NONLINEAR ANALYSIS OF IRREGULARITIES/DISCONTINUITIES IN HIGH-RISE CONCRETE SHEAR WALL BUILDINGS

by

Maryam Mahmoodi

B.A., Sharif University of Technology, 2005

M.Sc., University of Calgary, 2011

A THESIS SUBMITTED IN PARTIAL FULFILLMENT OF

THE REQUIREMENTS FOR THE DEGREE OF

DOCTOR OF PHILOSOPHY

in

THE FACULTY OF GRADUATE AND POSTDOCTORAL STUDIES

(Civil Engineering)

THE UNIVERSITY OF BRITISH COLUMBIA

(Vancouver)

December 2020

The following individuals certify that they have read, and recommend to the Faculty of Graduate and Postdoctoral Studies for acceptance, the dissertation entitled:

Nonlinear Analysis of Irregularities/Discontinuities in High-Rise Concrete Shear Wall Buildings

submitted by Maryam Mahmoodi in partial fulfillment of the requirements for

the degree of Doctor of Philosophy

in Civil Engineering

Examining Committee:

Professor Perry E. Adebar, Department of Civil Engineering
Supervisor

Professor Donald Anderson, Department of Civil Engineering
Supervisory Committee Member

Professor Terje Haukaas, Department of Civil Engineering
Supervisory Committee Member

Professor Shahria Alam, UBC-O School of Engineering
University Examiner

Professor Annalisa Meyboom, School of Architecture and Landscape Architecture
University Examiner

Abstract

State-of-the-art nonlinear analysis was used to investigate three different types of irregularities or discontinuities in high-rise concrete shear wall buildings. The objective was to develop knowledge that will assist practicing engineers who design buildings.

Overhanging wall discontinuity due to the wall above being longer than the wall below creates significant amplification of concrete compression strains immediately below the overhang. While the strains are highly nonlinear, the results of the current study were used to develop simple amplification factors for estimating the nonlinear strain increases from the results of linear finite element analysis, which can be done by practicing engineers. A simple safe limit for the maximum compression strain in a wall below an overhang determined from linear analysis is 0.001 in order to limit the nonlinear vertical compression strain in the zone below the overhang to 0.004.

A *discontinuity in lateral stiffness of building* occurs at grade level where the concrete diaphragms connect tower walls to foundation walls or at the top of podium levels. In design practice, these diaphragms are usually modelled as linear elastic members, and the choice of effective stiffness significantly influences how much force will go into the backstay force path. The effect of membrane forces on the flexibility of concrete diaphragms was investigated and a range of simplified models was presented. The nonlinear models provide a more accurate estimate of the diaphragm stiffness, while the simple upper and lower-bound (constant) stiffness models are much easier to use in practice. The influence of out-of-plane bending of the diaphragms on reducing membrane stiffness of the diaphragms was also investigated.

Sloped-column Irregularity is a new type of irregularity defined in the 2020 National Building Code of Canada for the seismic design of buildings as an outcome of the current study. Nonlinear time history analysis was used to investigate how the differential horizontal movement at the top and bottom of sloped columns causes vertical accelerations of the building mass. A simplified procedure was developed to account for the possible range of member stiffnesses and to account for vertical ground motions in a simplified way.

Lay Summary

Three different types of commonly occurring complexities in the architecture of high-rise concrete buildings were investigated using state-of-the-art nonlinear analysis to produce knowledge needed by structural engineers that design these buildings. When a concrete wall overhangs the wall below, the deformations of the wall causing damage in an earthquake are magnified beyond what can be estimated by the normal linear analysis tools. Amplification factors were developed to allow simple estimates to be made. The additional concrete walls in the lower levels of a building result in a discontinuity in the lateral stiffness of the building. Simple methods were developed for estimating the large forces that develop in the diaphragms that interconnect the walls in a building. Inclined gravity-load columns supporting the floors of high-rise buildings cause vertical movement of the building in an earthquake and the resulting additional forces must be accounted for. Simplified methods were developed for estimating these additional forces.

Preface

This dissertation entitled "Nonlinear Analysis of Irregularities/Discontinuities in High-Rise Concrete Shear Wall Buildings" is an original intellectual product of Maryam Mahmoodi under the supervision of Professor Perry Adebar.

A portion of Chapter 3 has been published in Adebar and Mahmoodi (2014), "Compression Failure of Thin Concrete Shear Walls with Overhanging Wall Above," Tenth U.S. National Conference on Earthquake Engineering, Anchorage, Alaska, US. A version of Chapter 3 is going to be submitted as a journal paper entitled "Compression Failure of Overhanging (Flag-Shaped) Walls". This paper includes the proposed simplified procedure and recommendations for designing a shear wall with an overhang.

Some contents of Chapter 4 have been published in Mahmoodi and Adebar (2018), "Nonlinear FE Analysis of Concrete Diaphragms Subjected to Backstay Forces in High-Rise Core Wall Buildings", Eleventh U.S. National Conference on Earthquake Engineering, Los Angeles, California, US.

A version of Chapter 4 will be published in Adebar and Mahmoodi (2020), "Influence of Diaphragm Flexibility on Backstay Forces in High-Rise Shear Wall Buildings: The Canadian Approach", 17th World Conference on Earthquake Engineering, Sendai, Japan.

A portion of Chapter 5 has been published in Mahmoodi and Adebar (2015), "Influence of Flexural Cracking on Stiffness of Concrete Diaphragms Supporting High-Rise Shear Walls", The 11th Canadian Conference on Earthquake Engineering, Victoria, BC, Canada.

A version of Chapter 4 and Chapter 5 is included in a paper entitled "Effective Stiffness of Concrete Diaphragms Subjected to Backstay Forces in High-Rise Core Wall Buildings" that is under preparation for submission as a journal paper. This paper includes the proposed simplified models for shear and flexural stiffnesses of concrete diaphragms and the recommendation for the shear stiffness of diaphragms taking account of out-of-plane loading.

Based on the study in Chapter 6, the 2020 edition of the National Building Code of Canada (NBCC) has defined a new type of irregularity that must be considered in the seismic design of buildings called “sloped-column irregularity”. A simple procedure for scaling the analysis results to avoid having to do multiple analyses with a range of stiffness values and vertical ground motions is provided in the commentary to the new provisions. A version of Chapter 6 will be published in Adebar and Mahmoodi (2020), “Sloped-Column Irregularity in High-Rise Shear Wall Buildings”, 17th World Conference on Earthquake Engineering, Sendai, Japan.

In addition, a version of Chapter 6 will be published as a journal paper which includes the effect of different parameters such as column characteristics, type of SFRS and horizontal and vertical accelerations on the sloped column seismic force demand, the proposed simplified procedure for estimating the maximum axial force in sloped columns, the influence of sloped-column irregularity on the seismic performance of SFRS and the maximum axial force in the sloped column supporting a single vertical mass.

Table of Contents

List of Tables

List of Figures

Acknowledgements

I would like to express my sincere gratitude to my supervisor, Professor Perry Adebar, for his professional supervision, guidance and continued encouragement during my research and preparation of this thesis. The completion of this thesis would have not been possible without his insightful comments and valuable feedback. His support is highly appreciated.

I would like to extend my appreciation to the members of my Supervisory Committee, Professor Haukaas and Professor Anderson for their useful suggestions and constructive comments.

I would like to thank the faculty and staff members of UBC Civil Engineering Department, who were always ready to assist me throughout my graduate studies.

Most importantly, I would like to express my deepest gratitude to my beloved family: my parents for their endless support, guidance and patience throughout my life, my husband and my son, Mohammad and Taha, my brother and my sister, Mohammad and Mahya, for their support and encouragement during hard times.

Dedicated to my mother, my father,

my husband and my son …

Chapter 1

Introduction

1.1 Background

Concrete shear walls are a popular lateral force resisting system for high-rise buildings in many countries around the world as they provide good lateral drift control when the building is subjected to wind or earthquake demands and are relatively simple to construct. All but a very few high-rise buildings in the lower mainland of British Columbia are concrete shear wall buildings. Older buildings, constructed up until about the mid-1980s, typically have thin lightly reinforced concrete walls distributed throughout the building. Since the 1980's virtually all new high-rise buildings in the lower mainland of BC have a large central concrete shear core wall that is designed to resist all the lateral loads from wind and earthquake (Adebar et al., 2017).

Concrete shear wall buildings with numerous walls distributed throughout the building continue to be a popular lateral force resisting system in other regions, such as Toronto where the seismicity is much lower than BC, and in South America, including countries where the seismicity is higher than BC. Concrete core wall buildings have recently become the system of choice in the seismically active regions of western United States in cities such as Seattle, San Francisco and Los Angeles.

It is relatively simple to design a concrete shear wall building that has uniform geometry over the height. In Canada, the seismic design of concrete shear wall buildings is normally done using linear response spectrum analysis to determine the seismic demands – forces and deformations. Simplified empirical methods are used to account for the nonlinear behaviour of the concrete shear walls (CSA, 2019). When a concrete shear wall building has a significant irregularity or discontinuity over the height, it becomes more challenging to ensure the building will perform well when subject to strong ground shaking due to an earthquake.

One significant discontinuity that occurs in all high-rise concrete shear wall buildings is the transition from the below-grade structure, which includes foundation walls, to the upper parts of the structure, which consists of only the tower shear walls. Many buildings have a podium structure above grade that includes additional concrete shear walls, in which case, the building has three different parts that have different geometry and hence different lateral stiffness – the below-grade portion, the podium structure, and the tower. Often the transition between the top of the podium structure and the tower walls causes the greatest design challenges.

In addition to the discontinuity that occurs where there is a sudden change in lateral stiffness of the building due to shear walls stopping at grade level or the top of the podium structure, concrete shear walls often have additional discontinuities created by architectural features of the building. Such discontinuities are usually referred to as building irregularities. One such feature is when the length of a shear wall suddenly changes at a certain elevation. When the wall length is less in the story above compared to the story below, the situation is similar (but less severe) to where a shear wall suddenly stops at some level. A completely different type of irregularity occurs where the wall length is larger in the story above compared to the story below. That is, where the wall above overhangs the wall below. This type of discontinuity, which is sometimes called a "flag wall," is herein referred to as an overhanging wall irregularity. A third type of irregularity that has recently become common is where the gravity-load columns are inclined from the vertical. This is referred to as a sloped-column irregularity. Each of these three types of discontinuities/ irregularities are discussed further below.

1.1.1 Overhanging Wall Irregularity

During the February 2010 Chile (Maule) Earthquake, a significant number of newly constructed concrete shear wall buildings were badly damaged. Concrete shear wall buildings in Chile typically have numerous thin concrete walls distributed throughout the building. For example, many of the partition walls in a high-rise residential building in Chile are concrete shear walls. One of the factors that led to new concrete shear wall buildings being badly damaged was overhanging wall irregularities such as the one shown in Figure 1.1.

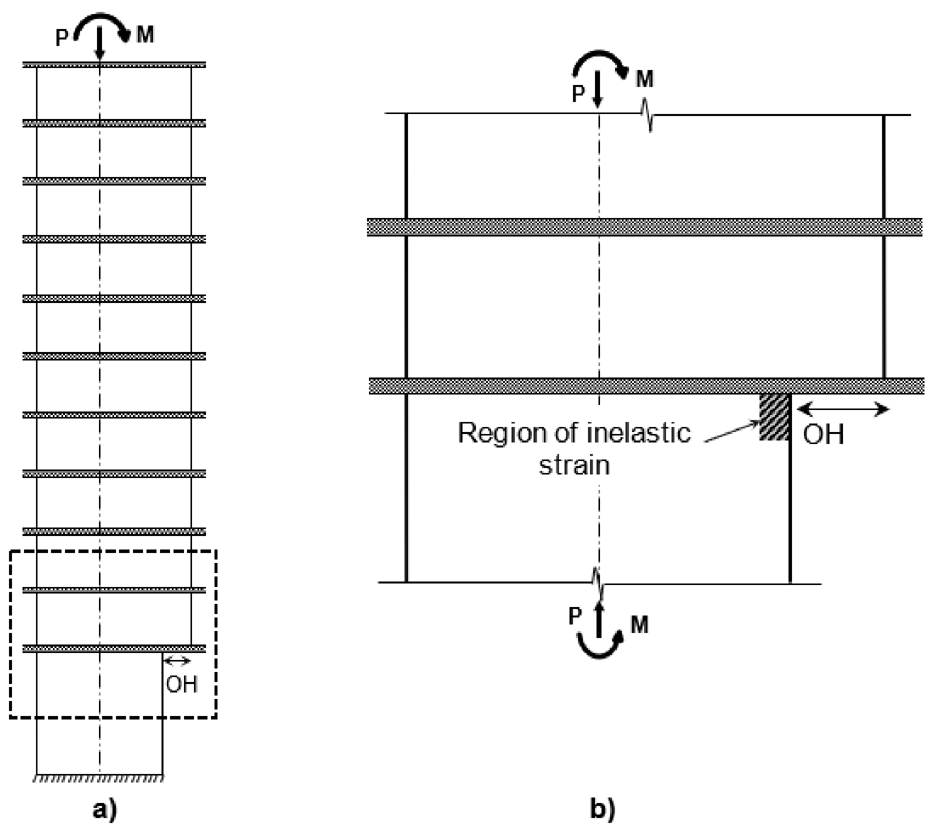

Figure 1.1 – Concrete shear wall with a geometrical discontinuity caused by an overhang (OH): (a) elevation of overall wall investigated in current study; (b) close-up of critical region around geometrical discontinuity

A review of the structural drawings of about 350 high-rise concrete buildings constructed in the city of Vancouver prior to 1980 revealed that about 25% of the buildings contain shear walls that have an overhanging wall irregularity (Yathon et.al., 2014). None of the concrete shear wall buildings in Vancouver has been subjected to significant ground motion; however, the seismicity of the region is such that these buildings could be subjected to very significant ground shaking similar to what occurred in Chile in 2010. Overhanging wall irregularities also often happen in the gravity-load walls of modern concrete shear wall buildings in the lower mainland of BC.

Compression failure at the end of a wall with an overhanging wall above occurs due to crushing of the concrete when the compression strain demand exceeds the compression strain capacity of the concrete. Confinement reinforcement will increase the compression strain capacity of the concrete. The ties around the concentrated vertical reinforcement at the end of the wall would have provided confinement of the concrete within the vertical reinforcement before they fractured. The concrete shear walls in the pre-1980 buildings in Vancouver that have overhanging wall irregularities do not have any confinement reinforcement. In fact, many of these walls have only a single layer of reinforcement. As a result, these overhanging wall irregularities will be even more vulnerable to damage than what occurred in Chile.

The main analytical tool that engineers use to assess the strength and deformation capacity of a concrete shear wall utilizes the plane sections assumption. That is, the vertical compression strain is assumed to vary linearly along the wall. This simple strain assumption is not valid within the discontinuity region near the wall overhang. Thus, the compression strain demands cannot be determined using this analytical tool.

State-of-the-art nonlinear finite element analysis was used in the current study to investigate the magnification of compression strains due to overhanging wall irregularities. The details of the study and the results that were obtained are presented in Chapter 3.

1.1.2 Discontinuity in Lateral Stiffness of Building

Figure 1.2 shows an example of a high-rise concrete core (shear) wall building where there is a significant discontinuity in the lateral stiffness of the building at grade level. Above grade, the lateral stiffness of the building is provided by the tower shear walls, which are shown as a central core. The tower shear walls continue below grade and there are additional foundation walls around the perimeter of the below-grade structure. These long foundation walls have very significant lateral stiffness compared to the tower walls.

If the concrete diaphragms that connect the foundation walls to the tower walls are assumed rigid, a large reaction force will develop in the top diaphragm as shown in Figure 1.2. This reaction is often larger than the total applied lateral load shown at about two-thirds the building height. Additional forces in the lower diaphragms below grade balance the large reaction force in the top diaphragm. Note that the shear force in the tower wall immediately below grade level is in the reverse direction from the base shear force, and if the foundation walls are stiff, this reverse shear force may be several times larger than the base shear force. The 'prying action' of the tower walls against the diaphragms supported by the foundation walls, as shown in Figure 1.2, is commonly referred to as the 'backstay effect.'

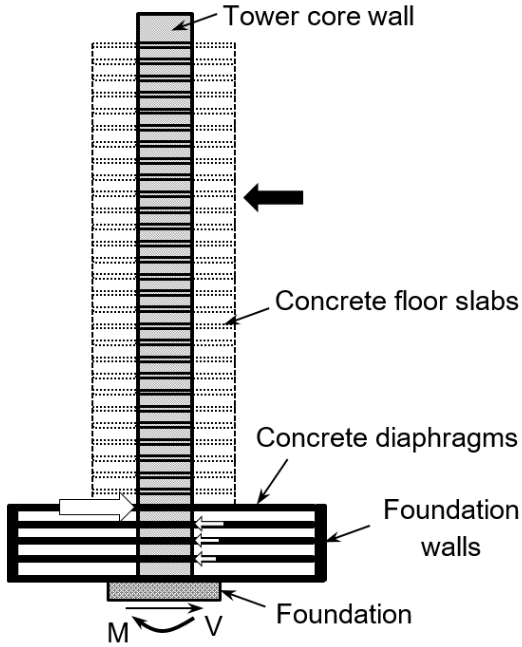

Figure 1.2 – Backstay forces in a high-rise concrete shear wall building; adapted from ATC-72-1, 2010

When the diaphragms connecting the tower walls to the foundation walls are modelled as semi-rigid, as they must be, the forces that develop in the diaphragms will depend on the assumed flexibilities of the diaphragms. As the diaphragms crack due to increased membrane forces plus out-of-plane bending, the flexibility increases and the membrane forces decrease. The diaphragm forces need to be accurately determined in order to determine the shear force and bending moment demands on the tower walls below grade and the design forces for the tower wall foundation.

State-of-the-art nonlinear finite element analysis was used in the current study to investigate the flexibility of concrete diaphragms resisting the backstay forces described above. The effect of membrane forces on the flexibility of concrete diaphragms is investigated in Chapter

4. The additional influence of out-of-plane bending of the diaphragms on reducing the flexibility of diaphragms subjected to backstay membrane forces is investigated in Chapter 5.

1.1.3 Sloped-Column Irregularity

Figure 1.3 shows a concrete shear wall building where the gravity-load columns along one side of the building are sloped over the first three floors. This sloped-column irregularity may have a very significant influence on the seismic response of the building.

Figure 1.3 – Example building with a sloped gravity-load columns (from http://skyscraperpage.com)

When the slab at level 3 in the building shown in Figure 1.3 moves horizontally within the plane of the outside surface of the building, the tops of the sloped columns will also move vertically. This will cause deformation demands on the slab at level 3. The vertical movement of the column at level 3 will also cause vertical movement of all the columns above that level. In addition to vertical movement of the columns due to horizontal movement of the sloped columns, horizontal acceleration at the top of the sloped column will cause vertical acceleration in all the columns above the sloped columns. These vertical accelerations will significantly influence the force demands in the sloped columns and may influence the overall seismic response of the building.

State-of-the-art nonlinear response history analysis was used to investigate the influence of sloped gravity-load columns in concrete shear wall buildings in Chapter 6.

1.2 Methodology and Objectives

In this thesis, three very different types of irregularity/discontinuity are investigated; however, the methodology used and the high-level goal is similar for each. State-of-the-art nonlinear analysis tools are used to investigate the phenomenon in such a way that a physical understanding is gained about the irregularity/discontinuity. This permits simple empirical methods to be developed that are not only consistent with the results of the nonlinear analysis, i.e., fit the data; but also are rational and provide insight to the designer about the phenomenon that they are designing. The main goal in each case is to develop simplified methods that can be used by practicing engineers to account for the irregularity/discontinuity in design practice.

The detailed objectives for each of the three different types of irregularity/discontinuity are as follows:

Overhanging wall discontinuity:

- Investigate how much the strains may increase because of the geometrical discontinuity caused by an overhanging wall.
- Investigate the relationship between the overhang length and the magnification of the strains.
- Investigate the influence of an overhang on the strength and flexibility of the shear wall.
- Investigate the effect of axial load applied to the wall and the reinforcement ratio at the wall boundaries on the flexibility and strength of the shear wall with an overhang.
- Develop a simplified procedure for estimating the magnification of strains due to the overhanging wall.
- Develop recommendations for designing a shear wall with an overhang.

Discontinuity in lateral stiffness of building – Effective stiffness of concrete diaphragms:

- Investigate the behaviour of concrete diaphragms subjected to large in-plane forces.
- Investigate the influence of reinforcement ratio and relative spans on the behaviour of diaphragms.
- Develop a simplified procedure for estimating the trilinear load-deformation relationship of concrete diaphragms, from which the effective shear and flexural stiffnesses can be calculated at any backstay force level.
- Develop simple and rigorous models for reduction in shear and flexural stiffnesses of concrete diaphragms for given backstay forces.
- Investigate the influence of flexural cracking on the in-plane shear stiffness of diaphragms.
- Determine the effects of different parameters including diaphragm length-to-depth ratio, diaphragm reinforcement ratio and magnitude of out-of-plane loads on the shear stiffness of one-way slabs.
- Develop a simplified model for the initial shear stiffness of cracked one-way slabs due to out-of-plane loading.
- Develop a recommendation for the shear stiffness of two-way slabs taking account of out-of-plane loading.

Sloped columns in high-rise core wall buildings:

- Investigate the sloped-column irregularity in high-rise core wall buildings and to understand the physics of the problem.
- Investigate if it is possible to model the distributed vertical mass supported by sloped columns as lumped mass.
- Investigate the influence of different parameters including sloped column characteristics (i.e., column type, column slope, column height and column base location) on the sloped column seismic force demand.
- Investigate the effect of horizontal and vertical acceleration and the type of SFRS on the sloped column axial force.

- Develop a simplified procedure for properly estimating the maximum axial force in sloped columns.
- Develop a simplified model for the amplification factor of the sloped column force.
- Validate the simplified model against the analysis results.
- Investigate the influence of sloped-column irregularity on the seismic behaviour of SFRS.
- Investigate the maximum axial force in the sloped column supporting a single vertical mass.

1.3 Thesis Organization

The thesis is organized into seven chapters and seven appendices as follows:

Chapter 2 presents the nonlinear analysis methods utilized in the current study. A brief description of the important characteristics of each computer program is provided, as is the material models used for concrete and reinforcing steel. A verification of the analysis method is provided for each type of problem.

Chapter 3 presents the investigation on overhanging wall irregularity. The chapter begins with an introduction of the compression failure of thin concrete shear walls. Then the details of the structure investigated in the current study are described. Two nonlinear finite element models used in the current study are presented, as is the validation of the models. An investigation is carried out to determine how much the strains may increase as a result of the geometrical discontinuity caused by an overhanging wall. The results of analyses are discussed and a simplified solution for estimating the magnification of the vertical compression strains and a possible approach for designing a shear wall with an overhang are proposed.

Chapter 4 presents the study on the in-plane stiffness of concrete diaphragms. The chapter includes a summary of previous work, recommendations by current design guidelines for shear and flexural stiffnesses of diaphragms, a comparison between nonlinear FE model and diaphragm test results. The parameters which have significant influence on the in-plane stiffness of diaphragms are evaluated. A simplified procedure is presented for estimating the trilinear load-deformation relationship of concrete diaphragms, from which the effective shear and flexural stiffnesses can be calculated at any backstay force level. Simple and rigorous models are proposed for reduction in shear and flexural stiffnesses of concrete diaphragms for given backstay forces.

The influence of out-of-plane flexural cracking on the in-plane shear stiffness of diaphragms is studied in Chapter 5. Both one-way and two-way floor slabs are examined. For one-way floor slabs, a parametric study is carried out to investigate the effects of different parameters. Two different analysis approaches are employed and results are compared. A simplified equation is developed for the initial stiffness of cracked diaphragms subjected to out-of-plane loading. To provide better understanding of the behaviour of two-way slabs, the behaviour of a shell element subjected to out-of-plane bending and twisting moments and an increasing in-plane shear force is evaluated. The applied nonlinear analysis approach is explained, and the results are presented. The recommendations for in-plane shear stiffness of two-way slabs are provided.

Chapter 6 presents the study on the sloped-column irregularity in high-rise core wall buildings. This chapter includes an introduction to sloped-column irregularity, an overview of the analysis of buildings with sloped columns, the description of the investigated high-rise building, the response spectrum analysis, the time history analysis and the seismic hazard used for the analysis. Then, modelling of vertical mass and the physics of the problem are also discussed. A parametric study using response spectrum analysis is conducted to investigate the influence of different parameters on the sloped column seismic force demand. Linear and nonlinear time history analyses are carried out and the results are discussed. Simplified procedure for the maximum column force is developed and a simplified equation is proposed for the amplification factor of the sloped column force. The simplified equation is compared with the analysis results. The influence of vertical acceleration on vertical columns is investigated. As an additional study, the influence of the sloped column on the SFRS and the sloped column supporting a single vertical mass are evaluated in this chapter.

A summary of the contributions and recommendations for future work are presented in Chapter 7.

Appendix A presents the details of the finite element models used for shear walls with an overhang irregularity investigated in Chapter 3. The finite element results for the shear wall with different overhang lengths are also included in Appendix A. Details of the diaphragm test by Nakashima (1986) is presented in Appendix B, while Appendix C presents the analysis results for the full range of concrete diaphragms studied in Chapter 4. The analysis results for all slabs investigated in Chapter 5 are included in Appendix D. Appendix E Presents the layout of the core wall used for the study of concrete shear wall buildings with the sloped-column irregularity in Chapter 6. Appendix F lists the analyzed cases for sloped-column irregularity investigated in Chapter 6 and Appendix G presents the analytical results for all different sloped columns studied in Chapter 6.

Chapter 2

Nonlinear Analysis Methods

2.1 Overview

In the current research, to investigate various types of discontinuities in concrete shear wall buildings, different nonlinear analysis methods were employed, including ABAQUS, VecTor2, Response-2000, Shell-2000 and PERFORM 3D. The descriptions of these computer programs are presented in the current chapter and a verification example is provided for each program.

ABAQUS is a powerful commercial program for NLFE analysis that has high-powered membrane elements. VecTor2 is a nonlinear finite element program for the analysis of two-dimensional reinforced concrete membrane structures. In this study, ABAQUS and VecTor2, were used to develop finite element models of the shear wall with overhanging wall irregularity which are presented in Chapter 3. In fact, VecTor2 was used to verify the results from ABAQUS and to provide additional insight into the problem.

VecTor2 was also used for the analysis of concrete diaphragms that resist significant backstay forces (as presented in Chapter 4). Since these diaphragms are relatively thick, the influence of out-of-plane loading moments due to the gravity loads is relatively small in these diaphragms compared to the large backstay forces. On the other hand, sometimes the diaphragms that resist backstay forces are kept the same thickness as regular floor slabs. Thus, these diaphragms are relatively thin, and the effect of out-of-plane loading can be quite significant. Shell-

2000 and Response-2000 were utilized to investigate the influence of out-of-plane bending cracks on the membrane stiffness of such diaphragms (as presented in Chapter 5).

PERFORM-3D is a powerful tool for inelastic analysis and performance assessment of structures. In this study, PERFORM-3D was used to conduct the time history analysis of high-rise core wall buildings with sloped-column irregularity which is presented in Chapter 6.

2.2 ABAQUS

ABAQUS is a computer program used for linear and nonlinear finite element modelling and analyses of structural and mechanical components and assemblies. ABAQUS/CAE makes it possible to easily visualize the finite element analysis results. ABAQUS is popular computer program used by researchers in engineering due to the comprehensive material modelling capability, and the ability to be customized. For instance, new materials can be simulated in ABAQUS as this program allows users to define their own material models.

Solution methods used by ABAQUS are implicit and explicit integrations. Implicit integration method needs to solve multiple coupled equations simultaneously; thus, this method needs repetitive calculations which takes a lot of space, but it is always stable. Explicit integration method is a step-by-step method using small time steps; hence it is more time-consuming and sometimes it is not stable. Since implicit method is more efficient for solving smooth nonlinear problems, this method was utilized in the current study.

2.2.1 Material Models for Concrete

In ABAQUS, there are two material models that can be used to model a reinforced concrete: concrete smeared cracking model and concrete damaged plasticity model. The concrete smeared cracking is a simpler model and computational faster compared to the concrete damaged plasticity model, as it does not model the stiffness degradation in compressive state.

In the current study, the concrete was modelled using the "concrete damaged plasticity" model of ABAQUS. This material model is a continuum, plasticity-based, damage model which accounts for the main two failure mechanisms – tensile cracking and compressive crushing of concrete. The propagation of the failure surface is controlled by two hardening variables linked to failure mechanisms under tension and compression loading, as follows (ABAQUS Analysis user's manual, 2016):

$$\tilde{\varepsilon}^{pl} = \begin{bmatrix} \tilde{\varepsilon}_t^{pl} \\ \tilde{\varepsilon}_c^{pl} \end{bmatrix} \tag{2.1}$$

where, $\tilde{\varepsilon}_t^{pl}$ and $\tilde{\varepsilon}_c^{pl}$ are tensile and compressive equivalent plastic strain, respectively. The strain rate decomposition is assumed to be:

$$\dot{\varepsilon} = \dot{\varepsilon}^{el} + \dot{\varepsilon}^{pl} \tag{2.2}$$

where, $\dot{\varepsilon}$ is the total strain rate, $\dot{\varepsilon}^{el}$ is the elastic strain rate, and $\dot{\varepsilon}^{pl}$ is the plastic strain rate.

The concrete damaged plasticity model combines the concepts of isotropic damaged elasticity with isotropic tensile and compressive plasticity to model the inelastic behavior of concrete. It also includes the combination of non-associated multi-hardening plasticity and scalar (isotropic) damaged elasticity to describe the irreversible damage that occurs during the fracturing process. The model considers the degradation of the elastic stiffness induced by plastic straining both in tension and compression.

Under uniaxial tension, the stress-strain relationship is linearly elastic until the value of the cracking stress, σ_{t0}, is reached which corresponds to the onset of micro cracking in the concrete material. Beyond the cracking stress, the formation of micro-cracks is represented by a softening stress-strain response. Under uniaxial compression, the stress-strain relationship is linear until the value of initial yield, σ_{c0}, is reached. Beyond that, the response is followed by strain hardening up to ultimate stress, σ_{cu}, and then strain softening. This model captures the main features of concrete response.

In ABAQUS, the stress-strain relationship is converted into stress versus plastic strain curves. Thus,

$$\sigma_t = \sigma_t\left(\tilde{\varepsilon}_t^{pl}, \dot{\tilde{\varepsilon}}_t^{pl}, \theta, f_i\right) \tag{2.3}$$

$$\sigma_c = \sigma_c\left(\tilde{\varepsilon}_c^{pl}, \dot{\tilde{\varepsilon}}_c^{pl}, \theta, f_i\right) \tag{2.4}$$

where, $\dot{\tilde{\varepsilon}}_t^{pl}$ and $\dot{\tilde{\varepsilon}}_c^{pl}$ are tensile and compressive equivalent plastic strain rates, respectively; θ is the temperature, and $f_i(i = 1,2, \dots)$ are other predefined field variables.

In ABAQUS, the degradation of the stiffness is considered by two damage parameters, d_t and d_c, which are function of the plastic strains, temperature, and field variables (ABAQUS Analysis user's manual, 2016):

$$d_t = d_t\left(\tilde{\varepsilon}_t^{pl}, \theta, f_i\right); \quad 0 \le d_t \le 1 \tag{2.5}$$

$$d_c = d_c\left(\tilde{\varepsilon}_t^{pl}, \theta, f_i\right); \quad 0 \le d_c \le 1 \tag{2.6}$$

The damage parameters can vary between zero, which represents the undamaged material, and one, representing total loss of strength.

The stress-strain relationships of the concrete material under uniaxial tension and compression loading are as follows, respectively (ABAQUS Analysis user's manual, 2016):

$$\sigma_t = (1 - d_t)E_0\left(\varepsilon_t - \tilde{\varepsilon}_t^{pl}\right) \tag{2.7}$$

$$\sigma_c = (1 - d_c)E_0\left(\varepsilon_c - \tilde{\varepsilon}_c^{pl}\right) \tag{2.8}$$

where, E_0 is the initial (undamaged) elastic stiffness of the material.

The effective tensile and compressive cohesion stresses are defined using Equations 2.9 and 2.9, respectively (Simulia, 2013):

$$\bar{\sigma}_t = \frac{\sigma_t}{(1 - d_t)} = E_0\left(\varepsilon_t - \tilde{\varepsilon}_t^{pl}\right) \tag{2.9}$$

$$\bar{\sigma}_c = \frac{\sigma_c}{(1 - d_c)} = E_0\left(\varepsilon_c - \tilde{\varepsilon}_c^{pl}\right) \tag{2.10}$$

The size of the yield (failure) surface is determined based on the effective cohesion stresses.

Tension stiffening is used to model the post-failure behaviour of the cocncrete material which allows to define the strain-softening behaviour for cracked concrete. Tension stiffening also allows for the influence of the reinforcement-concrete intreaction to be simulated in a simple way.

In ABAQUS, tension stiffening is defined by means of a post-failure stress-strain relation or by applying a fracture energy cracking criterion.

In reinforced concrete, the post-failure behaviour is generally defined by the post-failure stress as a function of the cracking strain, $\tilde{\varepsilon}_t^{ck}$. The cracking strain is determined based on the total strain minus the elastic strain which corresponds to the undamaged material (ABAQUS Analysis user's manual, 2016):

$$\tilde{\varepsilon}_t^{ck} = \varepsilon_t - \varepsilon_{t0}^{el} \tag{2.11}$$

where, $\varepsilon_{t0}^{el} = \sigma_t / E_0$. In ABAQUS, a lower limit equal to one-hundreth of the intial failure stress is applied on the post-failure stress in order to avoid potential numerical problems: $\sigma_t \geq \sigma_{t0}/100$.

2.2.2 Material Models for Reinforcement

In ABAQUS, the elastic part of the stress-strain relationship of reinforcement is modelled with Young's modulus, E_s, and Poisson's ratio, v. Plastic behaviour is defined as a tabular form with yield stress and corresponding plastic strain. In the current research, a bilinear stress-strain curve with strain hardening are used for reinforcement.

2.2.3 Verification

Genikomsou and Polak (2015) conducted nonlinear finite element analyses of reinforced concrete slab-column connections under static and pseudo-dynamic loadings. They investigated failure modes of slab-column connections in terms of ultimate load and cracking patterns. Computer program ABAQUS was used to perform the 3D finite element analyses. Different slab-column connections without shear reinforcement were simulated including interior slab-column specimens under static loading, interior specimens under static and reversed cyclic loadings, and edge specimens under static and horizontal loadings. In total, five specimens were simulated. Due to the symmetry of the specimens, one quarter of the control specimen and half of all other specimens were modelled in ABAQUS, as shown in Figure 2.1. 8-noded brick elements were used for concrete and 2-noded truss elements were used to mode reinforcement. The concrete damaged plasticity model was used for concrete material.

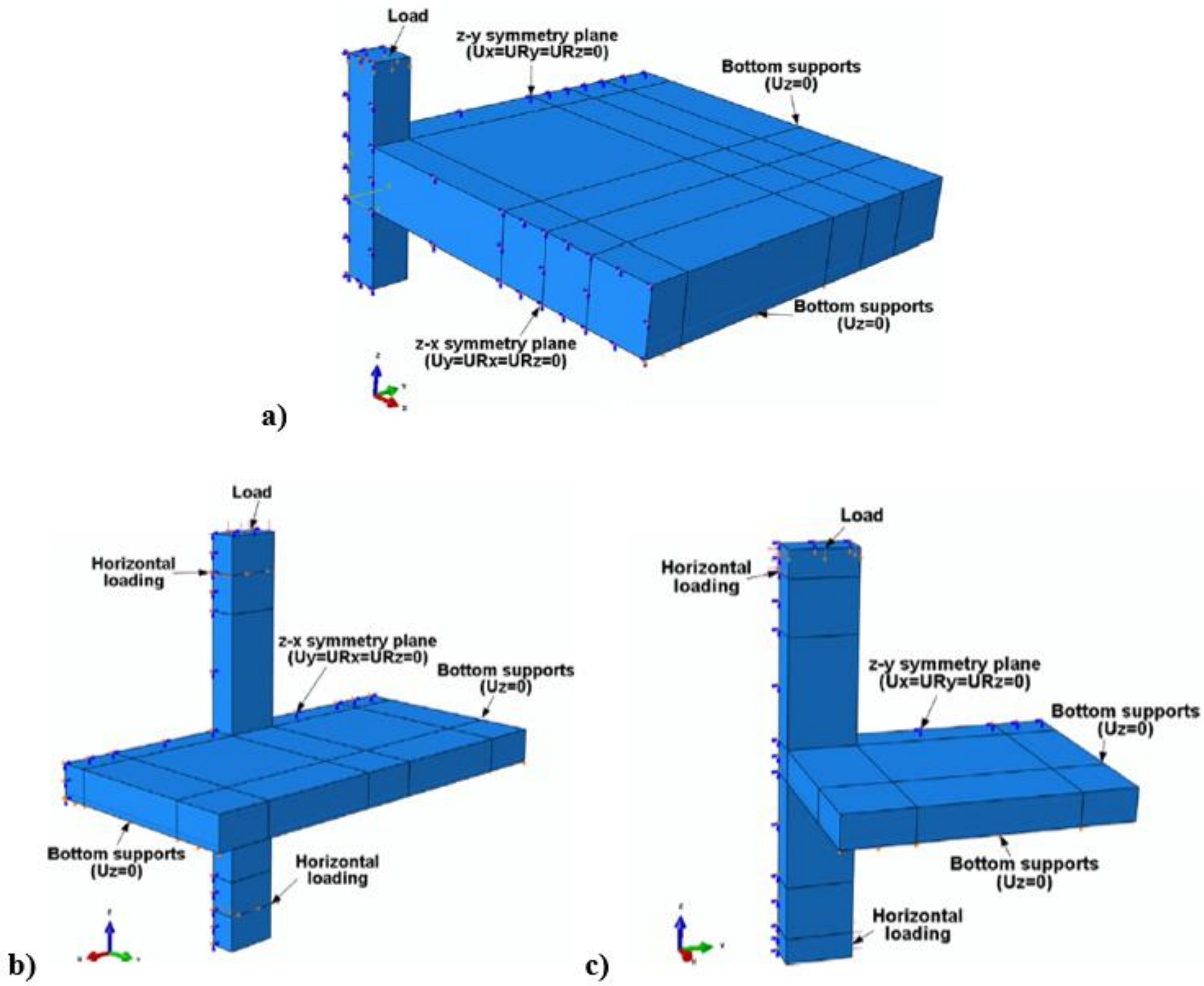

Figure 2.1 – Geometry and boundary conditions of specimens: (a) control specimen; (b) interior slabs; (c) edge slabs (Genikomsou and Polak, 2015)

The comparison of numerical and experimental results indicated that the ABAQUS model was able to properly predict the punching shear response of concrete slabs without shear reinforcement. Figure 2.2 presents the comparison of the results for three of the analyzed slabs. In addition, the finite element analysis results confirmed the ability of the model for providing insight into punching shear failure and crack formation of slabs.

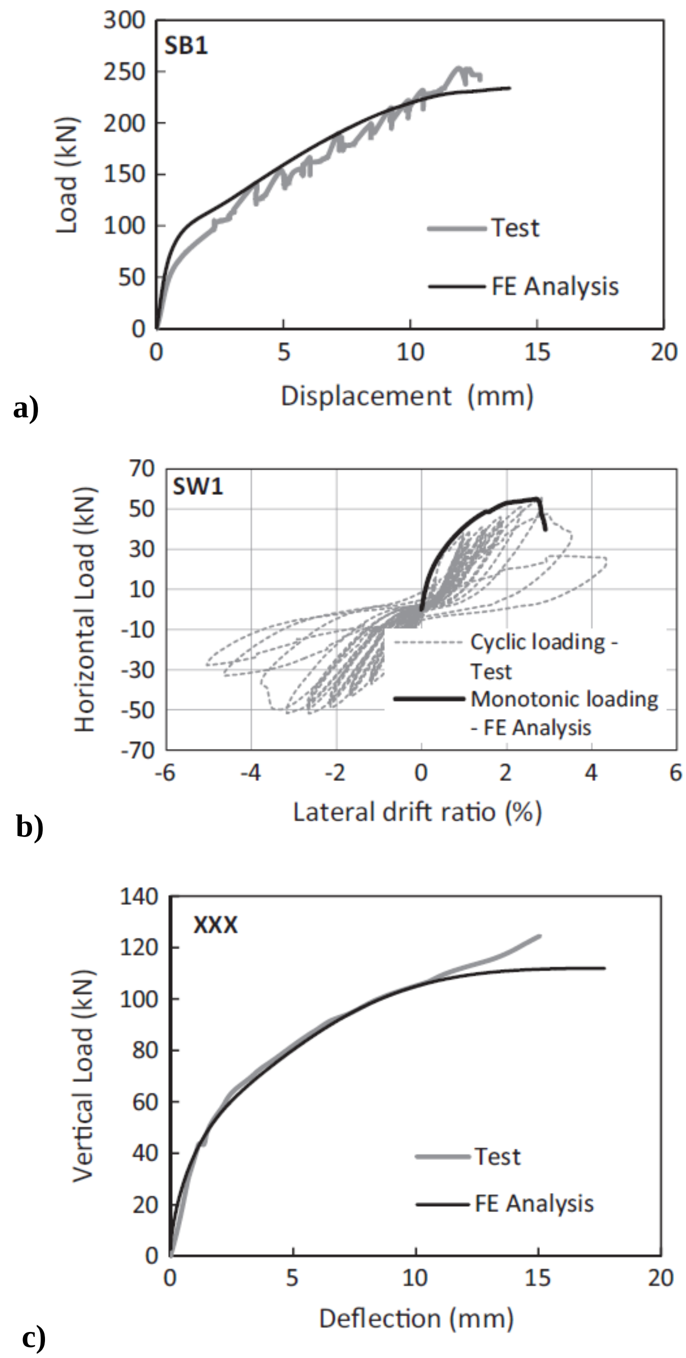

Figure 2.2 – Comparison between experimental and numerical results: (a) control specimen; (b) interior slab; (c) edge slab (Genikomsou and Polak, 2015)

2.3 VecTor2

VecTor2 is a computer program for the nonlinear finite element analysis (NLFEA) of two-dimensional reinforced concrete membrane structures subjected to quasi-static loading. In this section, a general overview of program VecTor2 developed by researchers at the University of Toronto is presented. The presented information comes directly from the VecTor2 and FormWorks User's Manual (Wong and Vecchio, 2002). In this research, program FormWorks is used as the pre-processor and program Augustus is used as the post-processor which provides graphical capabilities for the analysis results of VecTor2.

VecTor2 is based on the Modified Compression Field Theory (Vecchio and Collins, 1986) and the Disturbed Stress Field Model (Vecchio, 2000) which is a refinement of the Modified Compression Field Theory. These analytical models predict the response of reinforced concrete elements subject to in-plane normal and shear stresses by modelling cracked concrete as an orthotropic material with smeared, rotating cracks. Constitutive models for a variety of second-order effects, such as compression softening and tension stiffening are incorporated to accurately predict the response. In addition, VecTor2 can model concrete expansion and confinement, cyclic loading and hysteretic response, bond slip and crack shear slip deformations (Wong and Vecchio, 2002).

Program VecTor2 uses a fine mesh of low-powered finite elements which has the advantage of computational efficiency and numerical stability. The element library includes a 3-node constant strain triangle (with six degrees of freedom), and a 4-node plane stress rectangle or a 4-node quadrilateral element (with eight degrees of freedom) to model concrete with smeared reinforcement, and a 2-node truss bar element (with four degrees of freedom) to model discrete reinforcement. The reinforcement can be modeled as either smeared within concrete elements or as discrete bars using truss elements.

The program utilizes an incremental total load, iterative secant stiffness algorithm to produce an efficient and robust nonlinear solution. The element stiffness matrices are calculated and assembled at each load step. The nodal loads are computed and subsequently the nodal displacements are determined. These displacements are used to calculate strain tensor for each element, and then the principal strains are determined. Consequently, the stress tensor for concrete and steel are calculated in each element. Based on that, the secant moduli are computed, and compared to the secant moduli from the previous stress-strain state. The analysis for that load step is completed if the convergence is satisfactory and the analysis continues to the next step. Otherwise, the analysis is repeated using the new stress-strain state. The convergence is usually achieved after 10 to 30 iterations (Selby, Vecchio and Collins, 1996). This procedure continues until the target displacement or the specified force is reached, or until the structure becomes unstable.

2.3.1 Models for Concrete in Compression

Nonlinear functions are used to describe the stress-strain relationship of concrete in compression (Figure 2.3). The ascending and descending branches of the concrete response in uniaxial compression are defined with different models.

Compression pre-peak response models (ascending branch) calculate the concrete compressive stresses while the concrete compressive strain is less than the strain corresponding to the maximum compressive stress. In this research, the model proposed by Popovics for normal-strength concrete was used for the ascending curve of concrete compressive stress. The stress-strain relationship was described as (Wong and Vecchio, 2002):

$$f_{c2} = -\left(\frac{\varepsilon_{c2}}{\varepsilon_p}\right) f_p \frac{n}{n - 1 + \left(\varepsilon_{c2}/\varepsilon_p\right)^n} \qquad for \quad \varepsilon_p < \varepsilon_{c2} < 0 \tag{2.12}$$

$$n = \frac{E_c}{E_c - E_{sec}} \tag{2.13}$$

$$E_{sec} = \frac{f_p}{\left|\varepsilon_p\right|} \tag{2.14}$$

where,

f_{c2}: Average net concrete axial stress;

ε_{c2}: Average net concrete axial strain;

f_p: Peak concrete compressive stress;

ε_p: Concrete compressive strain corresponding to the peak concrete compressive stress;

n: Curve fitting parameter for stress-strain response of concrete in compression;

E_c: Concrete initial tangent stiffness;

E_{sec}: Concrete secant stiffness.

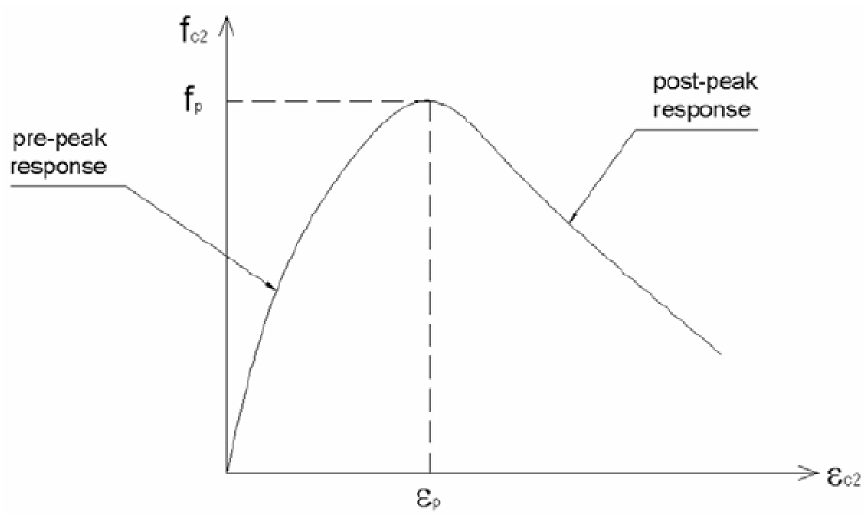

Figure 2.3 – Concrete compression response (Wong and Vecchio, 2002)

Compression post-peak response models (descending branch) calculate the concrete compressive stresses while the concrete compressive strain is greater than the strain corresponding to the maximum compressive stress. The stress-strain relationship was calculated as follows (Wong and Vecchio, 2002):

$$f_{c2} = (1-c)f_{c2}^{a} + cf_{c2}^{b} \;\; ; \quad \varepsilon_c < \varepsilon_c' < 0 \qquad (2.15)$$

$$c = 4\left(\frac{f_p - f_c'}{f_c'}\right) \;\; ; \quad 0 \leq c \leq 1 \qquad (2.16)$$

where,

c: Averaging factor which increases from zero to one as f_p increases from f_c' to $1.25f_c'$;

f_c': Concrete cylinder uniaxial compressive strength;

f_{c2}^{a}: Average concrete compressive stress contribution of unconfined concrete;

f_{c2}^{b}: Average concrete compressive stress contribution of confined concrete.

The stress contribution of unconfined concrete was determined using the Smith-Young model (Wong and Vecchio, 2002):

$$f_{c2}^{a} = -f_p\left(\frac{\varepsilon_{c2}}{\varepsilon_p}\right).exp\left(1-\frac{\varepsilon_{c2}}{\varepsilon_p}\right) \tag{2.17}$$

The stress contribution of confined concrete is determined using the Modified Park-Kent model (Wong and Vecchio, 2002):

$$f_{c2}^{b} = -\left[f_p + Z_m f_p\left(\varepsilon_{c2}-\varepsilon_p\right)\right] < \begin{cases} 0 & ;0 < f_p < f_c' \\ -0.2f_p & ;0 < f_c' < f_p \end{cases} \tag{2.18}$$

$$Z_m = \frac{0.5}{\left(\frac{3+0.29|f_c'|}{145|f_c'|-1000}\right)\left(\frac{\varepsilon_o}{-0.002}\right)+\left(\frac{|f_{c1}|}{170}\right)^{0.9}+\varepsilon_p} \tag{2.19}$$

where,

Z_m: Slope of compression post-peak descending curve;

ε_o: Concrete compressive strain corresponding to f_c';

f_{c1}: Average net concrete axial stress in the principal tensile direction.

In cracked concrete, compression softening is the reduction of compressive strength and stiffness of concrete due to transverse cracking and tensile straining. This reduction can considerably influence the stiffness, ultimate strength capacity and ductility of reinforced concrete structures.

In VecTor2, compression softening is determined by a softening parameter, β_d, which varies between zero and one. The compression softening models are classified into two types of strength-and strained softened models (Figure 2.4) and strength-only softened models (Figure 2.5) based on the calculation of β_d.

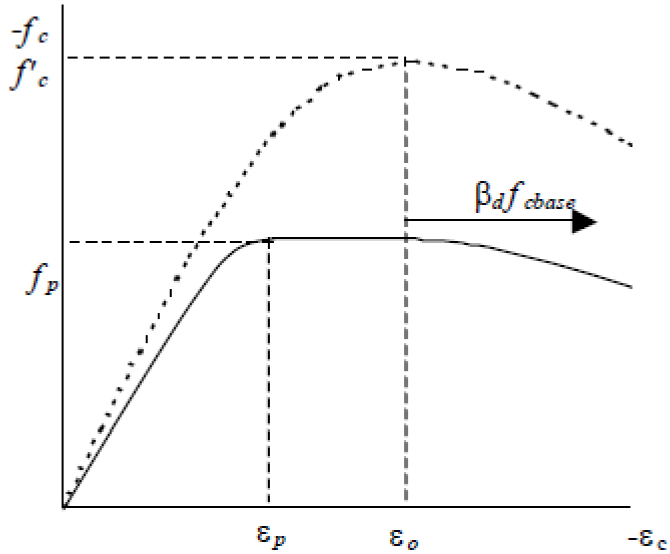

Figure 2.4 – Strength-and strained softened compression response (Wong and Vecchio, 2002)

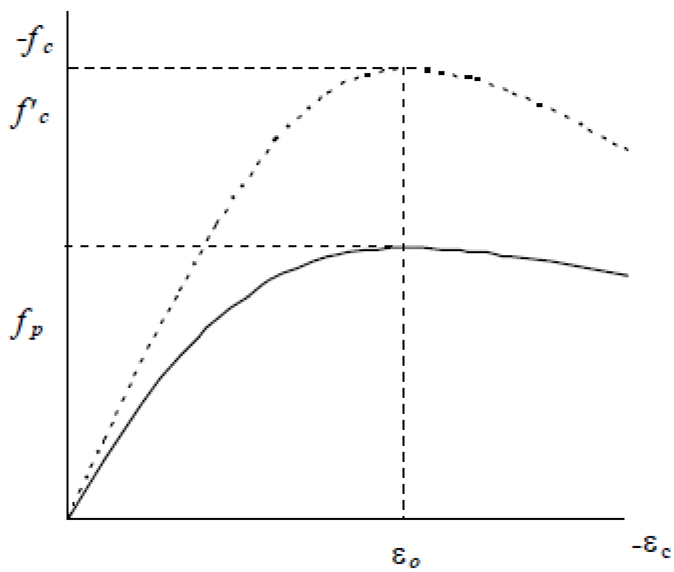

Figure 2.5 – Strength-only softened compression response (Wong and Vecchio, 2002)

The compression softening model used in this research to determine β_d is the Vecchio 1992-A ($\varepsilon_{c1}/\varepsilon_{c2}$-Form) model. This factor is applied to soften both the uniaxial compressive strength and its corresponding strain. The model is as follows (Wong and Vecchio 2002):

$$\beta_d = \frac{1}{1 + C_s C_d} \leq 1 \tag{2.20}$$

$$C_d = \begin{cases} 0 & ;\ r < 0.28 \\ 0.35(r - 0.28)^{0.8} & ;\ r > 0.28 \end{cases} \tag{2.21}$$

$$r = \frac{-\varepsilon_{c1}}{\varepsilon_{c2}} \leq 400 \tag{2.22}$$

$$f_p = \beta_d f_c' \tag{2.23}$$

$$\varepsilon_p = \beta_d \varepsilon_o \tag{2.24}$$

where,

C_s: Compression softening shear slip factor. It is assigned a value of one if shear slip is not considered, and 0.55 if it is considered;

C_d: Compression softening strain softening factor;

r: Ratio of the principal tensile strain to the principal compressive strain;

ε_{c1}: Average net concrete axial strain in the principal tensile direction.

2.3.2 Models for Concrete in Tension

Concrete is brittle in tension and its response can be divided into uncracked and cracked response (Figure 2.6). Before cracking, the response is considered to be linear-elastic (Wong and Vecchio 2002):

$$f_{c1} = E_c \varepsilon_{c1} \ ; \quad 0 < \varepsilon_{c1} < \varepsilon_{cr} \tag{2.25}$$

$$\varepsilon_{cr} = \frac{f_{cr}}{E_c} \tag{2.26}$$

where,

ε_{cr}: Concrete cracking strain;

f_{cr}: Concrete cracking stress.

After cracking, the tensile stresses in concrete gradually decrease to zero at the free surface of cracks as shown in Figure 2.6. In order to determine the average concrete tensile stresses in

VecTor2, the concrete tensile stresses due to tension stiffening and due to tension softening are calculated. The greater of the two values is considered as the average post-cracking tensile stress (Wong and Vecchio, 2002):

$$f_{c1} = Max\left(f_{c1}^{a}, f_{c1}^{b}\right) \ ; \quad 0 < \varepsilon_{cr} < \varepsilon_{c1} \tag{2.27}$$

where,

f_{c1}^{a}: Average concrete tensile stress due to tension stiffening;

f_{c1}^{b}: Average concrete tensile stress due to tension softening.

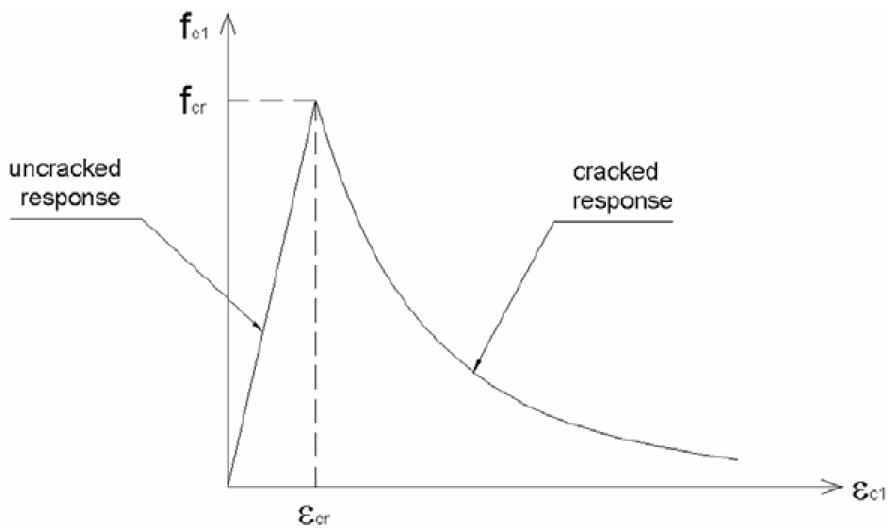

Figure 2.6 – Concrete tension response (Wong and Vecchio, 2002)

Tension stiffening is the existence of average concrete tensile stresses in the reinforced concrete between cracks in the vicinity of the reinforcement. Since these average concrete tensile stresses must be less than the cracking stress of concrete, they act over a large tributary area of the reinforcement. In VecTor2, for discrete reinforcement elements, their tributary area is delineated by a distance equal to 7.5 bar diameters from the reinforcement element (Wong and Vecchio, 2002).

Tension stiffening is considered by a gradually decreasing the average stress-strain response of concrete in tension and it is important for modelling the load-deformation behaviour of concrete structures. The magnitude of average tensile stresses due to tension stiffening is limited by both the yielding of reinforcement at the crack and the maximum shear stress at the crack when slip deformations are not considered.

In this research, the Modified Bentz 2003 model was used for tension stiffening which is the same as the Bentz 1999 model. Bentz (1999) assumed that the tension stiffening effect relies on the bond action and proposed a model which incorporates the bond characteristics of the reinforcement. Although the model was originally formulated for sectional analysis of reinforced concrete members, Vecchio adapted the model for VecTor2 to account for two-dimensional stress conditions. The post-cracking tensile stress-strain response of concrete is determined as (Wong and Vecchio, 2002):

$$f_{c1}^{a} = \frac{f_{cr}}{1 + \sqrt{c_t \varepsilon_{c1}}} \tag{2.28}$$

$$c_t = 2.2m \tag{2.29}$$

$$\frac{1}{m} = \sum_{i=1}^{n} \frac{4\rho_i}{d_{b_i}} \left|\cos\theta_{n_{ii}}\right| \tag{2.30}$$

where,

c_t: Coefficient that incorporates the influence of reinforcement bond characteristics;

m: Bond parameter, in millimeter;

ρ_i: Reinforcement ratio of each of the n reinforcement components;

d_{b_i}: Bar diameter;

θ_n: Angle between the normal to the crack surface and the longitudinal axis of reinforcement.

Tension softening is the presence of post-cracking tensile stresses in plain concrete. By increasing the tensile strains, the tensile stresses gradually decrease to zero. This phenomenon is attributable to the fact that concrete is not perfectly brittle.

Tension softening is important for the analysis of reinforced concrete structures, particularly in lightly reinforced regions. In this research, the linear model was used for the tension softening. This model does not consider the residual tensile stresses and is defined as follows (Wong and Vecchio, 2002):

$$\varepsilon_{ch} = \frac{2G_f}{L_r f_{cr}} \qquad 1.1\varepsilon_{cr} < \varepsilon_{ch} < 10\varepsilon_{cr} \tag{2.31}$$

$$f_{c1}^{b} = f_{cr}\left(1 - \frac{\varepsilon_{c1} - \varepsilon_{cr}}{\varepsilon_{ch} - \varepsilon_{cr}}\right) \geq 0 \tag{2.32}$$

where,

ε_{ch}: Characteristic strain;

G_f: Energy required to form a complete crack of unit area, it is assigned a value of 75 N/m;

L_r: Distance over which the crack is assumed to be uniformly distributed, it is assigned a value of half the crack spacing.

The concrete cracking stress usually decreases by increasing the compressive stresses acting transversely. Thus, the cracking stress does not remain constant and can be different from the specified concrete tensile strength, f_t'. In VecTor2, the cracking stress can be determined using the Mohr-Coulomb stress model which is defined as follows (Wong and Vecchio, 2002):

$$f_{cr} = f_{cru}\left(1 + \frac{f_{c2}}{f_c'}\right) \qquad 0.2f_t' \leq f_{cr} \leq f_t' \tag{2.33}$$

$$f_{cru} = 2C\,\frac{\cos\Phi}{1 + \sin\Phi} \tag{2.34}$$

$$C = f_c'\,\frac{1 - \sin\Phi}{2\cos\Phi} \tag{2.35}$$

where,

C: Cohesion;

Φ: Internal angle of friction, it is assigned a value of 37°.

2.3.3 Models for Slip Distortions in Concrete

Since VecTor2 has been formulated based on Disturbed Stress Field Model (DSFM), it can include the crack shear slip deformations. The DSFM eliminates the crack shear check requirement by considering the crack shear slip deformations. In this study, the model used to calculate the shear slip deformations is Hybrid-I model, which combines the Lai-Vecchio stress-based model with the constant rotation lag model. Therefore, the shear slip strains are calculated using both the stress-based model and the constant rotation lag model and the greater value is selected:

$$\gamma_s = Max(\gamma_s^a, \gamma_s^b) \tag{2.36}$$

where,

γ_s: Shear slip strain;

γ_s^a: Shear slip strain calculated from the stress-based model;

γ_s^b: Shear slip strain calculated form the constant rotation lag model.

According to the stress-based model, the shear slip along the crack is related to the local shear stress along the crack, which is calculated as follows (Wong and Vecchio, 2002):

$$\gamma_s^a = \frac{\delta_s}{s} \tag{2.37}$$

where,

δ_s: Shear slip;

s: Crack spacing.

Based on the constant rotation lag model, the post-cracking rotation of the principal stress field is related to the post-cracking rotation of the principal strain field (Wong and Vecchio, 2002):

$$\Delta\theta_\sigma = \begin{cases} \Delta\theta_\varepsilon & |\Delta\theta_\varepsilon| \leq \theta^l \\ \Delta\theta_\varepsilon - \theta^l & |\Delta\theta_\varepsilon| > \theta^l \end{cases} \tag{2.38}$$

where,

$\Delta\theta_\sigma$: Post-cracking rotation of the principal stress field;

$\Delta\theta_\varepsilon$: Post-cracking rotation of the principal strain field;

θ^l: Specified rotation lag. It is considered as 10° for unreinforced elements, 7.5° for uniaxially reinforced elements and 5° for biaxially reinforced elements.

The shear slip strain is calculated as follows:

$$\theta_\sigma = \theta_{ic} + \Delta\theta_\sigma \tag{2.39}$$

$$\gamma_s^b = \gamma_{xy} Cos2\theta_\sigma + \left(\varepsilon_{yy} - \varepsilon_{xx}\right) Sin2\theta_\sigma \tag{2.40}$$

where,

θ_σ: Inclination of the principal stress field;

θ_{ic}: Inclination of the principal stress field at cracking;

γ_{xy}: Total shear strain;

ε_{xx}: Total axial strain in the x direction;

ε_{yy}: Total axial strain in the y direction.

2.3.4 Models for Reinforcement

The ductile steel reinforcement model is used for the monotonic stress-strain response of reinforcement. A trilinear model consisting of a linear-elastic, a yield plateau and a linear strain hardening responses is utilized for reinforcement, as shown in Figure 2.7.

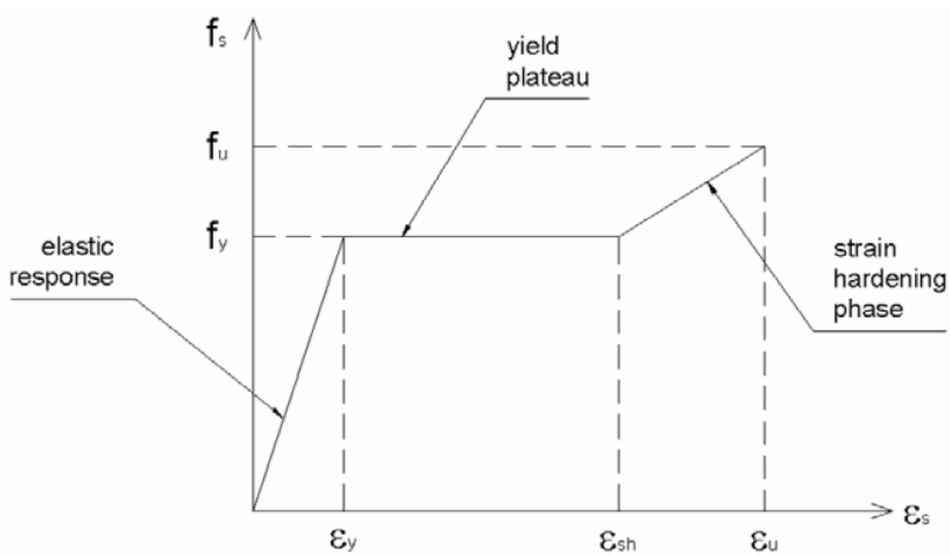

Figure 2.7 – Reinforcement compression and tension response (Wong and Vecchio, 2002)

The following expression is used for the reinforcement stress in tension and compression (Wong and Vecchio, 2002):

$$f_s = \begin{cases} E_s\varepsilon_s & |\varepsilon_s| \le \varepsilon_y \\ f_y & \varepsilon_{sh} < |\varepsilon_s| \le \varepsilon_{sh} \\ f_y + E_{sh}(\varepsilon_s - \varepsilon_{sh}) & \varepsilon_{sh} < |\varepsilon_s| \le \varepsilon_u \\ 0 & \varepsilon_{sh} < |\varepsilon_s| \end{cases} \tag{2.41}$$

$$\varepsilon_y = \frac{f_y}{E_s} \tag{2.42}$$

$$\varepsilon_u = \varepsilon_{sh} + \frac{f_u - f_y}{E_{sh}} \tag{3.43}$$

where,

f_s: Reinforcement stress;

E_s: Initial tangent stiffness or elastic modulus of reinforcement;

ε_s: Reinforcement strain;

ε_y: Yield strain;

ε_{sh}: Strain at the onset of strain hardening;

E_{sh}: Strain hardening modulus;

ε_u: Reinforcement ultimate strain;

f_u: Ultimate strength of reinforcement.

2.3.5 Verification

Bohl and Adebar (2011) validated the VecTor2 model by comparing the analytical results with the test results conducted by Adebar et. Al. (2007) on a slender reinforced concrete cantilever shear wall from the core of a high-rise building. The tested wall was 11.3 m high (h_w) and 1.625 m long (l_w) with the height-to-length ratio (h_w/l_w) of 7. The wall had a flanged cross section with a low percentage of vertical reinforcement (0.45%) and was subjected to a constant compressive axial load of $10\% f_c' A_g$. The wall was tested in the horizontal position due to the limited height of the laboratory. To prevent movement during the test, the wall base was post-tensioned to the floor. The cyclic lateral load was applied at the top of the wall.

The average compressive strength of concrete was 49 MPa. The average yield and ultimate strengths of the reinforcement were 455 MPa and 650 MPa, respectively. The purpose of the test was to investigate the effect of cracking on the effective stiffness of the wall considered for seismic analysis. According to the test results, the maximum displacement at the top of the wall was 281 mm, and the displacement prior to the yielding of the reinforcement was 46 mm. The total curvature capacity of the wall was 22 rad/km with the elastic portion of 2 rad/km. The curvature of the wall was measured at several locations over the height.

Bohl and Adebar (2011) modelled and analyzed the tested wall using VecTor2 in order to predict the curvature distribution along the height of the wall and to compare the predictions with the test results. The concrete was modelled using the low-powered rectangular and triangular elements with smeared reinforcement. Three different types of material were used to represent various regions of the wall. Smaller finite element mesh size was used near the base of the wall to have a better representation of the strain profile along the wall length. The horizontal and vertical displacements at the base of the wall were restrained. The total mesh consisted of 1487 nodes, 1360 rectangular elements and 60 triangular elements.

A monotonic lateral load was applied at the top of the wall in the displacement-controlled mode with increments of 0.2 mm. Since the envelopes for monotonic and cyclic loading were almost the same, applying a monotonic load was considered reasonable. In addition, a constant axial load of 1500 kN was applied equally distributed among the nodes at the top of the wall. This load did not include the self-weight of the wall.

The finite element model of the wall created in the FormWorks is shown in Figure 2.8. The curvatures of the wall at different locations over the height obtained from the VecTor2 model were compared with the observed curvatures from the experiment in Figure 2.9. As shown in Figure 2.9, there is very good agreement between the predicted and observed curvature distributions. Thus, the VecTor2 model could reasonably predict the curvature distribution of the wall.

Additionally, program VecTor2 is verified by comparing the results of NLFE analysis performed in VecTor2 with the concrete diaphragm test by Nakashima (1981). There is a good agreement between the experimental and analysis results for the load-deformation response. In addition to that, the VecTor2 does an excellent job of predicting the crack pattern observed in the test. Details of verification are presented in Section 4.5 of Chapter 4.

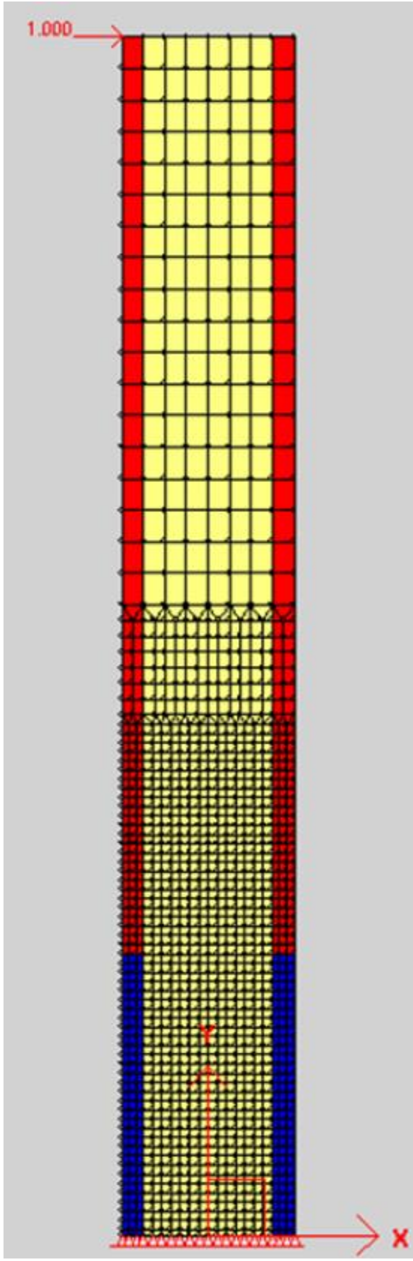

Figure 2.8 – Finite element model of UBC wall in FormWorks (Bohl, 2006)

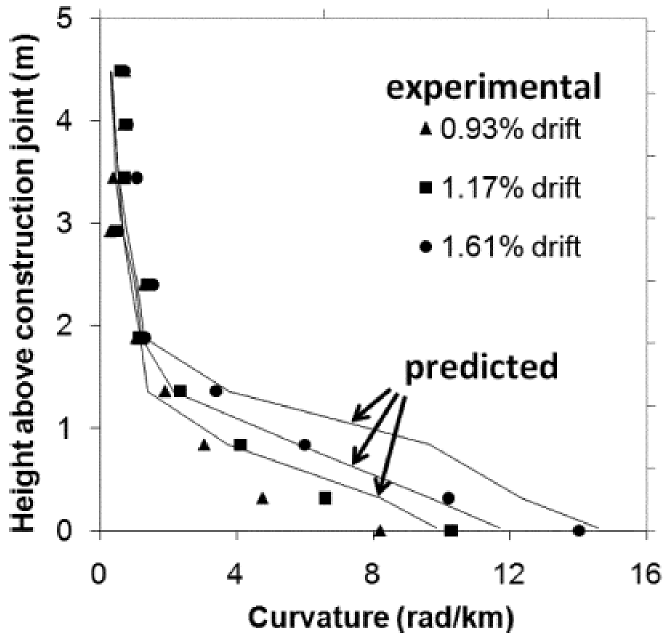

Figure 2.9 – Comparison of predicted and observed curvatures near base of tested wall (Bohl and Adebar, 2011)

2.4 Response-2000 and Shell-2000

Response-2000 and Shell-2000 are non-linear sectional analysis programs for the analysis of reinforced concrete elements subjected to shear. These programs are based on the Modified Compression Field Theory (Vecchio and Collins, 1986) and were developed over years 1996 to 1999 by Bentz (2000) at the University of Toronto.

In order to determine the response of a reinforced concrete structure under the effect of applied loads, the problem is broken into two interrelated parts. The first part is to determine the sectional forces at different locations in the structure due to the applied loads. For this part, it is usually assumed that the structure remains linearly elastic. The second part is to determine the response of a local section to the sectional forces which is known as ‘sectional analysis”. In this part, the nonlinear characteristics of cracked reinforced concrete are taken into account.

Program Response-2000 can calculate strength and deformation for beams and columns subjected to arbitrary combinations of axial load, bending moment and shear. Thus, this program can accurately model the behaviour of reinforced concrete. Response-2000 can also calculate the full member behaviour for a prismatic section. Program Shell-2000 is used for the analysis of plates and shells subjected to axial load, out-of-plane bending moments, twisting moment and in-plane and out-of-plane shear forces.

In these programs, the sectional analysis is implemented based on two primary assumptions. First, the engineering beam theory is valid which means that plane sections remain plane after deformation. Second, the net stress in the transverse direction is not significant which means that the concrete and transverse steel forces balance each other through the depth of the element. These assumptions are valid at a reasonable distance from the support and the load point.

In order to predict the response of an element, an analytical model is required to determine the stress resultants acting on the element due to the given deformations or to calculate deformations acting on the element due to the applied stress resultants.

2.4.1 Modified Compression Field Theory

The original form of the "Modified Compression Field Theory" (MCFT) was defined by Vecchio in 1982 based on the testing of 30 reinforced concrete panels subjected to uniform strains. The MCFT is a general model for the load-deformation response of cracked reinforced concrete subjected to shear. The MCFT models concrete considering concrete stresses in principal directions in addition to reinforcing axial stresses. The stress-strain relationship of concrete in compression and tension was derived from the tests conducted by Vecchio and verified against 250 experiments performed using two large special purpose testing machines at the University of Toronto.

The cracked concrete in reinforced concrete is treated as a new material in the MCFT model which is the most critical assumption in the model. The stress-strain relationship used for the cracked concrete was empirically defined which differs from the stress-strain relationship of a cylinder. Average strains were used for the stress-strain relationships which combined the effects of local strains at cracks, strain between cracks, bond slip and crack slip. In addition, average stresses were used which implicitly considered stresses between cracks, stresses at cracks, interface shear on cracks and dowel action. In order to make the use of average stresses and strains reasonable, a few cracks must be included in the calculations. Furthermore, an explicit check, called crack check, is required to ensure that the average stresses are compatible with actual cracked condition of the concrete. According to crack check, the average principal tensile stress in the concrete is limited to the maximum allowable stress determined based on the stress in steel at a crack and the ability of the crack surface to resist shear stresses.

The Modified Compression Field Theory for membrane elements is summarized in Figure 2.10.

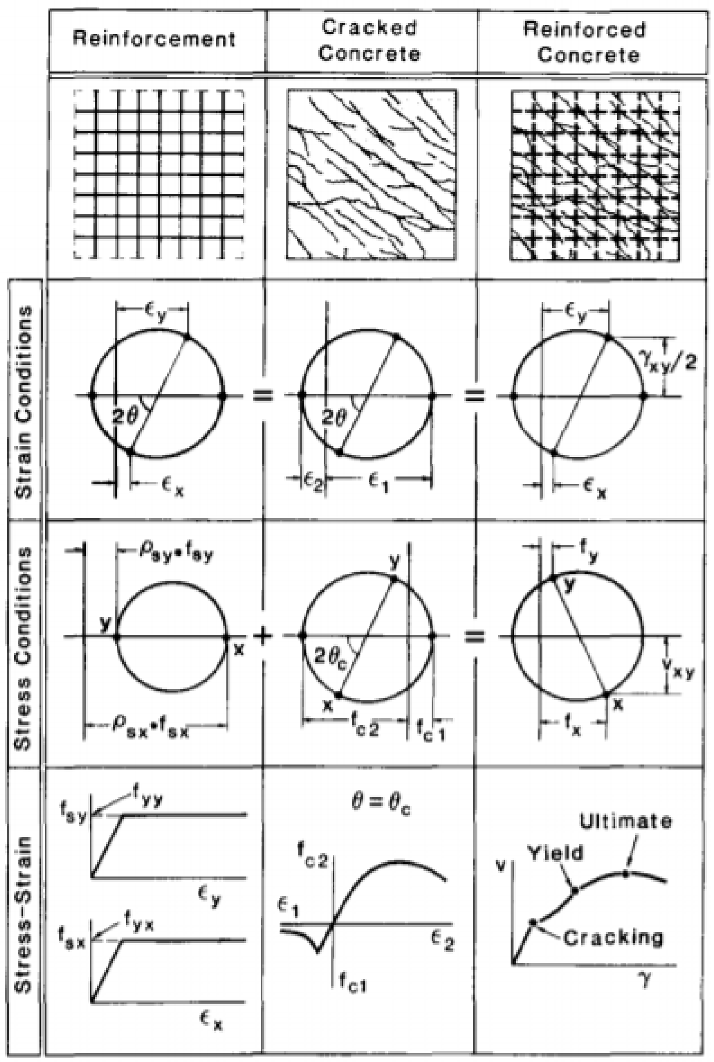

Figure 2.10 – The Modified Compression Field Theory for membrane elements (Vecchio and Collins, 1986)

The equilibrium equations shown in the left panel are the equations of a Mohr's circle of stress. The strain conditions are presented in the middle panel. According to MCFT, the angle of principal concrete stress is considered to be equal to the angle of principal strain. The concrete and steel stress-strain relationships in compression and tension are shown in the right panel. The components of the crack check are shown at the bottom of each panel.

The important aspects of the Modified Compression Field Theory (MCFT) are summarized as follows:

The average response of steel is approximated by bare bar behaviour in the MCFT. Porasz (1989) numerically demonstrated that this assumption is appropriate, and the corresponding error is relatively small.

It is assumed that concrete is able to carry the full cracking strength prior to cracking. Tensile stresses in the uncracked concrete between cracks stiffens the concrete after cracking. The following simple equation, originally proposed by Vecchio (1982), is used to model the behaviour of post-cracking, pre-reinforcement yielding tension stiffening of concrete. In fact, bond degradation, formation of new cracks and other damage mechanisms after cracking of concrete are modelled by the decrease in average tensile stress.

$$f_1 = \frac{f_{cr}}{1 + \sqrt{500\varepsilon_1}} \tag{2.44}$$

where,

f_{cr}: Concrete cracking strength;

f_1: Concrete principal tensile stress;

ε_1: Concrete principal tensile strain.

The stress-strain relationship of the concrete cylinder is used for the uncracked concrete in compression. According to Equation 2.37, the stress-strain curve is a function of both the principal compressive strain and the principal tensile strain of concrete. When the concrete is transversely cracked, the apparent concrete compressive strength is decreased. This effect was taken into account by the tensile strain component.

$$f_2 = \frac{f_c'}{0.8 + 170\varepsilon_1}\left[2\frac{\varepsilon_2}{\varepsilon_c'} - \left(\frac{\varepsilon_2}{\varepsilon_c'}\right)^2\right] \quad (2.45)$$

where,

f_c': Concrete compressive strength;

ε_c': Concrete strain corresponding to the concrete compressive strength;

f_2: Concrete principal compressive stress;

ε_2: Concrete principal compressive strain.

When concrete is subjected to shear, its behaviour becomes complicated due to the formation of new cracks and closure of some old cracks. In MCFT, this complex behaviour is modelled using a single set of parallel cracks with the average angle of principal compressive stress. The following equation is used to calculate the crack spacing based on the crack spacings in the two orthogonal x and y directions which can be estimated by the method presented by Collins and Mitchell (1991).

$$s_\theta = 1/\left(\frac{sin\theta}{s_x} + \frac{cos\theta}{s_y}\right) \quad (2.46)$$

where,

s_x: Crack spacing in principal stress direction;

s_y: Crack spacing in y direction;

s_θ: Crack spacing in principal stress direction;

θ: Angle of principal stress or strain.

Crack width is calculated as a product of the crack spacing and the principal tensile strain as follows:

$$w = s_\theta \varepsilon_1 \quad (2.47)$$

In the MCFT, the interface shear stress on a crack is limited which can be calculated by the equation derived by Walraven (1981). According to this equation, the shear stress limit is higher for larger aggregates or stronger concrete, while it is lower for larger crack width.

$$v_{ci} \leq \frac{0.18\sqrt{f_c'}}{0.31 + \frac{24w}{a + 16}} \tag{2.48}$$

where,

v_{ci}: Allowable shear stress on crack;

a: aggregate size.

Calculation of local reinforcement stress at a crack defines the crack check. The stress at a crack is computed for each direction of reinforcement and it should be smaller than the reinforcement yield stress. The Modified Compression Field Theory (MCFT) was extended to three-dimensional response by Kirschner (1986) and Adebar (1994).

2.4.2 Strain Compatibility Approach

The "Strain Compatibility Approach" was used to determine stress resultants in programs Response-2000 and Shell-2000. The first step in this approach is to consider appropriate assumptions for the strain distribution across the thickness of the element. Then, stresses corresponding to the strains are calculated based on the stress-strain relationships. Finally, the stress resultants are determined by integrating the calculated stresses over the appropriate areas.

2.4.3 Strain Assumptions

The strain within the element is defined based on the stresses considered in the element. For elements in which the out-of-plane shear stress is zero, the strain can be described by six variables including the membrane strains at the mid-surface, the curvatures and the shear strain gradient which is equal to twice the twist. It is assumed that each state of strain corresponds to only one set of stress resultants. Furthermore, the membrane strains are assumed to linearly vary over the thickness of the element.

For elements in which the out-of-plane shear is non-zero, the concrete has normal strains and shear strains in out-of-plane direction (i.e., z direction) which are determined from equilibrium for each integration point. Thus, the out-of-plane shear stresses in the concrete should be in equilibrium with the assumed shear stress distribution across the element thickness and the axial concrete stress in the z direction and the tension in the z reinforcement times the reinforcement ratio.

2.4.4 Verification

2.4.4.1 Response-2000

In order to verify Response-2000, the results of a concrete shear wall test conducted at the University of British Columbia are compared with those predicted by Response-2000 (Adebar and Ibrahim, 2002). The prototype wall was assumed to be 73.2 m high with a height-to-width ratio of 11. A ¼ scale model of the prototype wall (i.e., 18.3 m high) was considered for the test under seismic loading. The seismic loading was simulated by a triangular load distribution along the wall height which can be represented by the resultant lateral load at two-thirds of the wall height (i.e., 12.2 m from the base). Thus, a 12.2 m high wall specimen was considered for the test subjected to a single lateral load at the top of the wall.

The test specimen was a 12.2 m high by 1.625 m long with a flanged cross section. The web was 1219 mm long and 127 mm thick, and the flanges were 203 mm long and 308 mm thick. The vertical reinforcement in the flanges consisted of 5-10M reinforcing bars closed by 10M ties spaced at 64 mm in the lower 3 m of the wall and spaced at 152 mm in the remaining height of the wall. The web was reinforced by 10M bars spaced at 305 mm vertically and horizontally (Ibrahim, 2000). The cross section of the specimen and the details of reinforcement are shown Figure 2.11.

An axial load of 1500 kN ($10\%\ of\ f_c'\ A_g$) was applied to the wall during the test in addition to the lateral load at the top of the wall. The cylindrical compressive strength of concrete at the age of 140 days was 49 MPa. The yield and the ultimate strength of the reinforcing bars were determined to be 455 MPa and 650 MPa, respectively.

Simple hand calculations are performed to predict the bending moment-curvature response of the shear wall. It is assumed that the strain distribution varies linearly across the cross section according to the Euler- Bernoulli Beam Theory. The gross concrete cross section is used for calculations before cracking. After concrete cracks, the properties of a fully cracked member are used. It should be noted that the concrete tension stiffening is ignored in the hand calculations. In calculating the compression force in the concrete in the non-linear range, the equivalent uniform stress block is used and the concrete contribution in the tension side is neglected. A uniform shrinkage strain of -0.0004 is considered and the effect of creep is ignored. Also, the compression reinforcement is not considered. An elastic-perfectly plastic behavior with no strain hardening is assumed for the reinforcement steel.

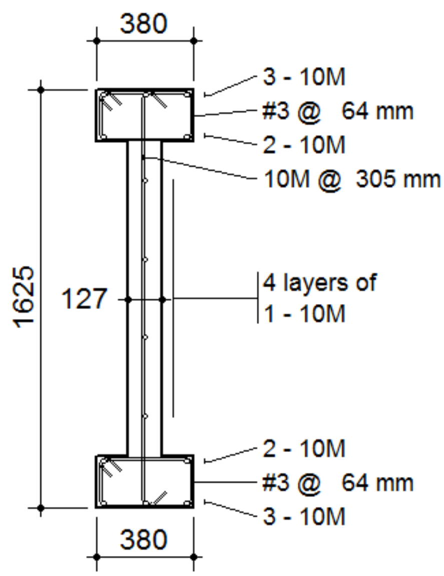

Figure 2.11 – Cross section of test specimen (Ibrahim, 2000)

The initial uncracked flexural rigidity, EI, is computed using the transformed moment of inertia of the cross section, I_{trans}, which is close to that of the gross section due to our lightly reinforced section. In order to determine the moment and curvature corresponding to the cracking point, the top strain is assumed while the bottom strain is the cracking strain. The iteration process continues until the axial force equilibrium is satisfied.

After the concrete cracks, each layer of the vertical reinforcing bars starts to yield. In order to predict these points, the bottom strain at the location of the reinforcing bars is set to the yielding strain of steel, $\varepsilon_{sy} = 0.00228$, and the compressive depth of concrete, c, is varied until the axial load equilibrium converges to the applied compressive load 1500 kN.

In order to determine the maximum flexural and curvature capacity, the concrete top strain is equal to the maximum compressive strain, $\varepsilon_{cu} = -0.0035$ and the concrete compression depth, c, is iterated until the axial equilibrium is satisfied. It should be noted that the curvature capacity is assumed to occur at the point of the flexural capacity for convenience.

In addition, the concrete shear wall cross section is modeled using Response-2000 with the above-mentioned material properties. The bending moment-curvature response is obtained for the two cases with and without tension stiffening. Figure 2.12 compares the moment-curvature response of the wall obtained from the hand calculation and Response-2000. It should be noted that the strain hardening is neglected in both the hand calculations and the Response-2000. As can be seen, hand calculations provide relatively conservative results for the moment-curvature response.

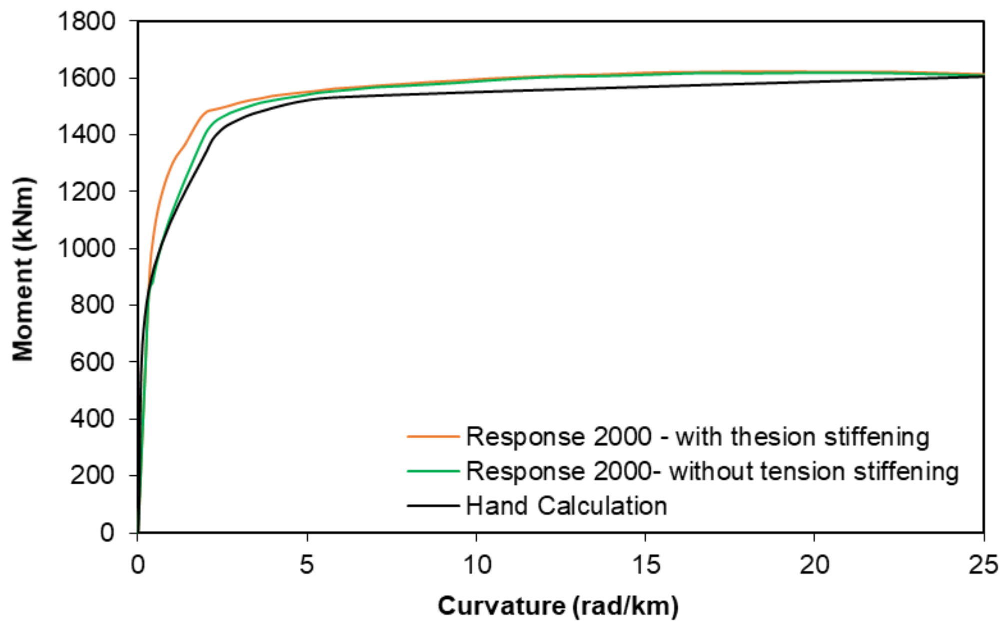

Figure 2.12 – Comparison of predicted moment-curvature response of the wall

The lateral load – displacement relationship of the tested wall is compared with the predicted results using Response-2000 in Figure 2.13. It is seen that Response-2000 curve with tension stiffening give the best prediction of the measured displacements. Increasing of discrepancy after yielding of reinforcements can be attributed to neglecting the effect of strain hardening of reinforcement. Thus, it can be concluded that Response-2000 is able to accurately predict the behaviour of the concrete shear wall.

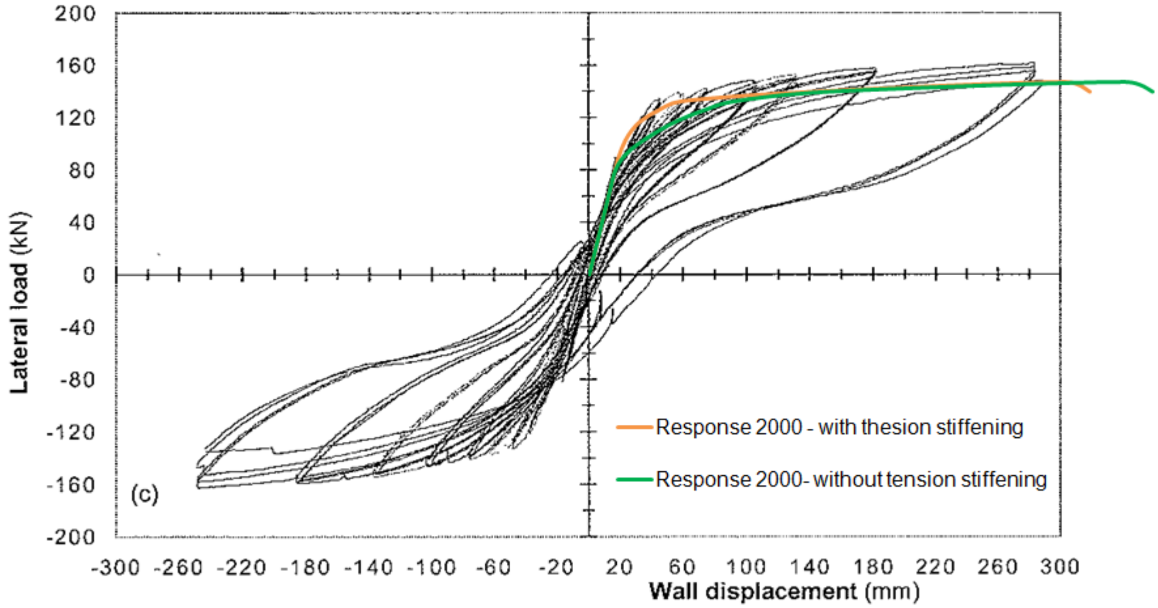

Figure 2.13 – Comparison of observed lateral load-displacement response with prediction by Response-2000

2.4.4.2 Shell-2000

Kirschner and Collins (1986) conducted a pilot series of experiments on shell elements. The two parameters varied in this series consisted of the amount of reinforcement in the y direction and the moment-to-shear ratio. Six specimens were tested in this series. Three specimens formed a subseries with increasing amounts of y reinforcement ($\rho_y = 0.163, 0.489,$ and 1.465) while three other specimens formed a subseries with increasing moment-to-shear ratios ($m_x/n_{xy} = 0.13\ m, 0.50\ m,$ and ∞). All the specimen size was 1524 mm by 1524 mm with the thickness of 285 mm. The amount of x reinforcement was kept constant ($\rho_x = 1.465$) for all tested specimens. The specimens were reinforced with two layers of reinforcement and the given reinforcement ratios were for one layer. It was intended to test a specimen large enough which was at full scale of floor or wall element of buildings.

Kirschner and Collins (1986) designed and built a testing facility for this experimental study which was capable of loading to failure relatively large reinforced concrete specimens. The shell element tester was designed such that the eight stress resultants, the three membrane forces

(n_x, n_y, n_{xy}) in the plane of the element; the three moments (m_x, m_y, m_{xy}) about in-plane axes, and two transverse shear forces (v_x, v_y) perpendicular to the plane, could be applied simultaneously or separately.

The shell element tester took the following approach to apply the eight stress resultants to the specimen: (1) only principal membrane forces were introduced into the specimen; (2) the moments were applied using couples along the element sides and lateral corner forces; (3) the out-of-plane shear forces were introduced by lateral forces along the element sides. Figure 2.14 shows the shell element tester. Twenty load application points were considered around the specimen perimeter, as shown in Figure 2.14. Forty 1000 kN hydraulic cylinders were required in the plane of the specimen (in-plane cylinders) for applying in-plane forces and another twenty 500 kN hydraulic cylinders were required perpendicular to the specimen (lateral cylinders) for applying out-of-plane loads.

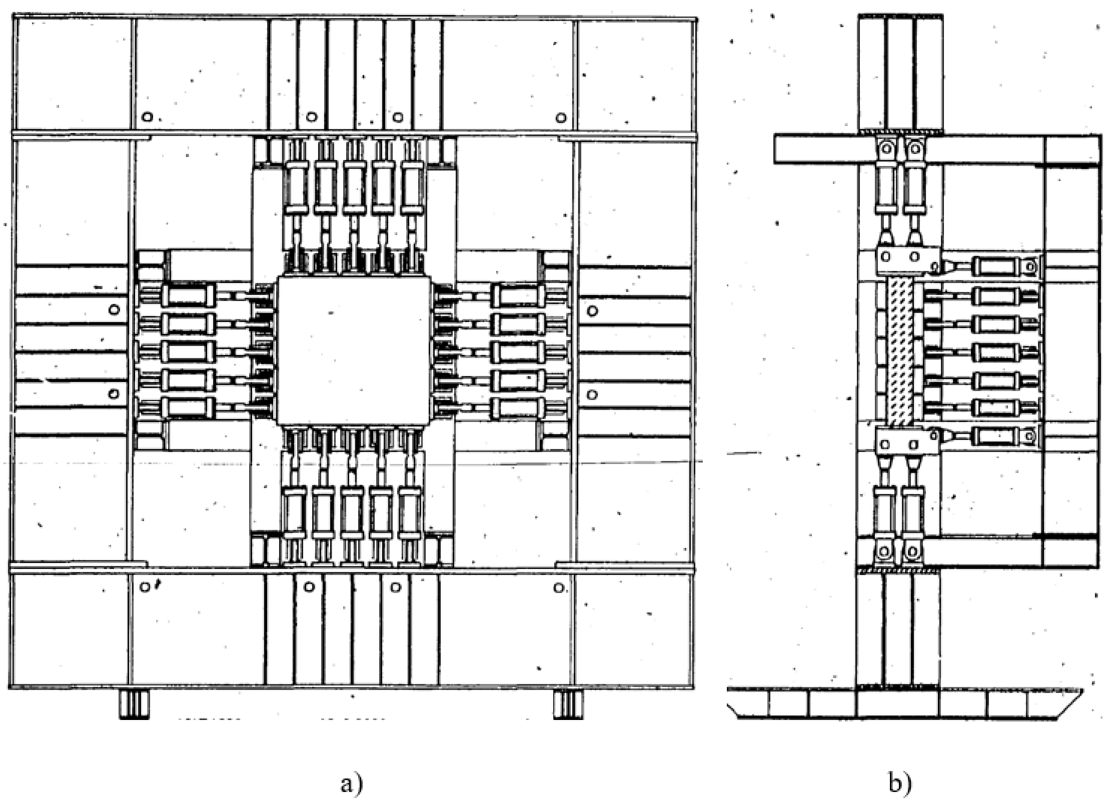

Figure 2.14 – Shell element tester: (a) plan view; (b) side view (Kirschner, 1986)

In order to verify Shell-2000, the tested specimens were analyzed using Shell-2000 and the results are compared with the experiment. Figures 2.15 to 2.20 present the comparisons for one of the specimens, loaded in combined moment and shear with a ratio (m_x/n_{xy}) of 500 mm. Predictions by Shell-2000 agree well with the experimental results. However, Shell-2000 predicts significant curvature in y direction while the test measured virtually none, as shown in Figure 2.19.

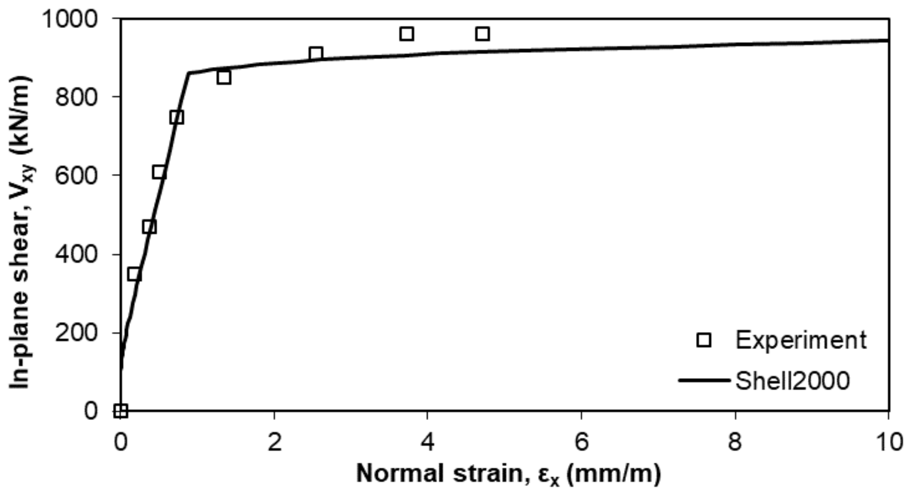

Figure 2.15 – Comparison of experimental results and predictions by Shell-2000 for in-plane shear versus normal strain in x direction

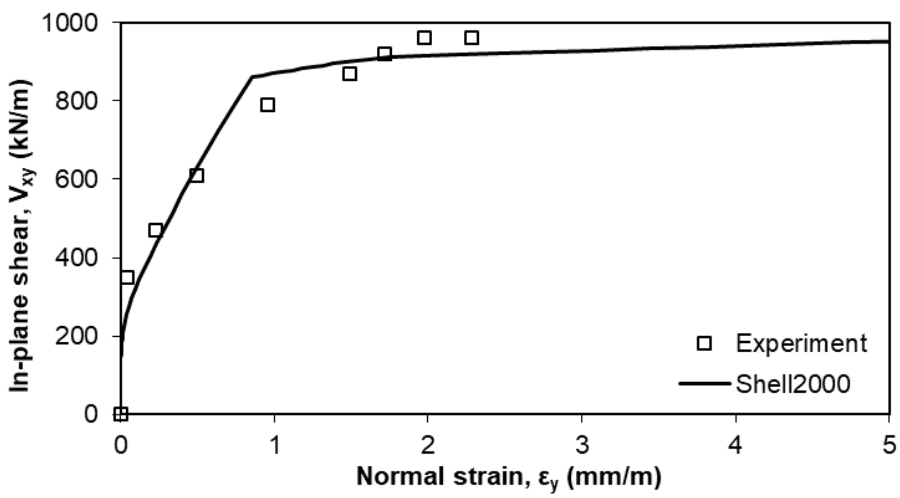

Figure 2.16 – Comparison of experimental results and predictions by Shell-2000 for in-plane shear versus normal strain in y direction

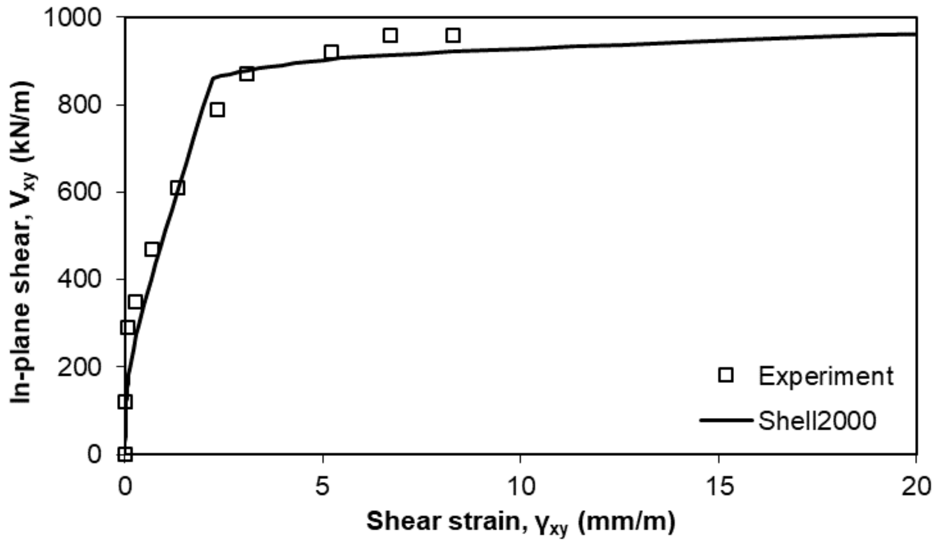

Figure 2.17 – Comparison of experimental results and predictions by Shell-2000 for in-plane shear versus shear strain

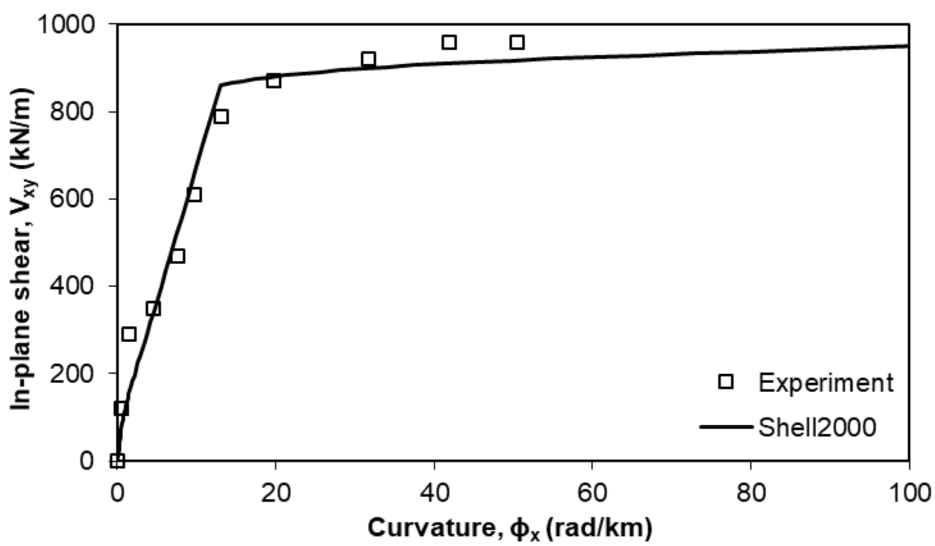

Figure 2.18 – Comparison of experimental results and predictions by Shell-2000 for in-plane shear versus curvature in x direction

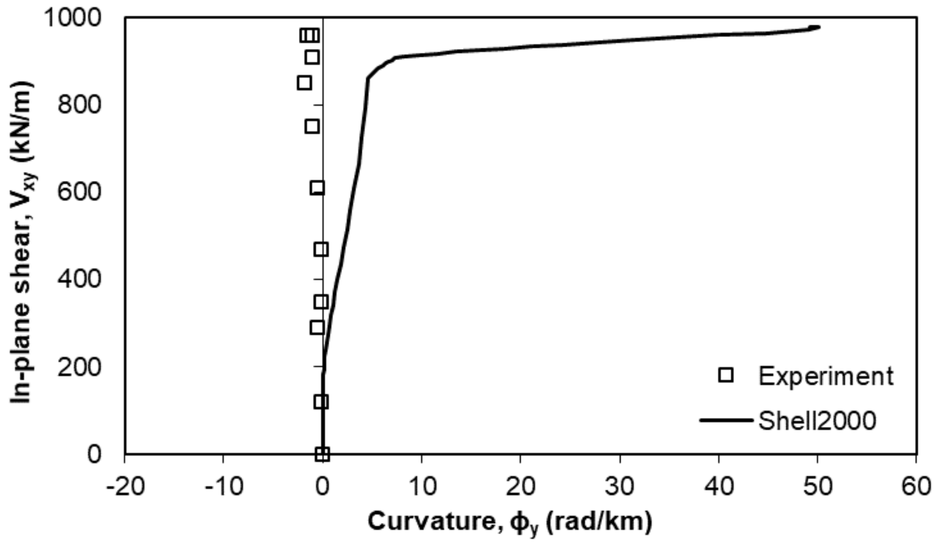

Figure 2.19 – Comparison of experimental results and predictions by Shell-2000 for in-plane shear versus curvature in y direction

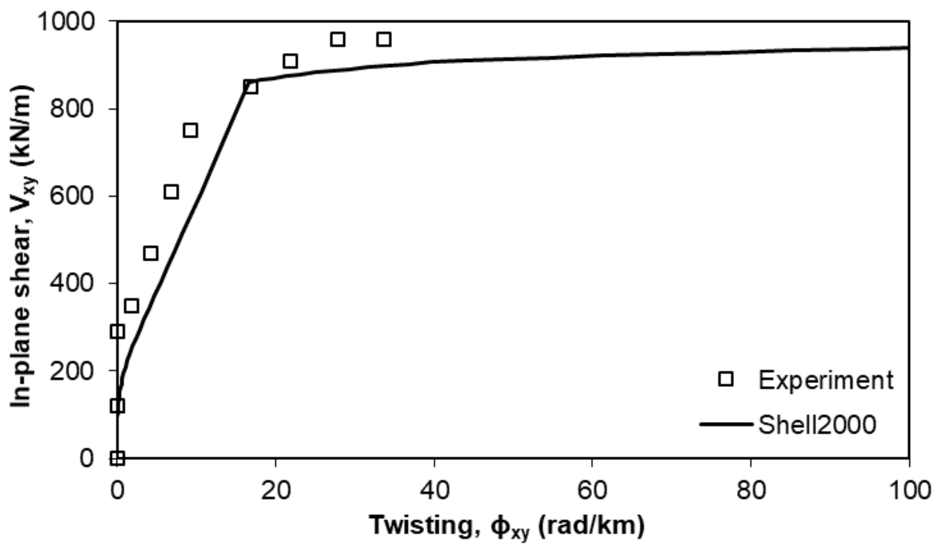

Figure 2.20 – Comparison of experimental results and predictions by Shell-2000 for in-plane shear versus twisting

2.5 PERFORM-3D

PERFORM-3D is a powerful tool for inelastic analysis and performance assessment of structures that allows the user to implement displacement-based design and to apply capacity design principles. PERFORM-3D uses the procedure for displacement-based design specified by ASCE 41 which can be applied to the retrofit of existing buildings and to the design of new buildings. However, PERFORM-3D is a general tool for implementing displacement-based design and it is not limited to ASCE 41.

Although PERFORM-3D has powerful capabilities for nonlinear analysis, it is not intended for general purpose inelastic analysis. It can help the user to identify weak points of the design and hence can guide to improve the design. Thus, it can be helpful to produce better designs, but it does not do the engineering.

PERFORM-3D includes different types of elements for modelling different parts of the structure, such as: frame element for beams, columns and braces, wall element for shear walls, slab element for floors, bar element with only axial stiffness, etc. In PERFORM-3D, most elements are made of a number of components. For instance, a beam element can consist of several components such as, end zone component, moment hinge component, shear hinge component, etc. PERFORM-3D uses the basic trilinear force-deformation relationship with optional strength loss for all inelastic components. This will be discussed in more details later.

In PERFORM-3D, deformation capacities can be specified for inelastic components for up to 5 performance levels. For inelastic components, deformation demand to capacity ratios are calculated, hence, these components can be checked to ensure they have sufficient ductility. For elastic components, PERFORM-3D computes the strength demand to capacity ratios to check whether these components have sufficient strength. Since the number of components with demand to capacity ratios can be large, PERFORM-3D considers limit states to group components with similar demand to capacity ratios. A usage ratio for each limit state is defined as the maximum demand to capacity ratio for any component in the limit state. In order to satisfy the performance requirements for a structure, usage ratios for all limit states should not exceed 1.0.

Both frame and shear wall structures can be modelled in PERFORM-3D using beam and column elements and plane wall elements, respectively. Wall elements can have inelastic behaviour in bending and shear. Beam element is used to model coupling beams with inelastic behaviour in either bending or shear. P-delta effects can be considered in PERFORM-3D.

PERFORM-3D can run different types of analysis including mode shapes, gravity loads, static push-over, response history for earthquake ground motion, response history for dynamic forces and response spectrum analysis. The strategies taken by PERFORM-3D for nonlinear analysis is very reliable, even when inelastic components have negative stiffness, and when the structure becomes unstable due to P-delta effects.

In PERFORM-3D, two different analysis sequences can be applied: standard and general. The standard analysis sequence includes: (1) apply gravity loads; (2) Run one or more static push-over analyses, with constant gravity load; (3) run one or more earthquake history analyses with constant gravity load. An example of the general sequence is a cyclic push-over analysis is as follows: (1) apply gravity loads; (2) add push-over loads to a specified drift in the positive direction; (3) add push-over loads to a specified drift in the positive direction; (2) add push-over loads to a specified drift in the negative direction; (4) progressively increasing the specified drift in each direction.

In PERFORM-3D, an analysis series is a series of analyses with a standard or general sequence. Some of the structure properties can be changed for each analysis series including the mass distribution and magnitude, the amount and type of damping for dynamic response history analysis, and the strengths and stiffnesses of the structural components. Thus, using this feature of PERFORM-3D makes it possible to change the structural properties of the model without creating a new analysis model.

A number of tools are included in PERFORM-3D for processing the analysis results which are used to study and check the behaviour of a structure. These tools are as follows: (1) deflected shapes, time histories of response quantities including nodal displacements, velocities and accelerations, element and component forces and deformations, and forces on structure sections; (2) hysteresis loops for inelastic components; (3) moment and shear diagrams for beams, columns, and shear walls; and (4) energy balance showing strain energy, kinetic energy, and damping energy (CSi Computers and Structures Inc.).

2.5.1 Fiber Section

A fiber section can have fibers of different material types, usually steel and concrete. In PERFORM-3D, cross sections for shear walls are always fiber sections. In addition, fiber sections can be used for frame elements, beams and columns.

Shear wall elements act essentially as beams, with bending, axial and shear deformations. Shear walls can be elastic or inelastic for shear by defining a shear material, and elastic or inelastic for bending, using fiber sections. In PERFORM-3D, there are two options for specifying the fibers in a fiber section: fixed size and auto size. For fixed size option, the area and coordinate location for each fiber in the cross section are specified. The width of the cross section is fixed, and it should be ensured that the element width is consistent with the cross-section width. Therefore, this option makes it possible to account for thickness variations in the wall. In addition, different reinforcement areas can be considered in different part of the section.

For auto size option, the wall thickness and the number of fibers in the cross section are specified. The width of the cross section is not fixed. When the cross section is assigned to an element, PERFORM-3D considers the cross-section width equal to the element width, and determines the fiber areas and coordinates. Thus, it is not possible to account for the variation of wall thickness over the element, and the reinforcement percentage is constant.

In PERFORM-3D, the transverse stiffness of the shear wall in the horizontal direction and the out-of-plane bending stiffness of the wall are assumed to be elastic. Furthermore, if inelastic shear is specified for the wall, limit states can be defined using strain capacities of the shear material. If elastic shear is specified, limit states are defined using the shear strength of the shear material. For elastic bending, limit states are defined using the stress capacities of the elastic material at locations where fibers are monitored, and for inelastic bending, limit states are defined using the strain capacities of the inelastic materials in the section at the same locations where the fibers are monitored (PERFORM Components and Elements, 2006).

In elastic fiber sections can be used for beam and column elements in PERFORM-3D. For beam sections, the fiber properties are used for axial force and in-plane bending only and the out-of-plane bending are considered to be elastic. For in-plane bending, P-M interaction is also accounted for in beam sections. For column sections, the fiber properties are used for bending about both axes and P-M-M interaction is accounted for. Shear and torsion are assumed to be elastic for both beam and column sections. In order to consider inelastic shear behaviour, shear hinge components can be used.

There are different types of materials are available to be used for fibers including steel material, concrete material, the materials used for the current study. PERFORM-3D allows to use up to 16 fibers for shear walls, up to 12 fibers for beam sections, and up to 60 fibers for column sections. It should be noted that using larger number of fibers results in the great increase of the computation time. Thus, the goal is to use the minimum number, especially for column sections, that gives reasonable results (PERFORM-3D User Guide, 2006).

2.5.2 Force-Deformation Relationship

In PERFORM-3D, each material has one or more actions (forces) and the corresponding deformations. For instance, for a simple material, the stress is the action and the strain is the deformation, and for a simple plastic hinge, the bending moment is the action and the hinge rotation is the deformation. The relationship between these two is the force-deformation relationship (F-D relationship). In PERFORM-3D, most of inelastic components have the form of trilinear relationship with optional strength loss for the F-D relationship, as shown in Figure 2.21.

The key points in the above diagram are as follows:

(1) Y Point is the first yield point, where the nonlinear behaviour begins.
(2) U Point is the ultimate strength point, where the maximum strength is reached.
(3) L Point is the ductile limit point, where significant strength loss begins.
(4) R Point is the residual strength point, where the minimum residual strength is reached.
(5) X Point is usually at a large deformation that there is no point to continue the analysis.

It is also possible to define components with different relationships for positive and negative deformations. In addition, some components have an elastic-perfectly-plastic (EPP) relationship rather than a trilinear relationship. In this case, the Y and U points are identical. To define a bilinear relationship with no strength loss, a large value should be specified for the deformation at U point. To define a bilinear relationship with strength loss, the deformation at U point should be specified slightly smaller than the deformation at L point.

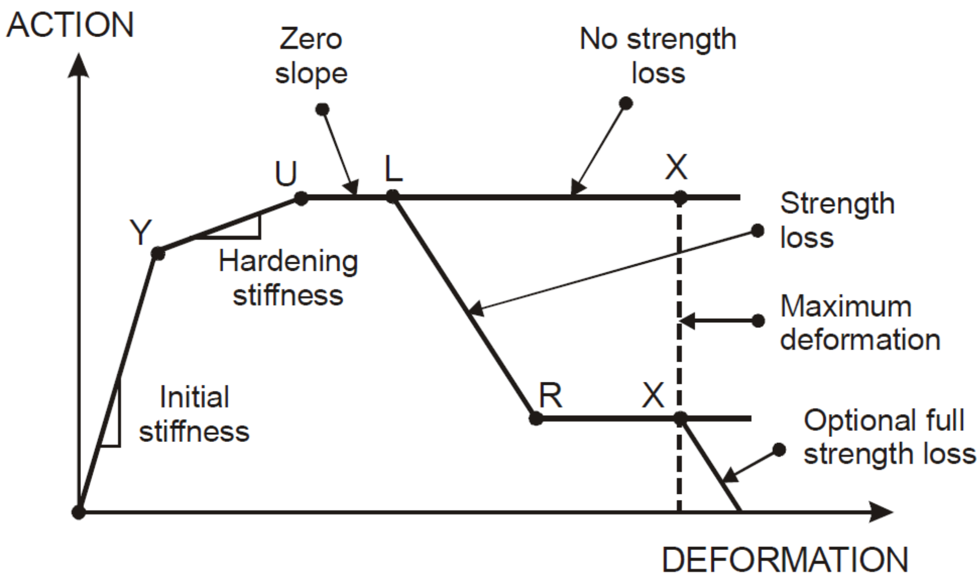

Figure 2.21 – PERFORM force-deformation relationship (PERFORM-3D User Guide, 2006)

It is also possible to define components with different relationships for positive and negative deformations. In addition, some components have an elastic-perfectly-plastic (EPP) relationship rather than a trilinear relationship. In this case, the Y and U points are identical. To define a bilinear relationship with no strength loss, a large value should be specified for the deformation at U point. To define a bilinear relationship with strength loss, the deformation at U point should be specified slightly smaller than the deformation at L point.

Brittle strength loss can occur due to different effects including tensile fracture, buckling, concrete crushing and concrete shear failure. When strength loss takes place in a component, the lost strength is redistributed to adjacent components which can result in a complex behaviour. In PERFORM-3D, considering the effect of strength loss in the analysis is optional, and it is recommended to specify it only if it is essential. It is not usually permissible for an inelastic component to deform beyond the L point as the deformation capacity is smaller than the L point deformation. For instance, the FEMA 356 usually allow deformation beyond the deformation at L point for secondary members at the collapse prevention performance level. The force-deformation relationships for FEMA 356 and PERFORM-3D are shown in Figure 2.22.

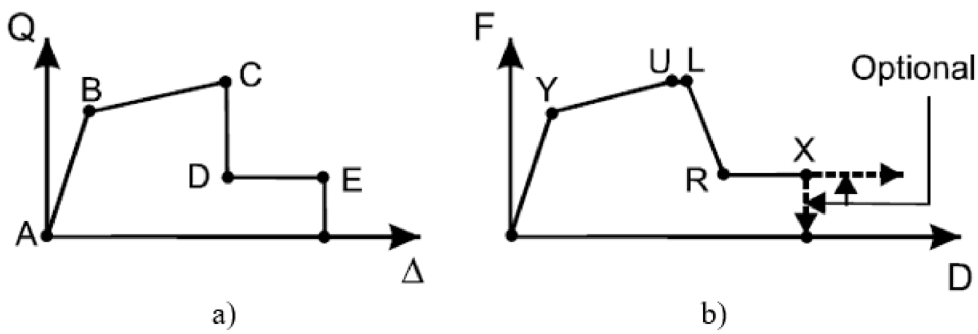

Figure 2.22 – Strength loss: (a) FEMA 356; (b) PERFORM-3D (PERFORM-3D User Guide, 2006)

According to FEMA 356, there is sudden strength loss at point C and total strength loss at point E (shown in Figure 2.22(a)). In PERFORM-3D, strength loss can be sudden or gradual which starts at point L. In fact, sudden strength loss is not realistic, and it is gradual in an actual structure. Thus, sudden strength loss is better to be avoided. Total strength loss is optional in PERFORM-3D.

2.5.3 Concrete Material

The hysteresis model for a concrete fiber in compression used by PERFORM-3D is shown in Figure 2.23. In this model, the unloading stiffness is considered to be equal to the initial elastic stiffness of concrete, and the dissipated energy is controlled by changing the reloading stiffness. Figure 2.23(a) shows reloading for the energy dissipation factor of 1.0, while Figure 2.23(b) shows reloading for the energy dissipation factor of less than 1.0. When the energy dissipation factor is zero, the unloading and reloading lines are identical, and no energy is dissipated.

In PERFORM-3D, it is possible to consider either finite or zero strength for concrete in tension. Figure 2.24 depicts unloading and reloading for finite tensile strength with no cyclic energy dissipation. In fact, PERFORM-3D considers independent behaviour for concrete in tension and compression. Therefore, compression crushing of concrete does not affect its behaviour in tension, and subsequently, cracking in tension does not influence its behaviour in compression.

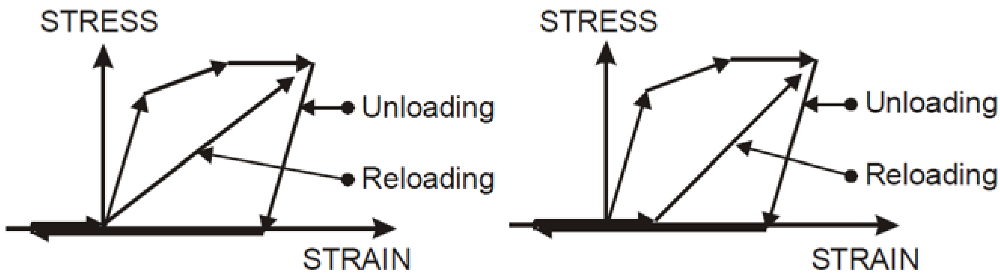

a) b)

Figure 2.23 – Concrete material in compression with unloading stiffness of: (a) 1.0; (b) less than 1.0 (PERFORM Components and Elements, 2006)

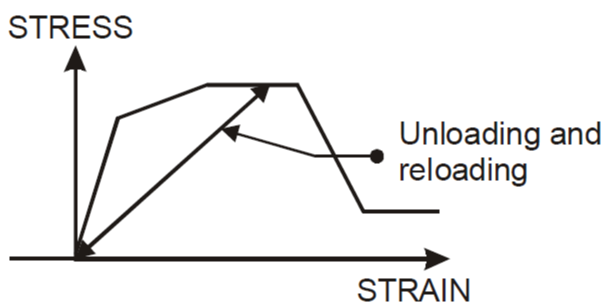

Figure 2.24 – Concrete material in tension (PERFORM Components and Elements, 2006)

2.5.4 P-Δ Effects

There are three different types of geometric nonlinearities including P-Δ, P-δ and large displacement effects which can cause nonlinear behaviour of elements and complete structures. PERFORM-3D has the option to include or ignore the geometric nonlinearity.

Two key assumptions are typically considered for small displacements analysis, as follows: (1) the linear geometric relationship is assumed between element deformations and node displacements; (2) the equations of equilibrium can be considered for the structure undeformed position. In fact, none of these assumptions are correct. The first assumption is mathematically correct when the displacements tend to zero. By increasing the displacements of the nodes, the relationship between the element deformations and node displacements becomes more nonlinear.

Due to the simple physical reason that the equilibrium should be satisfied in the deformed position of the structure, the second assumption is not correct. As the element deformations get larger, the second assumption becomes less correct.

True large displacements analysis accounts for both types of nonlinearity. P-Δ analysis retains the first assumption but considers the equilibrium in the structure deformed position. The difference between these analyses for a simple bar is illustrated in Figure 2.25.

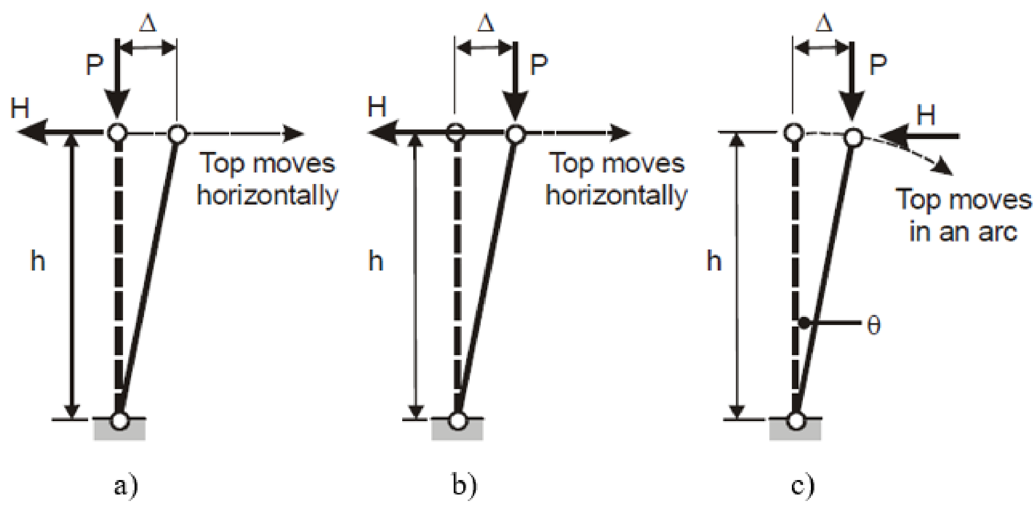

Figure 2.25 – Geometric nonlinearity: (a) small displacements; (b) P-Δ; (c) large displacements (PERFORM-3D User Guide, 2006)

For this example, assume the axial stiffness (EA) of the bar is very large, and accordingly, the axial extension of the bar is negligible. The three different theories are as follows:

Small displacements theory considers that the top of the bar moves horizontally, and the equilibrium can be considered in the undeformed position. Therefore, for all values of Δ the force H is zero ($H = 0$).

P-Δ theory assumes that the bar moves horizontally with zero axial extension, and the equilibrium is considered in the deformed position of the structure. Thus, $H = P\Delta/h$.

Large displacements theory assumes the top of the bar moves in an arc which results in vertical and horizontal movements of the top. The bar extension is considered to be zero; and the equilibrium is formed in the deformed position. Hence, $H = P\Delta/h \cos\theta$.

There is a small difference between the H value obtained from P-Δ theory and from large displacements theory. For instance, when $\Delta/h = 0.05$, P-Δ theory results in $H = 0.05V$ and large displacements theory gives $H = 0.05006V$. The difference is negligible. In addition, the vertical displacement predicted by large displacements theory is $0.00125h$, which is zero for P-Δ theory. Thus, there is not a significant error in most cases; hence, it can be concluded that P-Δ theory is accurate enough for most structures.

Figure 2.26 illustrates the simple bar structure where P-Δ theory is not accurate.

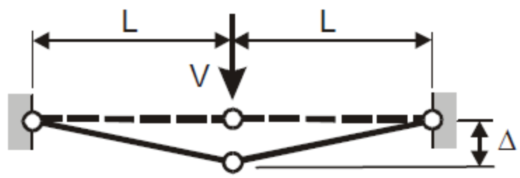

Figure 2.26 – Simple bar structure where P-Δ theory is not accurate (PERFORM-3D User Guide, 2006)

Based on small displacements theory, the stiffness of the structure is zero as the extension of the bars are zero. Thus, there is no axial force in the bars, and hence, the force V is zero for all deflections.

According to P-Δ theory, the force V is zero if the initial force in the bars is zero, as this theory assumes no extension of the bars. Large displacements theory predicts progressive increasing of V force as the deflection increases, since this theory accounts for the bar extension. By assuming the initial force in the bars equal to P in tension, P-Δ theory says the force remains constant and the relationship between the vertical force and the vertical displacement is linear ($V = 2P\Delta/L$). The stiffness ($2P/L$) is the geometric or initial stress stiffness of the two bars. Large displacements theory accurately predicts the stiffness which progressively increases with an initial stiffness of $2P/L$.

It should be noted that in most structures subjected to earthquake loads, the behaviour of the structure is mostly analogous to Figure 2.25 than to Figure 2.26. Thus, P-Δ theory works well for such cases and has the advantages of simplicity and less time-consuming compared to the large displacement theory. PERFORM-3D has the option to include or to ignore geometric nonlinearity. In the present version of PERFORM-3D, it is possible to consider P-Δ effects but not true large displacement effects.

Chapter 3

Compression Failure of Thin Concrete Shear Walls with Overhanging Wall Above

3.1 Introduction

Thin reinforced concrete walls that are 8 inches (200 mm) or less are a very cost-effective way of constructing buildings. They have been used in many countries around the world especially in South America and Europe. In February 2010, Chile experienced a very large earthquake (magnitude M8.8) and many of high-rise buildings with thin concrete walls were badly damaged. Most of damaged buildings were mainly new structures with 150 to 200 mm wall thicknesses built after year 2000 (Jünemann et al. 2012).

A common type of damage to high-rise concrete buildings was compression failure of thin concrete shear walls which was generally concentrated in the vicinity of discontinuities. Figure 3.1 shows an example of the type of damage that occurred. Compression failure of the concrete began on the left end of the wall, which is shown in the close-up photograph. Immediately above the damaged zone, the shear wall is longer and is connected to a transverse wall. That is, above the damaged zone, the wall has a “compression flange”. About 1.2 meters above the damage zone, the shear wall is longer and overhangs the wall below. The overhanging wall above and the transverse wall (compression flange) that suddenly stops in order to create an opening to accommodate parking created a significant geometrical discontinuity in the shear walls that resulted in the damage being concentrated immediately below the discontinuity (Adebar, 2013).

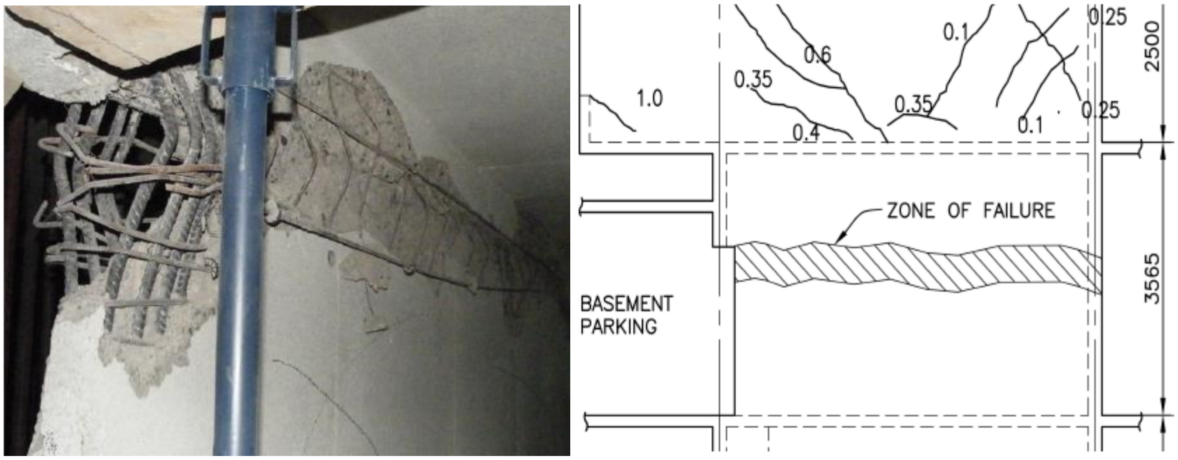

Figure 3.1 – Example damage to thin concrete shear walls during 2010 Chile Earthquake: close-up photo of damage (left); drawing showing location of damage (right) (Sherstobitoff et al., 2012)

In another large earthquake that occurred in the City of Christchurch, New Zealand approximately one year later, damage was again observed in thin concrete shear walls. The five-story Pyne Gould Building collapsed during the earthquake. It was reported that the compression failure of the east core wall caused the collapse (Beca, 2011). The wall thickness was 203 mm and it had a single layer of horizontal and vertical reinforcement with a diameter of 16 mm. The horizontal reinforcing bars were spaced at 380 mm which is acceptable according to current Canadian Concrete Code requirements. Based on the Code, the horizontal reinforcement shall be spaced at the smaller of three times the wall thickness or 500 mm. Another example was the compression failure of a concrete wall in the 22-story Grand Chancellor Hotel, one of the tallest buildings in Christchurch. The wall supported a significant load from a large transfer girder cantilevered over the wall (Elwood, 2012). As a result of the recent observations, the seismic safety of the many existing high-rise concrete buildings in Canada has become a serious concern.

A recent review of the structural drawings of about 350 high-rise concrete buildings constructed in the city of Vancouver prior to 1980 revealed that the majority of these buildings had thin concrete walls, 6 or 8 inches thick, as important vertical and lateral load resisting members. 25% of the buildings contain shear walls that have a significant geometrical discontinuity consisting of the wall with a step-back irregularity, shorter length shear wall supporting an overhanging shear wall above. Such walls have been called “flag walls” (Yathon et al., 2014).

Figure 3.2 shows an example of a typical wall with geometrical discontinuity that was investigated in the current study. In this case, the wall above overhangs the wall below on the right side. In order to evaluate the capacity of such a wall, design engineers use a sectional analysis for the shorter length wall below which does not account for the influence of the geometrical discontinuity. To evaluate the flexural capacity of the wall accounting for the applied axial load, the assumption of linearly varying vertical strains is used. This assumption is reasonable away from the discontinuity like at the bottom of the wall as shown in Figure 3.2(b).

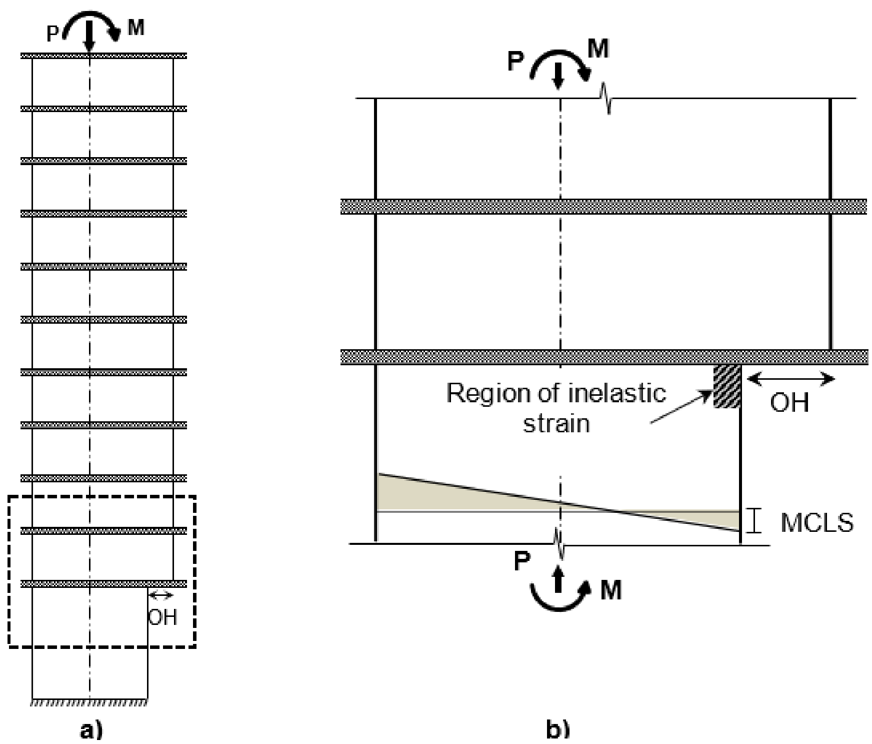

Figure 3.2 – Concrete shear wall with a geometrical discontinuity caused by an overhang (OH): (a) elevation of overall wall investigated in current study; (b) close-up of critical region around geometrical discontinuity

In addition to evaluating that the wall below has adequate bending strength, the engineer must evaluate if the wall has sufficient ductility. This would normally be done using a plane-sections analysis to determine the maximum compression strain in the concrete when the vertical tension reinforcement yields and after significant inelastic curvature occurs in the wall. The magnitude of the applied axial load and geometry of the wall will influence the result of the maximum compression strain. Generally, the reinforcement details at the flexural compression end of a wall will influence the acceptable compression strain. However, it is very difficult to provide significant confinement reinforcement at the end of a thin concrete shear wall. All of the thin concrete shear walls in the pre-1980 high-rise concrete buildings in Vancouver that have an overhanging wall discontinuity have no transverse ties at the end of the wall (Yathon et al., 2017). In fact, many of the walls have only a single layer of reinforcement. When concrete is unconfined, the maximum compression strain is usually limited to 0.003.

Recent experimental research conducted at the University of British Columbia has shown that thin concrete shear walls may have a significantly reduced compression strain capacity because the concrete cover on the reinforcement, which is damaged at strains as low as 0.002 or less, is a large portion of the total wall cross section (Adebar, 2013).

For unconfined high-rise shear walls, the ultimate compressive strain at failure should be conservatively reduced to the strain corresponding to the compressive strength of concrete (0.0018~0.0025) and the ductility should be determined according to this strain. It was suggested that the boundary confinement should be provided in the compression zone where the strain exceeds this ultimate strain (Kang et al. 2015). Results of experiments conducted by Shea and Wallace (2013) has also shown that thin wall boundary elements performed reasonably well when subjected to low compression strains (e.g., less than 0.003). Results indicated that thin walls subjected to moderate compression strains suddenly failed in compression.

It is believed that the reduced compression strain capacity is a significant part of the explanation for the recent failures of concrete walls in earthquakes. In addition, the geometrical discontinuity may cause a significant increase in strains immediately below the overhang. Thus, it is also believed that the increased compression strain demands that occur at geometrical discontinuities is the other important reason for the recent failures of concrete walls. This increase in strain cannot be quantified using the sectional model normally used by designers. In the current study, nonlinear finite element analysis is used to investigate how much the strains may increase as a result of the geometrical discontinuity caused by an overhanging wall.

The objective of the current study is to develop simplified procedures for estimating the magnification of strains due to the geometrical discontinuity caused by the overhanging wall, which can be used to estimate the likelihood of a compression failure in such a wall. This will provide engineers assessing the seismic safety of existing buildings with the "tools" they need to more accurately assess the risk of severe damage or collapse due to the compression failure of thin concrete shear walls with an overhanging wall discontinuity.

3.2 Description of Investigated Structure

Figure 3.2 describes the structure that was investigated in the current study. Figure 3.2(a) shows the elevation of overall wall, while Figure 3.2(b) depicts the close-up detail of the critical region around the geometrical discontinuity. At the base of the building, the shear wall was 4.0 m long. At 4.0 m up from the base of the wall, the length of the wall suddenly increases on the right-hand side. Five different sizes of overhangs (OH) were investigated: 0.2, 0.5, 1.0, 1.5 and 2.0 m. Above the level of the overhang, the wall had a uniform length of 4.2, 4.5, 5.0, 5.5 and 6.0 m, respectively.

The wall was subjected to a uniform bending moment over the height (zero shear force) in order to simplify the analysis. The bending moment was applied so that flexural compressive stresses developed on the side of the overhang (right-hand side). The height of the shear wall was definitely tall enough so that the details of how the bending moment was applied did not influence the strains in the region of the geometrical discontinuity. The wall was also subjected to a constant axial load equal to $10\% f_c' A_g$ based on the 4.0 m length of the lower portion of the wall (below the overhang). For simplicity, the base of the wall was assumed to be fully fixed against translational and rotational displacements. The thickness of all walls was assumed to be 200 mm (approximately 8 in). The flat plate concrete floor slabs were also 200 mm thick. One floor slab was located at the level of the overhang and the additional floor slabs were spaced at 2.5 m (center-to-center) above the overhang.

The concrete walls were reinforced with two layers of distributed reinforcement, 15M@400 mm on each face, which results in 0.5% distributed reinforcement in both vertical and horizontal directions. In the lower portion of the wall (below the overhang) 8-20M reinforcing bars were provided over a length of 400 mm (3% vertical reinforcement) as concentrated reinforcement at the compression end of the wall. This vertical reinforcement was extended up through a number of floor levels above the overhang. In addition, 3% vertical reinforcement was provided along 600 mm of the concrete wall on the tension side and over the full height of the wall. It was assumed that the ties around the concentrated reinforcement were not sufficient to justify an enhanced concrete response due to confinement. In order to control diagonal shear cracks and avoid shear critical issues in this study, additional distributed horizontal reinforcement (3%) was provided in the wall above the overhang.

3.3 Nonlinear Finite Element Analysis

Two primary methods utilized to investigate the response of reinforced concrete members are experimental and numerical approaches. The experimental method is one of the most reliable methods which has been widely used to study the behaviour of concrete structures. Although the accuracy of experimental results is high, it is time consuming and can be very costly. Finite element analysis as a numerical method is also widely used to analyze the behaviour of structures. The use of this method was very time consuming in last few decades, but nowadays, it has become much easier due to the use of powerful software and hardware capabilities.

In this study, nonlinear finite element (NLFE) analysis was employed to investigate the concrete compression strains at the geometrical discontinuity due to the presence of the overhang. Two different computer programs, ABAQUS (Simulia, 2013) and VecTor2 (Wong and Vecchio, 2002), were used to develop finite element models. ABAQUS is a powerful commercial program for NLFE analysis that has high-powered membrane elements. VecTor2 is a nonlinear finite element program for the analysis of two-dimensional reinforced concrete membrane structures. VecTor2 uses the constitutive models of the Disturbed Stress Field Model, which is a refinement of the Modified Compression Field Theory (Vecchio, 2000; and Vecchio and Collins, 1986). VecTor2 has a state-of-the-art material model for cracked reinforced concrete subjected to biaxial stresses; but has a limited number of low-powered elements. The entire wall was modelled using ABAQUS, while only the discontinuity region, above and below the overhang, was modelled using VecTor2. VecTor2 was used to verify the results from ABAQUS and to provide additional insight into the biaxial strains in the concrete wall immediately below the overhang.

3.3.1 ABAQUS Model

The 8-node quadrilateral membrane elements (M3D8) in ABAQUS were used for modelling both the concrete walls and slabs using a small mesh size of 100×100 mm in order to get a very detailed map of the stresses and strains immediately below the overhang. The floor slabs were simulated using high tensile strength concrete with concentrated horizontal reinforcement. Reinforcement was modelled as rebar layers (smeared reinforcement). The interaction between cracked concrete and reinforcing bars, i.e., bond stress, was modelled using tension stiffening in concrete. In total, seven different sections with different ratios of vertical and horizontal reinforcement and concrete tensile strength were created to represent various regions of the concrete wall in the finite element model. Details of each section properties are given in Appendix A.

The concrete was modelled using the "concrete damaged plasticity" model of ABAQUS described in Section 2.2.1. This material model is a continuum, plasticity-based, damage model which accounts for the main two failure mechanisms – tensile cracking and compressive crushing of concrete. The propagation of the failure surface is controlled by two hardening variables linked to failure mechanisms under tension and compression loading, respectively. The model combines the concepts of isotropic damaged elasticity with isotropic tensile and compressive plasticity to model the inelastic behavior of concrete. It also includes the combination of non-associated multi-hardening plasticity and scalar (isotropic) damaged elasticity to describe the irreversible damage that occurs during the fracturing process. The model considers the degradation of the elastic stiffness induced by plastic straining both in tension and compression.

The concrete compressive strength was considered as 30 MPa. The classic parabolic stress-strain relationship for concrete was used in compression up to the peak stress. As large compression strains occurred in only a small critical region immediately below the overhang where the wall was restrained from expanding, the concrete compression stress was assumed to be constant after reaching the peak stress, i.e., concrete was assumed to be perfectly plastic. This resulted in a very stable analysis. The tensile strength of concrete was 1 MPa. The concrete secant modulus of elasticity and Poisson's ratio was 23750 MPa and 0.2, respectively. The reinforcing bars were modelled as bilinear with yield strength and ultimate strength of 400 MPa and 650 MPa, respectively, until rupture at a strain of 0.05. This rupture strain is commonly used for concrete buildings (Adebar et al., 2005).

A sufficiently tall segment of shear wall which represented between 8 to 10-story building depending on the overhang size was modelled to minimize the influence of the boundary conditions on the strains in the region of the geometrical discontinuity. A foundation fixed against rotation and translation was used. Figure 3.3 depicts the geometry and boundary conditions of the ABAQUS model.

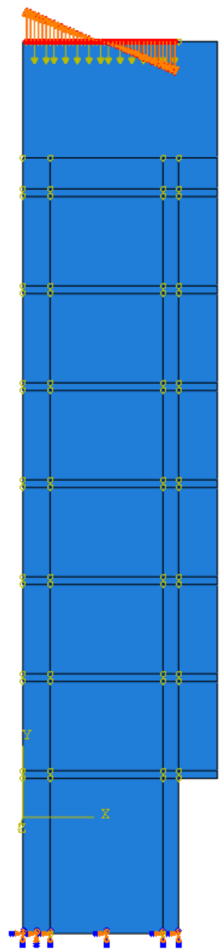

Figure 3.3 – Geometry and boundary conditions of the wall studied by ABAQUS

In the analysis by ABAQUS, the loads were applied in steps. In the first step, the axial load of 2400 kN, which corresponds to $10\% f_c' A_g$ of the lower wall was applied through the centre of the lower wall, as shown in Figure 3.3. The axial load of $10\% f_c' A_g$ is a typical value used as a compression load in shear walls in concrete buildings. In the subsequent steps, an increasing bending moment was applied as a force couple near the top of the wall. As the force couple was applied many stories above the overhang, the details of how the forces were applied did not influence the stresses and strains at the overhang.

3.3.2 VecTor2 Model

VecTor2 can predict the nonlinear response of large-scale tests of concrete shear walls subjected to earthquake loading (Palermo and Vecchio, 2007). This program uses a smeared, rotating-crack formulation for reinforced concrete based on the Modified Compression Field Theory (Vecchio and Collins, 1986) and the Distributed Stress Field Model (Vecchio, 2000). The reinforcement can be modelled as discrete truss bars or as smeared reinforcement. The second approach was used in the current study. VecTor2 accounts for compression softening due to transverse cracking, tension stiffening of reinforcement by concrete, and shear slip along crack surfaces.

VecTor2 has a limitation on the total number of elements that can be used in the model. Thus, only the one story above the overhang and the compression zone of the wall below overhang were included in the model, as shown in Figure 3.4. The wall modelled using ABAQUS is also shown in the figure with dashed lines. The length of the compression zone of the wall below the overhang was considered as 1.6 m based on the sectional analysis of the full wall.

In this model, the vertical and horizontal displacements of the wall were restrained at the top of the model (i.e., one story above the overhang), as shown in Figure 3.4. A monotonic axial load was applied at the bottom of the wall as a distributed load with an eccentricity, e, from the centre line of the lower wall. This load was equally distributed among 23 nodes over a length of 1.2 m at the compression end of the wall (see Figure 3.4). The eccentricity of the applied flexural compression force was selected such that no vertical tensile stresses in the portion of the wall modelled below the overhang. The load was applied in a force-controlled mode, in increments of 20 kN.

Low-powered rectangular membrane elements with distributed steel smeared in the element were used to model the reinforced concrete. For selecting an appropriate mesh refinement in VecTor2, Palermo and Vecchio (2007) suggested to use 14-16 elements in the shortest wall direction with a maximum aspect ratio of 1.5. Since VecTor2 uses low-powered elements, a smaller mesh size of 50 mm was selected compared to the ABAQUS model. This resulted in 32 elements with the aspect ratio of about 1 in the horizontal direction.

In addition, two 200 mm floor slabs were modelled using high tensile strength concrete with concentrated horizontal reinforcement, one at the level of the overhang and the other one spaced at 2.5 m above. Figure 3.5 shows the finite element model of the wall in FormWork. Eight concrete materials with different ratios of vertical and horizontal reinforcement and concrete tensile strength were used to represent various regions of the concrete wall in the finite element model which has been shown by different colors in Figure 3.5. Details of concrete materials used in the VecTor2 model are given in Appendix A.

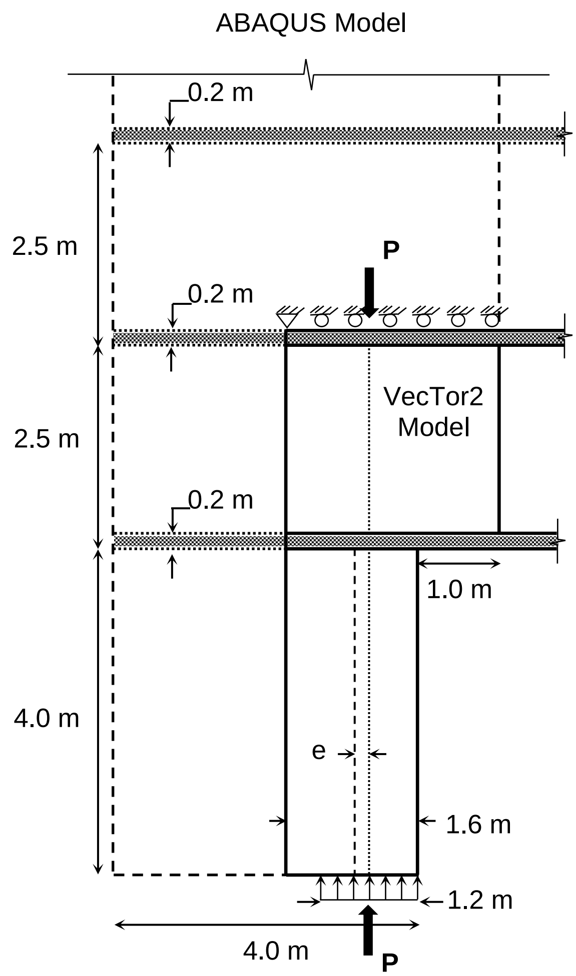

Figure 3.4 – Geometry and boundary conditions of the wall studied by VecTor2

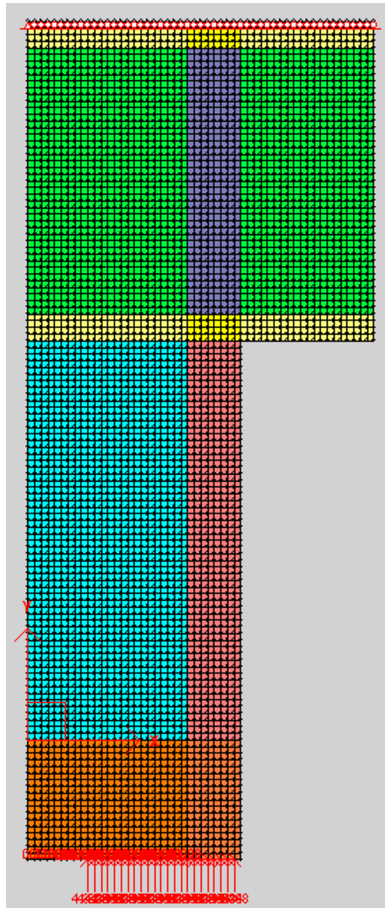

Figure 3.5 – Finite element model of the wall in FormWorks

3.4 Verification of Finite Element Models

In order to verify the finite element models of the shear wall with geometrical discontinuity, the results obtained from the two different models, the ABAQUS model and the VecTor2 model, were compared. Figure 3.6 compares the variation of concrete vertical compression strain at 50 mm below the overhang obtained from ABAQUS and VecTor2 analyses for 1.0 m overhang as the bending moment applied to the wall increases. The indicator of the applied loading, plotted on the horizontal axis, is the maximum compression linear strain (MCLS) in the uniform strain region below the discontinuity.

The results are surprisingly similar given that two nonlinear finite element models were very different in terms of the material models, the element types, mesh size and boundary conditions. The dotted line shows the variation of vertical compression strain from the linear finite element analysis. The variation of the maximum compression linear strain (MCLS) at 2 m below the discontinuity (uniform strain region of the wall) is also depicted by a thick solid line.

Figure 3.7 compares the variation of concrete horizontal tension strain at 50 mm below the overhang obtained from ABAQUS and VecTor2 analyses for 1.0 m overhang. While the vertical compression strains in the critical zone are caused by the applied vertical compression stresses, the horizontal tension strains in the region of biaxial compression stress are not associated with any applied tension stress. The horizontal tension strains were due to the transverse expansion from the large vertical compression strains. ABAQUS and VecTor2 use two different assumptions for Poisson's ratio in the nonlinear range.

In VecTor2 analysis, the variable Poisson's ratio model proposed by Kupfer et al. (1969) was used. In this model, the Poisson's ratio is constant as the compression strain reaches half of the compression strain corresponding to the peak compression stress (e.g., 0.001) and then increases nonlinearly up to 0.5 and again remains constant as the compression strain increases beyond the strain corresponding to the peak compression stress (e.g., a compression strain larger than about 0.002), as shown in Figure 3.8.

In ABAQUS analysis, the Poisson's ratio is initially constant and then increases nonlinearly even after the compression strain exceeds 0.002 (Figure 3.8). This model is consistent with observations from experiments that the volumetric expansion of concrete is due to the formation of micro and macro cracks in the cement paste around the aggregates. Therefore, the horizontal strains below the overhang obtained from the nonlinear finite element analysis by ABAQUS are considerably larger than those obtained from VecTor2 analysis. Figure 3.8 compares the Poisson's ratio models used in ABAQUS and VecTor2.

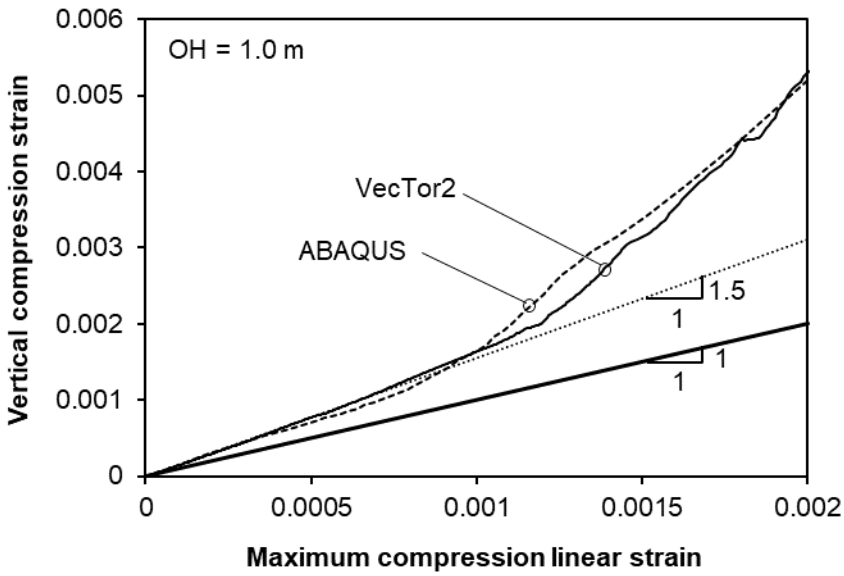

Figure 3.6 – Comparison of variation of vertical compression strain obtained from ABAQUS and VecTor2 analyses as the bending moment applied to the wall increases

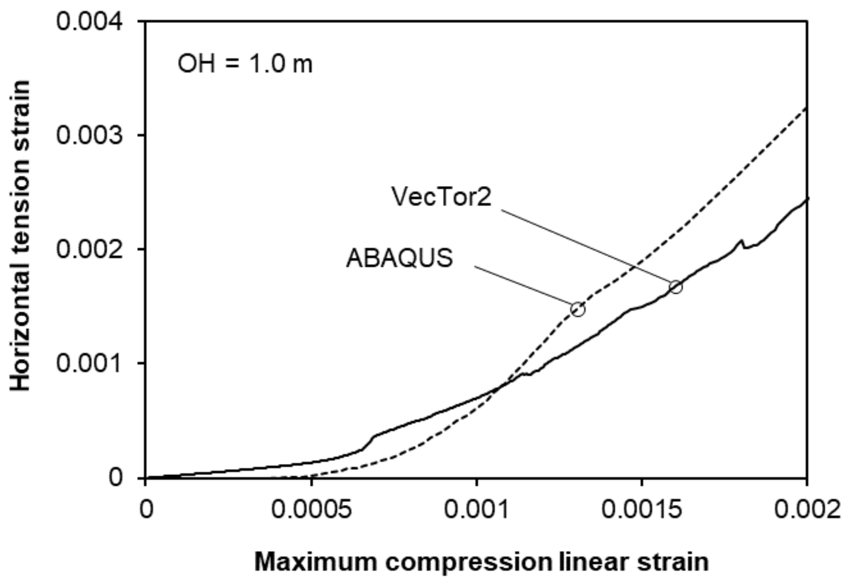

Figure 3.7 – Comparison of variation of horizontal tension strain obtained from ABAQUS and VecTor2 analyses as the bending moment applied to the wall increases

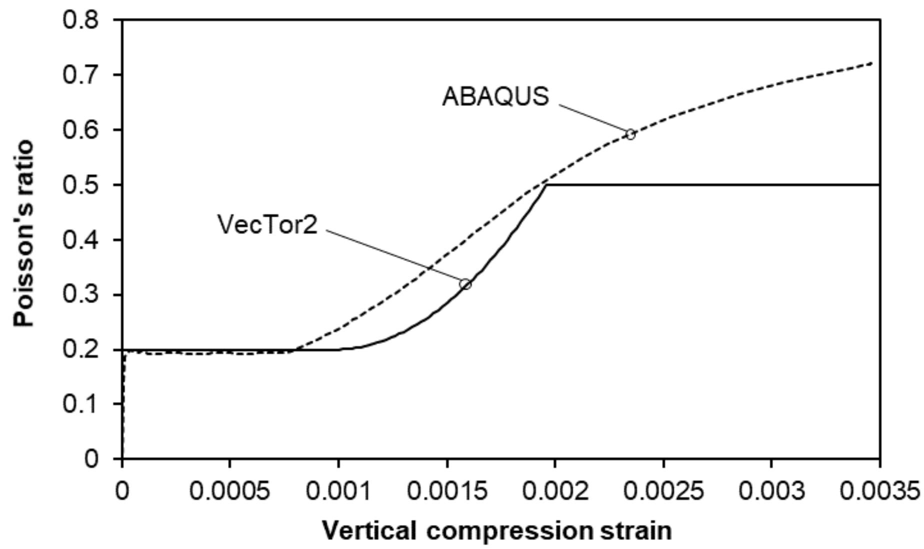

Figure 3.8 – Comparison of Poisson's ratio models used in ABAQUS and VecTor2

3.5 Analysis Results and Discussion

The results presented in this section are based on analyses using ABAQUS. Figure 3.9 illustrates the flow of concrete principal compression stress around the discontinuity. The inclination of the arrows shows the direction of the principal stress, while the length of the arrows indicates the magnitude of the principal compression stress. Above the discontinuity (not shown in figure), plane sections remain plane and the flexural compression is largest at the compression end of the wall. As this flexural compression approaches the discontinuity, it must flow diagonally towards the end of the shorter wall. The diagonal compression concentrates at the corner and is the largest in this zone.

The diagonal compression above the discontinuity is part of a shear flow that also includes diagonal tension that may crack the wall. As the wall above the discontinuity has a longer internal flexural lever-arm than the wall below, the flexural tension force in the vertical reinforcement at the left end of the wall reduces going from the lower to the upper level. The shear flow indicated by the diagonal compression flowing up and to the left from the discontinuity equilibrates this changing tension force.

Figures 3.10 and 3.11 depict the vertical profiles of strains along the compression edge of the lower wall for five different overhang lengths (OH) and two levels of maximum compression linear strain (MCLS) in the lower wall, 0.001 and 0.002, respectively. Figures 3.10(a) and 3.11(a) show the profile of vertical strains. The vertical compression strains are relatively uniform except within 200 mm below the overhang, which is equal to the wall thickness. The vertical strains increase nonlinearly within this distance. By increasing the maximum compression linear strain from 0.001 to 0.002, the vertical strains increase rapidly.

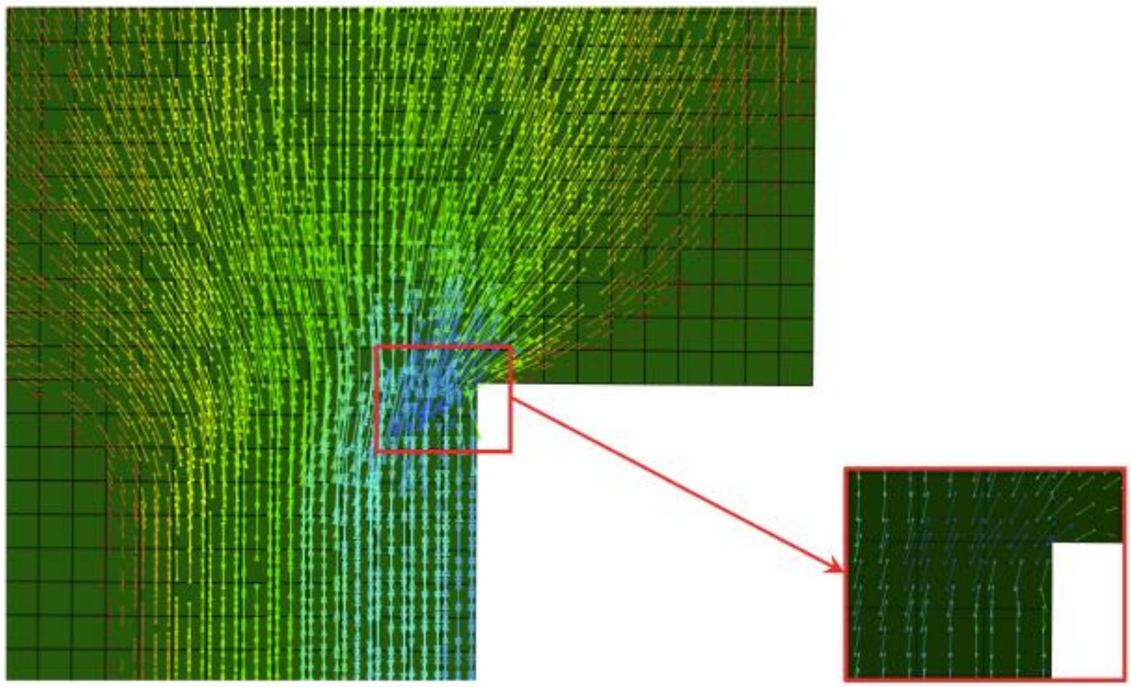

Figure 3.9 – Concrete principal compression stress directions showing the flow of forces in concrete around the discontinuity; the length and color of the arrows indicate the magnitude of the principal compression stress

The profiles of horizontal tension strains at the compression edge of the wall are shown in Figures 3.10(b) and 3.11(b). The horizontal tension strains considerably increase within 200 mm below the overhang similar to the vertical compression strain; however, the maximum horizontal strain occurs at about 50 mm below the overhang. At the point where the wall below meets the overhanging wall above (i.e., in the corner), the horizontal strain is compressive due to the diagonal compression stress flowing past the corner. The vertical profiles of strains along the compression edge of the lower wall for five different overhang lengths and the maximum compression linear strain (MCLS) of 0.0005 and 0.0015 are presented in Appendix A.

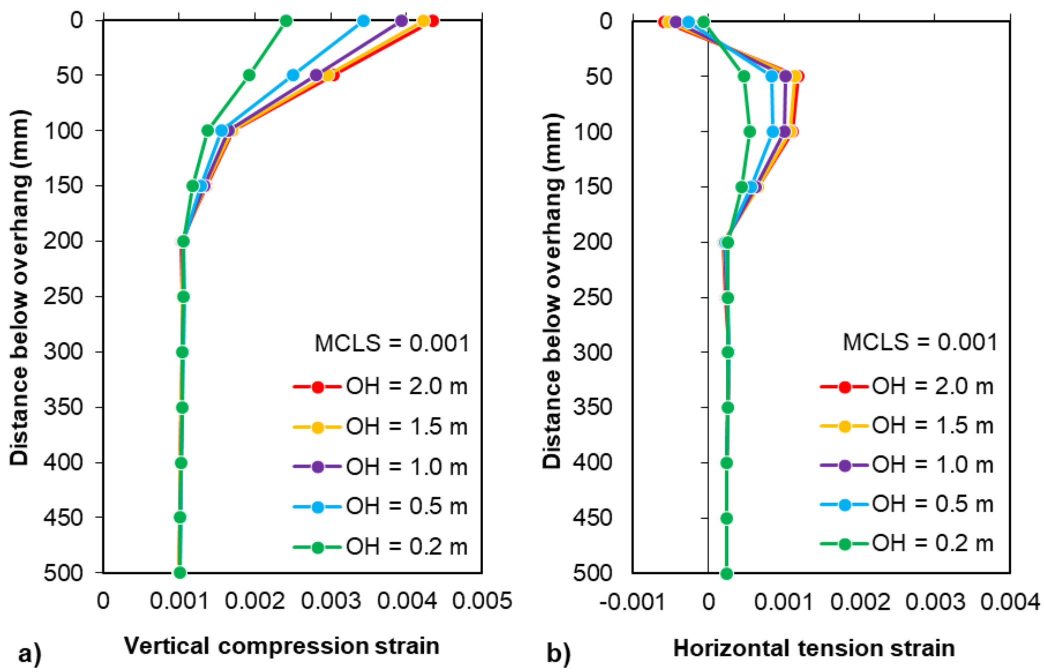

Figure 3.10 – Vertical profiles of strains for different overhang sizes when the maximum compression linear strain is 0.001: (a) vertical compression strain; (b) horizontal tension strain

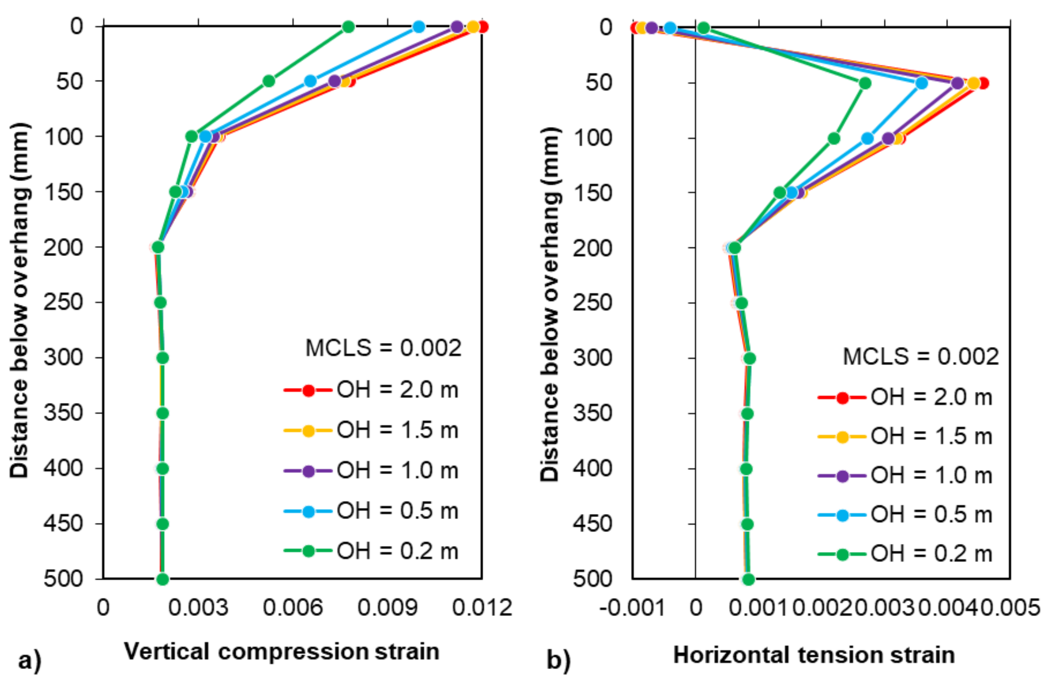

Figure 3.11 – Vertical profiles of strains for different overhang sizes when the maximum compression linear strain is 0.002: (a) vertical compression strain; (b) horizontal tension strain

Figure 3.12 compares the vertical profile of strains along the compression edge of the lower wall for the overhang length of 1.0 m and different levels of the maximum compression linear strain (MCLS) varying from 0.0005 to 0.002. The results for other overhang lengths are given in Appendix A. Figure 3.12(a) shows the profile of vertical strains while Figure 3.12(b) shows the profile of horizontal strains. The vertical and horizontal strains increase more nonlinearly below the overhang as the maximum compression linear strain (MCLS) increases from 0.0005 to 0.002.

At 400 mm below the overhang, the horizontal tension strains, shown in Figure 3.12(b), are equal to Poisson's ratio (0.2) times the vertical compression strains when the maximum compression linear strain (MCLS) is 0.001 or smaller. As the maximum compression linear strain (MCLS) increases, the horizontal tension strains increase considerably due to the nonlinear increase of the Poisson's ratio.

Figure 3.13 presents horizontal profiles of vertical strain along a 1000 mm length in flexural compression region of the lower wall for several distances below the overhang (DBO). The results are shown in Figure 3.13(a) and (b) for the case when the overhang length (OH) is 1.0 m and the maximum compression linear strain (MCLS) in the uniform strain region is 0.001 and 0.002, respectively. At 2 m below the discontinuity, there is a perfectly linear variation of vertical compression strains, shown as a thick solid line. By approaching closer to the overhang from the underside, the strain profiles tend to exhibit higher nonlinearity and the compression strains become significantly large at the outside edge of the wall.

The maximum vertical compression strain at the edge of the wall, at 50 mm below the overhang, is equal to 0.0028 and 0.0073, respectively. These correspond to the magnification factors of 2.8 and 3.7 on vertical strain from the maximum compression linear strain (MCLS) of 0.001 and 0.002, respectively. The horizontal profiles of vertical strains along the 1000 mm length in flexural compression region of the lower wall for other overhang lengths (0.2, 0.5, 1.5 and 2.0), and two levels of the maximum compression linear strain (MCLS = 0.001 and 0.002), are presented in Appendix A.

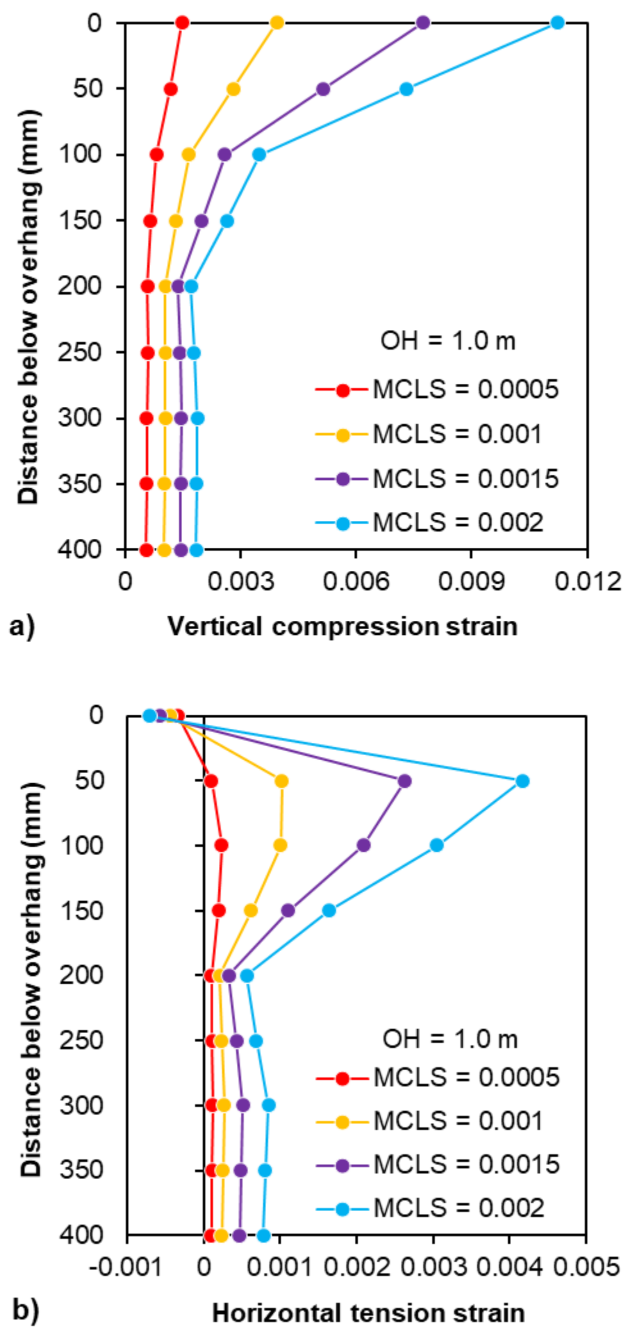

Figure 3.12 – Vertical profiles of strains for 1.0 m overhang when the maximum compression linear strain (MCLS) in the uniform strain region is 0.0005, 0.001, 0.0015, and 0.002: (a) vertical compression strain, and; (b) horizontal tension strain

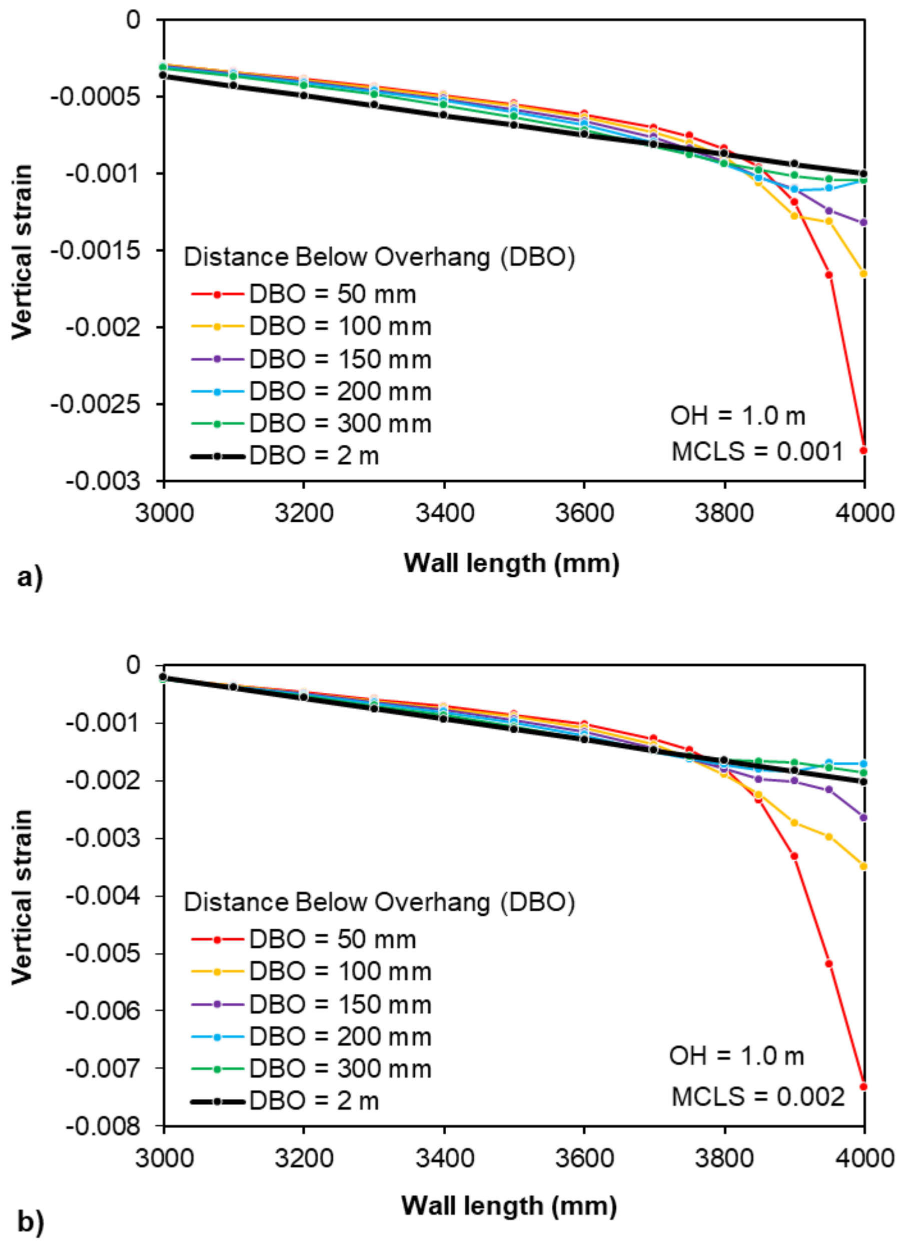

Figure 3.13 – Horizontal profiles of vertical compression strain in flexural compression region of lower wall for overhang length of 1.0 m and the maximum compression linear strain (MCLS) of: (a) 0.001, and (b) 0.002

Figure 3.14 shows the horizontal profile of vertical compression strains along a 200 mm length of the lower wall below the discontinuity for five different overhang lengths (OH). All results are shown at 50 mm distance below overhang (DBO) and for the two levels of maximum compression linear strain (MCLS), 0.001 and 0.002, upper and lower graphs, respectively. Note that the scales of the vertical (strain) axes are very different in upper and lower parts. The linear variation of the vertical compression strain at 2 m below the discontinuity is also included in Figure 3.14, shown by a thick solid line.

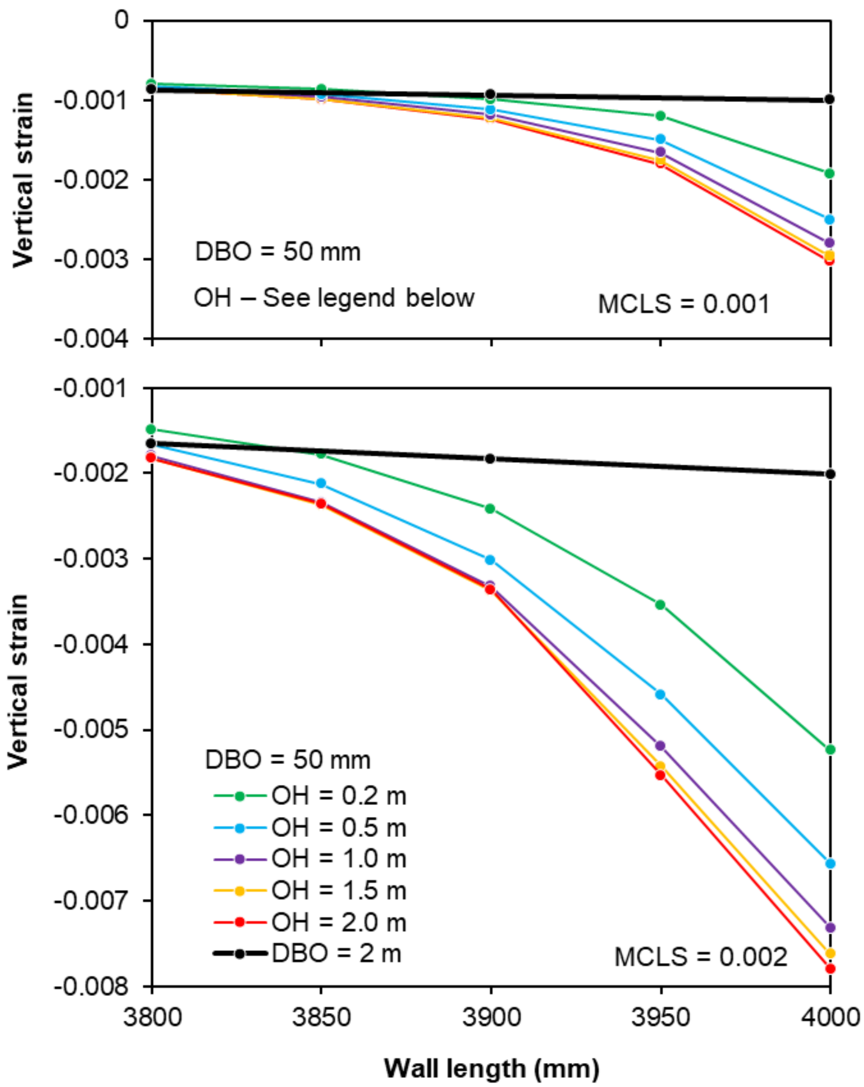

Figure 3.14 – Horizontal profiles of vertical compression strain at 50 mm below the overhang for different overhang lengths and two levels of the maximum compression linear strain (MCLS), 0.001 and 0.002

Figure 3.14 indicates that the maximum vertical compression strain is magnified due to the presence of overhang (geometrical discontinuity) in the wall. For five different overhang lengths of 0.2, 0.5, 1.0, 1.5 and 2.0, the magnification factors, defined as the ratio of the maximum compression strain at 50 mm distance below the overhang to the maximum compression linear strain (MCLS), are equal to 1.92, 2.51, 2.8, 2.97, and 3.03, respectively, when the maximum compression linear strain is 0.001. The maximum compression strains are magnified by a factor of 2.62, 3.29, 3.66, 3.82, and 3.90, respectively, for the case when the maximum compression linear strain (MCLS) is 0.002. According to Figure 3.14, it should be noted that as the maximum compression linear strain increases from 0.001 to 0.002 (a factor of 2), the vertical compression strains increase by a larger factor of 2.6.

From Figure 3.14, it is observed that the maximum vertical compression strain increases as the overhang length increases which is expected. One surprising result is how the magnification of the strain does not increase significantly as the length of the overhang increases. According to Figure 3.14, the magnification of vertical compression strain is large for a small overhang length and which does not increase noticeably with increasing overhang length. When the overhang length is only 0.2 m (small overhang length), the vertical compression strain is magnified by a factor of 1.9 and 2.6 for the maximum compression linear strain (MCLS) of 0.001 and 0.002, respectively.

When the overhang length is increased by a factor of 10 from 0.2 to 2.0 m, the corresponding magnification of the maximum vertical compression strain increases from 1.9 to 3.0 (factor of 1.6) when MCLS = 0.001, and from 2.6 to 3.9 (factor of 1.5) when MCLS = 0.002. Note that the maximum compression strains are very similar whether the overhangs are 1.0, 1.5 or 2.0 m long. That is, once the overhang is 1.0 m long, increasing the overhang length seems to have little influence on the magnification of the compression strains. The strain magnification factors are discussed further in reference to Figure 3.18.

Figure 3.15 illustrates the variation of vertical compression strains and horizontal tension strains at 50 mm below the overhang as the bending moment applied to the wall increases. The horizontal axis represents the maximum compression linear strain (MCLS) which is an indication of the applied loading. The dashed lines show the results from the linear finite element analysis which is commonly used by design engineers.

Figure 3.15(a) shows the variation of the vertical compression strains. The variation of the maximum compression linear strain (MCLS) at 2 m below the discontinuity is also shown in Figure 3.15(a) by a thick solid line. Figure 3.15(a) indicates that the vertical compression strain linearly increases for all five different overhang lengths up until the maximum compression linear strain (MCLS) in the uniform strain region is about 0.0008. Up to this level, the results obtained from linear and nonlinear finite element analyses are identical. As the maximum compression linear strain (MCLS) increases beyond 0.0008, the vertical strains increase nonlinearly until the maximum compression linear strain reaches about 0.0012. Beyond this point, the vertical strains continue to increase significantly in a linear way for all five overhang sizes. According to Figure 3.15(a), the vertical compression strains can reasonably be approximated by a trilinear curve.

The variation of horizontal tension strains is presented in Figure 3.15(b). It is indicated that the magnification of the horizontal strains occurs earlier and is larger compared to the vertical compression strains. A similar result that can also be inferred from Figure 3.15 is that the magnification of the strain does not increase significantly as the size of the overhang increases.

Moreover, an interesting observation is how the nonlinearity of the horizontal strains occurs at a smaller level of the maximum compression linear strain (MCLS) and how the deviation from the linear prediction is significantly larger than observed with the vertical compression strains. This can be attributed to the fact that the nonlinear horizontal strains are the product of the nonlinear vertical strains and a nonlinearly increasing Poisson's ratio.

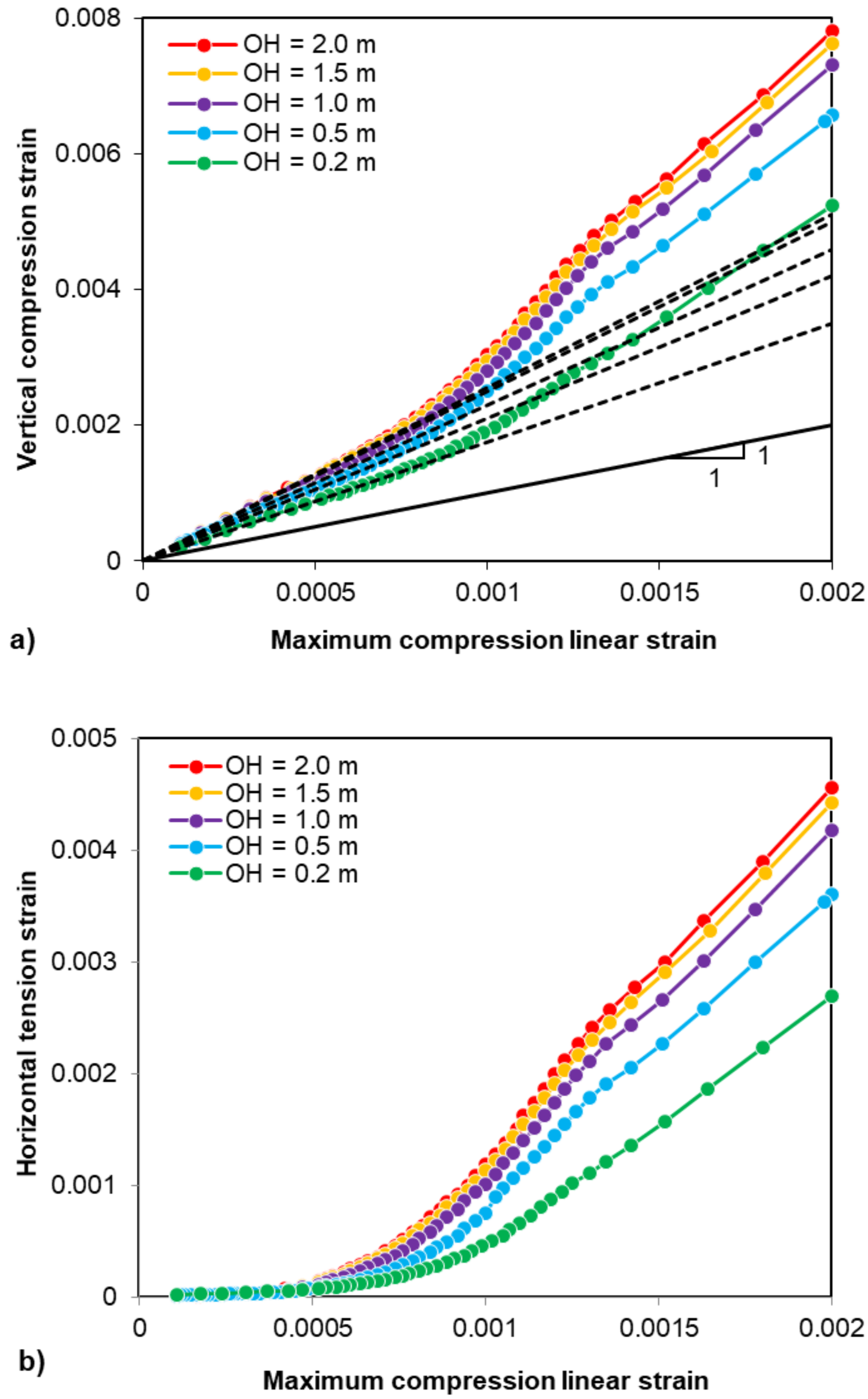

Figure 3.15 – Variation of concrete strains at face of wall at 50 mm below the overhang as the bending moment applied to the wall varies: (a) vertical compression strain, and; (b) horizontal tension strain

Figure 3.16 presents a contour of horizontal strains when the overhang size is 1.0 m, and the maximum compression strain in the uniform strain region is 0.002. The floor slab prevents horizontal expansion of the wall along the underside of the overhang. The horizontal strains are maximum at 50 to 100 mm below the overhang. The contours of horizontal strains shown in Figure 3.16 correlate very well with the locations of concrete crushing failures observed in such walls after the 2010 Chile Earthquake.

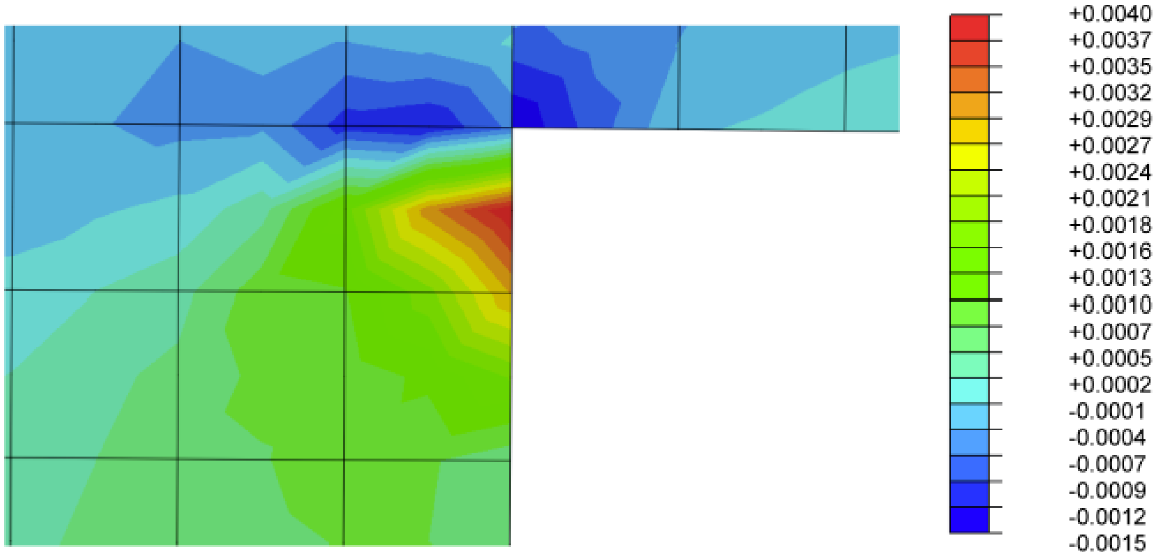

Figure 3.16 – Contours of horizontal stains for a 1.0 m overhang when the maximum compression strain in the uniform strain region is 0.002

An important question is when the concrete in a wall with such an overhang will begin to fail in compression. The experiments on thin walls suggest that if the end of the wall does not contain any ties, a brittle failure of concrete could happen at a very low compression strain (Adebar, 2013). If the end of the wall does contain reinforcement that will prevent a sudden brittle failure, the compression strain to cause a concrete compression failure will be larger. Numerous tests have been conducted at the University of Toronto on reinforced concrete wall elements to study the influence of biaxial strains on concrete compression failures (Vecchio and Collins, 1986). These tests have clearly demonstrated that what controls concrete compression failures in walls is the transverse tension strain. The larger the transverse tension strain, the softer and weaker the concrete is in compression. This phenomenon is closely related to the influence of confinement reinforcement. Confinement reinforcement prevents the lateral expansion of concrete, i.e., it reduces the transverse tension strain. Thus, the large horizontal strains that occur in the walls immediately below an overhang discontinuity are very important.

Figure 3.17 presents a summary of the principal strain components in the region with large inelastic strains immediately below the overhang for the case that the maximum compression linear strain (MCLS) in the uniform strain region is 0.002. The principal strains were determined from the strain components at the integration points of finite elements. The principal compression strain is plotted versus the principal tension strain. The combination of large principal tension strain with large principal compression strain is certain to result in significant damage of the concrete (Vecchio and Collins, 1986). The summary of the principal strains when the maximum compression linear strain is 0.001, is presented in Appendix A.

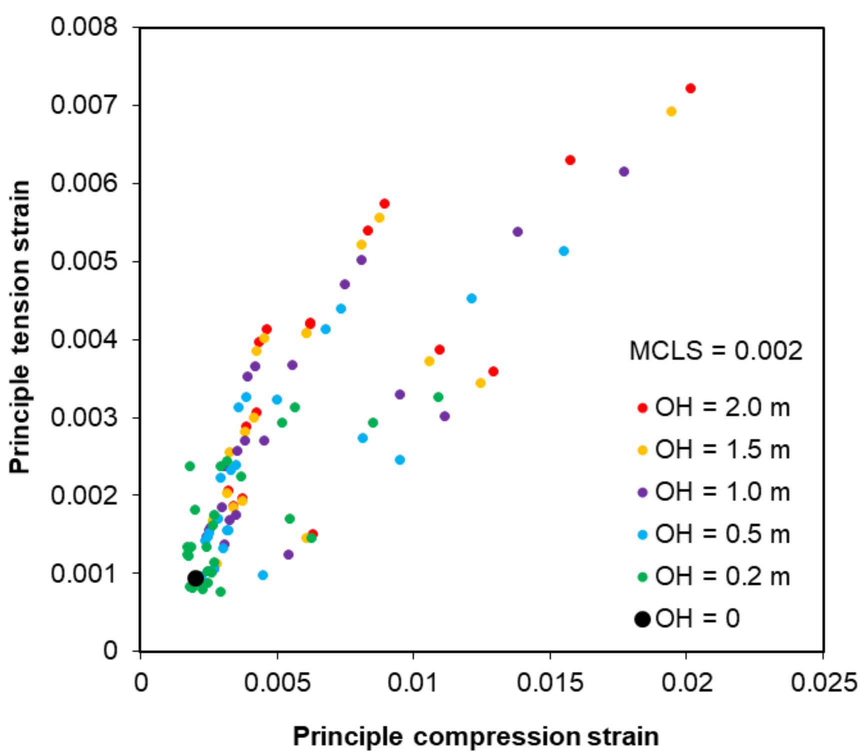

Figure 3.17 – Principal strain components in the wall immediately below the overhang when the maximum compression strain in the uniform strain region is 0.002

Amplifications of vertical compression strains at 50 mm below the overhang are shown in Figure 3.18. As indicated, there is significant amplification of concrete strains immediately below the geometrical discontinuity. In fact, large amplification of vertical compression strains occurred at small overhang size and did not increase considerably as the overhang became much larger. Figure 3.18(a) depicts the amplification of vertical compression strain at 50 mm below the overhang relative to the maximum compression linear strain (MCLS) in the uniform strain region. When the maximum compression linear strain (MCLS) increases up to 0.0008, the vertical compression strain was magnified by a constant factor of about 1.8, 2.2, 2.4, 2.5, 2.6 for the overhang length of 0.2, 0.5, 1.0, 1.5 and 2.0 m, respectively. By increasing the applied bending moment, the amplification of the vertical compression strain increases nonlinearly.

Figure 3.18(a) shows when the maximum compression linear strain (MCLS) increase to 0.002, the vertical compression strain is 2.62, 3.29, 3.66, 3.82 and 3.90 times larger than the maximum compression linear strain in the uniform strain region. It is the same result observed in Figure 3.14. The trilinear nature of the amplification is again clearly visible in Figure 3.18: constant amplification up to the maximum compression linear strain equal to 0.0008, rapidly increasing amplification as the maximum compression linear strain increases from 0.0008 to 0.0012, and smaller increase in amplification as the maximum compression linear strain increase above 0.0012.

Figure 3.18(b) presents the amplification of the vertical compression strain at 50 mm below the overhang obtained from the nonlinear finite element analyses relative to the one obtained from the linear finite element analysis. As shown in Figure 3.18(b), the magnification factor is constant and about 1 when the maximum compression linear strain (MCLS) is smaller than 0.0008. This explains that the vertical compression strain obtained from linear and nonlinear finite element analyses are almost identical up to this point. Beyond this point, the vertical compression strain from nonlinear analyses significantly increases in a nonlinear way. The trilinear nature of the amplification is again clearly visible in Figure 3.18: constant amplification up to an MCLS equal to 0.008, rapidly increasing amplification as MCLS increases from 0.0008 to 0.0012, and smaller increase in amplification as MCLS increases above 0.0012.

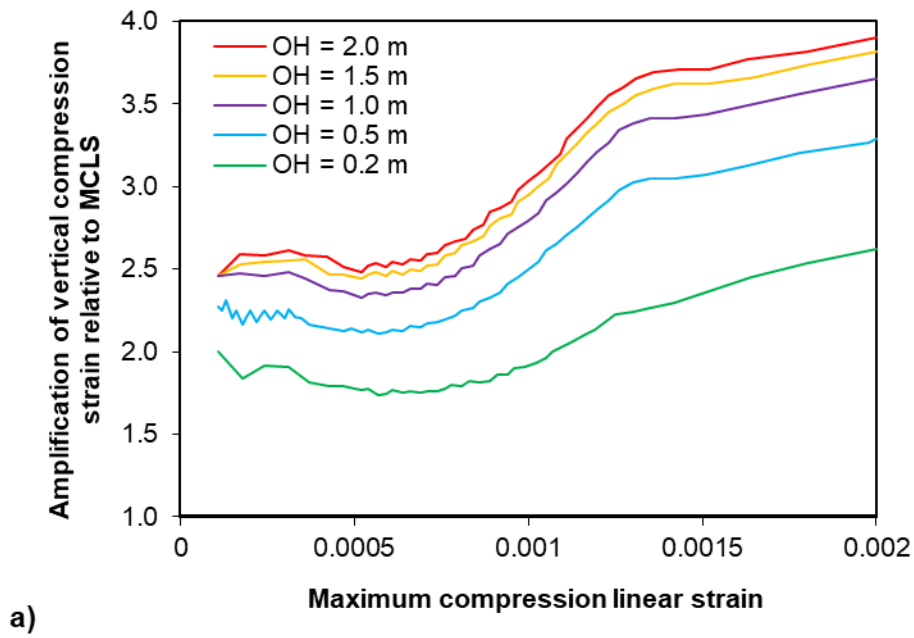

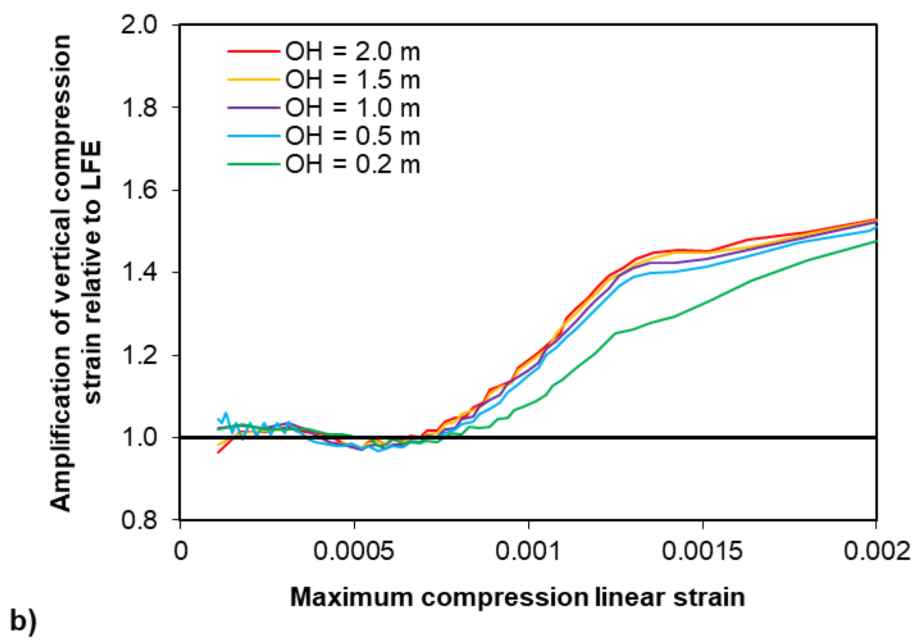

Figure 3.18 – Amplification of the vertical compression strain at 50 mm below the overhang relative to: (a) the maximum compression linear strain (MCLS) in the uniform strain region, and; (b) the vertical compression strain at 50 mm below the overhang obtained from the linear finite element analyses

Figure 3.18(b) demonstrated that the vertical compression strain at 50 mm below the overhang is magnified by a factor of about 1.5 for all five different overhang lengths when the maximum compression strain (MCLS) reaches 0.002. Figure 3.18(b) can be used to develop a simplified solution for estimating the magnification of the vertical compression strains. In fact, the vertical compression strain accounting for material nonlinearity can be safely estimated by applying a magnification factor of 1.5 to the results of linear finite element analysis.

If the maximum compression strains in the critical zone below an overhang become too large, the concrete will crush in that zone. If a wall sustains such damage during one cycle of an earthquake, the damaged wall will be even more susceptible to further damage in a subsequent cycle. Thus, the compression strains in the wall must be limited to prevent the start of damage. Tests on thin wall elements have demonstrated that crushing in a thin wall may occur at strains lower than 0.002 (Adebar, 2014). The critical zone below an overhang is subjected to biaxial compression stress, rather than uniaxial compression as applied in the wall element tests, and this suggests a higher limit on the vertical compression strain. A range of possible limits on the maximum vertical compression strain in the critical zone (of a wall without a large amount of confinement reinforcement) is 0.002 to 0.004.

Figure 3.19 presents the maximum compression linear strain (MCLS) in the uniform strain region below overhang (i.e., at 2.0 m below overhang) when the vertical compression strain at 50 mm below overhang is limited to 0.002 and 0.004. The results are shown for different lengths of overhang. Rectangular and circular points in Figure 3.19 show the results obtained from the analyses for strain of 0.002 and 0.004, respectively, which are connected by lines in order to better visualize the decreasing trend of the maximum compression linear strain.

Figure 3.19 illustrates that limiting the maximum vertical compression strain below overhang results in significant reduction in the maximum compression linear strain (MCLS). This reduction is about 50% (from 0.002 to 0.001) for 0.2 m overhang and about 60% (from 0.002 to 0.0008) for 2.0 m overhang when the vertical compression strain at 50 mm below overhang is limited to 0.002, and it is about 60% (from 0.004 to 0.0016) for 0.2 m overhang and 70% (from 0.004 to 0.0012) for 2.0 m overhang when the vertical compression strain at critical zone is limited to 0.004. In the other words, to limit the maximum vertical compression strain in the wall immediately below the overhang to 0.002, the maximum compression linear strain in the wall below the overhang must be limited to 0.001 for a 0.2 m overhang, and to 0.0008 for a 2.0 m overhang. In order to limit the maximum compression vertical strain to 0.004, the maximum compression linear strain must be limited to 0.0016 for a 0.2 m overhang and 0.0012 for a 2.0 m overhang.

A simple safe limit for the maximum compression linear strain in a wall below an overhang is 0.001 in order to limit the vertical compression strain in the zone below the overhang to 0.004. This simple rule is consistent with the observation from Figure 3.18(a) that an upper-bound (total linear and nonlinear) magnification of the vertical compression strains is equal to 4.0.

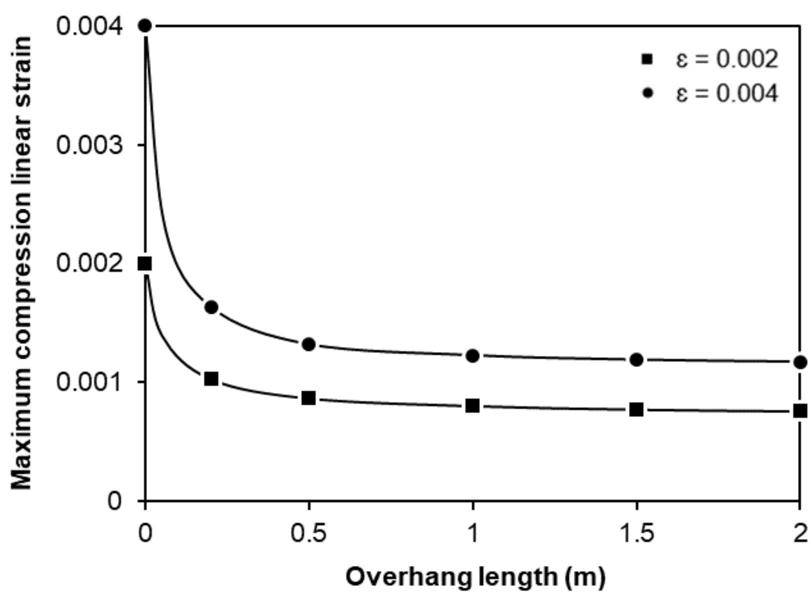

Figure 3.19 – Maximum compression linear strain (MCLS) for different overhang lengths when the vertical compression strain at 50 mm below overhang is 0.002 and 0.004

Figure 3.20 examines how the limit on the maximum vertical compression strain influences the bending moment capacity and curvature capacity of the wall below a 2.0 m long overhang. The effects of the axial compression applied to the wall and the reinforcement ratio at the wall boundaries were investigated. As aforementioned, the vertical compression strain at critical zone below overhang is limited to 0.002 or 0.004 depending on the confinement provided at the compression end of the wall.

Figure 3.20(a) shows the bending moment capacity ratio of the wall which was defined as the ratio of bending moment corresponding to the maximum compression linear strain (MCLS) at 2 m below overhang when the maximum compression strain at 50 mm below overhang is limited to 0.002 or 0.004 to the bending moment capacity of the wall (the ultimate compression strain of concrete is considered as 0.0035 according to CSA-A23.3).

Figure 3.20(b) shows the same ratio for the curvature of the wall which is used to calculate the displacement capacity of the wall. Rectangular and circular points in Figure 3.19 show the results obtained from the analyses which are connected by lines in order to better visualize the varying trend of the moment capacity and curvature capacity of the wall versus the axial compression load applied to the wall. Two different reinforcement ratios at the wall boundaries, 6-20M (2.2% vertical reinforcement) and 8-20M (3% vertical reinforcement) were considered for the analysis. The results of the wall with different overhang lengths (0.2, 0.5, 1.0 and 1.5 m) are presented in Appendix A.

According to Figure 3.20(a), the moment capacity of the wall reduces by only 20% when the maximum vertical compression strain at 50 mm below overhang is limited to 0.004 and the effect of axial load changing from 0% to $15\% f_c' A_g$ is negligible. However, when the maximum vertical compression strain is limited to 0.002, the moment capacity reduces by 30% and 40% for the axial load of 0% and $15\% f_c' A_g$, respectively. In addition, the analysis results have shown that the reinforcement ratio at the wall boundaries has quite small influence on the moment capacity of the wall.

The geometrical discontinuity (overhang) significantly influences the displacement capacity of the wall, as shown in Figure 3.20(b). The curvature ratio reduces by about 75% and 90% when the maximum vertical compression strain at 50 mm below overhang is 0.004 and 0.002, respectively. The level of axial load and reinforcement ratio at wall boundaries have negligible influences on the displacement capacity of the wall.

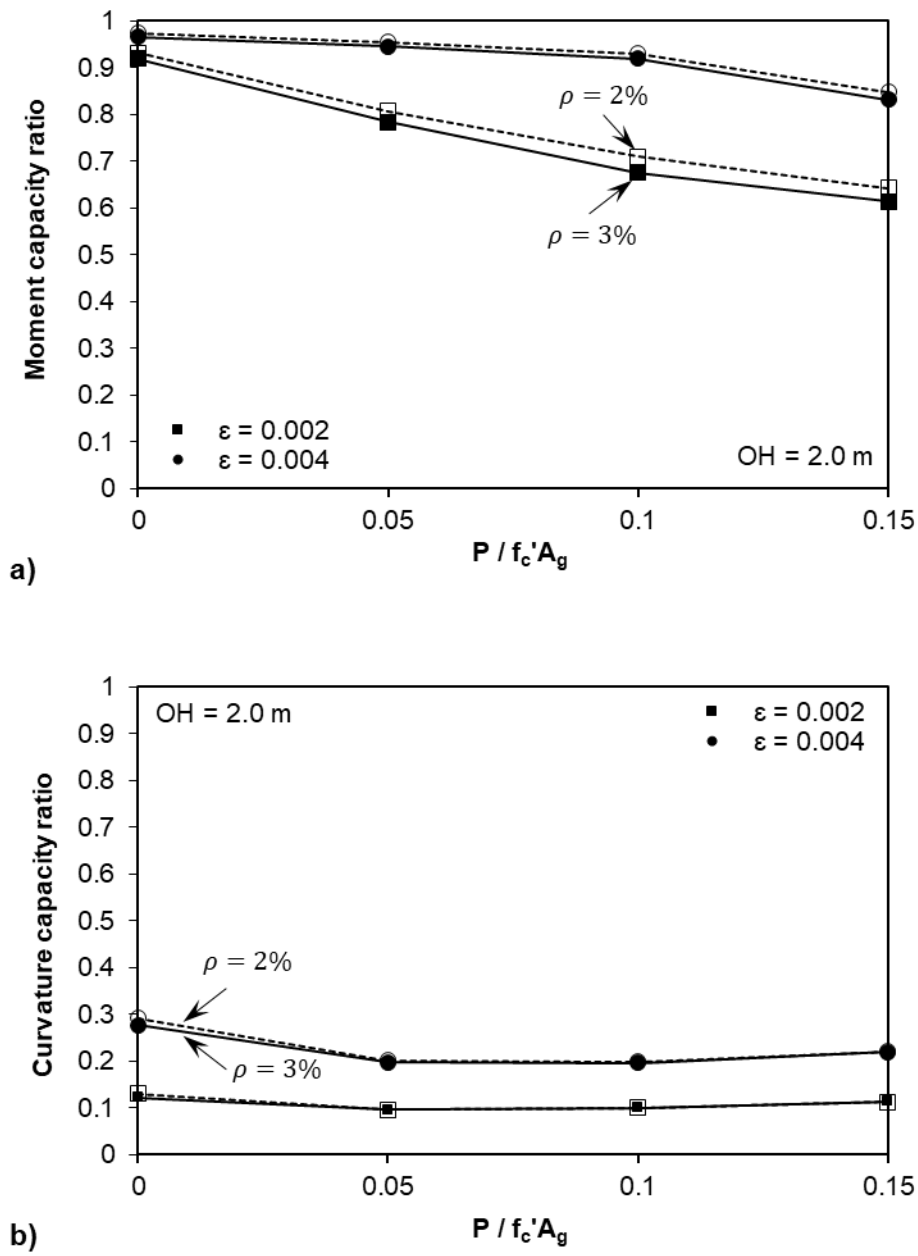

Figure 3.20 – Effect of axial load and allowable strain level at 50 mm below overhang on: (a) the moment capacity, and; (b) the curvature capacity of the wall

3.6 Summary and Conclusions

A wall overhang discontinuity occurs when the length of a shear wall is smaller in the lower level compared with the level above, and the shear wall above overhangs the shear wall below. The geometrical discontinuity due to the overhanging wall causes significant amplification of concrete strains immediately below the overhang. The flexural capacity of the shear wall can be evaluated using a plane-sections analysis of the shorter-length wall; however, the maximum compression strains in the wall below cannot be estimated by such an analysis.

Nonlinear finite element analysis was used to investigate the magnification of concrete strains because of the geometrical discontinuity caused by an overhanging wall. Five different sizes of overhangs (length of overhang) were investigated in this study. Two different computer programs were used to develop finite element models. VecTor2 was used to verify the results from ABAQUS and to provide additional insight into the biaxial strains in the concrete wall immediately below the overhang. The influence of the overhanging wall on the strength (bending moment capacity) and flexibility (curvature capacity) of the wall was examined considering the effect of the axial compression applied on the wall and the reinforcement ratio at the wall boundaries.

The analysis results demonstrated that the vertical compression strains along the compression edge of the wall are relatively uniform except within 200 mm below the overhang. The vertical strains increase nonlinearly within this distance. The horizontal tension strains also increase significantly; however, the maximum horizontal strain occurs at 50 mm below the overhang. The floor slab prevents horizontal expansion of the wall along the underside of the overhang. Thus, the horizontal strain is compressive due to the diagonal compression stress flowing past the corner where the wall below meets the overhanging wall above.

The results show that the geometrical discontinuity creates a large magnification of the strains in the shorter-length wall below the overhang. Surprisingly, large magnifications occur at very small overhang sizes and do not increase significantly as the overhangs become very large. For example, when the maximum compression linear strain (MCLS) in the uniform strain region below the discontinuity (which is indicator of applied loading) was 0.001, the magnification of the vertical strains was 1.9, 2.5, 2.8, 3.0 and 3.0 for overhang sizes of 0.2, 0.5, 1.0, 1.5 and 2.0 m.

The magnification of the horizontal tension strains is even larger in the critical region immediately below the discontinuity. The horizontal tension strains in the region of biaxial compression stress are not associated with any applied tension stress and are due to the transverse expansion from the large vertical compression strains. Such large horizontal tension strains reduce the ability of the concrete in the wall to resist vertical compression. It is believed that the combination of large horizontal tension strains and amplification of vertical compression strains explain the concrete compression failures observed in many thin shear walls with such discontinuities during the 2010 Chile Earthquake.

An interesting observation is how the nonlinearity of the horizontal strains occurs at a smaller level of the maximum compression linear strain (MCLS) and how the deviation from the linear prediction is significantly larger than observed with the vertical compression strains. This can be attributed to the fact that the nonlinear horizontal strains are the product of the nonlinear vertical strains and a nonlinearly increasing Poisson's ratio.

Analysis results was used to develop a simplified solution for estimating the magnification of the vertical compression strains due to the nonlinear material behaviour. Up to the maximum compression linear strain (MCLS) of 0.002, which is a large value for a wall with an overhang, an amplification factor of 1.5 applied to the results of a linear FE analysis provides a safe estimate of the vertical compression strains accounting for nonlinear material behaviour. With this amplification factor, a linear FE analysis can be used to make an estimate of the maximum vertical compression strains.

A possible approach to designing a shear wall with an overhang is to limit the maximum compression linear strain to a value that prevents the magnified compression strain below the overhang from exceeding an appropriate limit. A range of possible limits on the maximum vertical compression strain in the critical zone (of a wall without a large amount of confinement reinforcement) is 0.002 to 0.004. According to the analysis results, to limit the maximum vertical compression strain in the wall immediately below the overhang to 0.002, the maximum compression linear strain in the wall below the overhang must be limited to 0.001 for a 0.2 m overhang, and 0.0008 for a 2.0 m overhang. In order to limit the maximum compression vertical strain to 0.004, the maximum compression linear strain must be limited to 0.0016 for a 0.2 m overhang and 0.0012 for a 2.0 m overhang.

A simple safe limit that can easily be remembered is to limit the maximum compression linear strain in a wall below an overhang to 0.001 in order to limit the vertical compression strain in the zone below the overhang to 0.004. This simple rule is consistent with the observation from the analysis result that an upper-bound (total linear and nonlinear) magnification of the vertical compression strains is equal to 4.0.

Limiting the maximum compression linear strain in a wall below an overhang will limit the strength and the flexibility of the wall. According to analysis results, the bending moment capacity of the wall reduces by only 20% when the maximum vertical compression strain in the critical zone is limited to 0.004 pretty much independent of the axial compression applied to the wall. If the compression strain is to be limited to 0.002, the bending moment reduces by 30% at low axial compression levels and reduces by 40% at high axial compression levels.

The influence on the curvature capacity is much more significant. Independent of the axial compression applied to the wall, the curvature capacity reduces by 75% and 90% when the maximum compression strain is limited to 0.004 and 0.002, respectively. In addition, the analysis results have shown that the reinforcement ratio at the wall boundaries has negligible influence on the bending moment and curvature capacities of the wall.

Chapter 4

Effective In-Plane Stiffness of Concrete Diaphragms

4.1 Introduction

Concrete shear walls are popular seismic force resisting systems for high-rise buildings as they provide proper lateral drift control during earthquakes and are relatively simple to construct. A typical concrete high-rise building has shear walls located near the centre of the building plan to form the core of the building. The core shear wall system in a high-rise concrete building is known to be an efficient solution to both structural and architectural demands. This system with flat floor slabs has been increasingly used in North America. In most high-rise shear wall buildings, the core walls extend from the top of the tower down to the foundation and are supported near the base by a structure, which is entirely or partially below the base. In the upper levels of the buildings, the concrete floor slabs are usually modelled as rigid diaphragms that force the shear walls and gravity-load columns to undergo the same lateral deformation. Figure 4.1 shows the core shear wall system in a typical high-rise concrete building including the below grade portion of the building.

In the lower levels of the buildings, the large underground structure is surrounded by rigid perimeter foundation walls, as shown in Figure 4.1. The purpose of considering below-ground structures is typically to provide the required space for vehicle parking and shopping and commercial centers. The perimeter foundation walls possess high in-plane rigidity due to large dimensions, resulting in a quite rigid base structure. The foundation walls of high-rise buildings are significantly stiffer than the central core walls. As a result, the lateral seismic forces in high-rise walls are transferred to the perimeter foundation walls by interconnecting floor diaphragms below the base. The multiple levels of floor diaphragms also transfer the over-turning moments from the high-rise walls to the perimeter foundation walls.

If the floor slabs within a podium structure or below grade are modelled as rigid diaphragms, a large portion of the overturning moment in the core walls will be transferred into the perimeter foundation walls, rather than be transferred down to the foundation supporting the core walls. The reduction in bending moment in the high-rise walls is accompanied by a corresponding reverse shear force in the wall section below ground and the maximum bending moment (flexural plastic hinge) occurs above the diaphragms. This is commonly referred to as the 'backstay effect' phenomenon in high-rise concrete shear wall buildings.

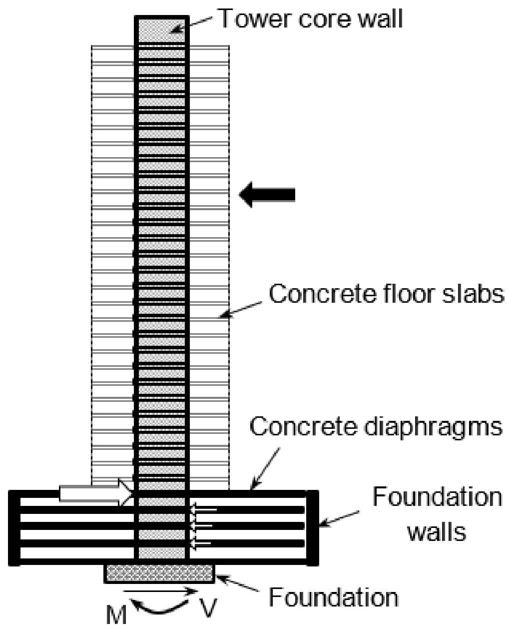

Figure 4.1 – Backstay forces in a high-rise concrete core wall building; adapted from ATC-72-1 (2010)

One of the important parameters that significantly affects the magnitude of the reverse shear force in the first level below the grade of high-rise structures is the stiffness of floor diaphragms. In fact, if the flexibility of the diaphragms is accounted for, due to cracking of the diaphragms, the lateral force and overturning moment that is transferred out of the core walls will be significantly reduced and the demands on the foundation of the core walls increased (Bevan-Pritchard, Man and Anderson, 1983; and Rad and Adebar, 2009).

Therefore, an important part of the seismic design of high-rise core wall buildings involves estimating the reduction in diaphragm stiffness due to forces developed within the diaphragms that connect the tower walls to a podium structure or below-grade basement walls. These diaphragms are usually modelled as elastic members, and the choice of effective stiffness significantly influences how much force will go into the backstay force path (podium or below-grade walls) versus the tower wall foundations. Given the difficulty in making accurate estimates, upper and lower-bound stiffness properties are usually used to bound the solution.

In the current study, nonlinear finite element (NLFE) analysis was employed to study the behaviour of concrete diaphragms subjected to backstay forces and to investigate the reduction in shear and flexural stiffness of diaphragms. The finite element analyses were performed using computer program VecTor2 which has a state-of-the-art material model for cracked concrete subjected to in-plane shear and normal forces. The analytical model was verified by comparing predictions against the results of a diaphragm test by Nakashima (1983).

The validated NLFE model was used to examine the influence of amount of diaphragm reinforcement (ranging from 0.5% to 2.0%) and relative spans of the diaphragm (parallel and perpendicular to the backstay forces). A simplified procedure is presented for estimating the trilinear load-deformation relationship of concrete diaphragms, from which the effective shear and flexural stiffnesses can be calculated at any backstay force level. In addition, simple and rigorous models are proposed for estimating the reduction in shear and flexural stiffnesses of concrete diaphragms for any backstay force level.

4.2 Background Literature

Few studies have been conducted on the backstay effect in a high-rise core shear wall below ground where large reverse shear forces due to the presence of rigid diaphragms and foundation walls is of considerable concern to engineers.

Bevan-Pritchard, Man and Anderson (1983) carried out a study on the reverse shear force at the sub-grade levels of a core shear wall in a high-rise concrete building subjected to seismic forces. Figure 4.2 shows the plan and elevation views of the investigated subgrade structure.

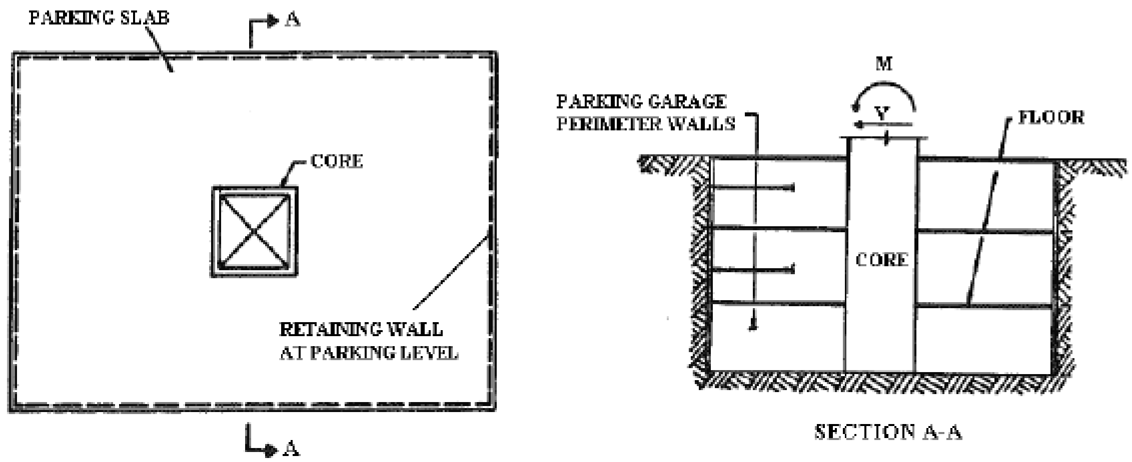

Figure 4.2 – Plan and elevation views of the sub-grade structure (Bevan-Pritchard, Man and Anderson, 1983)

They modelled the diaphragms that attached the core wall to the foundation walls below ground using line springs which accounted for in-plane bending, axial and shear deformation of parking floor slabs (Figure 4.3). In order to investigate the parameters that have most influence on the shear force distribution at sub-grade levels of the core wall, they performed several linear analyses. The influence of degree of fixity below the core wall foundation was examined by considering two extreme cases: a fully fixed support and a fully pinned support. The effect of stiffness of foundation walls and concrete floor slabs as well as the effect of shear deformation of the core wall on the magnitude of the reverse shear force were investigated.

The analysis results indicated that flexural and shear stiffness values of the foundation walls have little influence on magnitude of the shear force and bending moments developed in the core wall below ground. This was attributed to the large stiffness of foundation walls relative to the core wall. In addition, it was illustrated that the effect of shear deformation of the core wall was significant when perimeter foundation walls and the concrete floor slabs were assumed infinitely rigid.

They also proposed a formula for determining the stiffness of the springs used to model the floor diaphragms. In order to study the distribution of shear force and bending moment in the core wall below ground, they used upper and lower bounds equal to 100,000 kips/in and 3,000 kips/in for diaphragm stiffness. Comparison of obtained results showed that major influence on shear force distribution was caused by diaphragm stiffness rather than the shear deformation of core wall.

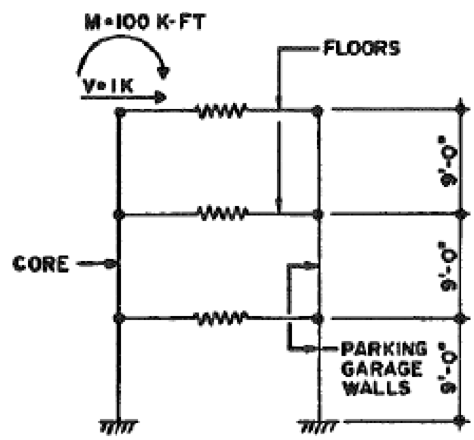

Figure 4.3 – Model used to study sub-grade structure by Bevan-Pritchard, Man and Anderson (1983)

According to this study, it was concluded that the actual behaviour of the sub-grade structure cannot be properly captured by using the assumption of rigid floor diaphragms. It was found that the stiffness of concrete diaphragms below the base level and the degree of fixity below the core wall foundation were the most important parameters that influence the distribution of shear force below ground. The study carried out by Bevan-Pritchard, Man and Anderson (1983) did not include any nonlinearity in the analytical model.

Rad and Adebar (2009) conducted a study with a variety of analyses including linear static analysis, nonlinear response history analysis (NLRHA) and nonlinear static analysis to better understand the reverse shear phenomenon. They used a horizontal linear spring at each floor level to represent the combined stiffness of diaphragms and foundation walls below grade (Figure 4.4). Rad and Adebar (2009) considered a simple model to estimate the lower-bound stiffness and range of the possible values for stiffness of the diaphragms.

A simply supported deep beam was used to model the action of the diaphragms transmitting the horizontal force to the foundation walls. The beam width and the beam span-to-depth ratio correspond to the slab thickness and the slab length-to-width ratio, respectively. It was found that for typical lengths of foundation walls, the stiffness is quite high such that a very small error results from simply assuming the foundation walls are infinitely rigid (Rad and Adebar, 2007). Therefore, rigid supports were assumed for the deep beam. Three values of diaphragm spring stiffness equal to $K1 = 1 \times 10^6\ kN/m$, $K2 = 10 \times 10^6\ kN/m$ and $K3 = 30 \times 10^6\ kN/m$ were considered which correspond to a range of average slab thicknesses from 200 mm to 400 mm, a range of slab length-to-width ratios from 0.5 to 2.0, and modulus of elasticity of 24000 MPa.

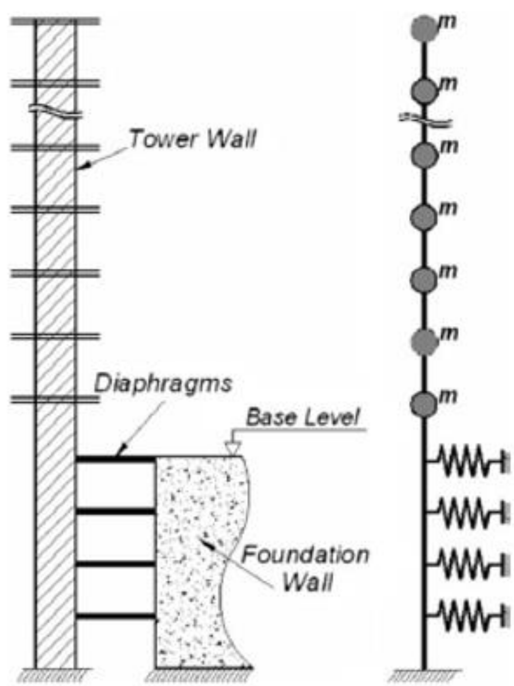

Figure 4.4 – Simplified analysis model of diaphragms below flexural hinge (Rad and Adebar, 2009)

They employed linear static analysis to investigate the effect of different parameters including diaphragm stiffness on relative magnitudes of the reverse shear force and the bending moment transmitted down the wall. Figure 4.5 shows the effect of diaphragm stiffness. As shown in Figure 4.4, the maximum reverse shear force decreases from about five times the base shear to slightly less than the base shear when the diaphragm spring stiffness reduces from $K30$ (rigid) to $K1$ (soft).

This illustrates how much the reverse shear force can be reduced due to the shear cracking of diaphragms. Cracking reduces the stiffness of floor diaphragms which reduces the reverse shear force. Since the shear behaviour of floor diaphragms is very complicated, it is difficult to use a simple model for the nonlinear behaviour of concrete diaphragms. Rad and Adebar (2009) proposed to consider the same nonlinear shear model used for shear walls, for concrete floor diaphragms when it is reasonable to assume that the reverse shear force is transmitted primarily to the in-plane foundation walls by compression and tension stresses in the diaphragm.

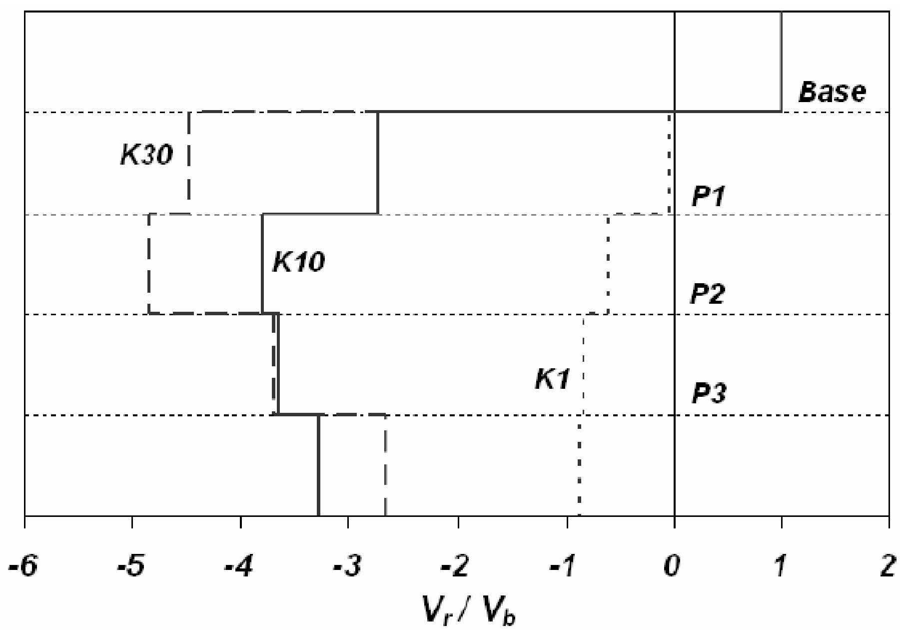

Figure 4.5 – Influence of diaphragm stiffness on reverse shear force below base (Rad, 2009)

Rad and Adebar (2009) recommended a procedure to deal with the reverse shear forces in high-rise tower walls connected to stiff base structures. They used the results of nonlinear response history analysis (NLRHA) to develop a simple linear static analysis procedure of the structure below the plastic hinge to estimate the design forces.

Tocci and Levi (2012) compared some of the possible options for modelling the base conditions of high-rise shear wall buildings, as shown in Figure 4.6. In their study, they focused on the effect of the ground floor diaphragm in contributing to the backstay effect. Figure 4.6(a) shows the most traditional model which is a simple cantilever. This model is not a good option as it underestimates the force demands in key elements.

The second model (Figure 4.6(b)) shows the extreme case of the backstay effect in which the floor diaphragms and foundation walls are very stiff and modelled as a pinned support. This model is very conservative for most conditions and the backstay effect may create conditions with much higher demands than expected in certain elements.

The more realistic model is the third one (Figure 4.6(c)) in which the ground floor restraint is model as a spring. This model produces results somewhere between the first and second models. The spring represents the cumulative stiffness of numerous elements in the building structure including diaphragm to core connection, diaphragm stiffness, diaphragm to foundation wall connection, foundation wall stiffness, foundation stiffness and passive soil resistance against foundation wall.

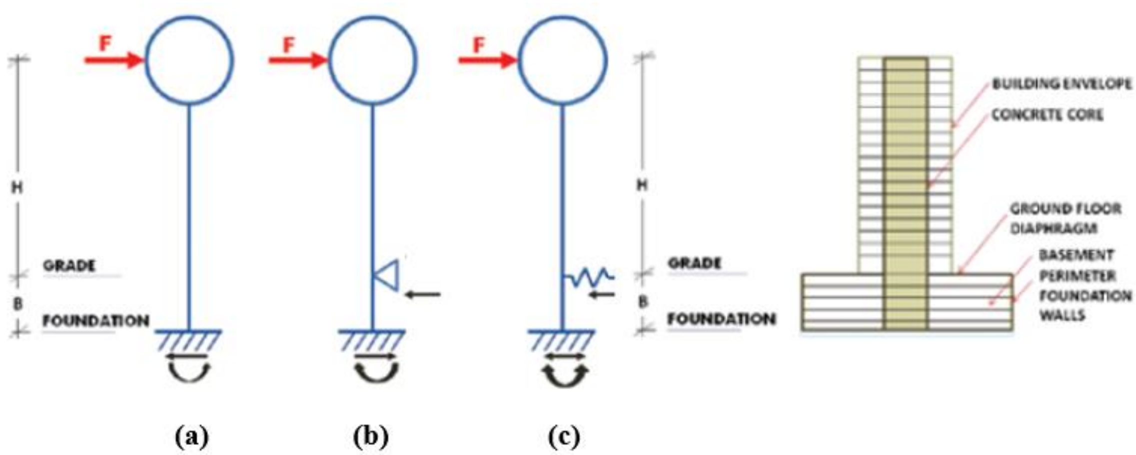

Figure 4.6 – Modelling options for base conditions in high-rise shear wall buildings (Tocci and Levi, 2012)

Tocci and Levi (2012) suggested that the first step in designing the high-rise shear wall is to assess whether the backstay effect is a consideration for the building under investigation. For buildings with backstay effect, they recommended considering reasonable extremes for both overestimation and underestimation conditions of backstay effect and design each element for the bounding condition which is referred to as bracketing. Unfortunately, this approach results in overdesign of some elements due to the lack of knowledge on this topic. As knowledge on the backstay effect in high-rise shear walls increases, the bracketing parameters will be refined and correspondingly the efficiency of design will be increased.

4.3 Current Design Guidelines

Some design guidelines provide recommendations on how to evaluate the backstay effect in tall buildings. Since the diaphragm stiffness significantly influences the seismic design forces in the building and due to the uncertainty in the best assumption for the diaphragm stiffness, all these design guidelines recommend the use of bracketing assumptions.

ASCE 7 (2010) permits to model reinforced concrete diaphragms as rigid elements as far as the span-to-depth ratio is less than or equal to 3 and there are no horizontal irregularities as defined in ASCE 7 Table 12.3-1. According to ASCE 7, the flexibility of diaphragms must be considered in all other cases as the stiffness assumptions used for diaphragm model influence the forces within the diaphragm as well as the distribution of forces among the vertical elements. This is particularly true at podium levels or the initial below-grade levels of high-rise structures.

Reduction in diaphragm stiffness due to cracking is approximated by applying a stiffness modifier to the diaphragm in-plane gross-section stiffness. These modifiers are commonly in the range of 0.15 to 0.5 for reinforced concrete diaphragms when analyzing the structure for design level earthquake demands (Nakaki, 2000). When the analysis results are sensitive to diaphragm stiffness, it is recommended to “bound” the solution by analyzing the structure with the upper-bound and lower-bound diaphragm stiffnesses. The design forces are selected as the largest values from the two analyses (NIST, 2016).

For seismic design of tall buildings, ATC-72-1 (2010) recommends a capacity design approach and nonlinear response history analysis of the structure using Maximum Considered Earthquake (MCE) level ground motions. In some cases, isolated models of particular diaphragms are required to ensure that the design satisfies equilibrium and compatibility requirements. In order to evaluate backstay effects, ATC-72-1 (2010) considers two seismic load paths which contribute to the overturning resistance of the building. The first load path is provided by the foundation below the tower core wall and known as overturning resistance. The second load path is provided by in-plane forces in floor diaphragms below grade and perimeter walls and known as backstay resistance (see Figure 4.1).

In order to design a building for backstay effects, ATC-72-1 (2010) recommends: (1) determining that each load path resists what portion of the building overturning, and (2) designing the structural elements of each load path with adequate strength. Therefore, it is required to consider the stiffness of the piles or the supporting soil below the tower wall foundation for the first load path and to consider the stiffness of the diaphragms and the perimeter walls for the second load path (backstay load path). In addition, sufficient stiffness and strength must be provided to all elements in both load paths.

Furthermore, the type and configuration of structural system influences the backstay effects. The central core wall systems rely more on the backstay load path compared to the more distributed seismic force resisting system over the building floor plan. Most of loads are transferred through the diaphragm located at the top of the podium (main backstay diaphragm). Thus, this diaphragm needs to be considerably thicker than other floor slabs.

Since the stiffness of critical elements in each load path is uncertain and influences the seismic design of the building, ATC-72-1 (2010) recommends the use of bracketing assumptions which means upper-bound and lower-bound stiffnesses should be considered for each element. In order to determine the governing design forces, two cases should be considered:

- *"Case 1 – Upper bound backstay effect*. A set of assumptions that provides an upper-bound estimate of forces in the backstay load path and a lower bound estimate of forces in the foundation below the tower. This case will govern the design forces for the podium floor diaphragms and perimeter walls, and the associated connections.

- *Case 2 – Lower bound backstay effect.* A set of assumptions that provides a lower-bound estimate of forces in the backstay load path and an upper-bound estimate of forces in the foundation below the tower. This case will govern the design forces for the tower foundation elements" (ATC-72-1, 2010).

Table 4.1 lists the recommended stiffnesses and bracketing upper-bound and lower-bound assumptions for the podium and tower elements, respectively. Based on Table 4.1, for in-plane shear stiffness of diaphragms, ATC-72-1 (2010) recommends using $0.5\mathrm{G_c A_g}$ for the upper-bound and between $0.05G_cA_g$ and $0.2G_cA_g$ for the lower-bound shear stiffness. For strong-axis flexural stiffness, ATC-72-1 (2010) recommends $0.5E_cI_g$ and $0.2E_cI_g$ for the upper and lower bounds, respectively.

Table 4.1 – Recommended stiffness assumptions for structural elements of a podium and foundation (ATC-72-1, 2010)

Structural element or property	**Assumption for Case 1**	**Assumptions for Case 2**	**Notes**
Concrete diaphragms / perimeter concrete walls – effective flexural stiffness (E_cI_{eff})	0.5 times gross section properties	0.2 times gross section properties, or fully cracked, transformed section properties	Flexural stiffness should be reduced for strain penetration effects. Including sources of additional deformation, such as strain penetration, can reduce effective stiffness to a small fraction of gross properties.
Concrete diaphragms / perimeter concrete walls – effective shear stiffness (G_cA)	0.5 times gross section properties	0.05 to 0.2 times gross section properties	Shear stiffness should be reduced upon initiation of diagonal cracking (when average shear stress exceeds $0.25\sqrt{f_c'}$ (MPa)).
Supporting soil / piles – vertical spring stiffness below perimeter concrete walls	Upper-bound soil properties	Lower-bound soil properties	A fixed base assumption can be used in lieu of upper-bound properties.
Supporting soil – horizontal spring stiffness on face of perimeter concrete walls	Lower-bound soil properties (alternatively soil springs can be omitted)	Upper-bound soil properties (will increase overall backstay effect, but will also take force out of diaphragms)	Passive resistance occurs in compression but not tension. The stiffness of passive resistance can be small compared to the stiffness of the perimeter walls, and thus can often be neglected.

LATBSDC (2017) and PEER (2017) provide a performance-based approach for seismic design and analysis of tall buildings. The procedure is based on capacity design principles followed by a series of performance-based design evaluations using two hazard levels: service level (43-year return period) and Maximum Considered Earthquake (MCE_R) level. The service-level evaluation shall be performed using three-dimensional linear or nonlinear dynamic analyses while three-dimensional nonlinear dynamic response analyses shall be employed for the MCE_R-level evaluation. The in-plane shear and flexural stiffnesses recommended by LATBSDC (2017) and PEER (2017) for non-pretensioned diaphragms are $0.4E_cA_g$ $(1.0G_cA_g)$ and $0.5E_cI_g$ for service-level evaluation and $0.1E_cA_g$ $(0.25G_cA_g)$ and $0.25E_cI_g$ for MCE_R-level evaluation, respectively.

Similar to ATC-72-1 (2010), LATBSDC (2017) also recommends conducting two sets of analyses to evaluate backstay effects using upper-bound (UB) and lower-bound (LB) stiffness assumptions for floor diaphragms at the podium and below. LATBSDC (2017) recommends the use of $0.5G_cA_g$ for the upper-bound and $0.25G_cA_g$ for the lower-bound in-plane shear stiffness. For the in-plane flexural stiffness of diaphragms, LATBSDC (2017) recommends using $0.25E_cI_g$ for the upper-bound and $0.1E_cI_g$ for the lower-bound flexural stiffness.

While ATC-72-1 (2010), LATBSDC (2017) and PEER (2017) recommend nonlinear response history analysis (NLRHA) of the entire building to estimate the design forces in the structure below the plastic hinge, the Canadian Concrete Design Handbook (2014) recommends linear static analysis of the structure below the plastic hinge to determine the design forces.

The Canadian Concrete Design Handbook (2014) recommendations are mainly from Rad and Adebar (2009) who used the results of NLRHA to develop a simple linear static procedure. Tables 4.2 and 4.3 summarize the analysis cases, and the applied forces and stiffness assumptions provided by the Canadian Concrete Design Handbook (2014) for the linear static analysis. An upper-bound overturning moment and either an upper-bound or lower-bound horizontal force should be applied to the structure below the plastic hinge (i.e., at the base of the plastic hinge). The lower-bound horizontal force is equal to zero which results in the maximum reverse shear force.

Table 4.2 – Linear static analysis cases (Canadian Concrete Design Handbook, 2014)

Case	Design forces (or deformation) to be determined
1	Maximum bending moments in *tower walls*; design forces for foundation below tower walls
2A	Forces in diaphragms, podium structure, other walls and associated connections
2B	Maximum (reverse) shear force in tower walls
3	Inter-story drift ratio of tower walls at top of structure restraining foundation movements

Table 4.3 – Stiffness and forces assumptions for different analysis cases (Canadian Concrete Design Handbook, 2014)

Applied forces and stiffness assumptions	**Case**			
	1	**2A**	**2B**	**3**
Applied overturning moment	M_n	M_p	M_p	M_n
Applied horizontal force	V @ M_n	V @ M_p	0	V @ M_n
Flexural stiffness of tower walls	**UB**	LB	LB	BE
Stiffness of footings and supporting soil/rock below tower walls	**UB**	LB	LB	BE
Shear stiffness of tower walls	LB	**UB**	**UB**	BE
Stiffness of ***diaphragms***	LB	**UB**	**UB**	BE
Stiffness of other walls, supporting footings and soil/rock	LB	**UB**	**UB**	BE
Lateral passive soil pressures on perpendicular foundation walls	LB	LB	**UB**	BE

M_n , M_p : nominal, probable bending moment capacity of tower walls accounting for level of axial compression
LB : lower-bound stiffness
UB : upper-bound stiffness
BE : best estimate

Above grade, the in-plane stiffness of concrete slabs is high in comparison to the lateral stiffness of walls. Thus, the Canadian Concrete Design Handbook (2014) recommends to model concrete slabs as rigid diaphragms at floor levels above grade. Since the stiffness of perimeter basement walls is considerably high, even small deformation of the diaphragm is significant and the flexibility of diaphragm should be taken into account. The Canadian Concrete Design Handbook (2014) states that the diaphragm must be modelled as linear elastic elements with a reduced effective stiffness to account for cracking.

Since the span-to-depth ratio of the diaphragm is very small, the shear is dominant in the diaphragm. The Canadian Concrete Design Handbook (2014) recommends using the same upper-bound shear stiffness used for the tower walls ($0.5\mathrm{G_c A_g}$) for the diaphragms.

According to the Canadian Concrete Design Handbook (2014), the lower-bound shear stiffness should be selected based on the amount and distribution of reinforcement provided in the diaphragm. For well distributed reinforcement, the lower-bound shear stiffness of $0.1G_cA_g$ can be used for diaphragms. When the provided reinforcement in the diaphragm is not known, a smaller lower-bound shear stiffness of $0.05G_cA_g$ should be applied. The recommended upper-bound and lower-bound flexural stiffness for diaphragm are $0.5E_cI_g$ and $0.2E_cI_g$, respectively, which are selected based on ATC-72-1 (2010).

Table 4.4 compares the recommendations from ATC-72-1, LATBSDC and the Canadian Concrete Design Handbook (2014) for upper and lower bounds shear and flexural stiffness of diaphragms. The upper bound shear stiffness proposed by the design guidelines, ATC-72-1 (2010), LATBSDC (2017) and the Canadian Concrete Design Handbook (2014) is identical. For the lower bound shear stiffness, LATBSDC (2017) proposed lager value compared to ATC-72-1 (2017) and the Canadian Concrete Design Handbook (2014). The upper bound and lower bound flexural stiffness recommended by LATBSDC (2017) is smaller than those proposed by ATC-72-1 (2010).

Table 4.4 – Comparison of current design practice recommendations for shear and flexural stiffness of concrete diaphragms

Diaphragm Stiffness	**Shear**		**Flexure**	
	UB	**LB**	**UB**	**LB**
ATC-72-1 (2010)	$0.5\mathrm{G_c A_g}$	$(0.05-0.2)G_c A_g$	$0.5E_c I_g$	$0.2E_c I_g$
LATBSDC (2017)	$0.5\mathrm{G_c A_g}$	$0.25\mathrm{G_c A_g}$	$0.25E_c I_g$	$0.1E_c I_g$
Canadian Concrete Design Handbook (2014)	$0.5\mathrm{G_c A_g}$	$(0.05-0.1)G_c A_g$	$0.5E_c I_g$	$0.2E_c I_g$

UB: upper-bound stiffness

LB: lower-bound stiffness

4.4 Nonlinear Finite Element Analysis

Nonlinear finite element analysis was used to investigate the reduction in shear and flexural stiffness of concrete diaphragms subjected to in-plane forces. Computer program VecTor2 (Wong and Vecchio, 2002) was used for the analysis as it utilizes state-of-the-art material models for cracked concrete elements subjected to in-plane shear and normal forces. VecTor2 is based on the Disturbed Stress Field Model (Vecchio, 2000), which is a refinement of the Modified Compression Field Theory (Vecchio and Collins, 1986).

In VecTor2, the concrete model accounts for the reduction in concrete compression strength and stiffness due to tensile straining and transverse cracking. The model also accounts for the crack shear-slip deformations by relating shear slip to local shear stresses along cracks. The model relates the post-cracking rotation of the principal stress field to the post-cracking rotation of the principal field using a rotation lag. The post-cracking tensile stresses between cracks due to bond between concrete and reinforcement (tension stiffening) are included in the model. In addition, the model accounts for the reduction in concrete cracking strength due to transverse compressive stresses. Nonlinear functions are used to describe the stress-strain relationship of concrete in compression and tension. The constitutive model used for reinforcement is trilinear, consisting of a linear-elastic response, a yield plateau, and a linear strain-hardening phase until rupture. Details of concrete and reinforcement models available in VecTor2 were presented in Section 2.3 of Chapter 2.

4-node plane stress rectangular elements of VecTor2 with eight degrees of freedom (DOF) were used to model concrete. Given the high number of bars at the top and bottom of the tested slab and uniformly distributed reinforcement in the studied diaphragms, the smeared reinforcement method was used to define reinforcing bars in the diaphragms. In this model, reinforcing bars were defined by the reinforcement ratio and uniformly distributed throughout the element. The concrete diaphragm was simulated using different concrete material types with different amount of reinforcement distributed in both directions of diaphragm.

4.5 Validation of NLFE Model

To validate the FE model, the results of NLFE analysis were compared with the concrete diaphragm test by Nakashima (1981). One of the most crucial in-plane characteristics of the floor slabs investigated by Nakashima (1981) was the in-plane stiffness of floor slabs. The test specimen chosen for this experimental study represented an interior panel of a floor system in a prototype building. It was supported by a shear wall on one edge and by columns on the opposite edge. Overhanging slabs, equal to one quarter of the panel dimension, were added on three sides to represent parts of the floor slabs of the adjacent bays. An intermediate scale ratio of 1:4.5 was selected. The basic panel was 1630 mm × 1630 mm and 40 mm thick, as shown in Figure 4.7. The prototype floor slab was designed according to the direct design method of ACI Code to ensure failure in the slabs. Summary of the experimental study including details of the arrangement and size of reinforcing bars are given in Appendix B.

Two types of concrete were used for the test specimen. The compressive strength of concrete was 27.6 MPa for the floor slabs and the walls and 34.5 MPa for the columns. Details of the material properties of concrete and reinforcing bars are given in Appendix B.

In order to facilitate the application of vertical load and provide access to the underside, the specimen was supported on four heavily reinforced concrete pedestals anchored to the floor of the testing laboratory, as illustrated in Figure 4.7. For the test of interest, the support condition provided to the wall was to prevent the wall from moving in the floor plane, while the columns were supported in free-to-slide conditions. The column in the free sliding condition did not offer any resistance to the applied lateral load and provided only a vertical reaction to the gravity load.

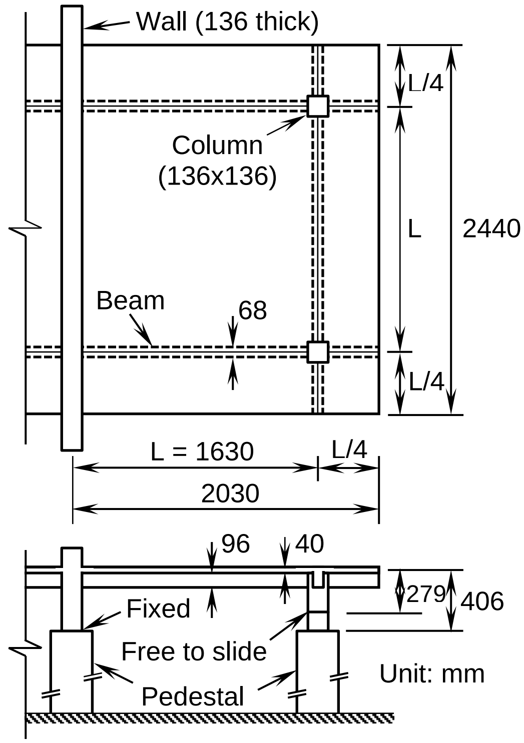

Figure 4.7 – Dimensions and supporting conditions of test specimen

The in-plane load was generated by a double-acting mechanical jack placed at the slab center-plane and acting against a heavy steel frame. To simulate the desired shear action, a steel frame was used to distribute the jack load to five embedded studs along the loading line at uniformly spaced distances of 540 mm, as depicted Figure 4.8. The frame and studs were carefully designed so that each stud would transmit approximately one fifth of the total applied load and the action would lie in the slab center-plane. The in-plane deflection of the slab along the loading line was measured by a linear variable differential transformer (LVDT) connected to the slab along the loading line (Figure 4.8).

Figure 4.9 shows the finite element model of the slab created in the pre-processor FormWorks. Fourteen concrete material types with different amounts of reinforcement in the both directions of slab were used to represent various regions of the slab in the finite element model, as depicted in Figure 4.9. Details of concrete materials used in the VecTor2 model are given in Appendix C. A total number of thirty-eight regions were created to represent the complicated arrangement of rebars in slab and beams. Details of reinforcement arrangement are presented in

Appendix B. The beams and the wall were modelled using elements with thicknesses equal to the beam depth and wall height, respectively. A finite element mesh with a mesh size of 34 × 34 mm was used for both slab and beams. The total mesh consisted of approximately 4680 nodes and 4530 rectangular elements.

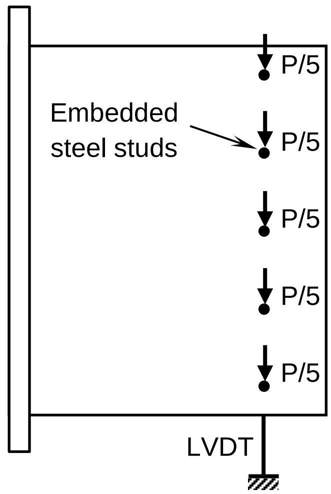

Figure 4.8 – Loading conditions and measurement in test

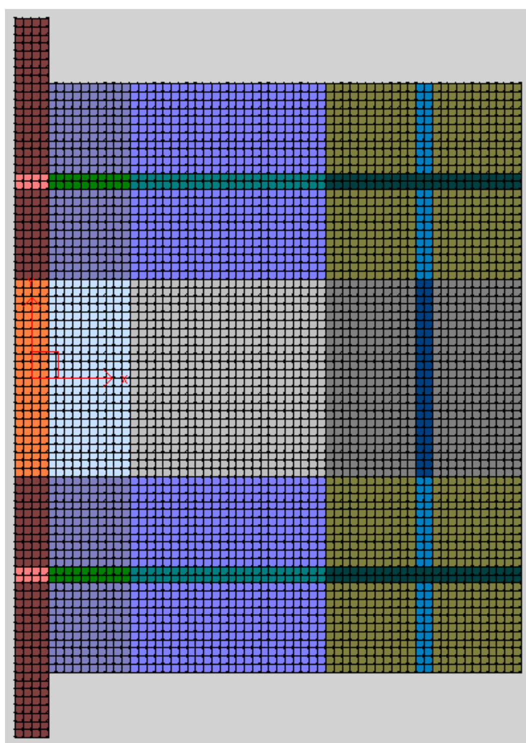

Figure 4.9 – Finite element model of the tested slab in FormWorks

The boundary condition was one of the challenging steps in the modeling procedure. Since the description for the boundary conditions given in Nakashima's report (1981) was not quite clear, two different boundary conditions were considered for the slab-wall junction to capture the closest results to the experiment. For the first boundary condition, the slab was completely fixed along the slab-wall interface (fixed support). The displacement of the slab along this line in both directions were restrained (Figure 4.10(a)). For the second boundary condition, the shear wall was also considered in the finite element model acting as a deep beam (beam support). The displacement in x direction was restrained along the wall length while the displacement in y direction was fixed at the bottom, as shown in Figure 4.10(b).

A sensitivity analysis was completed for the model with different boundary conditions. As expected, the slab with beam support exhibited more flexibility as compared to the fixed support. The most important influence of the two boundary conditions (i.e., fixed support and beam support) was noted on the cracking pattern and shear flow in the slab. The crack pattern and shear flow of the slab with beam support were similar to those observed in the experiment. Therefore, the beam support boundary condition was used for this analysis. The crack pattern and the shear flow of the slab analyzed with the fixed and beam supports are compared in Appendix C.

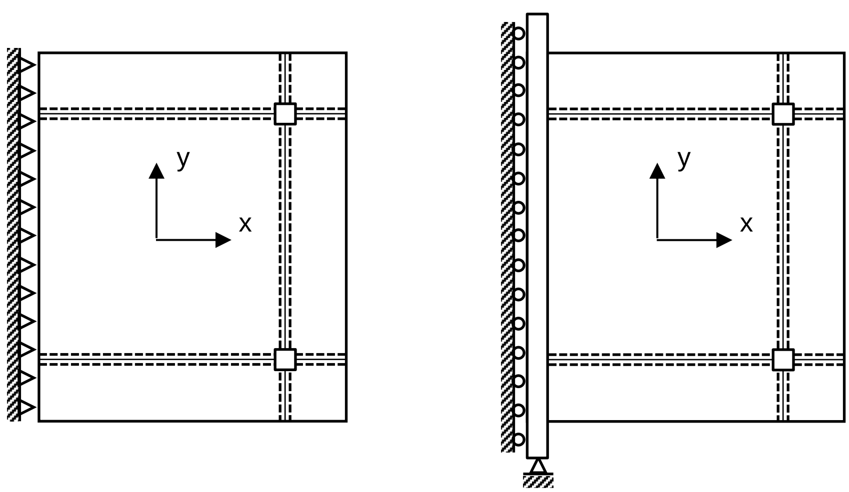

a) **b)**

Figure 4.10 – Two different boundary conditions: (a) fixed support; (b) beam support

A monotonic in-plane shear load in displacement-controlled mode with increment of 0.05 mm was applied along the centre line of the beam parallel to the shear wall (the loading line). The in-plane load was applied in very small increments since the model experienced a high degree of non-linearity under the loading conditions. To simulate the uniform shear stress in the slab, the in-plane shear force was applied to five nodes evenly spaced along the loading line (similar to the experiment). Since the scale ratio of 1:4.5 was used for the test specimen, the self-weight of the slab specimen was small as compared to the prototype floor slab and did not cause any cracks in the slab. Thus, the influence of the slab self-weight was neglected in the analysis.

A few pre-existing cracks were reported in the tested slab. These cracks could have been due to concrete shrinkage and/or the effect of other preliminary tests performed on the slab specimen. The influence of pre-existing cracks was taken into account in the VecTor2 model by reducing the tensile strength of concrete. The tensile strength of concrete was reduced to half and one-third of the concrete cracking strength.

Figure 4.11 compares the measured force-deformation response with the analytical prediction using the reduced tensile strength. As shown in Figure 4.11, there is a good agreement between the experimental and analysis results for the slab with tensile strength equal to one-third of the cracking strength ($f_t' = 0.1\sqrt{f_c'}$). The VecTor2 model was able to predict the force-deformation behaviour of tested slab quite accurately. The effect of shrinkage cracking was not included in the parametric study; thus, the reduction in tensile strength of concrete was not applied in the other analyses.

Since the figure of the force-deformation relationship reported in Nakashima's report was not clear enough to reproduce the test graphs, the data was taken from Chen's report (Chen, 1986). Chen (1986) carried out the same experimental study for waffle slabs and included Nakashima's test results for comparison.

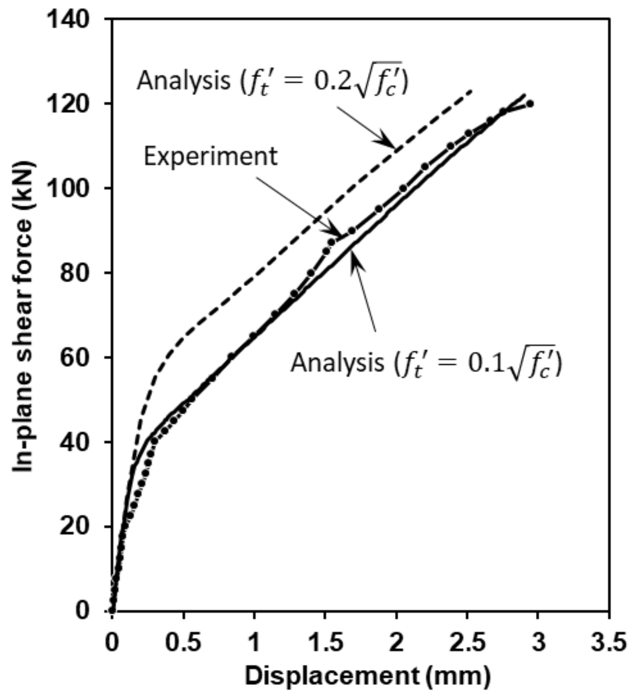

Figure 4.11 – Comparison of the observed and predicted force-deformation relationships

In addition to predicting the load-deformation response, the VecTor2 model did an excellent job of predicting the crack pattern observed in the test, which included 45-degree shear cracks between the loading line and the slab-wall junction. Flexural cracks also developed at the slab edge and extended in the slab parallel to the wall where some horizontal reinforcement was cut off. The VecTor2 model also correctly predicted that flexural failure controlled the capacity of the diaphragm.

Figure 4.12 compares the crack pattern of the slab observed in the experiment with the predicted one for the slab with beam support. Bold solid lines indicate "major cracks". The information regarding observed crack width was not given in Nakashima's report. For the VecTor2 model, different crack widths are schematically presented using lines with different thicknesses. Smaller crack spacing from analytical results can be attributed to the smaller tensile strength of concrete used for the analysis.

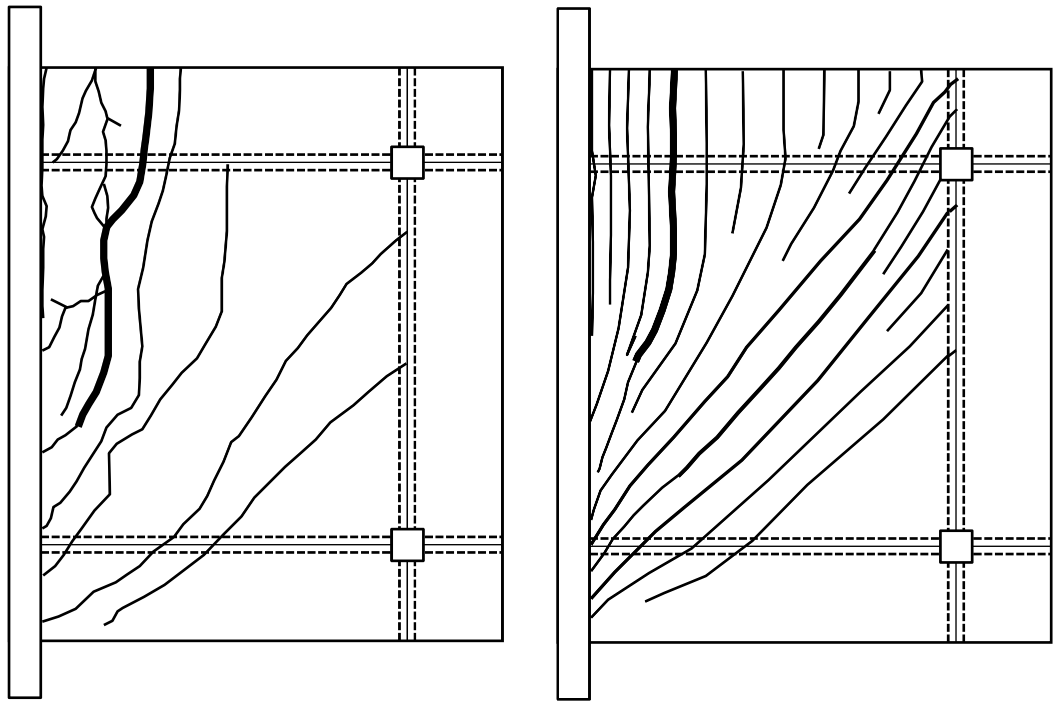

Figure 4.12 – Comparison of the observed (left) and predicted (right) crack patterns

4.6 Analytical Study

The VecTor2 NLFE model was used to investigate how a number of important parameters influence the effective stiffness of diaphragms subjected to large backstay forces. One of the main parameters was the amount of uniformly distributed reinforcement in the two span directions of the diaphragms. Three different reinforcement ratios ($\rho = A_s/A_g$) of 0.5%, 1.0% and 2.0%, representing lightly reinforced to heavily reinforced diaphragms, were investigated.

Another important parameter was the span lengths of the diaphragms parallel and perpendicular to the backstay forces. Figure 4.13 shows an overview of a concrete diaphragm investigated in the current study. Since it is assumed that small out-of-plane movement of the foundation walls is not resisted, the action of the diaphragms transmitting the backstay forces to the foundation walls can be modelled as a simply supported deep beam. The length of the diaphragm parallel to the applied backstay forces is called L_{SD} [see Figure 4.13(a)]. If the diaphragm is modelled as a beam, this span direction would be analogous to the shear depth (SD)

of the beam model. The clear span of the diaphragm from the core wall to the foundation walls resisting the backstay forces is called L_{SS} [see Figure 4.13(a)]. In the beam model of the diaphragm, this length is equivalent to the shear span (*SS*). The overall span length of the diaphragm in this direction is called L [see Figure 4.13(a)].

In the current study, the diaphragm aspect ratio is defined as the shear-span to shear-depth ratio of the diaphragm (L_{SS}/L_{SD}). The length of the core walls in the direction of the applied backstay forces is called L_w [see Figure 4.13(a)]. Three different lengths of 7, 10 and 12 m were used for L_w. The length of the core walls in the perpendicular direction to the backstay forces was assumed to be constant and equal to 6 m. Table 4.5 summarizes the different combinations of diaphragm span lengths, reinforcement ratios and core wall lengths that were investigated. A total number of nineteen diaphragms were analyzed, which were categorized into seven cases, listed in Table 4.5.

Further details of the diaphragms are summarized in the following. The thickness of all diaphragms (t_d) was 200 mm. The foundation walls, surrounding diaphragms had a uniform thickness ($t_w = 300$ mm). The thickness of the core wall was 400 and 600 mm in parallel and perpendicular directions to the backstay forces, respectively. The center-to-center height between floor diaphragms was assumed to be 3 m. The diaphragm with perimeter foundation walls behaved like an I-shaped deep beam, as depicted in Figure 4.13(c).

The concrete diaphragms were reinforced with two layers of uniformly distributed reinforcement, 10M@200 mm, 15M@200 mm and 15M@100 mm in both directions of diaphragm, which resulted in 0.5%, 1% and 2% reinforcement amount, respectively. The same reinforcement amount was provided to the foundation walls in longitudinal and transverse directions while the core wall was provided with 3% longitudinal and transverse reinforcement to avoid extensive cracking and failure in the core wall.

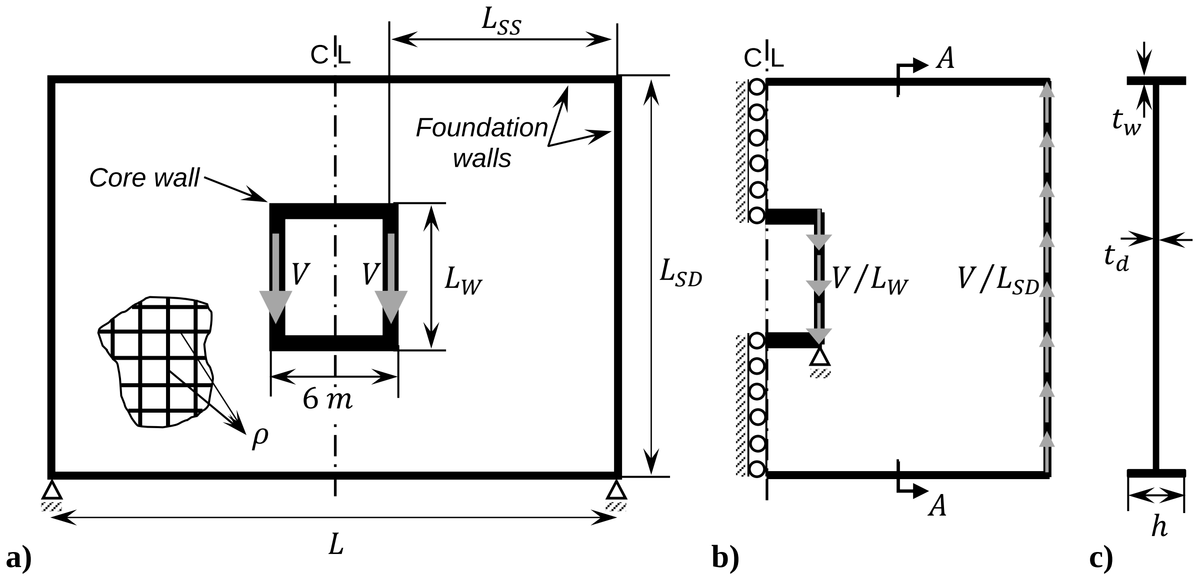

Figure 4.13 – Concrete diaphragm investigated in the current study, including core walls and perimeter foundation wall below grade: (a) overall diaphragm considered as a simply supported deep beam; (b) plan view of half-diaphragm model used due to symmetry; (c) elevation view of one diaphragm (section A-A)

Table 4.5 – Characteristics of analyzed diaphragms

Case	**1**	**2**	**3**	**4**	**5**	**6**	**7**
L **(m)**	42.0	42.0	30.0	30.0	21.0	42.0	30.0
L_{SS} **(m)**	18.0	18.0	12.0	12.0	7.5	18.0	12.0
L_{SD} **(m)**	21.0	30.0	21.0	30.0	42.0	21.0	30.0
L_w **(m)**	7.0	7.0	7.0	7.0	7.0	10.0 12.0	10.0 12.0
L/L_{SD}	2.0	1.4	1.4	1.0	0.5	2.0	1.0
L_{SS}/L_{SD}	0.9	0.6	0.6	0.4	0.2	0.9	0.4
L_w/L_{SD}	0.33	0.23	0.33	0.23	0.17	0.48 0.57	0.33 0.40
ρ (%)	0.5 1.0 2.0	0.5 1.0 2.0	0.5 1.0 2.0	0.5 1.0 2.0	0.5 1.0 2.0	1.0	1.0

h = 3.0 m; t_d = 200 mm; t_w = 300 mm

The boundary conditions used in the two-dimensional model of the diaphragm are illustrated in Figure 4.13(b). As the overall diaphragm is symmetrical, restraints in the horizontal direction (perpendicular to backstay forces) were introduced at the edges of the analyzed diaphragm at mid-span. The mechanism of transferring backstay forces from the foundation walls to the foundation is not completely known and requires performing three-dimensional nonlinear analysis. To eliminate the complexity of this mechanism and to simplify the analysis to a two-dimensional model, a uniformly distributed shear force was applied at the foundation wall along the diaphragm shear depth (L_{SD}), as shown in Figure 4.13(b). This force simulated the reaction of the support.

According to NIST (2016), it is reasonable to assume that the diaphragm shear is distributed uniformly along the width of the diaphragm when the diaphragm has chord reinforcement located near the extreme flexural tension edge of the diaphragm. In addition, the displacement at the bottom of the core wall was restrained in both perpendicular and parallel directions to backstay forces. A uniformly distributed backstay force of the same magnitude and in opposite direction was applied along the length of the core wall, as illustrated in Figure 4.13(b), to ensure the shear force was distributed uniformly along the core wall length (L_w) and to avoid stress concentrations at the bottom of the core wall.

The compressive strength of concrete was assumed to be 30 MPa and the secant modulus of elasticity was taken as 23,750 MPa. The tensile strength of concrete was assumed to be 1.8 MPa which corresponds to $1/3\sqrt{f'_c}$ and Poisson's ratio was assumed to be 0.15. All reinforcing bars had an actual yield strength of 400 MPa until strain hardening at a strain of 0.01. The ultimate strength and strain of reinforcing bars were 650 MPa and 0.05, respectively.

The nonlinear finite element analysis of concrete diaphragms was performed using VecTor2. Forty-one regions were created using seven concrete material models with different amount of reinforcement to represent various regions of the diaphragm in the VecTor2 model. Details of concrete material models are given in Appendix C. The uniformly distributed in-plane shear forces were applied along the core wall on the left side and along the foundation wall on the right side of the diaphragm. The in-plane shear forces were monotonically increased in a load-controlled mode. These shear forces equilibrated each other during the analysis. The element size of approximately 300 mm was used for the simulation of diaphragms. In order to apply the uniformly distributed shear forces along the center line of the core wall and the foundation walls, smaller element size was used at these locations. However, the element aspect ratio used in the finite element model remained between 1 and 2. As the influence of out-of-plane loading was not considered in this model, the gravity-load columns were not modelled. The thickness of the elements used for the core wall and foundation walls was equal to 3 m. Figure 4.13 depicts the finite element model of the diaphragm as well as the applied boundary conditions in the pre-processor FormWorks.

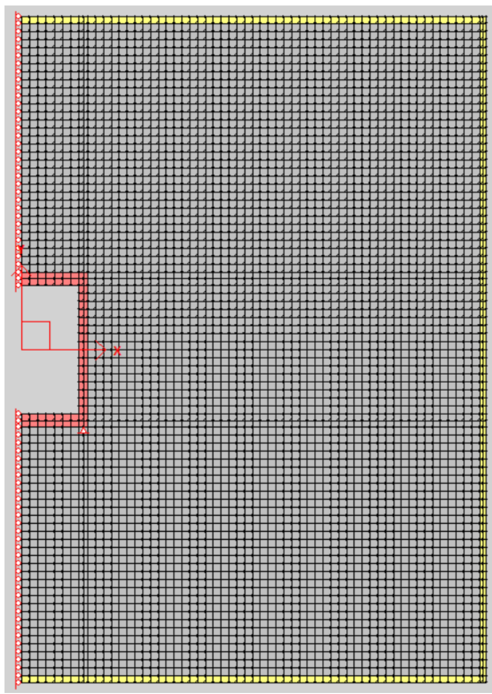

Figure 4.14 – Finite element model of the analyzed diaphragm in FormWorks

4.7 Discussion of Analysis Results

4.7.1 Load–Deformation Relationship of Concrete Diaphragms Subjected to Backstay Forces

Results from the analyses indicated that the load-deformation relationship of concrete diaphragms subjected to backstay forces can be represented fairly accurately by a trilinear curve. The load-deformation relationship of diaphragms Case 1, 2, 3, 4 and 5 with different span lengths

($L_{SS} \times L_{SD} = 18 \times 21, 12 \times 21, 18 \times 30, 12 \times 30, 7.5 \times 42$ m) and different reinforcement amounts (0.5%, 1% and 2%) are depicted in Figures 4.15 to 4.19, respectively. In these figures, the in-plane shear force versus the corresponding average displacement along the foundation wall was plotted for each analyzed diaphragm. The variation of displacement along the foundation wall, where the uniform in-plane shear forces were applied, was relatively uniform due to the significantly large in-plane stiffness of foundation walls.

Prior to cracking, the load-deformation relationship was linear for all diaphragms and the initial stiffness of the diaphragms remained constant and equal to the uncracked stiffness of diaphragms. Once cracking took place, the slope of the load-deformation curve decreased as the diaphragm became softer due to cracking. Since the diaphragms had relatively small aspect ratios (L_{SS}/L_{SD}), shear was dominant, hence diagonal (shear) cracks took place first in all analyzed diaphragms. Formation of diagonal (shear) cracks resulted in a small reduction in diaphragm stiffness. Once flexural cracking took place, the diaphragm became softer due to cracking and the diaphragm in-plane stiffness decreased noticeably. Thus, the slope of the load-deformation relationship of diaphragm reduced considerably. However, the relationship remained relatively linear after cracking. Significant reduction in diaphragm stiffness (significant change in the slope of the load-deformation diagram) occurred when the flexural cracks formed in the diaphragm.

As illustrated in Figures 4.15 to 4.18, the diaphragm reinforcement amount has a significant influence on the diaphragm strength as expected. The diaphragm strength reduces considerably as the reinforcement amount reduces from 2.0% to 0.5%. Also, the reduction in diaphragm strength is reversely proportional to the aspect ratio (L_{SS}/L_{SD}) of the diaphragm. By increasing the diaphragm aspect ratio from 0.4 to 0.9, the diaphragm strength reduces by about 85% and 60% when the reinforcement ratio varies from 2.0% to 1.0% and by about 50% and 35% when the reinforcement ratio varies from 2.0% to 0.5%.

As the aspect ratio (L_{SS}/L_{SD}) of the diaphragm reduces to 0.2 (Case 5), the diaphragm becomes more squat and totally shear-dominated. Therefore, the diaphragm exhibited brittle behaviour. The ultimate displacement of the diaphragm reduced and consequently the ductility of diaphragm significantly decreased, as shown in Figure 4.19. The analysis of the diaphragm Case 5 ($L_{SS}/L_{SD} = 0.2$) with 2% reinforcement amount was not completed due to some software errors.

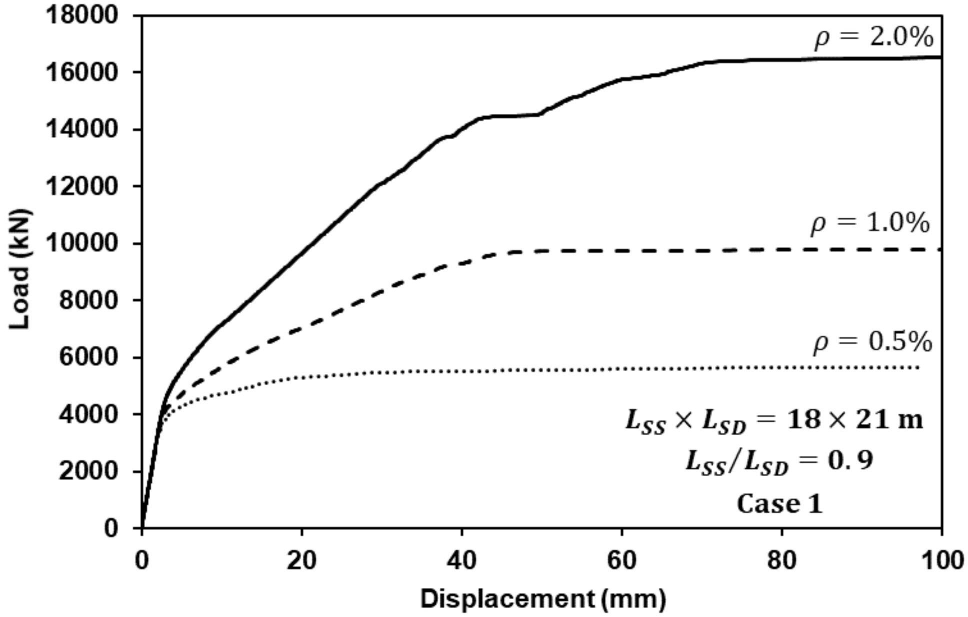

Figure 4.15 – Force-deformation relationship of diaphragm with $L_{SS} \times L_{SD} = 18 \times 21$ m (Case 1) and different reinforcement amount (0.5%, 1% and 2%)

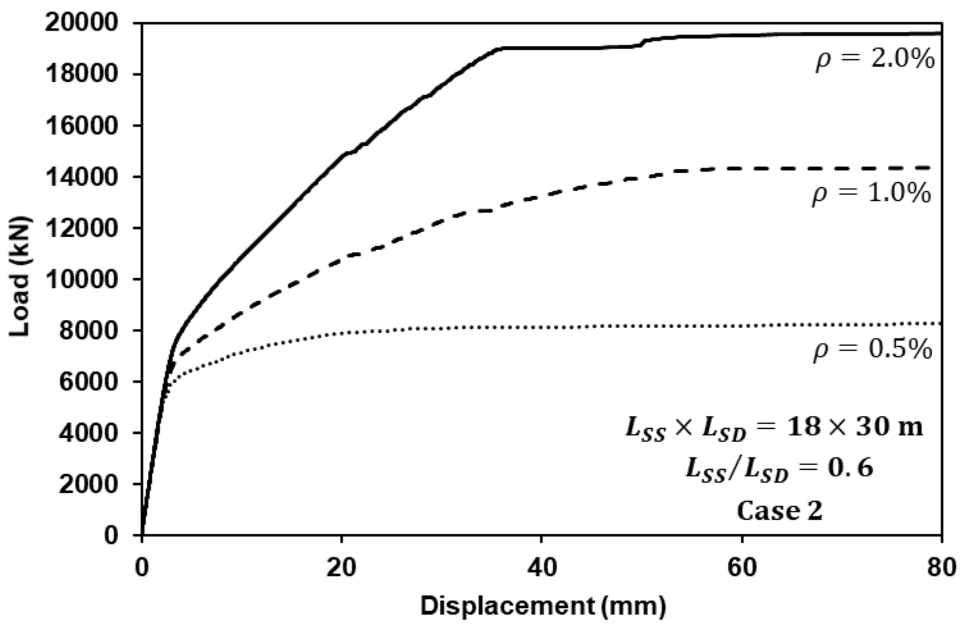

Figure 4.16 – Force-deformation relationship of diaphragm with $L_{SS} \times L_{SD} = 18 \times 30$ m (Case 2) and different reinforcement amount (0.5%, 1% and 2%)

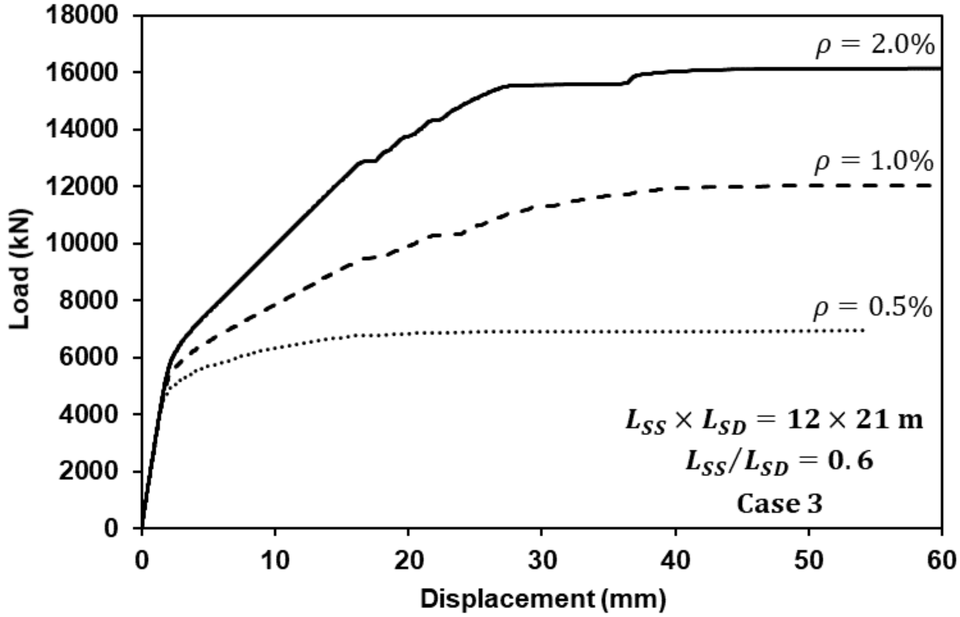

Figure 4.17 – Force-deformation relationship of diaphragm with $L_{SS} \times L_{SD} = 12 \times 21$ m (Case 3) and different reinforcement amount (0.5%, 1% and 2%)

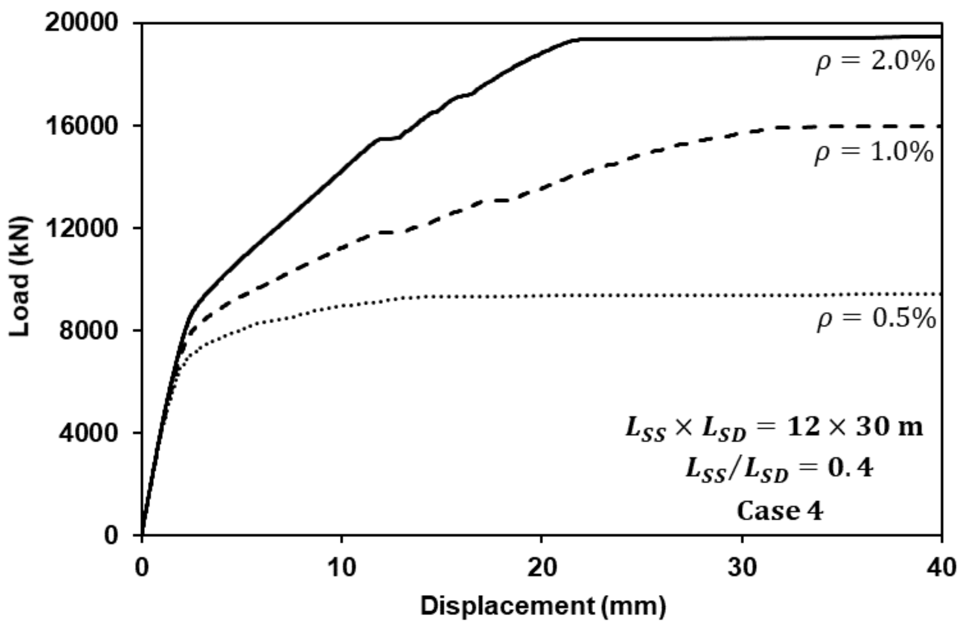

Figure 4.18 – Force-deformation relationship of diaphragm with $L_{SS} \times L_{SD} = 12 \times 30$ m (Case 4) and different reinforcement amount (0.5%, 1% and 2%)

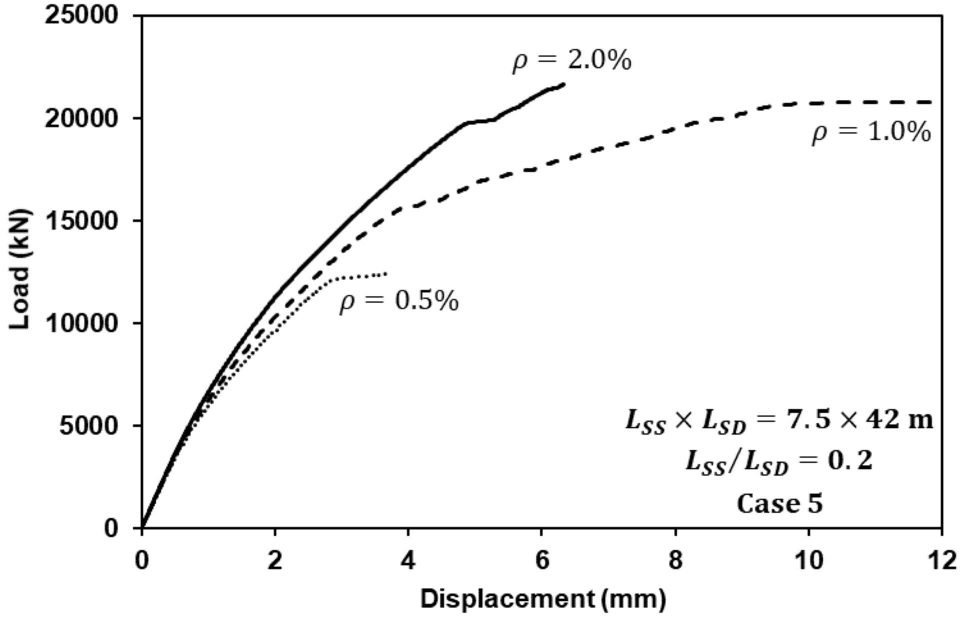

Figure 4.19 – Force-deformation relationship of diaphragm with $L_{SS} \times L_{SD} = 7.5 \times 42$ m (Case 5) and different reinforcement amount (0.5%, 1% and 2%)

4.7.2 Diaphragm Cracking Patterns

In order to better understand the load-deformation behaviour of diaphragms subjected to backstay forces, the cracking patterns of diaphragms at different load levels were investigated. Due to relatively small aspect ratios (L_{SS}/L_{SD}) of diaphragms, diagonal (shear) cracks took place first in all analyzed diaphragms. However, for the most slender diaphragms with aspect ratio of 0.9 (Case 1), flexural cracks formed shortly after diagonal cracks. Diagonal cracks first appeared in the diaphragm at the top corner of the core wall and extended diagonally with the angle of approximately 45° towards the foundation wall where the uniformly distributed shear loads were applied. In addition, few diagonal cracks formed along the bottom corner of the core wall.

Since the applied in-plane loads caused a strong-axis bending in the diaphragm, flexural (tension) cracks also formed in the flexural tension zone of diaphragms. Increase of applied in-plane load resulted in a large zone of flexural cracks. The location of diagonal and flexural cracks and the direction of crack extension are illustrated in Figure 4.20. Figure 4.20 shows cracking patterns for the diaphragm with $L_{SS} \times L_{SD} = 18 \times 30$ m (Case 2) and 1% reinforcement amount at the load V'_{FC} corresponding to the onset of flexural cracking (left) and at the load V_{FC}, which corresponds to the significant change in the slope of the load-deformation curve due to the flexural cracking (right). The in-plane shear force corresponding to each cracking pattern was included in the figure.

The cracking patterns of diaphragms with different aspect ratios and reinforcement amounts indicated that the shear was dominant in investigated diaphragms. Tables 4.6 and 4.7 show cracking patterns for analyzed diaphragms with different aspect ratios and reinforcement amount at the onset of flexural cracking and at a load level which the force-deformation curve bent and the slope of the curve significantly changed. Each column of Tables 4.6 and 4.7 compares the cracking pattern for diaphragms with the same aspect ratio while each row of the tables compares the cracking pattern for diaphragms with identical reinforcement amount.

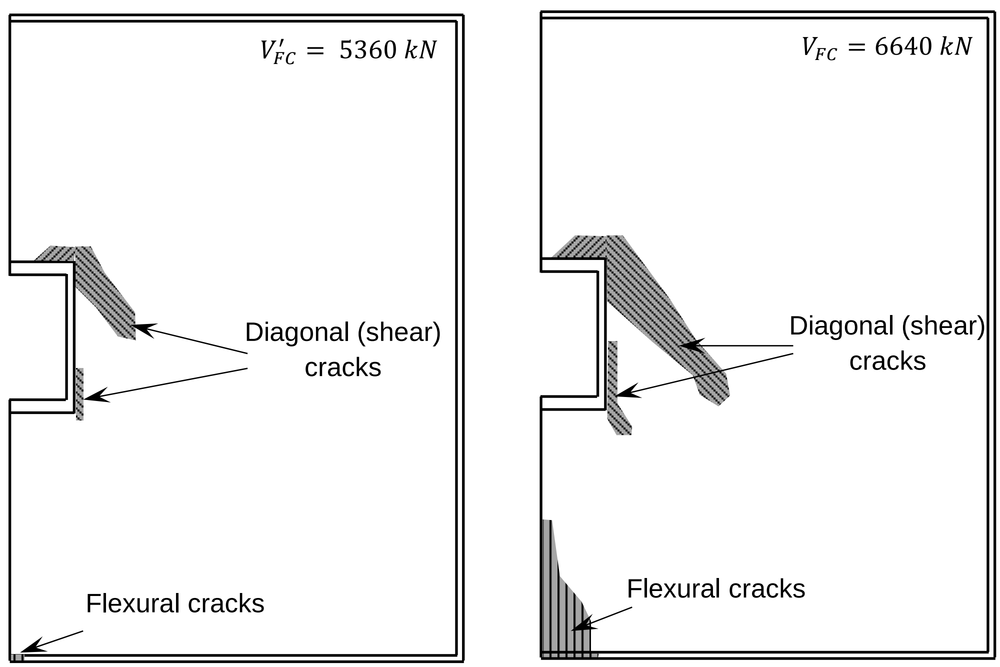

Figure 4.20 – Formation of diagonal (shear) cracks and flexural cracks in diaphragm at load V'_{FC} corresponding to the onset of flexural cracking (left) and at load V_{FC} corresponding to significant change in the slope of the load-deformation curve due to flexural cracking (right)

Table 4.6 – Cracking pattern for analyzed diaphragms at onset of flexural cracking

	$l_1/l_2 = 0.9$	$l_1/l_2 = 0.6$	$l_1/l_2 = 0.4$	$l_1/l_2 = 0.2$
ρ = 2%	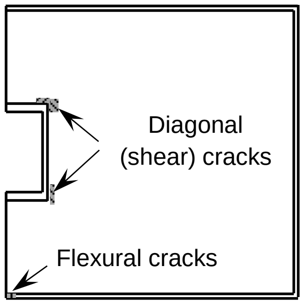	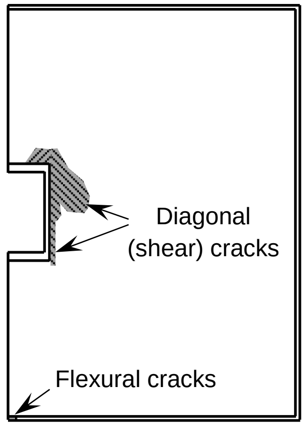	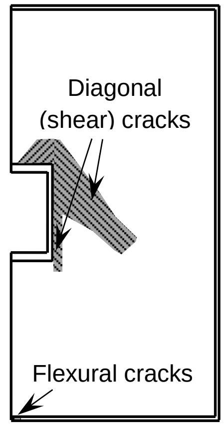	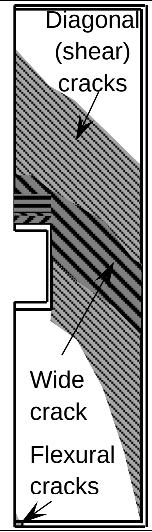
ρ = 1%	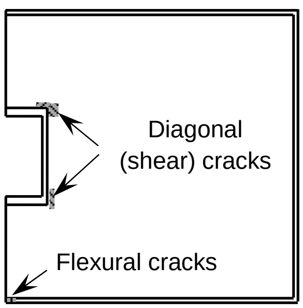	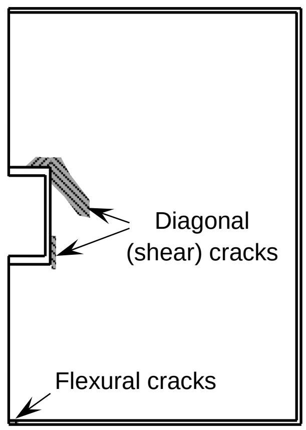	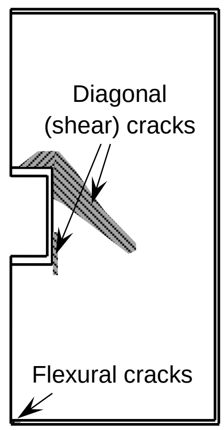	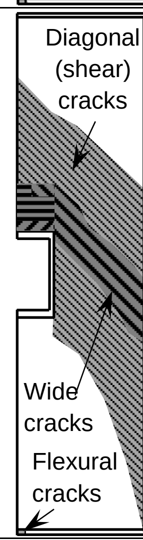
ρ = 0.5%	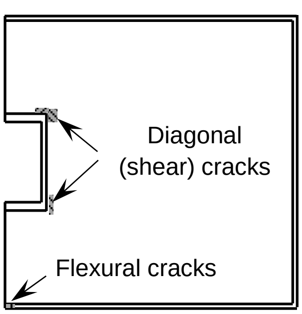	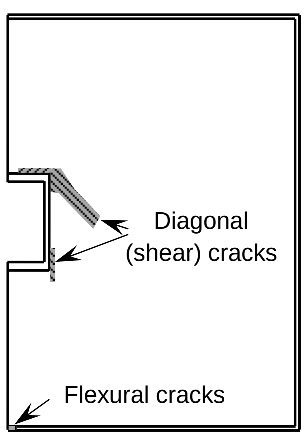	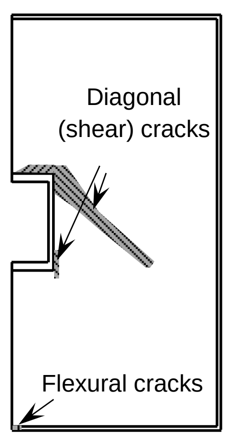	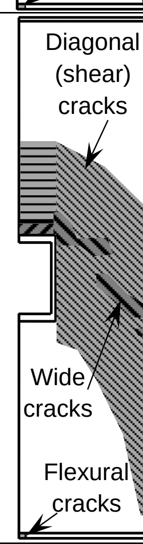

Table 4.7 – Cracking pattern for analyzed diaphragms at load V_{FC}

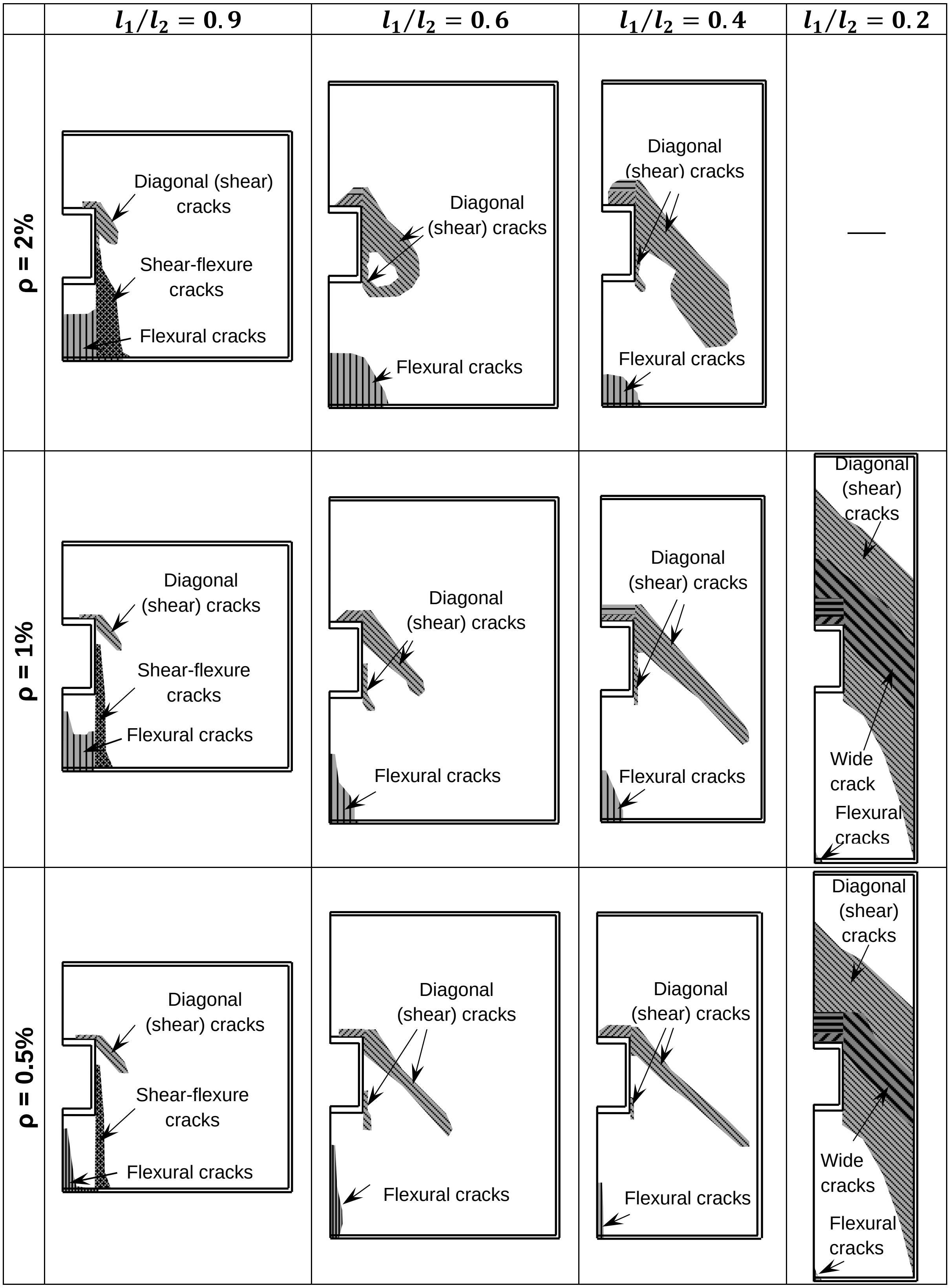

For diaphragms with the same reinforcement amount (move horizontally on the tables from left to right), more diagonal (shear) cracks formed as the aspect ratio of diaphragm decreases. Increasing the reinforcement amount of diaphragms with the same aspect ratio (move vertically on the tables from bottom to top) resulted in more flexural cracks along the diaphragm tension zone. This was attributed to the better crack control of diaphragm with larger amount of reinforcement.

For the most slender analyzed diaphragms (Case 1), shear-flexure cracks formed in the diaphragm as the flexural cracking occurred shortly after the diagonal cracking in the diaphragm. For the most squat analyzed diaphragms (Case 5), small area of flexural cracks occurred in the flexural (tension) zone of the diaphragms, while extensive diagonal (shear) cracks propagated all across the shear span of the diaphragms. The most squat diaphragm with the light reinforcement amount ($L_{SS}/L_{SD} = 0.2$ and $\rho = 0.5\%$) failed shortly after the formation of flexural cracks. As aforementioned, the analysis of the diaphragm Case 5 with 2% reinforcement amount was not completed due to some software errors.

4.7.3 Shear and Flexural Contributions to Total Displacement

Based on the results of this study, the shear deformation contributes between 70% and 100% of the total deformation depending on the aspect ratio of the diaphragm. Consequently, the flexural deformation contributes between 0% and 30% of the total displacement. Figure 4.21(a) and (b) present the load-deformation relationships of diaphragms with $L_{SS} \times L_{SD} = 18 \times 21$ m (Case 1) and $L_{SS} \times L_{SD} = 12 \times 30$ m (Case 4) and 1% reinforcement amount, respectively. The contributions of shear and flexural deformations to the total displacement are also shown in the figures, which are about 70% and 30% for diaphragm Case 1 and about 90% and 10% for diaphragm Case 4, respectively.

To determine the flexural deformation, the average curvatures were integrated over the diaphragm shear span (L_{SS}). The average curvature was considered as the slope of the line fitted to the normal strain profile in the horizontal direction. The shear deformation was obtained by subtracting the flexural deformation from the total deformation. To ensure that the calculated shear deformation is accurate, the average shear strains were integrated over the diaphragm shear span

(L_{SS}) to obtain the shear deformation. Comparison of the results has shown that VecTor2 is able to accurately predict the shear and flexural deformations of the diaphragm. Details of calculations and profiles of normal and shear strains are given in Appendix C.

The shear and flexural deformations obtained from linear finite element (LFE) analysis (dashed lines) are also shown in the figures. Since the diaphragms are squat, the shear deformation is dominant. By decreasing the diaphragm aspect ratio from 0.9 to 0.4, the flexural deformation of diaphragm considerably reduces and the shear deformation approaches to the total displacement of diaphragm. The calculated shear and flexural displacements indicate that the contributions of shear and flexural displacements to the total displacement remain approximately constant for diaphragms with the same aspect ratio independent of the reinforcement amount.

Figure 4.22 illustrates the contributions of flexural deformations for diaphragms Cases 1, 2, 3 and 4. The applied in-plane load was normalized with respect to the load V_{FC}, which corresponds to the significant change in the slope of the load-deformation curve due to the flexural cracking. Based on Figure 4.22, all analyzed cases exhibit a similar trend for contributions of flexural deformation. The flexural deformation slightly decreases when diagonal (shear) cracks form in the diaphragm. Upon the formation of flexural cracks, flexural deformation increased accordingly. By increasing the applied load, diagonal (shear) cracks are extended in the diaphragm, which result in some reduction in flexural contribution.

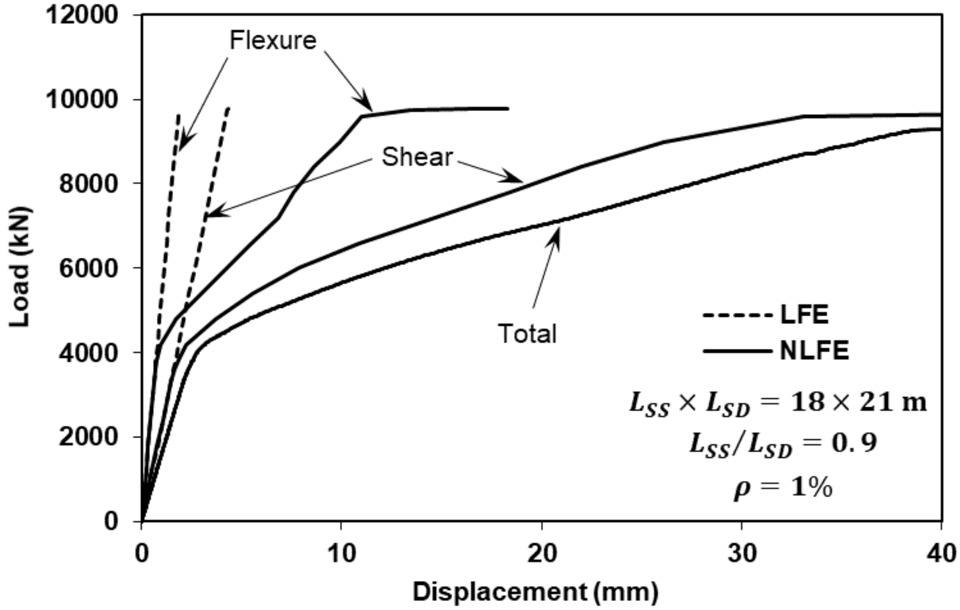

a)

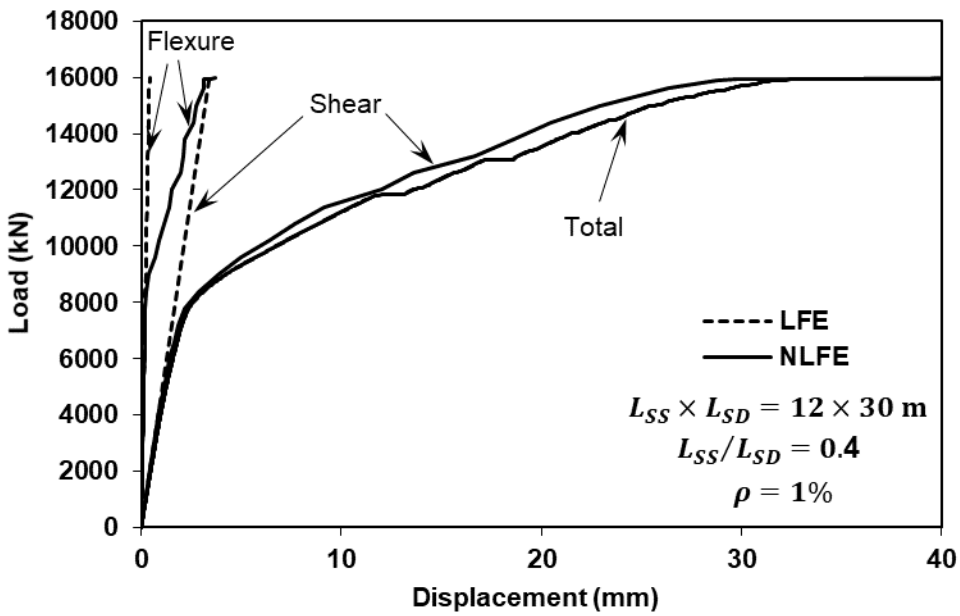

b)

Figure 4.21 – Force-deformation relationship showing portions due to shear and flexure for diaphragms with 1% reinforcement amount and aspect ratio (L_{SS}/L_{SD}) of: (a) 0.9 (Case 1); and (b) 0.4 (Case 4)

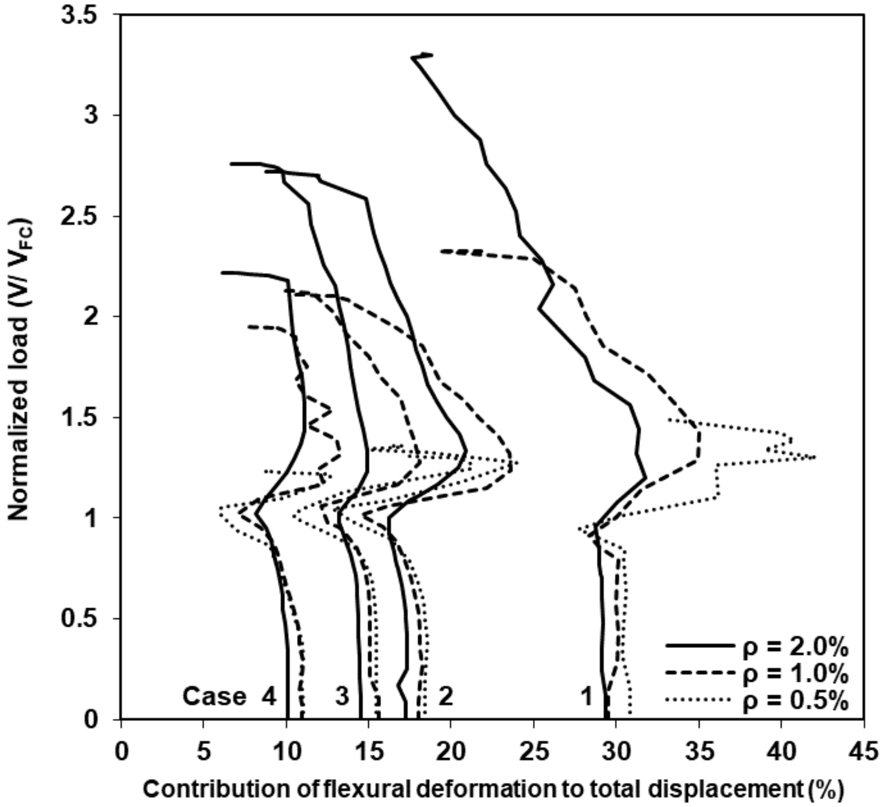

Figure 4.22 – Contribution of flexural deformation to total displacement for diaphragms Cases 1, 2, 3 and 4 with reinforcement amounts of 0.5%, 1.0% and 2.0%

4.7.4 Shear and Flexural Stiffness Reduction Factors

The load-deformation relationship of diaphragms indicates that the shear and flexural stiffnesses of diaphragm significantly reduce by increasing the applied in-plane shear forces. The stiffness reduction factor at each load level was defined as the ratio of the secant stiffness to the initial uncracked stiffness of diaphragm. In other words, the shear and flexural stiffness reduction factor was considered as the ratio of the linear shear or flexural displacement (obtained from linear finite element analysis) to the nonlinear shear or flexural displacement at each load level. Figures 4.22(a) and (b) present the shear, flexural and overall stiffness reduction factors versus load for diaphragms with $L_{SS} \times L_{SD} = 18 \times 21$ m (Case 1) and $L_{SS} \times L_{SD} = 12 \times 30$ m (Case 4) and 2% reinforcement amount, respectively.

One of the important conclusions obtained from Figure 4.23 is that the shear and flexural stiffness of diaphragm degrade simultaneously as the backstay force increases. For the most slender analyzed diaphragms ($L_{SS} \times L_{SD} = 18 \times 21$ m, Case 1) with the aspect ratio of 0.9, the flexural cracking occurred shortly after the shear (diagonal) cracking in the diaphragm. Thus, shear and flexural stiffnesses reduce concurrently. For other analyzed diaphragms with smaller aspect ratios (0.6 and 0.4), once the diagonal (shear) cracks occur, the diaphragm shear stiffness gradually reduces by about 15% while there is no reduction in flexural stiffness of diaphragms.

Formation of flexural cracks due to the strong-axis bending of diaphragms results in a significant reduction in both shear and flexural stiffnesses of diaphragms. By investigating the variation of shear strains before and after cracking of diaphragm, it is indicated that flexural cracking of diaphragm leads to extending cracks and a considerable increase in shear strain at the location of shear (diagonal) cracks. In fact, the less squat diaphragms (Case 1) with the aspect ratio close to 1 behave as a deep beam in which flexural cracks form in the flexural tension zone of diaphragm due to the effect of strong-axis bending. These flexural cracks trigger the formation of flexural-shear cracks in the diaphragm which extend towards the upper corner of the core where diagonal (shear) cracks formed. This results in the extending of shear cracks and the considerable increase of shear strains along the cracks.

The more squat diaphragms (Case 2, 3 and 4) with the aspect ratio between 0.3 and 0.7 are analogous to two beams located on each side of the core and bend simultaneously under the applied in-plane shear forces. Tensile stresses are developed in the flexural tension zone of each beam. Developed tensile stresses in the lower beam lead to the formation of flexural cracks in the diaphragm while developed tensile stresses in the upper beam trigger the extending of the shear (diagonal) cracks diagonally with the angle of approximately 45° towards the foundation walls where the uniformly distributed in-plane shear force were applied. Subsequently, the shear strain significantly increases along the cracks.

According to Figure 4.23, the overall stiffness reduction of diaphragms was noted to be similar to the shear stiffness reduction as all analyzed diaphragms were squat and shear-dominated and shear deformation formed the main portion of the total displacement.

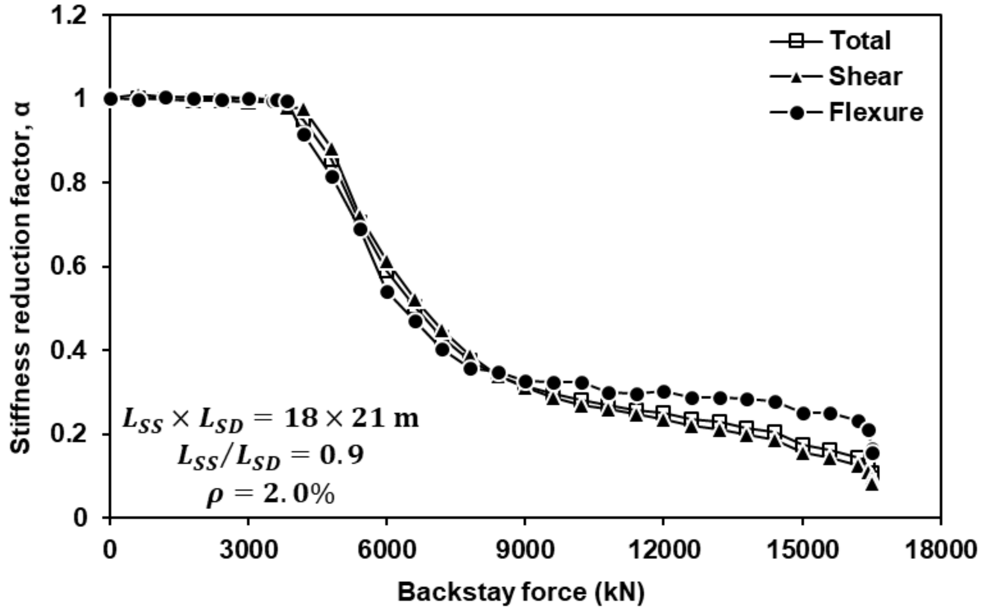

a)

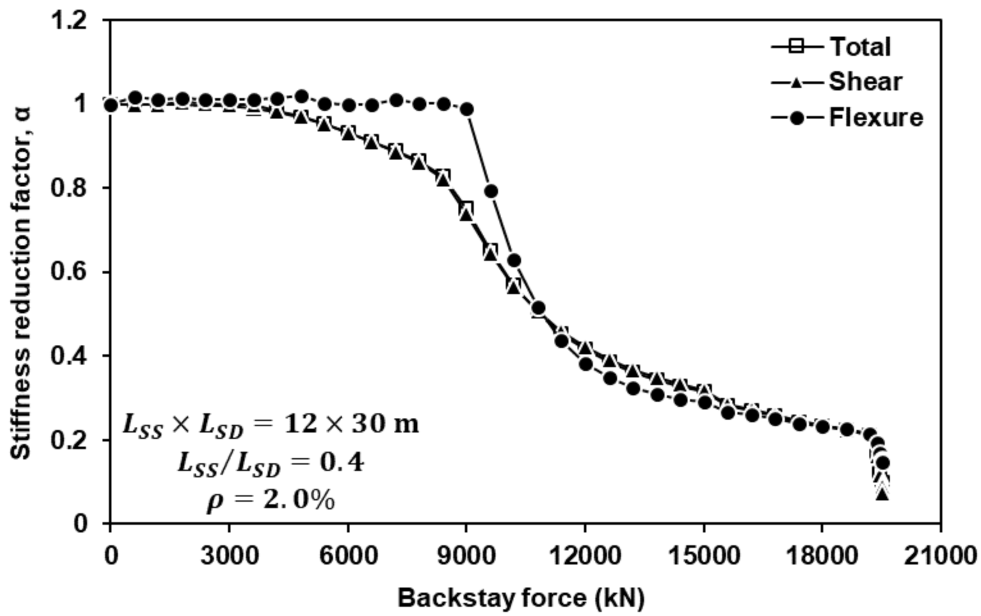

b)

Figure 4.23 – Shear and flexural stiffness reduction factors for diaphragms with 2% reinforcement amount and $L_{SS} \times L_{SD}$: (a) 18×21 m (Case 1); and (b) 12×30 m (Case 4)

Figure 4.24 presents the shear and flexural stiffness reductions for diaphragms with the aspect ratio of 0.6 (Case 2) and different reinforcement amounts, respectively. For lightly reinforced diaphragms (0.5% reinforcement), the shear and flexural stiffnesses sharply reduced by about 95% after flexural cracking, which can be estimated by a straight line.

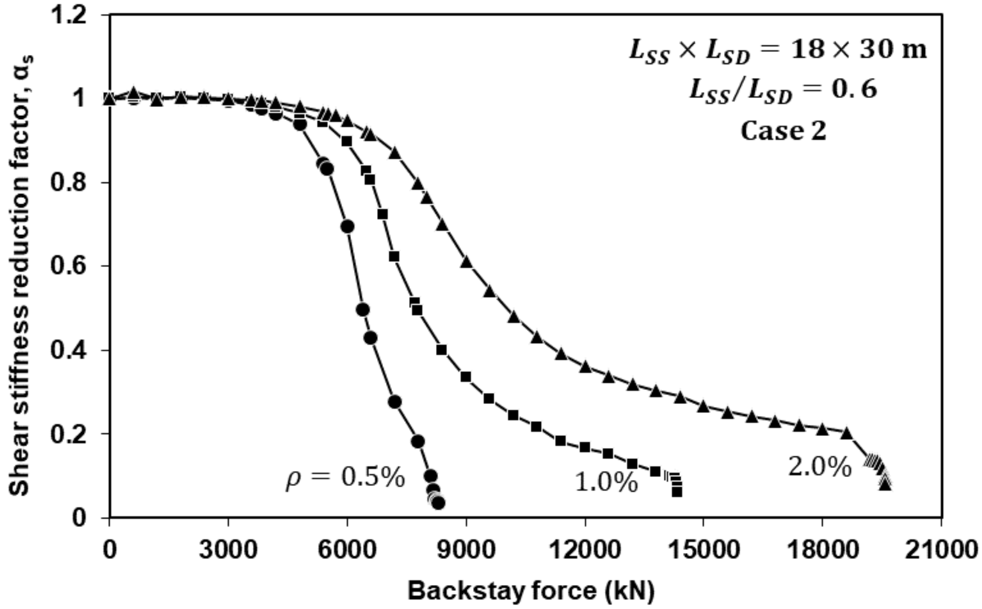

a)

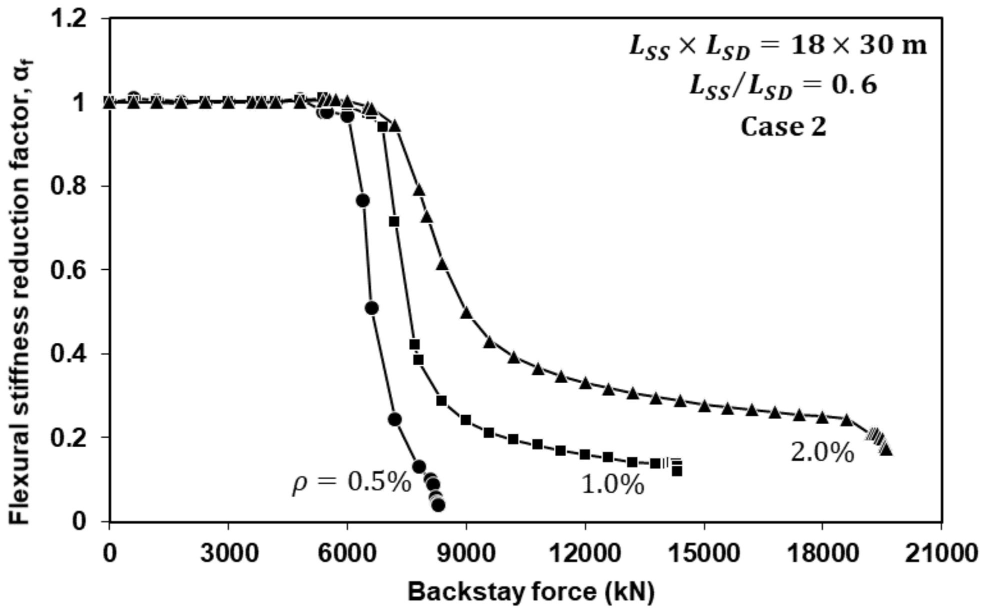

b)

Figure 4.24 – Stiffness reduction factors for diaphragms with $L_{SS} \times L_{SD} = 18 \times 30$ m (Case 2) and different reinforcement amount: (a) shear, α_s; and (b) flexure, α_f

For moderately and heavily reinforced diaphragms (1% and 2% reinforcement, respectively), there was a significant reduction in shear stiffness due to flexural cracking followed by a smooth reduction as the applied load approaches the diaphragm strength. The diaphragm shear stiffness reduced by about 85% and 75% for the reinforcement amounts of 1% and 2%, respectively.

The shear stiffness reduction for the most squat diaphragms (Case 5) with the aspect ratio of 0.2 are depicted in Figure 5.25. These diaphragms were noted to behave quite differently from other analyzed diaphragms due to the small aspect ratio. They failed as a result of extensive shear cracks while a small zone of tension cracks formed in the flexural tension zone. The shear stiffness reduces linearly upon the formation of diagonal (shear) cracks. Due to the small zone of flexural cracks, minor reduction in shear stiffness was observed due to flexural cracking. Therefore, the shear stiffness reduction can be estimated by a straight line. The curve for diaphragm with 2% reinforcement amount was not complete due to software limitation.

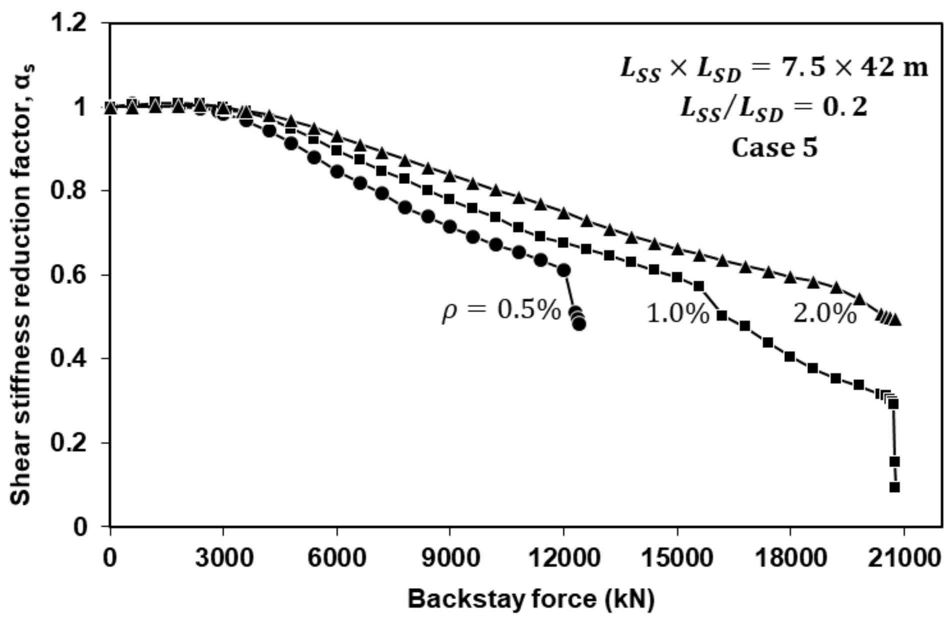

Figure 4.25 – Shear stiffness reduction factor, α_s, for diaphragms with $L_{SS} \times L_{SD} = 7.5 \times 42$ m (Case 5) and different reinforcement amount

4.8 Simplified Procedure for Estimating In-Plane Stiffness of Concrete Diaphragms

4.8.1 Trilinear Force-Deformation Relationship for Concrete Diaphragms

The analysis results indicate that the force-deformation relationship of concrete diaphragms subjected to backstay forces can be reasonably represented by a trilinear curve up to ultimate strength of diaphragm, V_N, as illustrated in Figure 4.26. The trilinear model is defined using the following five parameters: (1) the slope of the first line segment, K_1, (2) the slope of the second line segment, K_2, (3) the slope of the third line segment, K_3, (4) the load V_{SC} that defines the intersection of the first and second linear segments, and (5) the load V_{FC} that defines the intersection of the second and third linear segments.

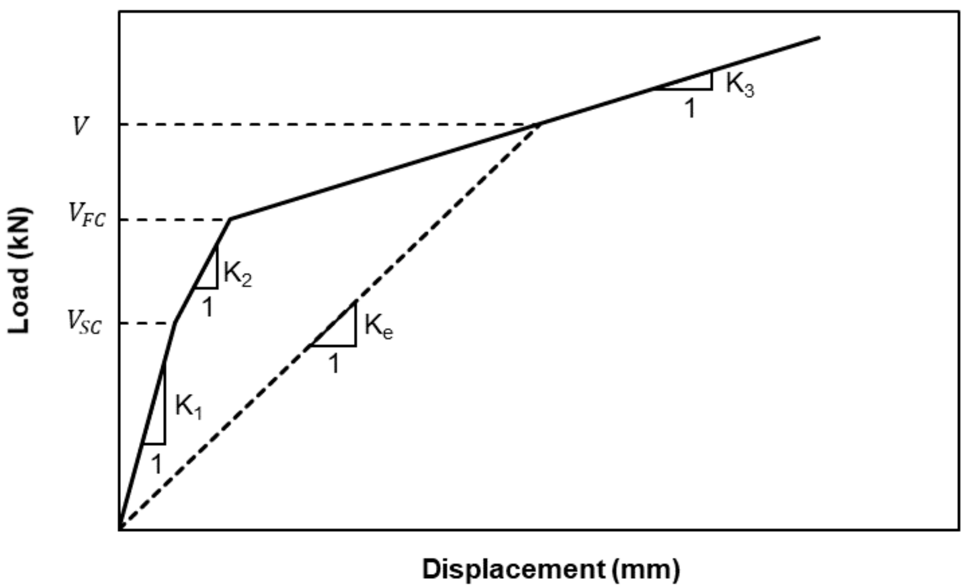

Figure 4.26 – Trilinear idealization of the force-deformation relationship of concrete diaphragms

The slope of the initial part (K_1) of the force-deformation curve is equal to the uncracked stiffness of diaphragm which depends on the geometry of diaphragm and concrete material properties. Once diagonal (shear) cracking took place, a small reduction occurred in the stiffness of diaphragm which is about 20%. However, this reduction varies slightly with the amount of reinforcement. From the analysis results of diaphragms, the ratio of cracked to uncracked diaphragm stiffness after diagonal (shear) cracking ($\alpha_1 = K_2/K_1$), can be calculated by the following equation:

$$\alpha_1 = 7.3\rho + 0.71 \tag{4.1}$$

where, ρ is the reinforcement ratio (A_s/A_g). Table 4.8 provides reasonable values for α_1 factor.

Table 4.8 – Values for α_1 factor

Reinforcement Ratio (%)	0.5	1	2
$\boldsymbol{\alpha_1 = K_2/K_1}$ **(%)**	75	80	85

By forming flexural cracks in the tension zone of diaphragm, the stiffness of diaphragm reduced significantly. The slope of the third line of the load-deformation model (K_3) depends primarily on the amount of reinforcement provided to the diaphragm. Equation (4.2), obtained from the analysis results, can be used to determine the ratio of cracked to uncracked diaphragm stiffness ($\alpha_2 = K_3/K_1$) after the formation of flexural cracks in the flexural zone of diaphragm:

$$\alpha_2 = 7.3\rho + 0.01 \tag{4.2}$$

Figure 4.27 presents the α_2 factor versus the diaphragm reinforcement amount. It is concluded that the ratio of the cracked stiffness of diaphragm to the initial diaphragm stiffness is independent of diaphragm geometry and concrete properties and is mainly proportional to the amount of reinforcement. Table 4.9 lists the appropriate values for α_2 factor of diaphragms with reinforcement ratios of 0.5%, 1% and 2%.

Table 4.9 – Values for α_2 factor

Reinforcement Ratio (%)	0.5	1	2
$\boldsymbol{\alpha_2 = K_3/K_1}$ **(%)**	5	8	16

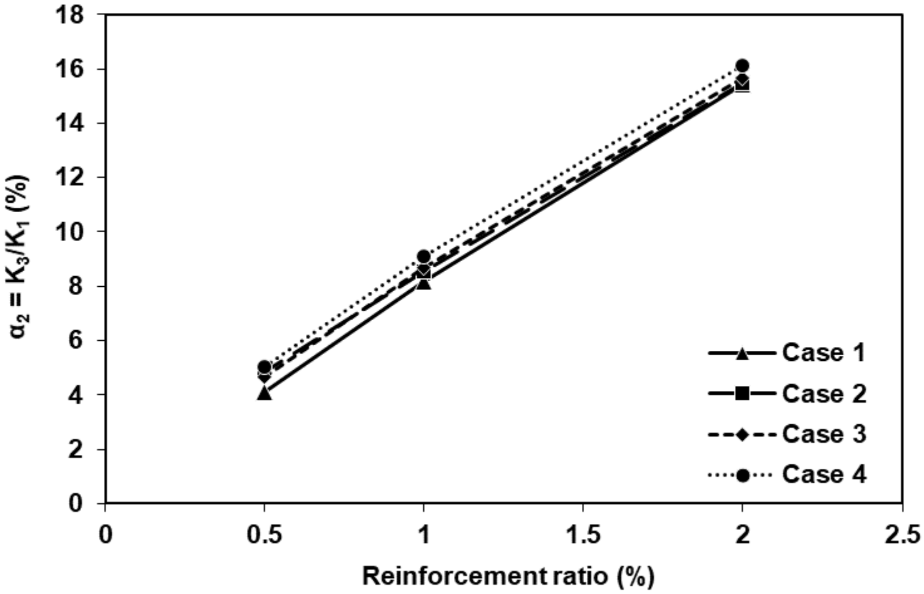

Figure 4.27 – Ratio of the tangent stiffness of diaphragm after flexural cracking to the uncracked stiffness of diaphragm versus reinforcement amount

The analysis results of diaphragms with different aspect ratios and different reinforcement amounts demonstrate that the magnitude of the load V_{SC}, which corresponds to the shear cracking (SC) of diaphragm, was independent of the diaphragm aspect ratio and reinforcement amount. The load V_{SC} exhibited an approximately similar magnitude for all analyzed diaphragms with the same core wall length (L_w). Thus, it was concluded that the shear (diagonal) cracking load V_{SC} depends on the length of the core wall which is a reasonable conclusion as all the applied in-plane shear forces should be transferred to the core wall. This load can be estimated by considering a uniform cracking shear stress ($0.3\sqrt{f_c'}$) over a factor of the core wall length ($a.L_W$) multiplied by the diaphragm thickness (t_d). In order to investigate the validity of this statement, two diaphragms with spans of $L_{SS} \times L_{SD} = 18 \times 21$ m and 12×30 m and 1% reinforcement (Cases 6 and 7) were analyzed with different core wall lengths of 10 and 12 m. The results of nineteen analyzed diaphragms, shown in Figure 4.28, indicate that the shear (diagonal) cracking load V_{SC} can be estimated by the following simplified equation:

$$V_{SC} = 0.45\sqrt{f_c'} \cdot L_W \cdot t_d \tag{4.3}$$

where, f_c' is the compressive strength of concrete.

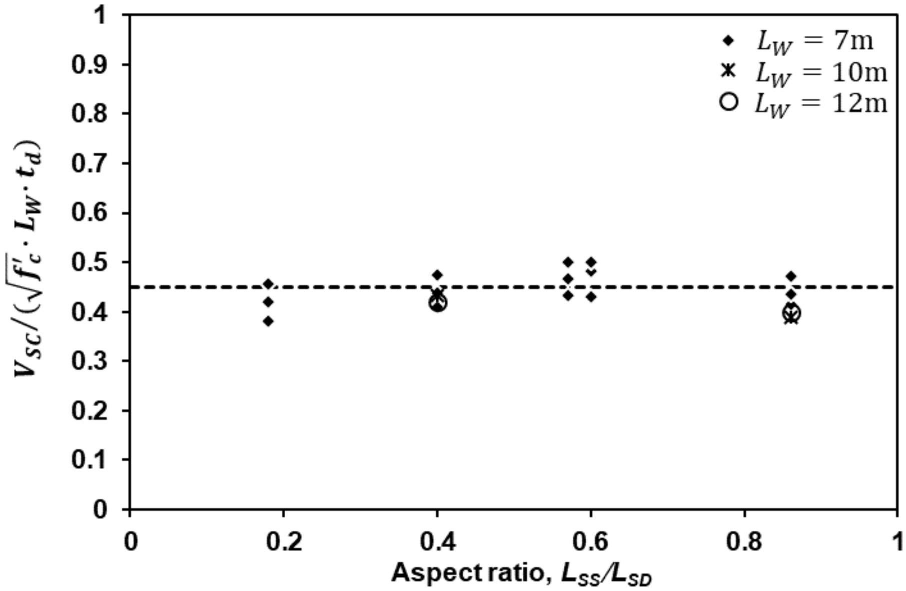

Figure 4.28 – Shear cracking load ratio, $V_{SC}/(\sqrt{f'_c} \cdot L_w \cdot t_d)$, for nineteen analyzed diaphragms with different aspect ratio (L_{SS}/L_{SD}) and core wall length (L_W)

Once flexural cracks formed in the diaphragm, the diaphragm became softer due to cracking. The load V_{FC} corresponds to the significant change in the slope of the load-deformation curve where the stiffness of diaphragm reduces noticeably. This observation can be attributed to a relationship between the load V_{FC} and flexural cracking. To determine the cracking moment at the onset of flexural cracking, the distribution of normal strain/stress in horizontal direction is assumed to be linear (plane sections remain plain) and the contribution of reinforcement is taken into account. The cracking moment based on the assumption of linear normal strain/stress (LNS) distribution can be calculated from Equation (4.4):

$$M_{LNS} = 0.33\sqrt{f'_c} \cdot S(1 + n\rho) \tag{4.4}$$

where, S is the elastic section modulus (I_g/c) and n is the modular ratio (E_s/E_c).

Since the distribution of strains does not remain linear as the diaphragm becomes deeper by decreasing the aspect ratio, the calculated cracking moment is larger than the actual cracking moment of the section. This discrepancy increases by decreasing the aspect ratio of diaphragm, which increases the degree of nonlinearity in the strain profile. Therefore, a correction factor is required to consider the effect of nonlinearity in the strain distribution. In addition, the load V_{FC} was defined at the intersection of the two linear segments where the slope of the load-deformation curve decreases significantly. This load is larger than the load at the onset of flexural cracking, V'_{FC}; hence, the second correction factor is applied to account for this difference. This correction factor increases as the diaphragm aspect ratio increases.

Thus, a correction factor (β) is defined as a ratio of the flexural cracking load V_{FC} corresponding to the significant change in the slope of the load-deformation curve, obtained from the analysis results, to the flexural cracking load V_{LNS} calculated based on the assumption of linear normal strain distribution. This correction factor combines the effects of the nonlinearity in strain distribution and the difference between the magnitude of the load at the onset of flexural cracking, V'_{FC}, and the load corresponding to the significant change in the slope of the load-deformation curve, V_{FC}. Analysis results demonstrate that the correction factor β mainly depends on the aspect ratio (L_{SS}/L_{SD}) of the diaphragm. The relationship of the correction factor to the diaphragm aspect ratio can be approximated by a straight line as follows (Equation 4.5):

$$\beta = 0.8(L_{SS}/L_{SD}) + 0.7 \qquad (0.3 < L_{SS}/L_{SD}) \tag{4.5}$$

hence, the load V_{FC} is determined as:

$$V_{FC} = \beta \cdot M_{LNS}/L_{SS} \tag{4.6}$$

It should be noted that Equation 4.6 is not appropriate to determine the load V_{FC} for the most squat analyzed diaphragms with the aspect ratio of 0.2 (Case5). These diaphragms behaved quite differently from other analyzed diaphragms due to the small aspect ratio. The failure occurred as a result of extensive shear cracks while a small zone of tension cracks formed in the flexural tension zone. Particularly, for the lightly reinforced diaphragm in this case, the failure was observed shortly after the formation of flexural cracks. Therefore, the aspect ratio was limited to greater than 0.3 in Equation 4.5.

The distribution of normal stresses in horizontal direction at load level V_{FC} obtained from the nonlinear analysis of diaphragms and the corresponding resultant forces are presented in Figures 4.29 and 4.31 for diaphragms $L_{SS} \times L_{SD} = 18 \times 21$ m and $L_{SS} \times L_{SD} = 12 \times 30$ m with

2% reinforcement amount, respectively. Figures 4.30 and 4.32 show the linear distribution of normal stress at the onset of flexural cracking and the resultant forces for the same diaphragms, respectively. In addition, the correction factor β determined based on Equation 4.5 and the corresponding load V_{FC} predicted for each diaphragm are given in the figures for comparison. There is a good agreement between the observed from analysis and predicted load V_{FC}. The results for the same diaphragms with 0.5% reinforcement amount are presented in Appendix C.

The proposed trilinear model for load-deformation relationship of concrete diaphragms can be also used to define the shear behaviour of the diaphragm by replacing the initial stiffness of diaphragm (K_1) with the uncracked shear rigidity of diaphragm ($G_c A_g$). Therefore, the shear behaviour of concrete diaphragms subjected to backstay forces can be illustrated by a trilinear curve.

The flexural stiffness of diaphragm reduces due to flexural cracking in the diaphragm. Therefore, prior to occurrence of flexural cracks there is no reduction in the flexural stiffness of diaphragm. The flexural behaviour of diaphragm can be also approximated by the proposed model for load-deformation relationship of diaphragm by using the uncracked flexural rigidity of diaphragm as the initial stiffness which remains constant up to the load V_{FC}. As a result, the flexural behaviour of diaphragms is defined as a bilinear relationship. Figure 4.33 compares the predicted and observed load-deformation curves for diaphragm with $L_{SS} \times L_{SD} = 12 \times 21$ m (Case 3) and 1% reinforcement amount. As shown, there is a good agreement between the predicted and analytical results. Comparison of predictions with analysis results for other analyzed diaphragms are given in Appendix C.

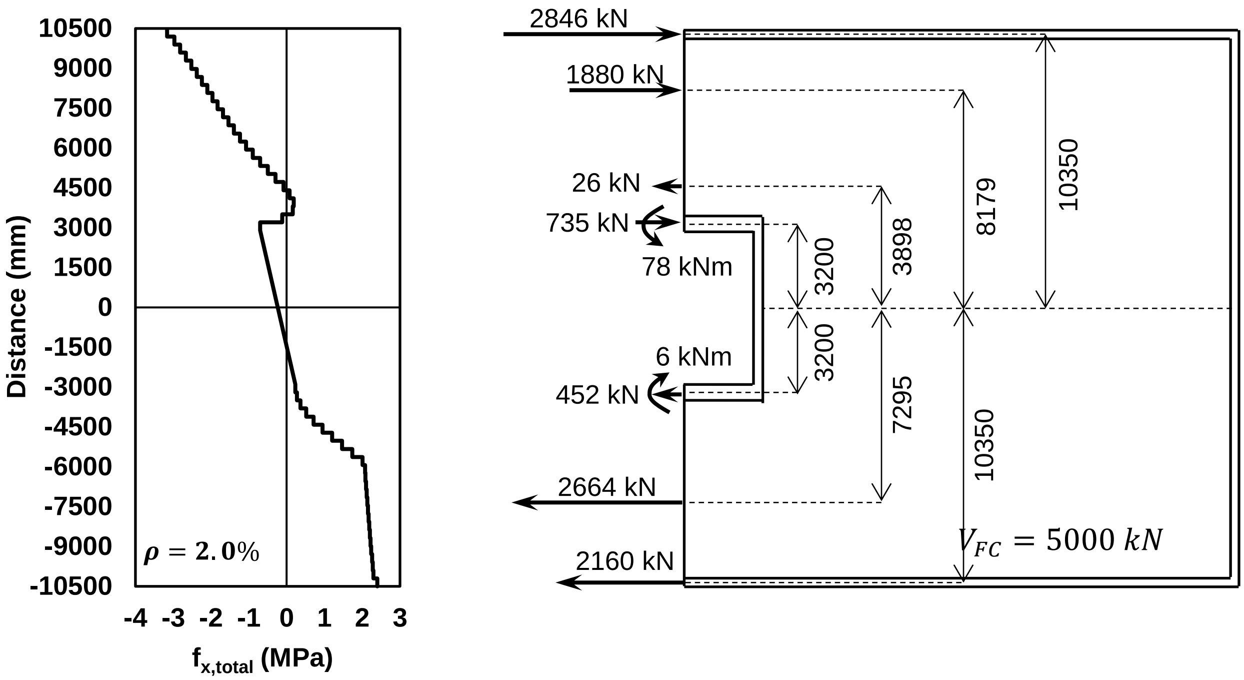

Figure 4.29 – Distribution of normal stresses at load level V_{FC} (left) and the corresponding resultant forces (right) for diaphragm $L_{SS} \times L_{SD} = 18 \times 21$ m with 2% reinforcement amount

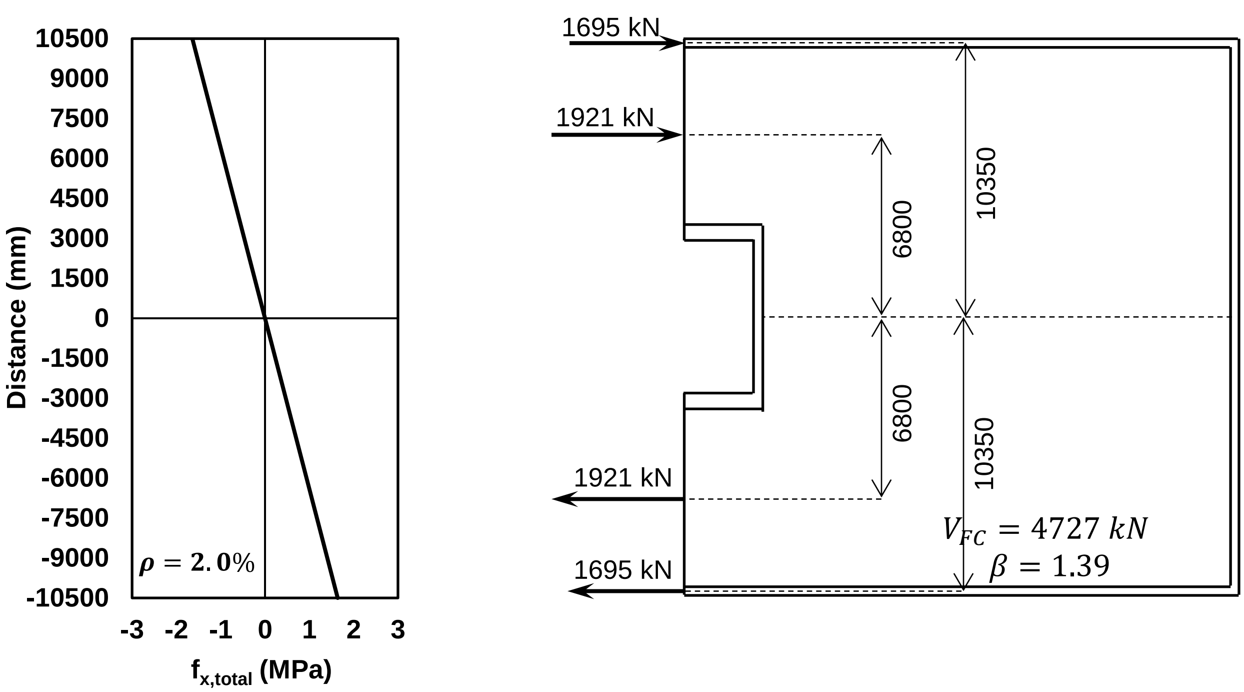

Figure 4.30 – Linear distribution of normal stresses at onset of flexural cracking (left) and the corresponding resultant forces (right) for diaphragm $L_{SS} \times L_{SD} = 18 \times 21$ m with 2% reinforcement amount

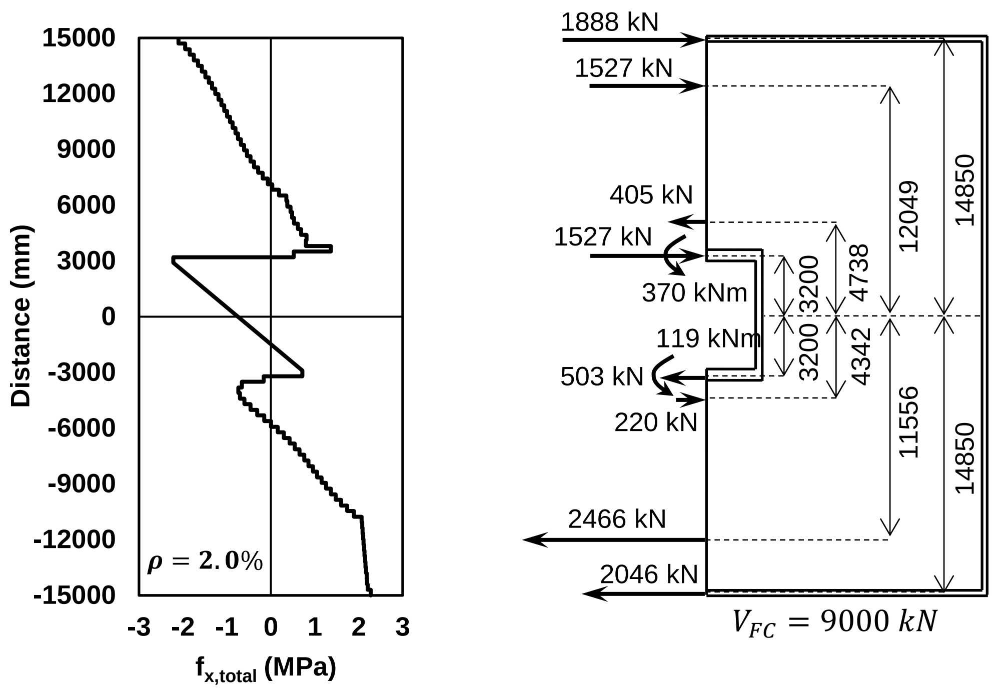

Figure 4.31 – Distribution of normal stresses at load level V_{FC} (left) and the corresponding resultant forces (right) for diaphragm $L_{SS} \times L_{SD} = 12 \times 30$ m with 2% reinforcement amount

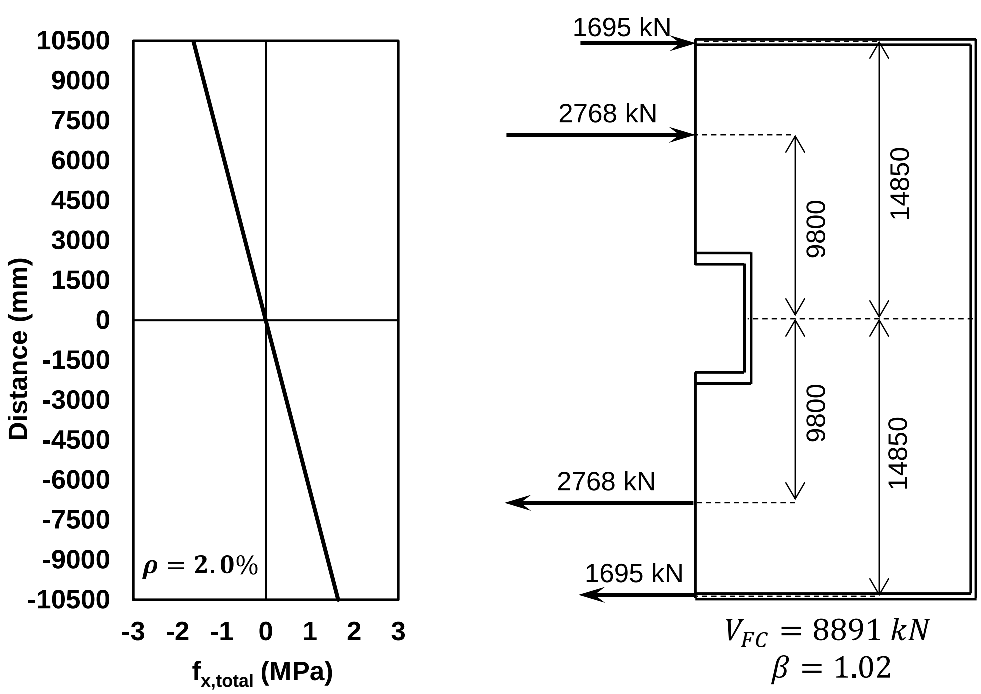

Figure 4.32 – Linear distribution of normal stresses at onset of flexural cracking (left) and the corresponding resultant forces (right) for diaphragm $L_{SS} \times L_{SD} = 12 \times 30$ m with 2% reinforcement amount

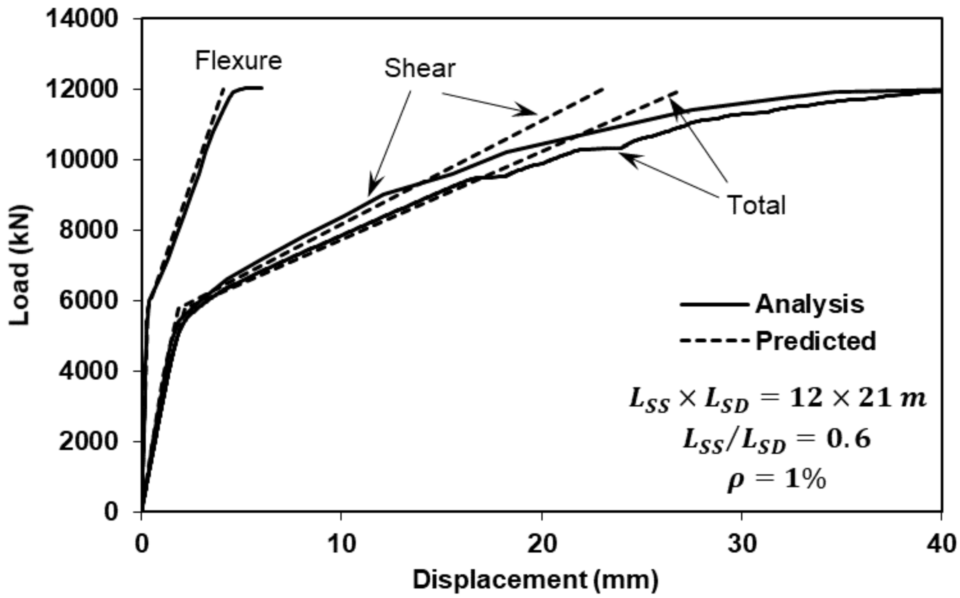

Figure 4.33 – Comparison of predicted and observed load-deformation relationships showing portions due to shear and flexure

4.8.2 Effective Shear and Flexural Stiffnesses

According to design guidelines, the diaphragm should be modelled as elastic elements using a linear model with an effective stiffness to account for cracking. In fact, the linear model is the appropriate model for diaphragms since the diaphragms are expected to remain elastic under the design forces. As the force-deformation behaviour of diaphragms is approximated by a trilinear model as shown in Figure 4.33, the shear and flexural stiffness reductions of diaphragms can be estimated at different backstay force level, V, as follows:

$$V \leq V_{SC}: \qquad \alpha_s = \alpha_f = 1 \tag{4.7}$$

$$V_{SC} < V \leq V_{FC}: \qquad \alpha_s = \frac{\alpha_1 V}{(\alpha_1 - 1)V_{SC} + V}, \quad \alpha_f = 1 \tag{4.8}$$

$$V_{FC} < V: \qquad \alpha_s = \frac{\alpha_1 \alpha_2 V}{\alpha_2(\alpha_1 - 1)V_{SC} + (\alpha_2 - \alpha_1)V_{FC} + \alpha_1 V} \tag{4.9}$$

$$\alpha_f = \frac{\alpha_2 V}{(\alpha_2 - 1)V_{FC} + V}$$

where, α_s and α_f are the shear and flexural stiffness reduction factors, respectively. The effective shear and flexural stiffnesses of diaphragm can be calculated as the shear or flexural stiffness reduction factor times the shear or flexural rigidity of diaphragm, respectively. Thus, the effective shear and flexural stiffnesses of diaphragm are a function of the backstay force, V and decrease with increasing the backstay force. The accuracy of the proposed procedure is validated against the results of NLFE analysis of concrete diaphragms.

Figures 4.34 and 4.35 compare the predicted shear and flexural stiffness reduction factors of concrete diaphragms with the analysis results for diaphragm with $L_{SS} \times L_{SD} = 12 \times 21$ m (Case 3) and 1% reinforcement, respectively. As seen, there is a good agreement between the predictions and analytical results. In addition, the upper bound and lower bound shear and flexural stiffnesses recommended by ATC-72-1 are shown in Figures 4.34 and 4.35. As aforementioned, ATC-72-1 recommends the upper bound of $0.5\mathrm{G_c A_g}$ and $0.5\mathrm{E_c I_g}$ for shear and flexural stiffnesses of diaphragms, respectively. This reduced upper bound could be to capture the effects of out-of-plane flexural cracking due to the gravity loads and possible shrinkage cracks in the diaphragms which will be investigated in Chapter 5. Comparisons of the predicted shear and flexural stiffness reduction factors with the analysis results for other analyzed diaphragms are presented in Appendix C.

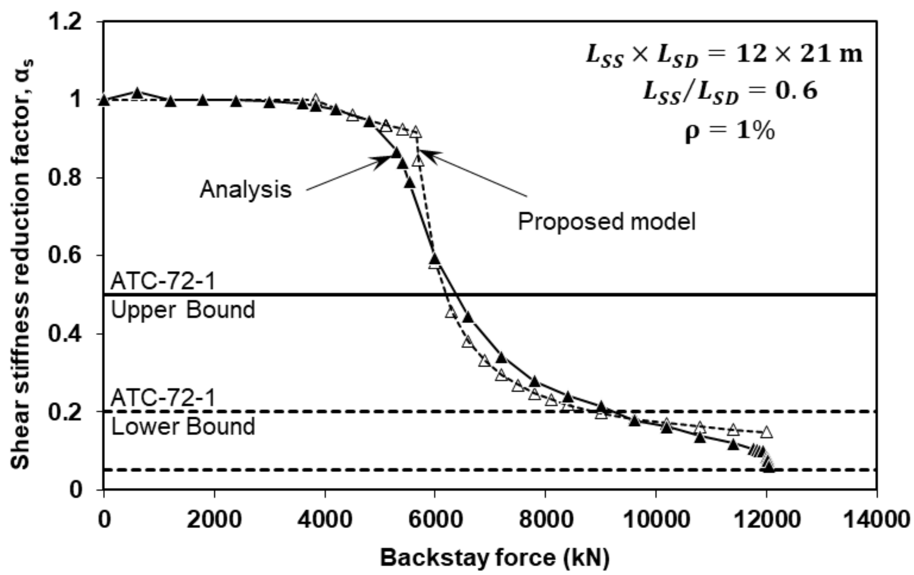

Figure 4.34 – Comparison of shear stiffness reduction factor obtained from analysis and proposed model for diaphragm with $L_{SS} \times L_{SD} = 12 \times 21$ m (Case 3) and $\rho = 1.0\%$

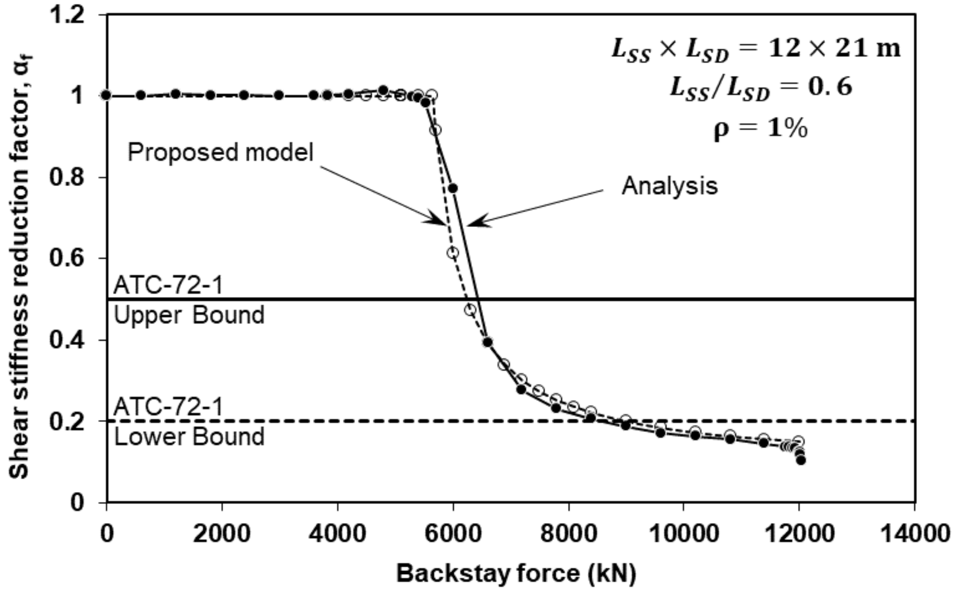

Figure 4.35 – Comparison of flexural stiffness reduction factor obtained from analysis and proposed model for diaphragm with $L_{SS} \times L_{SD} = 12 \times 21$ m (Case 3) and $\rho = 1.0\%$

4.8.3 Rigorous Model for Shear and Flexural Stiffnesses of Diaphragms

The effective shear and flexural stiffnesses of concrete diaphragms subjected to backstay forces can be accurately determined at each backstay force level based on the developed model for the load-deformation relationship of diaphragms. However, design engineers are interested in simpler and more practical approaches for estimating the effective diaphragm stiffness in order to evaluate the backstay effect in high-rise core wall buildings. Therefore, the proposed model was made one step simpler yet rigorous as accounts for the continuous reduction in the diaphragm shear stiffness as the backstay forces increase.

In order to compare the shear reduction factors for all analyzed diaphragms with different aspect ratios and different reinforcement amounts, the relationship between effective shear stiffness and backstay force were divided into three parts: (1) from zero loading to diagonal (shear) cracking – no reduction in shear stiffness (shear reduction factor is equal to 1); (2) from shear cracking to flexural cracking – the shear stiffness reduces by about 15%; and (3) from flexural cracking to failure of the diaphragm – shear stiffness reduces to about 20% of the initial shear stiffness.

Figure 4.36 compares the relationship between the shear stiffness reduction factor and the backstay force for diaphragms Cases 1, 2, 3 and 4 with 1% and 2% reinforcement amount (gray lines). Interestingly, the trend of the shear stiffness reduction was similar for analyzed diaphragms with different aspect ratios ranging from 0.4 to 0.9. It revealed that the degradation of diaphragm shear stiffness is independent of diaphragm aspect ratio specifically after flexural cracking. Moreover, the diaphragm reinforcement amount has negligible influence on the shear stiffness reduction of concrete diaphragms.

According to the proposed rigorous model presented in Figure 4.36, the shear stiffness of slender diaphragms (i.e., diaphragms with the aspect ratio of greater than 0.3, $L_{SS}/L_{SD} > 0.3$) remains constant and equal to the initial shear stiffness of diaphragm prior to the diagonal (shear) cracking. Then, it gradually reduces to 85% prior to the flexural cracking. Upon the formation of flexural cracks, the shear stiffness significantly reduces to about 35% of the initial stiffness when the backstay forces reach to 25% of the diaphragm resistance after the flexural cracking. After this point, the shear stiffness gradually degrades to about 15% of the initial shear stiffness of diaphragm at the time of failure.

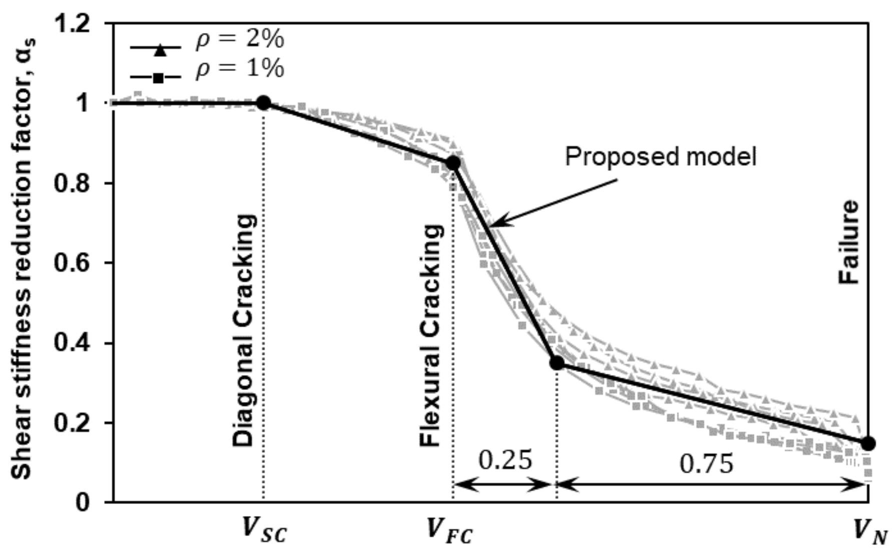

Figure 4.36 – Rigorous model for effective shear stiffness of slender concrete diaphragms with $L_{SS}/L_{SD} > 0.3$

Consequently, the relationship between flexural reduction factor and backstay force were separated into two ranges: (1) from zero loading to flexural cracking – no reduction in flexural stiffness (flexural reduction factor is equal to 1); and (2) from flexural cracking to failure of diaphragm – flexural stiffness significantly reduces. The relationship between flexural stiffness reduction factors and backstay force for diaphragms Cases 1, 2, 3 and 4 with 1% and 2% reinforcement amount (gray lines) are shown in Figure 4.37. Similarly, the analysis results indicated that the reduction in diaphragm flexural stiffness is independent of diaphragm aspect ratio. However, the diaphragm reinforcement amount has small influence on the flexural stiffness reduction of concrete diaphragms, as illustrated in Figure 4.37.

Based on the proposed rigorous model, the flexural stiffness of slender diaphragms is equal to the initial flexural stiffness of diaphragm prior to flexural cracking. By the formation of flexural cracks, the flexural stiffness considerably decreases to about 35% of the initial flexural stiffness when the backstay forces reach to 20% of the diaphragm resistance after the flexural cracking. Then, the flexural stiffness gradually reduces to about 20% of the initial flexural stiffness of diaphragm at the time of failure.

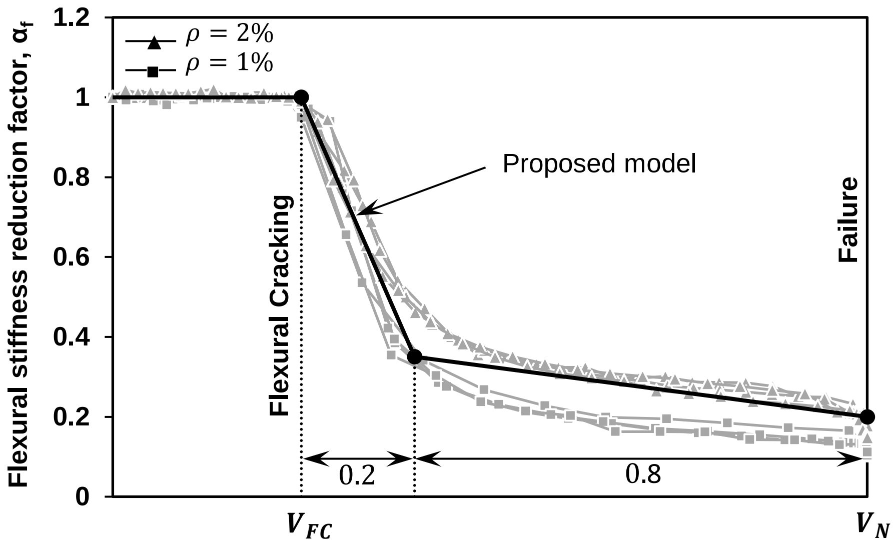

Figure 4.37 – Rigorous model for effective flexural stiffness of slender concrete diaphragms with $L_{SS}/L_{SD} > 0.3$

Figure 4.38 presents the relationship between shear stiffness reduction factors and backstay force for diaphragms Case 5 with 1% and 2% reinforcement ratios. The reduction in shear stiffness of diaphragms with 1% and 2% reinforcement amounts coincided, which confirms that the shear stiffness reduction factor of squat diaphragms is independent of diaphragm reinforcement amount.

The proposed rigorous model for shear stiffness of squat diaphragms (i.e., diaphragms with the aspect ratio of 0.3 or smaller, $L_{SS}/L_{SD} \leq 0.3$) is illustrated in Figure 4.38. The shear stiffness remains constant and equal to the initial shear stiffness of diaphragm until shear (diagonal) cracks formed. Formation of shear cracks results in considerable decrease in shear stiffness of diaphragms which reduces to about 35% of the initial shear stiffness at the time of failure. As shown in Figure 4.38, the reduction in shear stiffness for squat diaphragms can be properly estimated by a straight line.

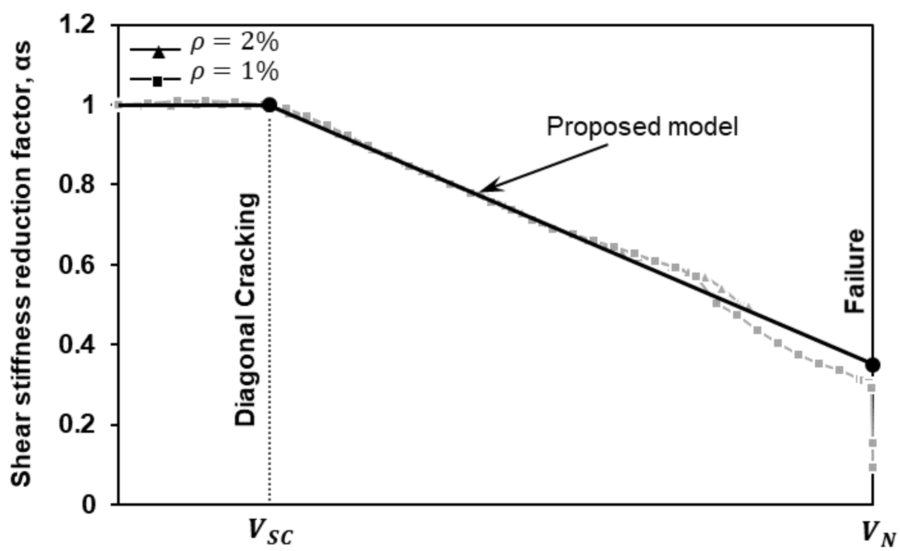

Figure 4.38 – Rigorous model for effective shear stiffness of squat concrete diaphragms with $L_{SS}/L_{SD} \leq 0.3$

4.8.4 Simple Model for Diaphragm Stiffness

There are quite different models ranging from complex to simple can be proposed for the effective stiffness of concrete diaphragms according to the analysis results. Figures 4.39 and 4.40 illustrate relatively simple models for shear and flexural stiffnesses of slender concrete diaphragms with the aspect ratio of greater than 0.3 ($L_{SS}/L_{SD} > 0.3$), respectively. Although the shear stiffness of diaphragms continuously degrades by increasing the backstay forces, the assumption of constant values for the upper bound and the lower bound of shear stiffness are reasonable in order to make the model simple and practical.

The straight lines in Figure 4.39 show the upper bound (solid lines) and lower bound (dashed lines) for the shear stiffness of diaphragms. Before diagonal (shear) cracking, the upper bound and lower bound for shear stiffness reduction factor are coincided and equal to 1. After shear cracking takes place, the upper bound remains unchanged equal to 1 while the lower bound reduces to 0.85 due to diagonal (shear) cracking. By formation of flexural cracks, there is a considerable reduction in both upper bound and lower bound shear stiffnesses. The upper bound reduces to 0.5 while the lower bound decreases to 0.25, as shown in Figure 4.39. The proposed model shows a reasonable match with analysis results and it is relatively simple.

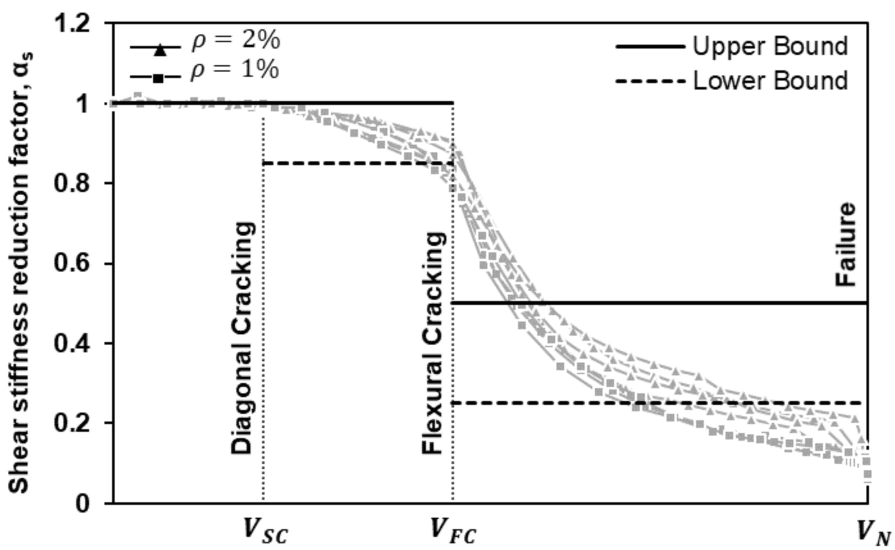

Figure 4.39 – Simple model for effective shear stiffness of slender concrete diaphragms with $L_{SS}/L_{SD} > 0.3$

Figure 4.40 presents the simple model proposed for the flexural stiffness of slender diaphragms. The upper bound and lower bound considered for the flexural stiffness reduction factor after flexural cracking are 0.5 and 0.2, respectively. The simple model for the stiffness of squat concrete diaphragms is illustrated in Figure 4.41. According to this model, the upper bound for the shear stiffness reduces to 0.8 while the lower bound decreases to 0.4.

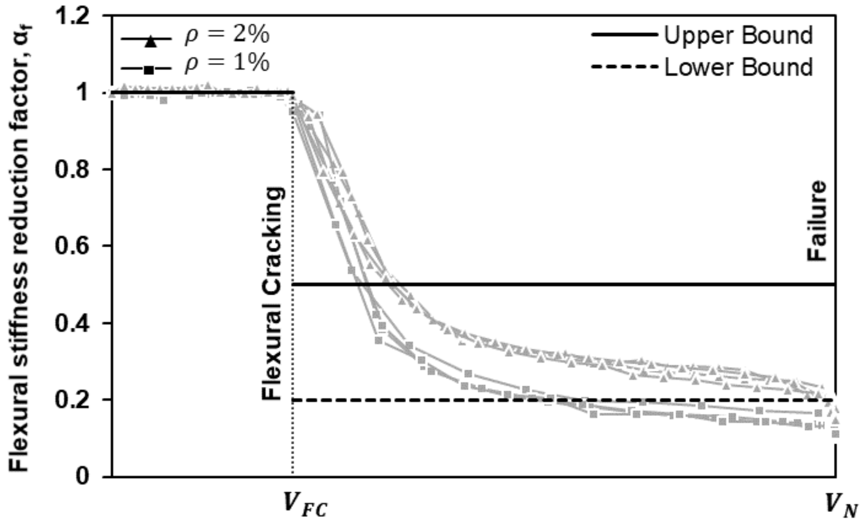

Figure 4.40 – Simple model for effective flexural stiffness of slender concrete diaphragms with $L_{SS}/L_{SD} > 0.3$

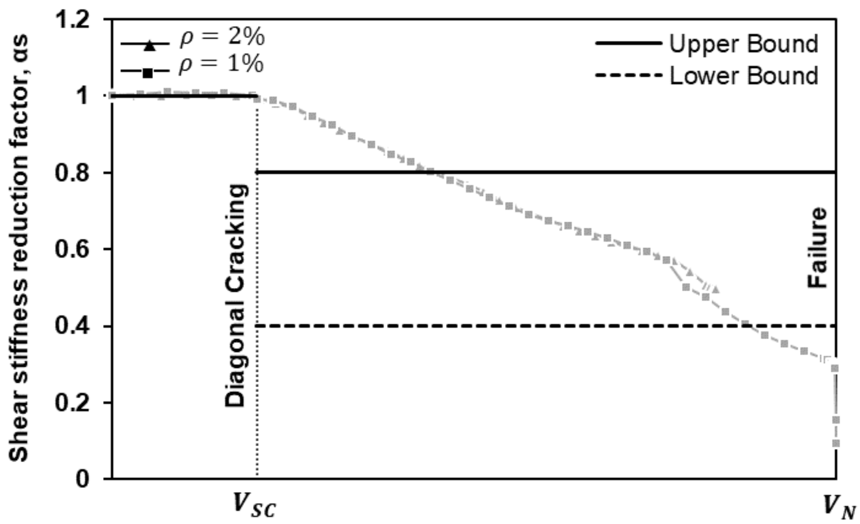

Figure 4.41 – Simple model for effective shear stiffness of squat concrete diaphragms with $L_{SS}/L_{SD} \leq 0.3$

4.8.5 Summary of Simplified Models

The proposed rigorous and simple models for the shear and flexural stiffnesses of concrete diaphragms subjected to backstay forces can be summarized as follows:

Definition of parameters utilized in the simplified models:

L: Overall diaphragm length (out-to-out of foundation walls) perpendicular to applied shear force

L_{SS}: Diaphragm shear span, equal to length of diaphragm perpendicular to applied shear force (center-to-center of core wall and foundation wall)

L_{SD}: Diaphragm shear depth, equal to length of diaphragm parallel to applied shear force (to outside of foundation walls)

L_W: Length of core wall parallel to applied shear force

t_d: Thickness of diaphragm

t_W: Thickness of foundation walls

h: Story height, equal to half of height of upper and lower stories

V: Applied shear force

M_{LNS}: Strong-axis bending moment at the onset of flexural cracking based on the assumption of linear normal stress (LNS) distribution

- Calculate an estimate of the shear force at diagonal (shear) cracking, V_{SC}:

  $$V_{SC} = 0.45\sqrt{f_c'} \cdot L_W \cdot t_d \tag{4.3}$$

- Calculate an estimate of the shear force at flexural cracking, V_{FC}, for slender diaphragms ($L_{SS}/L_{SD} > 0.3$):

  $$V_{FC} = \beta \cdot M_{LNS}/L_{SS} \tag{4.6}$$

  $$\beta = 0.8(L_{SS}/L_{SD}) + 0.7 \tag{4.5}$$

  $$M_{LNS} = 0.3\sqrt{f_c'} \cdot S(1 + n\rho) \tag{4.4}$$

  where,
  $n = E_s/E_c$
  $\rho = A_s/A_g$
  $S = I_g/c$

Tables 4.10 to 4.13 summarize the rigorous model for flexural and shear stiffnesses of slender and squat concrete diaphragms, respectively.

Table 4.10 – Rigorous model for flexural stiffness of slender diaphragms ($0.3 < L_{SS}/L_{SD}$)

Shear Force Level	**Shear Stiffness Reduction ($\boldsymbol{E_c I_e / E_c I_g}$)**
$\boldsymbol{V = V_{FC}}$	1
$\boldsymbol{V = 0.2(V_N - V_{FC})}$	0.35
$\boldsymbol{V = V_N}$	0.15

Linear interpolation between the points

Table 4.11 – Rigorous model for shear stiffness of slender diaphragms ($0.3 < L_{SS}/L_{SD}$) when $V_{SC} < V_{FC}$

Shear Force Level	**Shear Stiffness Reduction ($\boldsymbol{G_c A_{ve} / G_c A_{vg}}$)**
$\boldsymbol{V = V_{SC}}$	1
$\boldsymbol{V = V_{FC}}$	0.85
$\boldsymbol{V = 0.25(V_N - V_{FC})}$	0.35
$\boldsymbol{V = V_N}$	0.15

Linear interpolation between the points

Table 4.12 – Rigorous model for shear stiffness of slender diaphragms ($0.3 < L_{SS}/L_{SD}$) when $V_{SC} \geq V_{FC}$

Shear Force Level	**Shear Stiffness Reduction ($\boldsymbol{G_c A_{ve} / G_c A_{vg}}$)**
$\boldsymbol{V = V_{FC}}$	1
$\boldsymbol{V = 0.25(V_N - V_{FC})}$	0.35
$\boldsymbol{V = V_N}$	0.15

Linear interpolation between the points

Table 4.13 – Rigorous model for shear stiffness of squat diaphragms ($L_{SS}/L_{SD} \leq 0.3$)

Shear Force Level	Shear Stiffness Reduction ($\boldsymbol{G_c A_{ve}/G_c A_{vg}}$)
$\boldsymbol{V = V_{SC}}$	1
$\boldsymbol{V = V_N}$	0.35

Linear interpolation between the points

Tables 4.14 to 4.17 summarize the simple upper-bound and lower-bound estimates for flexural and shear stiffnesses of slender and squat concrete diaphragms, respectively.

Table 4.14 – Simple model for flexural stiffness of slender diaphragms ($0.3 < L_{SS}/L_{SD}$)

Shear Force Level	Flexural Stiffness Reduction ($\boldsymbol{E_c I_e/E_c I_g}$)	
	Upper Bound	Lower Bound
$\boldsymbol{V < V_{FC}}$	1	1
$\boldsymbol{V_{FC} \leq V}$	0.5	0.2

Table 4.15 – Simple model for shear stiffness of slender diaphragms ($0.3 < L_{SS}/L_{SD}$) when $V_{SC} < V_{FC}$

Shear Force Level	Shear Stiffness Reduction ($\boldsymbol{G_c A_{ve}/G_c A_{vg}}$)	
	Upper Bound	Lower Bound
$\boldsymbol{V \leq V_{SC}}$	1	1
$\boldsymbol{V_{SC} < V \leq V_{FC}}$	1	0.85
$\boldsymbol{V_{FC} < V}$	0.5	0.25

Table 4.16 – Simple model for shear stiffness of slender diaphragms ($0.3 < L_{SS}/L_{SD}$) when $V_{SC} \geq V_{FC}$

Shear Force Level	Shear Stiffness Reduction (G_cA_{ve}/G_cA_{vg})	
	Upper Bound	**Lower Bound**
$\boldsymbol{V < V_{FC}}$	1	1
$\boldsymbol{V_{FC} \leq V}$	0.5	0.25

Table 4.17 – Simple model for shear stiffness of squat diaphragms ($L_{SS}/L_{SD} \leq 0.3$)

Shear Force Level	Shear Stiffness Reduction (G_cA_{ve}/G_cA_{vg})	
	Upper Bound	**Lower Bound**
$\boldsymbol{V < V_{SC}}$	1	1
$\boldsymbol{V_{SC} \leq V}$	0.8	0.4

4.9 Summary and Conclusions

An important aspect of the seismic design of high-rise core wall buildings involves determining the forces within the diaphragms connecting the tower walls to the below-grade foundation walls. These diaphragms are usually modelled as linear elastic members, and the assumed effective stiffness of the diaphragms significantly influences how much of the lateral force will go into each of the two possible force paths: (i) into the below-grade foundation walls (backstay force path) and (ii) remain in the tower walls and transfer down to the wall foundations.

In the current study, nonlinear finite element (NLFE) model VecTor2 was used to study the behaviour of concrete diaphragms subjected to backstay forces and to investigate the reduction in shear and flexural stiffnesses of concrete diaphragms as the backstay forces increase. The VecTor2 model was verified by comparing predictions against the results of a diaphragm test by Nakashima (1981). The validated NLFE model was used to examine the influence of amount of uniformly distributed reinforcement in the two span directions of the diaphragm and the span lengths of the diaphragm (parallel and perpendicular to the backstay forces). A total of 19 different building diaphragms were analyzed in the current study.

The analysis results demonstrated that the load-deformation relationship for concrete diaphragms subjected to backstay forces can be accurately represented by a trilinear curve. Prior to cracking, the load-deformation relationship is linear and the stiffness of the diaphragms is equal to the uncracked stiffness. The slope of the load-deformation curve reduces after the diaphragm develops significant cracking. Diagonal (shear) cracks occur first; but this only reduce the shear stiffness of the diaphragm by a small amount, and does not influence the flexural stiffness. When flexural cracking occurs in the flexural tension zone of the diaphragm, both the shear and flexural stiffnesses reduce significantly.

A number of the observations from the current study on concrete diaphragms are consistent with what would be expected if the diaphragm were considered as a narrow deep beam. The diaphragm strength is a function of the amount of diaphragm reinforcement (analogous to distributed horizontal and vertical reinforcement in a deep beam), and the shear span-to-shear depth ratio of the diaphragm.

The crack patterns that developed in the diaphragms were studied in order to better understand the reasons for the change in diaphragm stiffness. More diagonal (shear) cracks form in the diaphragms as the shear-span to shear-depth ratio of the diaphragms is reduced. Increasing the amount of reinforcement (for a constant shear-span to shear-depth ratio) results in more flexural cracks, which can be attributed to the better crack control of the diaphragm with larger amounts of reinforcement.

The biaxial strains from the finite element analysis was converted into flexural and shear deformation components. The flexural deformation was determined by integrating the average curvatures over the diaphragm span and the shear deformations were determined by integrating the shear strains. The results indicated that the shear deformation contributes between 70% and 100% of the total deformation depending on the shear span-to-shear depth ratio of the diaphragm. Conversely, the flexural deformation contributes no more than 30% of the total displacement. According to the analysis results, the contributions of shear and flexural deformations to the total displacement remain relatively unchanged for diaphragms with the same aspect ratio regardless of the reinforcement amount.

The secant slope of the load-deformation relationship defines the effective stiffness of diaphragm at a particular backstay load level. The relationship between effective stiffness and backstay force is initially constant due to the initial uncracked portion of the load-deformation relationship. Formation of diagonal (shear) cracks causes a small reduction in the shear stiffness. For lightly reinforced diaphragms, the shear and flexural stiffnesses reduces sharply due to the flexural cracking of diaphragm. For moderately and heavily reinforced diaphragms, there is an initial significant reduction in shear and flexural stiffnesses, followed by a more gradual reduction as the backstay forces increase. One of the most important observations from the current study is that the shear and flexural stiffnesses of the diaphragm degrade simultaneously after flexural cracking of the diaphragms.

Diaphragms with very low shear-span to shear-depth ratios behave differently than more slender diaphragms. The failure of these diaphragms occurred because of extensive shear cracks with only a small zone of cracking in the flexural tension zone. The shear stiffness reduces linearly with an increase in backstay forces after the formation of diagonal (shear) cracks and flexural cracks.

A trilinear model was presented for the load-deformation relationship of concrete diaphragms. The model uses five parameters to define the curve: (1) the slope of the first line segment, K_1, (2) the slope of the second line segment, K_2, (3) the slope of the third line segment, K_3, (4) the load V_{SC} corresponding to the shear cracking (SC) of the diaphragm that defines the intersection of the first and second linear segments, and (5) the load V_{FC} corresponding to the flexural cracking (FC) of the diaphragm that defines the intersection of the second and third linear segments. The details of how to determine each parameter is given in Section 4.8.1.

The proposed trilinear model for load-deformation relationship of concrete diaphragms can be also used to define the shear response of the diaphragm by replacing the initial stiffness of diaphragm (K_1) with the uncracked shear rigidity of diaphragm ($G_c A_g$). The shear behaviour of concrete diaphragms subjected to backstay forces is accurately represented by a trilinear curve. The flexural response of a diaphragm can also be approximated by the proposed model by using the uncracked flexural rigidity of diaphragm as the initial stiffness which remains constant up to the flexural cracking load, V_{FC}. The analysis results have shown that prior to occurrence of flexural cracks, there is no reduction in the flexural stiffness of diaphragm. Thus, the flexural behaviour of diaphragms is defined as a bilinear relationship.

The shear and flexural stiffness reductions for diaphragms can be estimated at different backstay force level using the proposed model. In this study, the stiffness reduction factor at each load level is defined as the ratio of the secant stiffness to the initial uncracked stiffness of diaphragm. The effective shear and flexural stiffnesses of diaphragm were calculated as the shear or flexural stiffness reduction factor times the shear or flexural rigidity of diaphragm, respectively. The accuracy of the proposed procedure was validated against the results of NLFE analysis of concrete diaphragms.

As design engineers are interested in an even simpler approach for estimating the effective diaphragm stiffness, the proposed model was further simplified. The shear reduction factors for all analyzed diaphragms with different aspect ratios and different reinforcement amounts were compared by dividing the relationship between effective shear stiffness and backstay force into three parts: (1) from zero loading to diagonal (shear) cracking – no reduction in shear stiffness (shear reduction factor is equal to 1); (2) from shear cracking to flexural cracking – the shear stiffness reduces by about 15%; and (3) from flexural cracking to failure of the diaphragm – shear stiffness reduces to about 20% of the initial shear stiffness. Independent of shear-span to shear-depth of the diaphragm and the amount of reinforcement, the shear reduction factors follow a similar decreasing trend as the backstay forces increase.

The relationship between flexural reduction factor and backstay force were separated into two ranges: (1) from zero loading to flexural cracking – no reduction in flexural stiffness (flexural reduction factor is equal to 1); and (2) from flexural cracking to failure of diaphragm – flexural stiffness significantly reduces. The analysis results indicated that the reduction in diaphragm flexural stiffness was also independent of diaphragm aspect ratio. However, the diaphragm reinforcement amount was shown to have a small influence on the flexural stiffness reduction of concrete diaphragms.

In summary, different models have been developed for determining the effective stiffness of diaphragms subjected to backstay forces. The more rigorous model accounts for the continuous reduction in diaphragm stiffness as the backstay forces increase, and as a result, provides an accurate estimate of the diaphragm stiffness. On the other hand, simple upper-bound and lower-bound estimates of the effective stiffness were also presented and these can be more readily used by design engineers in practice.

Chapter 5

Influence of Out-of-Plane Bending Cracks on In-Plane Stiffness of Diaphragms

5.1 Introduction

Often in shear wall buildings, the concrete diaphragms that resist significant backstay forces are relatively thick and heavily reinforced. The influence of out-of-plane bending moments applied to the slab due to the superimposed gravity loads and self-weight of the slabs is relatively small for such thick slabs compared to the large backstay forces. On the other hand, sometimes the diaphragms that resist backstay forces are kept the same thickness as regular floor slabs. One of the reasons that has been used to justify this is that the thin diaphragms would crack thereby reducing the backstay forces.

In this chapter, the question of how much the flexural cracking due to out-of-plane bending moments influences the membrane stiffness of the diaphragms is investigated. The results of this study are relevant only to the thin diaphragms. Both one-way and two-way slabs are investigated, and given the significance of the shear stiffness of the diaphragms, as presented in Chapter 4, the strong-axis bending stiffness of the diaphragms is not considered. A computer program that has a state-of-the-art material model for cracked-concrete subjected to shear (such as VecTor2) and also has the capability to model membrane shear, out-of-plane bending and strong-axis bending of the diaphragm was not readily available.

A parametric study was carried out on continuous one-way floor slabs to investigate the effects of different parameters including the diaphragm length-to-depth ratio, the diaphragm reinforcement ratio and the magnitude of out-of-plane loads. Two different approaches were employed. In the first approach, the one-way slab was subjected to the out-of-plane bending and an increasing in-plane tensile force. The shear stiffness of the diaphragms was determined based on an effective modulus of elasticity of cracked concrete. In the second approach, the one-way slab was subjected to the out-of-plane bending and an increasing in-plane shear force. The purpose of using two different approaches for the analysis of one-way slabs was to validate the analyses, as no experimental test results for a slab subjected to out-of-plane loads and an increasing in-plane shear force were available in the literature. In addition, the analysis of a one-way slab subjected to out-of-plane bending moments and axial tension is more "transparent," easier to understand, than shear analysis.

Nonlinear analysis was also conducted to study the influence of out-of-plane loading on the shear stiffness of thin two-way slabs. The two-way slabs were subjected to combined out-of-plane bending moments (flexural bending moments about x-axis, flexural bending moments about y-axis and torsional bending moments), and in-plane shear force.

5.2 In-Plane Shear Stiffness of One-Way Slabs Subjected to Out-of-Plane Loads

The numerical investigation includes the evaluation of the effect of different parameters on the stiffness of concrete diaphragms. These parameters include the diaphragm length-to-depth ratio, diaphragm reinforcement ratio and loading conditions. In this study, one span of a continuous concrete slab with a unit width was used in the analyses. The thickness of all analyzed slabs was 200 mm (approx. 8 in.). The slab lengths were assumed to be 4 m (short span) and 7 m (long span) representing the slab length-to-depth ratios of 20 and 35, respectively. The slab was analyzed under two different vertical loading conditions. The first loading case (Case 1) includes the dead load only (self-weight of the slab, 4.8 kPa, plus a superimposed dead load of 1.5 kPa). The second loading case (Case 2) includes the dead load plus live load (6.3 kPa + 2.4 kPa). For simplicity, the translational and rotational displacements were assumed to be restrained on both ends of the one-way slab (fixed supports).

Two different reinforcement ratios (A_s/A_g), representing lightly reinforced and heavily reinforced slabs were selected. For the slabs with light reinforcement, the ratio of the top and bottom reinforcement was considered to be 0.5% and 0.25%, respectively. For the slab with heavy reinforcement, the ratio of the top and bottom reinforcement was 1% and 0.75%, respectively.

The compressive strength of concrete was assumed to be 30 MPa and the secant modulus of elasticity was taken as 23,750 MPa. The tensile strength of concrete was assumed to be 1.8 MPa which corresponds to $1/3\sqrt{f_c'}$. All reinforcing bars were assumed to be grade 400 MPa with actual yield strength of 400 MPa and the modulus of elasticity of 200,000 MPa.

The 7 m slab with light and heavy reinforcement under Case 1 loading condition was designated LR-C1-7 and HR-C1-7, in which "LR" and "HR" stand for light reinforcement and heavy reinforcement, respectively. "Cn" indicates the loading case and the last number is the slab length. Similar designations were used for other analyzed members. A total number of eight slabs were analyzed. Table 5.1 lists the characteristics of each analysis. Since the slab is symmetric with respect to its centre-line, half of the slab was considered for the analysis.

Two different approaches were employed to analyze the slab and evaluate the in-plane shear stiffness of diaphragms. In the first approach, after applying the service loads, the slab was subjected to an increasing tensile force and the effective modulus of elasticity of cracked reinforced concrete was estimated using a simple equation developed in this study. Then, the shear stiffness of the diaphragms is calculated based on the effective modulus of elasticity of cracked concrete. In the second approach, the slab was subjected to an increasing in-plane shear force after applying the gravity loads. In this case, the shear stiffness of diaphragms is equal to the slope of the shear-deformation curve.

Table 5.1 – Characteristics of analyzed slabs

Slab	Reinforcement Ratio (As/Ag)	Loading (kPa)	Slab Length (m)
	Top / Bottom		
LR-C1-4	0.005 / 0.0025	6.3	4
LR-C2-4	0.005 / 0.0025	8.7	4
HR-C1-4	0.01 / 0.0075	6.3	4
HR-C2-4	0.01 / 0.0075	8.7	4
LR-C1-7	0.005 / 0.0025	6.3	7
LR-C2-7	0.005 / 0.0025	8.7	7
HR-C1-7	0.01 / 0.0075	6.3	7
HR-C2-7	0.01 / 0.0075	8.7	7

5.2.1 Analysis of One-Way Slabs Subjected to Axial Tension and Out-of-Plane Loads

In order to analyze the slab under the effect of axial tension and out-of-plane bending moment simultaneously, half of the slab length was evenly divided into twenty segments. For each loading case, the magnitude of the service moment was determined at twenty-one sections along the slab span including both ends. The computer program Response-2000 was used to perform the sectional analysis for each section subjected to the calculated bending moment and increasing tensile force with an increment step of 1 kN. The tensile force was increased until the failure of the section was reached.

The strain at mid-height of the slab along the half of the slab span was plotted for different magnitudes of the applied tensile force. Figure 5.1 depicts the variation of the strain along half of the span for the 7 m slab with light reinforcement under Case 2 loading condition (LR-C2-7). Linear interpolation was used to evaluate the strain values at each location between the analyzed sections along the slab. By taking the average of these strains, the amount of strain along the slab for the specified axial load was evaluated. Since the slab is symmetric with respect to its centre-line, half of the slab was considered for the analysis. As shown in Figure 5.1, large tensile strains were developed at supports due to the application of out-of-plane moments. By increasing the tensile force, tensile strains were considerably increased at supports and mid-span where flexural cracks formed due to out-of-plane moments.

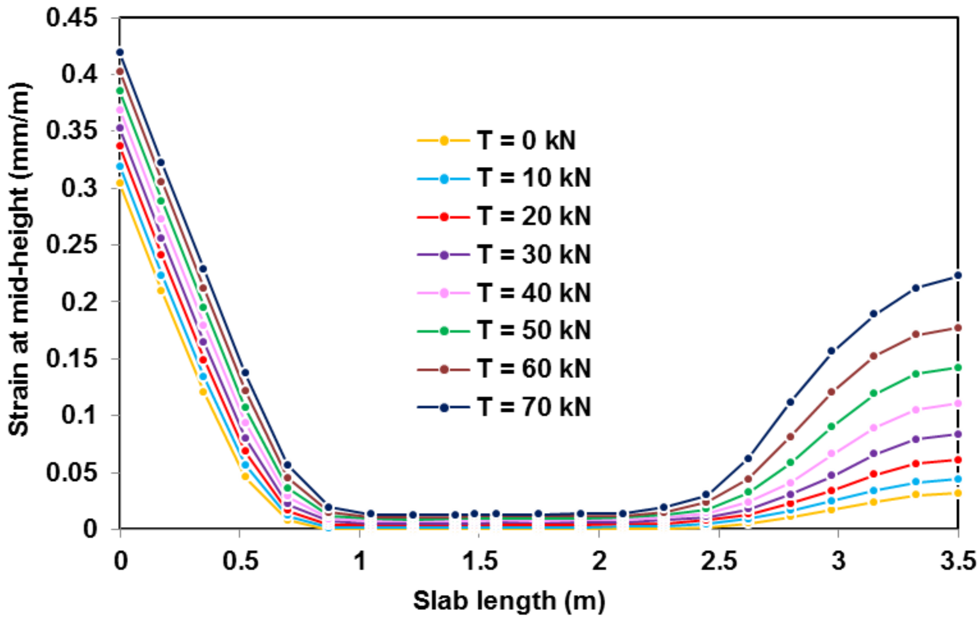

Figure 5.1 – Variation of strain at mid-height along the half span of slab LR-C1-7 (LR=0.005/0.0025; C1=6.3 kPa; L=7 m)

Figures 5.2(a) and (b) compare the ratios of the service bending moment (M_s) to the capacity moment (M_n) and to the cracking moment (M_{cr}) of the slab for the eight analyzed slabs. In Figures 5.2(a) and (b), the horizontal axis is normalized based on the slab length. The capacity moment of the slab was calculated based on the thickness of the slab and the amount of longitudinal reinforcement. Due to the unsymmetrical top and bottom reinforcement, the bending moment resistance of the slab at mid-span and the supports is not similar. The service moment depends on the applied service gravity loads on the slab as well as the slab length. Therefore, the ratio of the service to the capacity moment is different for the eight analyzed members as shown in Figure 5.2(a). The 7 m slab with light reinforcement and Case 2 loading condition showed a higher ratio of the service moment to the moment capacity at supports and at the mid-span.

The cracking moment was computed based on the thickness of the slab and the concrete tensile strength. Since the slab thickness and concrete tensile strength remained unchanged, the cracking moment was the same and equal to 12 kNm for all slabs. Therefore, the slabs with the same length and loading case show a similar ratio of the service moment to the cracking moment (e.g., LR-C1-7 and HR-C1-7 have the same service to cracking moment ratio). According to Figure

5.2(b), flexural cracking due to gravity loads occurred at mid-span and at both supports of the 7 m slabs, while flexural cracking did not occur in the 4 m long slabs.

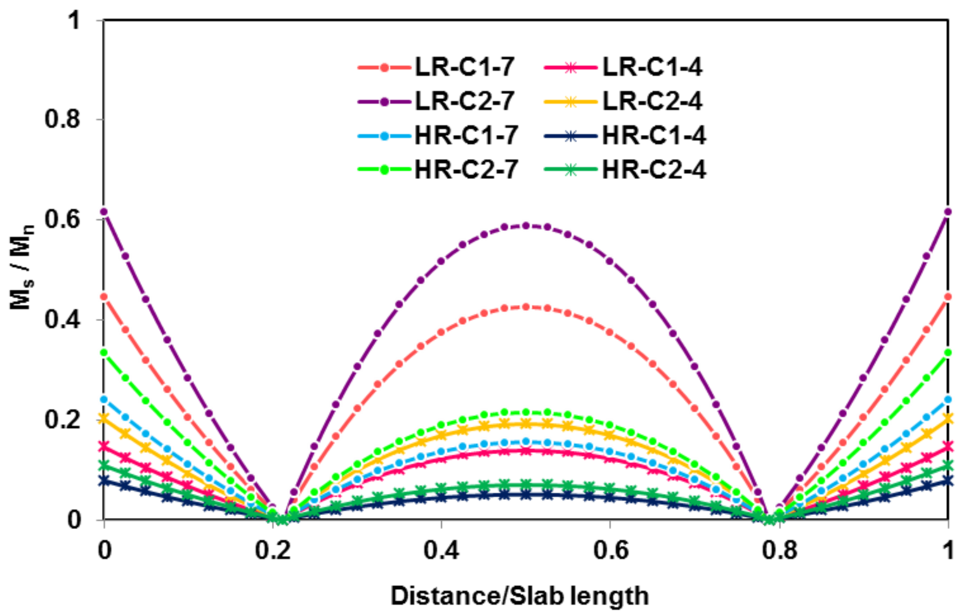

a)

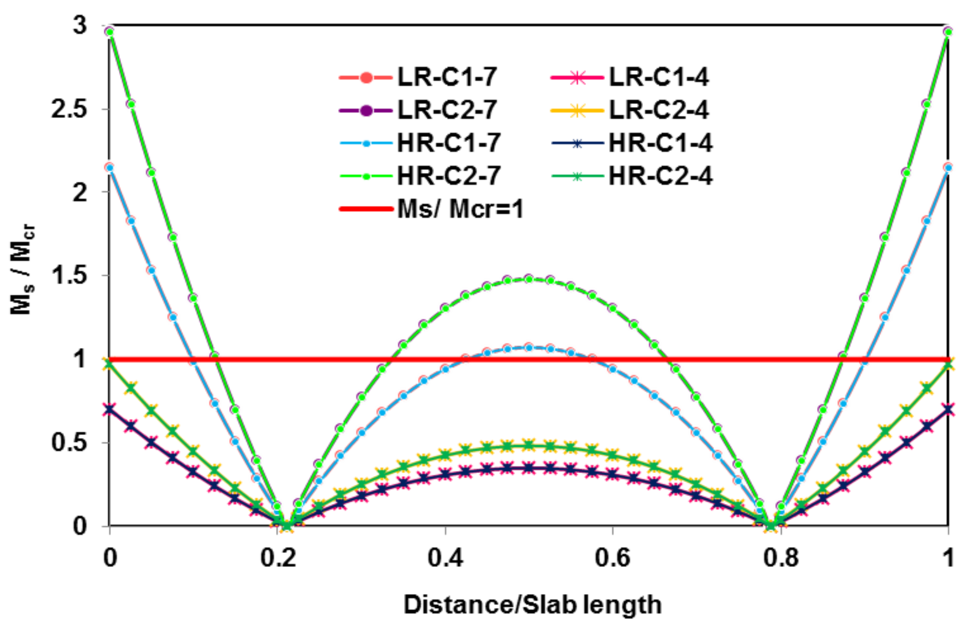

b)

Figure 5.2 – Ratio of the service-level bending moment M_s to: (a) the nominal bending moment capacity M_n; and (b) the cracking bending moment M_{cr} of the slabs

5.2.1.1 Tensile Force-Deformation Behaviour of One-Way Slabs

The tensile force versus average strain curves for the 4 m slabs with light reinforcement and two out-of-plane loading cases are shown in Figure 5.3. The results are compared to the curve obtained from the analysis of the slab subjected to pure axial tension force. When the slab is subjected to pure tension, the full cracking strength of concrete is mobilized. The cracking force is very large, and contribution from concrete drops rapidly after cracking.

Increasing the applied tension force causes the stiffness of the slab to decrease until the reinforcement reaches the yield level. Due to the asymmetry of the top and bottom reinforcement, the bottom reinforcement yields first and causes strain gradient through the section. A bending moment is developed due to the strain gradient which results in a compression force in the section. Consequently, the tensile strength decreases and the top reinforcement yields. Concrete contributes to resisting the axial force until both top and bottom reinforcement yields.

The results show that the initial stiffness of the 4 m slabs was exactly the same as that of the slab subjected to pure tension. Although for 4 m slabs, no stiffness reduction was observed, the cracking force of the slab was significantly reduced due to the effect of the out-of-plane bending moment. As shown in Figure 5.4, flexural cracking does not occur in 4 m slabs due to the applied gravity loads. Therefore, the initial stiffness of the slab did not decrease. However, a small amount of reduction in the strength of the slab was observed.

Figures 5.5 and 5.6 depict the axial force versus average strain curves obtained from the analyses of the 7 m slabs with light and heavy amount of reinforcement, respectively. The results are compared to the ones obtained from the analysis of the slab subjected to tension force only (no gravity loads). The closed-up details of the initial stiffness for the two plots are shown in Figure 5.7.

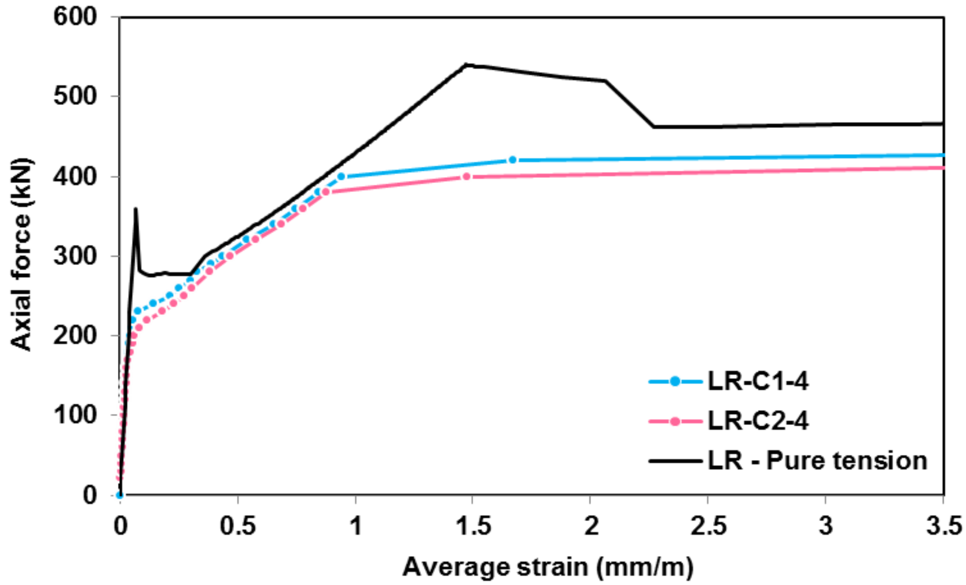

Figure 5.3 – Axial force versus average strain for 4 m long slabs with light reinforcement (LR=0.005/0.0025; C1=6.3 kPa; C2=8.4 kPa; L=4 m)

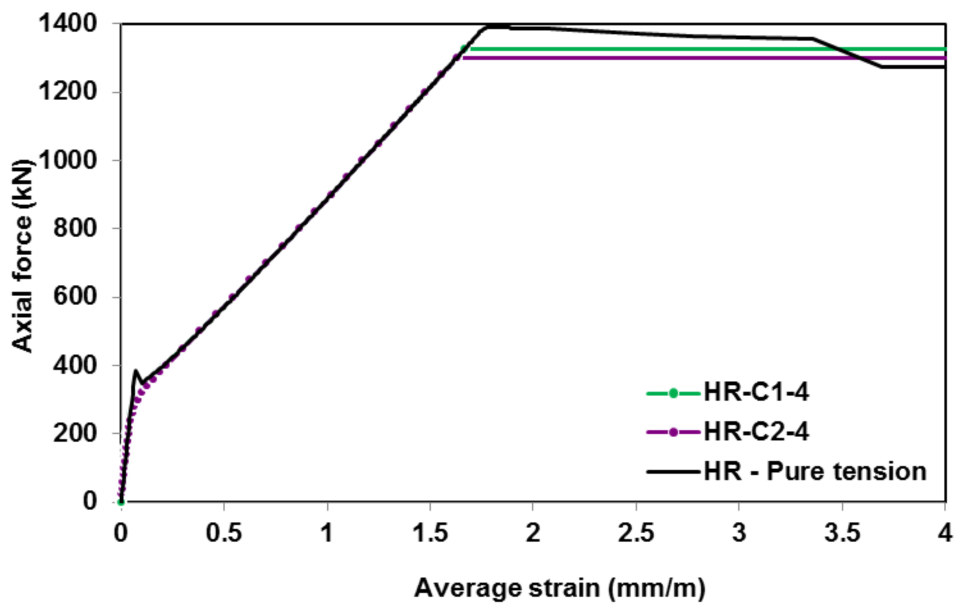

Figure 5.4 – Axial force versus average strain for 4 m long slabs with heavy reinforcement (HR = 0.01/0.0075; C1 = 6.3 kPa; C2 = 8.4 kPa; L = 4 m)

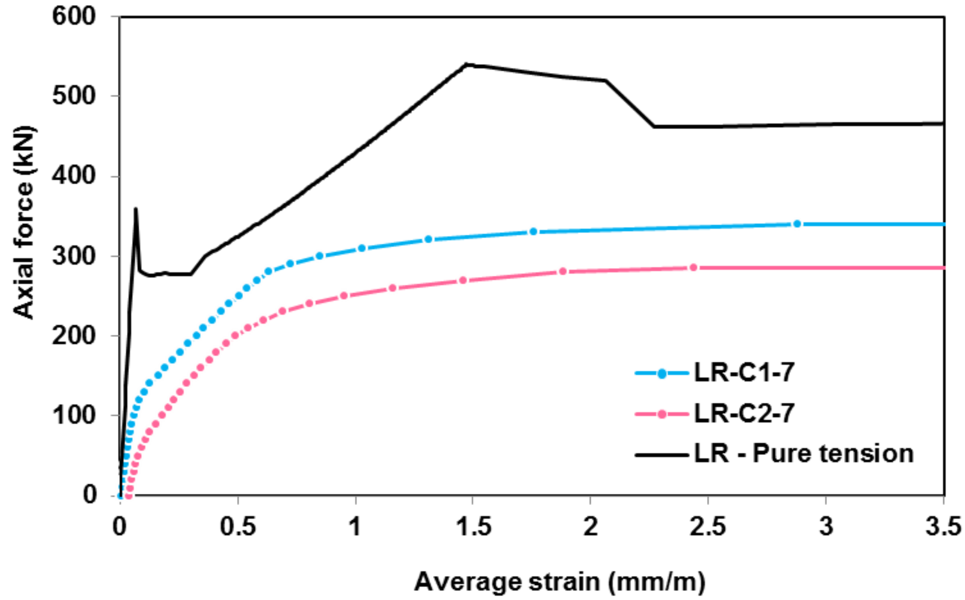

Figure 5.5 – Axial force versus average strain for 7 m slabs with light reinforcement (LR = 0.005/0.0025; C1 = 6.3 kPa; C2 = 8.4 kPa; L = 7 m)

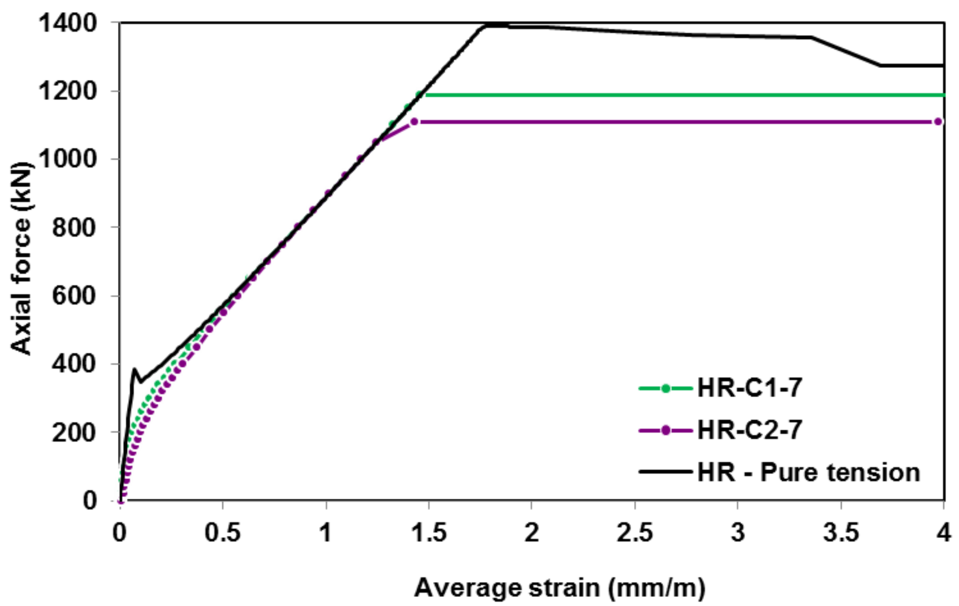

Figure 5.6 – Axial force versus average strain for 7 m slabs with heavy reinforcement (HR = 0.01/0.0075; C1 = 6.3 kPa; C2 = 8.4 kPa; L = 7 m)

Comparison of Figures 5.5 and 5.6 demonstrates that the out-of-plane bending moment considerably influences the behaviour of the tensile force - average strain of the diaphragm when the magnitude of the applied tensile force is relatively small. For heavily reinforced slabs, the yield strength of the slab is large and the influence of out-of-plane bending moment diminishes by increasing the applied tensile force. Thus, the tensile force - average strain curve of the slab would converge to that of the diaphragm subjected to the pure tension. However, for lightly reinforced slabs, the effect of out-of-plane bending moment is more dominant.

It is observed that the initial stiffness of the 7 m concrete floor slabs decreases significantly. This can be explained by the fact that these slabs were cracked at the location of supports and mid-span due to gravity loads before the application of the tensile force. Therefore, the cracking of the slab caused by the vertical loads is believed to be responsible for this stiffness reduction. In addition, an appreciable reduction in the tensile strength of the 7 m slabs with light reinforcement is observed.

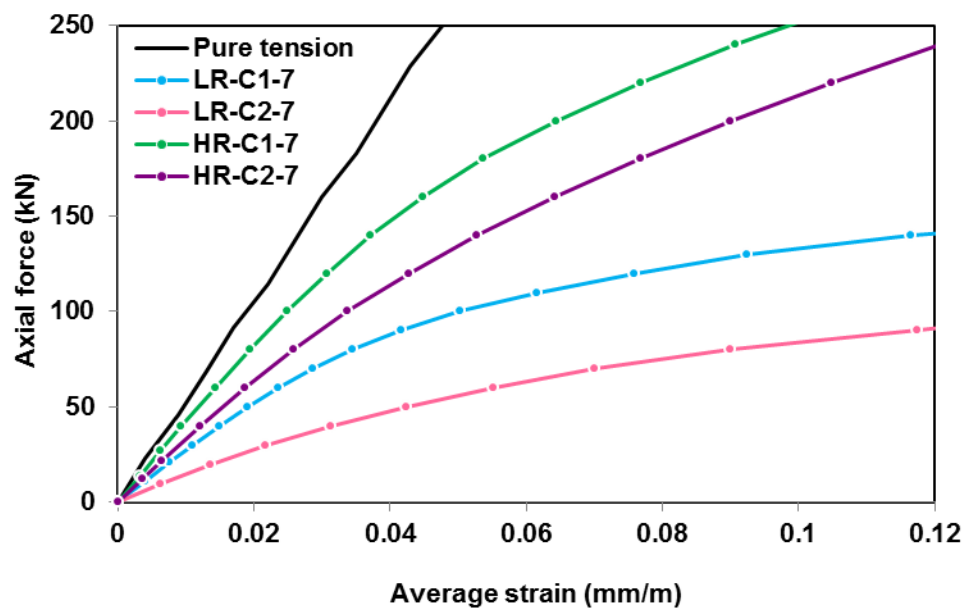

Figure 5.7 – Comparison of the initial potion of the axial force-average strain relationships for all 7 m long continuous slabs

According to Figure 5.7, it is obvious that the initial stiffness reduction of the slab LR-C2-7 is larger than that of the other slabs. This can be explained by looking at the strain values along the slabs. Figure 5.8 compares the variation of strains at mid-height of the slab along the half of the span for all 7 m slabs when the applied axial force is 50, 100 and 150 kN. The strain values are substantially larger for the slab LR-C2-7 along the span. By increasing the applied force, the strain values increase significantly for the slabs LR-C1-7 and LR-C2-7.

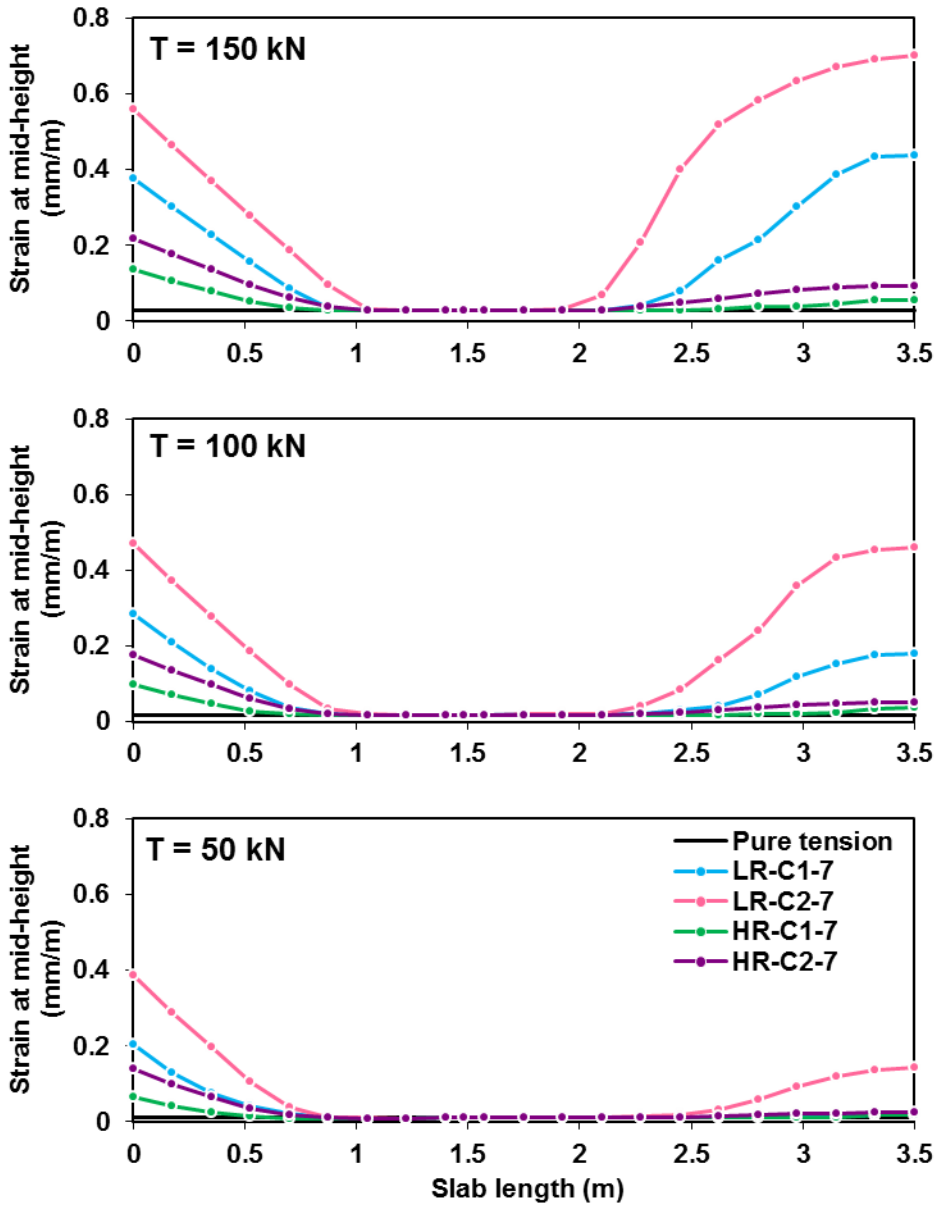

Figure 5.8 – Variation of axial strain at mid-height of slab at different locations along the half span for 7 m long continuous slabs when the axial force applied at mid-depth is 50, 100 and 150 kN; slab mid-span is at 3.5 m

Comparison of the strain values of the slabs LR-C1-7 and LR-C2-7 indicates that the difference in the magnitude of the applied service bending moments (different loading cases) caused a larger number of cracks along the slab and consequently larger strains in the slab LR-C2-7. Moreover, the difference between the strains of the slabs LR-C2-7 and HR-C2-7 can be attributed to the fact that the amount of reinforcement has a direct effect on the yield force as well as the crack control. The larger the reinforcement ratio, the larger the yield force and the smaller the strain values along the slab length.

5.2.1.2 Diaphragm Tensile Stiffness

Figure 5.9 illustrates the tensile stiffness reduction versus the average strain at the mid-height of the slab for the initially cracked slab due to the presence of the gravity loads. By comparing the results of the lightly and heavily reinforced slabs under two loading conditions (i.e., Case1 and Case2), it can be concluded that the effect of loading conditions (magnitude of bending moments) are more significant at small average strain levels. This effect becomes negligible at higher strain levels as depicted in Figure 5.9. In other words, for the slabs with the same reinforcement ratios, the tensile stiffness reduction factor converges to the same value as the average strain at mid-height of the slab increases.

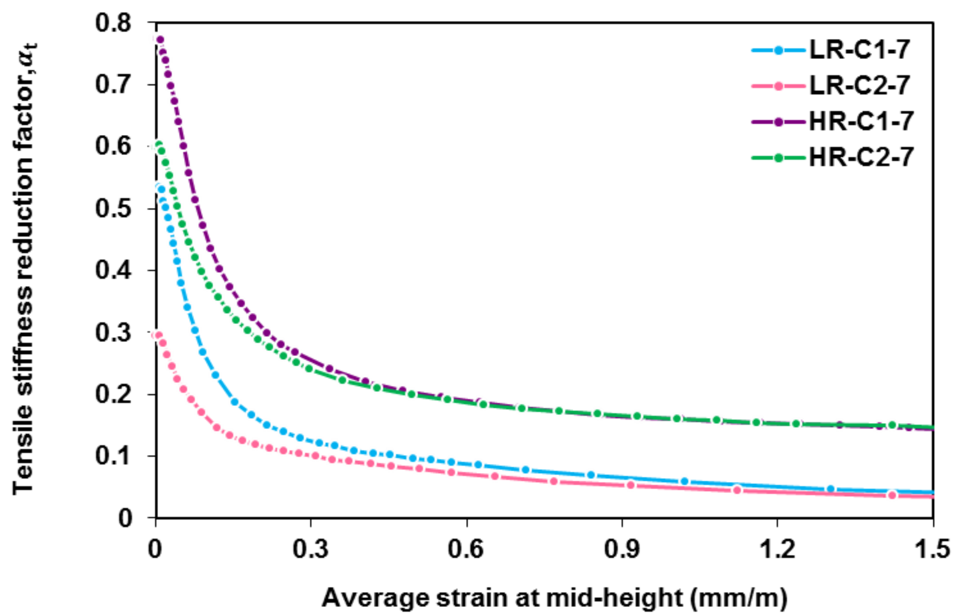

Figure 5.9 – Ratio of secant stiffness to tangent stiffness versus average strain for all 7 m long continuous slabs

It was observed that when the magnitude of the service moment is less than the cracking moment of the diaphragm ($M_s < M_{cr}$), there would be no reduction in the initial stiffness of the diaphragm. In this case, the force-deformation relationship of the diaphragm can be reasonably approximated by a trilinear model. Figure 5.10 illustrates the developed trilinear model for force-deformation relationship of diaphragms remained uncracked under service loads. The trilinear relationship is defined by four parameters: (1) the slope of the first straight line segment, $E_c A_g$, (2) the slope of the second straight line segment, T_n/ε_y, (3) the tensile force off-set (shown by "x" in Figure 5.10), $f_{cr} A_c/2$, and (4) the tensile strength of the section subjected to bending moment and tension force, T_y.

The gross section stiffness, $E_c A_g$, is mathematically defined as a product of the concrete modulus of elasticity and the gross sectional area. The second parameter can be determined as a ratio of the tensile strength of the section, T_n, to the yield strain of steel, ε_y, which is approximately 0.002 for steel Grade 400. The tensile strength of the section can be obtained by hand calculation and primarily depends on the amount of reinforcement. In fact, this parameter is equal to the product of the modulus of elasticity of steel and the area of reinforcing bars, $E_s A_s$, for a section with symmetric top and bottom reinforcement. However, for the section with unsymmetrical reinforcement, there would be some reduction in the tensile strength of the section due to the strain gradient which should be considered in the calculation. The third parameter is the distance "x" as shown in Figure 5.10. This distance is defined as the tensile force difference between the second line segment of the trilinear model and the line representing no tension stiffening effect of concrete (green line in Figure 5.10) at a certain level of strain. This parameter is approximated by half of the cracking force of the section, where $f_{cr} = 1/3\sqrt{f'_c}$ is the cracking strength of concrete. The final parameter that is required to define the trilinear force-deformation relationship of uncracked diaphragms is the tensile strength under the bending moment and the tension force simultaneously, T_y, which corresponds to the force that both top and bottom reinforcements yield. In order to define this parameter, the tensile strength of the slab should be calculated at the most critical sections along the slab which are at the supports and mid-span. The smaller of the obtained values is considered as the tensile strength of the slab.

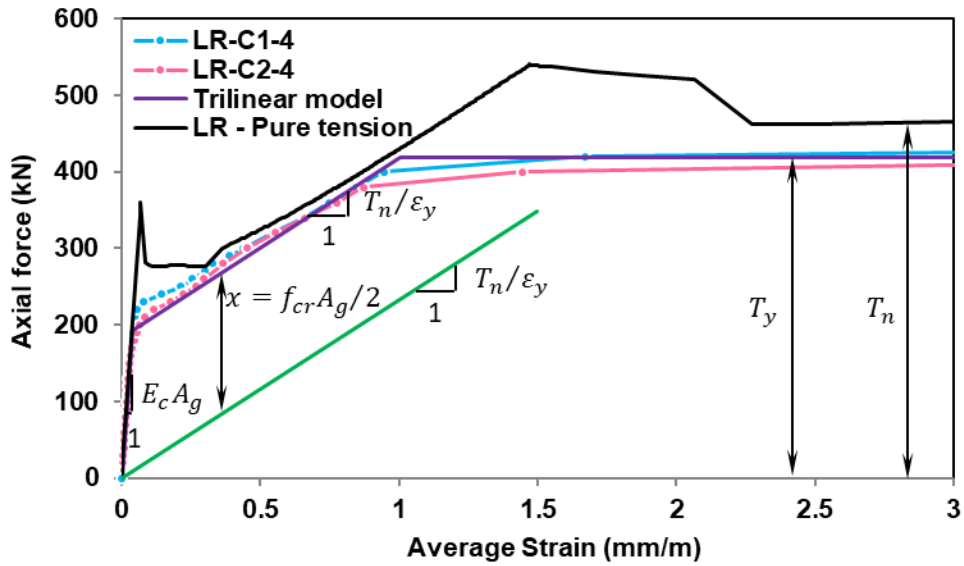

Figure 5.10 – Trilinear idealization of the force-deformation relationship for uncracked diaphragms

When the magnitude of the applied service moment is larger than the cracking moment of the diaphragm ($M_s > M_{cr}$), the flexural cracking occurs in the diaphragm. It is indicated that the flexural cracking significantly reduces the initial stiffness of the concrete floor diaphragms. The more cracking in the diaphragm, the larger reduction in the initial stiffness of diaphragm. Two main parameters that influence the extent of cracking along the diaphragm length are the magnitude of the applied service loads and the diaphragm reinforcement ratio.

Since displacements involve the integration of strains along the length of a diaphragm, the stiffness is related to average strains. In fact, for the initial stages of the analysis, when the applied tensile force is small, the stiffness can be defined as the ratio of the tensile force to the average strain along the diaphragm ($K = \Delta T/\Delta\varepsilon$). Based on that, the following simple equation was developed to evaluate the initial stiffness of diaphragms cracked under gravity loads:

$$\frac{1}{K} = \frac{\alpha_1^2}{2E_s A_s^-} + \frac{\alpha_2^2}{4E_s A_s^+} + \frac{\alpha_3}{E_c A_c} \tag{5.1}$$

where $\alpha_1 = 0.42(1 - \frac{M_{cr}}{M_s^-})$ and $\alpha_2 = 0.58\sqrt{1 - \frac{M_{cr}}{M_s^+}}$ are determined as a ratio of the cracked length to the diaphragm length at supports and mid-span, respectively. $\alpha_3 = 1 - (\alpha_1 + \alpha_2)$ is defined as a ratio of the uncracked length to the diaphragm length as shown in Figure 5.11. Detailed calculations are presented in Appendix D. E_s and E_c are the modulus of elasticity of the steel and concrete, respectively. A_s^-, A_s^+ and A_c are the area of top and bottom reinforcement and the concrete cross sectional area, respectively.

The first term of the equation is proportional to the average of strain increment along the cracked length of the diaphragm at supports due to the small increase of the tensile force. The second term reflects the contribution of the average strain increment along the cracked length of the diaphragm at mid-span. Finally, the third term is obtained from the elastic strain increment along the uncracked length of the diaphragm due to the tensile force increment.

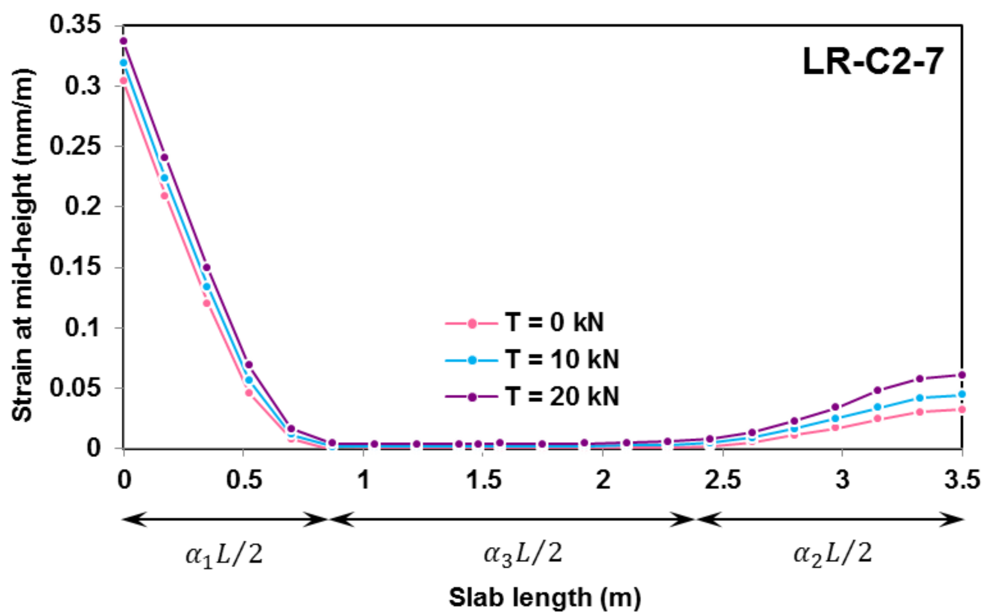

Figure 5.11 – Variation of axial strain at mid-height of slab along the half span for a 7 m slab with light reinforcement showing portions of slabs uncracked and cracked at support and mid-span due to out-of-plane loading

In order to validate the proposed equation for the reduced initial stiffness of the cracked diaphragm, the diaphragm stiffnesses predicted by the proposed simple model are compared to that obtained from the analyses in Figure 5.12. Table 5.2 summarizes the initial stiffness values obtained from the analysis and predicted by the proposed model. As seen in Table 5.2, there is a good agreement between the results. However, the predicted stiffnesses are larger than the tangent stiffnesses calculated from the analyses. Therefore, the proposed simplified model estimates the initial stiffness of cracked diaphragms conservatively which is more desirable for the purpose of this study. In fact, smaller stiffness values would result in smaller reverse shear force which may lead to underestimating the design of the wall against shear forces.

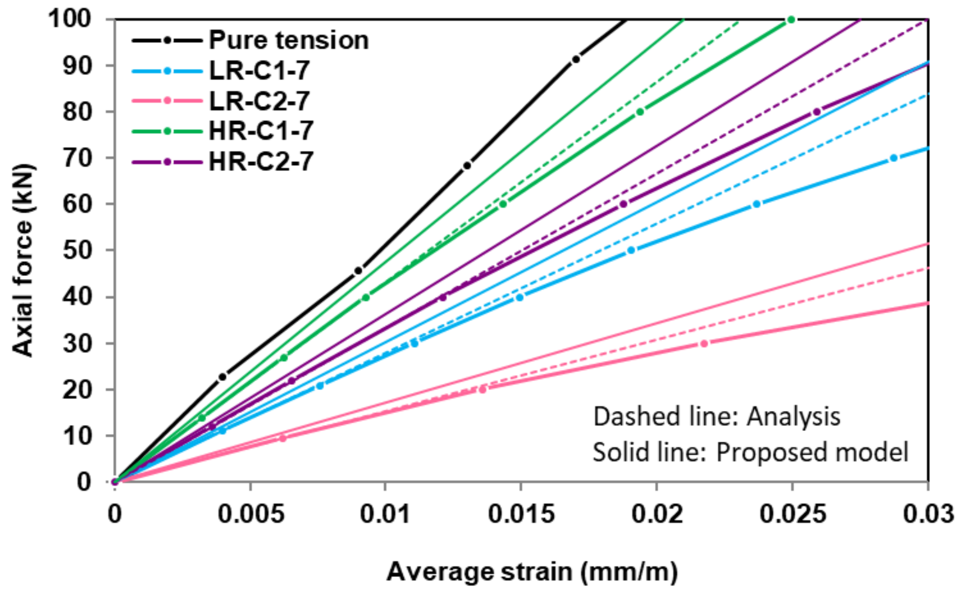

Figure 5.12 – Comparison of the initial stiffness of diaphragm predicted by the proposed model with that obtained from analyses for all 7 m slabs

Table 5.2 – Comparison of the initial stiffness of diaphragm predicted by the proposed model and obtained from analyses

Slab	Initial tensile stiffness (EA)		Error (%)
	Analysis	Model	
LR-C1-7	2798.8	3030.3	8
LR-C2-7	1545.9	1709.4	12
HR-C1-7	4330.0	4761.9	10
HR-C2-7	3338.3	3636.4	9

Finally, the effective modulus of elasticity of cracked reinforced concrete can be approximated by dividing the tensile stiffness of the diaphragm, K, by the cross-sectional area of diaphragm, A_c.

Equation (5.1) can be simplified by dividing both sides of the equation by the modulus of elasticity of concrete times the gross cross-sectional area of concrete, $E_c A_c$, as follows:

$$\frac{1}{\alpha} = \frac{\alpha_1^2}{2n\rho_s^-} + \frac{\alpha_2^2}{4n\rho_s^+} + \alpha_3 \tag{5.2}$$

where, α is the reduction factor by which the modulus of elasticity of concrete is reduced due to flexural cracking of diaphragms. In other words, α is the ratio of the effective modulus of elasticity of cracked reinforced concrete to the modulus of elasticity of concrete. *n* is the modular ratio, which is the ratio of modulus of elasticity of steel to modulus of elasticity of concrete.

5.2.1.3 Diaphragm Shear Stiffness

In order to evaluate the shear stiffness of the concrete diaphragm, a simply supported deep beam was considered as shown in Figure 5.13. The rigid foundation walls were assumed to perform as lateral supports due to their high lateral stiffness. The core wall's action was modelled by applying two concentrated forces at the location of the shear walls. Only the shear deformation of the diaphragm was taken into account and the flexural deformation was ignored which is relatively small. Therefore, the stiffness of the diaphragm mainly depends on the shear modulus of the diaphragm.

The applied shear forces from core walls are transferred to the perimeter foundation walls through the diaphragms. Thus, the diaphragms behave similar to membrane elements, as shown in Figure 5.13. In order to account for the influence of flexural cracking, the reinforced concrete slab can be considered as an orthotropic material with reduced modulus of elasticity due to the influence of the flexural cracking. The effect of cracking was assumed in one direction only which is the case in one-way slabs. Cracking of concrete reduces the stiffness of floor diaphragms and the shear reverse force would be accordingly reduced.

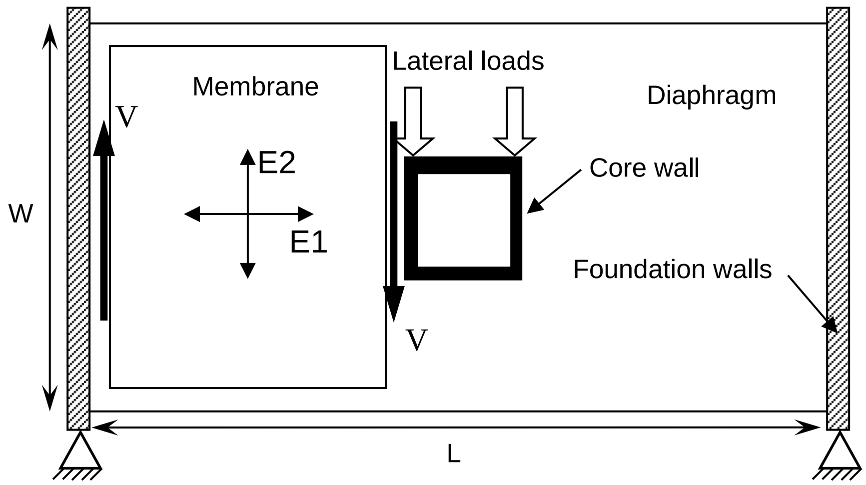

Figure 5.13 – Simplified model to define diaphragm stiffness

Based on the literature, the shear modulus of reinforced concrete diaphragms with orthotropic material properties can be predicted by Equation (5.3) which was proposed by Huber (1923) and followed by other researchers in mechanics such as Cheng and He (1984) and Bert (1985):

$$G = \frac{\sqrt{E_1 E_2}}{2(1 + \sqrt{\nu_{12}\nu_{21}})} \tag{5.3}$$

Huber used geometric mean in predicting the shear modulus of reinforced concrete slabs. The modulus of elasticity of concrete in the direction of cracking can be determined based on the present study. After cracking of concrete, the Poisson's ratio was assumed to remain unchanged and equal to 0.25 which is its value for concrete in both orthogonal directions. In fact, prior to cracking, the Poisson's ratios, ν_{12} and ν_{21} are identical and equal to 0.25. After cracking, ν_{12} increases gradually to a higher value of about 1.9 and ν_{21} decreases rapidly to a small value and then gradually approaches zero (Zhu, 2000). When ν_{21} approaches zero, the product of the Poisson's ratios becomes close to zero. Therefore, the denominator of the Equation (5.3) becomes approximately equal to 2 and it would be 2.5 for uncracked concrete. This would be equivalent to the condition that the shear modulus of the cracked concrete becomes larger than that of the uncracked concrete which is not acceptable. Therefore, the assumption of equal Poisson's ratios of 0.25 in both orthogonal directions is more reasonable. After defining the shear modulus of cracked concrete, the diaphragm stiffness can be simply determined based on the diaphragm length-to-width ratio (L/W). In fact, the stiffness of the diaphragm is the shear force per unit deflection of the beam at the location of the applied shear force.

According to Equations (5.2) and (5.3), the in-plane shear stiffness of diaphragms is reduced by a factor of $\sqrt{\alpha}$ due to the application of one-way bending in a one-way slab. Figure 5.14 provides the in-plane shear reduction factor due to the one-way flexural cracking of the slab for different amount of reinforcement controlling the flexural cracks (ρ^- is the top reinforcement ratio and ρ^+ is the bottom reinforcement ratio). In this graph, the compressive strength of concrete and the modulus of elasticity of steel are assumed as typical values of 25 MPa and 200,000 MPa, respectively, which gives the modular ratio of 8. The ratio of maximum negative bending moment M^- to the cracking moment M_{cr} expresses the degree of flexural cracking.

Figure 5.14 indicates that the in-plane shear stiffness of diaphragms decreases significantly by increasing the maximum negative moment applied to the diaphragms due to service loads. As aforementioned, the degree of flexural cracking is expressed by ratio of the maximum negative moment to the cracking moment. The larger this ratio, the more flexural cracks will exist in the diaphragm, which results in a smaller initial in-plane shear stiffness of the diaphragm. In addition, Figure 5.14 shows that the initial shear stiffness decreases considerably by reducing the amount of flexural reinforcement.

The reduction factor would be equal 1.0 when the moment ratio is less than 1.0 which means that no flexural cracking occurs in the slab. When the maximum negative moment increases beyond the cracking moment, the initial shear stiffness of the slab begins to reduce due to the formation of flexural cracks. When the moment ratio is greater than 1 but smaller than 2, the reduction factor is identical for slabs with equal top and bottom reinforcement and slabs with twice as much top reinforcement as bottom reinforcement. This can be attributed to the fact that when the moment ratio is between 1 and 2, flexural cracks form only at supports (where the top reinforcement carries the tension force due to the negative bending moment). Since the amount of top reinforcement is similar for these two slabs, the reduction factor is identical. When the moment ratio is beyond 2, the initial shear stiffness significantly decreases as flexural cracks form at the supports and mid-span. Slabs with smaller bottom reinforcement ratios experience more significant reduction in initial shear stiffness. For large moment ratios, M_{max}/M_{cr}, the shear stiffness reduction factor varies between 0.47 and 0.75 depending on the quantity of reinforcement in the diaphragms.

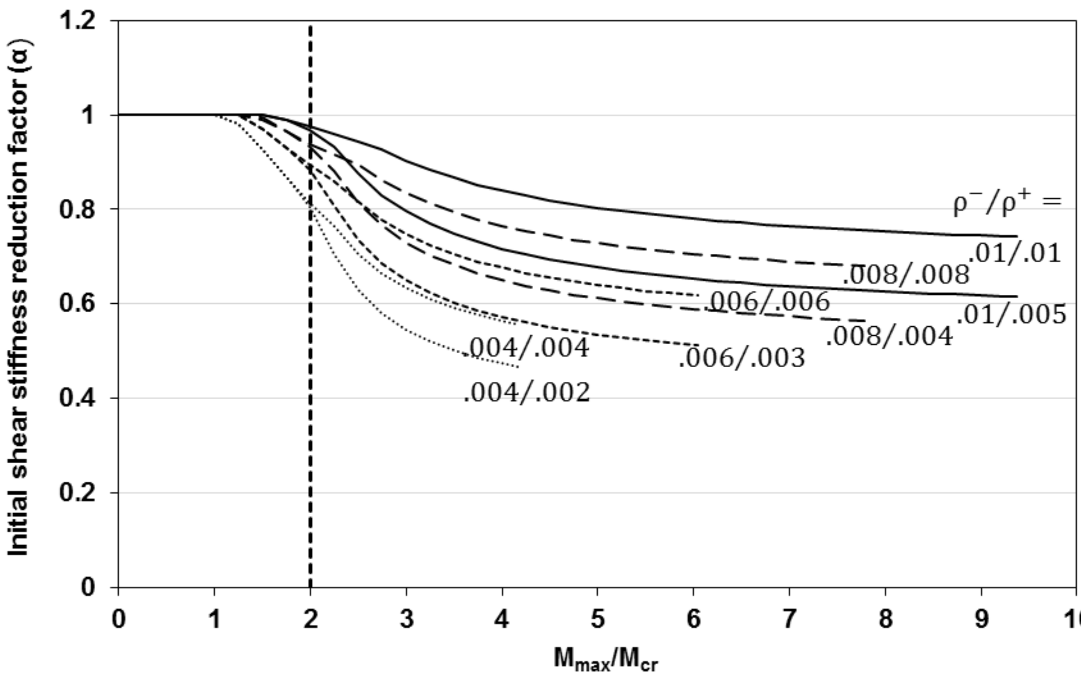

Figure 5.14 - Reduction of initial shear stiffness of diaphragms due to one-way bending for different amounts of flexural reinforcement and out-of-plane loading

5.2.2 Analysis of One-Way Slabs Subjected to In-Plane Shear and Out-of-Plane Loads

In the second approach, the slab was subjected to an increasing in-plane shear force after the application of gravity loads. The shear stiffness of the diaphragms was assumed equal to the slope of the shear-deformation curve.

In order to analyze the slab under the effect of shear and out-of-plane bending moment simultaneously, half of the slab length was evenly divided into twenty elements. For each loading case, the magnitude of the service moment was determined for each element along the slab span. The computer program Shell-2000 was employed to carry out the analysis for each element subjected to the calculated bending moment and increasing shear force with an increment step of 1 kN. The shear force was increased until the failure of the element was reached.

Figure 5.15 shows the shear force – shear strain relationship for some selected elements along the slab. As shown, the shear strain considerably increases in the elements with large out-of-plane bending moments (at supports). However, as the in-plane shear force increases and the elements are fully cracked, the shear force – shear strain curves for all elements converge to that of the element subjected to pure shear force (see Figure 5.15).

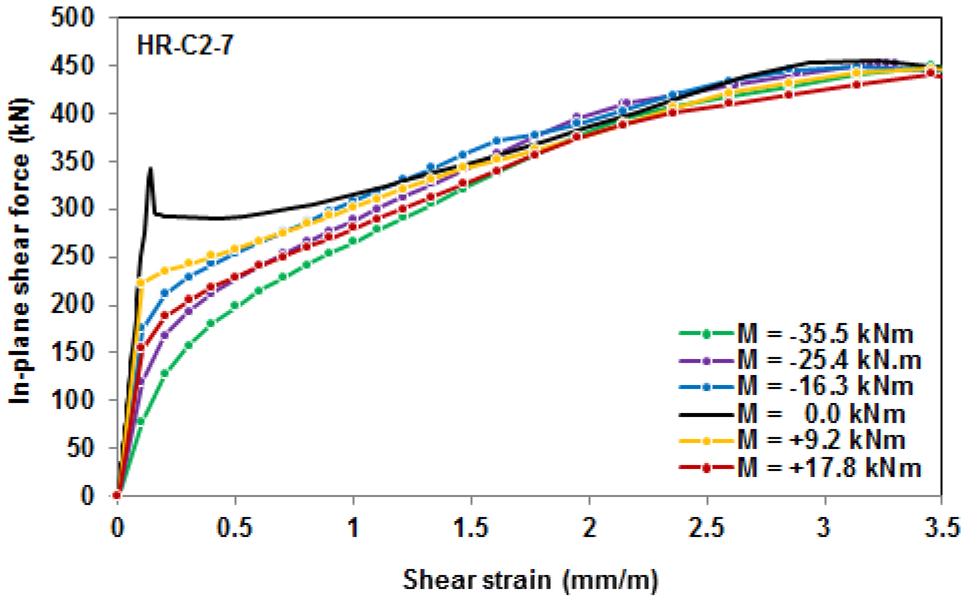

Figure 5.15 – In-plane shear force versus shear strain at different locations along a 7 m long slab with heavy reinforcement

The shear strain values at specified shear force levels were evaluated using linear interpolation for all elements along the slab. By taking the average of these strains at each shear force level, the shear force – average shear strain relationship of the slab was determined.

5.2.2.1 Shear Force-Deformation Behaviour of One-Way Slabs

Figures 5.16 to 5.19 illustrate the shear force – average shear strain curves for 4 m and 7 m slabs heavily and lightly reinforced (four cases in total). The curves obtained from the analysis of the slabs subjected to pure shear force (no out-of-plane loads) are also shown in the figure for comparison. The results of the slabs subjected to the pure in-plane shear force indicates a high cracking force which is reduced significantly after the formation of cracks in the slab.

As shown in Figures 5.16 and 5.17, the initial shear stiffness of the 4 m slabs subjected to the in-plane shear and out-of-plane loads is identical to that of the slab subjected to the pure in-plane shear. Therefore, no reduction is observed in the initial shear stiffness of 4 m slabs, similar to the results obtained from the first approach. However, the cracking force of the slab is significantly reduced due to the effect of the out-of-plane bending moment. Furthermore, small reduction in the strength of 4 m slabs with light reinforcement is observed.

According to Figure 5.18, the gravity (out-of-plane) loads results in some reduction in initial shear stiffness of heavily reinforced 7 m slabs. However, the shear strength of slabs is not affected considerably. By reducing the amount of reinforcement in the slab, the effect of gravity loads becomes more noticeable (Figure 5.19). In addition to the significant reduction in initial shear stiffness of the slabs, the shear strength of the slab reduces consequently. As aforementioned, the developed bending moments due to 6.3 kPa (Case 1) and 8.7 kPa (Case 2) gravity loads are larger than the cracking moment, at supports and mid-span of 7 m slabs. Thus, the flexural cracks form in the slab which is believed to be responsible for the initial shear stiffness reduction and shear strength loss in the slabs.

5.2.2.2 Shear Stiffness Degradation

Shear stiffness reduction factor versus applied in-plane shear force is illustrated in Figure 5.20 for 7 m slabs. The shear stiffness reduction factor at each shear force level is defined as the ratio of the secant shear stiffness of slabs subjected to the out-of-plane loads and an in-plane shear force to the initial shear stiffness of the slab subjected to a pure shear force (no out-of-plane loads). Based on this definition, the reduction of 16% and 30%, and 33% and 54% is observed in initial shear stiffness of heavily reinforced slabs HR-C1-7 and HR-C2-7 and lightly reinforced slabs LR-C1-7 and LR-C2-7, respectively. As expected, larger initial stiffness reduction occurs in lightly reinforced slabs. In addition, it is indicated that increasing out-of-plane loads lead to greater initial stiffness reduction in slabs.

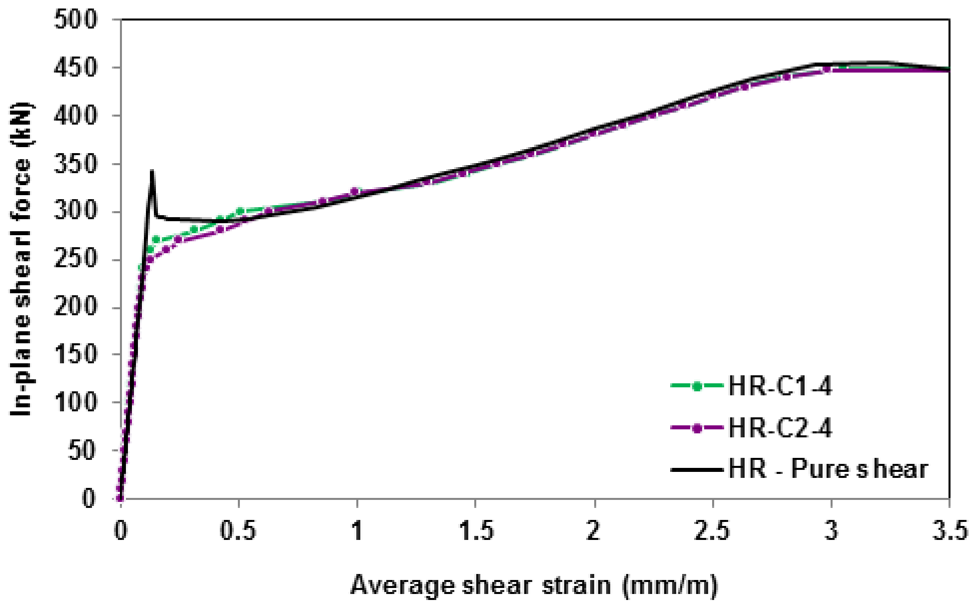

Figure 5.16 – In-plane shear force versus average shear strain for 4 m slabs with heavy reinforcement (HR = 0.01/0.0075; C1 = 6.3 kPa; C2 = 8.4 kPa; L = 4 m)

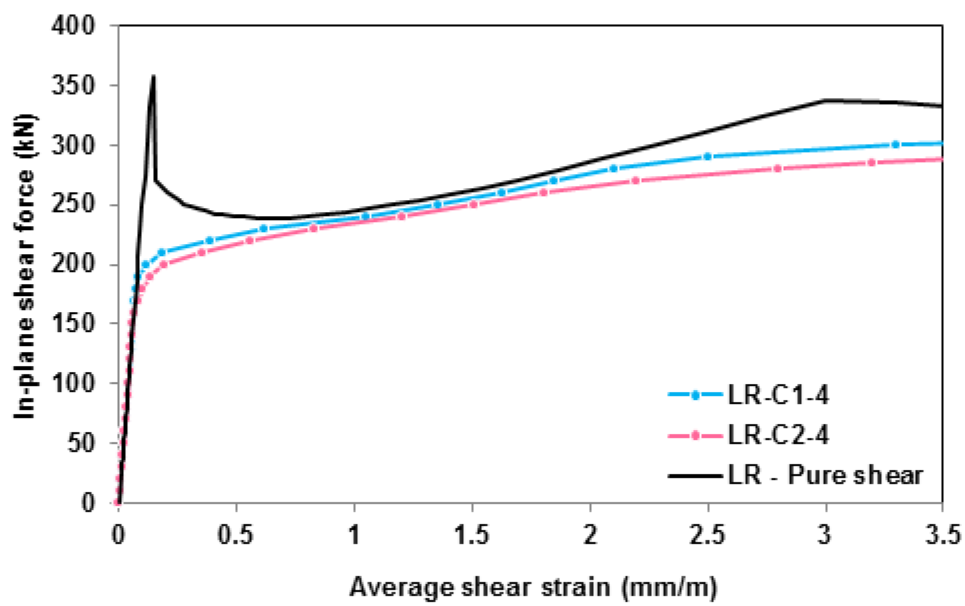

Figure 5.17 – In-plane shear force versus average shear strain for 4 m slabs with light reinforcement (LR = 0.005/0.0025; C1 = 6.3 kPa; C2 = 8.4 kPa; L = 4 m)

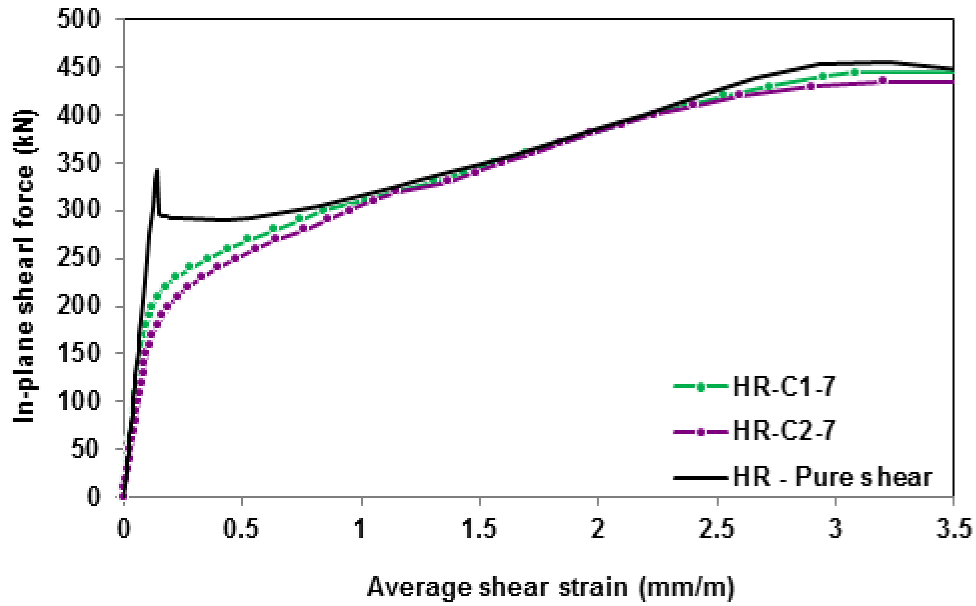

Figure 5.18 – In-plane shear force versus average shear strain for 7 m slabs with heavy reinforcement (HR = 0.01/0.0075; C1 = 6.3 kPa; C2 = 8.4 kPa; L = 7 m)

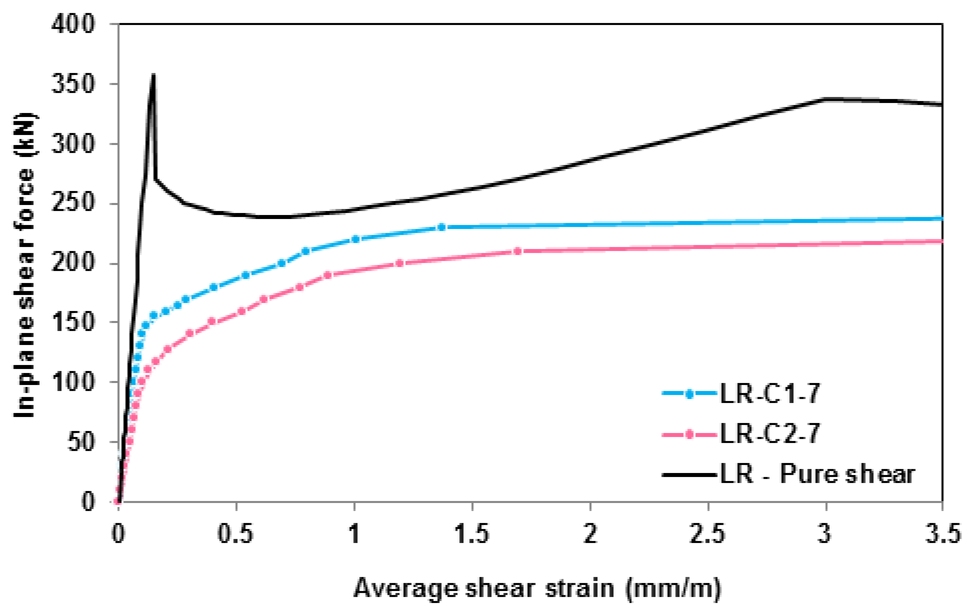

Figure 5.19 – In-plane shear force versus average shear strain for 7 m slabs with light reinforcement (LR = 0.005/0.0025; C1 = 6.3 kPa; C2 = 8.4 kPa; L = 7 m)

According to Figure 5.20, further reduction in shear stiffness gradually occurs due to the formation of diagonal cracks in the slab. Extending the diagonal cracks through the depth of the slab results in a significant reduction in the shear stiffness of the slab. Interestingly, Figure 5.20 shows that the stiffness reduction factor curves for the slabs subjected to identical out-of-plane loads follow the same reduction trend although the amount of reinforcement is different in these slabs. This means that the shear stiffness reduces with the same rate after diagonal cracking take places in these slabs (e.g., HR-C1-7 and LR-C1-7). In fact, the degree of flexural cracking is similar in these slabs due to the same amount of applied out-of-plane loads. Thus, it is highlighted that the degree of flexural cracking due to gravity loads plays an important role in the stiffness reduction of slabs.

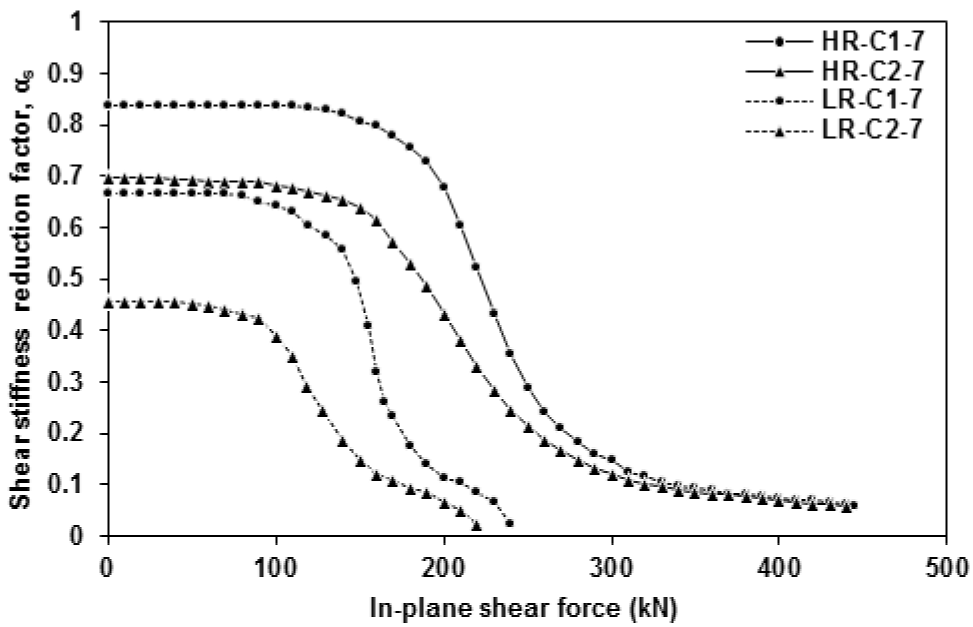

Figure 5.20 – Shear stiffness reduction factor for 7 m slabs

5.2.2.3 Comparison of Results from Two Approaches

Table 5.3 compares the reduction in initial shear stiffness of one-way 7 m slabs analyzed using two different presented approaches. There is good agreement between the results – the differences are less than 13%. However, the results obtained from the second approach (slab subjected to out-of-plane loads and in-plane shear) indicate relatively greater reduction in initial shear stiffness of the slabs. This is because the shear loading of a slab is more complicated than the simple approach.

Nevertheless, the good agreement between the results of the two completely different approaches can be considered as reasonable validation of the results.

Table 5.3 – Comparison of the reduction in initial shear stiffness of analyzed slabs

Slab	Reduction in initial shear stiffness		Difference (%)
	Tension approach	Shear approach	
LR-C1-7	0.71	0.67	6
LR-C2-7	0.53	0.46	13
HR-C1-7	0.89	0.84	4
HR-C2-7	0.78	0.70	10

5.3 In-Plane Shear Stiffness of Two-Way Slabs Subjected to Out-of-Plane Loads

Computer program Shell-2000 was used to conduct an investigation of the effect of out-of-plane loading on the in-plane shear stiffness of two-way flat plate slabs. Three simplifying assumptions were used, and these are discussed in detail in the following section.

5.3.1 Nonlinear Analysis of Two-Way Slabs

Nonlinear analysis was conducted to study the reduction in shear stiffness of two-way slabs subjected to out-of-plane loads and in-plane shear force. The computer program Shell-2000 was used for the analysis because it has a state-of-the-art material model for cracked concrete elements subjected to in-plane and out-of-plane forces.

The flexural bending moments in the slab (m_x and $m_y, kNm/m$) and the twisting bending moment in the slab ($m_{xy}, kNm/m$) were determined using a linear finite element analysis of the slab subjected to out-of-plane loads. These bending moments were assumed to remain constant as the in-plane shear force was increased until shear failure occurred in the slab. The distribution of membrane shear stress was assumed to be uniform across the diaphragm width, which is a reasonable assumption for the diaphragms with chord reinforcement located near the extreme flexural tension edge of the diaphragm (NIST, 2016). Finally, the effect of strong-axis bending of the diaphragm was ignored based on the results from the study in Chapter 4.

The in-plane shear force - shear strain behaviour of each element subjected to the out-of-plane moments and the in-plane shear force was obtained for all the elements in the slab. The shear displacement of the slab and average shear strain of the slab was calculated by integrating the shear strain along the slab span for each shear force level. As done previously, the shear stiffness reduction factor at each load level was defined as the ratio of the secant stiffness at a load level to the initial shear stiffness of the slab element subjected to in-plane shear force only.

Since the mechanism of transferring gravity loads in two-way slabs is much more complex than in one-way slabs, the effect of out-of-plane flexural bending moments (m_x and $m_y, kNm/m$) and the twisting bending moment ($m_{xy}, kNm/m$) on the shear behaviour of a shell element was investigated in detail.

5.3.2 Effect of Out-of-Plane Bending and Twisting Moments on Shear Behaviour of Reinforced Concrete Shell Elements

In one-way slabs, the effect of gravity loads is transferred primarily in one direction and the one-way out-of-plane bending occurs in that direction. In two-way slabs, the load path is not clearly defined. The slab transfers the gravity load in two perpendicular directions; however, the amount carried in each direction depends on the ratio of span lengths in the two directions, the type of supports and other factors. Therefore, two-way out-of-plane bending plus twisting occurs in the slab.

In order to better understand the effect of out-of-plane bending moments ($m_x, m_y, kNm/m$) and twisting moment ($m_{xy}, kNm/m$) on the shear behaviour of concrete slabs, the shear behaviour of one concrete shell element was investigated under different combinations of out-of-plane moments. For this purpose, a shell element with the thickness of 200 mm and two different reinforcement amount of 1% and 2% equally distributed in both x and y directions was analyzed using Shell-2000.

The concrete compressive strength was 30 MPa and the concrete secant modulus of elasticity was 23,750 MPa. The reinforcing bars were modelled using trilinear model with yield strength of 400 MPa until strain hardening at a strain of 0.01 and ultimate strength of 650 MPa at a rupture strain of 0.05. The modulus of elasticity of steel was assumed to be 200,000 MPa.

Figure 5.21 shows the shear behaviour of concrete shell element, with 2% reinforcement amount, subjected to one-way out-of-plane bending ($m_x, kNm/m$) and in-plane shear. The magnitude of the out-of-plane bending was kept constant for each analysis while the in-plane shear was increased with an increment step of 1 kN up to the failure of the element. The analysis was repeated with different magnitude of m_x ranging from zero to 60 kNm/m which is about 6 times the cracking moment ($M_{cr}, kNm/m$) of the element. Figure 5.21(a) shows the shear behaviour of the element up to failure while Figure 5.21(b) shows the close up of the initial slope. As shown in Figure 5.21, the flexural cracks due to the one-way bending significantly influence the initial stiffness and the strength of the element.

Figure 5.22 presents the analysis results of the shell element with 2% reinforcement amount subjected to two-way bending ($m_x, m_y, kNm/m$) with m_x/m_y ratio of 1. Also, the results are compared to those of the one-way bending. As expected, two-way bending causes larger reduction in initial shear stiffness and strength of the shell element compared to the same magnitude of one-way bending. However, the reduction in strength due to the out-of-plane bending moments can be compensated by increasing the amount of tension reinforcement.

When the magnitude of the out-of-plane bending moment is large enough to crack a considerable portion of the element in both directions (perpendicular to the reinforcement in horizontal and vertical directions), the initial shear stiffness of the element reduces remarkably. However, by increasing the shear force, the direction of the cracks changes to diagonal and the element regains the shear stiffness.

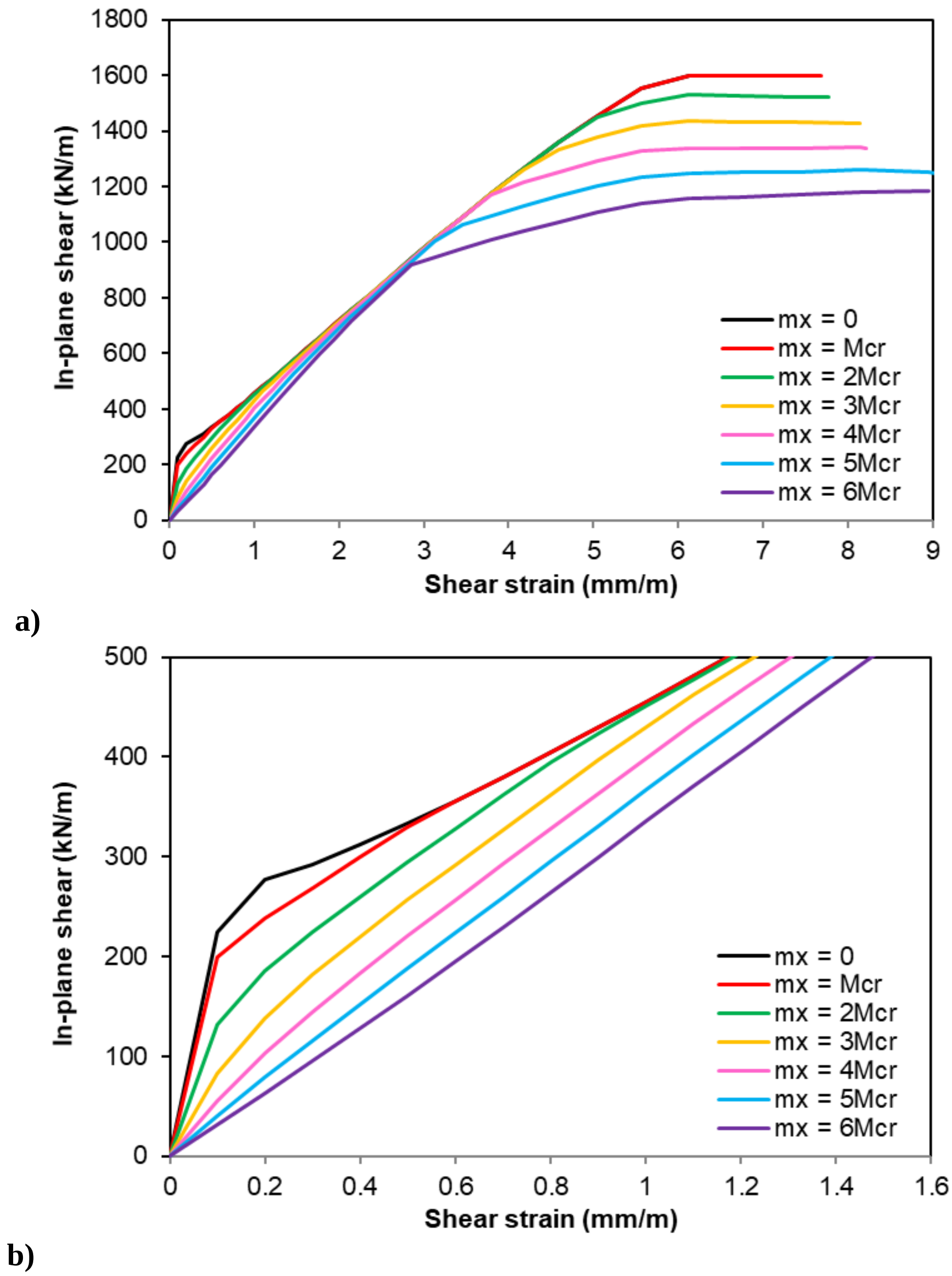

Figure 5.21 – Effect of one-way bending on shear behaviour of a shell element subjected to different levels of out-of-plane bending moment (as a ratio of the bending moment to cause initial cracking $\boldsymbol{M_{cr}}$): (a) shear force-shear strain relationship up to failure; (b) close up of initial slope

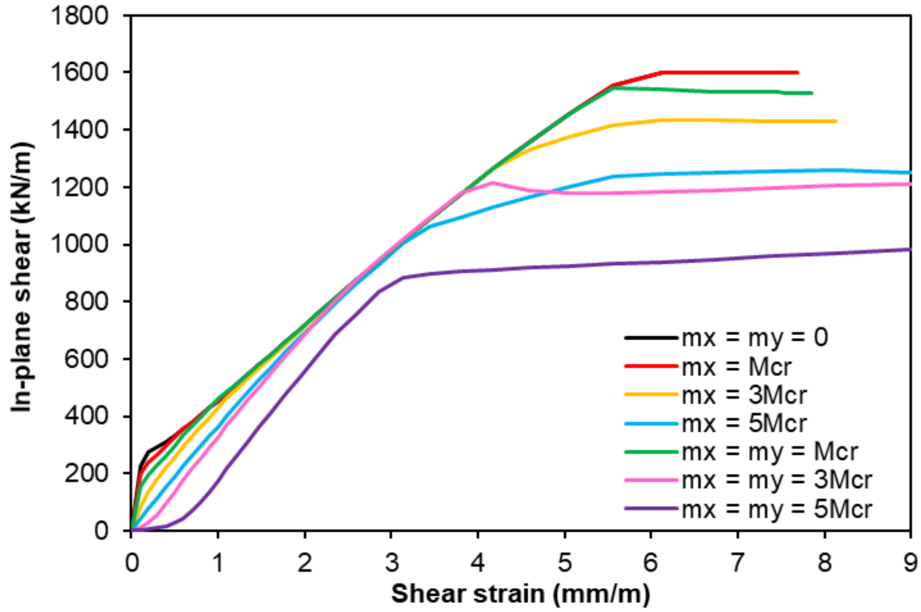

a)

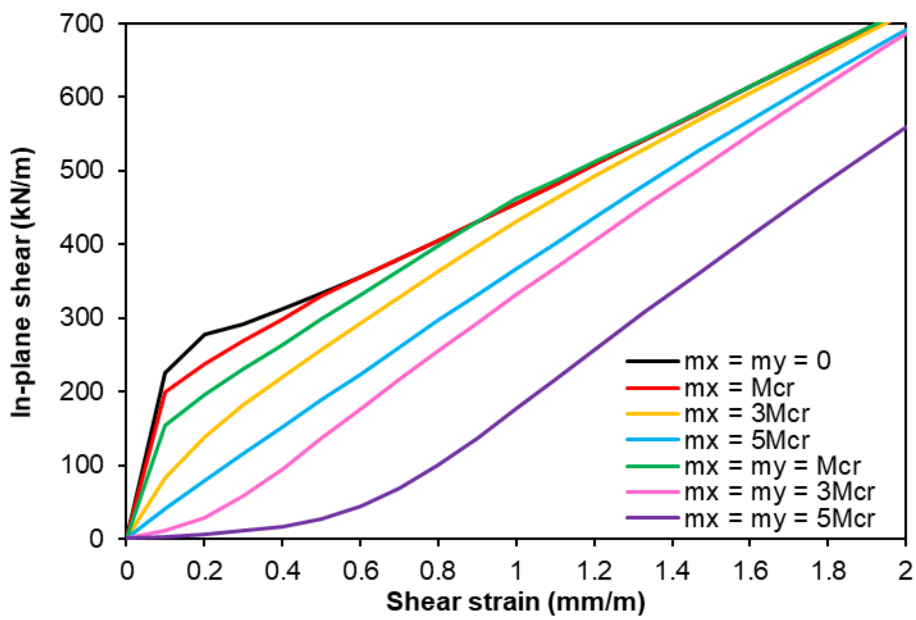

b)

Figure 5.22 – Effect of two-way bending on shear behaviour of a shell element (m_x/m_y=1): (a) shear force-shear strain relationship up to failure; (b) close up of initial portion

Figure 5.23 depicts the shear force – shear strain relationship of the shell element subjected to different combinations of two-way bending. The interesting point is that the shear behaviour of the element is almost identical for the cases where the summation of bending moments in horizontal and vertical directions is the same. This phenomenon can be explained by the following simple equation proposed by Gerin and Adebar (2004) for the shear strain:

$$\gamma_{hv} = \varepsilon_h + \varepsilon_v - 2\varepsilon_{45} \quad (5.4)$$

where ε_h and ε_v are the normal strains in the horizontal and vertical reinforcement directions, respectively; and ε_{45} is the normal strain at 45° to the reinforcement in the direction closest to the principal compression strain direction which depends on the magnitude of the shear stress. According to Equation (5.4), the shear strain remains unchanged as far as the summation of the normal strains does not change. Since the amount of reinforcement in the horizontal and vertical directions is identical in this example, the shear strain is about the same for the cases with identical summation of bending moments in the horizontal and vertical directions.

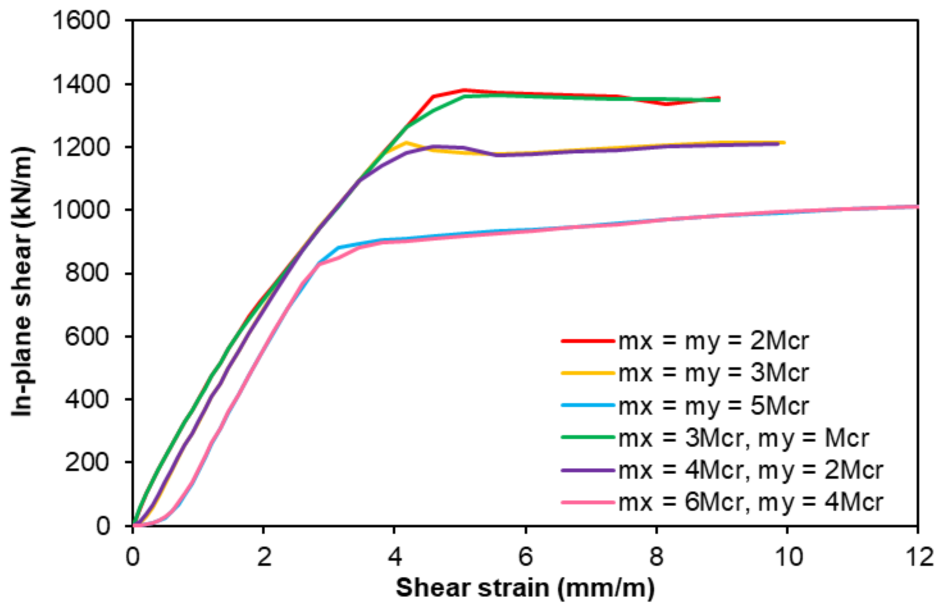

Figure 5.23 – Comparison of shear behaviour of a shell element subjected to different combinations of two-way bending

The shear behaviour of the shell element subjected to constant twisting moments and an increasing in-plane shear is depicted in Figure 5.24. It is observed that the twisting moment significantly reduces the initial shear stiffness and strength of the element. In addition to substantial strength degradation, increasing of twisting moment results in brittle failure of the shell element due to concrete crushing. In other words, by increasing the twisting moment, the failure mode of the shell element changes from ductile failure due to yielding of longitudinal reinforcement to brittle failure due to crushing of concrete. However, this is not of concern in two-way slabs as the magnitude of the twisting moments is not that large to cause such a problem.

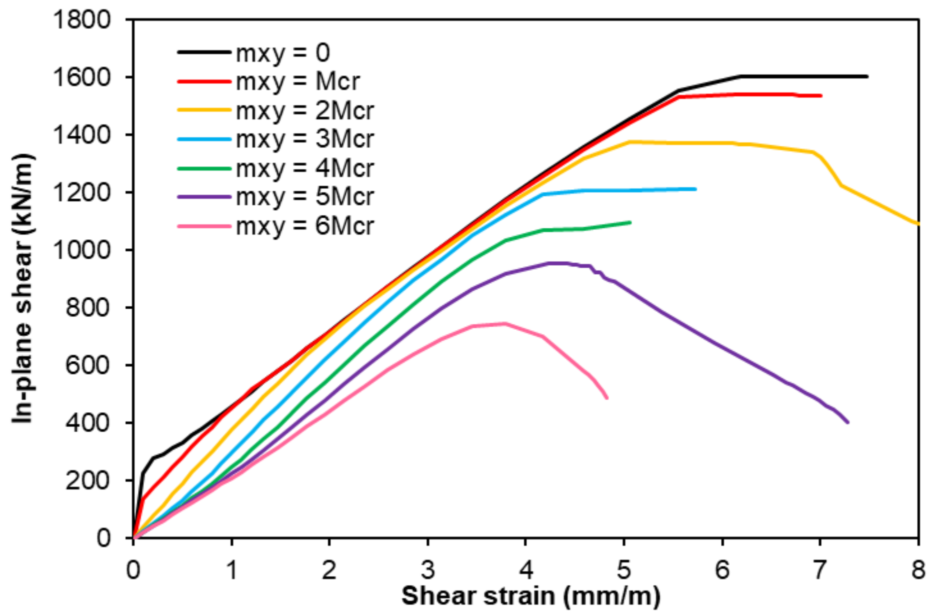

Figure 5.24 – Effect of a twisting moment (m_{xy}) on shear behaviour of a shell element

Figure 5.25 presents the shear force – shear strain relationship of the shell element subjected to different combinations of two-way bending and twisting moments and an increasing in-plane shear. As shown, when the two-way bending moments and the twisting moment applied in the same direction (either positive or negative), a positive initial shear strain (shear strain at zero shear force) occurs in the element. When the directions of the bending moments and twisting moment are opposite to each other, a negative initial shear strain takes place. The initial shear strain value depends on the magnitude of the applied twisting and bending moments. In addition, the element subjected to the bending and twisting moments with opposite directions exhibits lager strength. However, in this case, when the bending and twisting moments become large, the element fails in a brittle manner, as shown in Figure 5.25 (comparing blue and purple curves).

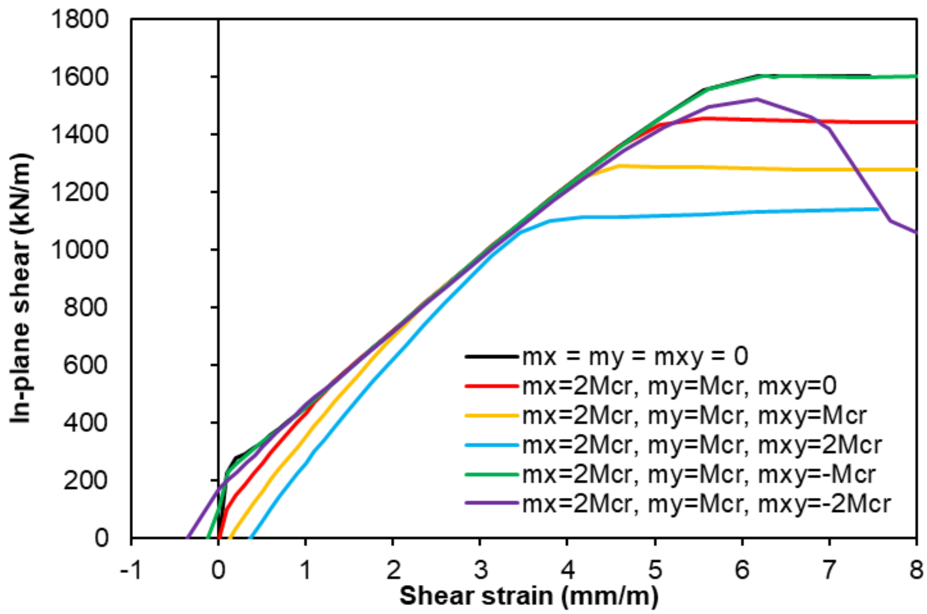

Figure 5.25 – Influence of two-way bending and twisting moments (m_x, m_y, m_{xy}) on shear behaviour of a shell element

5.3.3 Analysis of Two-Way Slabs Subjected to In-Plane Shear and Out-of-Plane Loads

In addition to the analysis of slab elements presented above, analysis was done on a complete bay of a two-way flat plate slab. The slab was 200 mm thick and had a span of 7 m. Thus, the span to depth ratio of the slab was 35, which typical for a concrete slab not thickened because of the large backstay forces. The concrete slab was reinforced with two layers of 15M@100 mm in each direction. Additional concentrated top slab reinforcement was provided around the column area where the magnitude of negative bending moments is large. This is consistent with the concentrated mat reinforcement that is provided in practice. The material properties used for the concrete and steel were the same as those used for the analysis of the shell element. The slab was analyzed under the service gravity load which accounts for the effect of dead load (self-weight of slab, 4.8 kPa, plus the superimposed dead load, 1.5 kPa) and the live load (2.4 kPa). Thus, the total applied gravity load was equal to 8.7 kPa.

As the slab is symmetrical about four axes (horizontal and vertical axes, and two diagonal axes) in terms of dimension, reinforcement amount and loading, only one-eighth of the slab needed to be analyzed. However, the one-eighth of the slab was analyzed twice, once with positive twisting moments and once with negative twisting moments as the twisting moments are only symmetrical about two diagonal axes. For the analysis, the slab was divided into elements with a mesh size of 500×500 mm.

The linear distribution of the out-of-plane moments in the continuous two-way slab was obtained from the linear finite element analysis of the slab subjected to the gravity loads by ABAQUS. For this purpose, the middle bay of a fully loaded continuous two-way slab with three bays in each direction was considered. Figures 5.26 and 5.27 depict the distribution of bending moments and twisting moment in the slab, respectively. As the investigated slab was symmetrical about the horizontal and vertical axes, the distribution of the bending moments in x and y directions (m_x and m_y, kNm/m) was identical in magnitude. Thus, only the distribution of the bending moment in x direction is shown in Figure 5.26 and by a 90-degree rotation of the graph, the distribution of the bending moment in y direction can be visualized.

Initially, the slab supports were modelled as point loads. This resulted in extremely large bending moments at the supports. For example, when the mid-span positive bending moment was 16 kNm/m, the negative bending moment at the support was 176 kNm/m. When the supports were changed to 600×600 mm columns, only the bending moments close to the supports were affected. The maximum negative bending moment reduced to 98 kNm/m.

Figures 5.27(a) and (b) show the 3D and plan views of the twisting moment distribution, respectively. The magnitude of the twisting moment increases near the supports. A transparent surface of zero twisting moment is also shown in Figure 5.27(a) to more clearly visualize the variation of the twisting moment in a symmetric two-way slab.

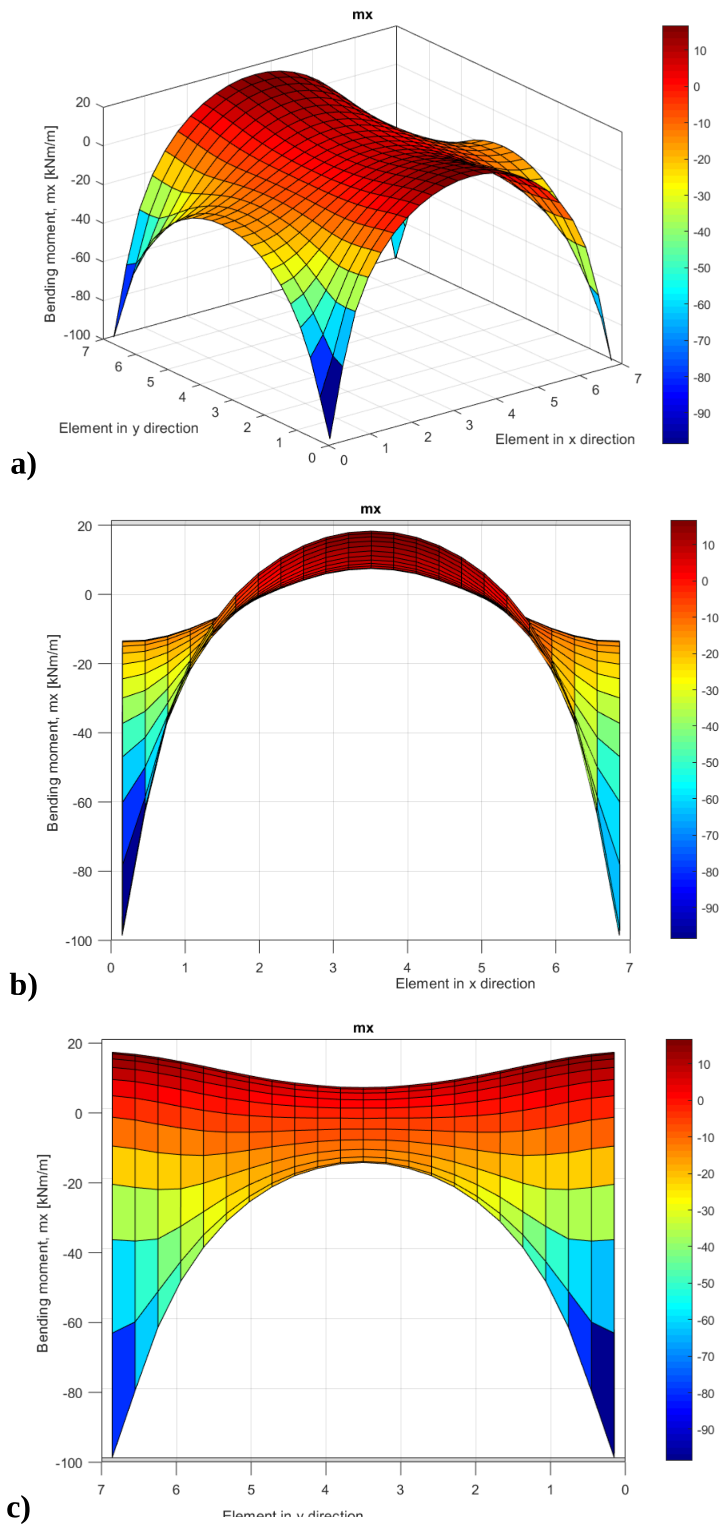

Figure 5.26 – Linear distribution of out-of-plane bending moment in x direction (m_x, kNm/m): (a) 3D view; (b) side view for elements in x direction; (c) side view for elements in y direction

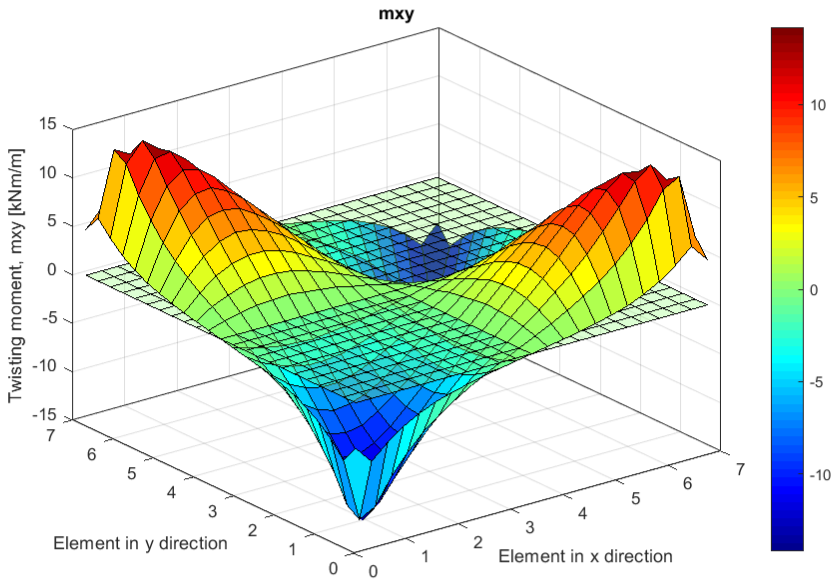

a)

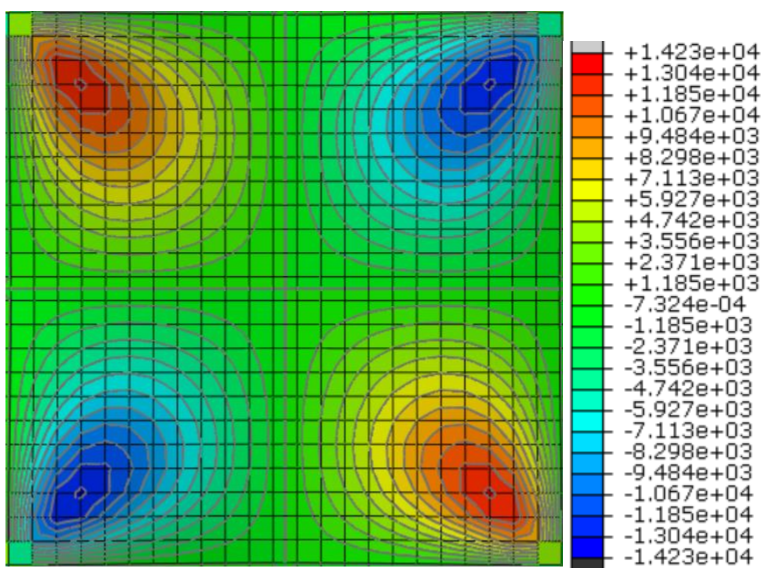

b)

Figure 5.27 – Linear distribution of twisting moment in two-way slabs ($m_{xy}, kNm/m$): (a) 3D view; (b) plan view

As shown in Figure 5.27(a), the twisting moment diagram is symmetrical about two diagonal axes of the slab. However, it is symmetrical about four axes (horizontal and vertical axes and two diagonal axes) in terms of the magnitude, as illustrated in Figure 5.27(b).

In order to analyze the slab under the effect of out-of-plane moments, the magnitude of the moments was obtained at the center of each element. Then the elements were analyzed using Shell-2000 under the effect of applied moments and an increasing in-plane shear force up to failure. The average of shear strains of the elements was calculated at each shear force level which gives the shear force – shear strain behaviour of the entire slab. The displacement of the slab due to the applied in-plane shear force was calculated by integrating the average shear strain over the slab span perpendicular to the applied shear force. Thus, the shear force – shear displacement relationship of the analyzed slab was determined as presented in Figure 5.28. Figure 5.28(a) shows the shear force – shear displacement relationship of the slabs while Figure 5.28(b) shows the close-up detail of the initial shear stiffness of the slabs.

The shear behaviour of the analyzed two-way slab was compared with the results of an identical slab loaded in one-way bending with fixed end supports at both ends of the slab which result in the maximum negative moment in the slab (Figure 5.28). Furthermore, the results were compared to the shear behaviour of a shell element subjected to an in-plane shear force only which represents the shear behaviour of a slab without out-of-plane loading. Figure 5.28 illustrates that the out-of-plane loading considerably influences the initial shear stiffness of the slab as well as the slab shear strength.

As shown in Figure 5.28, the two-way bending causes larger reduction in initial shear stiffness and subsequently strength of the slab compared to the one-way bending. This can be attributed to the fact that the two-way bending results in more extensive cracking especially close to the supports compared to the one-way bending due to the same out-of-plane loading. After the slab bay is fully cracked due to the applied in-plane shear force and the weak-axis bending, the shear force – deformation curve is merged to that of the slab subjected to the in-plane shear force only (without the weak-axis bending).

Shear stiffness degradation of analyzed slabs are depicted in Figure 5.29. It was indicated that the out-of-plane loading of slab considerably affects the initial shear stiffness of the slab reducing from 1 to about 0.75 due to the one-way bending and to about 0.5 due to the two-way bending of the slab. Thus, it has been shown that larger reduction occurs in the initial shear stiffness of the two-way slab compared to the one-way slab.

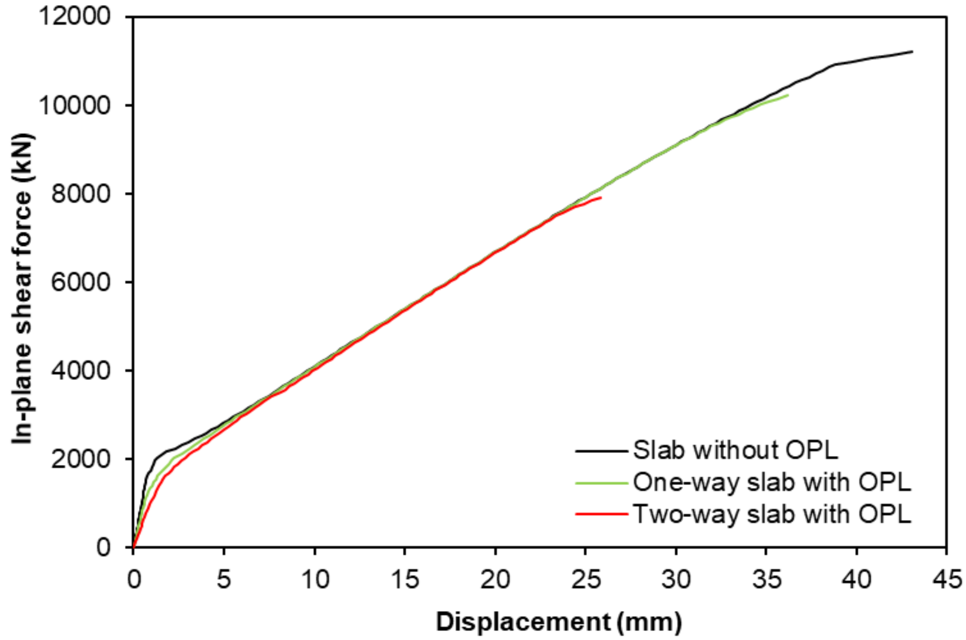

a)

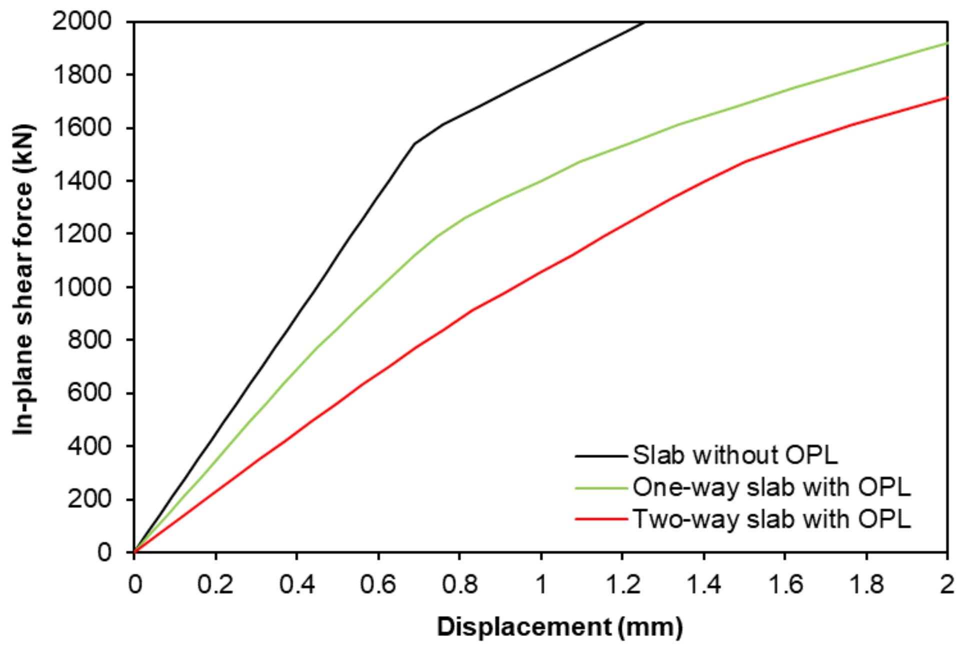

b)

Figure 5.28 – Shear force-displacement relationship of one-way and two-way slabs subjected to out-of-plane loads (OPL): (a) shear behaviour up to failure; (b) close-up detail of initial stiffness

By increasing the in-plane shear force, diagonal shear cracks formed in the slab which results in significant reduction in the shear stiffness of the slab. In the slab analysis using Shell-2000, it is assumed that the applied in-plane shear force causes a uniform shear stress in the slab. Therefore, the slab is fully cracked when the applied shear force becomes large enough. Beyond this point, the shear stiffness of the slab remains relatively constant which produces the flat portion of the shear stiffness reduction curve. It continues until the yielding of the reinforcement is reached. As the slab fully cracked, the effect of out-of-plane loading decreases and the shear stiffness of the slab with different boundary and out-of-plane loading conditions converges, as shown in Figure 5.29.

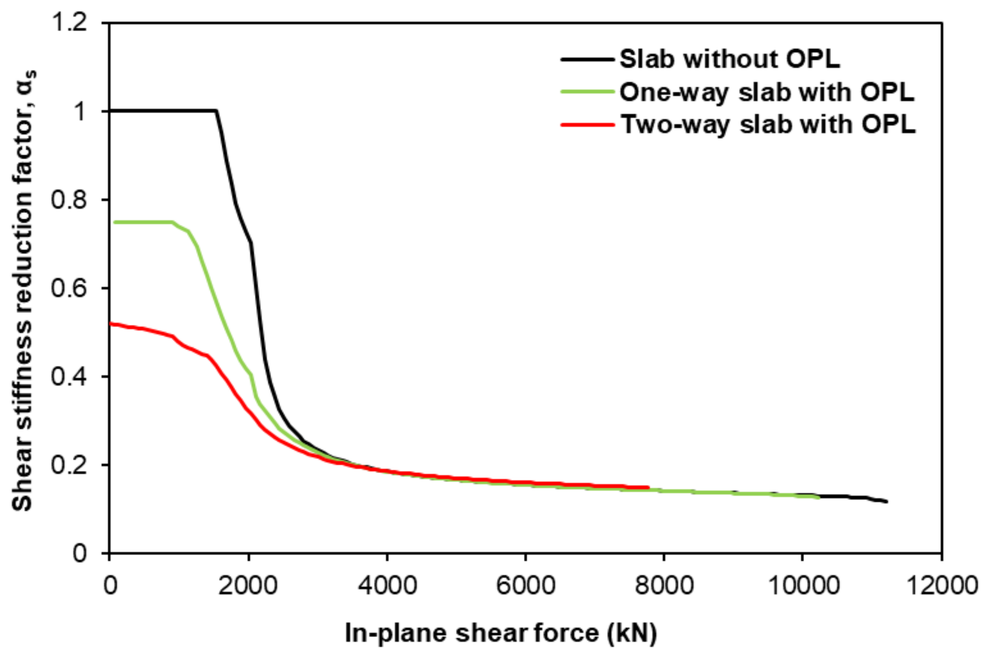

Figure 5.29 – Effect of out-of-plane loading (OPL) on membrane shear stiffness degradation of one-way and two-way slabs

The distribution of shear strain in the slab at different load levels were investigated in order to better understand the effect of out-of-plane loading on the shear behaviour of two-way slabs. Figure 5.30 shows the 3D view of the shear strain distribution for the analyzed two-way slab at the shear force of 700 kN. The average shear strain is depicted by a transparent surface in Figure 5.30 which is about 0.09 mm/m at the noted shear force level. As shown in Figure 5.30, the shear strain dramatically increases or decreases close to the support areas.

As the discussed above, the flexural bending moments and twisting bending moments (m_x, m_y and m_{xy}) are large near the column supports in two-way slabs. The large twisting moments (m_{xy}) near the columns cause diagonal cracks on both sides of the element which are perpendicular to each other. Also, large out-of-plane bending moments (m_x and m_y) near columns cause membrane tensions on one side and flexural compressions on the other side of the element. Applying in-plane shear also results in the formation of diagonal cracks in the element. The diagonal crack due to the twisting moment is aligned with the diagonal crack due to the in-plane shear on one side of the element. When the large membrane tensions caused by out-of-plane bending moments (m_x and m_y) are on the same side as where the diagonal cracks are aligned, the shear strain becomes very large. Inversely, when the aligned diagonal cracks form on the flexural compression side of the element, the shear strain reduces, as illustrated in Figure 5.30.

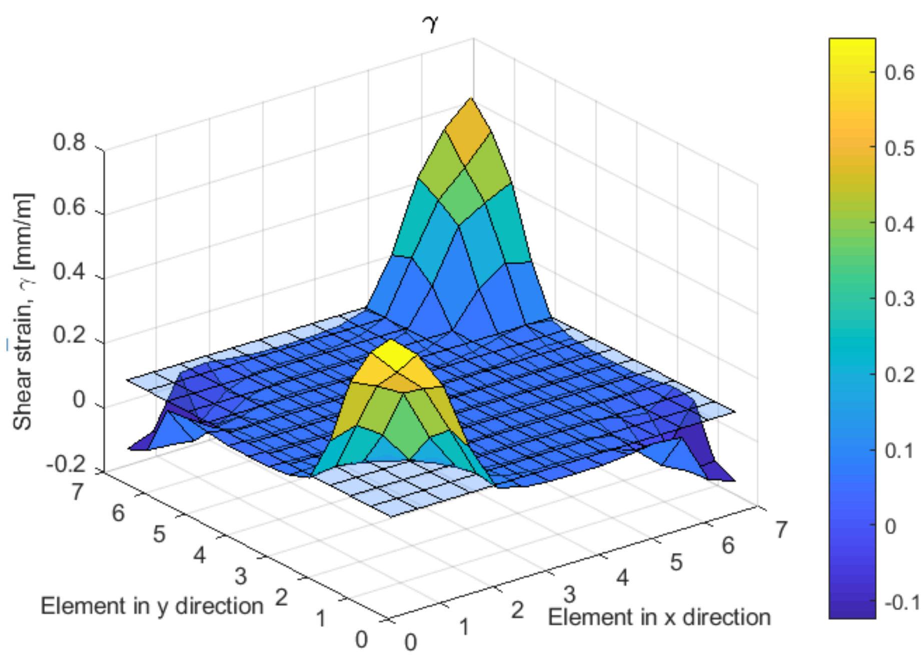

Figure 5.30 – Shear strain variation in analyzed two-way slab subjected to out-of-plane loads and in-plane shear at shear force level of 700 kN

In order to clearly visualize the variation of the shear strain in the slab, the shear strain in half of the slab at different rows of elements in x direction are plotted. Figures 5.31 and 5.32 depict the variation of shear strain when the slab was subjected to out-of-plane loads only ($V = 0\ kN$)

and when the slab was subjected to out-of-plane loads and in-plane shear force of 700 kN, respectively.

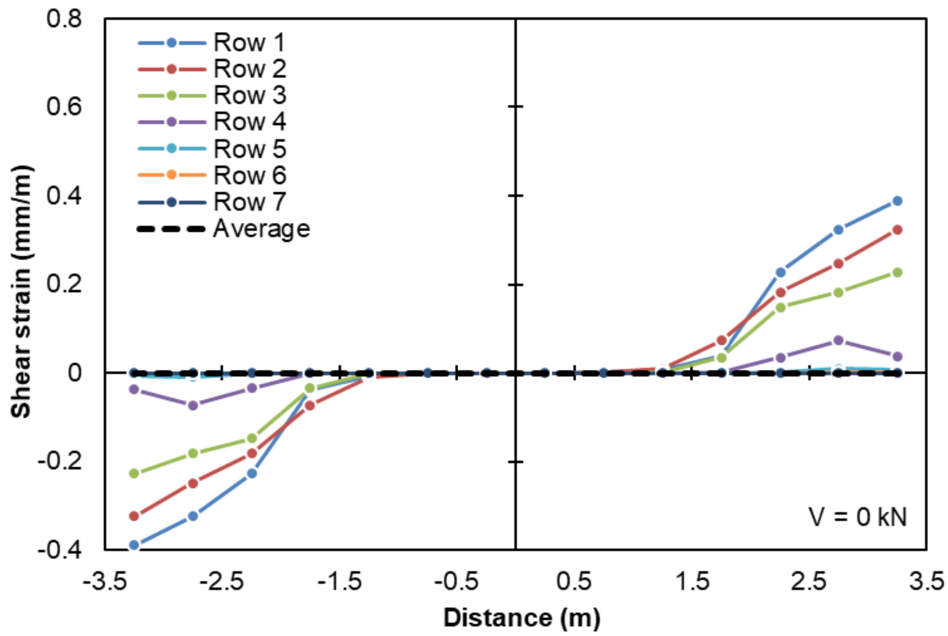

Figure 5.31 – Variation of shear strain in half of the analyzed slab subjected to out-of-plane loads only ($V = 0\ kN$)

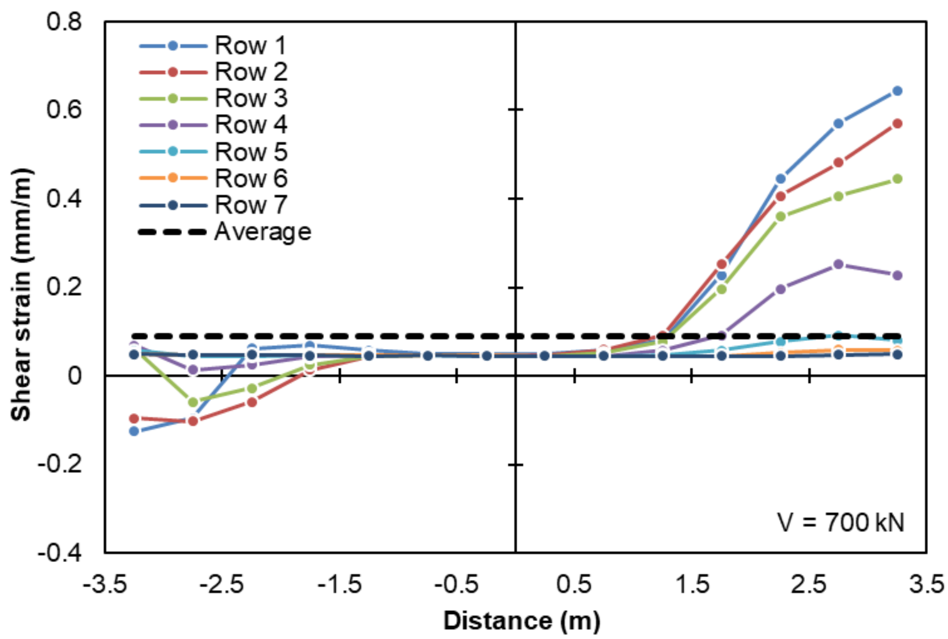

Figure 5.32 – Variation of shear strain in half of the analyzed slab subjected to out-of-plane loads and in-plane shear force of 700 kN

Prior to applying in-plane shear force, shear strains near columns are identical in magnitude but opposite in direction which is in accordance with the distribution of the twisting moment in the slab. At this point, the average shear strain in the slab was equal to zero as expected. Except for the elements close to the support areas (i.e., columns) where the out-of-plane moments are considerably large, the rest of the elements in the slab remained uncracked (Figure 5.31).

Applying in-plane shear force results in increasing shear strains in the direction of the shear force. Therefore, shear strain increases at two opposite corners where the aligned diagonal cracks due to the twisting moment and the shear force, and the large membrane tensions due to the bending moments form on the same side. At the other opposite corners, the shear strains decrease in magnitude. As a result, the average shear strain increases in the slab (Figure 5.32). By increasing the in-plane shear force, the influence of the out-of-plane moments becomes negligible while the effect of shear force becomes dominant. Diagonal cracks form in all the elements in the slab and consequently, shear strains increase in the slab in the direction of the shear force.

The analysis result show that the influence of the distributed reinforcement in the slab on the initial shear stiffness is not considerable since most of the elements in the slab remain uncracked under the effect of out-of-plane loads except for the areas close to the supports. As aforementioned, these areas are typically provided with concentrated mat reinforcement. Thus, the amount of concentrated reinforcement can affect the initial shear stiffness of the slab. Figure 5.33 compares the shear stiffness degradation in the slab for two cases of out-of-plane loadings, 6.3 kPa representing the dead load (self-weight of slab, 4.8 kPa, plus the superimposed dead load, 1.5 kPa), and 8.7 kPa representing the dead load and the live load (2.4 kPa).

The amount of concentrated reinforcement close to support areas is reduced from 4% for the case of out-of-plane load of 8.7 kPa to 3% for the case of out-of-plane load of 6.3 kPa. About 50% reduction in the initial shear stiffness of two-way slabs occurs due to the out-of-plane loads. If the amount of concentrated reinforcement for the case of 6.3 kPa out-of-plane load remains the same as 4%, the initial shear stiffness of the slab reduces about 40%, as shown in Figure 5.33. In fact, flexural cracking due to the out-of-plane loading is controlled more effectively when the amount of concentrated reinforcement increases close to the support areas where the out-of-plane moments are noticeably large.

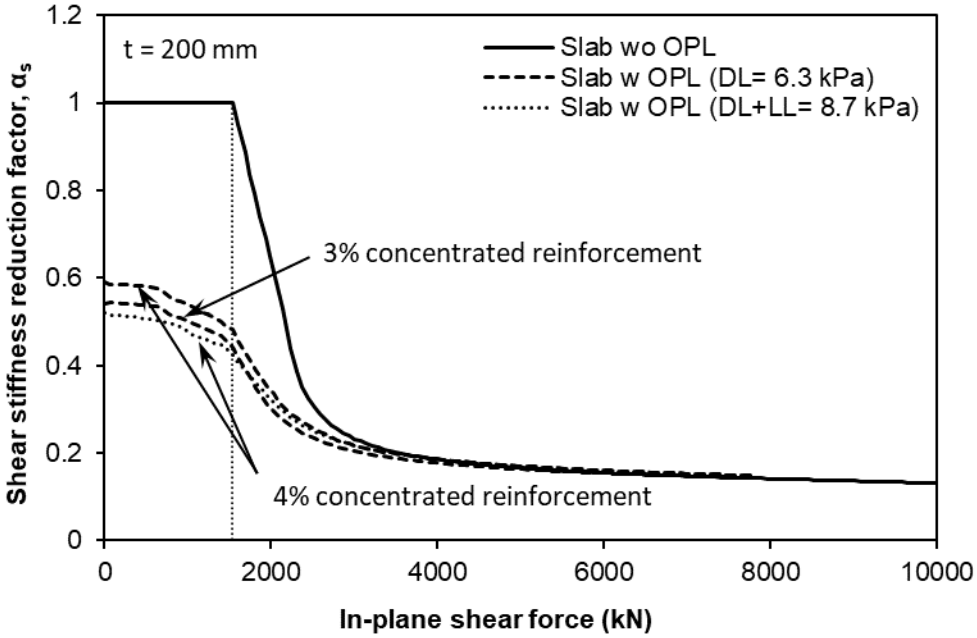

Figure 5.33 – Shear stiffness reduction in two-way slab with the thickness of 200 mm

The reduction in the initial shear stiffness is reduced when the area of slab affected by the flexural cracking due to the out-of-plane load is reduced. One way to decrease the effect of flexural cracking is to increase the thickness of the slab. Thus, the slab thickness was increased to 300 mm in this analysis. Although the out-of-plane load increased due to the increase in the self weight of the slab, the number of cracked elements in the slab reduces. Accordingly, the reduction in the initial shear stiffness of the slab is about 70% and 60% for the two cases of out-of-plane loading (dead load only, and dead load plus live load), respectively. Figure 5.34 depicts the shear stiffness reduction in the slab with the thickness of 300 mm and for the two out-of-plane loadings.

According to the analysis results, the flexural cracking due to the weak axis bending of concrete diaphragms can result in the reduction of the initial shear stiffness up to 50%. Depending on the extend of flexural cracks in the slab, the reduction in the initial shear stiffness can vary. The fewer flexural cracks form in the slab due to the out-of-plane loads, the smaller is the reduction in the initial shear stiffness of the slab.

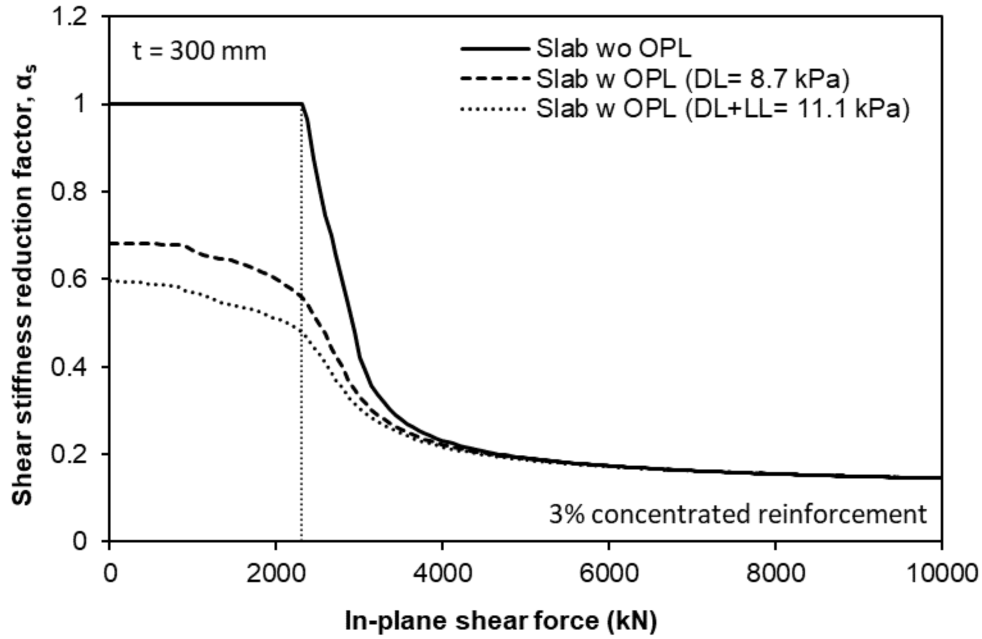

Figure 5.34 – Shear stiffness reduction in two-way slab with the thickness of 300 mm

5.4 Summary and Conclusions

The objective of the study presented in this chapter was to investigate the potential impact of out-of-plane bending moments on the in-plane shear stiffness of diaphragms resisting backstay forces. As strong-axis bending of the diaphragms were found to be much less important than shear stiffness in Chapter 4, it was not considered in this phase of the research. Nonlinear analyses were conducted on continuous one-way and two-way concrete floor slabs subjected to out-of-plane bending. Two out-of-plane load cases were considered, dead load only and dead load plus full live load. In addition, a number of different span lengths and diaphragm thicknesses were investigated.

For continuous one-way slabs subjected to in-plane shear and weak-axis bending (out-of-plane loads), the application of out-of-plane loads cause the formation of flexural cracks at the supports and at the mid-span where the maximum negative and positive bending moments occur, respectively. These flexural cracks reduce the initial shear stiffness of the slab. The more flexural cracking, the larger the reduction in initial shear stiffness of the slab. This is confirmed by the analysis results of the one-way slabs with two different levels of out-of-plane load. In addition, the amount of reinforcement has considerable influence on the initial shear stiffness. Heavily reinforced one-way slabs exhibit smaller reductions in initial shear stiffness compared to the lightly reinforced slabs.

As the in-plane shear is increased, the shear stiffness reduces similar to what was observed in Chapter 4. The shear stiffness of a diaphragm subject to large in-plane shear stresses is independent of the level of initial cracking due to out-of-plane loading. That is, the out-of-plane loading influences the initial shear stiffness; but not the final shear stiffness of the diaphragm when the diaphragm is fully cracked.

For two-way slabs subjected to in-plane shear force and weak-axis bending (out-of-plane loads), larger reduction in initial shear stiffness is observed. This is attributed to the different distribution of bending moments in one-way and two-way slabs. In one-way slab, the slab is subjected to one-way bending which causes flexural cracks in one direction at the supports and the mid-span, while in two-way slabs, the slab is subjected to two-way bending as well as the twisting moments which results in more complicated cracking pattern especially at the corners of the slab. The combination of large negative two-way bending and negative twisting moment generates the maximum shear strain at two opposite corners of the slab and the combination of large negative two-way bending and positive twisting moment produces the minimum shear strain at the other two opposite corners when the applied in-plane shear force is small (initial portion). When the direction of diagonal cracks due to the twisting moment is aligned with the direction of diagonal cracks due to the applied shear force, this leads to a significant increase in the shear strain and consequently, a considerable reduction occurs in the shear stiffness of diaphragms.

The important conclusion of this chapter is that cracking due to out-of-plane loading of diaphragms can significantly reduce the initial membrane shear stiffness of the diaphragms. The reduction in initial shear stiffness is larger in two-way slabs because of twisting moments near the supports, which cause membrane shear cracks at different levels through the thickness of the diaphragms. Once the in-plane shear force is large enough to cause the diaphragm to be fully cracked, the influence of the initial cracking due to out-of-plane loading disappears.

Chapter 6

Sloped-Column Irregularity in High-Rise Core Wall Buildings

6.1 Introduction

Architects are increasingly looking for ways to make their building different from other buildings. One way that this is being accomplished is by inclining the gravity-load columns in various arrangements. Figures 6.1 and 6.2 show two examples of such buildings constructed in Vancouver, Canada. Figure 6.1 shows the Telus Garden building, while Figure 6.2 shows the Vancouver House building. In Vancouver House, the “sloped columns” are formed by in-plane offsets of the columns/bearing walls from one floor to the next.

The important characteristics of sloped columns can be defined by four parameters. The first is whether the sloped columns are in a symmetric or asymmetric arrangement. Telus Garden is an example of sloped columns forming a symmetric structure, while Vancouver House is an example of sloped columns forming an asymmetric structure. Another important parameter is the slope of the column relative to the vertical axis. The sloped columns in the Telus Garden building have an angle of 13 deg. to the vertical, while the sloped columns in the Vancouver House building have a slope of about 17 degrees. The remaining two parameters that define a sloped-gravity load column are the starting point (base) of the columns and height of the building over which the columns are sloped. In the Telus Garden building, the sloped columns start at grade level and go up for five floors, while in the Vancouver House building, the sloped columns start at about Level 8 and go up for about 30 stories.

Figure 6.1 – Symmetric sloped column - Telus Garden, Henriquez Partners Architects (left: https://dailyhive.com, right: https://skyscraperpage.com)

Figure 6.2 – Asymmetric sloped column - Vancouver House, Bjarke Ingels Group (left: http://thecdr.ca/6jk, right: photo by P. Adebar)

With asymmetrical arrangements of sloped columns, shear walls in the building are subjected to additional shear force and bending moments due to gravity loads. These constant lateral forces cause the lateral displacements of a building to progressively increase during an earthquake. Based on the work of Dupuis, et. al. (2014), a new type of irregularity called "Gravity-Induced Lateral Demand (GILD)," was introduced in the 2015 edition of the National Building Code of Canada. Engineers are required to conduct a nonlinear analysis to determine the inelastic displacement demands on the building when the GILD irregularity is large. For a symmetrical arrangement of sloped columns, the horizontal components of the gravity forces in the sloped columns balance each other. A static analysis suggests that there will be no force demands on the shear walls due to symmetrical sloped columns, and therefore there is no GILD.

When a sloped column has different horizontal movement at the top and bottom of the column, there will also be vertical movement of the sloped column. This will cause the slabs connected to the columns to move vertically, which can result in additional bending moments in the slabs and additional axial forces in the columns. Similarly, differential horizontal acceleration at the top and bottom of sloped columns will result in the vertical acceleration of the mass supported by the columns.

The objective of the current study was to investigate the influence of sloped gravity-load columns on the seismic response of high-rise shear wall buildings. This study was mainly focussed on the maximum increase in the axial force applied to sloped columns during an earthquake, as this was felt to be a critical issue. An outcome of the current investigation is a new type of irregularity, called "sloped-column irregularity," being introduced into the 2020 edition of National Building Code of Canada (NBCC).

6.2 Seismic Analysis of Buildings with Sloped Column

6.2.1 Overview of Analysis

The influence of different characteristics of sloped columns was investigated. Both symmetric and asymmetric arrangements of sloped columns were included in the study. The slope of the gravity-load columns varied from 0 to 45 degrees from the vertical. The height of the sloped portion of the columns varied from 3 stories to 16 stories, and the location of the base of the sloped portion of the columns varied from the ground level up to the 8th floor level.

In addition, the influence of the type of seismic force resisting system (SFRS) in the direction of the column slope was investigated. Typical high-rise buildings in Canada have a core with cantilever shear walls in one direction and coupled shear walls in the other direction. Thus both cantilever shear walls and coupled walls were included in the investigation.

An important parameter that influences the response of a building with sloped columns is the ratio of the vertical mass supported by the sloped columns to the total horizontal mass. The ratio of the vertical to horizontal mass per floor level varied from 2% to 60% at the floor levels supported by the sloped columns. The lower-bound value is from the case where only one of many columns in the building are inclined, while the upper bound is from the case where most or all of the gravity-load columns are inclined. Table 6.1 summarizes the range of investigated parameters.

Table 6.1 – Investigated parameters

Parameter	**Description**
Type of Sloped column	Symmetric and asymmetric
Slope of column	0 to 45 deg.
Location of column base	Ground to 8th story
Height of sloped column	3 to 16 stories
Type of SFRS	Shear wall and coupled wall
Vertical mass per floor supported by sloped column (m_v/m_h)	2% to 60%

A series of analytical studies were conducted to investigate the influence of sloped gravity-load columns on the seismic response of concrete shear wall buildings. Three different types of dynamic analysis were employed in the study including response spectrum analysis (RSA), linear time history analysis (LTHA) and nonlinear time history analysis (NLTHA). Horizontal and vertical excitations were considered for the analyses. According to Clause 4.1.8.8 of NBCC 2015, since the SFRS components of investigated structure were oriented along a set of orthogonal axes, independent analyses about each principal axis of the structure were performed.

Response spectrum analysis (RSA) is typically used by design engineers to do the seismic analysis of buildings in Canada. In the current study, response spectrum analysis was mainly used to understand the physics of the problem and to develop the simplified procedure for the maximum axial force in the sloped column. The 5% damped design spectra for horizontal and vertical excitations, which will be defined in Section 6.2.5, were used for the analysis. For modal combination, CQC rule was applied since the natural frequencies of contributing modes were closely spaced when the maximum force occurred in the sloped column. SRSS rule was used for directional combination as the structure was independently analyzed in each horizontal direction.

To further investigate the seismic behaviour of buildings with sloped column irregularity, linear and nonlinear time history analyses (LTHA and NLTHA) were conducted at the hazard level of interest. Each horizontal component of selected ground motions was applied simultaneously with the vertical component. Equivalent viscous damping of 2.5% was considered for the analysis according to Guidelines for Performance-Based Seismic Design of Tall Buildings (TBI, 2017). In addition, P-Delta effects were included in the model. The many different types of analyses were conducted to better understand the physics of the problem and to accurately evaluate the seismic behaviour of high-rise buildings with sloped columns especially the axial force demand in the sloped columns.

It should be noted that the gravity-load columns including the sloped column were modelled as linear elastic members in all linear and nonlinear analyses. The sloped column was considered as a single element extending over a certain height of the building. The columns above and below the sloped column were connected to the core using rigid slabs at each floor level. The sloped column was considered on one side (e.g., the right side) of the building as a symmetric or asymmetric column, as shown in Figure 6.9. To ensure the gravity-load columns did not contribute to the lateral resistance of the building, all columns were modelled with moment releases at both ends.

The soil-structure interaction was neglected in all models. The base of the core walls was assumed to be fixed against translational and rotational movements while the base of the column was assumed to be restrained against translational movements only.

6.2.2 Description of Building

In this study, a typical modern shear wall building was used for the linear and nonlinear dynamic analyses. A 30-story residential building with a ductile core was taken from Chapter 11 of the CAC Concrete Design Handbook (Mitchell, Paultre and Adebar, 2015). The core consists of ductile shear walls in one direction and ductile coupled walls in the perpendicular direction. Figure 6.3 shows the core walls, which contains elevator shafts and a stair shaft.

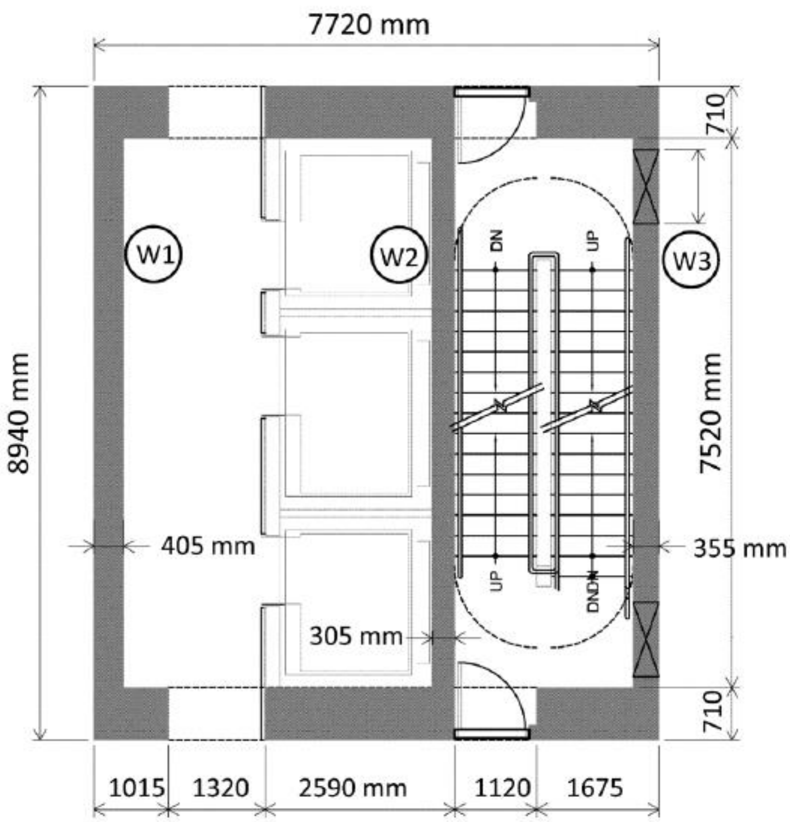

Figure 6.3 – Plan view of core walls (Mitchell, Paultre and Adebar, 2015)

The building has 30 stories above the grade and 5 stories below the grade. It should be noted that the below grade stories were not considered in the analysis. Building height from grade level to the top of roof slab is 85.1 m. Overall dimensions of floor plates above the grade are 25.9 x 25.9 m with the thickness of 190 mm. The height of first story is 4.46 m while it is 2.78 m for the second story and above (center-to-center of floor slabs).

As illustrated in Figure 6.3, the core consists of three C-shaped cantilever walls, labelled W1, W2 and W3, with an overall length of 8.94 m and web thicknesses of 405, 305 and 355 mm, respectively. The thickness of all wall flanges is 710 mm and the overall length of the core in the coupled wall direction is 7.72 m. The depth and length of coupling beams between walls W1 and W2 are 595 mm and 1320 mm, respectively, and are 695 mm and 1120 mm between walls W2 and W3. The gravity-load frame in the building consists of flat plate floor slabs with the thickness of 190 mm supported on 12 gravity-load columns spaced evenly around the perimeter of the building (four per side). However, the gravity-load columns were not considered in the current study except for one side of the building in each principal direction. The four columns on the side of interest (e.g., the right side of the building) were combined as a single column that was aligned with the center of mass and center of rigidity of the building to avoid any torsional effect in the building.

The concrete compression strength varies over the height of the core walls as follows: above level 20, $f_c' = 30$ MPa; levels 11 to 20, $f_c' = 35$ MPa; and below level 11, $f_c' = 45$ MPa. All reinforcement in the building is grade 400 MPa. In the current study, the concrete compressive strength was assumed to be 45 MPa and kept constant over the height of core walls. The secant modulus of elasticity was taken as 31,855 MPa and the Poisson's ratio was assumed to be 0.2. In addition, the vertical reinforcement provided at grade level of the building (given in Appendix E) was extended up through the entire height of core walls.

The concrete density of 24 kN/m^3 was used to calculate dead loads due to self-weight of the building. The superimposed dead load from finishes and partitions was 0.72 kN/m^2 and from cladding around perimeter of building was 1.9 kN/m. Thus, the calculated horizontal seismic mass was 505 ton (about 5000 kN/g) per typical floor. The mass of the top floor and the first floor were 629 ton (6174 kN/g) and 644 ton (6321 kN/g), respectively. The vertical mass was determined based on the tributary area of the sloped gravity-load column, which was about 20%

of the horizontal mass per floor. Therefore, the vertical component of mass was considered as 101 ton (1000 kN/g) per floor in the analyses.

6.2.3 Response Spectrum Analysis Model

Two computer programs SAP2000 and ETABS were employed to perform response spectrum analysis of the building with sloped columns. A two-dimensional model (linear stick model) of the core walls and the sloped column was created in SAP2000. This simple model was used to conduct a series of analyses for understanding the physics of problem.

Figure 6.4 depicts the 2D model of the 30-story building in the shear wall direction with a 17-degree asymmetric sloped column extended over sixteen stories which starts from the 8^{th} story to the 24^{th} story similar to the Vancouver House example. The core walls were modelled using I-section frame elements in the shear wall direction. The floor slabs that connect the gravity-load columns to the shear walls were modelled as rigid frame elements with pinned connections.

Figure 6.4 – 2D model of the core with a 17-degree asymmetric sloped column extended over 16 stories from the 8^{th} story to the 24^{th} story in SAP2000

A three-dimensional model of core walls was developed in ETABS using thin shell elements that were generated by automated rectangular meshing. The building was analyzed as a two-dimensional model in each principal direction independently. Floor slabs were also modelled using shell elements with automatic meshing. The floor slabs were considered as rigid diaphragms. Figures 6.5(a) and (b) show the ETABS model of a 30-story building in both shear wall direction and coupled wall direction with a 9-degree asymmetric and symmetric sloped columns, respectively.

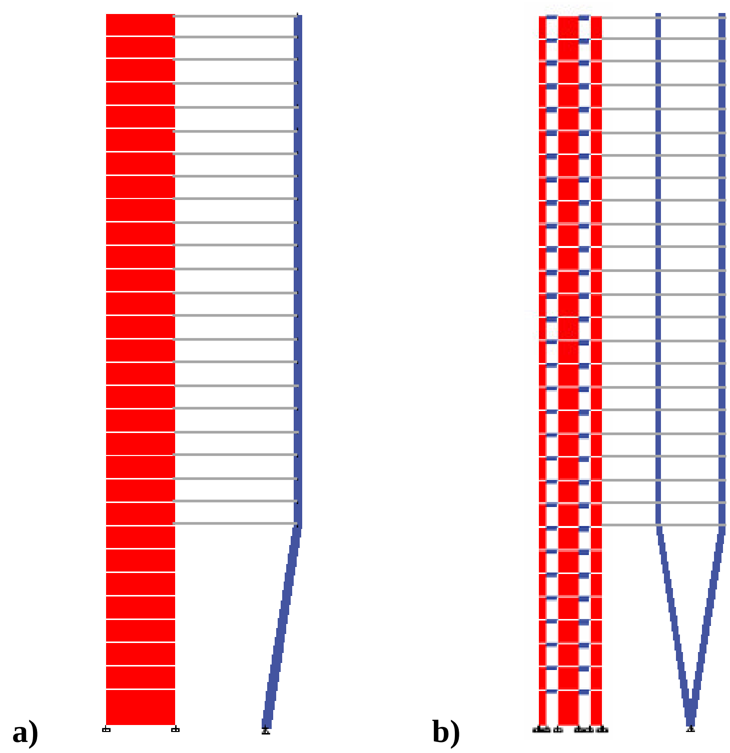

Figure 6.5 – ETABS model of: (a) the core in shear wall direction with a 9-degree asymmetric sloped column extended over 8 stories from ground, and (b) the core in the coupled wall direction with a 9-degree symmetric sloped column extended over 8 stories from ground

Reduced section properties in accordance with Clause 21.2.5.2 of CSA Standard A23.3-2014 were used to account for cracking of concrete in shear walls. Since coupling beams were designed with diagonal reinforcement, their effective shear and flexural rigidities were $E_c A_{ve} = 1.2 \times 0.45 E_c A_g$ and $E_c I_e = 0.25 E_c I_g$, respectively. The correction factor of 1.2 was considered for the effective shear area due to the fact that ETABS uses a shear area of $A_{ve} = 5/6\, A_g$. Different reduction factors, ranging from 0.5 to 1.0, were assumed for axial and flexural rigidities of core walls. The reduced axial rigidity mostly influences the flexural stiffness of the coupled walls while the reduced in-plane flexural rigidity controls the flexural stiffness of the cantilever walls (shear walls).

6.2.4 Response History Analysis Model

In order to conduct the time history analysis, two-dimensional models of core walls in both shear wall direction and coupled wall direction were developed in PERFORM-3D. In PERFORM-3D, cross sections used for shear walls are fiber sections. In the current study, both elastic and inelastic fiber sections were utilized to conduct linear and nonlinear time history analyses. Similar data is required to define the elastic and inelastic fiber sections in PERFORM-3D except for the material types used for concrete and steel in each section. Figure 6.6 illustrates inelastic concrete and steel materials used for the inelastic fiber section.

The fiber section in the shear wall direction was defined as an I-shaped section while it was defined as three T-shaped sections connected using coupling beams in the coupled wall direction. Wall sections used the fiber properties for axial force and in-plane bending and were considered to be elastic for shear, torsion and out-of-plane bending. For coupled walls, coupling beams were modelled as elastic members in bending with inelastic shear hinge in the middle. Inelastic shear hinge material model used for coupling beams is presented in Figure 6.7.

In PERFORM-3D, inelastic materials (e.g., concrete and steel) are defined as a piece-wise linear model, as illustrated in Figure 6.6. In order to verify the nonlinear model of shear walls, a push-over (nonlinear static) analysis was conducted on the isolated shear wall (without sloped column). The moment-curvature response of the shear wall at grade level was presented in Figure 6.8. In addition, the sectional analysis of the wall was performed using Response-2000, which has the state-of-the-art material models for concrete in nonlinear range. As illustrated in Figure 6.8, there is a good agreement between the moment-curvature responses of the wall obtained from two different analyses.

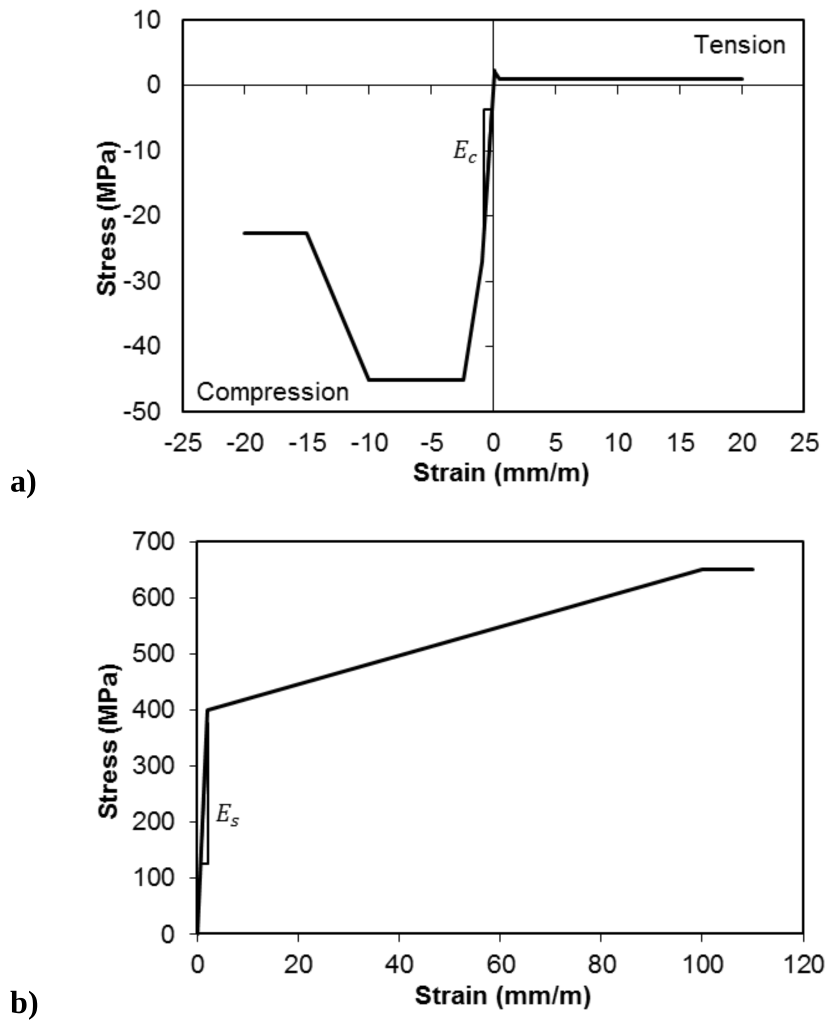

Figure 6.6 – Inelastic material models in PERFORM-3D model: (a) concrete; (b) steel

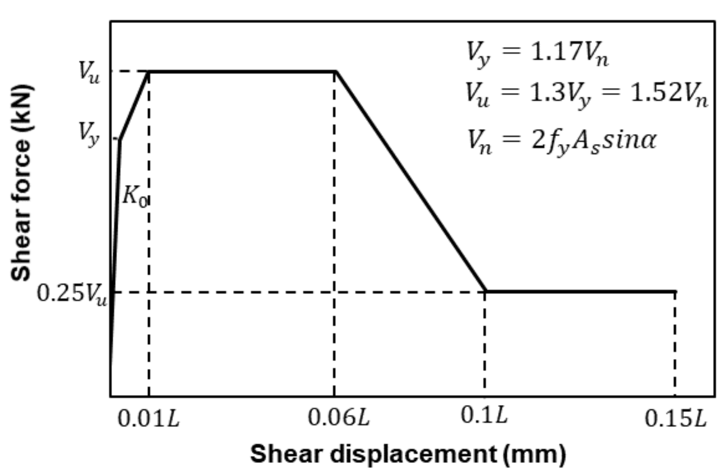

Figure 6.7 – Inelastic shear hinge properties used for coupling beams

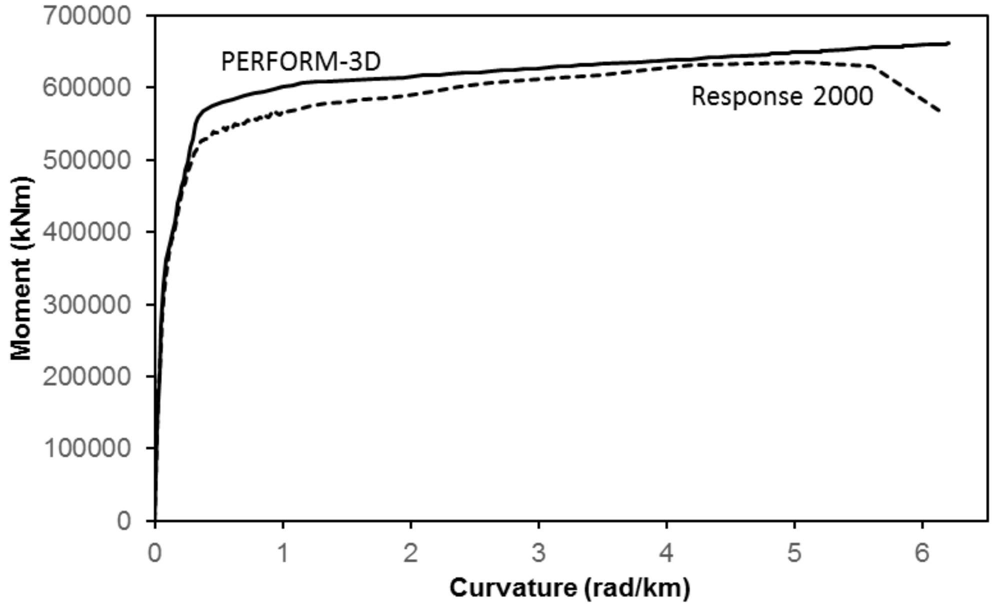

Figure 6.8 – Comparison of moment-curvature response of the shear wall obtained from PERFORM-3D and Response-2000

In order to account for the energy dissipation that is not considered by the analysis model, a small amount of equivalent viscous damping should be included in linear and nonlinear response history analyses. The equivalent viscous damping can be represented through modal damping and mass and stiffness proportional Rayleigh damping. However, it should be checked that the modes of the response that significantly contribute to the calculated demands are not overdamped. ATC-72-1 and other recent research publications such as Cruz and Miranda (2016) and Bernal et al. (2015) concluded that damping in tall buildings is less than that in low-rise buildings based on the evidence from measured building data. Figure 6.9 depicts equivalent viscous damping versus building height recommended by ATC-72-1. According to Figure 6.9, viscous damping should not be taken less than 0.025 for MCE (maximum considered earthquake) analysis. Since the height of the investigated structure is 85.1 m, the damping ratio of 2.5% was considered for the linear and nonlinear time history analyses. It should be noted that 2.3% of damping ratio was applied as modal damping and 0.2% of that was assumed as Rayleigh damping.

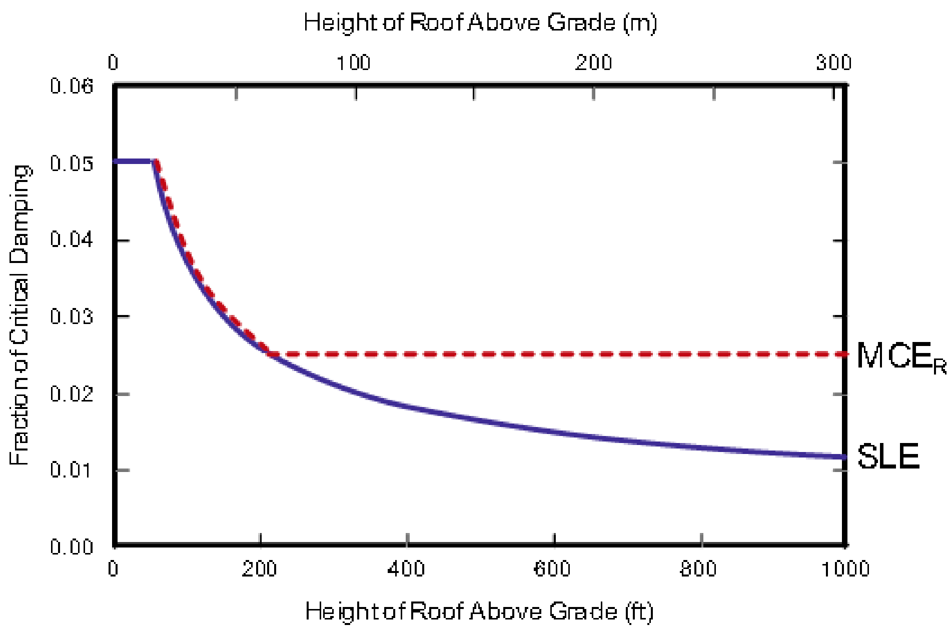

Figure 6.9 – Equivalent viscous damping versus building height (ATC-72-1, 2010)

To investigate the sloped column irregularity in high-rise concrete buildings, more than hundred linear and nonlinear dynamic analyses were performed in the current study. Each analysis case was designated with the type of SFRS (shear wall, SW, or coupled wall, CW), the type of sloped column (symmetric, S, or asymmetric, A), the slope of the column with regard to the vertical in degree, D, the height of the column in number of stories, S, and the location of the column base from the ground in number of stories. Thus, SW-A-17D-16S-8, for example, indicates the case with SFRS in the shear wall direction and asymmetric sloped column with the slope of 17 degrees extended over 16 stories starting from the 8th story to the 24th story. All analyzed cases are listed in Appendix F.

6.2.5 Seismic Hazard

In Southwestern BC, three distinctive sources of earthquakes are active: crustal events which occur along shallow faults; intraslab (subcrustal) events which occur deep within subducting tectonic plates; and interslab (subduction) events, which are caused by slip between subducting tectonic plates. All three sources impact the seismic hazard in Vancouver, depending on the fundamental period of structure and the distance of the site from the source.

The 5% damped Uniform Hazard Spectrum (UHS) with 2% chance of exceedance in 50 years hazard level, corresponding to the return period of 2475 years, for Site Class C (average shear wave velocity between 360 and 760 m/s) is shown in Figure 6.10. The UHS data points are given in the 2015 NBCC for Vancouver, Canada. This UHS was used as the target spectrum for selection and scaling of the ground motions.

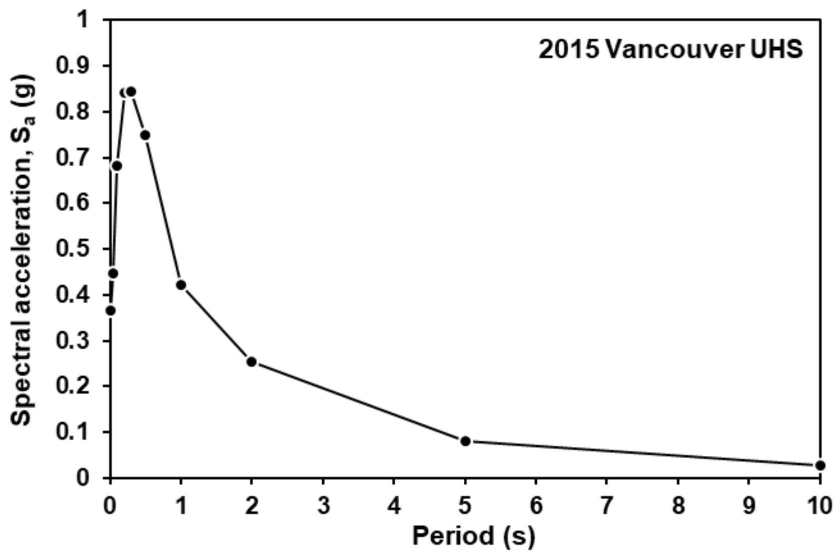

Figure 6.10 – Vancouver UHS for the return period of 2475 years (2% in 50 years)

6.2.5.1 Horizontal and Vertical Design Spectra

The horizontal design spectrum was obtained using the UHS and appropriate site coefficients recommended by National Building Code of Canada, NBCC 2015 (Clause 4.1.8.4). The 5% damped horizontal design spectrum is presented in Figure 6.11. For the vertical design spectrum, the standard engineering rule-of-thumb was used which assumes the ratio of vertical to horizontal spectral accelerations ($S_{a,v}/S_{a,h}$) is equal to $2/3$. Figure 6.11 also depicts the 5% damped vertical design spectrum. The design spectra were utilized in the response spectrum analysis of the building with sloped column, while the selecting and scaling of ground motions for time history analysis were performed using UHS.

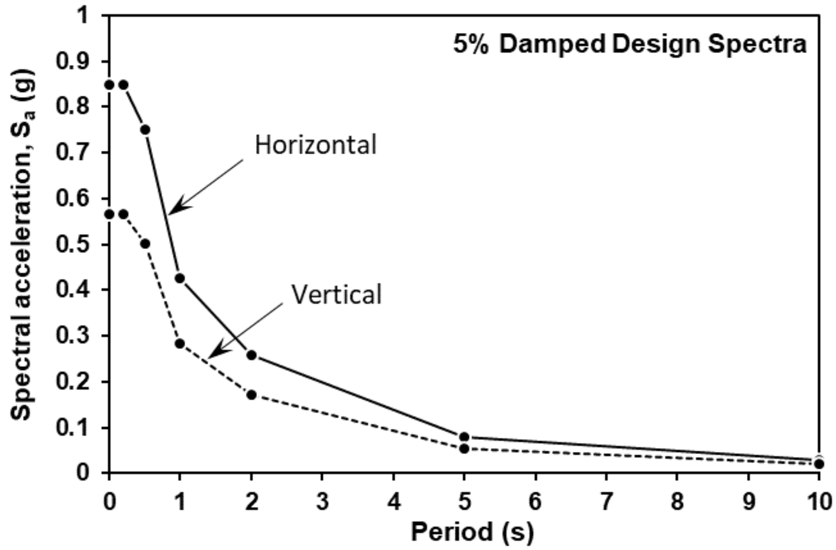

Figure 6.11 – Horizontal and vertical design spectra for site class C and the return period of 2475 years (2% in 50 years)

6.2.5.2 Selected and Scaled Ground Motions

LATBSDC (2017) recommends a minimum of 11 ground motions each containing two horizontal components to be considered for the time history analysis. For the vertical component of ground motions, the vertical component that accompanies pairs of selected horizontal motions should be used. The same scaling factor should be applied to both vertical and horizontal components.

For selecting and scaling the ground motions to the UHS, a period range of interest, T_R, should be selected. This period range includes the periods of the modes that considerably contribute to the dynamic response of the structure. According to NBCC 2015, the ground motions should be scaled in an appropriate manner over the interest period range, T_R, of $0.2T_1$ to $1.5T_1$, where T_1 is the fundamental lateral period of the structure. Figure 6.12 illustrates the period range for scaling of ground motions. The period range of $0 - 7.0$ s was used by Finn and Bebamzadeh (2017) for scaling of ground motions in order to cover potential shallow crustal and deep subcrustal ground motions effecting shorter periods.

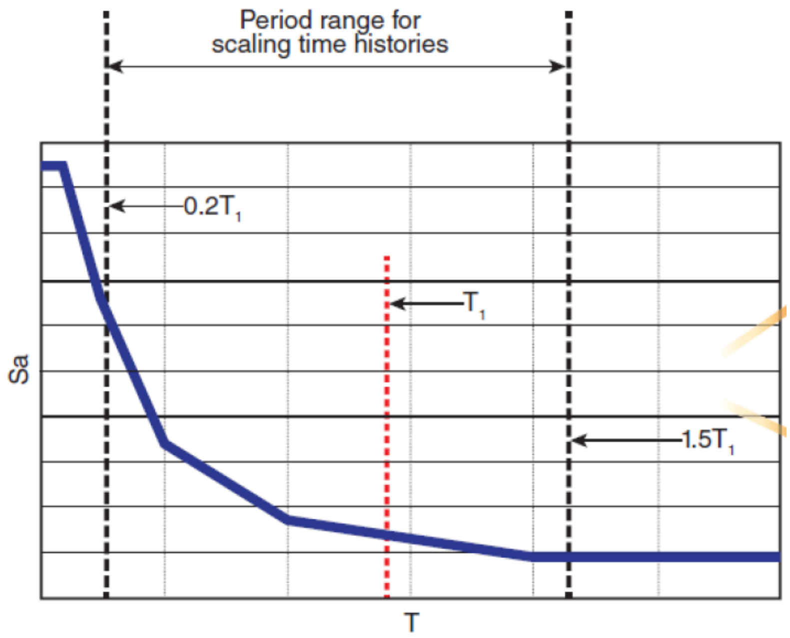

Figure 6.12 – Period range for scaling ground motion time histories (Commentary J NBCC 2015)

According to Commentary J NBCC 2015, there are two methods, Method A and B, for the selection of time histories for nonlinear dynamic analysis. Method A has been used by Finn and Bebamzadeh (2017). Based on Method A, ground motion records should be selected to cover appropriate portions of the interest period range, T_R, considering the tectonic regime and the dominant magnitude and distance which control the site condition and its seismic hazard. Each period portion forms a scenario-specific period range, T_{RS}.

For locations such as South-West British Columbia, where earthquakes from different sources (e.g., crustal, intraslab and interslab events) contribute to the hazard, a minimum of one scenario-specific period range, T_{RS}, should be determined for each source contributing to the hazard. It should be noted that the scenario-specific period ranges, T_{RS}, should cover the interest period range, T_R, although they may overlap each other. In addition, the mean of scaled ground motion records should not be smaller than 90% of the target spectrum. The scenario-specific period ranges selected by Finn and Bebamzadeh (2017) for Vancouver are listed in Table 6.2 and shown in Figure 6.13.

Table 6.2 – Selected scenario-specific period range, $\boldsymbol{T_{RS}}$

Source	Period Range, $\boldsymbol{T_{RS}}$ (s)
Crustal	0 – 0.8
Subcrustal	0 – 1.5
Subduction	0.9 – 7.0

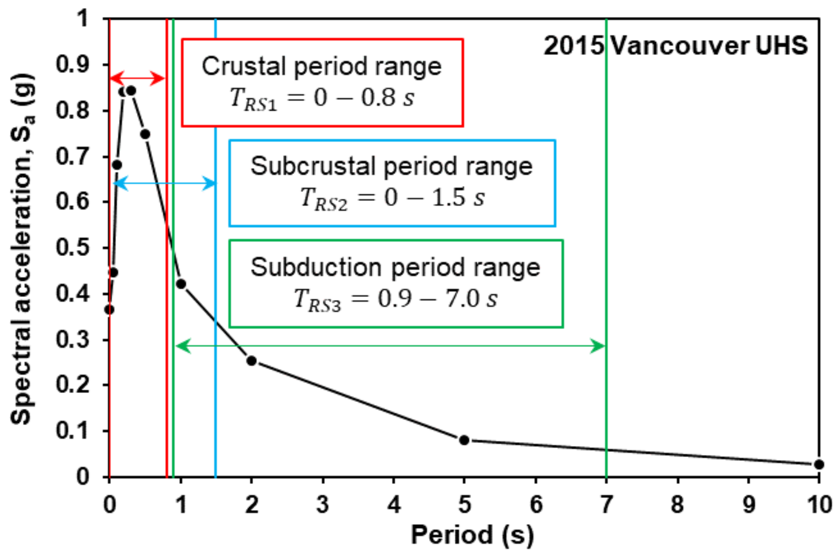

Figure 6.13 – Selected scenario-specific period ranges, T_{RS}

Finn and Bebamzadeh (2017) selected records from events that occurred in tectonic settings similar to those in Southwestern BC which are crustal, intraslab (subcrustal) and interslab (subduction) sources. Crustal records were taken from PEER database and subcrustal and subduction records were taken from S2GM database (Bebamzadeh, 2015; Bebamzadeh and Ventura, 2015). The total database consists of over 6000 crustal records, over 800 subcrustal records and over 1100 subduction records from over 130 unique events. Tables 6.3, 6.4 and 6.5 summarize the selected crustal, subcrustal and subduction records and associated parameters, respectively. The geometric mean of the horizontal acceleration components at each recording site were linearly scaled to match the target spectrum over the appropriate scenario-specific period range, T_{RS}. The Mean Squared Error (MSE; PEER, 2010) was computed between each scaled geomean and the target spectrum over the scenario-specific period range.

Table 6.3 – Vancouver crustal record summary

Record Number	Event Name	Source	Scale Factor	Magnitude	Epicentral Distance (km)	Vs30 (m/s)
1	Kern County	Crustal	2.23	7.36	359	385.43
2	San Fernando	Crustal	1.38	6.61	375	450.28
3	Tabas_ Iran	Crustal	1.11	7.35	401	471.53
4	Imperial Valley-06	Crustal	1.84	6.53	207	471.53
5	Corinth_ Greece	Crustal	1.54	6.6	271	361.4
6	Loma Prieta	Crustal	1.45	6.93	148	488.77
7	Loma Prieta	Crustal	0.61	6.93	222	594.83
8	Loma Prieta	Crustal	1.10	6.93	184	380.89
9	Landers	Crustal	2.40	7.28	184	359
10	Chi-Chi_ Taiwan	Crustal	1.08	7.62	330	520.37
11	Chi-Chi_ Taiwan	Crustal	0.99	7.62	334	614.98

Table 6.4 – Vancouver subcrustal record summary

Record Number	Event Name	Source	Scale Factor	Magnitude	Epicentral Distance (km)	Vs30 (m/s)
1	Nisqually_1437	Subcrustal	3.34	6.8	28.4	312
2	Nisqually_1416	Subcrustal	2.33	6.8	53.4	327.66
3	Geiyo_EHM005	Subcrustal	3.06	6.4	41.02	501.42
4	Geiyo_YMG018	Subcrustal	1.62	6.4	40	499.35
5	Nisqually_1421	Subcrustal	2.76	6.8	45.3	347.17
6	Nisqually_0725a	Subcrustal	3.29	6.8	20.3	416
7	Nisqually_5121	Subcrustal	3.25	6.8	15.6	312.42
8	Geiyo_EHM015	Subcrustal	1.19	6.4	60.61	417.15
9	Olympia_OLY0	Subcrustal	1.70	7.1	39	------
10	El_Salvador_VS	Subcrustal	1.23	7.6	96.6	------
11	PugetSound_OLY0	Subcrustal	2.51	6.7	89	------

Table 6.5 – Vancouver subduction record summary

Record Number	Event Name	Source	Scale Factor	Magnitude	Epicentral Distance (km)	Vs30 (m/s)
1	Tohoku_AOM008	Subduction	3.87	9	359	458
2	Tohoku_CHB013	Subduction	2.29	9	375	374
3	Tohoku_TKY006	Subduction	2.52	9	401	411
4	Tohoku_MYG005	Subduction	1.16	9	207	427
5	Tohoku_IWT022	Subduction	3.59	9	271	758
6	Hokkaido_HKD107	Subduction	2.40	8	148	565
7	Hokkaido_HKD127	Subduction	2.70	8	222	603
8	Hokkaido_HKD104	Subduction	2.51	8	184	384
9	Hokkaido_HKD105	Subduction	1.34	8	184	568
10	Maule_stgolaflorida	Subduction	2.31	8.8	330	685
11	Maule_STL	Subduction	1.40	8.8	334	------

Eleven records with the lowest MSE were selected for each scenario-specific period range (sources). It should be noted that the mean of the selected 11 records should not be smaller than 90% of UHS at any period within the scenario-specific period range, T_{RS}. Figures 6.14, 6.15 and 6.16 present the geomean of horizontal spectral values for the scaled crustal, subcrustal and subduction records, respectively, in addition to the Vancouver UHS.

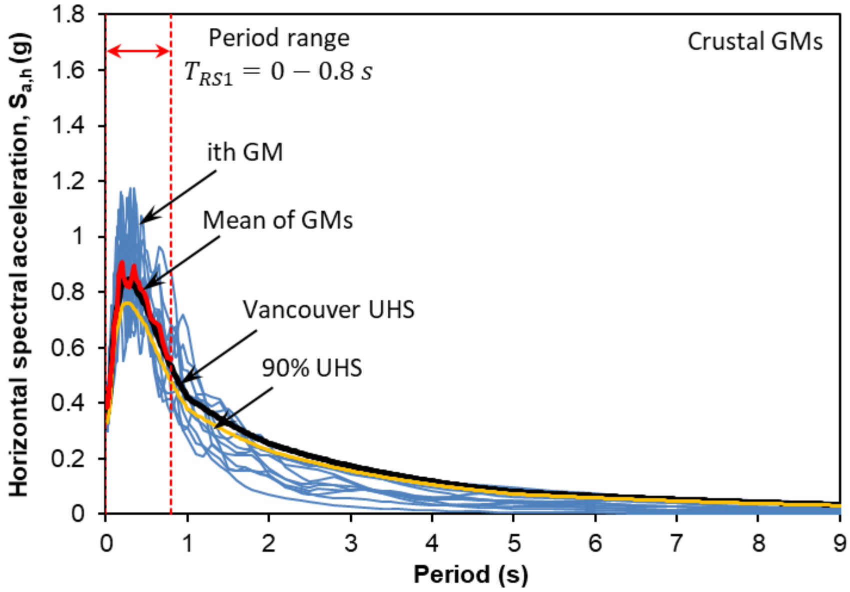

Figure 6.14 – Horizontal Spectra of selected crustal ground motion records

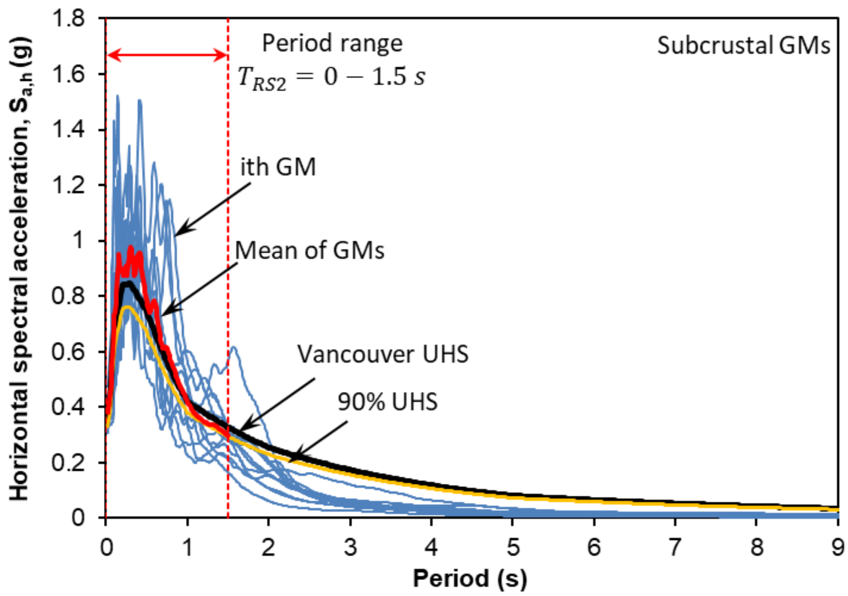

Figure 6.15 – Horizontal Spectra of selected subcrustal ground motion records

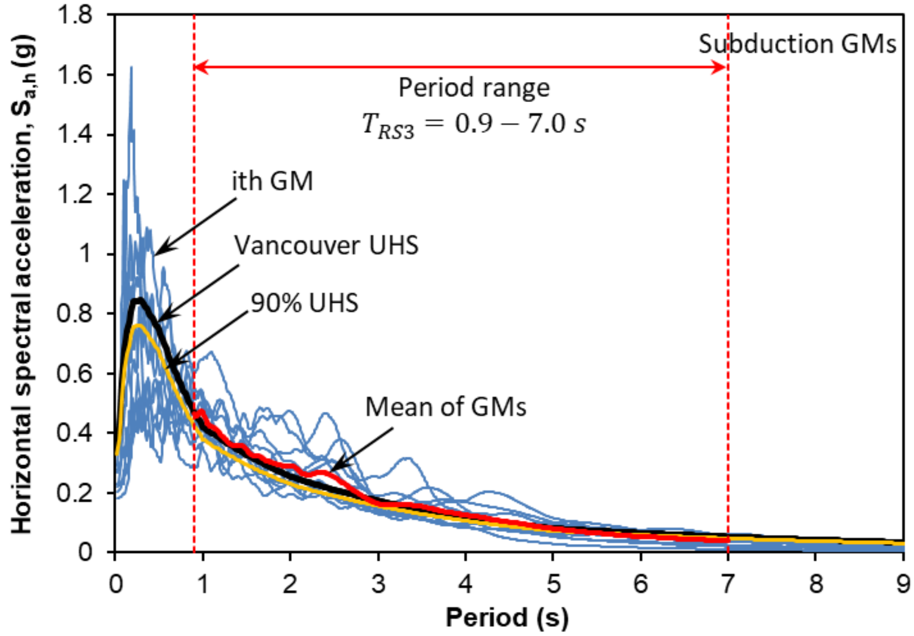

Figure 6.16 – Horizontal Spectra of selected subduction ground motion records

Figures 6.17, 6.18 and 6.19 show the vertical spectral values for the scaled crustal, subcrustal and subduction records, respectively, as well as 2/3 of the Vancouver UHS. It should be noted that the vertical component of ground motion records was scaled by the same factor as associated horizontal components.

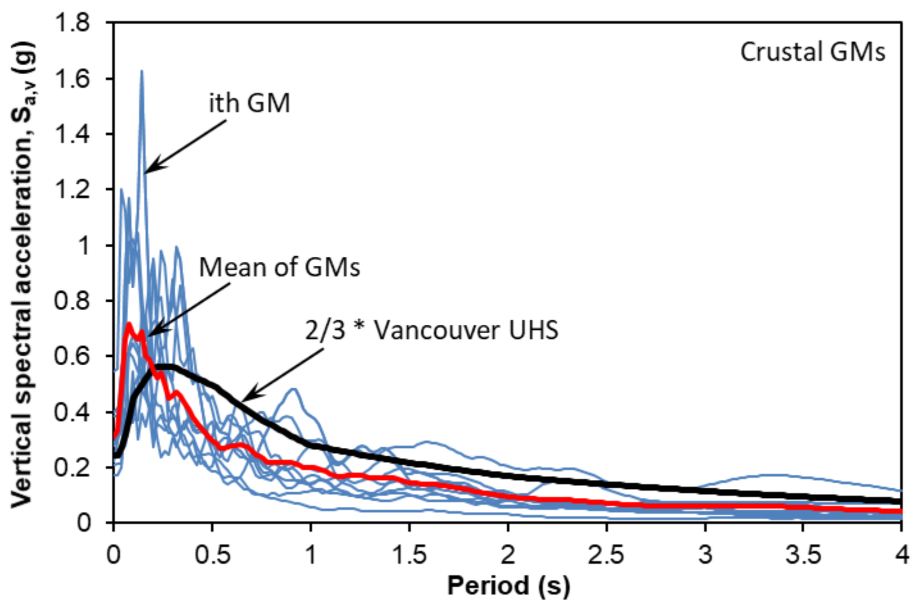

Figure 6.17 – Vertical Spectra of selected crustal ground motion records

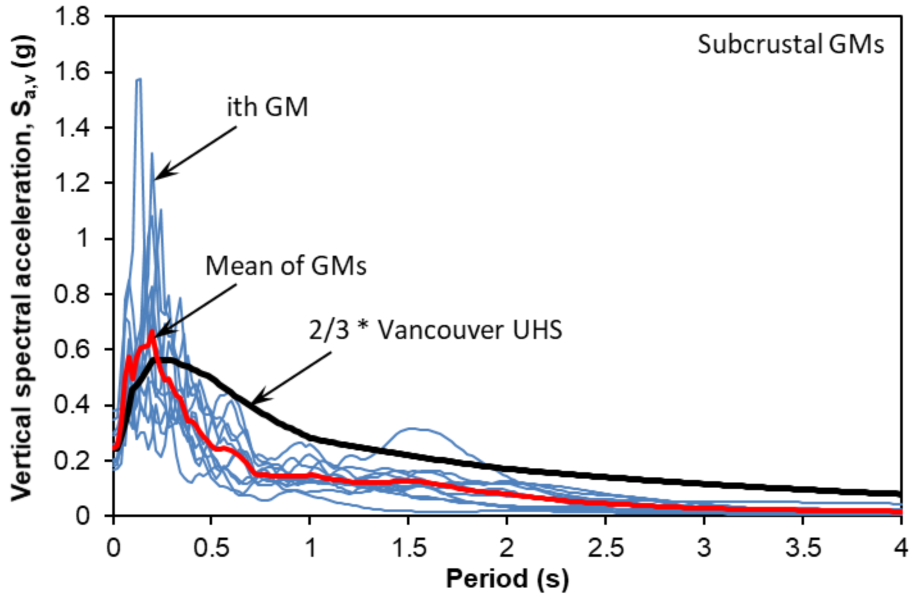

Figure 6.18 – Vertical Spectra of selected subcrustal ground motion records

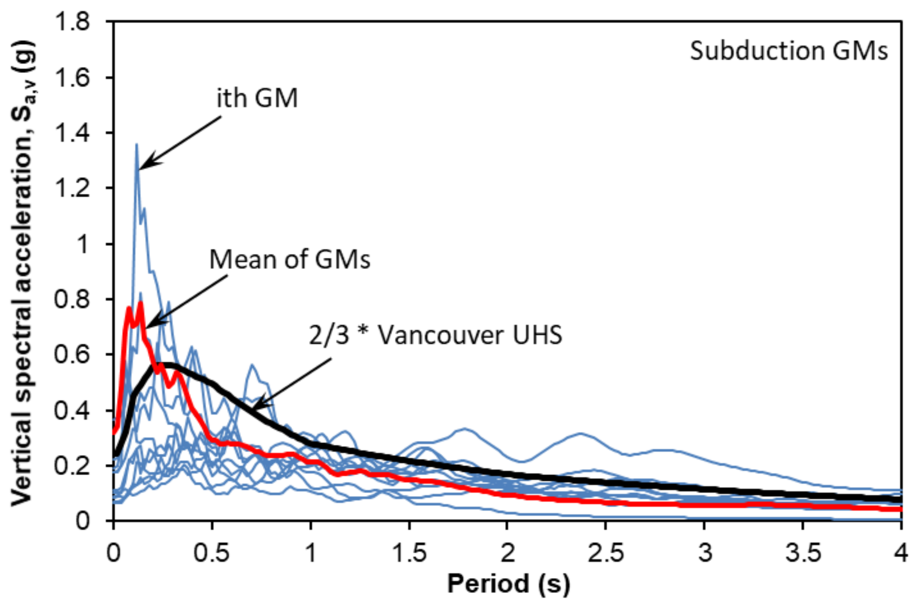

Figure 6.19 – Vertical Spectra of selected subduction ground motion records

6.3 Modelling Vertical Mass

The seismic mass should be calculated based on the seismic weight of the building, including the dead load and superimposed dead load. In two dimensional dynamic analyses of high-rise buildings, horizontal seismic mass can be modelled as a concentrated mass at each floor level, m_h, as shown in Figure 6.20. This is a reasonable assumption as slabs (above the base) are modelled as rigid diaphragms.

Modelling the vertical component of mass is a more challenging problem in seismic analysis of buildings due to the out-of-plane flexibility of slabs. Larger number of modes should be included in the dynamic analysis to capture the response of flexible slabs in the vertical direction, which makes the analysis more complicated. The aim of this part of the study was to investigate if it is possible to model the vertical seismic mass supported by the sloped column as concentrated (lumped) mass at each floor level above the column, m_v, as shown in Figure 6.20.

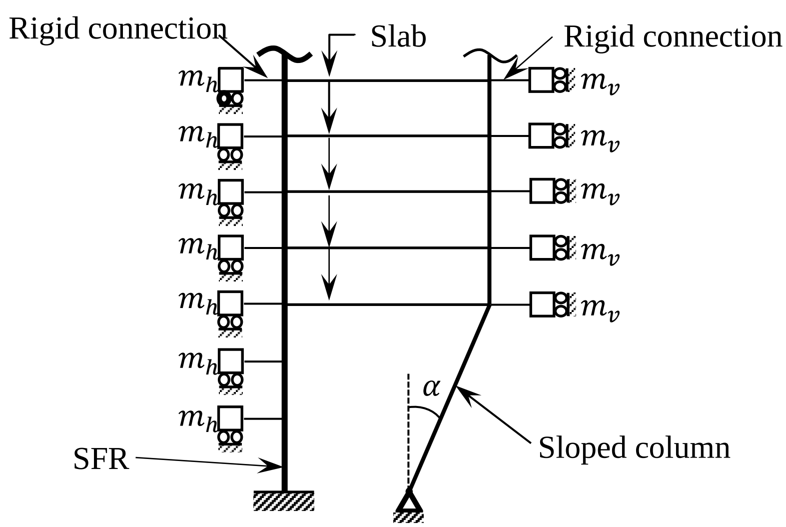

Figure 6.20 – Concentrated horizontal and vertical mass models

In order to evaluate the accuracy of this simplification, the response spectrum analysis of a slab supported on four columns with horizontally distributed vertical mass was performed using ETABS in the vertical direction (Figure 6.21(a)). The results of analysis were compared with those obtained form the analysis of a column with lumped mass on the top (Figure 6.21(b)). The magnitude of the concentrated mass was determined based on the tributary area of the column, which is equal to the seismic mass of the one quarter of the slab, as shown in Figure 6.21(a). The vertical design spectrum presented in Figure 6.11 was used for the response spectrum analysis, which was defined as 2/3 of the horizontal design spectrum.

Tables 6.6 and 6.7 summarize the modal periods and mass participation factors, for the first six modes of each model, respectively. There is only one mode for the concentrated mass model as it is a single-degree of freedom system while a larger number of modes should be included for the distributed mass model to capture more than 98% of horizontally distributed vertical mass participation. Twelve modes were considered for the analysis in this study. Table 6.8 compares the increase in the axial force of the column obtained from concentrated and distributed vertical mass models, which are 56.5% and 52.8%, respectively. There is a good agreement between the results. However, the small discrepancy occurred due to the difference in the modal period of the models.

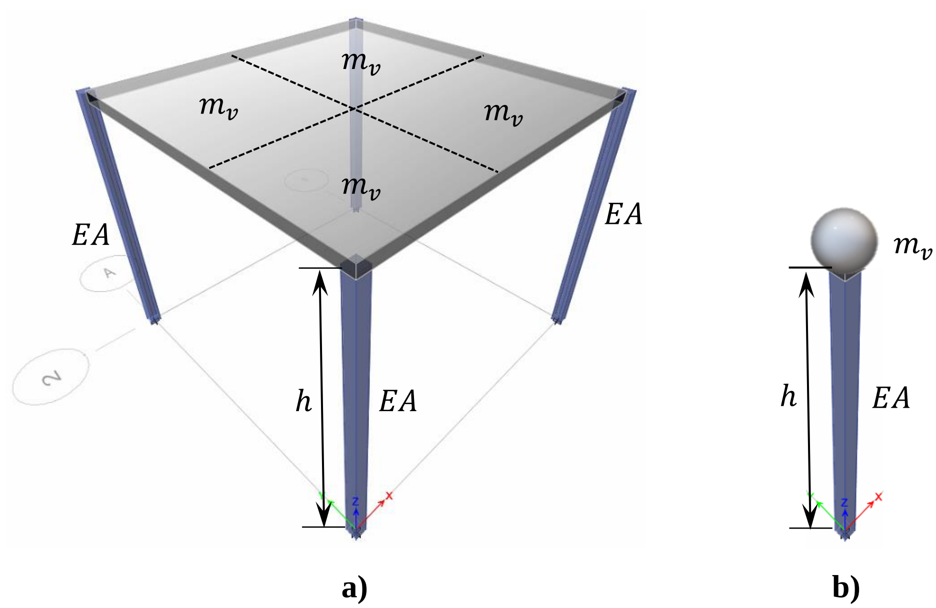

Figure 6.21 – Vertical mass models: (a) distributed; (b) concentrated

In addition, the number of stories was increased to twenty for the two vertical mass models. The same amount of distributed and concentrated vertical mass was assumed at each floor level. The axial force of the column at the first story from the two vertical mass models are compared in

Table 6.8. Although the column force obtained from the two models are identical, there is a significant reduction in the column force of the twenty-story system compared to the one-story system.

In fact, by increasing the number of stories, the total vertical mass increases and the system becomes more flexible which results in the increase of modal periods of the system as given in Table 6.6. It should be noted that the modal periods and mass participation factors obtained from two vertical mass models for the twenty-story system are close. According to the vertical design spectrum, the spectral acceleration values decrease by increasing the modal period. Consequently, the column axial force reduces. In a real structure, the primary vertical mode occurs in higher modes with modal period close to the plateau part of the spectrum (e.g., the maximum spectral acceleration value). Thus, a constant spectrum equal to the maximum of the vertical design spectral acceleration value (0.565g) was used for the response spectrum analysis and the results are presented in the Table 6.8 for comparison.

This study has indicated that there is a good agreement between the results of the distributed and concentrated vertical mass models. Hence, modelling the vertical mass supported by the sloped column as a concentrated (lumped) mass is a reasonable assumption that simplifies the modelling process and analysis.

Table 6.6 – Modal periods

No. of Story	**Vertical Mass Model**	**Period (s)**					
		1	**2**	**3**	**4**	**5**	**6**
1	Concentrated	0.201	-	-	-	-	-
	Distributed	0.342	0.130	0.129	0.092	0.080	0.074
20	Concentrated	2.096	0.699	0.420	0.301	0.236	0.194
	Distributed	2.113	0.751	0.502	0.409	0.364	0.339

Table 6.7 – Modal mass participation factors

No. of Story	Vertical Mass Model	Mass Participation Factor (%)					
		1	**2**	**3**	**4**	**5**	**6**
1	Concentrated	100	-	-	-	-	-
	Distributed	97.73	0	0	0	0	0.55
20	Concentrated	85.19	8.97	2.92	1.29	0.66	0.37
	Distributed	85.19	8.96	2.90	1.28	0.65	0.36

Table 6.8 – Column force increase from concentrated and distributed vertical mass models

No. of Story	Vertical Mass Model	Column Force Increase (%)	
		Vertical Design Spectrum	**Constant Spectrum**
1	Concentrated	56.5	56.5
	Distributed	52.8	55.2
20	Concentrated	14.9	48.5
	Distributed	14.9	48.5

6.4 Variation of Column Force over Height

To evaluate the variation of column force over the height of building (i.e., above and below sloped column), two different cases of sloped column were investigated using response spectrum analysis (RSA). The first case was a sloped column with an angle of 17 deg. starting at the 8th story and going up for 16 stories which is similar to Vancouver House building. Thus, there are eight columns below the sloped column and six columns above the sloped column. Response spectrum analysis was carried out for three different vertical to horizontal mass ratios of 0.02, 0.05 and 0.2 per floor (m_v/m_h). According to RSA results, column force below the sloped column is constant and equal to the vertical component of the axial force in the sloped column, while the column force above the sloped column increases by going up to the top of the building. Table 6.9 summarizes the column force over the height of the building. For this case, there is about 2% change in the column force above and below the sloped column.

Table 6.9 – Variation of column force above and below sloped column for the case of sloped column with slope of 17 deg. starting at 8th story and going up for 16 stories

Column Location		Increase in Column Force* (%)		
		$m_v/m_h = 0.02$	$m_v/m_h = 0.05$	$m_v/m_h = 0.2$
Above sloped column	Level 30	64.1	70.3	64.3
	Level 29	64.0	70.1	64.2
	Level 28	63.7	69.8	63.9
	Level 27	63.4	69.5	63.5
	Level 26	63.0	69.0	63.0
	Level 25	62.5	68.5	62.4
Sloped column	Level 8 to 24	61.8	67.8	61.8
Below sloped column	Level 1 to 8	61.8	67.8	61.8

* SW-A-17D-16S-8

The second analyzed case was a sloped column with the slope of 45 deg. starting at the 3rd floor and going up for 3 floors. For this case, the column force changes by about 25%, 25% and 20% above and below the sloped column for the mass ratios of 0.02, 0.05 and 0.2, respectively, as given in Table 6.10. In order to investigate the effect of building height on the variation of column force above the sloped column, the height of the building was increased from 30 to 50 stories. Table 6.11 lists the increase in the column force for the 50-story building. Similar to the 30-story building, the column force varies by about 25% over the building height for the mass ratios of 0.02 and 0.05.

Table 6.10 – Variation of column force above and below sloped column for the case of sloped column with slope of 45 deg. starting at 3rd story and going up for 3 stories in a 30-story building

Column Location		Increase in Column Force* (%)		
		$\boldsymbol{m_v/m_h = 0.02}$	$\boldsymbol{m_v/m_h = 0.05}$	$\boldsymbol{m_v/m_h = 0.2}$
Above sloped column	Level 30	101.9	97.9	82.2
	Level 25	99.5	95.0	79.4
	Level 20	94.4	89.8	75.6
	Level 15	88.3	83.9	71.1
	Level 10	82.0	77.4	66.1
	Level 7	78.0	73.3	62.8
Sloped column	Level 3 to 6	76.6	71.9	61.7
Below sloped column	Level 1 to 3	76.6	71.9	61.7

* SW-A-45D-3S-3 (30-story building)

Figures 6.22 and 6.23 summarize the analysis results. Figures 6.22(a) and (b) compare the variation of the column force and the percentage increase in the column force (defined as the ratio of the increase in the column force to the gravity load resisted by the column which can be determined from a simple static analysis), respectively, over the height of the 30-story building for the two cases of sloped column with slopes of 17 and 45 deg. starting at 8th story and 3rd story and going up for 16 stories and 3 stories (17D-16S-8 and 45D-3S-3). Figures 6.23(a) and (b) also compare the column force and the percentage increase in column force, respectively, for the case of sloped column (45D-3S-3) in 30-story and 50-story buildings. Presented analysis results are for the vertical to horizontal mass ratio of 0.05 per floor and the column stiffness of $1.0E_cA_g$.

According to Figures 6.22(a) and 6.23(a), the column force increases as the total vertical mass supported by the column increases. Thus, the maximum column force increase occurs at the level of sloped column. Although the percentage increase in the column force has the largest value at the uppermost level of the building (Figures 6.22(b) and 6.23(b)), the magnitude of the column force at this level is considerably smaller than that at the level of sloped column. Therefore, the focus of this study is on the maximum force increase in the sloped column.

Table 6.11 – Variation of column force above and below sloped column for the case of sloped column with slope of 45 deg. starting at 3rd story and going up for 3 stories in a 50-story building

Column Location		Increase in Column Force* (%)		
		$m_v/m_h = 0.02$	$m_v/m_h = 0.05$	$m_v/m_h = 0.2$
Above sloped column	Level 50	92.1	78.9	63.6
	Level 45	91.2	77.7	62.4
	Level 40	89.0	75.1	60.0
	Level 35	85.9	71.8	57.3
	Level 30	82.3	68.5	54.6
	Level 25	78.5	65.3	51.9
	Level 20	74.7	62.1	49.3
	Level 15	70.9	58.8	46.7
	Level 10	67.0	55.6	44.1
	Level 7	65.6	53.5	42.5
Sloped column	Level 3 to 6	64.8	52.8	41.9
Below sloped column	Level 1 to 3	64.8	52.8	41.9

* SW-A-45D-3S-3 (50-story building)

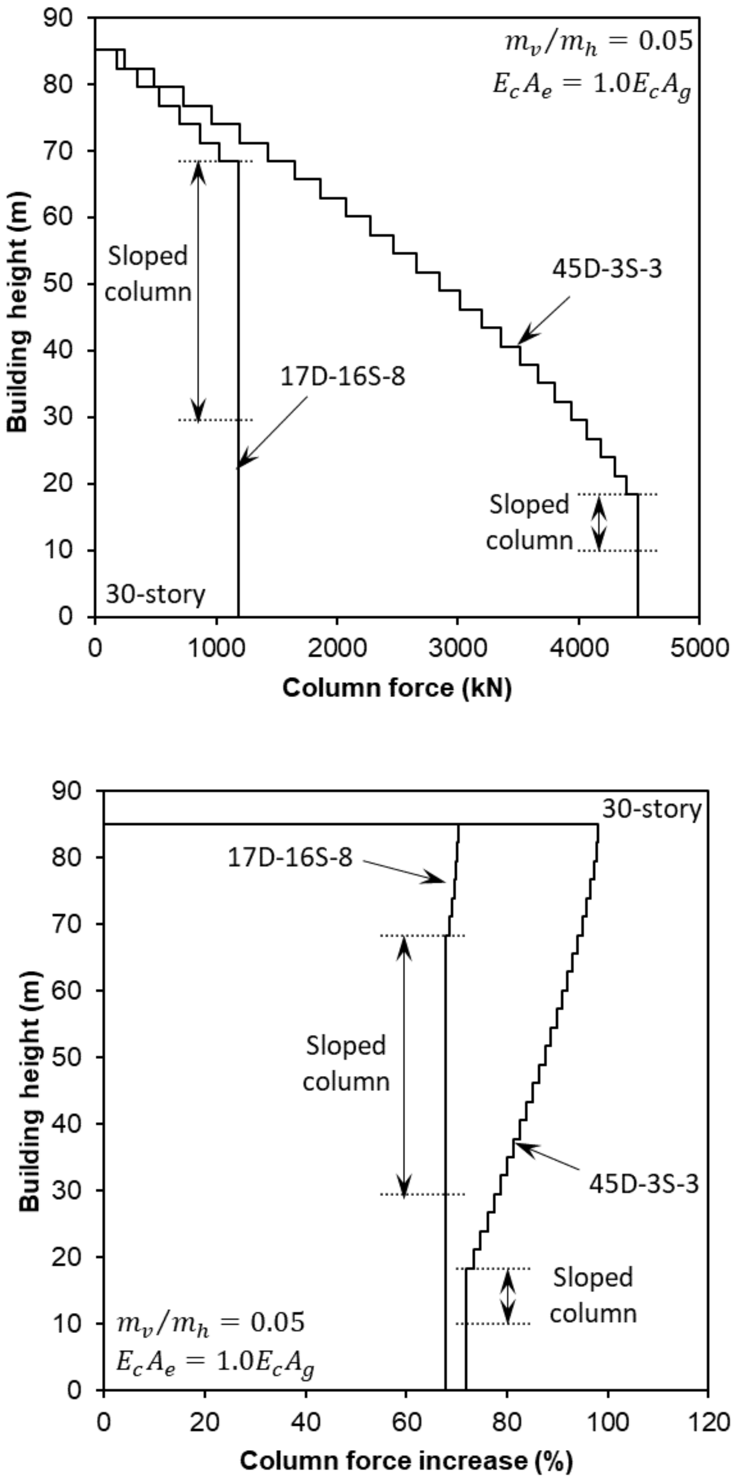

a)

b)

Figure 6.22 – Variation of column force over building height for asymmetric sloped columns of 17D-16S-8 and 45D-3S-3 in a 30-story building: (a) column force, and (b) percentage increase in column force

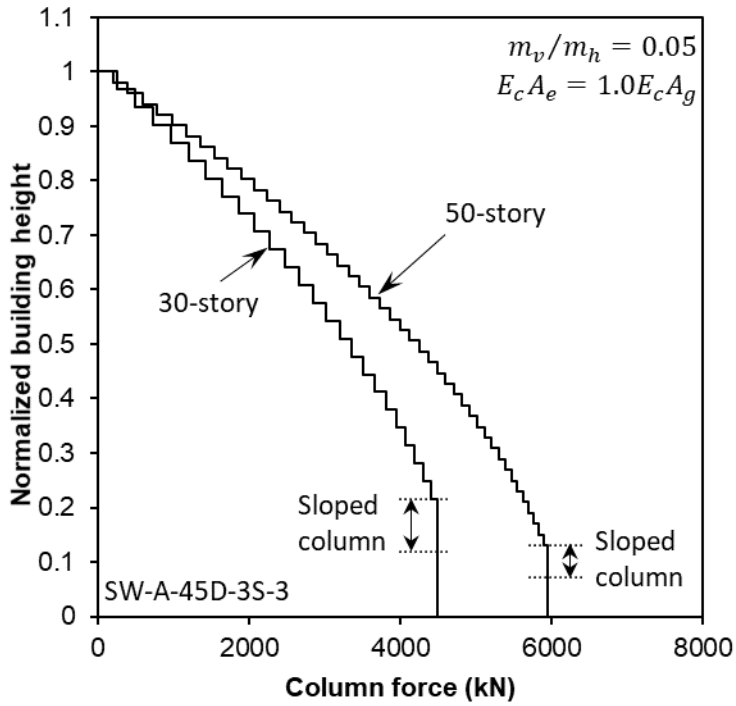

a)

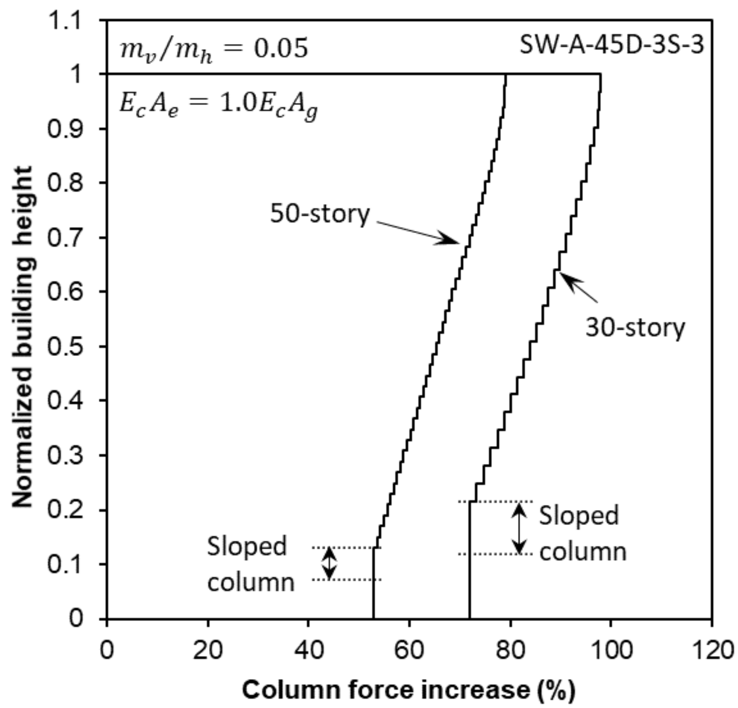

b)

Figure 6.23 – Variation of column force over building height for an asymmetric sloped column of 45D-3S-3 in 30-story and 50-story buildings: (a) column force, and (b) percentage increase in column force

6.5 Understanding Physics of Problem

6.5.1 Coupling of Modes

Figure 6.24 shows the influence of column stiffness on the axial force of the sloped column. In this case, the linear dynamic analysis was conducted in the shear (cantilever) wall direction of a 30-story building with asymmetric sloped columns with an angle of 3 deg. extended over 16 stories starting at grade (SW-A-3D-16S-0). The results are presented in terms of the percentage increase in the sloped column force relative to the gravity load resisted by the column. The analysis results indicated that the peaks in the column force occur when the first vertical mode is coupled with one of the lateral modes (e.g., 2nd mode, 3rd mode, 4th mode, …). In fact, when the degree of coupling of vertical and lateral modes increases, the force in the sloped column increases consequently. Thus, the column force is highly sensitive to the stiffness of the column. A small change in the column stiffness can result in either large increase or decrease in the column force. Table 6.12 gives the modal properties (period, horizontal and vertical mass contributions) for seven cases with varying column stiffness near the maximum peak in the column force.

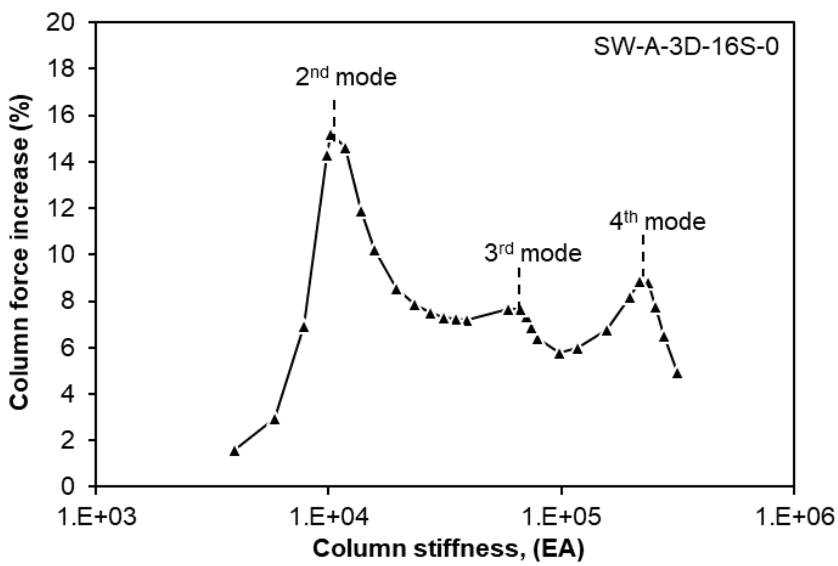

Figure 6.24 – Influence of column stiffness on column force for case of sloped column with slope of 3 deg. and height of 16 stories starting from ground (3D-16S-0); peaks of curve result from coupling of first vertical mode with lateral modes

Table 6.12 – Modal properties for seven cases with varying column stiffness

Column stiffness modifier	Increase in column force	Modal period (s)						Horizontal mass contribution (%)						Vertical mass contribution (%)					
EA	(%)	1	2	3	4	5	6	1	2	3	4	5	6	1	2	3	4	5	6
0.6	7.9	3.59	0.59	0.39	0.22	0.12	0.10	63	20	0	7	4	0	0	0	99	0	0	1
0.5	8.6	3.59	0.59	0.43	0.22	0.12	0.11	63	20	0	7	4	0	0	0	99	0	0	1
0.4	10.2	3.59	0.59	0.48	0.22	0.12	0.12	63	20	0	7	4	0	0	0	98	0	0	1
0.3	14.6	3.59	0.60	0.55	0.22	0.14	0.12	63	19	1	7	0	4	0	3	96	0	1	0
0.26	15.2	3.59	0.60	0.59	0.22	0.15	0.12	63	9	11	7	0	4	0	50	49	0	1	0
0.2	6.9	3.59	0.68	0.59	0.22	0.17	0.12	63	0	20	7	0	4	0	98	1	0	1	0
0.1	1.6	3.59	0.96	0.59	0.24	0.22	0.13	63	0	20	0	7	0	0	99	0	1	0	0

SW-A-3D-16S-0

Table 6.12 indicates that when the degree of coupling of vertical and lateral modes considerably increases, the additional column force increases significantly. The maximum increase in the sloped column force occurs when the second lateral mode is fully coupled with the first vertical mode.

Figure 6.25 shows the schematic view of coupling of the second lateral mode with the first vertical mode for the case of an asymmetric sloped column with the slope of 17 deg. starting at grade and going up for 16 floors in the shear wall direction (SW-A-17D-16S-0). Figures 6.25(a), (b) and (c) depict the upward movement of vertical mass, undeformed shape of the system and the downward movement of vertical mass, respectively.

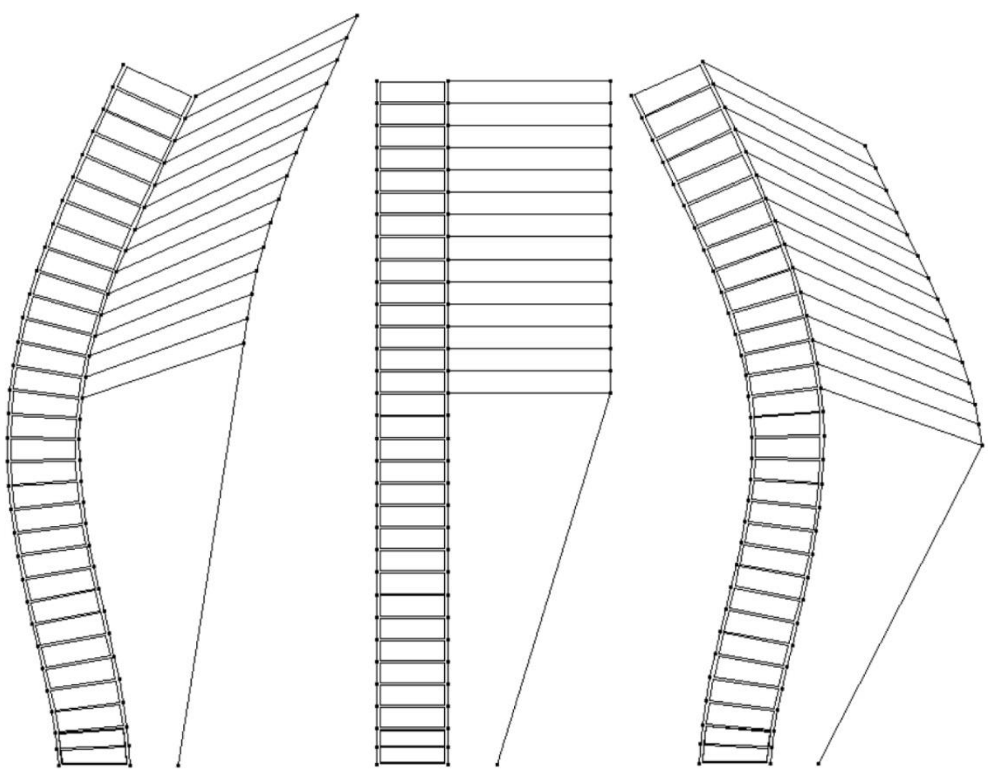

a) **b)** **c)**

Figure 6.25 – Coupling of the second lateral mode with the first vertical mode for a 30-story building with asymmetrical sloped columns: (a) upward movement of vertical mass; (b) undeformed shape of structure; (c) downward movement of vertical mass

There are different modal combination rules used for response spectrum analysis to determine the peak value of the total response. Figure 6.31 compares two popular rules: the square-root-of-sum-of-squares (SRSS) rule and the complete quadratic combination (CQC) rule. As is well-known, the SRSS rule provides good estimates for systems with well-separated natural frequencies. The CQC rule overcomes the limitation of the SRSS rule and is applicable to a wider class of structures even with closely-spaced frequencies. Figure 6.30 clearly illustrates the limitation of the SRSS rule. As the degree of coupling increases, the modes are closely-spaced and the SRSS rule is misleading. By decreasing the degree of coupling, the modes are well-separated and the SRSS and CQC modal combination rules yield the same results.

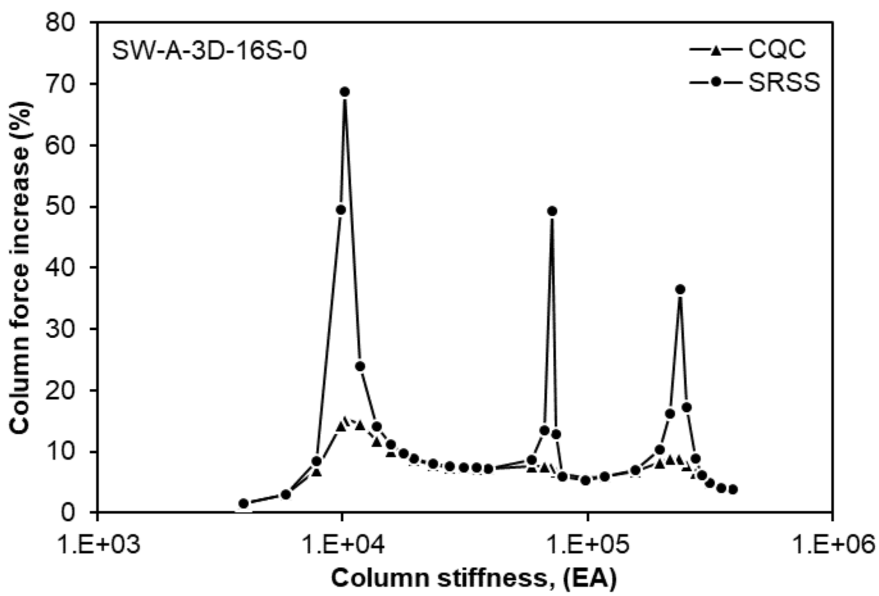

Figure 6.26 – Comparison of CQC and SRSS modal combination methods

6.5.2 Differential Vertical and Horizontal Accelerations

The differential horizontal acceleration at the top and bottom of the sloped column results in vertical acceleration of the mass supported by the column. Additional vertical accelerations occur due to the dynamic properties of the sloped column in the vertical direction. Figures 6.27 and 6.28 compare the normalized column force with normalized differential vertical and horizontal accelerations, respectively. As illustrated in Figure 6.27, the column force is directly related to the differential vertical acceleration at the top and bottom of the sloped column. There is a small discrepancy between the normalized column force and the normalized differential horizontal acceleration (Figure 6.28). If the columns are modelled as rigid members, there is a direct relationship between the differential vertical and horizontal accelerations that only depends on the slope of the column.

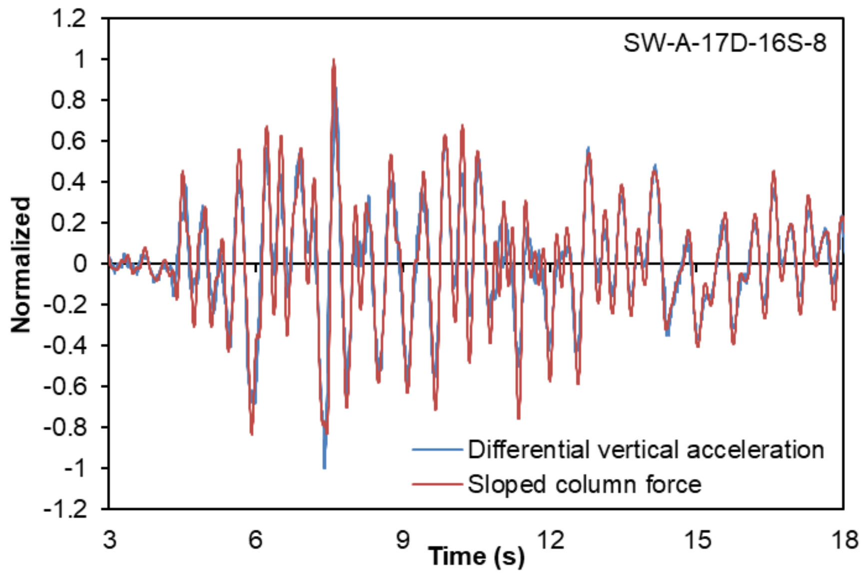

Figure 6.27 – Comparison of normalized differential vertical acceleration and normalized column force

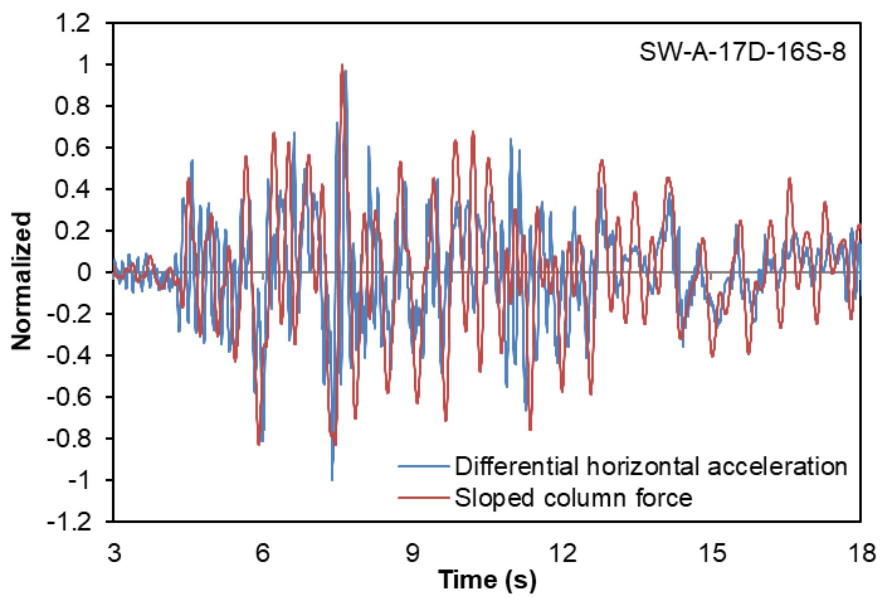

Figure 6.28 – Comparison of normalized differential horizontal acceleration and normalized column force

6.6 Parametric Study Using Response Spectrum Analysis

A parametric study was conducted using response spectrum analysis (RSA) to evaluate the effect of different characteristics of a sloped column and the ratio of the vertical mass supported by the sloped columns to the total horizontal mass on the column force.

6.6.1 Horizontal versus Horizontal and Vertical Accelerations

To evaluate the effect of vertical accelerations on the sloped column force, the system with sloped column was analyzed with horizontal excitation and horizontal plus vertical excitations. Figure 6.29 presents the analysis results for the case of sloped column with angle of 17 deg. starting from 8th story and going up for 16 stories. The vertical acceleration considerably increases the column force. The influence of vertical acceleration is more significant when the degree of coupling is low. In the other words, by increasing the degree of coupling of lateral and vertical modes (where peak column force occurs), the effect of vertical acceleration reduces. This can be attributed to the fact that the effect of horizontal acceleration significantly increases by increasing the degree of coupling of modes.

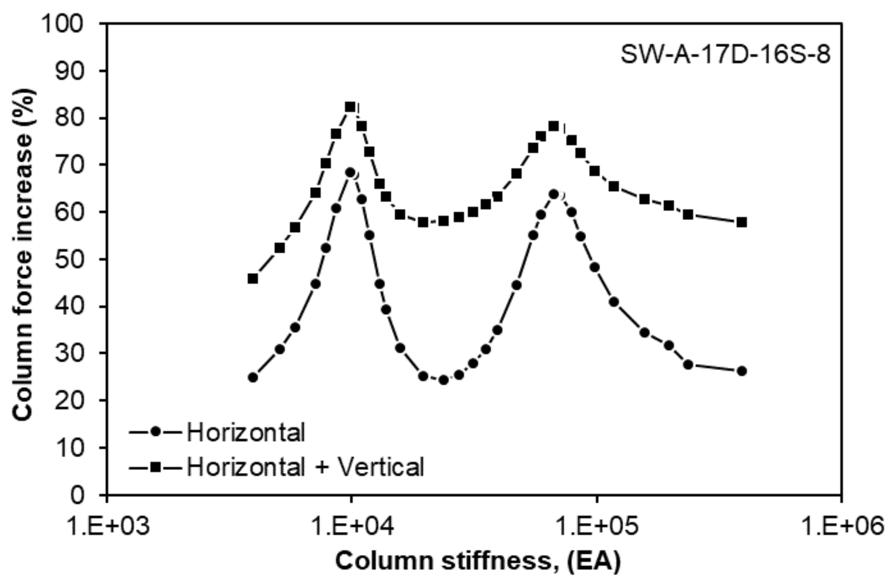

Figure 6.29 – Increase in column force for the case of sloped column with slope of 17 deg. and height of 16 stories starting from 8th story (17D-16S-8) subjected to horizontal excitation and horizontal plus vertical excitations

6.6.2 Effect of Column Slope on Maximum Column Force

The influence of column slope on the sloped column force is illustrated in Figure 6.30 for the cases of sloped columns with varying slopes between 0 to 20 deg. starting at 8th story and going up for 16 stories subjected to horizontal and horizontal plus vertical excitations. Due to horizontal acceleration, the column force relatively linearly increases as the slope of the column from vertical becomes larger (i.e., the sloped column becomes less steep). Including vertical acceleration results in considerable increase in the column force especially for steeper (closer to vertical) sloped columns since the influence of vertical accelerations are more dominant due to additional vertical accelerations. However, the increase in the column force is more gradual compared to the case without vertical ground motion.

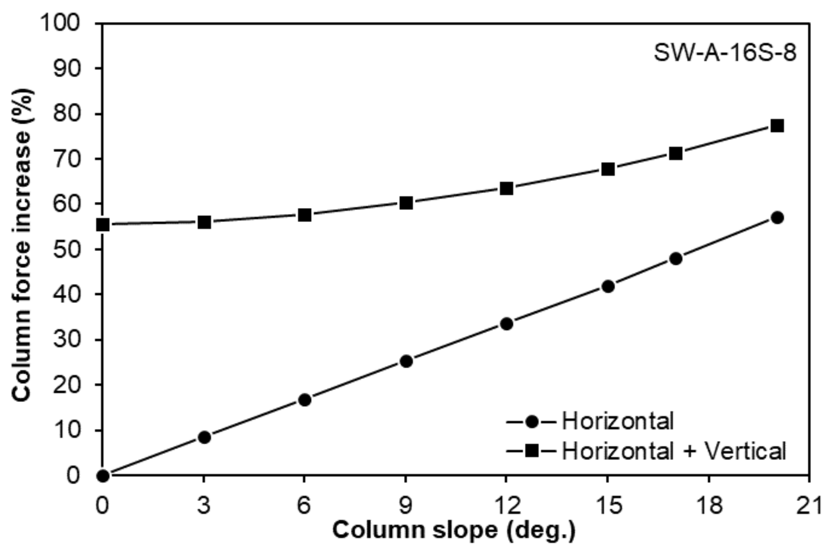

Figure 6.30 – Influence of column slope (varying from 0 to 20 deg.) on column force

Figure 6.31 depicts the column force versus the column stiffness for three different column slopes of 3, 12 and 20 degrees. As shown in Figure 6.31, the increase in the column force is highly sensitive to the axial stiffness of sloped columns. The peaks in the column force increase take place at about the same column stiffness for columns with different slopes.

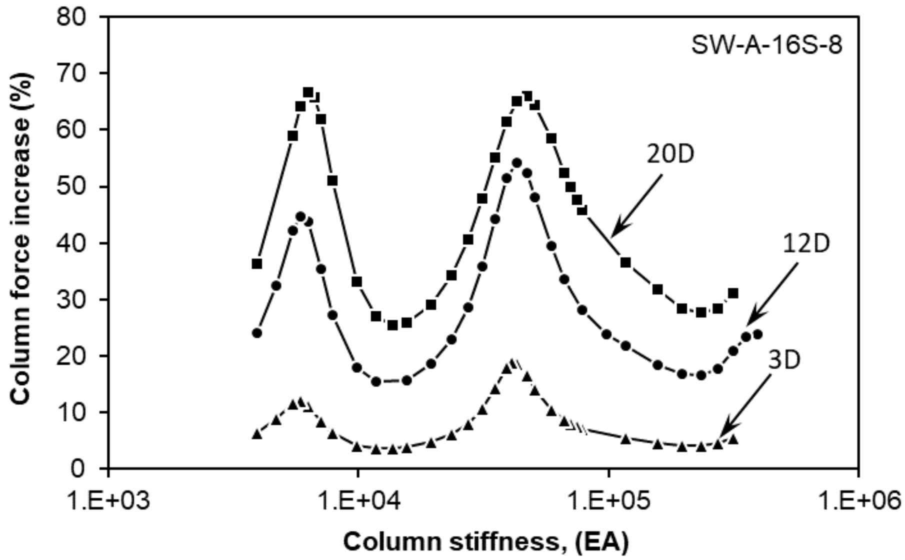

Figure 6.31 – Increase in sloped column force versus column stiffness for asymmetric sloped column extended over 16 stories starting from the 8th story with three different column slopes of 3, 12 and 20 deg.

6.6.3 Effect of Column Height on Maximum Column Force

The height of sloped column considerably affects the maximum column force. Figure 6.32 shows the column force versus column stiffness for the case of sloped column with slope of 3 deg. and two different column heights of 4 and 16 stories starting at grade. As the column height increase from 4 stories to 16 stories, the column force significantly increases.

Analysis results indicated that the maximum column force occurs due to the coupling of the first vertical mode with the second and forth lateral modes for the column heights of 16 and 4 stories, respectively. In fact, changing the height of sloped column results in the change of the seismic properties of the system in the vertical direction (e.g., the stiffness of the column and the total vertical mass supported by the sloped column) which shifts the coupled mode.

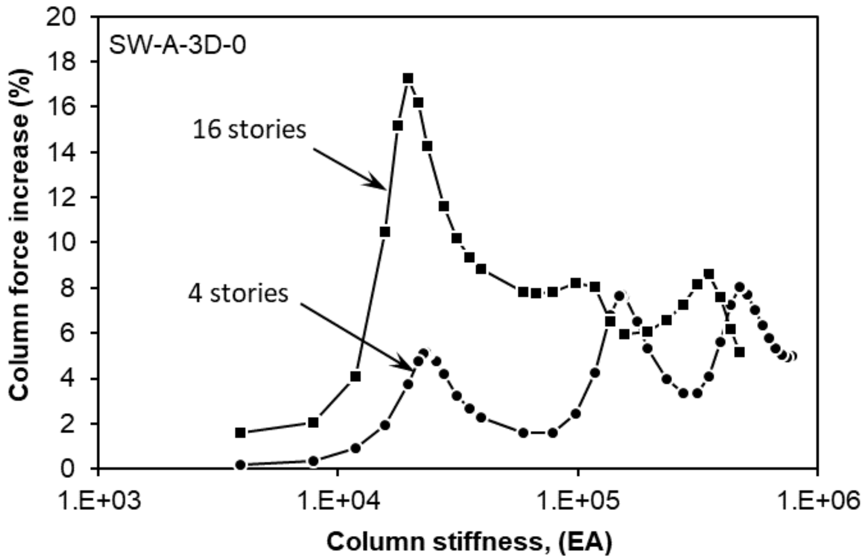

Figure 6.32 – Increase in sloped column force versus column stiffness for two different column heights of 4 and 16 stories

6.6.4 Effect of Column Base Location on Maximum Column Force

The other investigated characteristic of sloped column is the location of the sloped column base. Figure 6.33 depicts the column force versus column stiffness for two sloped columns with a slope of 20 deg. extending over 16 stories and starting at grade and at 8th story. When the base of the sloped column is moved up from the grade to higher levels, the peaks of the column force curve changes accordingly.

For example, maximum increase in the column force occurs due to the coupling of the first vertical mode with the second lateral mode when the base of the sloped column is located at the grade. Moving up the base from the grade to 8th story results in two similar peaks in the curve which occur due to the coupling of the first vertical mode with the second and third lateral modes. This considerable change happens as the total vertical mass supported by the sloped column changes. In fact, the change in the dynamic properties of the vertical system is responsible for the change in the column force curve.

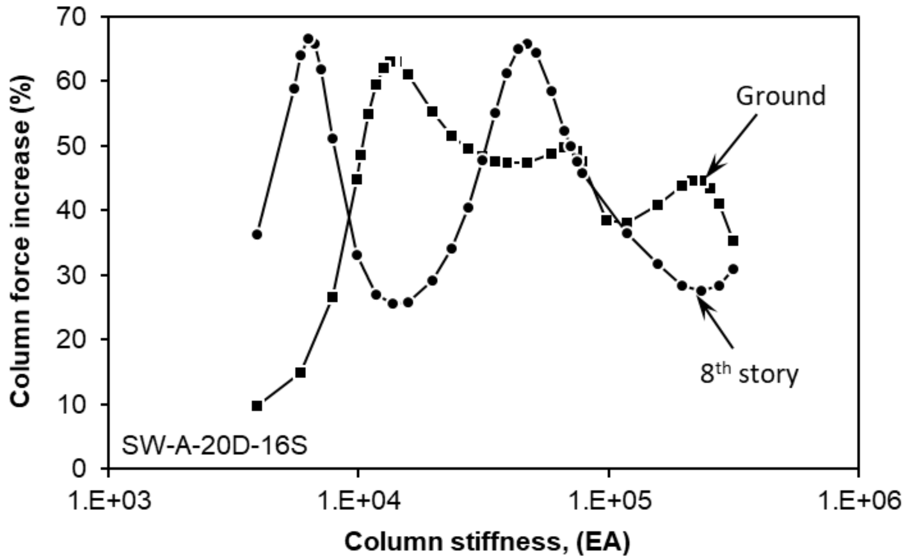

Figure 6.33 – Increase in sloped column force versus column stiffness for the sloped column 20D-16S with two different column base locations: at grade and at 8^{th} story

6.6.5 Effect of Vertical Mass on Maximum Column Force

The amount of the vertical mass supported by the sloped column also influences the maximum column force increase. The percentage increase in the column force versus the column stiffness is shown in Figure 6.34 for the case of an asymmetric sloped column with a slope of 9 deg. starting at grade and going up for 8 stories (9D-8S-0) in shear (cantilever) wall and coupled wall directions. The vertical to horizontal mass ratio per floor varies from 2 to 60%.

It was indicated that the maximum percentage increase in the column force increases as the mass ratio per floor (m_v/m_h) decreases for sloped columns in both shear wall and coupled wall directions. For instance, the maximum column force increase is about 30, 26 and 20% for the mass ratio of 2, 20 and 60%, respectively, for the sloped column in shear wall direction and similarly, it is about 28, 26 and 22% in the coupled wall direction. This can be attributed to the fact that the differential horizontal acceleration at top and bottom of the sloped column causes larger vertical acceleration in smaller vertical mass. Although the percentage increase in the column force (defined as the ratio of increase in the column force to the gravity load of the column) has the larger value for smaller mass ratio, the magnitude of the column force is smaller than that of the sloped column with larger vertical mass.

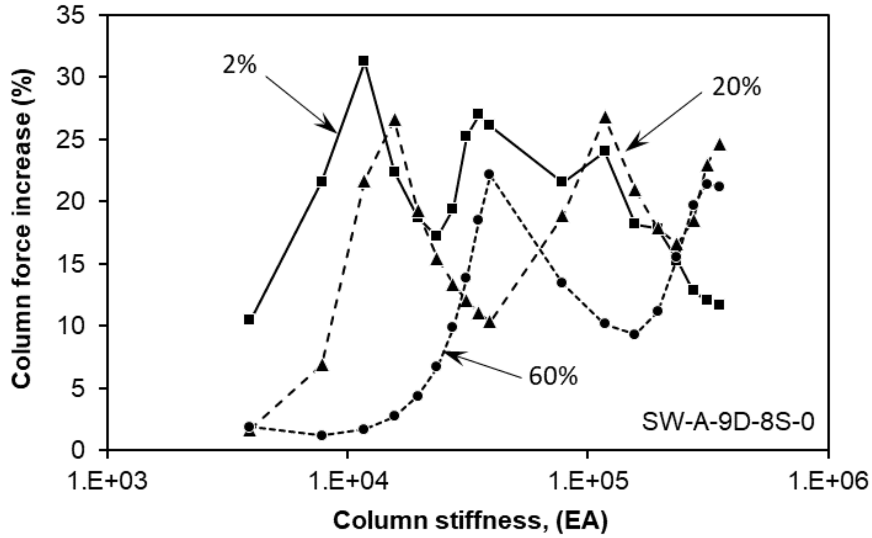

a)

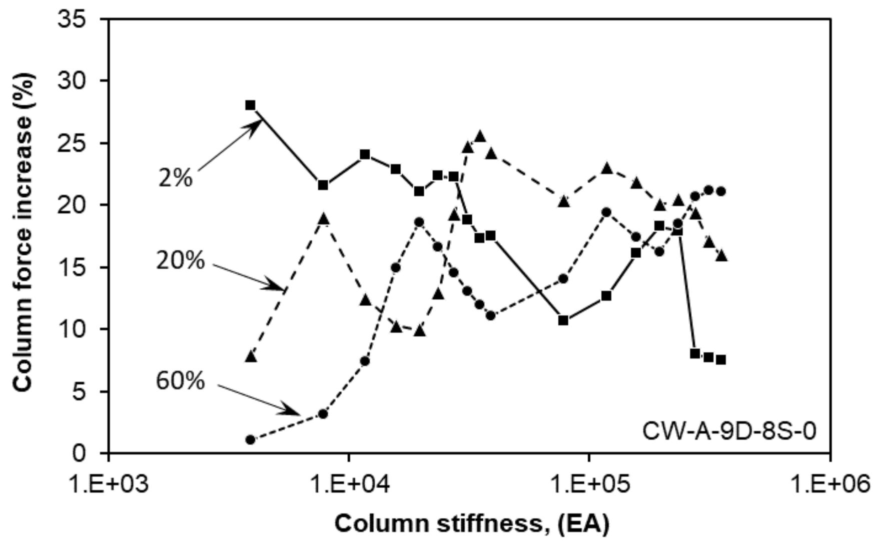

b)

Figure 6.34 – Increase in sloped column force versus column stiffness for the sloped column 9D-8S-0 with three different vertical to horizontal mass ratios of 2, 20 and 60% in: (a) shear wall direction; and (b) coupled wall direction

6.6.6 Effect of SFRS Stiffness on Maximum Column Force

The effect of the stiffness of the lateral system (SFRS) on the increase in the sloped column force was investigated. Figure 6.35 shows the increase in the column force versus column stiffness for the case of an asymmetric sloped column with a slope of 17 deg. starting at grade and going up for 16 stories. The 30-story building was analyzed in the shear (cantilever) wall direction. Upper-bound and lower bound stiffnesses of $1.0E_cI_g$ and $0.5E_cI_g$ were considered for the lateral system.

The shear wall flexural rigidity was reduced by 50% in order to represent the increase in flexibility of a shear wall due to flexural cracking.

The lateral systems with uncracked ($1.0E_cI_g$) and cracked ($0.5E_cI_g$) flexural rigidities are analogous to the systems behaving linearly and nonlinearly, respectively. As shown in Figure 6.35, the column force is sensitive to the stiffness of structural members. Depending on the axial stiffness of the sloped column, the analysis of the linear system results in a larger column force increase compared to that of the nonlinear system and vice versa. Therefore, an important point derived from Figure 6.35 is that it is not possible to estimate the additional column force for nonlinear system by analyzing the linear system and scaling the obtained column force similar to what is done for shear wall buildings without sloped-column irregularities. Thus, the possible range of stiffnesses for structural members should be considered to determine the maximum increase in the column force. This will be discussed in more detail in Section 6.7.

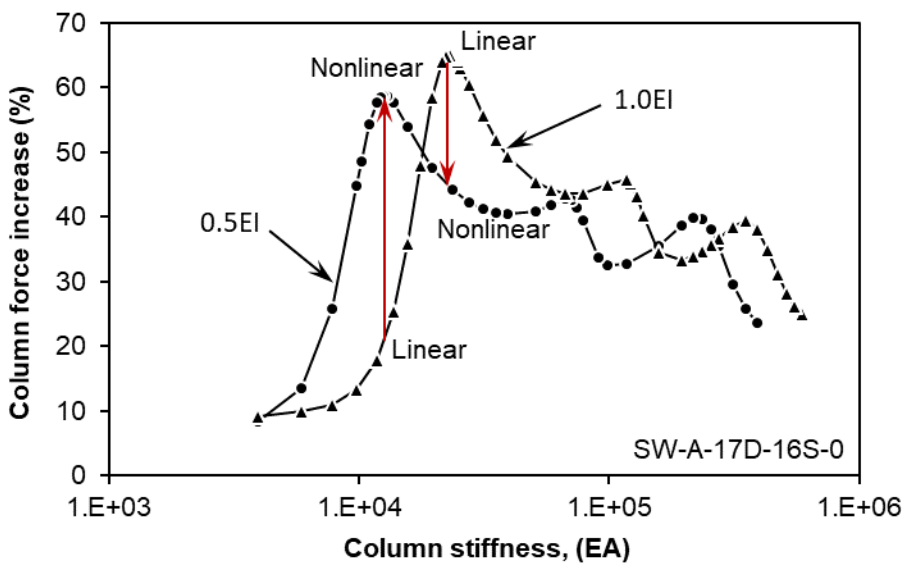

Figure 6.35 – Increase in sloped column force versus column stiffness for SFRS stiffness of $0.5E_cI_g$ and $1.0E_cI_g$

6.6.7 Shear Wall versus Coupled Wall SFRS

The increase in column force for sloped columns with different characteristics subjected to horizontal and horizontal plus vertical excitations in shear wall and coupled wall directions are compared in Figures 6.36 to 6.38. Figure 6.36 shows the increase in column force for three different sloped columns with angles of 3, 6 and 9 deg. starting at grade and going up for 16 stories. Figure 6.37 presents the additional force in the sloped columns with the angle of 3 deg. starting at grade and going up for 4, 8 and 16 stories. Increase in column force for three different sloped columns with the angle of 6 deg. starting at grade, at 4th story and at 8th story and going up for 16 stories are illustrated in Figure 6.38.

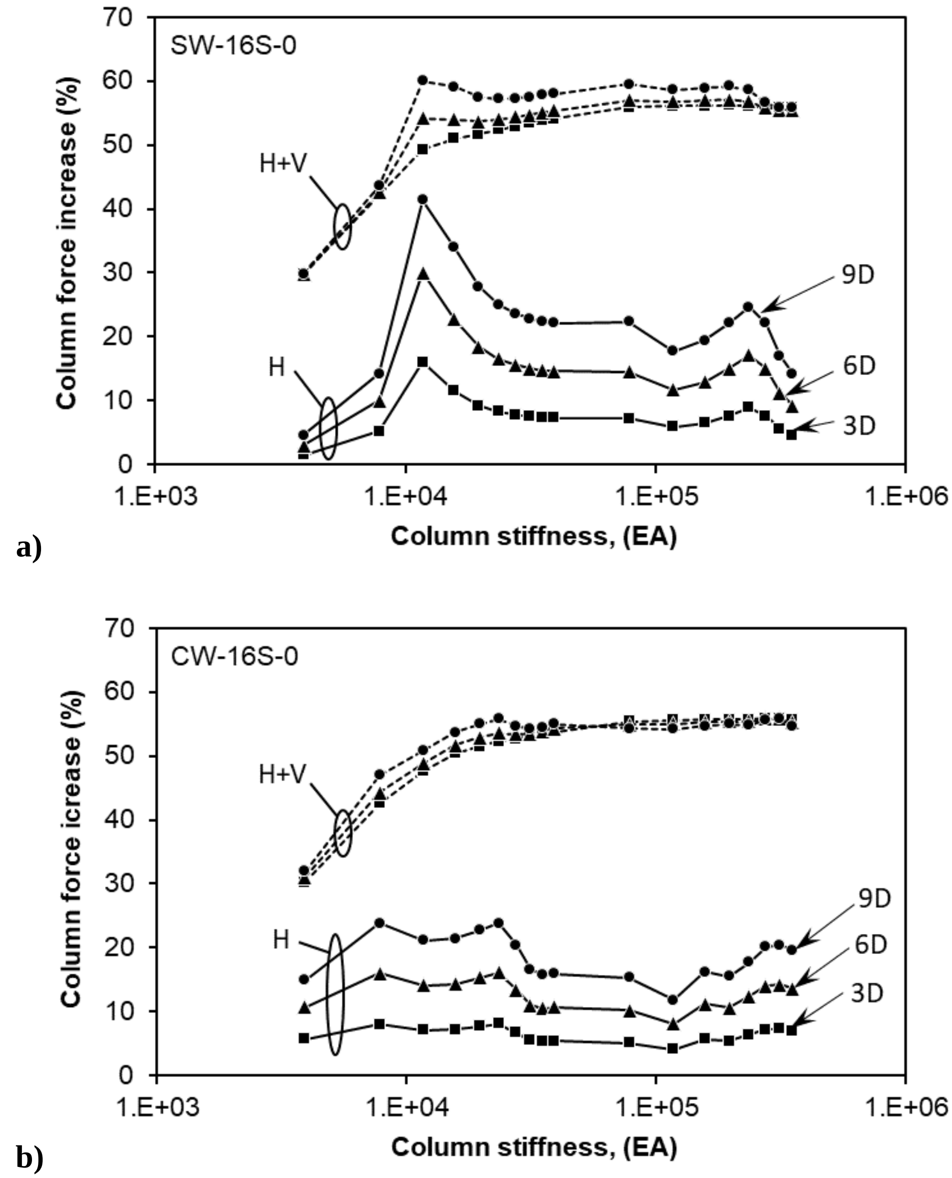

Figure 6.36 – Increase in sloped column force versus column stiffness for three different sloped columns with angles of 3, 6 and 9 deg. starting at grade and going up for 16 stories subjected to horizontal and horizontal plus vertical excitations in: (a) shear wall direction; and (b) coupled wall direction

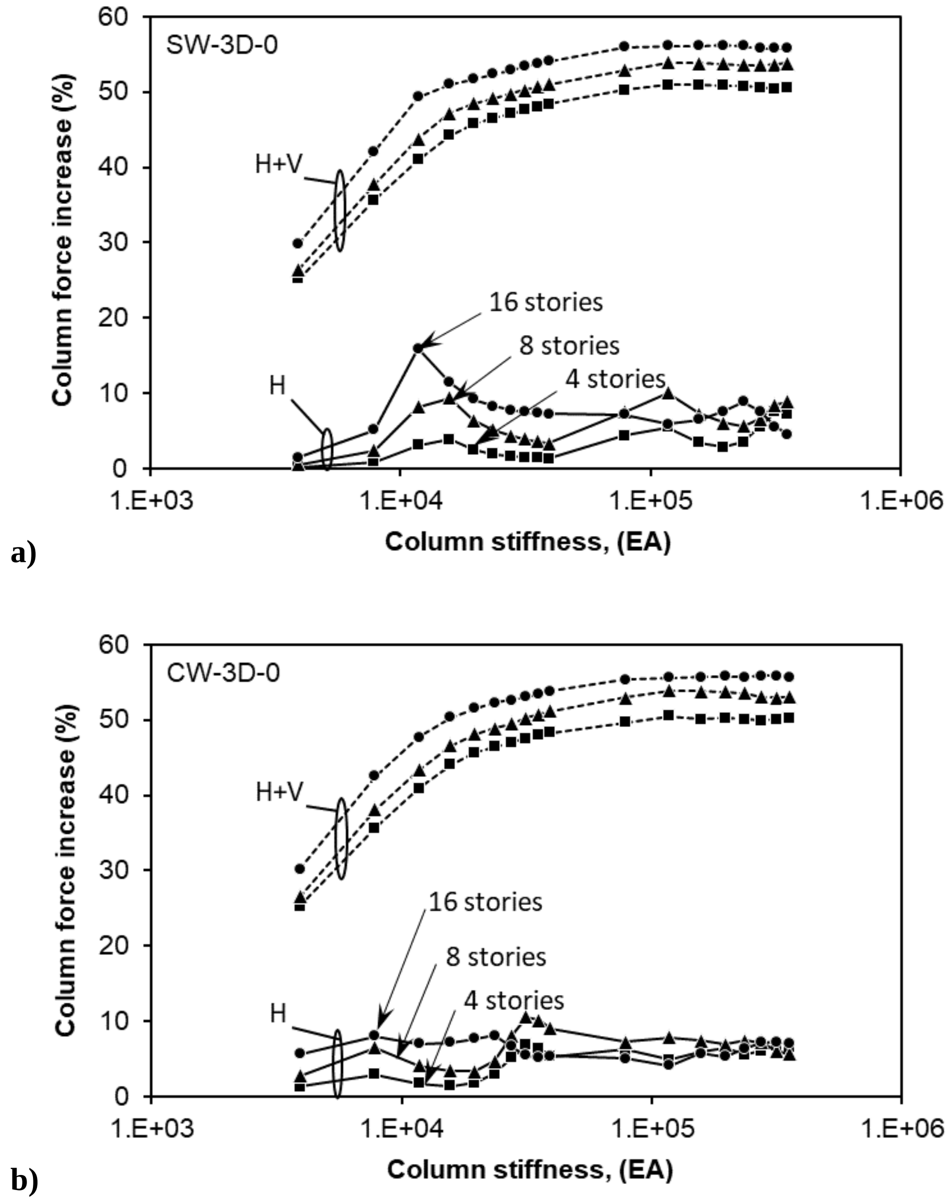

Figure 6.37 – Increase in sloped column force versus column stiffness for three different sloped columns with an angle of 3 deg. starting at grade and going up for 4, 8 and 16 stories subjected to horizontal and horizontal plus vertical excitations in: (a) shear wall direction; and (b) coupled wall direction

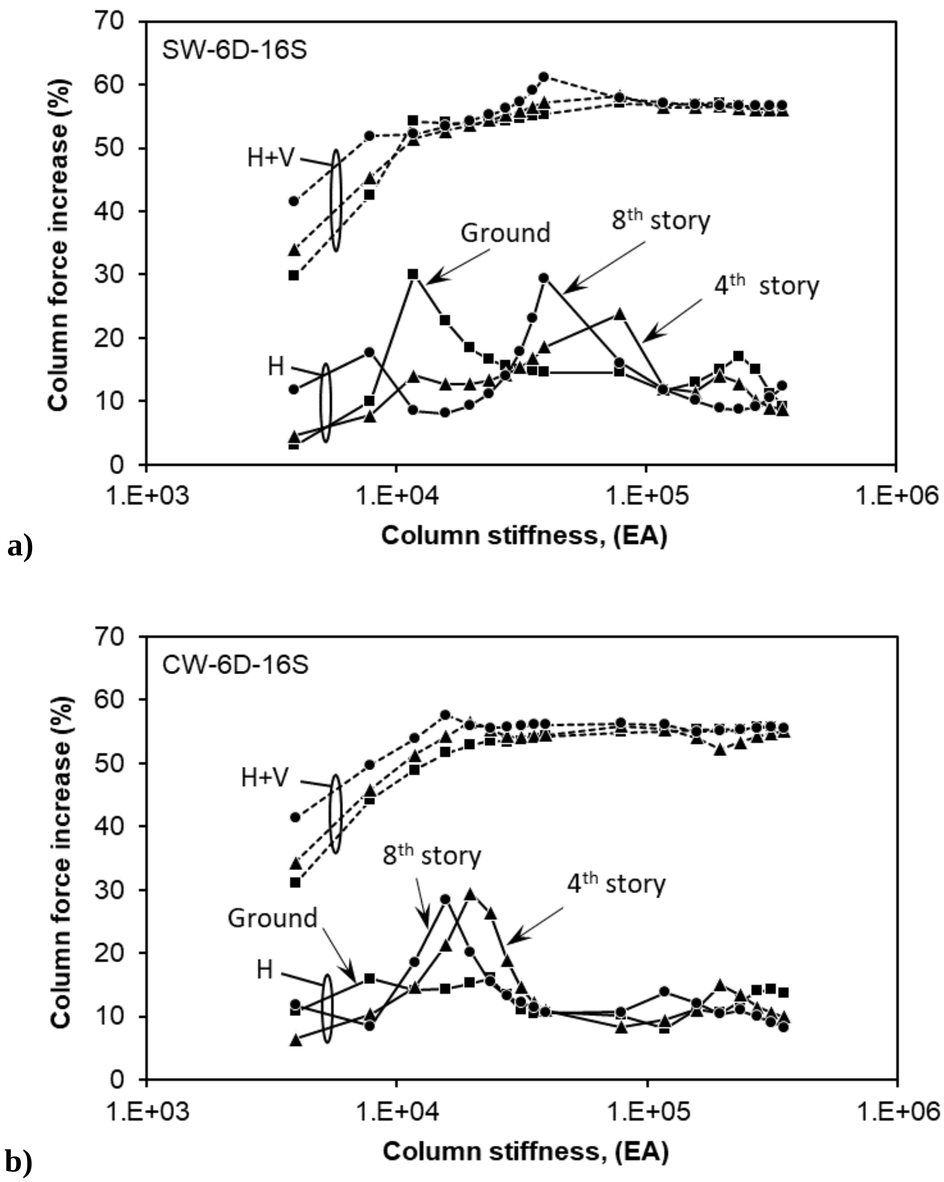

Figure 6.38 – Increase in sloped column force versus column stiffness for three different sloped columns with an angle of 6 deg. starting at grade, at 4th story and at 8th story and going up for 16 stories subjected to horizontal and horizontal plus vertical excitations in: (a) shear wall direction; and (b) coupled wall direction

For all analyzed cases, it was observed that the sloped columns in the shear wall direction are more critical due to the larger maximum column force. Thus, the time history analysis was mainly focused on sloped columns in the shear wall direction. However, some nonlinear time history analyses were performed with sloped columns in coupled wall direction for comparison.

6.6.8 Symmetric versus Asymmetric Sloped Columns

Figure 6.39 compares the increase in the column force versus column stiffness for symmetric and asymmetric sloped columns with different slopes of 3, 6 and 9 deg. starting at grade and going up for 16 stories in shear wall (Figure 6.39(a)) and coupled wall (Figure 6.39(b)) directions. The results from both horizontal and horizontal plus vertical excitations are shown in Figure 6.44.

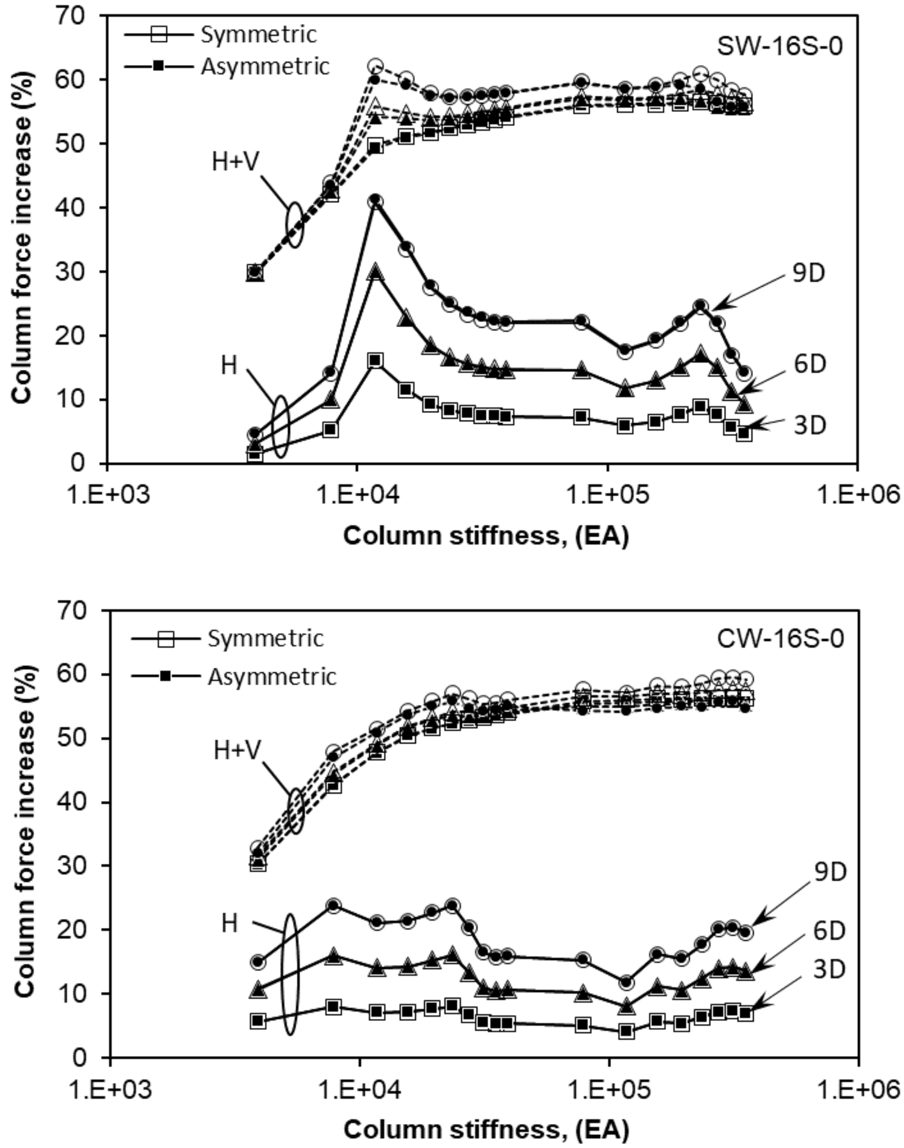

a)

b)

Figure 6.39 – Comparison of increase in column force for symmetric and asymmetric sloped columns with different slopes of 3, 6 and 9 deg. starting at grade and going up for 16 stories in: (a) shear wall direction; and (b) coupled wall direction

For the analysis, the total vertical mass supported by the symmetric sloped column (two opposing sloped columns connected together) was considered to be identical to that supported by the asymmetric sloped column (one sloped column in one direction). In addition, the total cross-sectional area of the symmetric sloped column was assumed to be equal to that of the asymmetric sloped column.

According to the analysis results, the percentage increase in the column force is identical for symmetric and asymmetric sloped columns with the same characteristics. This is the case for sloped column in both shear wall (Figure 6.39(a)) and coupled wall (Figure 6.39(b)) directions subjected to horizontal and horizontal plus vertical accelerations. Therefore, only asymmetric sloped column was used for the linear and nonlinear time history analyses.

6.7 Time History Analysis Results

Figure 6.40 compares the axial force in the column obtained from the response spectrum analysis (RSA) with those obtained from the linear time history analysis (LTHA) for an asymmetric sloped column with different slopes ranging from 0 to 20 deg. starting at the 8^{th} story and going up for 16 stories. Figure 6.40(a) shows the results for horizontal excitations while Figure 6.40(b) presents the results for horizontal plus vertical excitations. Response spectrum analysis is an approximate solution and is relatively equal to the mean of linear time history analysis for 11 selected and scaled ground motions. However, there was some differences between RSA results and the mean of LTHA results for analysis with horizontal and vertical excitations. This discrepancy can be attributed to the fact that the vertical components of ground motions were scaled with the same factor used for horizontal components of ground motions. This means that the vertical components were not scaled to the 2/3 of the horizontal design spectrum that was used for RSA with vertical excitations.

The results of nonlinear time history analysis (NLTHA) versus linear time history analysis (LTHA) for increase in the axial force of sloped column are plotted in Figure 6.41. Each point in Figure 6.41 represents the results for one ground motion. The analysis results are from the case of an asymmetric sloped column with the slope of 17 deg. extended over 16 stories starting from the 8^{th} story. The results are shown for three different combinations of horizontal and vertical mass per floor level. Nonlinear analysis has shown that the changes in the stiffness of the lateral system (e.g., shear wall) due to flexural cracking of concrete walls can cause the coupling of vertical and lateral modes to either increase or decrease dramatically. This results in significant changes in the column force. Therefore, the ratio of percentage increase in the column force obtained from linear and nonlinear models varies considerably. This means that the linear model can result in a larger column force increase compared to the nonlinear model as shown by black dots in the figure and sometimes the linear model can give lower increase in the column force (yellow dots shown in Figure 6.41).

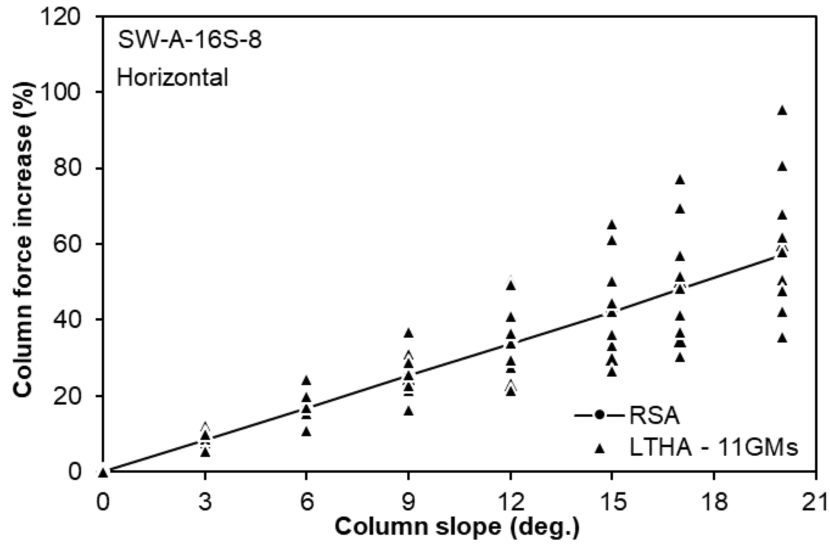

a)

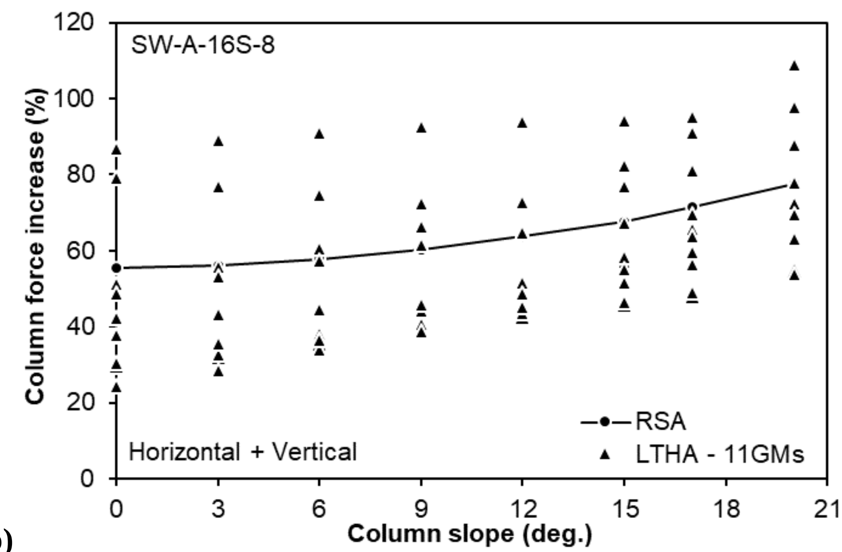

b)

Figure 6.40 – Comparison of axial force in column with different slope ranging from 0 to 20 deg. obtained from RSA and LTHA for: (a) horizontal excitations; (b) horizontal and vertical excitations

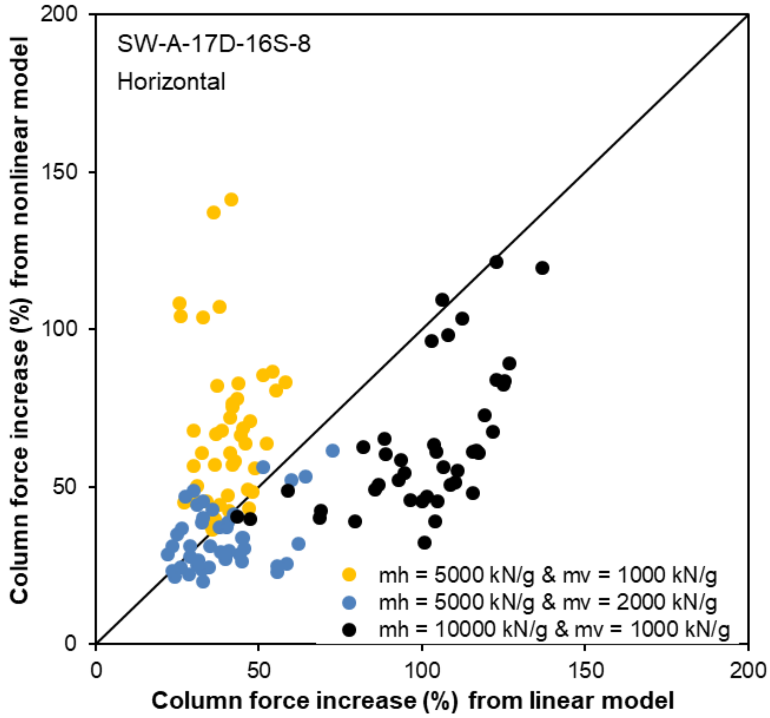

a)

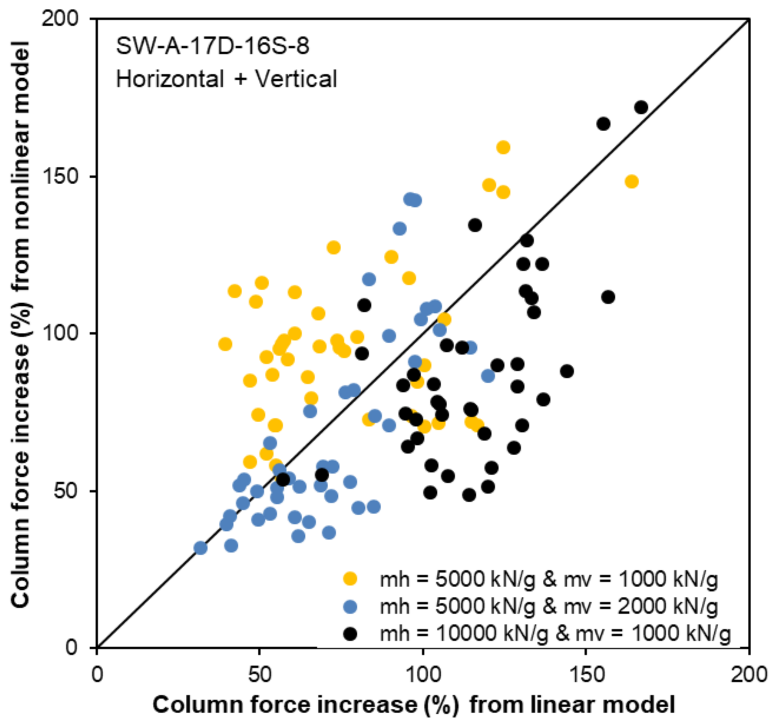

b)

Figure 6.41 – Comparison of axial force in the sloped column obtained from linear and nonlinear time history analyses for an asymmetric sloped column with the slope of 17 deg. Starting at story 8 and going up for 16 stories subjected to: (a) horizontal excitation; (b) horizontal + vertical excitations

To further investigate the effect of stiffness of structural members on the sloped column force, linear and nonlinear time history analyses were conducted for sloped column with various vertical to horizontal mass ratios per floor (m_v/m_h) ranging from 5 to 60%. Three ground motions were selected for the analyses. Figure 6.42 presents the percentage increase in the column force versus the mass ratio. By changing the mass ratio, the degree of coupling of vertical and lateral modes varies for linear and nonlinear analyses. In nonlinear analyses, the stiffness of shear wall changes due to cracking which has a significant influence on the coupling of vertical and lateral modes. As shown in Figure 6.42, for smaller mass ratios, the increase in column force obtained from nonlinear analyses is larger than those from linear analyses, while by increasing the mass ratio, column forces from nonlinear analyses considerably reduces and becomes smaller than those from linear analyses. Similar conclusion was made from Figure 6.35, which illustrates the effect of SFRS stiffness on the column force (obtained form RSA).

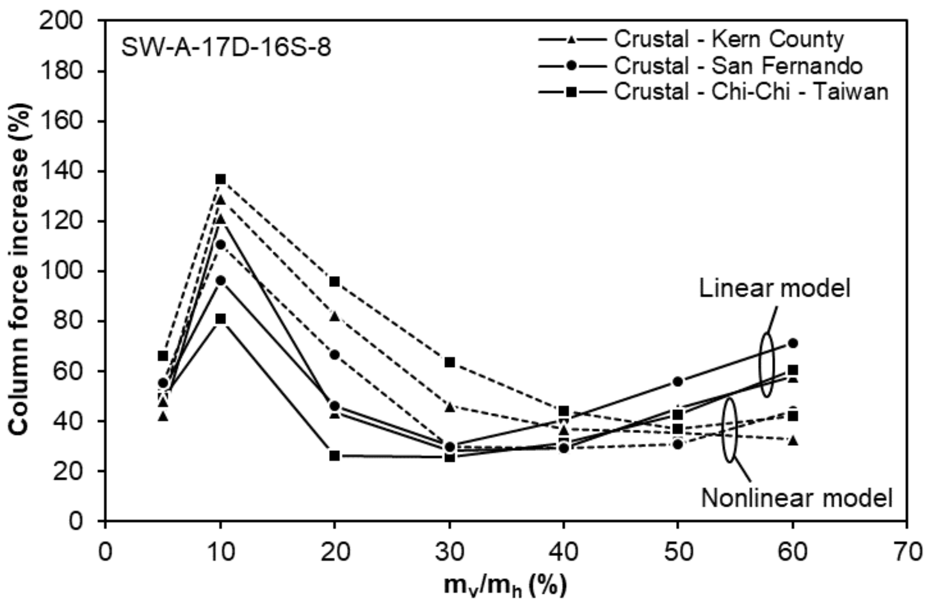

Figure 6.42 – Increase in column force versus vertical to horizontal mass ratio per floor (m_v/m_h) from linear and nonlinear models

Several arrangements of effective stiffness over the height of the shear wall were investigated in order to achieve an accurate estimate of the axial force in the sloped column from linear analysis. Figure 6.43 depicts the moment – rotation response of the shear wall at the base from liner model with $E_cI_e = 0.5E_cI_g$ and nonlinear model. The rotation of the base of the shear wall versus time is shown in Figure 6.44 and the axial force in the sloped column is presented in Figure 6.45. The axial force was normalized with respect to the maximum column force from nonlinear analysis.

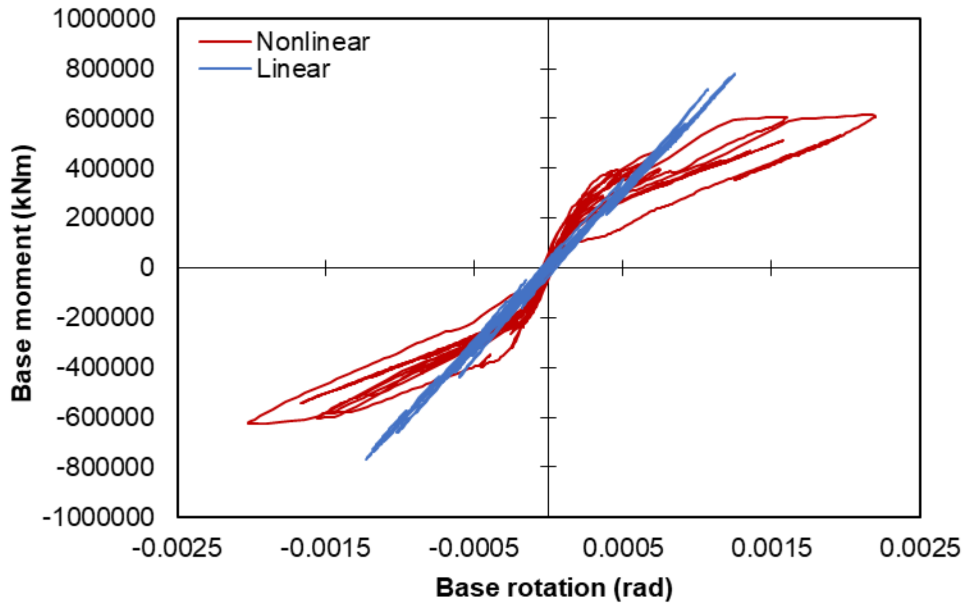

Figure 6.43 – Comparison of moment – rotation hysteresis loops at the base of shear wall from linear model with $E_c I_e = 0.5 E_c I_g$ and nonlinear model

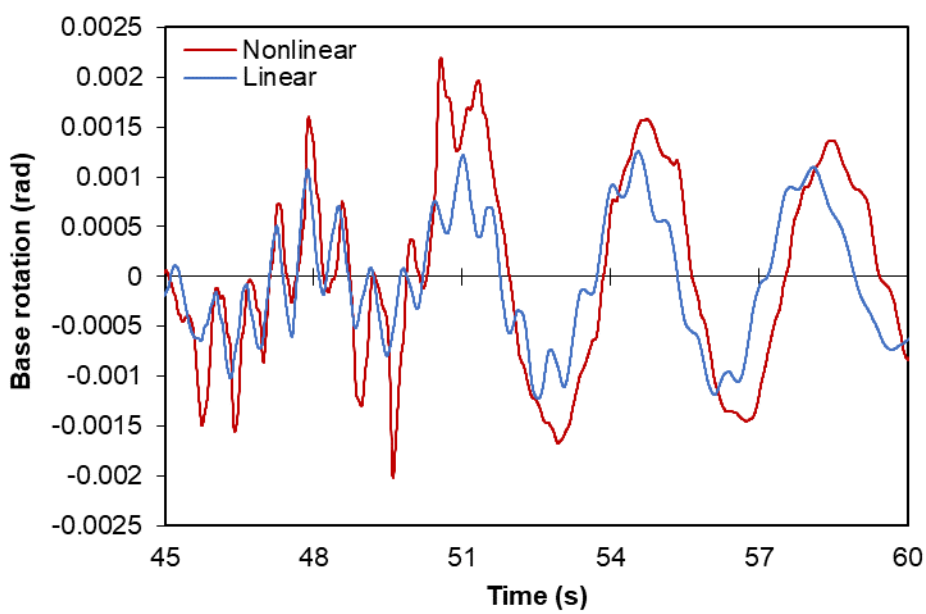

Figure 6.44 – Comparison of rotation at the base of shear wall from linear model with $E_c I_e = 0.5 E_c I_g$ and nonlinear model

Figure 6.45 demonstrates that estimating the effective stiffness of the lateral system does not lead to a good estimate of the axial force in the sloped column. Thus, it makes no sense to do a detailed estimate of the stiffness of the lateral system and use it for estimating the maximum increase in the column forces. Thus, a possible range of stiffness values should be considered for structural members to determine the maximum additional force in the sloped column.

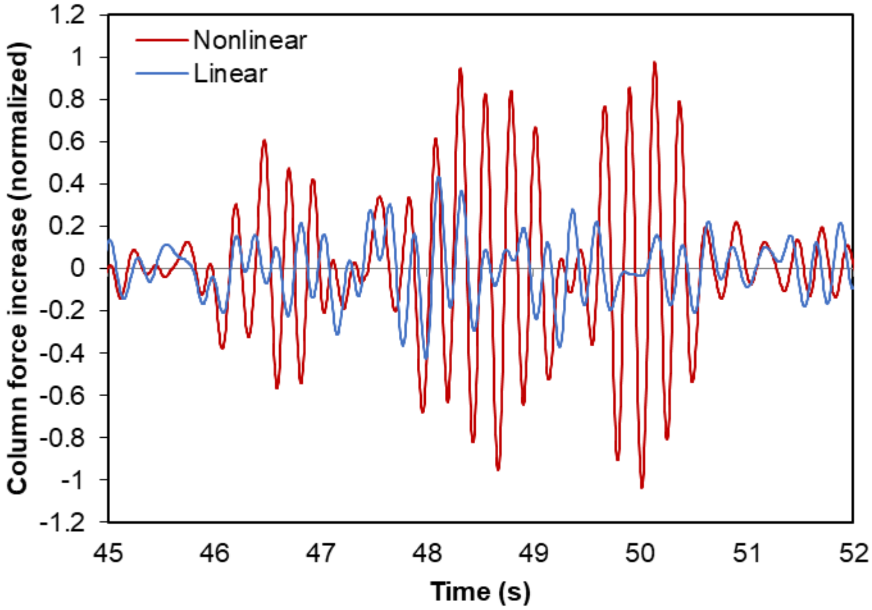

Figure 6.45 – Comparison of normalized increase in sloped column force from linear model with $E_c I_e = 0.5 E_c I_g$ and nonlinear model

6.8 Simplified Procedure for Maximum Column Force

6.8.1 Background and Derivation

As mentioned previously, the axial force in the sloped column is highly sensitive to the stiffness of the structural members. By changing the stiffness values, the column force significantly changes due to the increase or decrease in the coupling of lateral and vertical modes. In order to determine the maximum increase in the sloped column forces, the response spectrum analysis was conducted for different sloped column cases with different characteristics (column slope ranging from 0 to 20 deg., column height of 4 and 16 stories and column base at ground and at the 8th story). The vertical to horizontal mass ratio per floor varies from 5 to 60%. In total, thirty different cases were analyzed. For each case, the column axial stiffness varied between $0.1E_c A_g$ to $10E_c A_g$ to define the peaks in the column forces. The 30-story core wall building was analyzed in the shear (cantilever) wall direction in all the current analyses. Since similar results were obtained for symmetric and asymmetric sloped column (Figure 6.39), only asymmetric sloped column was considered for the current analyses.

The RSA results indicated that the coupled vertical and lateral modes mainly contribute to the maximum column forces. Thus, the maximum increase in the column force can be calculated by considering only the contribution of two coupled modes to the static response, r^{st}, of the analysis. By multiplying the static response of the modes of interest by the spectral acceleration, S_a, of each mode and applying the CQC method of the response spectrum analysis, a fairly good estimate of the peak force can be achieved. Table 6.13 compares the maximum force obtained from SAP2000 (including contributions of the first twelve modes) and from hand calculation (including contributions of two coupled modes only) for some of the analyzed cases. There is a good agreement between the results.

Table 6.13 – Comparison of maximum column force obtained from SAP2000 (including contributions of first twelve modes) and hand calculations (including contributions of two coupled modes only)

Case*	Maximum Column Force Increase (%)		Difference (%)
	SAP2000	Hand Calculation	
3D-16S-0	17.3	17.3	0.0
3D-16S-8	18.9	19.0	0.5
12D-16S-0	54.3	54.2	0.2
12D-16S-8	54.9	53.6	2.4
20D-16S-0	69.6	69.4	0.3
20D-16S-8	66.7	66.4	0.4

* Asymmetric sloped column in shear (cantilever) wall direction

Figure 6.46 shows an example of the coupling of vertical and lateral modes for the case of sloped column with a slope of 3 deg. starting at grade and going up for 16 stories (3D-16S-0). The lateral modes are shown in Figure 6.46(a) while the vertical modes are shown in Figure 6.46(b).

The horizontal axis in Figure 6.46(a) indicates the movement of horizontal mass, and the vertical axis in Figure 6.46(b) indicates the vertical movement of vertical mass.

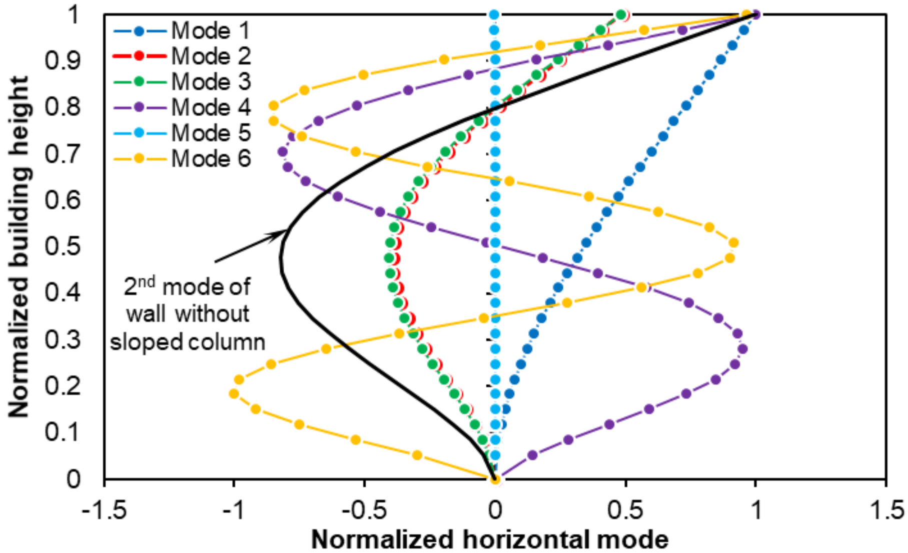

a)

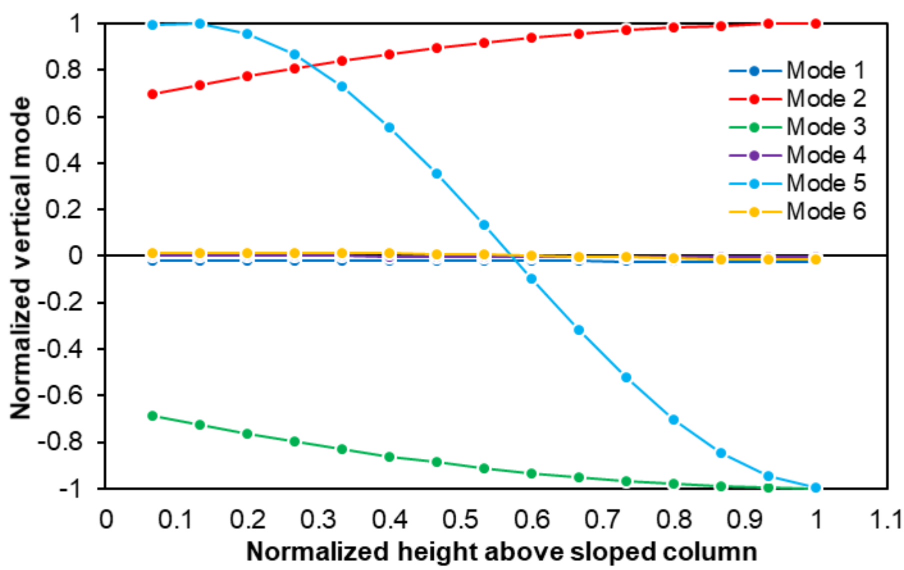

b)

Figure 6.46 – First six modes of a 30-story building with asymmetric 3 deg. sloped columns starting at grade and going up 16 floors (3D-16S-0): (a) lateral modes; (b) vertical modes

In this example, the first vertical mode was coupled with the second lateral mode. The modes were normalized to have a unit value as the maximum value in each mode. As shown in Figure 6.46, the summation of the second and third modes (the two coupled modes that cause the maximum column force) is about the second mode of the wall without sloped column. Investigating the analysis results has revealed that this is the case for all analyzed cases. Thus, the summation of the two normalized coupled modes of the wall with sloped column is approximately equal to the equivalent normalized mode of the wall without sloped column.

The maximum column force obtained from the analysis including contributions of the first twelve modes and from the hand calculation using lateral modes of the wall and including only contributions of the two coupled modes are compared in Table 6.14 for some of analyzed cases. There is a good agreement between the results. Therefore, the maximum column force can be calculated using the modes of the lateral system (e.g., shear wall) without sloped column, which is much easier for design engineers to determine.

Table 6.14 – Comparison of maximum column force obtained from analysis (including contributions of first twelve modes) and hand calculations (using lateral modes of wall and including contributions of two coupled modes only)

Case*	Maximum Column Force Increase (%)		Difference (%)
	SAP2000	Hand Calculation	
3D-16S-0	17.3	19.5	11.3
3D-16S-8	18.9	18.0	4.8
12D-16S-0	54.3	57.4	5.4
12D-16S-8	54.9	48.6	11.5
20D-16S-0	69.6	71.0	2.0
20D-16S-8	66.7	67.2	0.7

* Asymmetric sloped column in shear (cantilever) wall direction

According to the analysis results, the maximum increase in column force can occur due to the coupling of the vertical mode with one of the lateral modes (e.g., 2nd mode, 3rd mode, …) depending on the sloped column characteristics while the stiffness of the lateral system is unchanged. The common feature between these cases is the frequency ratio of the two coupled modes resulting in the maximum increase in column force. This frequency ratio mainly depends on two parameters. Figure 6.47 presents the frequency ratio of coupled modes versus the column slope for different analyzed cases. The linear relationship between the frequency ratio of the coupled modes resulting in the maximum increase in the column force and the slope of the column remains relatively unchanged, no matter which lateral mode is coupled with the vertical one.

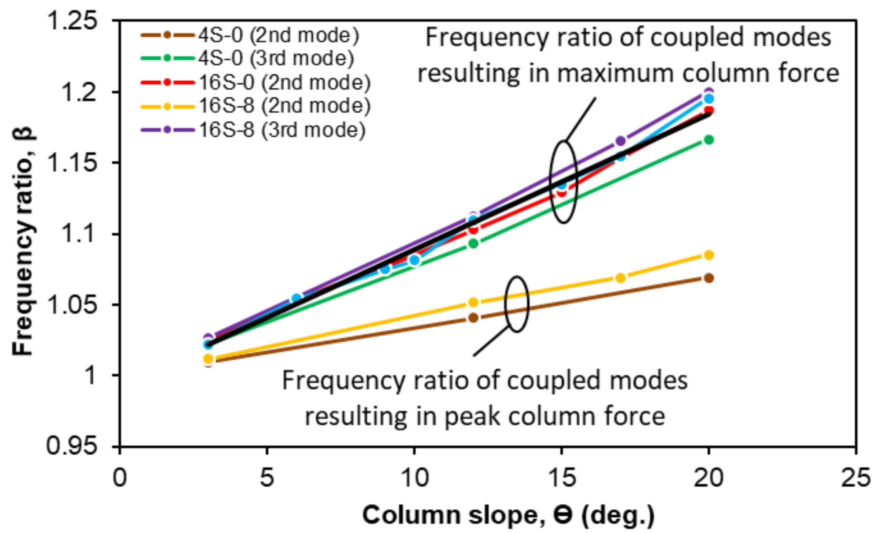

Figure 6.47 – Frequency ratio of coupled modes resulting in maximum increase in column forces and peak increase in column force versus column slope for some analyzed cases

The analysis results have shown that the second parameter that significantly affects the frequency ratio of the coupled modes is the vertical to horizontal mass ratio per floor (m_v/m_h). Figure 6.48 illustrates how frequency ratio increases by increasing the mass ratio and slope of the column. The following empirical equation was proposed for frequency ratio of the two coupled modes resulting in the maximum column force, β:

$$\beta = (0.03\, m_v/m_h + 0.004) \cdot \theta + 1 \qquad (6.1)$$

where, θ is the slope of the column in degree, and m_v/m_h is the vertical to horizontal mass ratio per floor.

The variation of column force versus mass ratio per floor is depicted in Figure 6.49 for different column slope. The maximum increase in the column force increases by decreasing the mass ratio per floor and increasing the slope of the column.

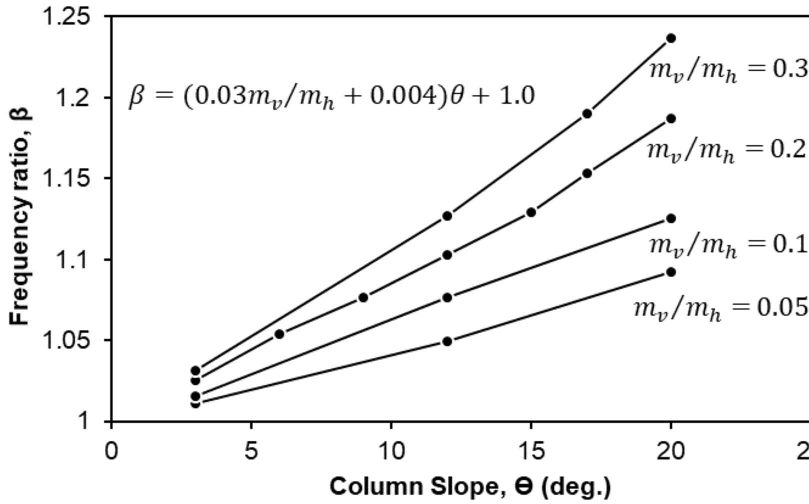

Figure 6.48 – Frequency ratio of coupled modes resulting in the maximum increase in column force versus column slope for different ratios of vertical to horizontal mass per floor ranging from 5 to 30 %

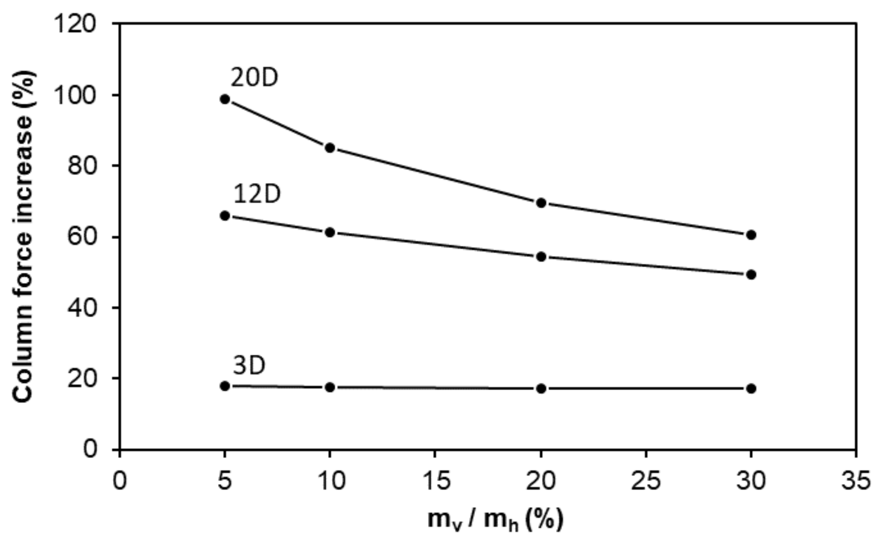

Figure 6.49 – Influence of vertical to horizontal mass ratio per floor on the axial force of sloped columns with different angles

Based on the CQC method, the correlation coefficient is required to determine the maximum column force which depends on the frequency and damping ratios. Some researchers proposed equations for the correlation coefficient. The Rosenblueth-Elorduy equation was used for the correlation coefficient in the current study by assuming the same damping ratio for the two coupled modes which is as follows (Chopra, 2012):

$$\rho = \frac{\xi^2(1+\beta)^2}{(1-\beta)^2 + 4\xi^2\beta} \tag{6.2}$$

where, ξ is the damping ratio. Figure 6.50 shows Equation 6.2 for the correlation coefficient, ρ, plotted as a function of modal frequency ratio, $\beta = w_i/w_n$, for three different damping values of 0.02, 0.05 and 0.1. It is observed that the correlation coefficient rapidly diminishes as the modal frequency ratio increases or decreases (i.e., the two natural frequencies move farther apart) especially the case at small damping values. Depending on damping value, the narrow range of frequency ratio around 1 with significant values changes. This range is $1/1.35 \leq \beta \leq 1.35$ for 5% damping while it is $1/1.13 \leq \beta \leq 1.13$ for 2% damping. It is now clear for structures with well-separated frequencies, the correlation coefficient vanishes and the CQC rule approaches to the SRSS rule.

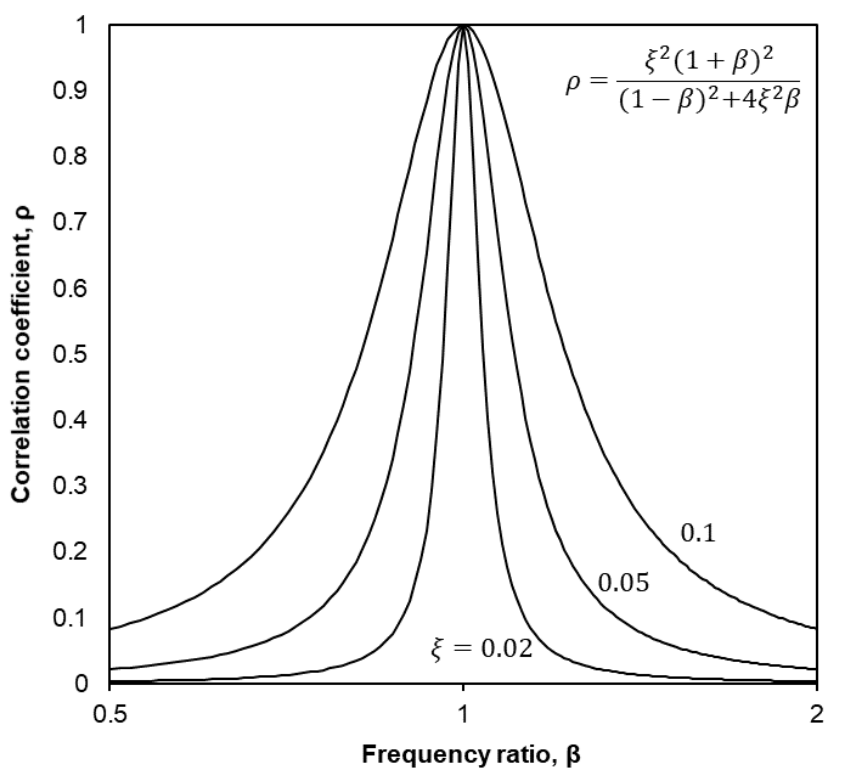

Figure 6.50 – Variation of correlation coefficient, ρ, with modal frequency ratio, β, for three damping values of 0.02, 0.05 and 0.1

As mentioned earlier, the maximum increase in column force can occur due to the coupling of the vertical mode with one of the lateral modes (e.g., 2nd, 3rd or 4th mode). In order to simplify the procedure, it was assumed that the first vertical mode is always coupled with the second lateral mode. This assumption is conservative as the coupling of the vertical mode with the second lateral mode results in a larger column force compared to the coupling of the vertical mode with a higher lateral mode.

The next step in determination of the maximum column force without performing series of analysis with a range of stiffnesses for structural members is to calculate the static response using the second lateral mode of the shear wall (lateral system). It should be noted that the normalized second mode for high-rise shear walls has typical values of 1 at top and about 1.25 at mid-height (Yathon, 2011).

For the simplified method, the two coupled modes are constructed by assuming the second mode of the lateral system is normalized to get 0.5 value at the top for horizontal degrees of freedom (horizontal masses). For one of the coupled modes, constant positive unit values were considered for the vertical degrees of freedom (vertical masses) while for the other coupled mode, constant negative unit values were assumed. In addition, horizontal and vertical masses per floor were assumed to be uniform. In order to compute the static response of the analysis, the spatial distribution of the excitation vector, $\boldsymbol{s}$, and correspondingly the modal participation factor, Γ, should be calculated for the constructed coupled modes (Chopra, 2012):

$$\boldsymbol{s} = \mathbf{m}\boldsymbol{\iota} \tag{6.3}$$

$$\Gamma = \frac{\boldsymbol{\varphi_n^T} \cdot \boldsymbol{s}}{M_n} \tag{6.4}$$

where, $\mathbf{m}$ is the mass matrix and $\boldsymbol{\iota}$ is the influence vector. $\boldsymbol{\varphi_n^T}$ and M_n are transpose of constructed mode and the generalized modal mass, respectively.

Thus, the static response can be simply calculated as follows:

$$r^{st} = \frac{0.14 M_h M_v}{0.085 M_h + M_v} \tag{6.5}$$

where, M_h and M_v are total horizontal mass and total vertical mass supported by sloped column, respectively. Finally, the maximum increase in the column force, r_o, due to horizontal plus vertical excitations can be determined as:

$$r_o = \sqrt{r_{o,h}^2 + r_{o,v}^2} = M_v \cdot S_{a,h} \cdot \sqrt{\left(\frac{S_{a,v}}{S_{a,h}}\right)^2 + \frac{1-\rho}{25(0.085 + M_v/M_h)^2}} \tag{6.9}$$

where, $r_{o,h}$ and $r_{o,v}$ are additional column forces due to horizontal and vertical excitations, respectively. $S_{a,h}$ and $S_{a,v}$ are maximum spectral accelerations from horizontal UHS and from vertical spectrum (e.g., $2/3\, S_{a,h}$), respectively.

6.8.2 Summary of Simplified Procedure

The simplified procedure was developed to provide an upper-bound estimate of the maximum axial forces in the sloped gravity-load columns in high-rise shear wall buildings. A number of simplifying assumptions were made : (1) it was assumed that the second lateral mode of the shear walls is coupled with the first vertical mode; (2) the maximum value of the design spectrum for short periods ($T \leq 0.2\ s$) was used; and (3) both the horizontal mass per floor and the vertical mass per floor were assumed to be uniform over the height of the building and over the floors supported by the sloped column, respectively. This procedure can be used instead of conducting numerous analyses with a range of stiffness values for the sloped columns and the shear walls. The effect of vertical ground accelerations was included in the procedure. The simplified procedure can be summarized as follows:

Definition of parameters utilized in the simplified procedure:

M_v: Total vertical mass supported on sloped column

M_h: Total horizontal mass

m_v: Uniform vertical mass per floor

m_h: Uniform horizontal mass per floor

θ: Column slope (deg.)

ξ: Damping ratio

$S_{a,h}$: Maximum spectral acceleration from horizontal UHS

$S_{a,v}$: Maximum spectral acceleration from vertical spectrum (e.g., $2/3\, S_{a,h}$)

1. Determine the static response, r^{st}:

$$r^{st} = \frac{0.14M_v}{0.085 + M_v/M_h} \tag{6.5}$$

2. Calculate the frequency ratio, β:

$$\beta = (0.03\, m_v/m_h + 0.004) \cdot \theta + 1 \tag{6.1}$$

3. Determine the correlation coefficient, ρ:

$$\rho = \frac{\xi^2(1+\beta)^2}{(1-\beta)^2 + 4\xi^2\beta} \tag{6.2}$$

For damping ratio of 0.025:

$$\rho = \frac{[0.05 + (7.5\, m_v/m_h + 1)\theta \times 10^{-4}]^2}{[0.05 + (3\, m_v/m_h + 0.4)\theta \times 10^{-2}]^2 - 0.000975(3\, m_v/m_h + 0.4)\theta} \tag{6.6}$$

4. Calculate the maximum increase in the column force, r_o:

- Horizontal excitation:

$$r_{o,h} = r^{st} \cdot S_{a,h}\sqrt{2(1-\rho)} \tag{6.7}$$

- Vertical excitation:

$$r_{o,v} = S_{a,v} \cdot M_v \tag{6.8}$$

- Horizontal + vertical excitations:

$$r_o = \sqrt{r_{o,h}^2 + r_{o,v}^2} \tag{6.9}$$

5. Calculate the amplification factor:

$$Amplification\ factor = 1 + r_o/(M_v \cdot g) \tag{6.10}$$

6.8.3 Simplified Equation for Maximum Column Force

According to the procedure presented above, the maximum column force can be estimated by multiplying the axial force due to the gravity loads by the following amplification factor (Equation 6.9):

$$Amplification\ factor = \tag{6.9}$$

$$1 + S_{a,h} \cdot \sqrt{\left(\frac{S_{a,v}}{S_{a,h}}\right)^2 + \frac{1 - \frac{[0.05 + (7.5\, m_v/m_h + 1)\theta \times 10^{-4}]^2}{[0.05 + (3\, m_v/m_h + 0.4)\theta \times 10^{-2}]^2 - 0.000975(3\, m_v/m_h + 0.4)\theta}}{25(0.085 + M_v/M_h)^2}}$$

This equation is based on the rigorous calculation of the correlation coefficient. A simpler mathematical expression that gives very similar results is as follows:

$$Amplification\ factor =$$

$$1 + S_{a,h} \cdot \sqrt{\left(\frac{S_{a,v}}{S_{a,h}}\right)^2 + \frac{1 - 1.16 \cdot e^{-\theta(0.6 m_v/m_h + 0.06)}}{25(0.08 + M_v/M_h)^2}} \tag{6.10}$$

Figure 6.51 compares the amplification factor for the column force obtained from Equation 6.9 (exact equation) and Equation 6.10 (simplified equation). There is very good agreement between the two equations and thus the simplified equation can be used.

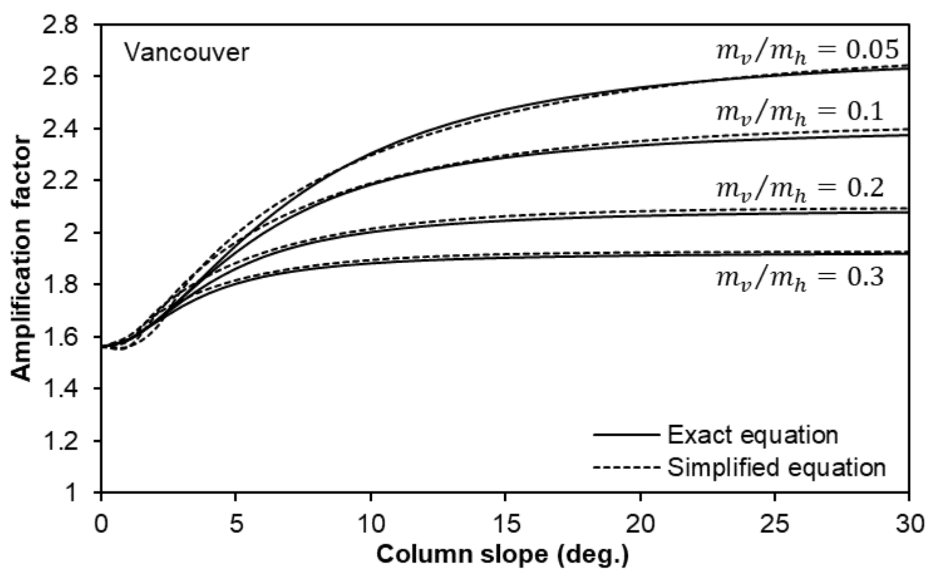

Figure 6.51 – Comparison of axial force amplification factor for sloped column obtained from exact and simplified equations

A further simplification was achieved by assuming the ratio of spectral vertical acceleration to spectral horizontal acceleration equal to 2/3.

$$Amplification\ factor = 1 + S_{a,h}(0.2) \cdot \sqrt{0.4 + \frac{1 - e^{-(\theta - 2)(0.6 m_v/m_h + 0.07)}}{25(0.08 + M_v/M_h)^2}} \tag{6.11}$$

Figure 6.52 compares the results from this further simplified expression with the results from the rigorous expression. The simplified expression gives similar results as the rigorous expression at larger column slopes.

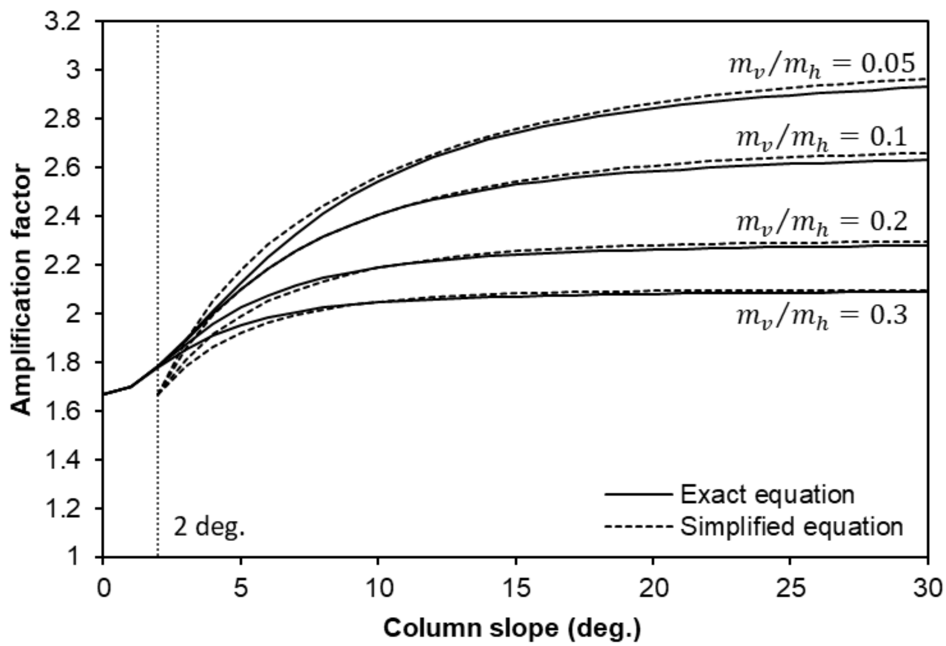

Figure 6.52 – Comparison of axial force amplification factor for sloped column obtained from exact and simplified equations

6.8.4 Comparison of Simplified Procedure with Nonlinear Analysis Results

In order to evaluate the simplified procedure, the maximum increase in the column force obtained from nonlinear time history analysis was compared with the upper-bound estimate predicted by the simplified equation. Two cases of sloped columns were considered for the analysis, an asymmetric sloped column with an angle of 17 deg. starting at 8^{th} floor and going up for 16 floors

(17D-16S-8) and an asymmetric sloped column with an angle of 45 deg. starting at 3rd floor and going up for 3 floors (45D-3S-3). The 30-story building was analyzed in the shear (cantilever) wall direction.

The increase in the sloped column force from 22 ground motions (11×2 horizontal components of ground motions from crustal sources) are shown in Figures 6.53 and 6.54 for sloped columns 17D-16S-8 and 45D-3S-3, respectively. These figures illustrate the distribution of NLTHA results for a specific column stiffness. Furthermore, the mean of NLTHA results (dotted line) and the maximum additional force predicted by the simplified equation (solid line) are depicted in the figures. Each of these figures can be replaced by a bar showing the maximum, minimum and mean of the results in addition to the mean plus and minus one standard deviation of the results, as shown in Figure 6.55.

As previously mentioned, three distinctive sources of earthquakes are active in Southwestern BC: crustal, subcrustal and subduction events. All three sources contribute the seismic hazard in Vancouver. Nonlinear time history analyses were carried out for the two cases of sloped columns using selected ground motions from three sources. Figures 6.55(a) and (b) compare the increase in the column force for the two cases of sloped columns, 17D-16S-8 and 45D-3S-3, subjected to three sources of ground motions.

According to the results, crustal and subcrustal events are more critical for the current study as expected. This can be attributed to the fact that the scenario-specific period range, T_{RS}, determined for crustal and subcrustal sources covers shorter periods compared to that for the subduction source. Since the coupling of lateral and vertical modes occur in the second or higher modes (with shorter periods), selected crustal and subcrustal ground motions cause larger increase in the sloped column force.

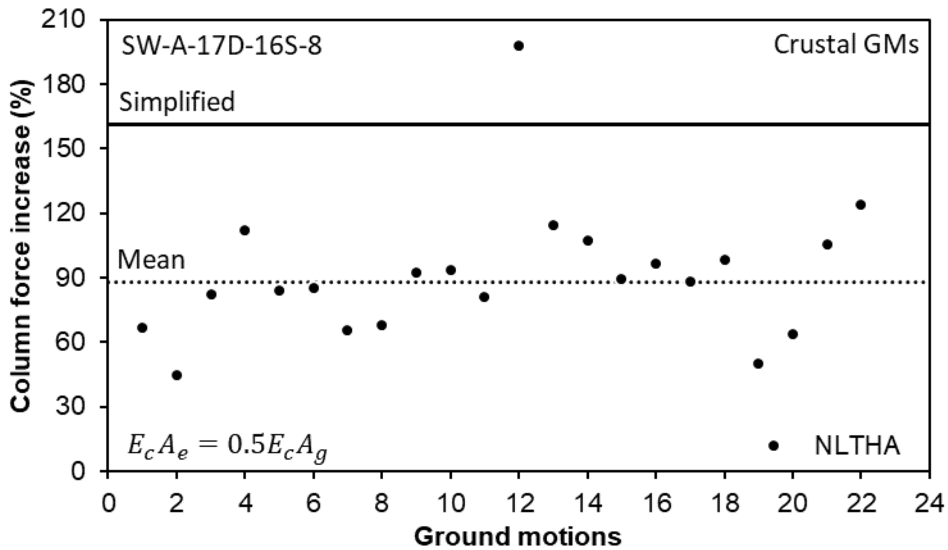

Figure 6.53 – Comparison of increase in column axial force obtained from simplified procedure and NLTHA for the case of sloped column with the slope of 17 deg. starting at 8th floor and going up for 16 floors (17D-16S-8)

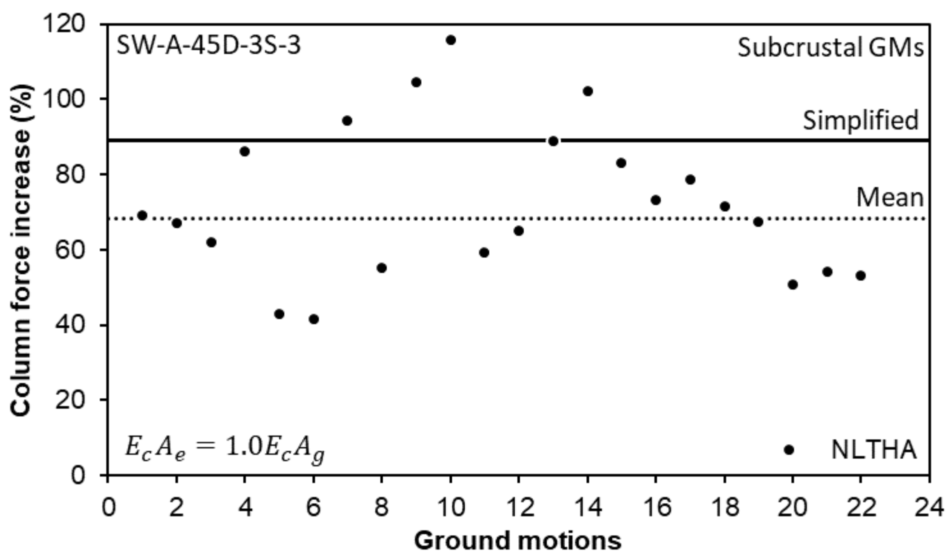

Figure 6.54 – Comparison of increase in column axial force obtained from simplified procedure and NLTHA for the case of sloped column with the slope of 45 deg. starting at 3rd floor and going up for 3 floors (45D-3S-3)

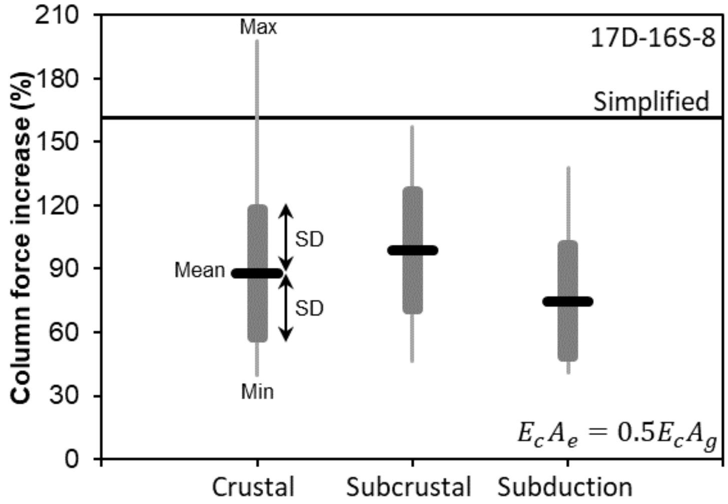

a)

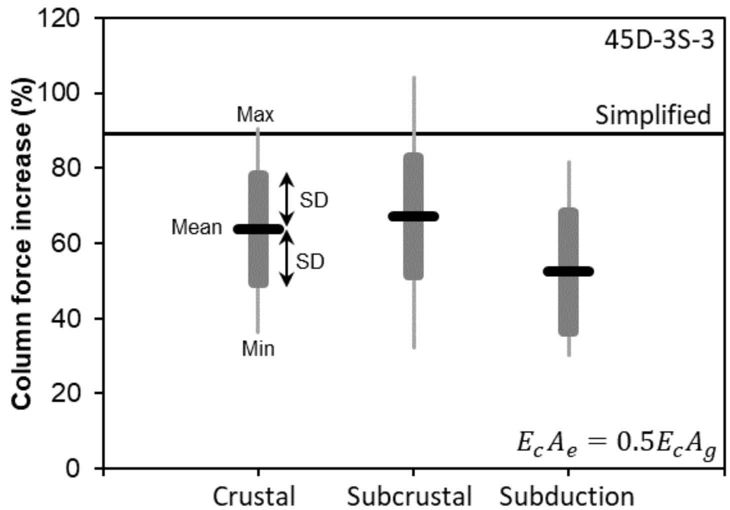

b)

Figure 6.55 – Comparison of the increase in axial force of column from three sources of earthquakes in BC for the case of sloped column: (a) 17D-16S-8 and (b) 45D-3S-3

Figures 6.56 to 6.59 present the comparison of the maximum increase in the sloped column force obtained from NLTHA and predicted by the simplified equation for the two cases of sloped columns: 17D-16S-8 and 45D-3S-3. The column stiffness for NLTHA varies between the range of $0.1E_cA_g$ and $1.0E_cA_g$ to determine the maximum increase in the column force for sloped columns in the shear wall direction. The NLTHA for sloped columns in the coupled wall direction was performed with two column stiffnesses of $0.5E_cA_g$ and $1.0E_cA_g$ for comparison.

Figures 6.56 and 6.57 show the results for crustal ground motions while Figures 6.58 and 6.59 show the results for subcrustal ground motions. Based on analysis results, the additional force in the sloped column considerably varies by increasing the column stiffness.

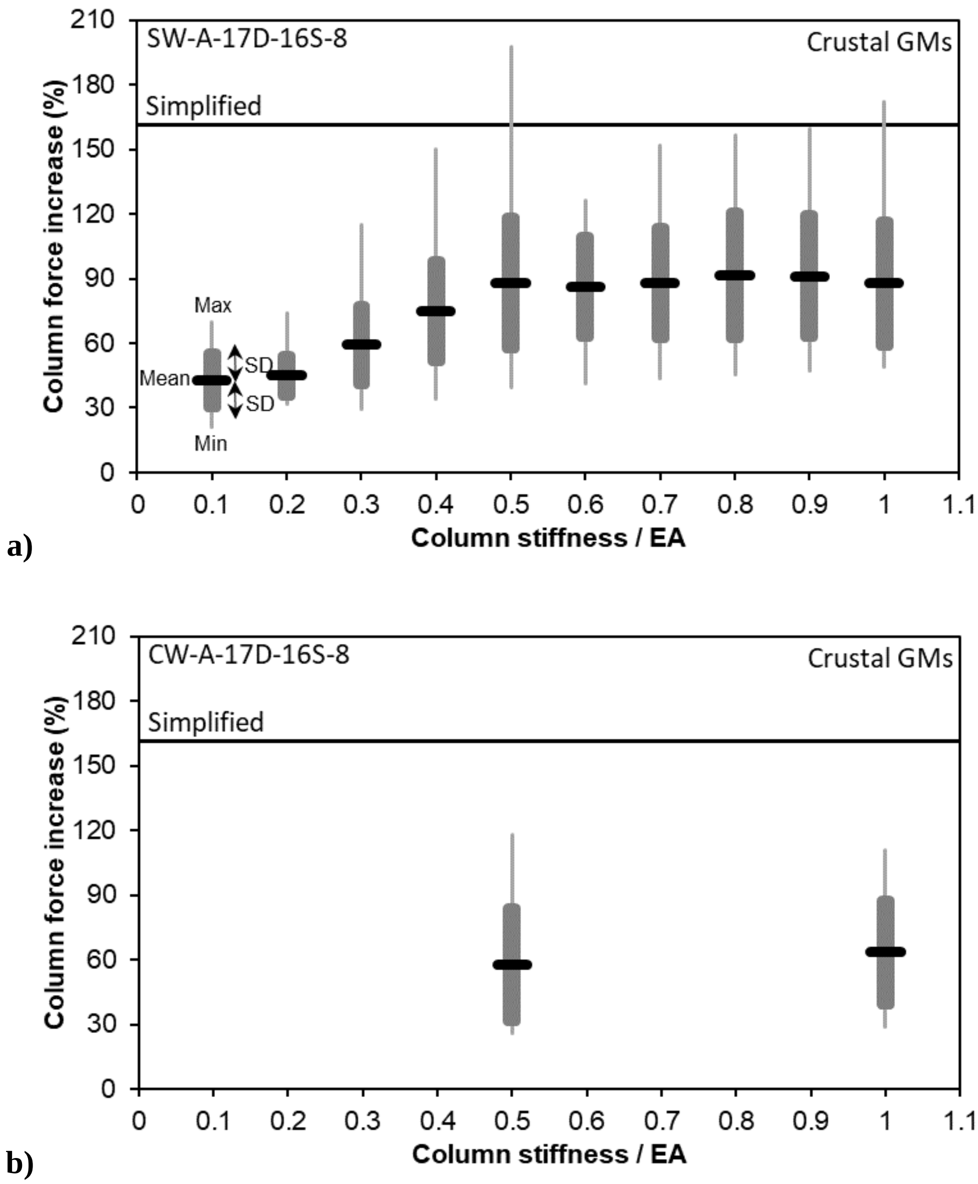

Figure 6.56 – Comparison of increase in column force obtained from simplified procedure and NLTHA with crustal ground motions for different stiffnesses of sloped column 17D-16S-8 in: (a) shear wall direction; and (b) coupled wall direction

The simplified method results in a good estimate for the maximum increase in the sloped column force. Comparison of the results for sloped columns in shear wall direction with those in coupled wall direction confirmed the conclusion from RSA which indicated the maximum increase in the column force in shear wall direction is more critical.

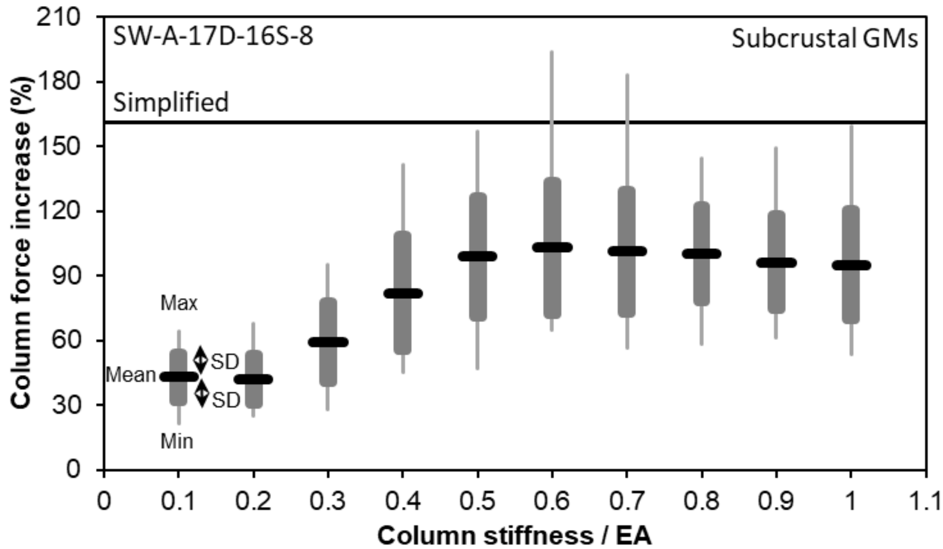

a)

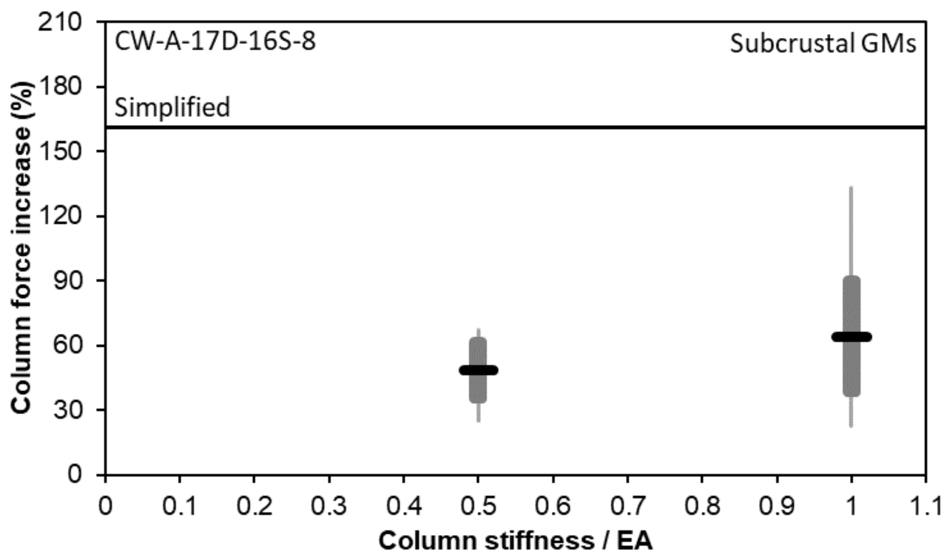

b)

Figure 6.57 – Comparison of increase in column axial force obtained from simplified procedure and NLTHA with subcrustal ground motions for different stiffnesses of sloped column 17D-16S-8 in: (a) shear wall direction; and (b) coupled wall direction

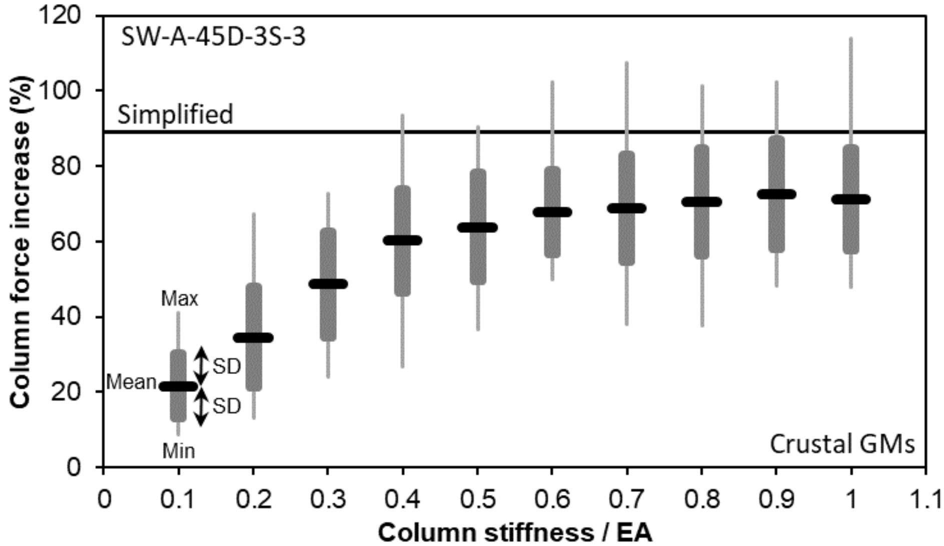

a)

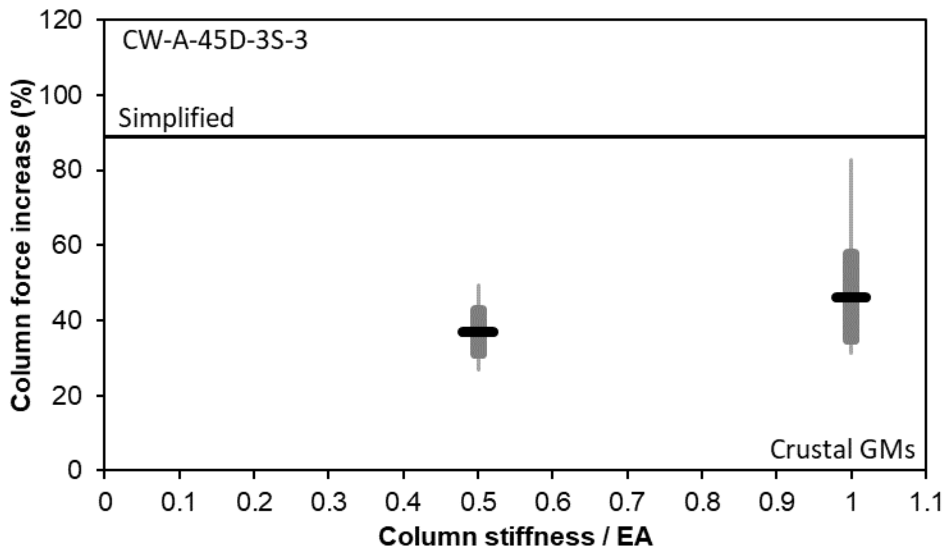

b)

Figure 6.58 – Comparison of increase in column axial force obtained from simplified procedure and NLTHA with crustal ground motions for different stiffnesses of sloped column 45D-3S-3 in: (a) shear wall direction; and (b) coupled wall direction

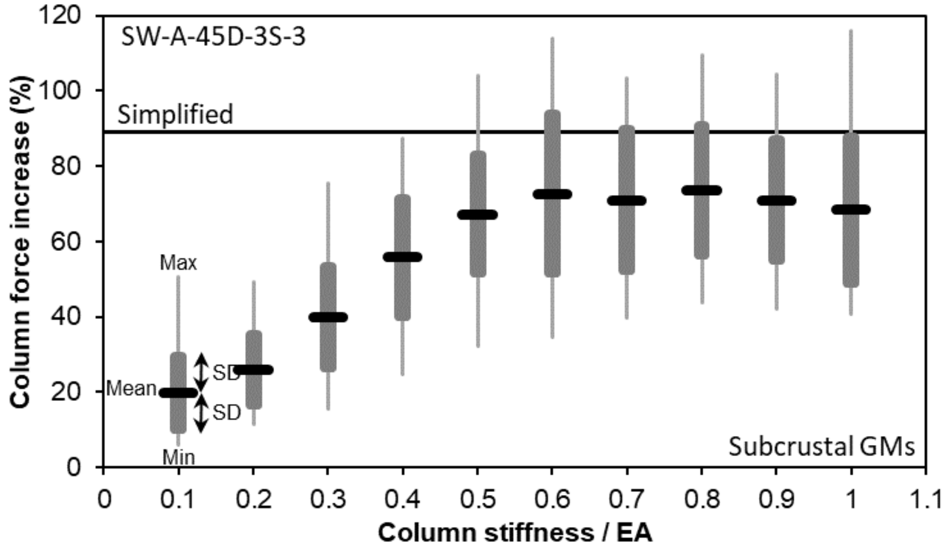

a)

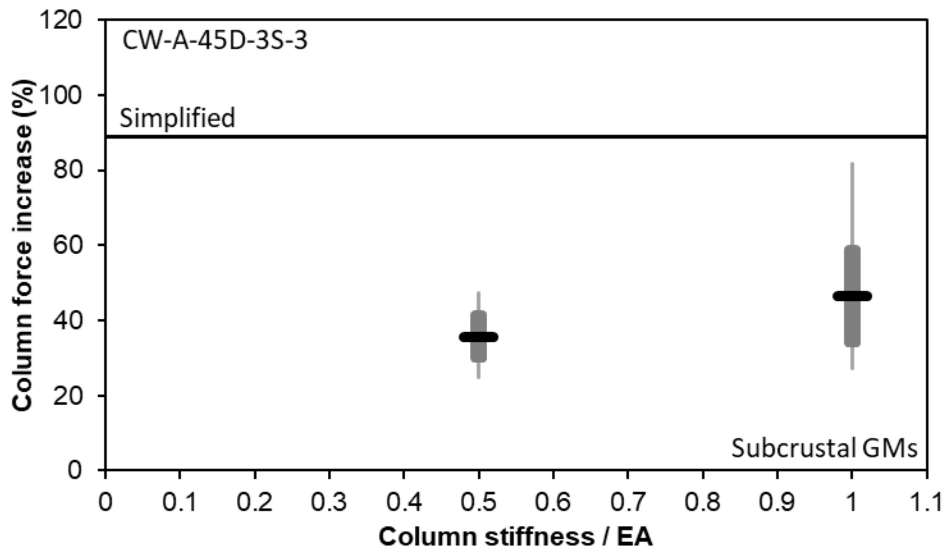

b)

Figure 6.59 – Comparison of increase in column axial force obtained from simplified procedure and NLTHA with subcrustal ground motions for different stiffnesses of sloped column 45D-3S-3 in: (a) shear wall direction; and (b) coupled wall direction

Figures 6.60 and 6.61 also compare the increase in the column force for sloped columns in the shear wall and coupled wall directions directly for two different column stiffnesses of $0.5E_cA_g$ and $1.0E_cA_g$.

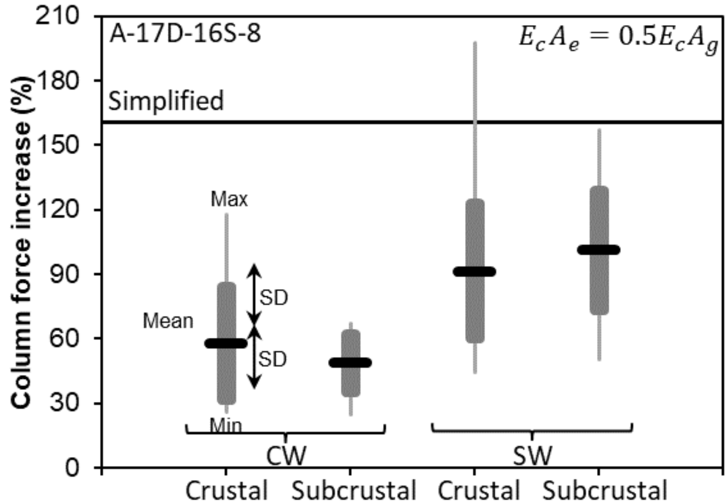

a)

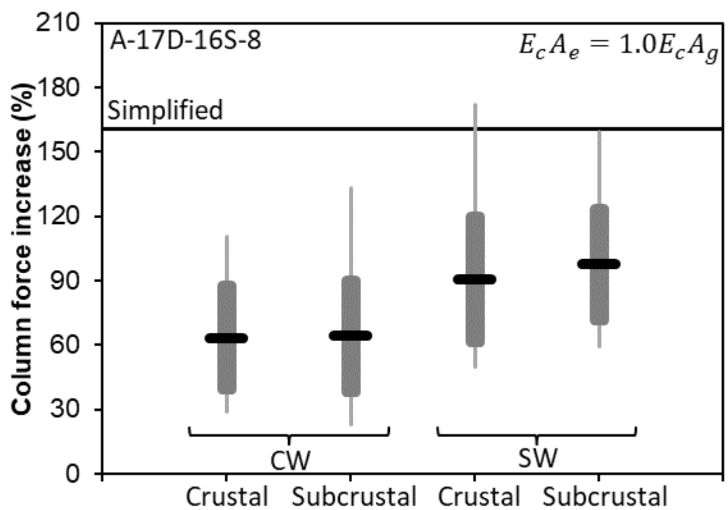

b)

Figure 6.60 – Comparison of increase in column force for the case of asymmetric sloped columns with the angle of 17 deg. starting from 8th story and going up for 16 stories (17D-16S-8) obtained from NLTHA in coupled wall and shear wall directions with column stiffness of: (a) $0.5E_CA_g$; and (b) $1.0E_CA_g$

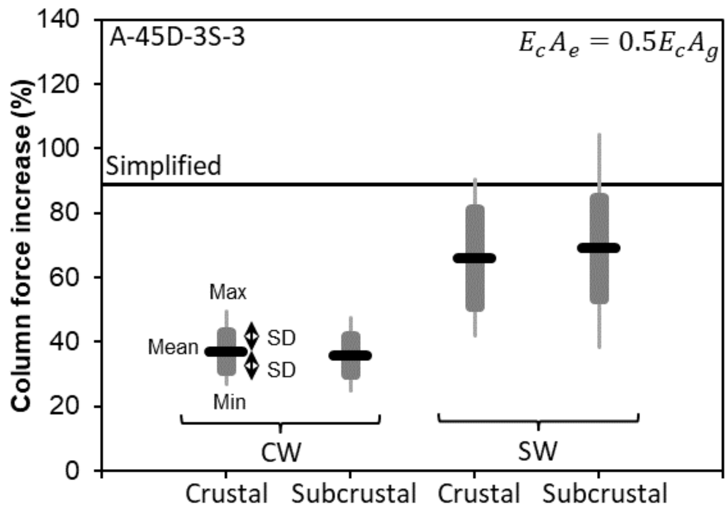

a)

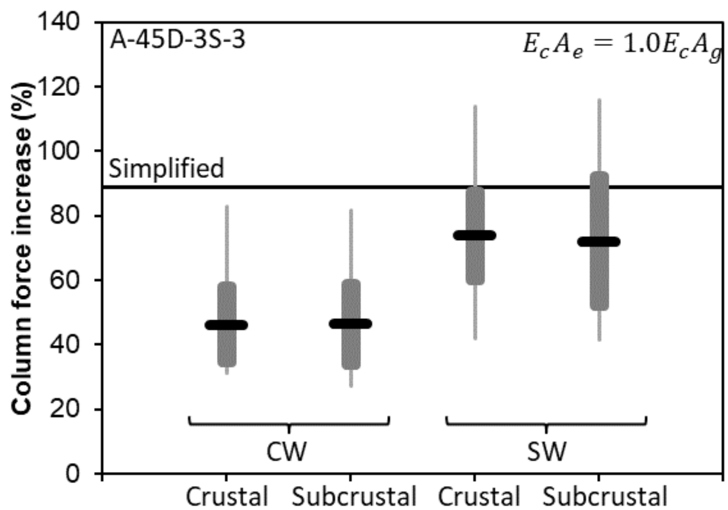

b)

Figure 6.61 – Comparison of increase in column force for the case of asymmetric sloped columns with the angle of 45 deg. starting from 3rd story and going up for 3 stories (45D-3S-3) obtained from NLTHA in coupled wall and shear wall directions with column stiffness of: (a) $0.5E_CA_g$; and (b) $1.0E_CA_g$

6.8.5 Influence of Vertical Acceleration on Vertical Columns ($\theta = 0$)

Vertical accelerations are usually ignored in the seismic design of buildings. The current study has demonstrated that vertical accelerations have a significant influence on sloped columns. As the slope of the columns was reduced to zero (columns approached being vertical) the influence of the vertical accelerations did not disappear. Thus, a study was done to examine the influence of vertical acceleration on vertical gravity-load columns. Response spectrum analysis and nonlinear time history analysis of the building were conducted in the shear wall direction. Figure 6.62 compares the additional force in the column at the first floor obtained from RSA and NLTHA. The vertical to horizontal mass ratio per floor (m_v/m_h) was 0.2. The NLTHA results from 11 crustal and subcrustal ground motions are shown in Figures 6.62(a) and (b), respectively. The solid line depicts RSA result, while the dotted line shows the mean of NLTHA results.

Gravity-load columns are designed for 1.4 times the dead load. Both RSA and NLTHA results indicate vertical accelerations may increase the column force more than 40%. For crustal ground motions, the RSA and mean of NLTHA results are similar. For some crustal ground motions, the column force is even larger than the RSA result. By looking at the vertical spectra of ground motions, it was revealed that these ground motions have larger spectral acceleration values compared to the vertical response spectrum at the period of interest which is equal to the period of the first vertical mode (e.g., $T_3 = 0.334\ s$ in this case). Thus, analysis results indicated that the effect of vertical accelerations should be considered for seismic design of buildings.

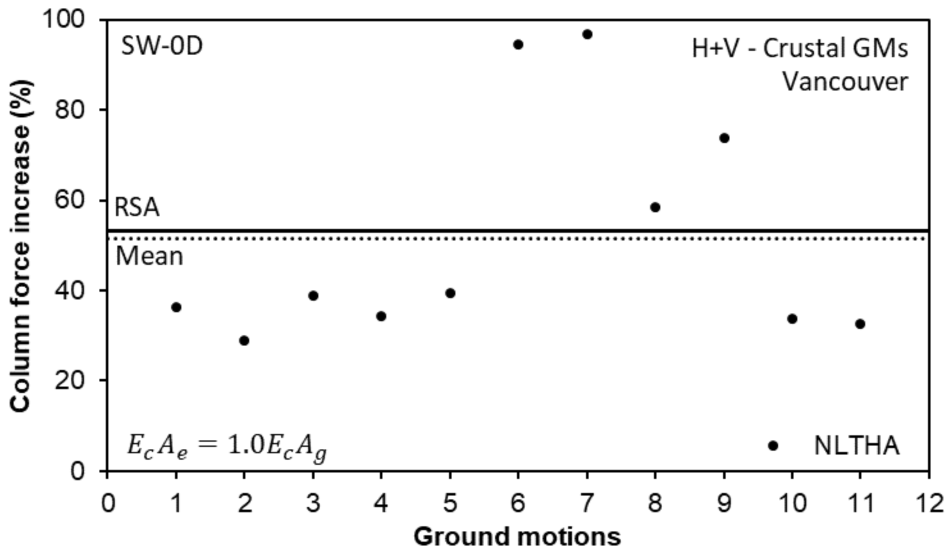

a)

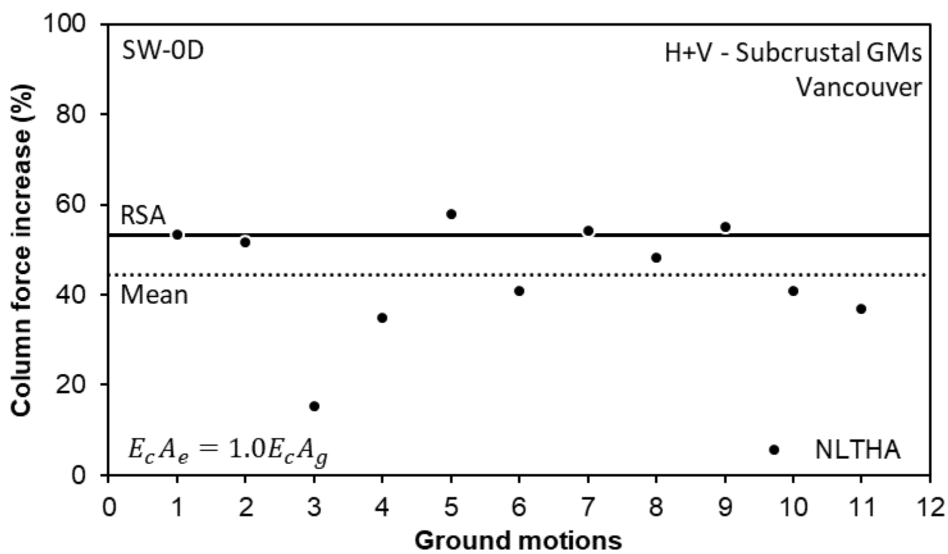

b)

Figure 6.62 – Increase in column axial force due to vertical acceleration obtained from RSA and NLTHA for: (a) crustal ground motions; and (b) subcrustal ground motions

6.9 Additional Study

Additional analyses were conducted to investigate the influence of sloped gravity-load columns on the seismic force resisting system (SFRS) of the building and to evaluate the axial force in a sloped column supporting a single vertical mass. The results of these studies are presented here.

6.9.1 Influence of Sloped Gravity-Load Columns on SFRS

Nonlinear time history analysis was used to evaluate the effect of sloped column on the seismic force resisting system (SFRS). NLTHA results have indicated that sloped column irregularities considerably influence the performance of the lateral system (SFRS) in high-rise buildings. Figure 6.63 shows shear force envelopes from 22 ground motions (11×2 horizontal components of ground motions) for a case of sloped column with the angle of 45 deg. starting from the 3rd story and going up for 3 stories. The black line shows mean of the shear envelopes for the system with sloped column while the red line shows the mean of the shear envelopes for the system without sloped column. Shear envelopes for the system without sloped column are not shown in the figure.

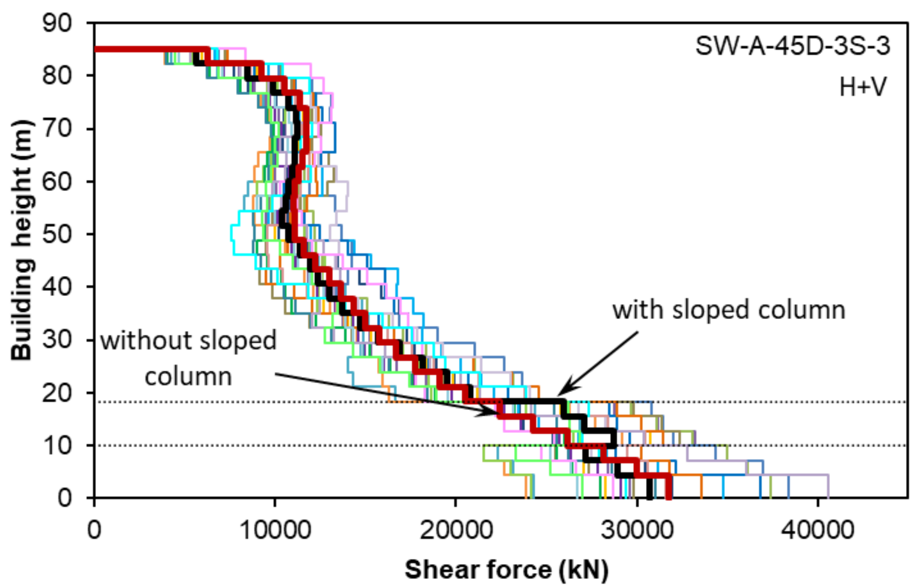

Figure 6.63 – Shear force envelopes for the system without sloped column and with 45 deg. sloped columns starting at 3rd story and going up 3 stories (45D-3S-3) from 22 ground motions

The mean of the shear envelopes for the system with and without sloped column are clearly depicted in Figure 6.64. The shear force in the lateral system increases significantly at the location of sloped column as illustrated in Figure 6.64. Apparently, this shear force increase occurs due to the horizontal component of the axial force in the sloped column. However, the magnitude of the shear increase calculated based on the mean of shear envelopes for the system with and without sloped column is smaller than the horizontal component of the maximum axial force occurring in the sloped column.

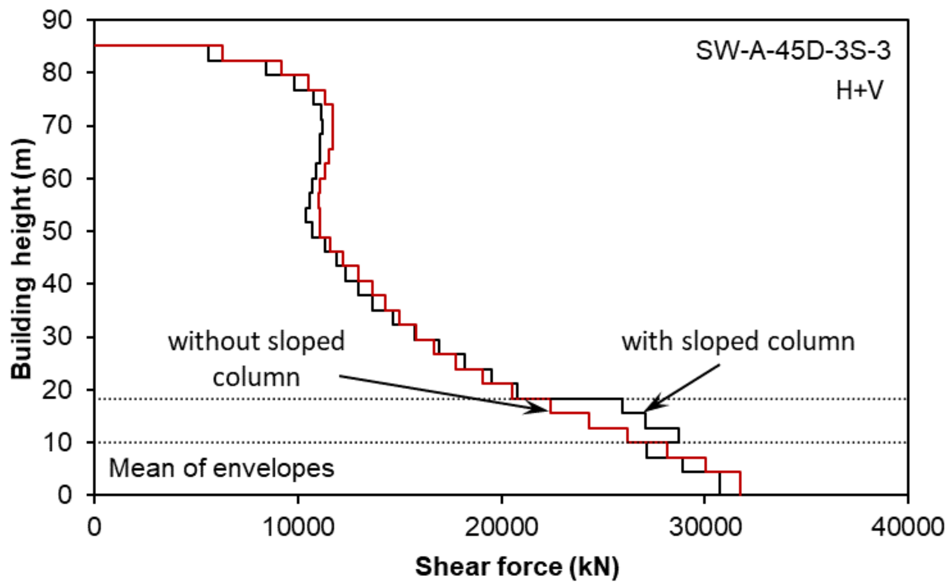

Figure 6.64 – Mean of shear envelopes from 22 ground motions for the system with and without sloped columns

By closely looking at the story shear over the building height at different time intervals for one ground motion (e.g., Loma Prieta), it is indicated that the sudden change in the seismic shear force in SFRS is equal to the horizontal component of the axial force in the sloped column at the time of interest. Figure 6.65 shows the story shear at three different time intervals for Loma Prieta earthquake and Table 6.15 gives the vertical component of the axial force in the sloped column at each time instant. Since the slope of the column is 45 deg. in this case, the vertical and horizontal components of the force in the column is identical. Therefore, the increase or decrease in the shear force at each time instant is approximately identical to the vertical component of the column force.

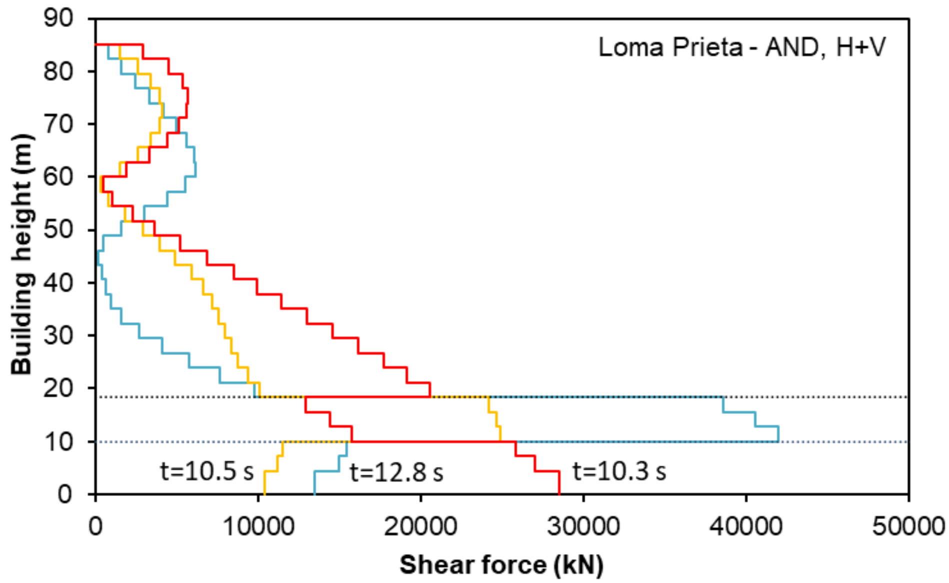

Figure 6.65 – Shear force at three different time instants for one ground motion

Table 6.15 – Column force at each time instant

Time (s)	Column force (kN) (vertical component)
10.3	-9112.8
10.5	13569.8
12.8	26663.0

Figure 6.66 compares the story shear over the building height at two different time instants with shear envelopes of the system with and without sloped column for Loma Prieta earthquake. The maximum column force is about to occur at the time instant of 12.8 s. However, there is a significant difference between the story shear and the shear envelope except for the stories that the sloped column is extended over.

According to the analysis results, one of the simplest though conservative way for estimating the influence of sloped column on the seismic shear force demand of SFRS is to calculate the horizontal component of the maximum sloped column force determined from the simplified procedure and increase the shear force in the SFRS obtained from the mean of shear envelopes of the system without sloped column by this amount.

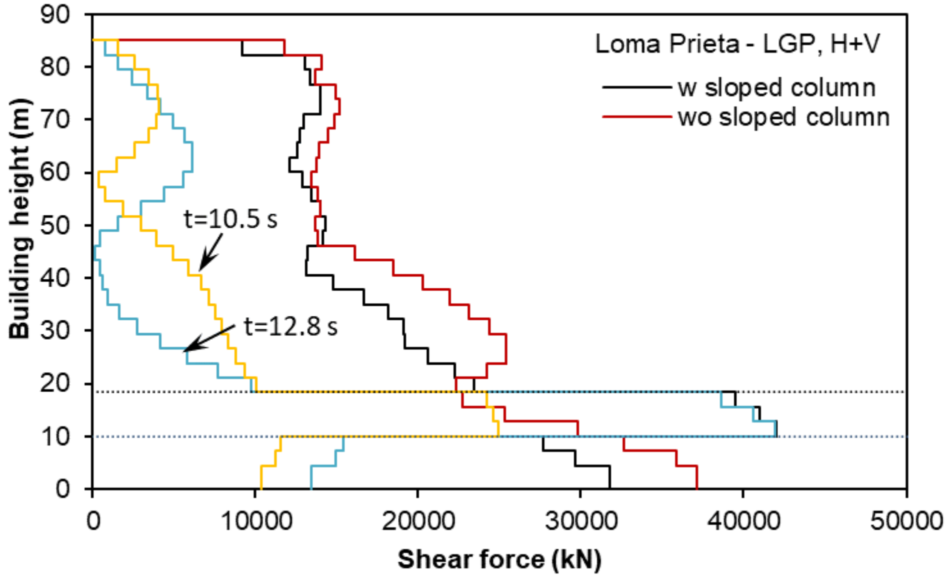

Figure 6.66 – Comparison of the shear force at different time instants with the shear force envelopes of the system with sloped column (black line) and without sloped column (red line) for one ground motion

The bending moment envelopes of the system with and without sloped column are shown in Figure 6.67 from 22 ground motions (11×2 horizontal components of ground motions) for the case of sloped column with the angle of 45 deg. starting from the 3rd story and going up 3 stories. Similarly, the black line shows the mean of the bending moment envelopes for the system with sloped column and the red line depicts the mean of the bending moment envelopes for the system without sloped column. Bending moment envelopes for the system without sloped column are not shown in the figure. The mean of bending moment envelopes for the system with and without sloped column are compared with the yielding moment and flexural strength of the SFRS in Figure 6.68. On average, yielding of flexural reinforcement in SFRS takes place over the height of the first story.

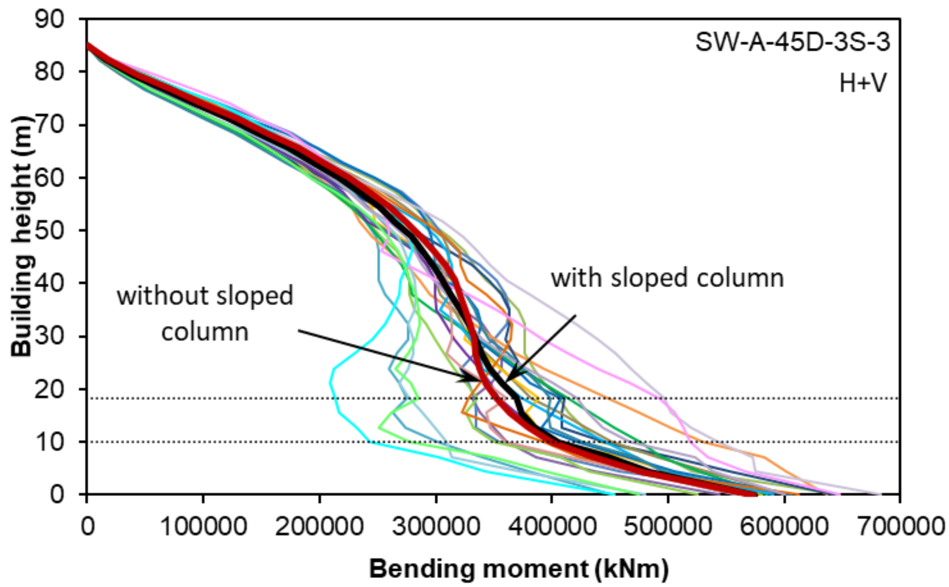

Figure 6.67 – Bending moment envelopes for the system without sloped column and with sloped column of 45 deg. starting from 3rd story and going up for 3 stories (45D-3S-3) from 22 ground motions

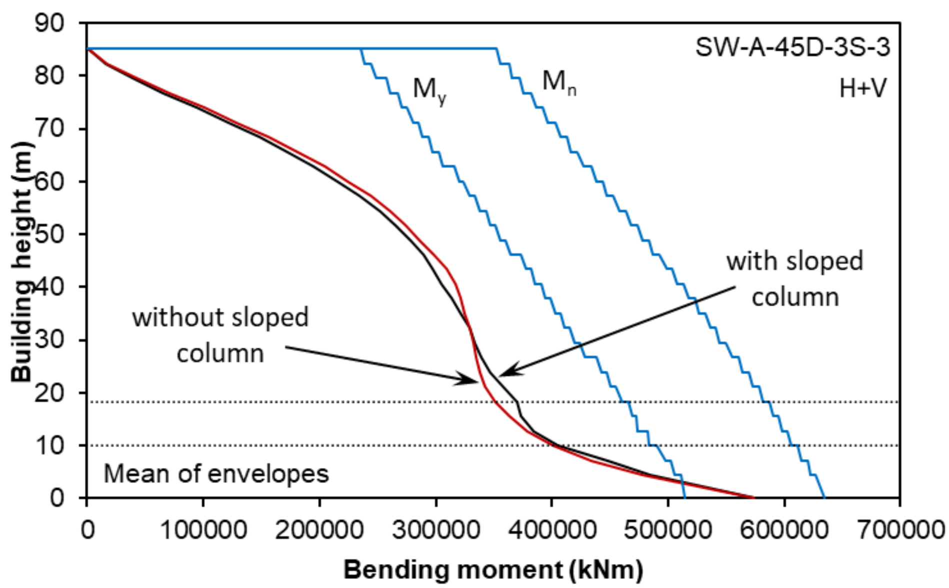

Figure 6.68 – Comparison of the mean of bending moment envelopes for the system with and without sloped column with the yielding moment and flexural strength of SFRS

6.9.2 Sloped Column Supporting a Single Vertical Mass

The simplified method developed in the current study was based on the assumption of uniformly distributed vertical mass per floor over the specific height of the high-rise building. However, in some cases, a single vertical mass is supported by the sloped column such as canopies. Response spectrum analysis was employed to determine the maximum increase in sloped column force for different sloped column stiffnesses ranging from $0.1E_cA_g$ to $10E_cA_g$. Figure 6.69 depicts the variation of increase in the column force with column stiffness for the case of sloped column with the angle of 45 deg. supporting a single vertical mass at the first floor above grade. The ratio of vertical to horizontal mass per floor (m_v/m_h) was 0.2 while the ratio of total vertical to horizontal mass (M_v/M_h) was small and about 0.007. According to RSA results, due to the small vertical mass, the vertical mode has a short period, which is coupled with higher lateral modes. In the above case, the maximum column force occurs due to the coupling of the vertical mode with the fifth lateral mode, which resulted in about 80% increase in the column force.

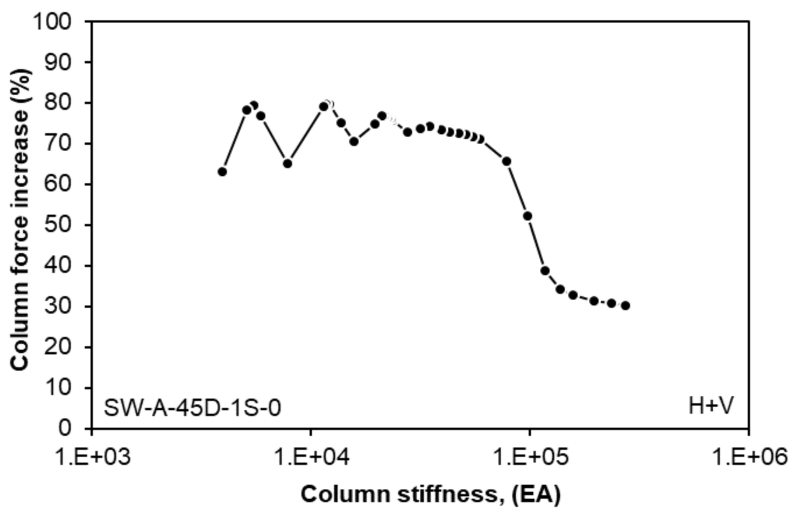

Figure 6.69 – Column force increase for the case of sloped column with slope of 45 deg. supporting a single vertical mass ($m_v/m_h = 0.2, M_v/M_h = 0.007$) located at first floor above grade (45D-1S-0) obtained from RSA

Nonlinear time history analysis was carried out using crustal and subcrustal ground motions. Both horizontal and vertical accelerations were applied. Two different effective axial stiffnesses of $0.5E_cA_g$ and $1.0E_cA_g$ were considered for the analysis. Figures 6.70 and 6.71 show force increase in the sloped column from 22 crustal and subcrustal ground motions (11×2

horizontal components of ground motions), respectively. Figures 6.70(a) and 6.71(a) present the NLTHA results for column effective stiffness of $E_cA_e = 0.5E_cA_g$, while Figures 6.70(b) and 6.71(b) present the results for column effective stiffness of $E_cA_e = 1.0E_cA_g$. The mean of NLTHA results are shown in the figures with a dotted line. The NLTHA results are compared with the maximum increase in column force determined using the simplified method (solid black line).

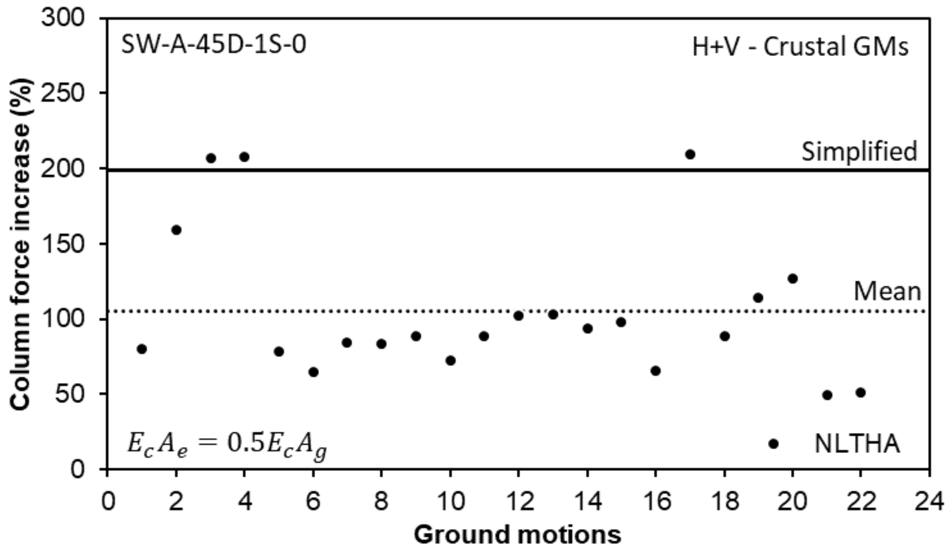

a)

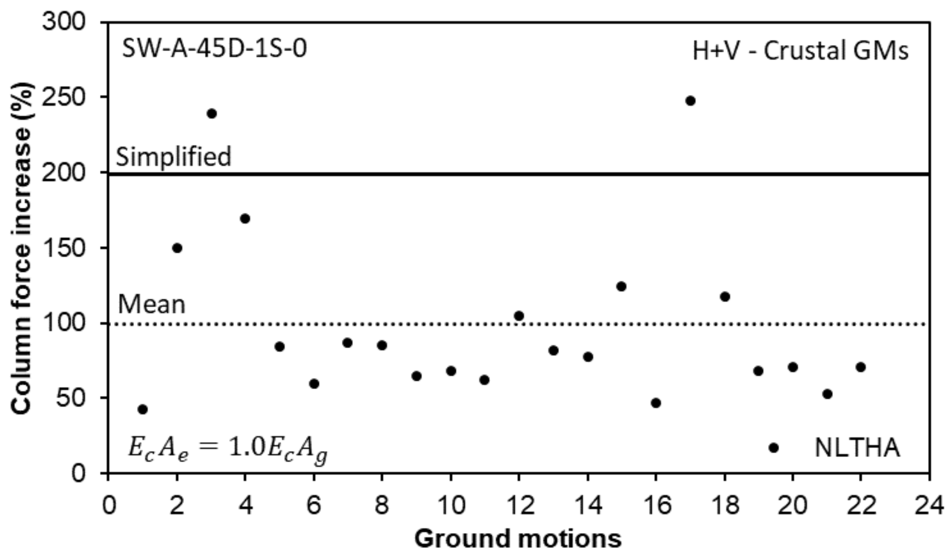

b)

Figure 6.70 – Comparison of column force obtained from NLTHA with crustal GMs and simplified procedure for the case of sloped column with slope of 45 deg. supporting a single vertical mass (45D-1S-0) and the effective axial stiffness (E_cA_e) of : (a) $0.5E_cA_g$, and (b) $1.0E_cA_g$

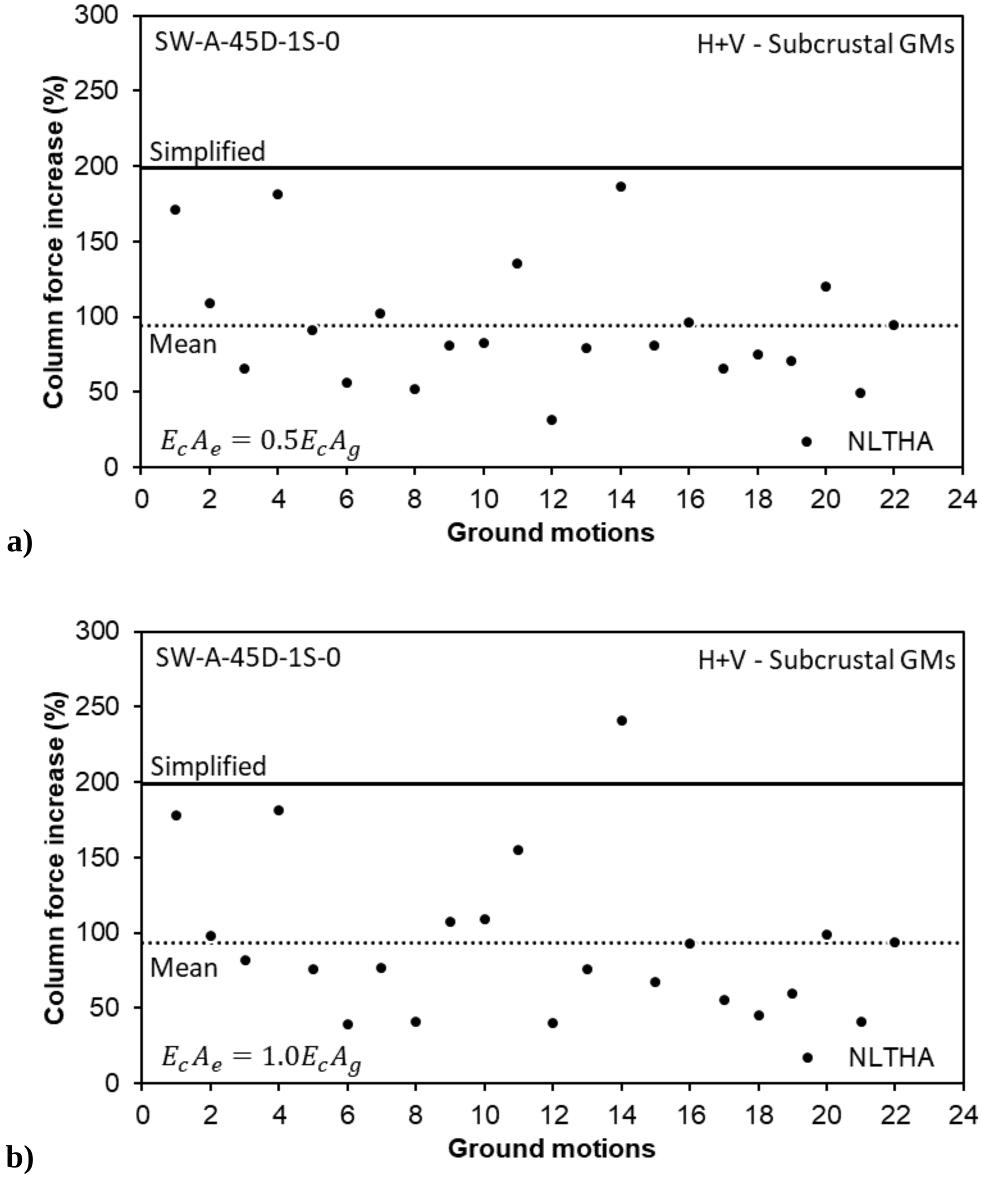

Figure 6.71 – Comparison of axial column force obtained from NLTHA with subcrustal GMs and simplified procedure for the case of sloped column with slope of 45 deg. supporting a single vertical mass (45D-1S-0) and the effective axial stiffness (E_cA_e) of : (a) $0.5E_cA_g$, and (b) $1.0E_cA_g$

Summary of all NLTHA results are presented in Figure 6.72. It is concluded that the simplified method reasonably estimates the maximum axial force in the sloped column. In fact, the simplified method predicts the upper-bound to the NLTHA results for the case of sloped column supporting a single vertical mass. There is a considerable difference between the mean of NLTHA results and the upper-bound in this case.

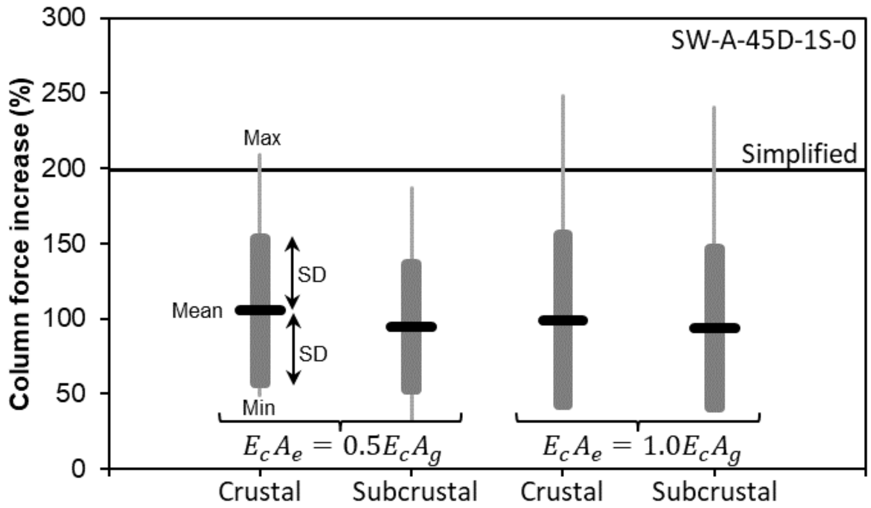

Figure 6.72 – Summary of NLTHA results for increase in sloped column force with crustal and subcrustal GMs and different effective axial stiffnesses of sloped column with the slope of 45 deg. supporting a single vertical mass and comparison of results with the simplified procedure

6.10 Summary and Conclusions

In order to investigate the influence of sloped gravity-load columns on the seismic response of concrete shear wall buildings, a variety of analytical studies were conducted for a range of different types of sloped gravity-load columns. The characteristics of sloped gravity-load columns can be described by four aspects: (i) whether the arrangement of sloped columns is symmetric or asymmetric, (ii) the slope of the column from the vertical axis, (iii) the location of the column base relative to the base of the building, and (iv) the height (e.g., number of stories) that the sloped column extends over the building.

Linear and nonlinear dynamic analyses including the response spectrum analysis (RSA) and time history analyses (THA) were carried out on a typical high-rise core wall building with cantilever shear walls in one direction and coupled shear walls in the perpendicular direction. Three sets of 11 ground motions (33 ground motions in total) from three different earthquake sources in western Canada (crustal, intraslab and interplate) were used for the time history analyses. The 5% damped Uniform Hazard Spectrum (UHS) with a 2% chance of exceedance in

50 years for Vancouver, Canada was used for the response spectrum analysis and for scaling the ground motions. The ratio of vertical to horizontal spectral accelerations was assumed to be $2/3$.

All gravity-load columns, including the sloped columns, were modelled as linear elements, while the shear walls were modelled as either linear or nonlinear elements depending on the type of analysis. An investigation was conducted to determine if the vertical mass could be reasonably modelled using concentrated (lumped) masses on the columns. This approach was found to greatly simplify the modelling of the vertical modes and gave very similar results.

The differential horizontal acceleration at the top and bottom of the sloped column causes vertical acceleration of the mass supported by the column. This results in additional axial forces in gravity-load columns, additional shear forces and bending moments in shear walls, and additional forces in floor slabs. Vertical ground motions cause additional vertical acceleration of the mass supported on the sloped column, which increases the seismic forces in these columns and the supported members (slabs and walls). The differential horizontal movement at the top and bottom of the sloped columns generates vertical movements in the gravity-load frame which need to be accounted for in the seismic design of the buildings with sloped columns.

The analysis results indicated that the seismic forces in a sloped gravity-load column is highly sensitive to the axial stiffness of the column. Small changes in the stiffness of the column can result in very large increases or very large decreases in the column force. The seismic forces in the sloped columns are due to the coupling of the lateral modes of the shear walls with the vertical modes of the mass supported on the columns. The degree of coupling of lateral and vertical modes depends on the column axial stiffnesses. When the first vertical mode is fully coupled with a lateral mode of the shear wall, the maximum increase occurs in the axial force of the column.

A parametric study was conducted to evaluate the effect of different characteristics of a sloped column and the ratio of the vertical mass supported by the sloped columns to the total horizontal mass on the column force. The results were presented in terms of the percentage increase in the sloped column force relative to the gravity load resisted by the column. The analysis showed that the maximum column force increases as the slope of the column (angle relative to the vertical) is increased. When vertical ground motion is included, a vertical column (zero slope) is subjected to a force larger than the gravity force. As the column is sloped, that force increases further but more gradually than the increase when there is no vertical ground movement.

An important parameter that affects the maximum force generated in the sloped column is the ratio of the vertical mass supported on the sloped columns to the total horizontal mass. The maximum percentage increase in the column force decreases as the ratio of vertical to horizontal mass per floor increases. This can be attributed to the fact that the differential horizontal acceleration at the top and bottom of the sloped column causes larger vertical acceleration in smaller vertical mass supported on the column. For the sloped columns with higher mass ratios, the absolute maximum increase in the column force is larger as these columns resist larger gravity loads (which is expected).

The results of analysis have shown that the maximum percentage increase in the column force was similar for symmetric and asymmetric arrangements of the sloped column (with the same characteristics). It should be noted that the total vertical mass supported on sloped columns and the total cross-sectional area of the columns were identical for both arrangements. Thus, only the asymmetric arrangement of sloped columns was considered for the time history analysis.

The influence of the type of shear wall system in the building (cantilever walls versus coupled walls) was also examined. It was observed that the seismic forces in sloped gravity-load columns are larger in the shear wall (cantilever wall) direction. Most of the analysis in this study were focussed in this direction.

One of the important observations of the current study is that the change in the stiffness of the shear walls (i.e., lateral system) due to flexural cracking may either increase or decrease coupling of lateral and vertical modes. Thus, nonlinearity of shear walls results in significant changes in the seismic forces in sloped columns; sometimes higher forces and other times lower forces depending on the degree of coupling. The sloped column force is highly sensitive to the stiffness of the shear walls. Since it is difficult to accurately determine the effective stiffness of the shear walls, a range of stiffness values needs to be considered to safely estimate the maximum increase in the sloped column axial force.

A simplified procedure was developed to provide an upper-bound estimate of the maximum axial forces in the sloped gravity-load columns in high-rise shear wall buildings. A number of simplifying assumptions were made: (1) the first vertical mode is coupled with the second lateral mode of shear walls; (2) the maximum value of the design spectrum for short periods ($T \leq 0.2\ s$) is used; and (3) both the horizontal mass per floor and the vertical mass per floor are uniform over the height of the building and over the floors supported by the sloped column, respectively. A damping ratio of 2.5% was used. The procedure can be used instead of conducting numerous analyses with a range of stiffness values for the sloped columns and the shear walls. Also, the procedure includes the effect of vertical ground accelerations. The developed equation was further simplified by using a simpler form for the mathematical expression and considering additional simplifying assumptions. The simplified equation provides an amplification factor that is multiplied by the portion of the gravity load supported on the top of the sloped column to give the maximum seismic force in a sloped gravity-load column. The results of the simplified solution were found to be in reasonable agreement with the results from nonlinear time history analysis of a shear wall building with different arrangements of sloped columns in both shear wall and coupled wall directions. The simplified procedure gives a very reasonable upper-bound estimate of the maximum increase in the sloped column force.

An additional study was conducted to investigate the influence of the sloped columns on the response of the seismic force resisting system (SFRS) of the building. Sloped columns can cause a significant increase in the seismic shear demands in SFRS at the location of the sloped column over the building height. A simple and conservative approach for estimating the shear force demand on SFRS in high-rise shear wall buildings with sloped columns is to increase the seismic shear force demand in the SFRS by the horizontal component of the maximum seismic force in the sloped gravity-load column determined from the simplified procedure.

Generally, in high-rise buildings, the vertical mass is distributed over the height of the building through floor slabs, and the presented simplified procedure was developed based on this assumption. However, it was found that this procedure can be also applied to the buildings with sloped columns supporting a single lumped vertical mass in order to make a reasonable upper-bound estimate for the maximum column force.

As an outcome of the current study, the 2020 edition of the National Building Code of Canada has defined a new type of irregularity called “sloped-column irregularity” that must be considered in the seismic design of buildings. A sloped-column irregularity shall be considered to exist when a vertical member, inclined more than 2 deg. from the vertical, supports a portion of the weight of a structure in axial compression.

Chapter 7

Conclusions and Future Work

7.1 Summary and Conclusions

Concrete shear wall systems are the most commonly used lateral force resisting system in high-rise buildings in Canada. One of the most challenges aspects of designing high-rise concrete shear wall buildings is accounting for the influence of discontinuities and irregularities in the structure, particularly when the structure is subjected to force or displacement demands in the nonlinear range of the structure.

The focus of this thesis was to investigate a number of challenging discontinuities/ irregularities in concrete shear wall buildings to better understand the nonlinear behaviour of the structure. The general approach taken was to use state-of-the-art nonlinear analysis tools in order to investigate the phenomenon in such a way that a physical understanding was gained about the irregularity/discontinuity. The main goal in each case was to develop simplified methods that can be used by practicing engineers to account for the irregularity/discontinuity in design practice.

Three different types of discontinuity/irregularity in high-rise concrete shear wall buildings were investigated: (i) overhanging wall discontinuity due to the wall above being longer than the wall below (Chapter 3), (ii) discontinuity in lateral stiffness of building, for example at grade level, and the backstay force transfers in the diaphragms that result from this (Chapters 4 and 5), (iii) gravity-load columns inclined from the vertical (Chapter 6).

A brief summary of the methodology and the high-level conclusions for each case is presented below.

7.1.1 Overhanging Wall Irregularity

Nonlinear finite element analysis was used to study the stresses and strains near an overhanging wall irregularity in shear walls. Five different sizes of overhangs (length of overhang) were investigated.

The membrane strains in the wall below the overhang are magnified by the stress flow past the overhang. Very large magnifications occur with small overhang sizes; but do not increase significantly, as the overhang length is increased.

A traditional plane-sections analysis can be used to estimate the vertical compression strains in the smaller shear wall at some distance below the overhang; however, such an analysis underestimates the maximum compression strains immediately below the overhang. Along the compression edge of the lower wall, the maximum compression strains increase nonlinearly towards the overhang. The horizontal tension strains also increase significantly below the overhang, and while the maximum compression strain occurs immediately below the overhang, the maximum horizontal strain occurs a short distance (e.g., 50 mm) below the overhang. The nonlinear increases of the horizontal strains is larger and occurs at lower stress level than the nonlinear increase in compression strains. This can be explained by the fact that the nonlinear horizontal strains are the product of the nonlinear vertical strains and a nonlinearly increasing Poisson's ratio.

It is believed that the combination of large horizontal tension strains and the magnified vertical compression strains resulted in the concrete compression failures observed in thin shear walls with overhanging wall irregularity during the 2010 Maule (Chile) Earthquake such as the case shown in Figure 1.1.

Design engineers typically do not have access to state-of-the-art nonlinear finite element analysis tools for concrete structures, and it would not be practical to use such analysis for design work. Thus, a simplified solution was developed for using the results from linear finite element analysis, or a plane sections analysis, which design engineers are more likely to have access to. A simple safe limit for the maximum compression strain determined from a linear analysis is 0.001 in order to limit the vertical compression strain in the zone below the overhang, accounting for nonlinear amplification of the strains, to less than 0.004. Limiting the maximum compression strain in a wall below an overhang to this level means limiting the maximum bending moment applied to the wall to 80% of the capacity. That is, to prevent a compression failure of the wall immediately below the overhang, the wall below must be protected from being loaded beyond 80% of its capacity.

See Chapter 3 for further details about overhanging wall irregularities.

7.1.2 Discontinuity in Lateral Stiffness of Buildings – Effective Stiffness of Concrete Diaphragms

At the levels where there is a discontinuity in the lateral stiffness of the building due to the termination of shear walls, e.g., at grade level or top of the podium level, large backstay forces develop in the diaphragms that interconnect the shear walls. As there are multiple paths for the lateral forces to take, the magnitude of the backstay forces is sensitive to the assumed effective stiffnesses of the diaphragms. A variety of nonlinear analysis methods were used to investigate concrete diaphragms subjected to backstay forces to determine the reduction in effective stiffnesses of concrete diaphragms due to cracking of concrete.

If the diaphragms are thick, heavily reinforced slabs designed to resist large backstay (membrane) forces, any (transverse) gravity loads applied to the diaphragms will have minimal influence on the cracking of the diaphragms. This more common case is the subject of Chapter 4, where 19 different building diaphragms were analyzed using nonlinear finite element analysis ignoring the effect of gravity loads on the diaphragms. On the other hand, if the diaphragms are not designed for the backstay forces, as sometimes happens, the additional cracking due to bending of the slab may be significant, and this situation was investigated in Chapter 5.

The results of the nonlinear finite element analysis presented in Chapter 4 indicates that the shear deformations of the diaphragm contribute between 70% and 100% of the total deformation depending on the shear span-to-shear depth ratio of the diaphragm. Surprisingly, the formation of diagonal (shear) cracks in the diaphragms cause only a small reduction in the shear stiffness of the diaphragms. For lightly reinforced diaphragms, the shear and flexural stiffnesses reduce sharply when flexural cracking due to strong-axis bending of diaphragms occurs. For moderately and heavily reinforced diaphragms, there is an initial reduction in shear and flexural stiffnesses when flexural cracking occurs, followed by a more gradual reduction as the backstay forces (and level of flexural cracking) increase. One of the most important observations from the current study is that the shear and flexural stiffnesses of the diaphragm degrade simultaneously and are primarily dependant on flexural cracking due to strong-axis bending of the diaphragms.

A trilinear model was presented for the load-deformation relationship of concrete diaphragms subjected to backstay forces. Piece-wise linear relationships are used prior to shear cracking, between shear cracking and strong-axis flexural cracking, and after strong-axis flexural cracking. Simplified procedures were developed for estimating the diaphragm forces that result in shear cracking and flexural cracking of the diaphragms. A trilinear model can also be used to represent the separate shear and strong-axis flexural deformation components of the diaphragms.

As the effective stiffness is defined as the secant stiffness to any load level, the piece-wise linear load-deformation model described above results in a nonlinear relationship between effective stiffness and load level. A one-step simplified model results from assuming a linear relationship between the applied load level and the effective stiffness of the diaphragms. The relationship can be further simplified by separating the relationship between effective stiffness and applied load level into different relationships for slender diaphragms (shear span to depth ratios larger than 0.3) and squat diaphragms (shear span to depth ratios less than or equal to 0.3).

The linear variation of effective stiffness with load level will require an iterative solution for solving the diaphragm forces if a linear model is used for the diaphragms, as is usually the case. Thus, an even further simplification was developed – upper-bound and lower-bound effective stiffness values over different ranges of load levels. This is the type of effective stiffness model currently used in practice, and thus the recommendations developed here can be directly implemented into practice without a change in analysis approach.

The results of Chapter 5 indicate that flexural cracking of thin diaphragms due to out-of-plane loading results in a significant reduction in the initial shear stiffness of slabs as the slab is not uncracked when the initial backstay forces are applied. The reduction in initial shear stiffness is more significant for two-way slabs due to the effect of two-way bending and twisting of the slabs, which causes more cracks and more complex cracking patterns in the slab compared to one-way slabs. For example, torsion of the slab may cause membrane shear cracks at certain levels in the slab. The results of the study presented in Chapter 5 can be used to provide a guidance on the reduction in shear stiffness of thin diaphragms due to out-of-plane loading.

7.1.3 Sloped-Column Irregularity

To investigate the influence of sloped gravity-load columns on the seismic response of concrete shear wall buildings, a variety of analytical studies were conducted for a range of different types of sloped gravity-load columns. Linear and nonlinear dynamic analyses including the response spectrum analysis (RSA) and time history analyses (THA) were carried out on a typical high-rise core wall building with cantilever shear walls in one direction and coupled shear walls in the perpendicular direction. All gravity-load columns, including the sloped columns, were modelled as linear elements, while the shear walls were modelled as either linear or nonlinear elements depending on the type of analysis. It was confirmed that vertical mass supported by sloped columns could be modelled as a concentrated mass to avoid having to include the floor slabs in the model, which would greatly increase the number of vertical modes of vibration.

The differential horizontal movement at the top and bottom of the sloped columns generates vertical movements in the gravity-load frame that need to be accounted for in the seismic design of the buildings with sloped columns. Differential horizontal acceleration at the top and bottom of the sloped column causes vertical acceleration of the mass supported by the column, which results in additional axial forces in gravity-load columns, additional shear forces and bending moments in shear walls, and additional forces in floor slabs. Vertical ground motions cause additional vertical acceleration of the mass supported on the sloped column.

The seismic forces in the sloped columns are due to the coupling of the lateral modes of the shear walls with the vertical modes of the mass supported on the columns. The degree of coupling of lateral and vertical modes depends on the column axial stiffnesses and the stiffnesses of the lateral force resisting system. When the first vertical mode is fully coupled with a lateral mode of the shear wall, the maximum increase occurs in the axial force of the column. The axial force increases are similar for symmetric and asymmetric arrangements of the sloped column and are generally larger in the shear wall (cantilever wall) direction compared to cantilever wall direction of the building. The maximum column force increases as the slope of the column (angle relative to the vertical) is increased, and the percentage increase in column force increases as the ratio of vertical to horizontal mass per floor decreases – a smaller vertical mass is accelerated vertically more easily.

The seismic forces in a sloped gravity-load column are highly sensitive to the axial stiffness of the column and the flexural stiffness of the lateral force resisting system (walls). Small changes in the stiffness of the column or the walls can result in large increases or large decreases in the column force. Since it is difficult to accurately determine the effective stiffness of the shear walls, a range of stiffness values needs to be considered to safely estimate the maximum increase in the sloped column axial force.

A simplified expression was developed to provide an upper-bound estimate of the maximum axial forces in sloped gravity-load columns in high-rise shear wall buildings. The procedure can be used instead of conducting numerous analyses with a range of stiffness values, and it explicitly accounts for the effect of vertical ground accelerations. The simplified solution was found to give a very reasonable upper-bound estimate of the maximum increase in the sloped column force when compared with the results from nonlinear time history analysis. The simplified procedure can be used for sloped columns supporting vertical mass distributed over a building height or supporting a single concentrated vertical mass.

Sloped columns can cause an increase in the seismic shear demands in SFRS at the elevation of the slope change in the column. A simple and conservative approach for estimating the shear force demand on SFRS in high-rise shear wall buildings with sloped columns is to increase the seismic shear force demand in the SFRS by the horizontal component of the maximum seismic force in the sloped gravity-load column determined from the simplified procedure.

7.2 Summary of Significant Contributions

A detailed summary of the conclusions from the investigation of each type of discontinuity/irregularity is summarized at the end of each chapter, and the important conclusions are further summarized in the sections above. In this section, a very brief high-level summary is given of the original and significant contributions made in this thesis looking “across” the three problems.

The three types of discontinuities/irregularities that were investigated in this thesis are issues that can significantly affect the design of high-rise concrete shear wall building and/or can significantly affect the performance of high-rise concrete shear wall buildings in an earthquake. For two of these, overhanging wall irregularity and sloped-column irregularity, no previous research has been done on these important problems prior to the current work. For the third problem, lateral stiffness discontinuity in shear walls causing large backstay forces, very limited work has previously been done to determine the effective stiffness of the diaphragms at different levels of backstay forces, which is the focus of the current study.

For all three discontinuities/irregularities, state-of-the-art nonlinear analyses were used in this thesis to investigate the problem. The nonlinear analysis tools were validated against experimental results wherever possible. For cases where the model could not be experimentally validated, multiple solutions were developed and the similarity of these provide the confirmation.

For each case, the nonlinear analysis models were used to study a wide range of parameters in order to gain a simple understanding of the “physics” of the irregularity /discontinuity. In the case of the overhanging wall irregularity, the simple explanation is that the overhang causes a magnification of the vertical compression strains and an even larger magnification of the horizontal tension strains, which together cause the early crushing of concrete. For the concrete diaphragms subjected to large backstay forces, it is flexural cracking due to strong-axis bending of diaphragms that causes large reductions in shear and flexural stiffness of the diaphragms. Finally, for sloped-column irregularity, it is the coupling of the vertical modes of the gravity frame with a lateral mode of the shear walls that causes large vertical acceleration of the mass supported by the sloped columns.

For each problem, simple engineering solutions were presented for how to deal with the problem. These solutions were based on a rational model rather than being purely empirically based (e.g., fit to the data). In a number of cases, multiple solutions with different levels of simplification and accuracy were presented. For the effective stiffness of concrete diaphragms subjected large backstay forces, three different models were presented for how the effective stiffness varies (nonlinear, linear, constant) between certain force levels. The nonlinear variation of stiffness is the most accurate, while the constant variation of stiffness is the easiest to implement. For the overhanging wall irregularity, a strain amplification factor was determined, which allows the magnified strains to be estimated from a linear analysis, and a simple strength-based limited was presented for avoiding concrete crushing. Finally, for sloped-column irregularity, a closed-form solution was presented for estimating the percentage increase in axial force in sloped columns due to vertical accelerations, which avoids the need for multiple analyses with different stiffness assumptions.

Finally, it is important to highlight the impact (or potential impact) of the research presented in this thesis. As already mentioned, the 2020 edition of the National Building Code of Canada has defined a new type of irregularity called "sloped-column irregularity" as a direct result of the work presented here. The 2014 edition of CSA Standard A23.3 (adopted in the 2018 BC Building Code) has a new requirement (Clause 21.5.2.2.9) requiring designers to conduct an analysis that considers the lower-bound and upper-bound value of effective stiffness of the diaphragms resisting backstay forces. The range of effective stiffness models presented here are exactly what designers need to implement these new building code requirements. Finally, the study on overhanging wall irregularity has clearly explained many of the unexpected failures of thin concrete shear walls observed because of the 2010 Maule (Chile) Earthquake. Thus, the information presented here gives designers the information they need to avoid such failures in buildings.

7.3 Recommendations for Future Work

The study on sloped-column irregularity is the first of its kind and had a limited scope. Only high-rise concrete shear wall buildings were investigated. Sloped-gravity load columns occur in many different types of buildings, e.g., frame buildings, low-rise buildings, etc., and additional work needs to be done to investigate this type of irregularity in these other building types.

Additional work can also be done investigating sloped-gravity columns in concrete shear wall buildings. For example, in the current study, the diaphragms connecting the sloped columns to the shear walls were modelled as rigid. It is expected that any flexibility of the diaphragm will have a similar effect as additional flexibility in the columns or shear walls – it may increase or decrease the axial force in the sloped column depending on the coupling of the modes. Nonetheless, this should be investigated.

The problem of discontinuity in lateral stiffness of concrete shear walls causing backstay forces is a complex problem that requires further work. For example, how the foundation walls transfer the lateral forces to the foundation with limited axial compression on these walls needs to be investigated. Also, the influence of the soil surrounding the foundation walls needs to be better understood.

The overhanging wall irregularity was the simplest of the three problems and extensive work was done on this. Nonetheless, additional work could be done. In the current study, the concrete in the wall was assumed unconfined as confinement reinforcement is rarely used in Canada. Other countries do provide a higher level of confinement reinforcement and therefore work could be done to investigate confined concrete walls. A three-dimensional nonlinear finite element model of the wall could be used to understand the variation of strains through the thickness of the wall.

Bibliography

ABAQUS Analysis user's manual (2016). Dassault Systems Simulia Corp., Providence, RI, USA; 2016.

Adebar, P.E. (2013). "Compression failure of thin concrete walls during 2010 Chile earthquake: lessons for Canadian design practice", *Canadian Journal of Civil Engineering*, Vol. 40, No. 8, pp. 711-721.

Adebar, P.E. and Collins, M.P. (1994). "Shear Design of Concrete Offshore Structures", *AC1 Structural Journal*, Vol. 91, No. 3, 1994, pp. 324-335.

Adebar, P. and Ibrahim, A.A. (2002). "Simple nonlinear flexural stiffness model for concrete structural walls", Earthquake Spectra, Vol. 18, No. 3, pp. 407-426.

Adebar, P.; Ibrahim, A. M. M.; and Bryson, M. (2007). "Test of a High-Rise Core Wall: Effective Stiffness for Seismic Analysis", *ACI Structural Journal*, V. 104, No. 5, Sept.-Oct. 2007, pp. 549-559.

Adebar, P., Mutrie, J., DeVall, R. (2005), "Ductility of concrete walls: the Canadian seismic design provision 1984 to 2004", *Canadian Journal of Civil Engineering*, Vol. 32, No. 6, Dec. 2005, 1124-1137.

ASCE (2010). *Minimum design loads for building and other structures (ASCE/SEI 7-10)*, American Society of Civil Engineers, Reston, VA.

ATC 72 (2010). ATC-72-1: *Interim Guidelines on Modeling and Acceptance Criteria for Seismic Design and Analysis of Tall Buildings*, Applied Technology Council, Redwood City, CA.

Bentz, E.C. (2000), "Sectional Analysis of Reinforced Concrete", PhD Thesis, Department of Civil Engineering, University of Toronto, 2000.

Bentz, E.C., Collins, M.P. (2000). "Response 2000." www.ecf.utoronto.ca/~bentz/r2k.htm.

Bernal, D., Döhler M., Kojidi S. M., Kwan K., Liu, Y. (2015). “First mode damping ratios for buildings”, *Earthq. Spectra*, 31(1): 367–381.

Bohl Arbulu, A. G. (2007), “Plastic Hinge Length in High-Rise Concrete Shear Walls”, MASc thesis, Department of Civil Engineering, University of British Columbia, Vancouver, BC, Canada, 2007, 250 pp.

Bohl, A. and Adebar, P. (2011). “Plastic Hinge Lengths in High-Rise Concrete Shear Walls”, *ACI Structural Journal*, V. 108, No. 2, March-April 2011, pp. 148-158.

Collins, M.P. and Mitchell, D. (1991), “Prestressed Concrete Structures”, Prentice Hall, Englewood Cliffs, 1991, 766 pp.

Chopra, A.K., (2012). “Dynamics of Structures: Theory and Applications to Earthquake Engineering”, Fourth Edition, Pearson Education Inc., publishing as Prentice Hall, One Lake Street, Upper Saddle River, Boston, MA.

Cruz C., Miranda E. (2016). “Evaluation of damping ratios for the seismic analysis of tall Buildings”, ASCE, *J. Struct. Eng.*, ASCE, DOI: 10.1061/(ASCE)ST.1943-541X.0001628.

CSA Standard A23.3 (2014). Design of Concrete Structures, CSA Standards Association, Mississauga, Ont.

CSI Computers and Structures Inc., https://www.csiamerica.com/products/perform-3d

Dupuis M.R., Elwood K.E., Best T., Anderson D.L. (2014). “Seismic performance of shear wall buildings with gravity-induced lateral demands”, *Canadian Journal of Civil Engineering*, 41 (4): 323–332.

Elwood, K.J. (2013), “Performance of concrete buildings in the 22 February 2011 Christchurch earthquake and implications for Canadian codes”, *Canadian Journal of Civil Engineering*, Vol. 40, pp.759-776.

FEMA 356 (2000). *Prestandard and Commentary for the Seismic Rehabilitation of Buildings*, Federal Emergency Management Agency and American Society of Civil Engineers, Reston, Virginia.

Finn, L., Bebamzadeh, A. (2017). “Ground Motions Selection and Scaling for St. Paul’s Hospital, Vancouver, BC”, Report prepared for: IBI Group and Fast + Epp, July 2017.

Genikomsou, A.S., Polak, M.A. (2015). “Finite element analysis of punching shear of concrete slabs using damaged plasticity model in ABAQUS”, *Journal of Engineering Structures*, 98 (2015), pp. 38-48.

Ibrahim A.M.M. (2000). “Early Crushing Failure of High-Rise Shear Walls with no Boundary Confinement”, PhD Dissertation, Department of Civil Engineering, University of British Columbia.

Kang, S.M., Park, H.G. and Kim, J.Y. (2015), “Investigating the Behaviour of Reinforced Concrete Shell Elements”, *Advances in Structural Engineering*, Vol. 18, No. 7, pp. 1029-1042.

Kirschner, U. (1986), “Investigating the Behaviour of Reinforced Concrete Shell Elements”, PhD Dissertation, Department of Civil Engineering, University of Toronto, 221 pp.

Kirschner, U. and Collins, M.P. (1986), “Investigating the Behaviour of Reinforced Concrete Shell Elements”, Publication No 86-09, Department of Civil Engineering, University of Toronto, Sep. 1986, 209 pp.

Kupfer, H., Hilsdorf, H.K.and Rusch, H. (1969), “Behavior of Concrete under Biaxial Stress”, *ACI Structural Journal*, Vol. 87, No. 2, pp.656-666.

LATBSDC (2017). Los Angeles Tall Buildings Structural Design Council: *An Alternative Procedure for Seismic Analysis and Design of Tall Buildings Located in the Los Angeles Region*, Los Angeles, CA.

Mitchell, D., Paultre, P, and Adebar, P. (2015). Chapter 11, CAC Concrete Design Handbook.

Naeim, F., Lew, M., Carpenter, L.D., Youssef, N.F., Rojas, F., Saragoni, G.R. and Adaros, M.S. (2011). "Performance of tall buildings in Santiago, Chile during 27 February 2010 offshore Maule, Chile earthquake", The *Structural Design of Tall and Special Buildpngs*, Vol. 20, pp.1-16.

National Building Code of Canada (2015). National Research Council Canada.

PEER. (2010). *Technical Report for the PEER Ground Motion Database Web Application*. Pacific Earthquake Engineering Research Center, University of California, Berkeley, Ca.

PERFORM Components and Elements for PERFORM-3D and PERFORM-COLLAPSE (2006), CSi Computers and Structures Inc., CA, USA.

PERFORM-3D User Guide (2006), "Nonlinear Analysis and Performance Assessment for 3D Structures", CSi Computers and Structures Inc., CA, USA.

Porasz, A. (1989), "An Investigation of the Stress-Strain Characteristics of High Strength Concrete in Shear", M.ASc. Thesis, University of Toronto, 1989.

Sherstobitoff, J., Cajiao, P., and Adebar, P. (2012), "Repair of an 18-story shear wall building damaged in the 2010 Chile earthquake", *Earthquake Spectra*, Vol. 28 (S1), pp. S335-S348.

Simulia. *Abaqus Unified FEA Software*, Providence, RI, USA.

Structural Commentaries (2015). User's Guide – NBCC 2015: Part 4 of Division B. Canadian Commission on Building and Fire Codes. National Research Council Canada.

TBI (2017). Tall Buildings Initiative: *Guidelines for Performance-Based Seismic Design of Tall Buildings*. Pacific Earthquake Engineering Center, Report No. 2017/06.

Vecchio, F. J. (2000), "Disturbed Stress Field Model for Reinforced Concrete: Formulation", *Journal of Structural Engineering*, ASCE, V. 126, No. 9, 2000, pp. 1070-1077.

Vecchio, F.J. and Collins, M.P. (1982), "The Response of Reinforced Concrete to In-Plane Shear and Normal Stresses", *Publication No.* 8243, Department of Civil Engineering, University of Toronto, 1982, 332 pp.

Vecchio, F. J., and Collins, M. P. (1986). “The Modified Compression-Field Theory for Reinforced Concrete Elements Subjected to Shear”, ACI Structural Journal, Proceedings V. 83, No. 2, Mar.-Apr. 1986, pp. 219-231.

VecTor Analysis Group Website, University of Toronto: www.civ.utoronto.ca/vector/

Walraven, J.C. (1981). “Fundamental Analysis of Aggregate Interlock”, *Journal of the Structural Division*, ASCE, Vol. 107 No. ST11, Nov. 1981 pp. 2245-2270.

Wong, P. S., and Vecchio, F. J. (2002). “VecTor2 and FormWorks User’s Manual”, *Report*, Department of Civil Engineering, University of Toronto, Toronto, ON, Canada, 2002, 232 pp.

Yathon, J. S. (2011). “Seismic Shear Demand in Reinforced Concrete Cantilever Walls”, M.Sc. Thesis, Department of Civil Engineering, The University of British Columbia, Vancouver, Canada, pp. 155.

Yathon J, Adebar P, Elwood, K. (2017). “A Detailed Inventory of Non-Ductile Concrete Shear Wall Buildings,” *EERI Spectra*, May 2017, Vol. 33, No. 2, pp. 605-622.

Yathon, J.S., Elwood, K.J., and Adebar, P.E. (2014). “Seismic characteristics of pre-1980 tall reinforced concrete buildings in Vancouver,” *Proceedings of the 10th National Conference in Earthquake Engineering*, EERI, Anchorage, AK, 2014.

Appendices

Appendix A Material Model Parameters and Analysis Results for Concrete Shear Walls with Overhanging Wall Irregularity

Material Parameters Used in ABAQUS and VecTor2 Models

Table A.1 gives the details of material parameters used for different sections in ABAQUS model.

Table 0.1 – Material properties for different concrete sections in ABAQUS model of the overhanging wall

Section	$f'_c\ (MPa)$	$f'_t\ (MPa)$	ρ_x (%)	ρ_y (%)
1	30	1	0.5	0.5
2	30	1	3	0.5
3	30	5	0.5	3
4	30	5	3	3
5	30	20	0.5	1
6	30	20	3	1

Eight different concrete materials were used to represent various regions of the wall in the VecTor2 model. Tables A2 to A.5 lists the properties of concrete materials.

Table A.2 – Properties of Material 1 and Material 2 in VecTor2 model of the overhanging wall

Concrete Properties	Material 1		Material 2	
Thickness (mm)	200		200	
Cylinder Compressive Strength (MPa)	30		30	
Tensile Strength (MPa)	1.83		1.83	
Poisson's Ratio	0.2		0.2	
Reinforcement Properties	x-direction	y-direction	x-direction	y-direction
Reinforcement ratio (%)	0.5	0.5	0.5	3
Reinforcement diameter (mm)	11.3	16	11.3	19.5
Yield Strength (MPa)	400	400	400	400
Ultimate Strength (MPa)	650	650	650	650
Elastic Modulus (MPa)	200,000	200,000	200,000	200,000
Strain Hardening Strain (mm/m)	7	7	7	7

Table A.3 – Properties of Material 3 and Material 4 in VecTor2 model of the overhanging wall

Concrete Properties	Material 3		Material 4	
Thickness (mm)	200		200	
Cylinder Compressive Strength (MPa)	60		60	
Tensile Strength (MPa)	60		60	
Poisson's Ratio	0.2		0.2	
Reinforcement Properties	x-direction	y-direction	x-direction	y-direction
Reinforcement ratio (%)	0.5	0.5	0.5	3
Reinforcement diameter (mm)	11.3	16	11.3	19.5
Yield Strength (MPa)	400	400	400	400
Ultimate Strength (MPa)	650	650	650	650
Elastic Modulus (MPa)	200,000	200,000	200,000	200,000
Strain Hardening Strain (mm/m)	7	7	7	7

Table 0.4 – Properties of Material 5 and Material 6 in VecTor2 model of the overhanging wall

Concrete Properties	Material 5		Material 6	
Thickness (mm)	200		200	
Cylinder Compressive Strength (MPa)	30		30	
Tensile Strength (MPa)	20		20	
Poisson's Ratio	0.2		0.2	
Reinforcement Properties	x-direction	y-direction	x-direction	y-direction
Reinforcement ratio (%)	3	0.5	3	3
Reinforcement diameter (mm)	16	16	16	19.5
Yield Strength (MPa)	400	400	400	400
Ultimate Strength (MPa)	650	650	650	650
Elastic Modulus (MPa)	200,000	200,000	200,000	200,000
Strain Hardening Strain (mm/m)	7	7	7	7

Table 0.5 – Properties of Material 7 and Material 8 in VecTor2 model of the overhanging wall

Concrete Properties	Material 7		Material 8	
Thickness (mm)	200		200	
Cylinder Compressive Strength (MPa)	30		30	
Tensile Strength (MPa)	5		5	
Poisson's Ratio	0.2		0.2	
Reinforcement Properties	x-direction	y-direction	x-direction	y-direction
Reinforcement ratio (%)	3	0.5	3	3
Reinforcement diameter (mm)	16	16	16	19.5
Yield Strength (MPa)	400	400	400	400
Ultimate Strength (MPa)	650	650	650	650
Elastic Modulus (MPa)	200,000	200,000	200,000	200,000
Strain Hardening Strain (mm/m)	7	7	7	7

Nonlinear Finite Element Analysis Results

The vertical profiles of strains along the compression edge of the lower wall for five different overhang lengths and the maximum compression linear strain (MCLS) of 0.0005 and 0.0015 are presented in Figures A.1 and A.2.

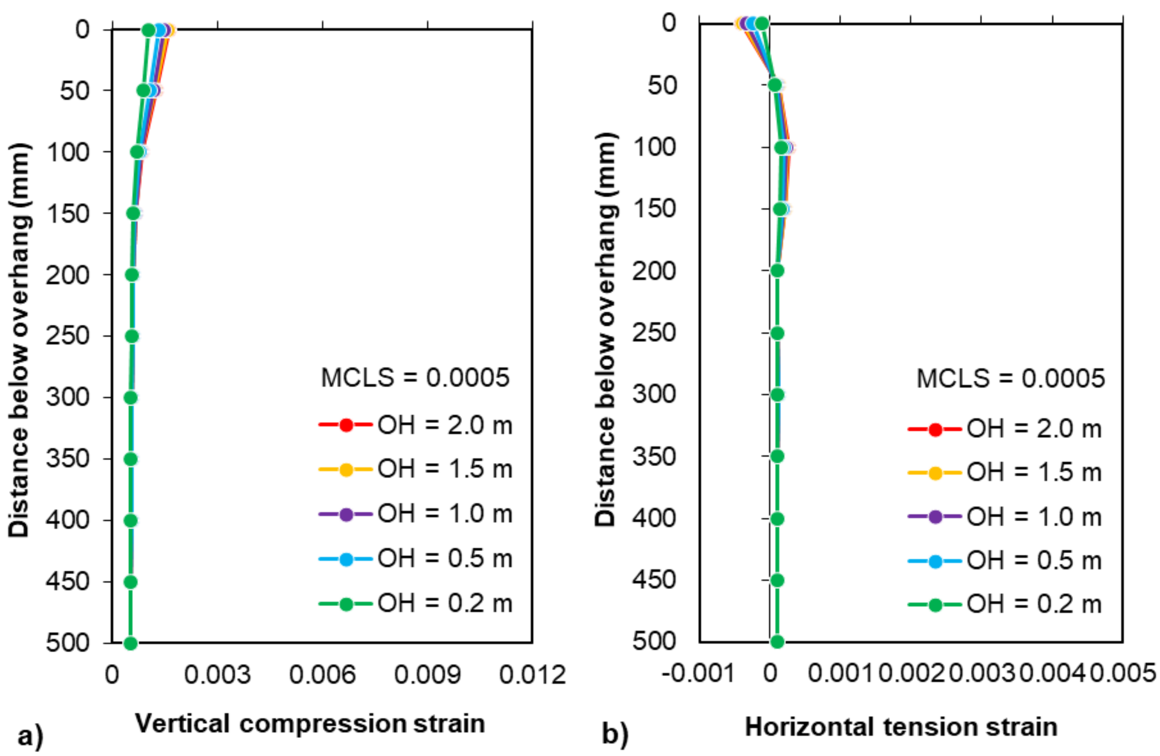

Figure A.1 – Vertical profiles of strains for different size of overhangs when the compression strain in the uniform strain region is 0.0005: (a) vertical compression strain; (b) horizontal tension strain

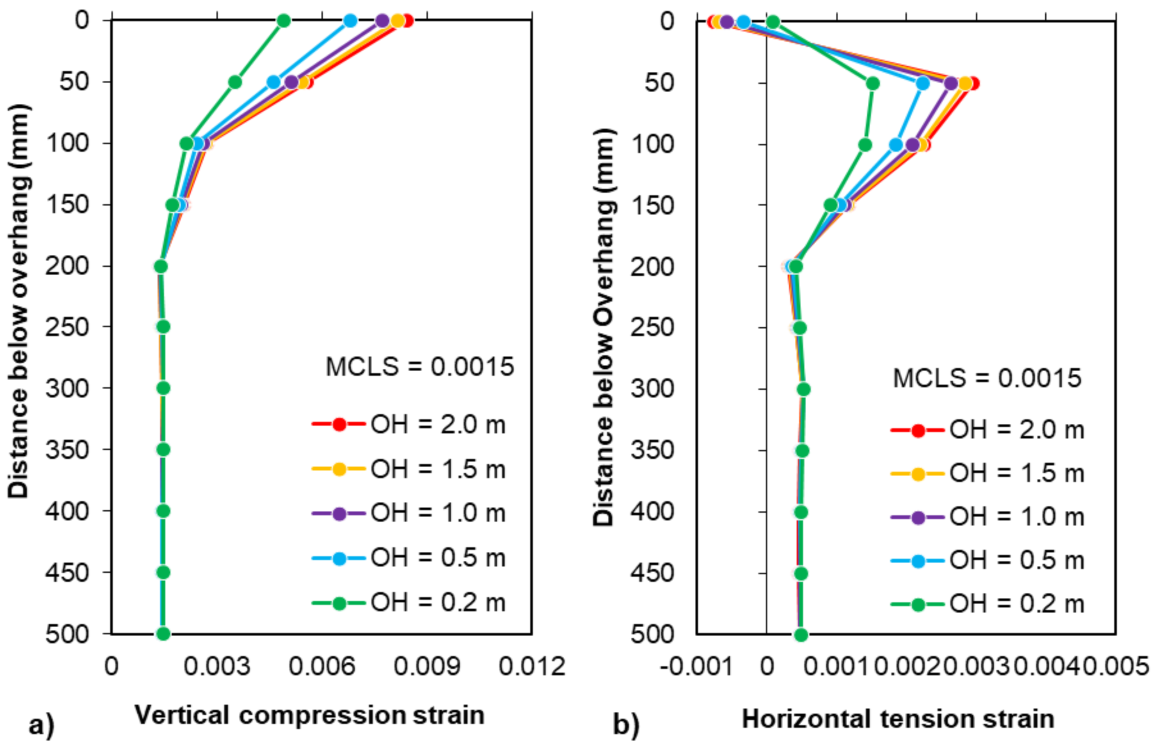

Figure A.2 – Vertical profiles of strains for different size of overhangs when the compression strain in the uniform strain region is 0.0015: (a) vertical compression strain; (b) horizontal tension strain

Figures A.3 to A.6 show the vertical profile of strains along the compression edge of the lower wall for different overhang lengths of 0.2, 0.5, 1.5 and 2.0 m at different levels of the maximum compression linear strain (MCLS) varying from 0.0005 to 0.002, respectively.

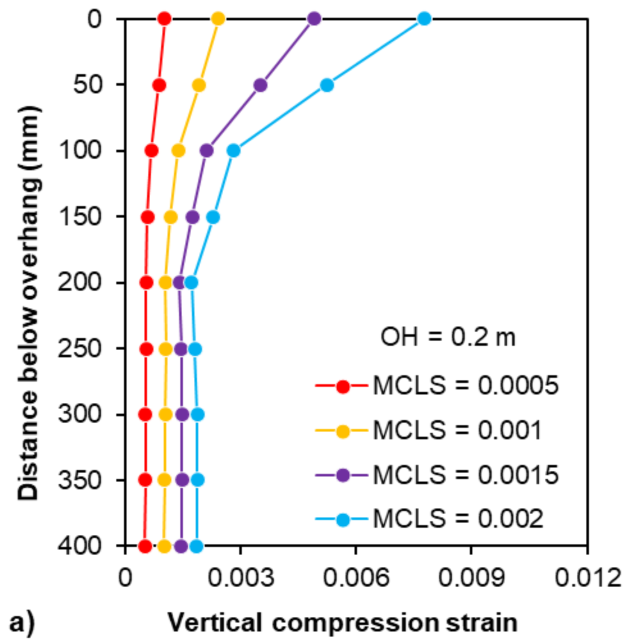

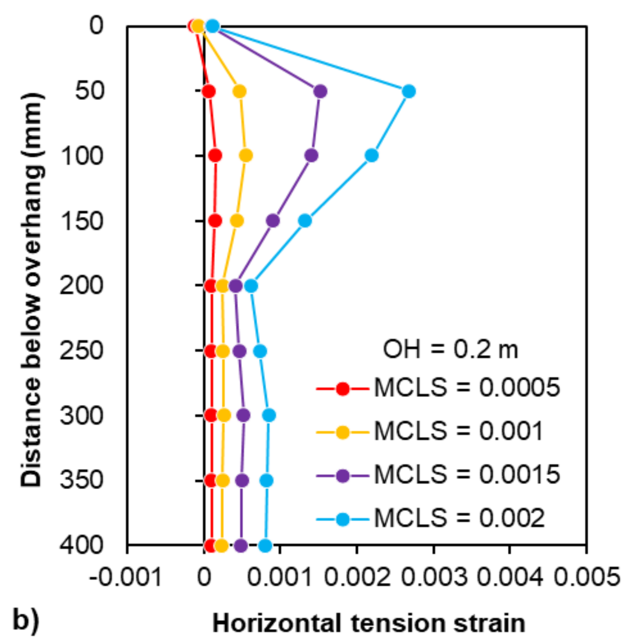

Figure A.3 – Vertical profiles of strains for 0.2 m overhang when the maximum compression linear strain (MCLS) in the uniform strain region is 0.0005, 0.001, 0.0015, and 0.002: (a) vertical compression strain, and; (b) horizontal tension strain

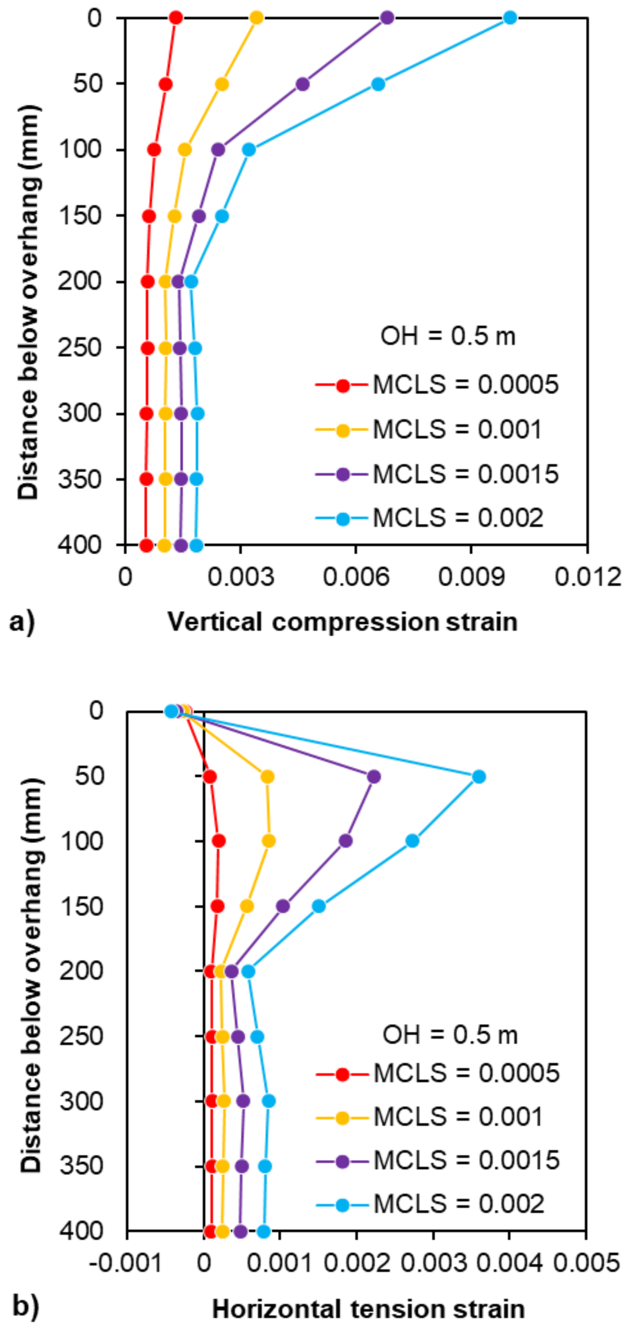

Figure A.4 – Vertical profiles of strains for 0.5 m overhang when the maximum compression linear strain (MCLS) in the uniform strain region is 0.0005, 0.001, 0.0015, and 0.002: (a) vertical compression strain, and; (b) horizontal tension strain

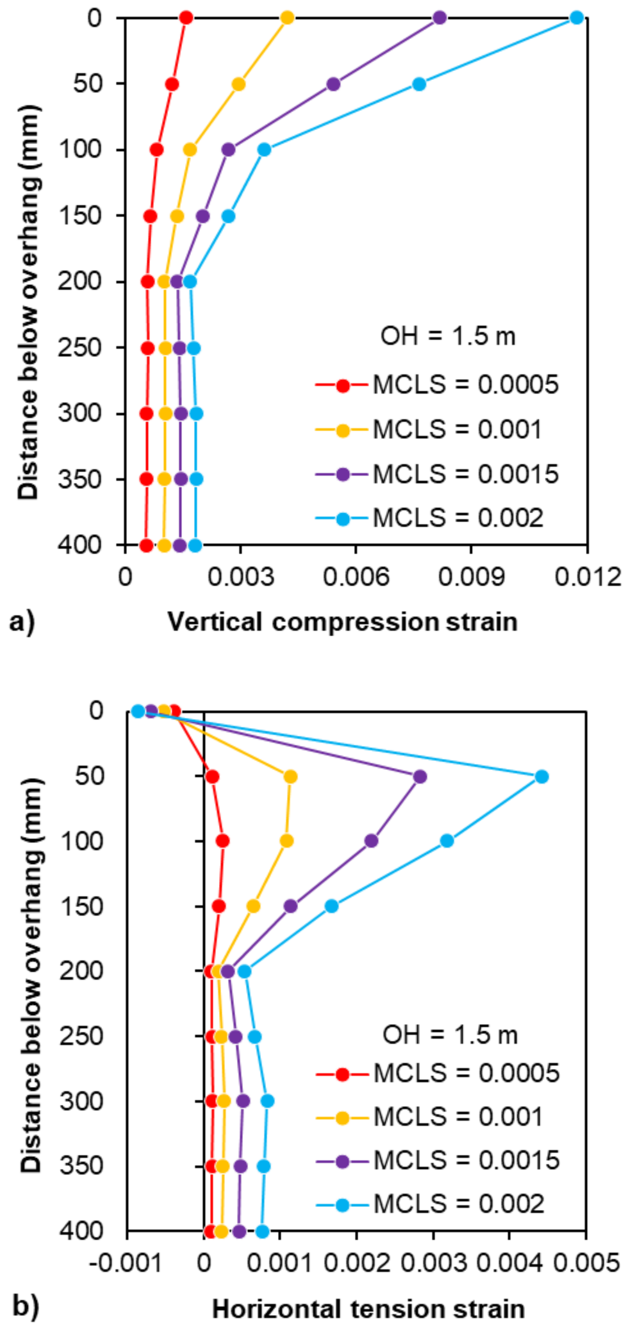

Figure A.5 – Vertical profiles of strains for 1.5 m overhang when the maximum compression linear strain (MCLS) in the uniform strain region is 0.0005, 0.001, 0.0015, and 0.002: (a) vertical compression strain, and; (b) horizontal tension strain

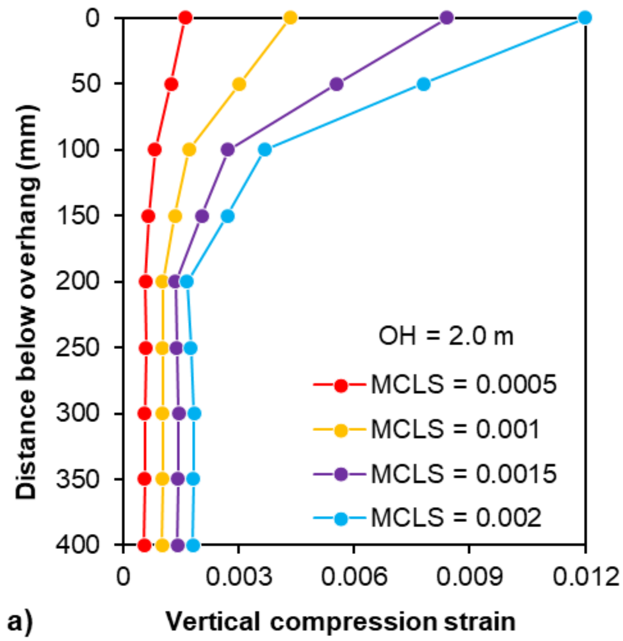

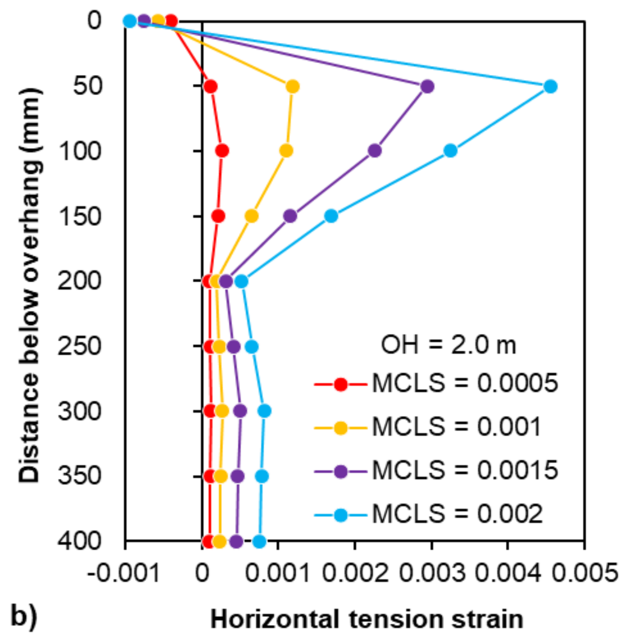

Figure A.6 – Vertical profiles of strains for 2.0 m overhang when the maximum compression linear strain (MCLS) in the uniform strain region is 0.0005, 0.001, 0.0015, and 0.002: (a) vertical compression strain, and; (b) horizontal tension strain

Figures A.7 to A.10 depict the horizontal profiles of vertical strains along the 1000 mm length in flexural compression region of the lower wall for overhang lengths of 0.2, 0.5, 1.5 and 2.0, and two levels of the maximum compression linear strain (MCLS = 0.001 and 0.002).

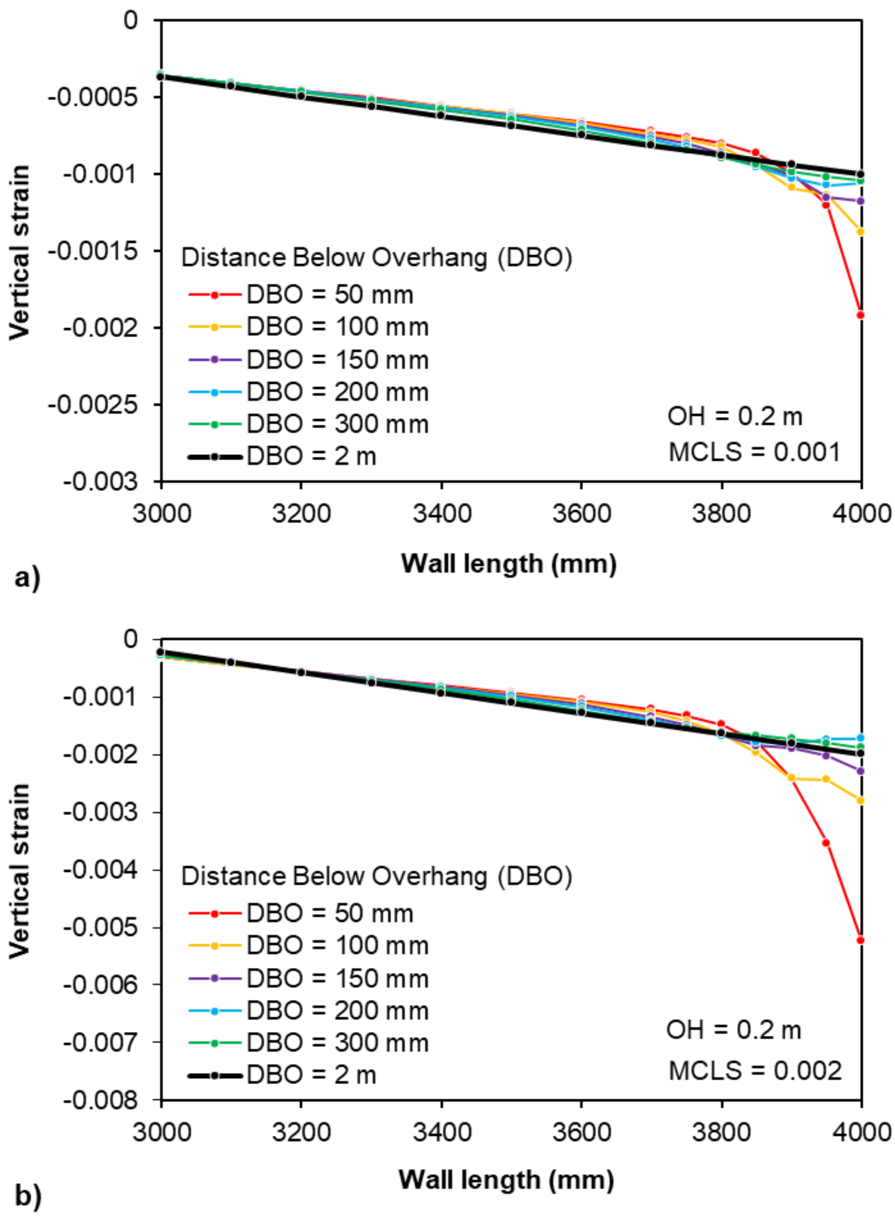

Figure A.7 – Horizontal profiles of vertical compression strain in flexural compression region of lower wall for overhang length of 0.2 m and the maximum compression linear strain (MCLS) of: (a) 0.001, and (b) 0.002

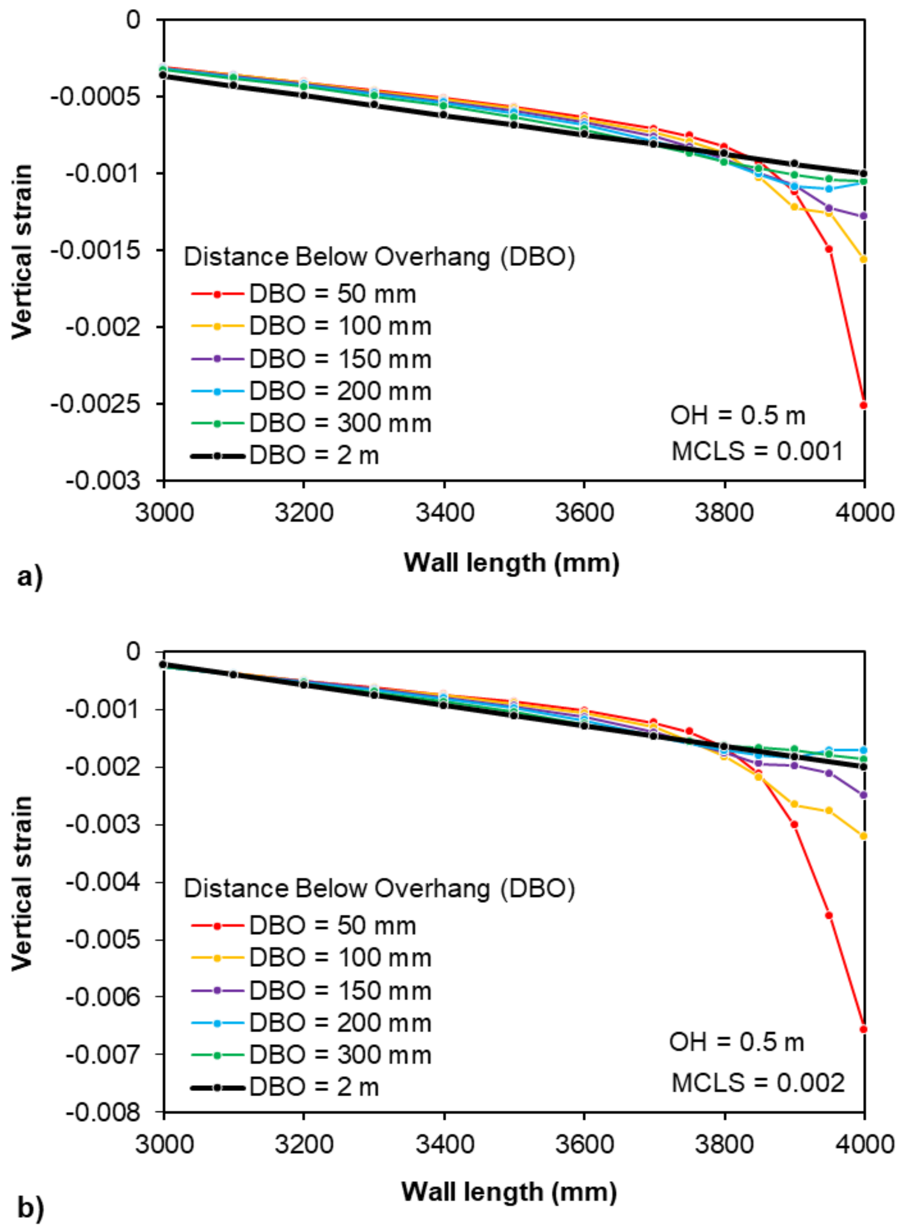

Figure A.8 – Horizontal profiles of vertical compression strain in flexural compression region of lower wall for overhang length of 0.5 m and the maximum compression linear strain (MCLS) of: (a) 0.001, and (b) 0.002

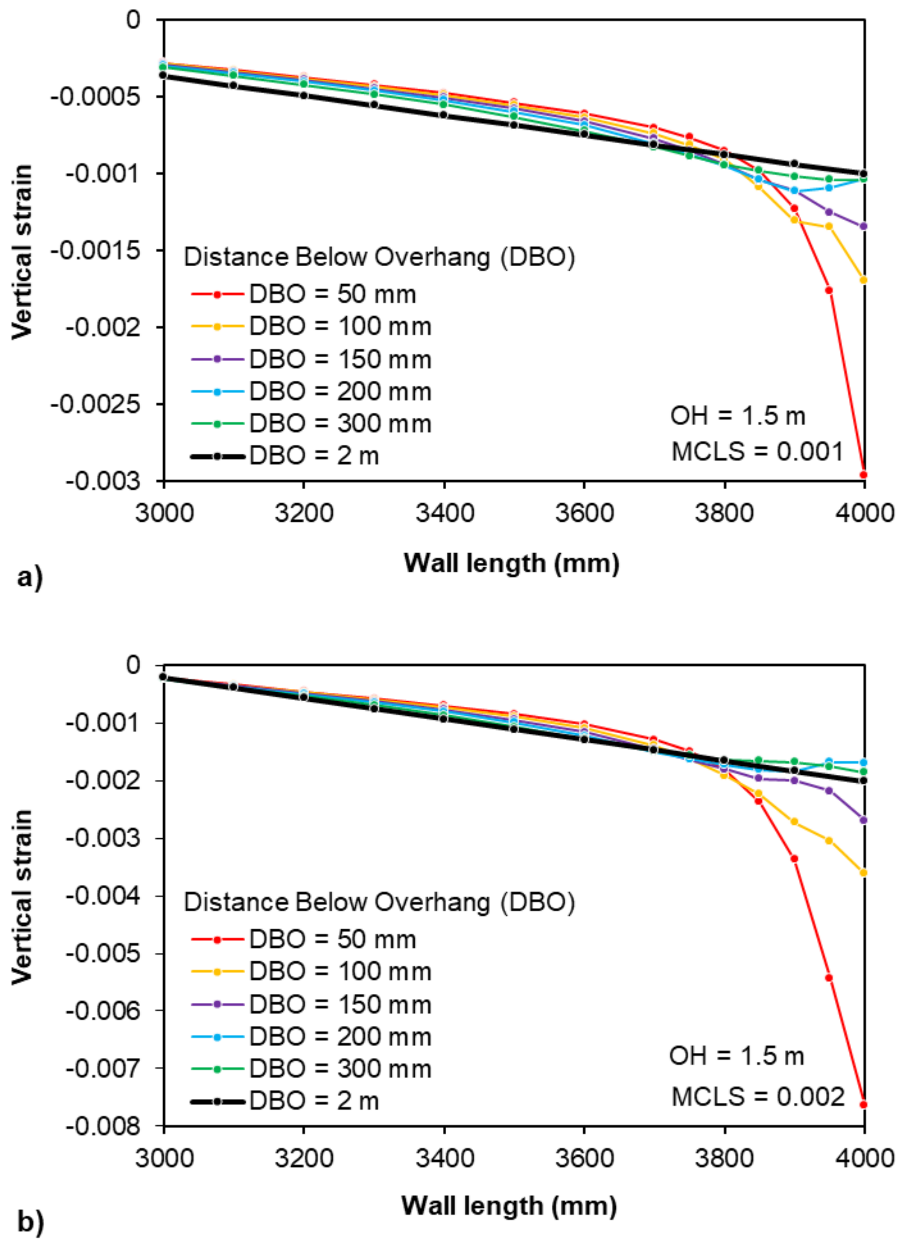

Figure A.9 – Horizontal profiles of vertical compression strain in flexural compression region of lower wall for overhang length of 1.5 m and the maximum compression linear strain (MCLS) of: (a) 0.001, and (b) 0.002

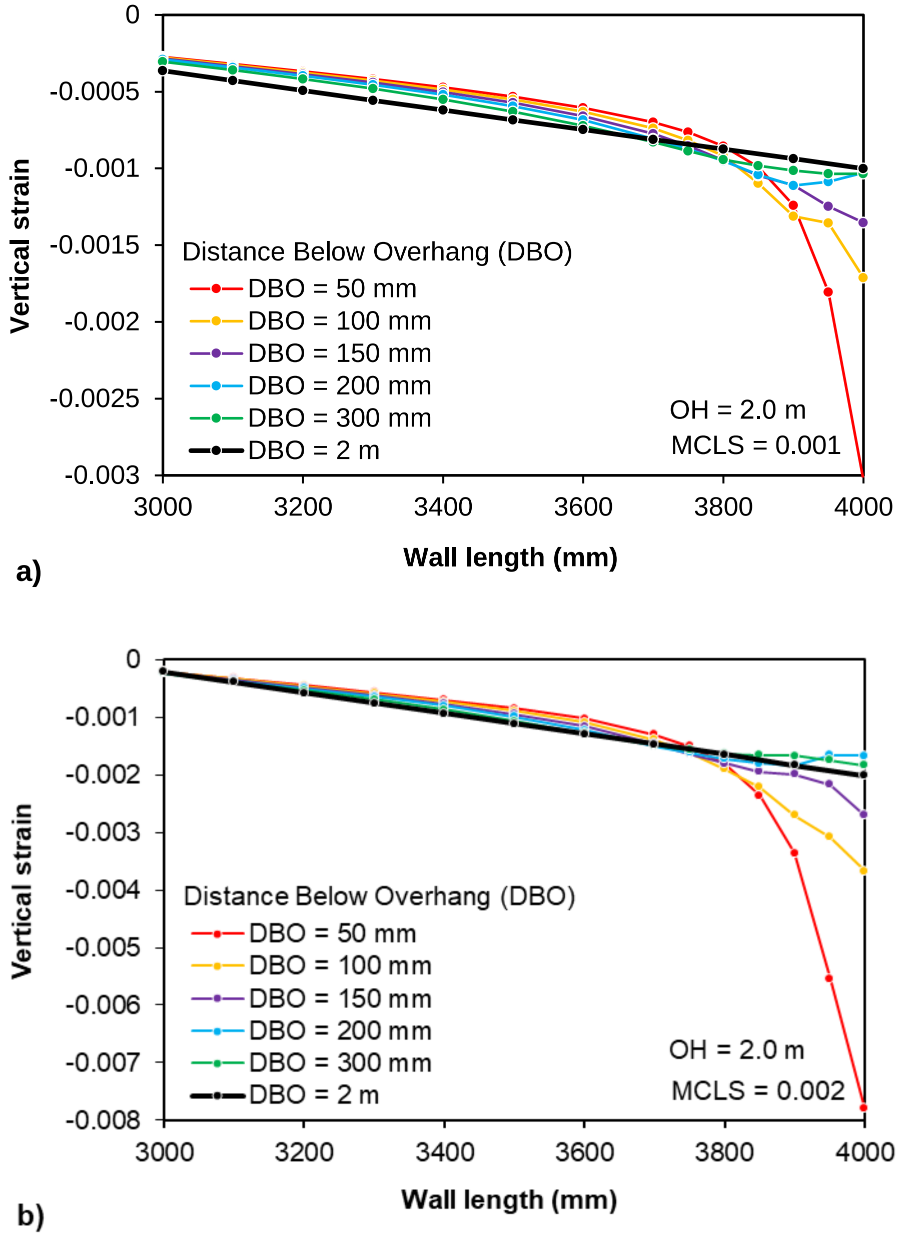

Figure A.10 – Horizontal profiles of vertical compression strain in flexural compression region of lower wall for overhang length of 2.0 m and the maximum compression linear strain (MCLS) of: (a) 0.001, and (b) 0.002

Figure A.11 presents a summary of the principal strain components in the region with large inelastic strains immediately below the overhang for the case that the maximum compression linear strain (MCLS) in the uniform strain region is 0.001.

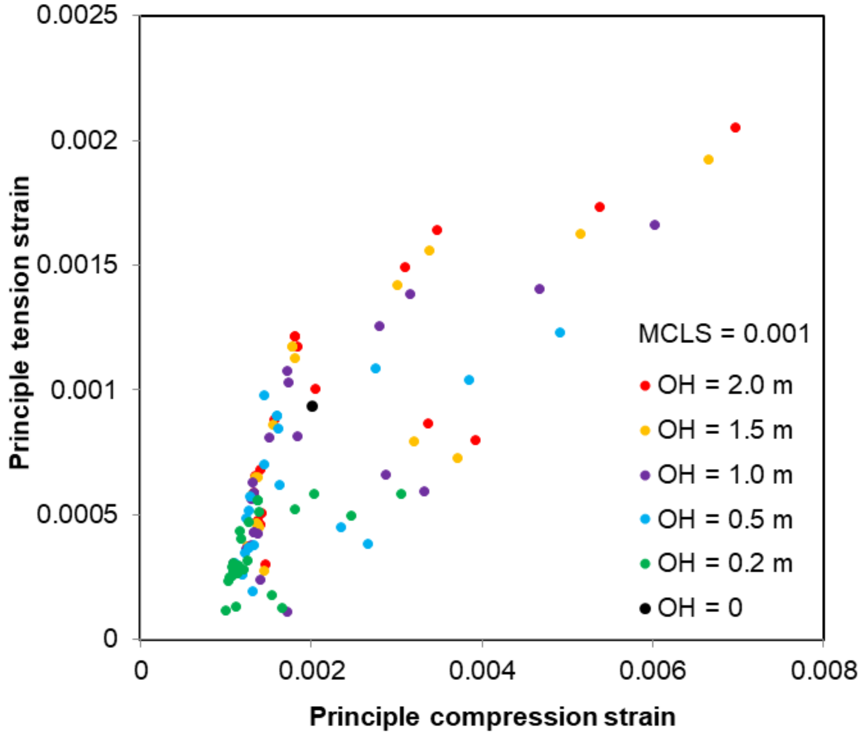

Figure A.11 – Principal strain components in the wall immediately below the overhang when the maximum compression strain in the uniform strain region is 0.001

The effect of axial load, reinforcement ratio and allowable strain level at 50 mm below overhang on the bending moment and curvature capacities of the wall for different overhang lengths of 0.2, 0.5, 1.0 and 1.5 m are shown in Figures A.12 to A.15, respectively.

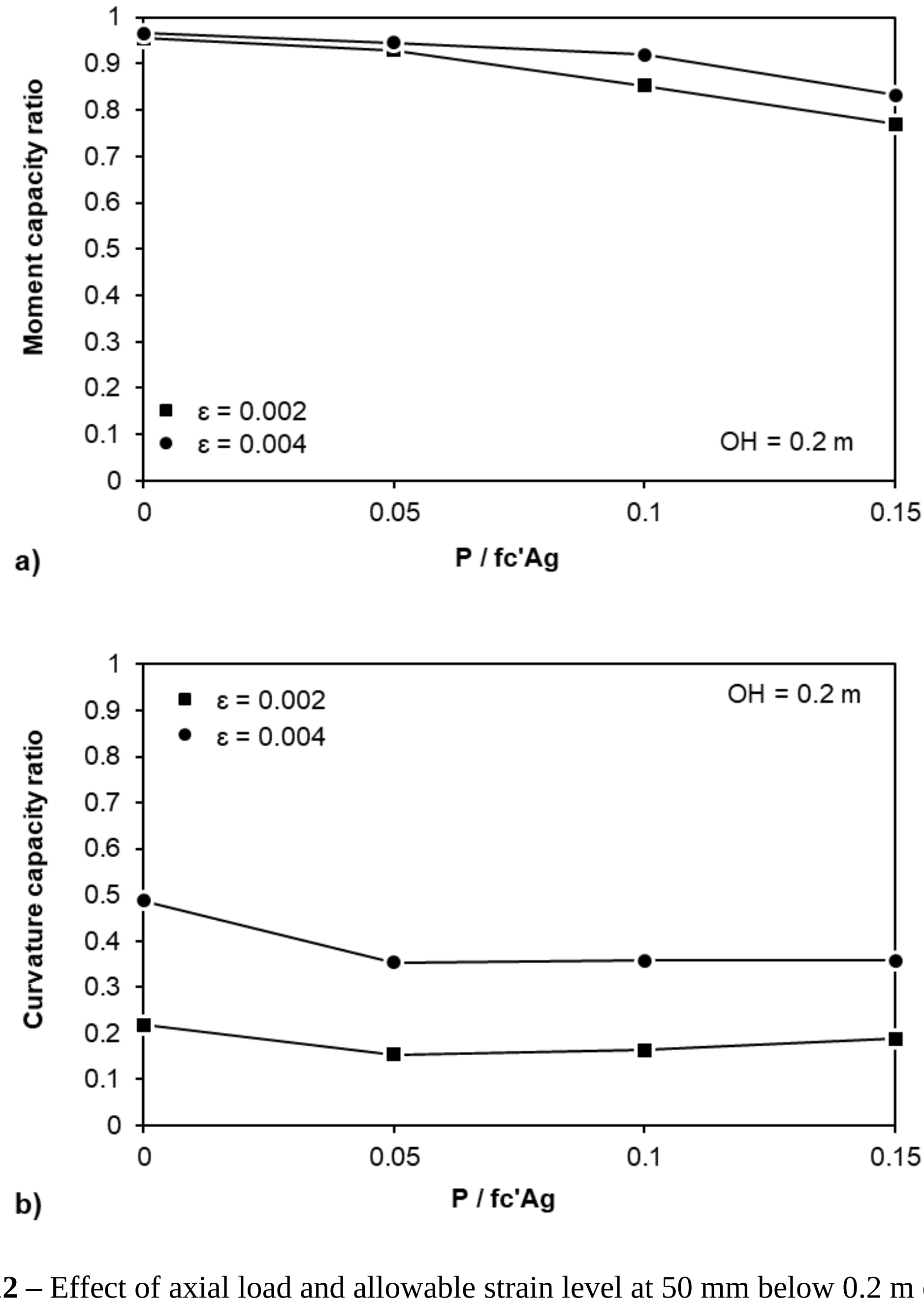

Figure A.12 – Effect of axial load and allowable strain level at 50 mm below 0.2 m overhang on: (a) the moment capacity, and; (b) the curvature capacity of the wall

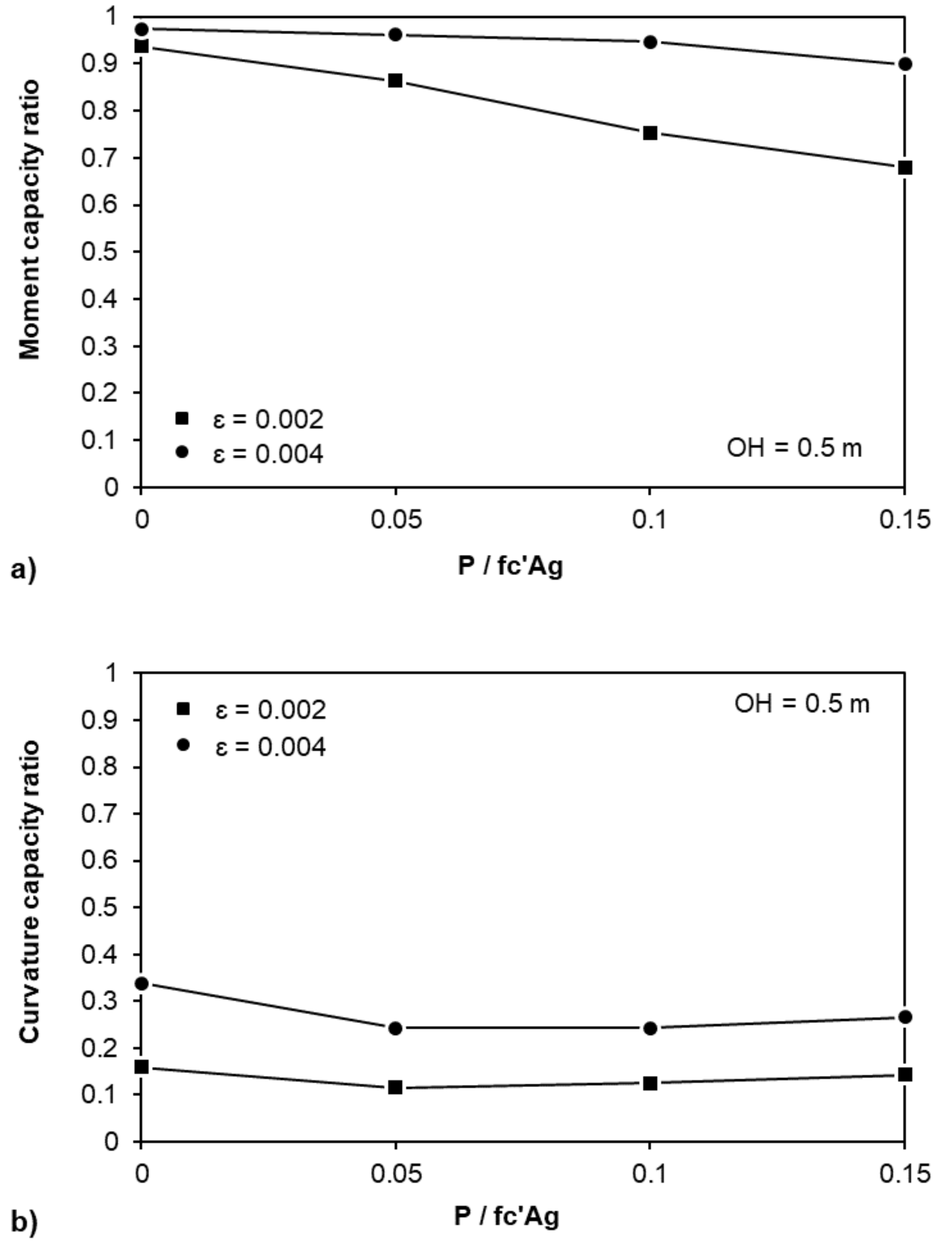

Figure A.13 – Effect of axial load and allowable strain level at 50 mm below 0.5 m overhang on: (a) the moment capacity, and; (b) the curvature capacity of the wall

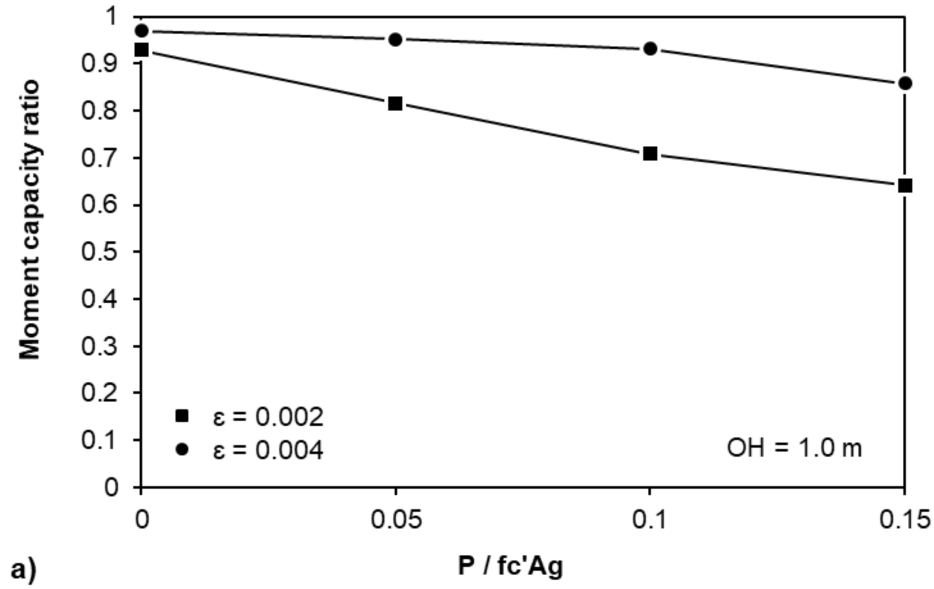

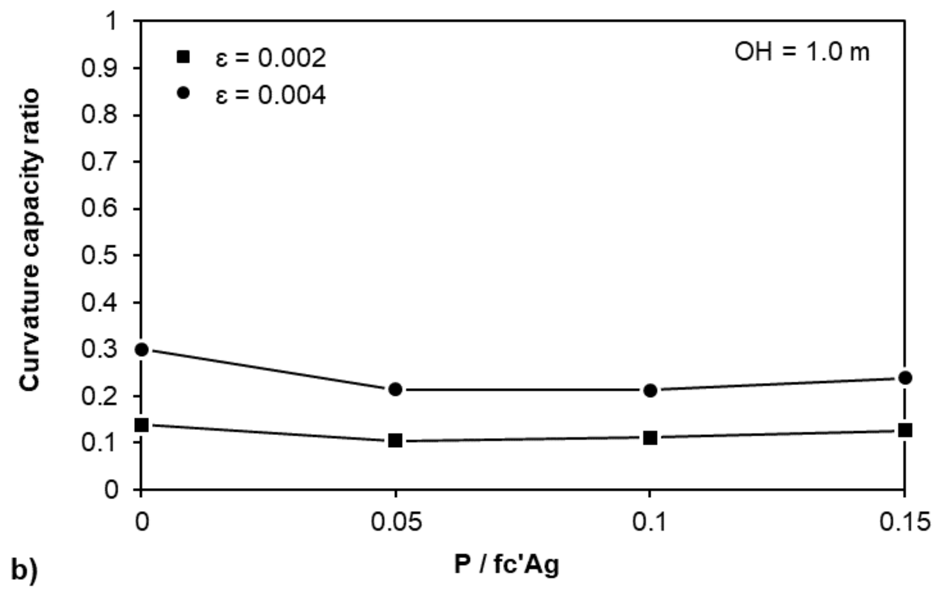

Figure A.14 – Effect of axial load and allowable strain level at 50 mm below 1.0 m overhang on: (a) the moment capacity, and; (b) the curvature capacity of the wall

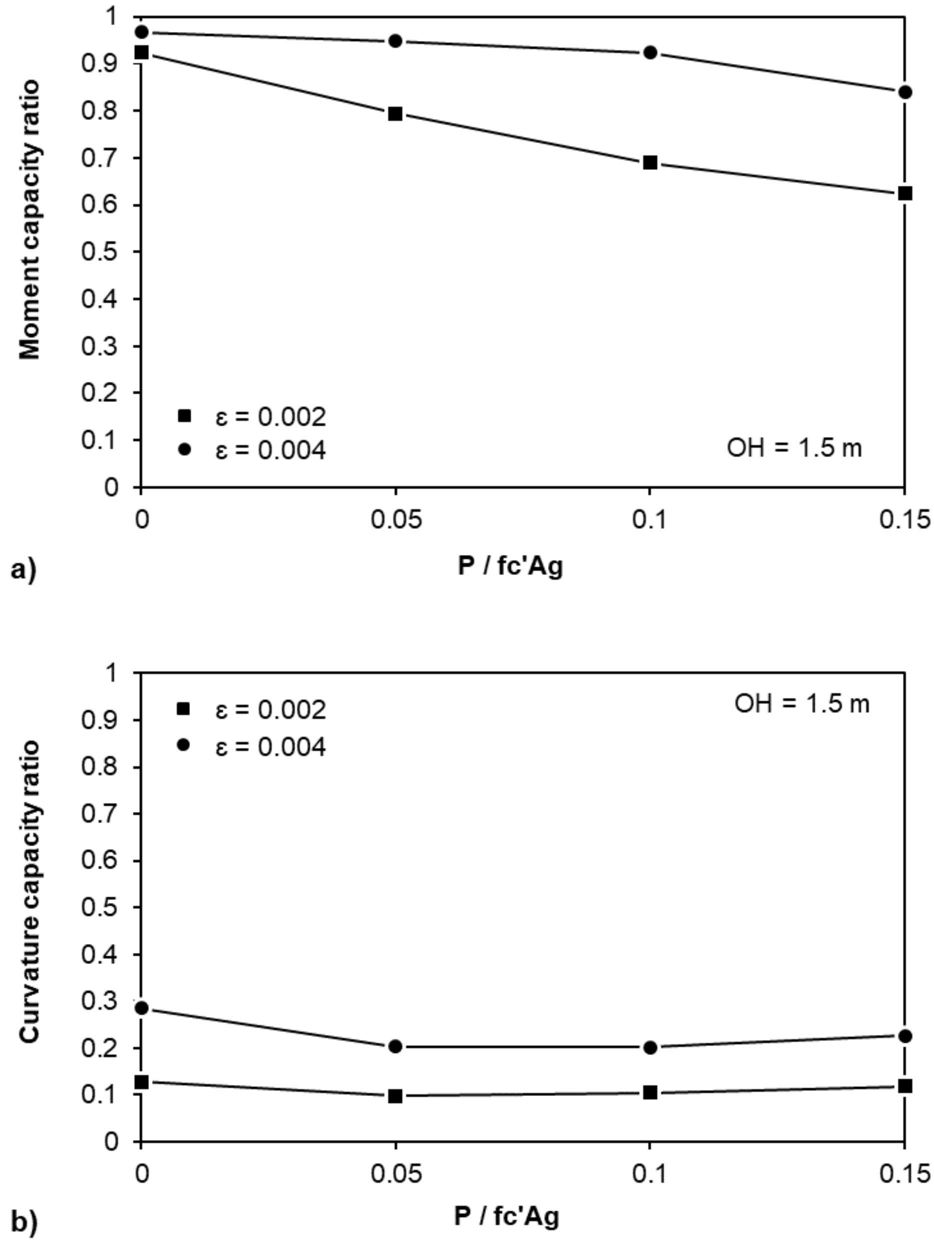

Figure A.15 – Effect of axial load and allowable strain level at 50 mm below 1.5 m overhang on: (a) the moment capacity, and; (b) the curvature capacity of the wall

Appendix B Diaphragm Test by Nakashima (1981)

The study by Nakashima (1981) was proposed to investigate the in-plane characteristics of reinforced concrete floor slabs under various loading and supporting conditions and to provide meaningful information for the design of the floor slabs. This study was concentrated on the floor slab system with edge beams, referred to as the beam-supported slab (slab-on-beam) system. The prototype floor slab for test specimens was isolated from a rectangular multi-story, multi-bay reinforced concrete building, in which earthquake resistance was provided by shear walls. Seismic forces at various floor levels were transmitted to the walls by the diaphragm action of the floor slabs. Structural dimensions were chosen to represent a building of medium to high rise. The center-to-center span length of slab panels were 7320 mm in both directions, the columns were 610 mm × 610 mm with no capital, the slab was 180 mm thick, and the beams were 610 mm × 310 mm in their cross sections. A portion of the plan view of the prototype floor system is shown in Figure B.1.

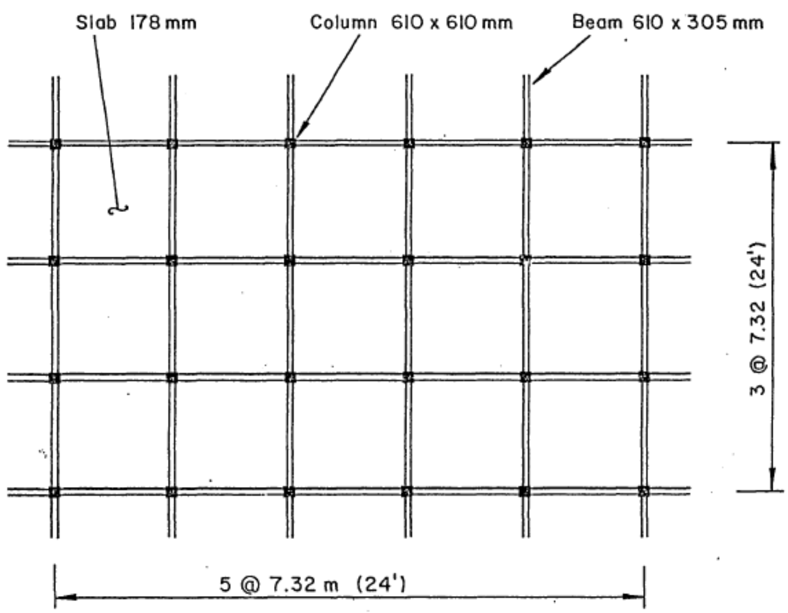

Figure B.1 – Prototype floor slab (Nakashima, 1981)

Special care was given to the size of reinforcing bars. Figure B.2 shows the arrangement of the reinforcing bars and Table B.1 lists the dimension, the design moment, and the area. The table shows that the temperature requirement (0.0018 times the gross area) controls the amount of steel required at many critical sections. Two specimens were constructed and casted at the same time. The two specimens are labelled B-l specimen and B-2 specimen. Two kinds of concrete were prepared: 27.6 MPa for the floor slabs and the walls and 34.5 MPa for the columns. Sixteen 76 mm × 150 mm and ten 150 mm × 300 mm concrete test cylinders were made from each batch of concrete. The specimens and cylinders were cured for fourteen days under moist burlap at room temperature. On the fifteenth day after the placing, the burlap was removed. The specimens and concrete test cylinders were then air-cured until tested.

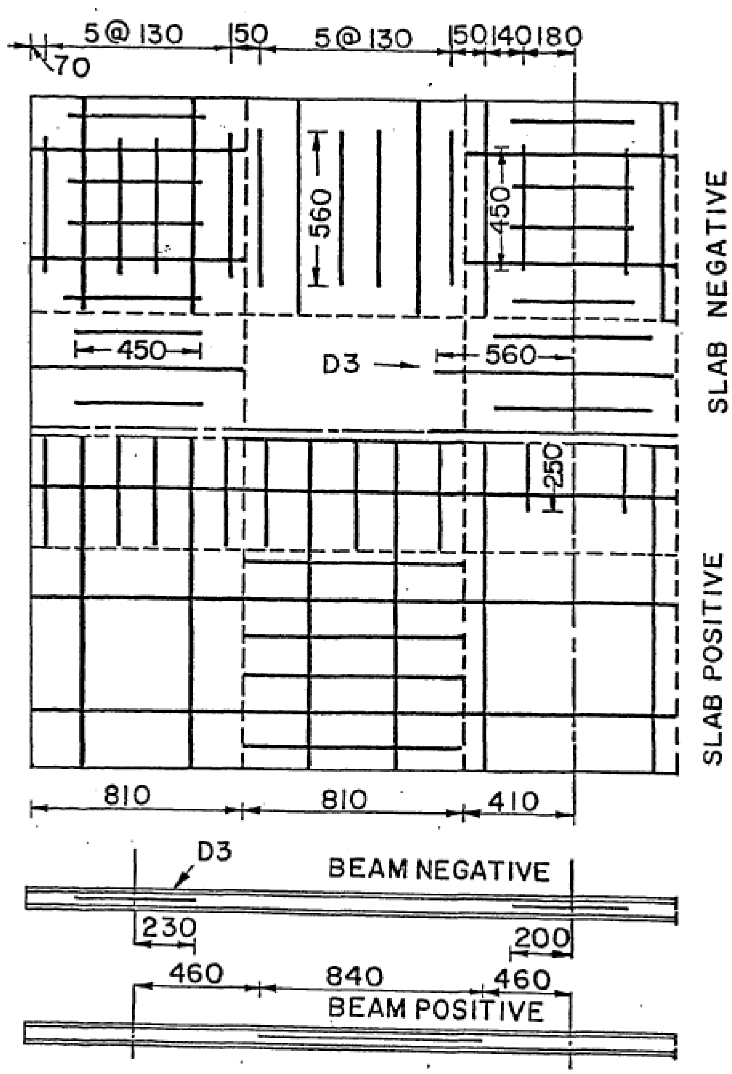

Figure B.2 – Reinforcement detail in concrete slab and beam (Nakashima, 1981)

Two kinds of concrete were used in the test specimens: 27.6 MPa concrete and 34.5 MPa concrete for each of the two specimens, B-l and B-2. Standard cylinder tests were performed at ages of seven and twenty eight days. On the first day of slab specimen testing, four more concrete test cylinders were tested to obtain modulus of elasticity, Poisson's ratio, and compressive strength. The ages of concrete at these tests were 52 days for specimen B-l and 109 days for specimen B-2. Table B.2 lists the compressive strength, the tensile strength, the modulus of elasticity, and the Poisson's ratio of the concrete at the beginning of slab specimen testing.

Table B.1 – Design detail of concrete slab (Nakashima, 1981)

	Strip	Sign	A_s Required (mm^2)	A_s Provided	Required Steel Ratio	Over Rein-forcement Ratio	Over-Strength Ratio
1	Column	Negative	58*	D2.0 x 6	0.0018	1.3	2.9
		Positive	58*	D2.5 x 2 + D2.0 x 4	0.0018	1.5	5.6
	Column	Negative Interior	58*	D2.0 x 6	0.0018	1.3	4.1
	Middle	Negative	61	D2.0 x 6	0.0019	1.3	1.3
		Positive	58*	D2.5 x 2 + D2.0 x 4	0.0018	1.5	5.6
	Middle	Negative Interior	120	D3.0 x 7	0.0038	1.1	1.1
2	Column	Negative	58*	D2.0 x 6	0.0018	1.3	2.8
		Positive	58*	D2.0 x 6	0.0018	1.3	5.0
	Column	Negative Interior	29*	D2.0 x 2	0.0018	1.1	2.2
		Positive Interior	29*	D2.0 x 2	0.0018	1.1	4.1
	Middle	Negative	67	D2.0 x 6	0.0021	1.2	1.2
		Positive	58*	D2.0 x 5	0.0018	1.1	1.9

* Controlled by temperature requirement

** Based on flexural resistance

Table B.2 – Material properties of concrete

Concrete	f_c' (MPa)	f_{sp} (MPa)	E_c (GPa)	υ
B-1	28.0	2.13	21	0.13
B-2	29.0	2.40	22	0.14

Deformed reinforcing bars of three sizes were used in the test slab specimens: D2.0, D2.5, and D3.0. The mechanical characteristics of these bars were determined by basic tension tests. The test was repeated four times for each size of reinforcing bar. Table B.3 lists the yield stress, the yield strain, the ultimate stress, the ultimate strain, and the modulus of elasticity of these bars. The values listed in the table represent the averages of the results of the four tests.

Table 0.3 – Material properties of reinforcing bars

Size	$A_b\ (mm^2)$	$f_y\ (MPa)$	$\varepsilon_y\ (m/m)$	$f_u\ (MPa)$	$\varepsilon_u\ (m/m)$	$E_s\ (GPa)$
D2.0	13.4	368	1.93×10^{-3}	411	78.3×10^{-3}	191
D2.5	17.2	609	3.11×10^{-3}	668	49.2×10^{-3}	196
D3.0	21.5	590	2.72×10^{-3}	590	62.5×10^{-3}	190

The out-of-plane (vertical) load was applied as a series of concentrated forces, spaced at 540 mm (one-third panel dimension) center-to-center in each direction. Inserts were placed at the center of each ninth portion of each panel for the application of these loads, as shown in Figure B.3. A series of statically determinate levers was devised so that all point loads would be equal. A preliminary elastic analysis showed that a series of concentrated forces could reasonably simulate the uniformly distributed vertical load on the slabs. The vertical (gravity) load simulator was designed so that substantial displacement of the specimen would be permitted in the direction of the in-plane loading without affecting either the direction or the magnitude of the applied vertical load.

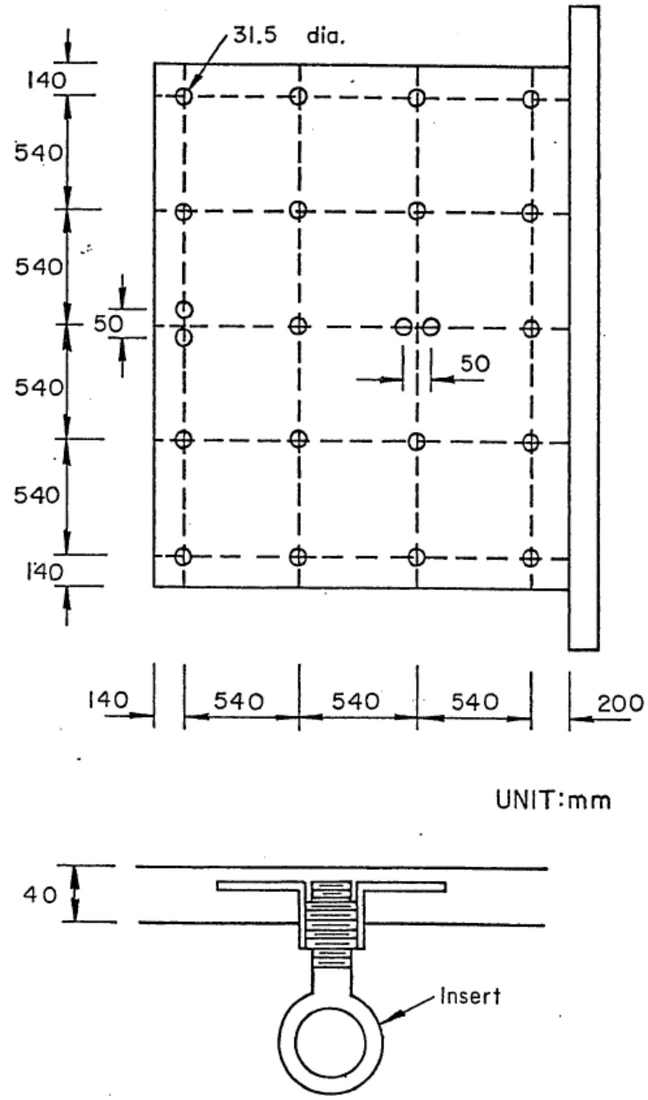

Figure B.3 – Application of the out-of-plane load and embedded inserts in slab (Nakashima, 1981)

Appendix C Material Model Parameters and Analysis Results for Concrete Diaphragms

Material Properties Used for VecTor2 Model of Tested Diaphragm by Nakashima (1981)

Tables C.1 to C.11 lists the properties of concrete materials used in the VecTor2 model of the tested diaphragm by Nakashima (1981).

Table 0.1 – Properties of Material 1 in VecTor2 model of the tested diaphragm by Nakashima

Concrete Properties	Material 1		
Thickness (mm)	40		
Cylinder Compressive Strength (MPa)	29		
Tensile Strength (MPa)	1.56		
Poisson's Ratio	0.14		
Reinforcement Properties	x-direction		y-direction
Reinforcement ratio (%)	0.46	0.105	0.163
Reinforcement diameter (mm)	3	2.5	2
Yield Strength (MPa)	590	609	368
Ultimate Strength (MPa)	590	668	411
Elastic Modulus (MPa)	190,000	196,000	191,000
Strain Hardening Strain (mm/m)	10	10	10

Table 0.2 – Properties of Material 2 in VecTor2 model of the tested diaphragm by Nakashima

Concrete Properties	Material 2		
Thickness (mm)	40		
Cylinder Compressive Strength (MPa)	29		
Tensile Strength (MPa)	1.56		
Poisson's Ratio	0.14		
Reinforcement Properties	x-direction		y-direction
Reinforcement ratio (%)	0.163	0.105	0.207
Reinforcement diameter (mm)	2	2.5	2
Yield Strength (MPa)	368	609	368
Ultimate Strength (MPa)	411	668	411
Elastic Modulus (MPa)	191,000	196,000	191,000
Strain Hardening Strain (mm/m)	10	10	10

Table 0.3 – Properties of Material 3 in VecTor2 model of the tested diaphragm by Nakashima

Concrete Properties	Material 3		
Thickness (mm)	40		
Cylinder Compressive Strength (MPa)	29		
Tensile Strength (MPa)	1.56		
Poisson's Ratio	0.14		
Reinforcement Properties	x-direction		y-direction
Reinforcement ratio (%)	0.245	0.105	0.248
Reinforcement diameter (mm)	2	2.5	2
Yield Strength (MPa)	368	609	368
Ultimate Strength (MPa)	411	668	411
Elastic Modulus (MPa)	191,000	196,000	191,000
Strain Hardening Strain (mm/m)	10	10	10

Table 0.4 – Properties of Material 4 in VecTor2 model of the tested diaphragm by Nakashima

Concrete Properties	Material 4			
Thickness (mm)	136			
Cylinder Compressive Strength (MPa)	29			
Tensile Strength (MPa)	1.56			
Poisson's Ratio	0.14			
Reinforcement Properties	x-direction		y-direction	
Reinforcement ratio (%)	0.245	0.105	0.248	0.725
Reinforcement diameter (mm)	2	2.5	2	2.5
Yield Strength (MPa)	368	609	368	609
Ultimate Strength (MPa)	411	668	411	668
Elastic Modulus (MPa)	191,000	196,000	191,000	196,000
Strain Hardening Strain (mm/m)	10	10	10	10

Table 0.5 – Properties of Material 5 in VecTor2 model of the tested diaphragm by Nakashima

Concrete Properties	Material 5			
Thickness (mm)	40			
Cylinder Compressive Strength (MPa)	29			
Tensile Strength (MPa)	1.56			
Poisson's Ratio	0.14			
Reinforcement Properties	x-direction		y-direction	
Reinforcement ratio (%)	0.248	0.106	0.163	0.082
Reinforcement diameter (mm)	2	2.5	2	2.5
Yield Strength (MPa)	368	609	368	609
Ultimate Strength (MPa)	411	668	411	668
Elastic Modulus (MPa)	191,000	196,000	191,000	196,000
Strain Hardening Strain (mm/m)	10	10	10	10

Table 0.6 – Properties of Material 6 in VecTor2 model of the tested diaphragm by Nakashima

Concrete Properties	Material 6			
Thickness (mm)	40			
Cylinder Compressive Strength (MPa)	29			
Tensile Strength (MPa)	1.56			
Poisson's Ratio	0.14			
Reinforcement Properties	x-direction		y-direction	
Reinforcement ratio (%)	0.165	0.106	0.248	0.083
Reinforcement diameter (mm)	2	2.5	2	2.5
Yield Strength (MPa)	368	609	368	609
Ultimate Strength (MPa)	411	668	411	668
Elastic Modulus (MPa)	191,000	196,000	191,000	196,000
Strain Hardening Strain (mm/m)	10	10	10	10

Table C.7 – Properties of Material 7 in VecTor2 model of the tested diaphragm by Nakashima

Concrete Properties	Material 7			
Thickness (mm)	40			
Cylinder Compressive Strength (MPa)	29			
Tensile Strength (MPa)	1.56			
Poisson's Ratio	0.14			
Reinforcement Properties	x-direction		y-direction	
Reinforcement ratio (%)	0.248	0.083	0.248	0.106
Reinforcement diameter (mm)	2	2.5	2	2.5
Yield Strength (MPa)	368	609	368	609
Ultimate Strength (MPa)	411	668	411	668
Elastic Modulus (MPa)	191,000	196,000	191,000	196,000
Strain Hardening Strain (mm/m)	10	10	10	10

Table 0.8 – Properties of Material 8 in VecTor2 model of the tested diaphragm by Nakashima

Concrete Properties	Material 8			
Thickness (mm)	136			
Cylinder Compressive Strength (MPa)	29			
Tensile Strength (MPa)	1.56			
Poisson's Ratio	0.14			
Reinforcement Properties	x-direction	y-direction		
Reinforcement ratio (%)	0.331	0.7	0.538	0.106
Reinforcement diameter (mm)	2	3	2	2.5
Yield Strength (MPa)	368	590	368	609
Ultimate Strength (MPa)	411	590	411	668
Elastic Modulus (MPa)	191,000	190,000	191,000	196,000
Strain Hardening Strain (mm/m)	10	10	10	10

Table C.9 – Properties of Material 9 in VecTor2 model of the tested diaphragm by Nakashima

Concrete Properties	Material 9		
Thickness (mm)	136		
Cylinder Compressive Strength (MPa)	29		
Tensile Strength (MPa)	1.56		
Poisson's Ratio	0.14		
Reinforcement Properties	x-direction		y-direction
Reinforcement ratio (%)	0.973	0.106	0.245
Reinforcement diameter (mm)	2	2.5	2
Yield Strength (MPa)	368	609	368
Ultimate Strength (MPa)	411	668	411
Elastic Modulus (MPa)	191,000	196,000	191,000
Strain Hardening Strain (mm/m)	10	10	10

Table 0.6 – Properties of Material 10 in VecTor2 model of the tested diaphragm by Nakashima

Concrete Properties	Material 10		
Thickness (mm)	136		
Cylinder Compressive Strength (MPa)	29		
Tensile Strength (MPa)	1.56		
Poisson's Ratio	0.14		
Reinforcement Properties	x-direction		y-direction
Reinforcement ratio (%)	0.89	0.106	0.331
Reinforcement diameter (mm)	2	2.5	2
Yield Strength (MPa)	368	609	368
Ultimate Strength (MPa)	411	668	411
Elastic Modulus (MPa)	191,000	196,000	191,000
Strain Hardening Strain (mm/m)	10	10	10

Table 0.7 – Properties of Material 11 in VecTor2 model of the tested diaphragm by Nakashima

Concrete Properties	Material 11			
Thickness (mm)	136			
Cylinder Compressive Strength (MPa)	29			
Tensile Strength (MPa)	1.56			
Poisson's Ratio	0.14			
Reinforcement Properties	x-direction		y-direction	
Reinforcement ratio (%)	0.621	0.7	0.248	0.106
Reinforcement diameter (mm)	2	3	2	2.5
Yield Strength (MPa)	368	590	368	609
Ultimate Strength (MPa)	411	590	411	668
Elastic Modulus (MPa)	191,000	190,000	191,000	196,000
Strain Hardening Strain (mm/m)	10	10	10	10

Material Properties Used for VecTor2 Model of Investigated Diaphragms

Tables C.12 to C.16 lists the properties of seven concrete material models used to represent various regions of the investigated diaphragms in the VecTor2 model.

Table 0.12 – Properties of Material 1 and Material 2 in VecTor2 model of investigated diaphragms

Concrete Properties	Material 1		Material 2	
Thickness (mm)	200		3000	
Cylinder Compressive Strength (MPa)	30		30	
Tensile Strength (MPa)	1.82		1.82	
Poisson's Ratio	0.15		0.15	
Reinforcement Properties	x-direction	y-direction	y-direction	Out-of-plane
Reinforcement ratio (%)	0.5	0.5	3	3
Reinforcement diameter (mm)	10	10	20	20
Yield Strength (MPa)	400	400	400	400
Ultimate Strength (MPa)	650	650	650	650
Elastic Modulus (MPa)	200,000	200,000	200,000	200,000
Strain Hardening Strain (mm/m)	10	10	10	10

Table 0.13 – Properties of Material 3 and Material 4 in VecTor2 model of investigated diaphragms

Concrete Properties	Material 3		Material 4	
Thickness (mm)	3000		3000	
Cylinder Compressive Strength (MPa)	30		30	
Tensile Strength (MPa)	1.82		1.82	
Poisson's Ratio	0.15		0.15	
Reinforcement Properties	x-direction	Out-of-plane	y-direction	Out-of-plane
Reinforcement ratio (%)	3	3	0.5	0.5
Reinforcement diameter (mm)	20	20	10	10
Yield Strength (MPa)	400	400	400	400
Ultimate Strength (MPa)	650	650	650	650
Elastic Modulus (MPa)	200,000	200,000	200,000	200,000
Strain Hardening Strain (mm/m)	10	10	10	10

Table 0.14 – Properties of Material 5 in VecTor2 model of investigated diaphragms

Concrete Properties	Material 5	
Thickness (mm)	3000	
Cylinder Compressive Strength (MPa)	30	
Tensile Strength (MPa)	1.82	
Poisson's Ratio	0.15	
Reinforcement Properties	x-direction	Out-of-plane
Reinforcement ratio (%)	0.5	0.5
Reinforcement diameter (mm)	10	10
Yield Strength (MPa)	400	400
Ultimate Strength (MPa)	650	650
Elastic Modulus (MPa)	200,000	200,000
Strain Hardening Strain (mm/m)	10	10

Table 0.15 – Properties of Material 6 in VecTor2 model of investigated diaphragms

Concrete Properties	Material 6		
Thickness (mm)	3000		
Cylinder Compressive Strength (MPa)	30		
Tensile Strength (MPa)	1.82		
Poisson's Ratio	0.15		
Reinforcement Properties	x-direction	y-direction	Out-of-plane
Reinforcement ratio (%)	3	3	3
Reinforcement diameter (mm)	20	20	20
Yield Strength (MPa)	400	400	400
Ultimate Strength (MPa)	650	650	650
Elastic Modulus (MPa)	200,000	200,000	200,000
Strain Hardening Strain (mm/m)	10	10	10

Table 0.16 – Properties of Material 7 in VecTor2 model of investigated diaphragms

Concrete Properties	Material 7		
Thickness (mm)	3000		
Cylinder Compressive Strength (MPa)	30		
Tensile Strength (MPa)	1.82		
Poisson's Ratio	0.15		
Reinforcement Properties	x-direction	y-direction	Out-of-plane
Reinforcement ratio (%)	0.5	0.5	0.5
Reinforcement diameter (mm)	10	10	10
Yield Strength (MPa)	400	400	400
Ultimate Strength (MPa)	650	650	650
Elastic Modulus (MPa)	200,000	200,000	200,000
Strain Hardening Strain (mm/m)	10	10	10

Crack Patterns for Diaphragms with Fixed and Beam Supports

The location and direction of major cracks are more visible in the crack pattern of the slab shown in Figures C.1(left) and C.2(left). In order to depict the location and direction of other cracks (i.e. diagonal tension cracks) in the slab more clearly, the principal tensile strains of the slab are also shown in Figures C.1(right) and C.2(right). The inclination of the arrows shows the direction of the principal tensile strains and the direction of cracks is perpendicular to the direction of the principal tensile strains. According to the principal tensile strain diagram (Figure C.1, right), the direction and location of shear cracks developed in the slab with fixed support were not compatible with those observed in the experiment. Consequently, the shear flow in the slab was not in accordance with the experiment. Thus, the fixed support was not a good option for modelling the boundary condition of the slab. The slab with beam support exhibited more promising results in terms of crack pattern and shear flow in the slab which is in very good agreement with the experimental results.

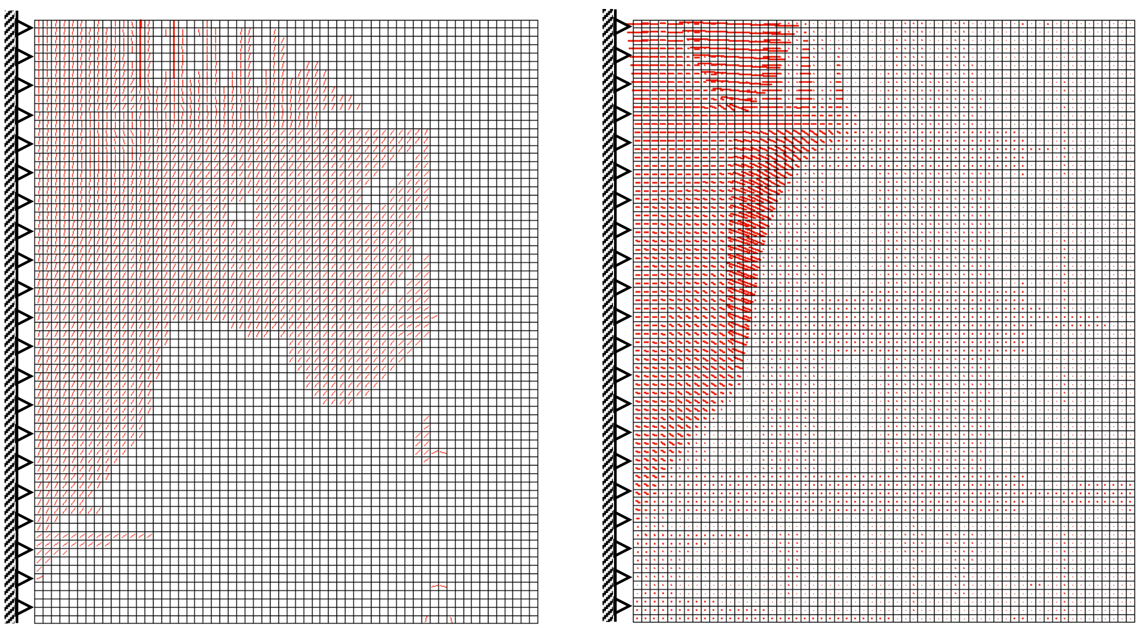

Figure C.1 – Crack pattern (left) and principal tensile strain direction (right) of slab with fixed support

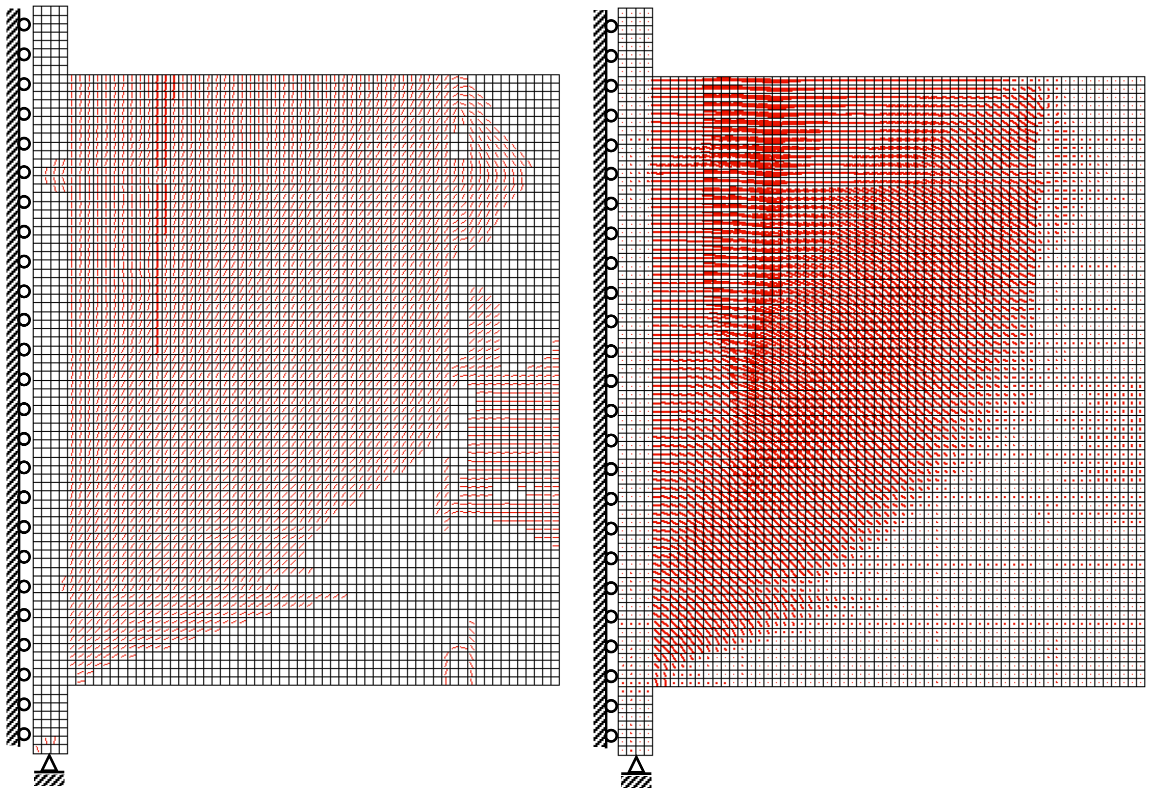

Figure C.2 – Crack pattern (left) and principal tensile strain direction (right) of slab with beam support

Calculation of Shear and Flexural Deformations

To determine the flexural deformation, the average curvatures were integrated over the diaphragm shear span (L_{SS}). The average curvature was considered as the slope of a line fitted to the normal strain profile in horizontal direction, ε_x. The shear deformation was obtained by subtracting the flexural deformation from the total deformation. In addition, the average shear strains were integrated over the diaphragm shear span (L_{SS}) to obtain the shear deformation. Comparison of the results confirms VecTor2 is able to accurately predict the shear and flexural deformations of the diaphragm.

Figures C.3 and C.4 present normal strain profiles in horizontal direction (over the diaphragm shear depth, L_{SD}) for diaphragms with aspect ratios of 0.4, 0.6 and 0.9 and 1% reinforcement amount before cracking (linear range) and after flexural cracks took place (nonlinear range) close to the core and at mid-shear span, respectively. The best fitted line obtained from the linear regression was also shown in the figures. The horizontal strain was normalized with regard to the cracking strain (ε_{cr}) of diaphragm which depends on the compressive strength of concrete and modulus of elasticity of concrete and was identical for all analyzed diaphragms.

Figure C.3(a) depicts the horizontal strain profiles in linear range (before cracking) close to the core wall which shows sudden variations due to the discontinuity caused by the core wall. However, the strain profiles can still be approximated by a straight line. As shown in Figure C.3(a), the strain profiles were relatively linear for diaphragm with the aspect ratio of 0.9 and became nonlinear by decreasing the aspect ratio even before cracking (linear range). Figure C.4(a) depicts the horizontal strain profiles in linear range at mid-shear span. After cracking, the degree of nonlinearity of strain profiles increases considerably which made the estimation of curvature complicated. For simplification, a straight line was also fitted to each strain profile and the slope of the line was considered as the average curvature. As shown in Figures C.3(b) and C.4(b), this approach is relatively reasonable. However, it can result in some errors by underestimating or overestimating the curvature. Since the contribution of flexural displacement in the total displacement is small, these errors could be neglected.

Figures C.5 and C.6 present shear strain profiles (over the diaphragm shear depth, L_{SD}) for diaphragms with aspect ratios of 0.4, 0.6 and 0.9 and 1% reinforcement amount before cracking (linear range) and after shear (diagonal) cracks took place (nonlinear range) close to the core and at mid-shear span, respectively. The average shear strain was also shown in the figures with dashed line. The shear strain was normalized with regard to the cracking shear strain (γ_{cr}) of diaphragm.

Figure C.5(a) depicts the shear strain profiles in linear range (before cracking) close to the core wall showing sudden variations due to the discontinuity caused by the core wall. As shown in Figure C.5(a), the shear strain profiles were relatively identical for diaphragms with different aspect ratios of 0.4, 0.6 and 0.9 before diagonal cracking. Figure C.6(a) depicts the shear strain profiles in linear range at mid-shear span which have parabolic shape. After shear cracking, the shear strain increases considerably at the location of shear cracks, as shown in Figures C.5(b) and C.6(b).

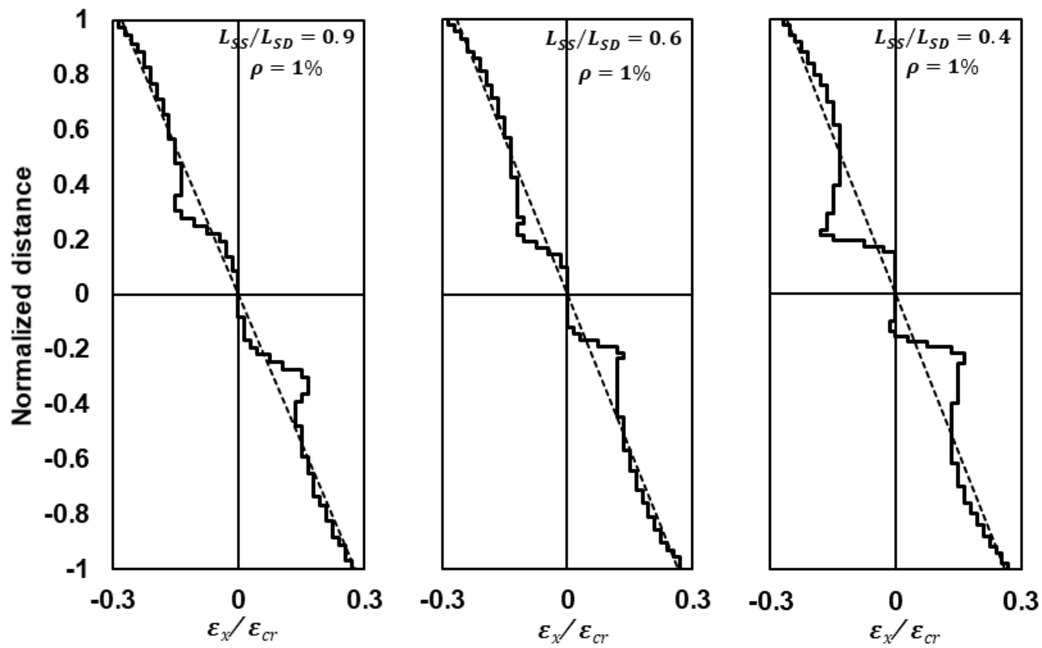

a)

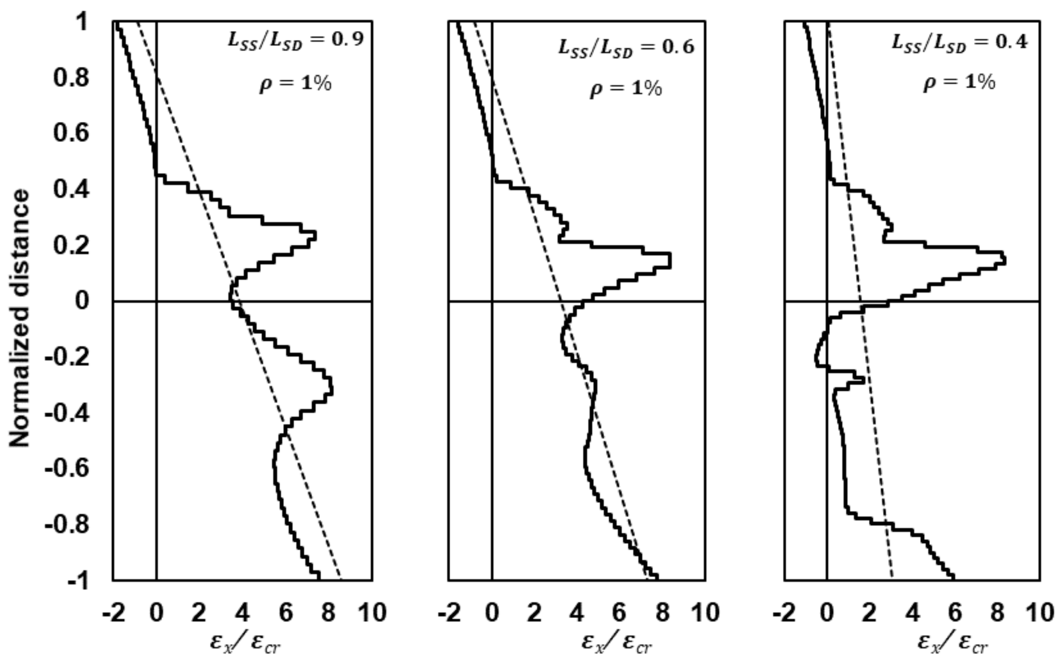

b)

Figure C.3 – Normal strain profiles for diaphragms with aspect ratio of 0.9, 0.6 and 0.4 and 1% reinforcement amount close to the core wall: (a) before cracking (linear range); and (b) after cracking (nonlinear range)

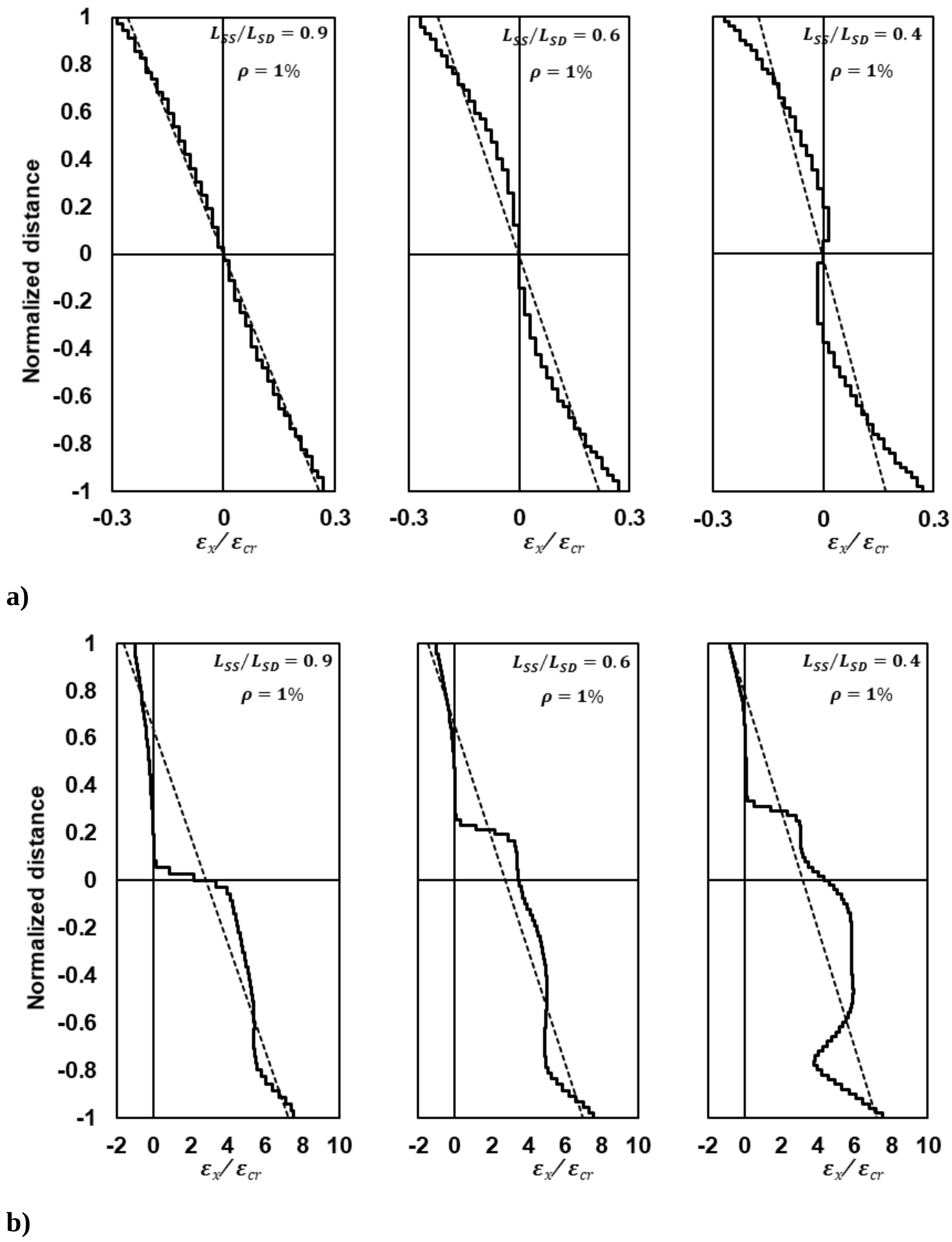

Figure C.4 – Normal strain profiles for diaphragms with aspect ratio of 0.9, 0.6 and 0.4 and 1% reinforcement amount at mid-shear span: (a) before cracking (linear range); and (b) after cracking (nonlinear range)

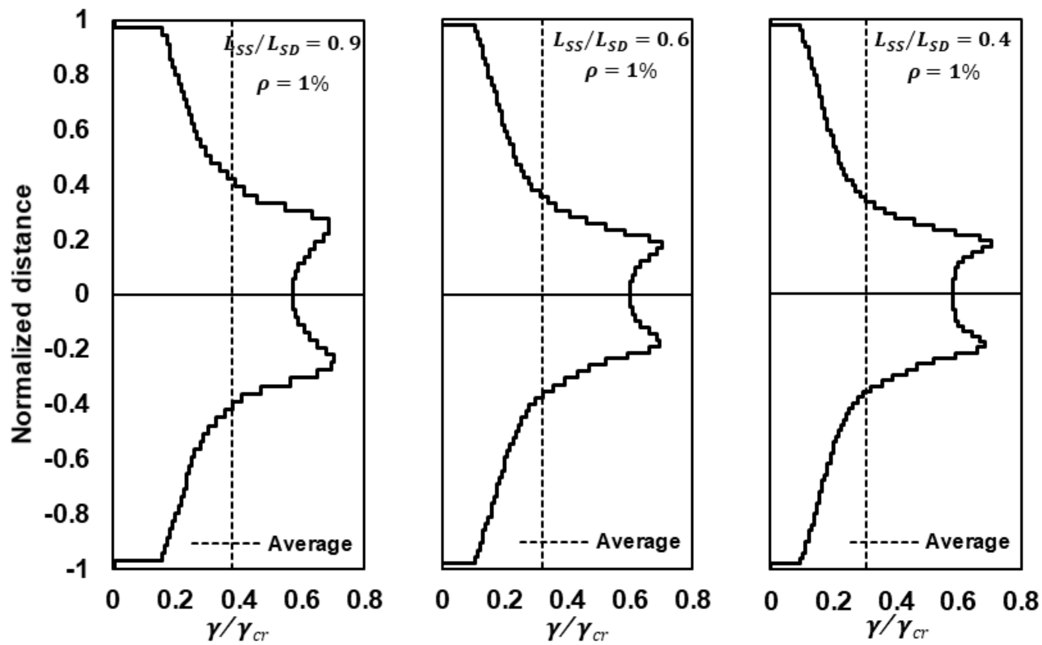

a)

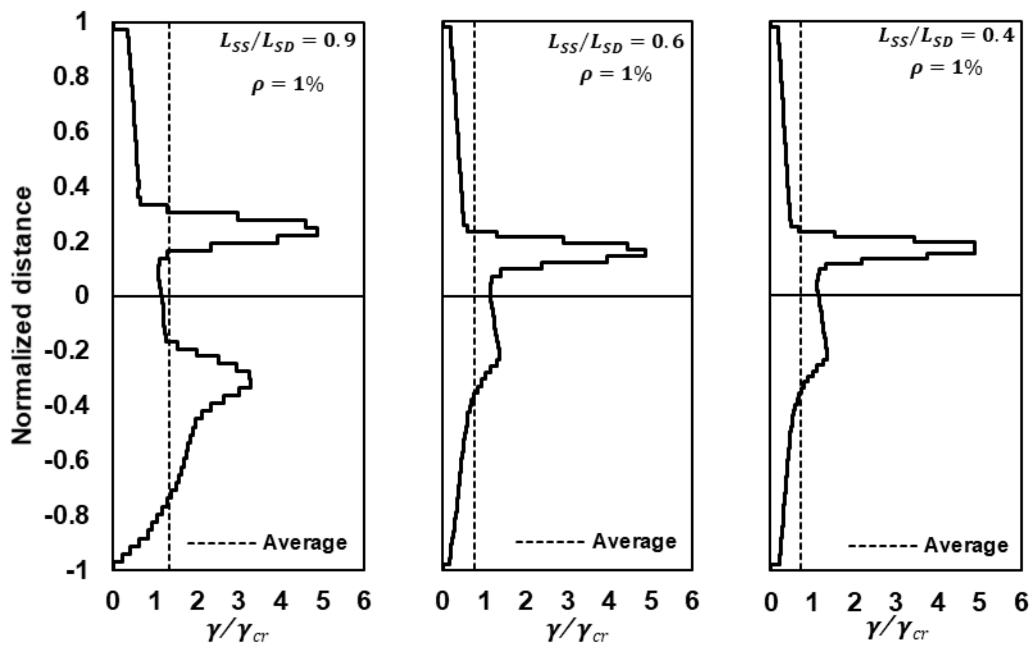

b)

Figure C.5 – Shear strain profiles for diaphragms with aspect ratio of 0.9, 0.6 and 0.4 and 1% reinforcement amount close to the core wall: (a) before cracking (linear range); and (b) after cracking (nonlinear range)

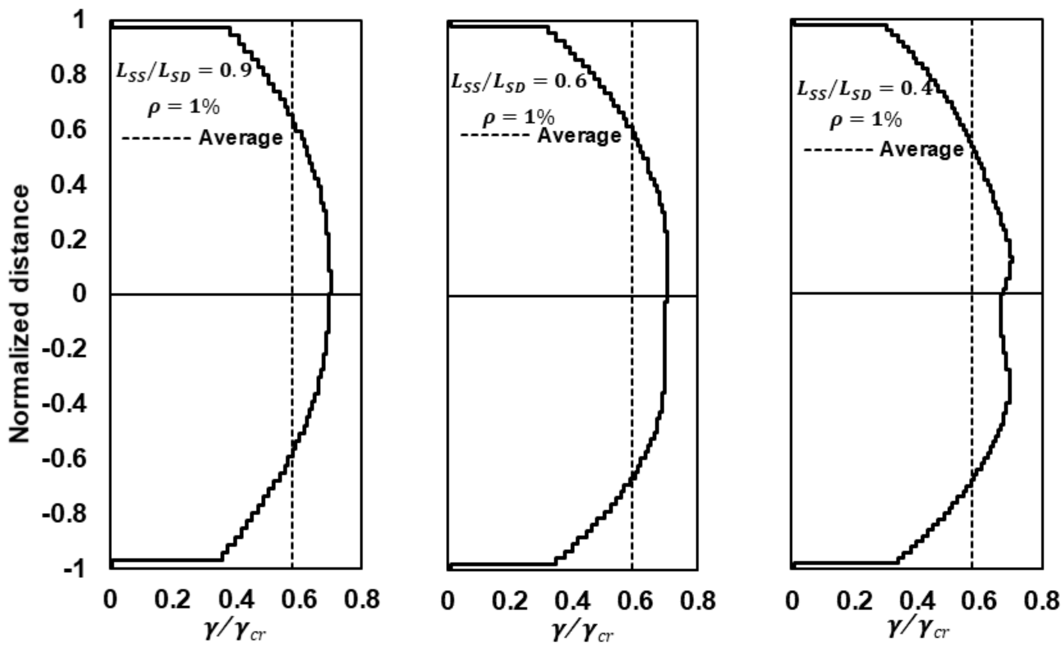

a)

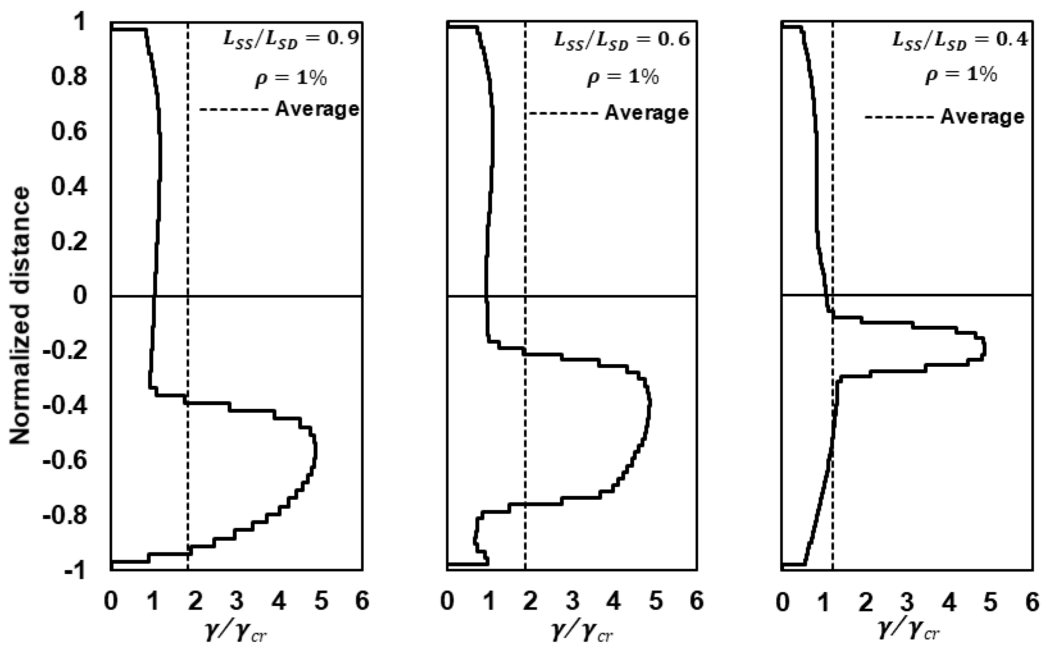

b)

Figure C.6 – Shear strain profiles for diaphragms with aspect ratio of 0.9, 0.6 and 0.4 and 1% reinforcement amount at mid-shear span: (a) before cracking (linear range); and (b) after cracking (nonlinear range)

Shear and Flexural Contributions to Total Displacement

Figures C.7 to C.16 present the load-deformation relationships of diaphragms Cases 1, 2, 3 and 4 with different reinforcement amount, respectively. The contributions of shear and flexural deformations to the total displacement are also shown in the figures.

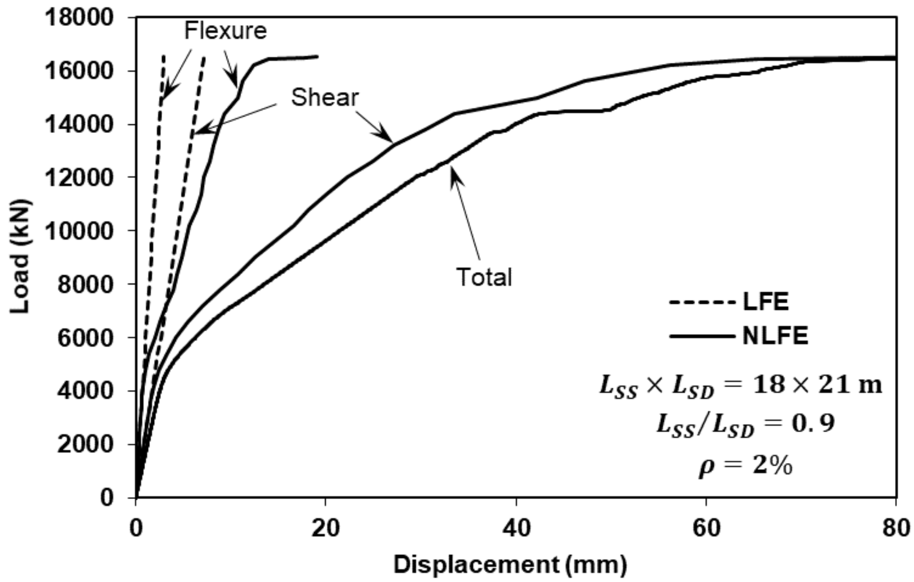

Figure C.7 – Force-deformation relationship showing portions due to shear and flexure for diaphragm with $L_{SS} \times L_{SD} = 18 \times 21$ m (Case 1) and $\rho = 2\%$

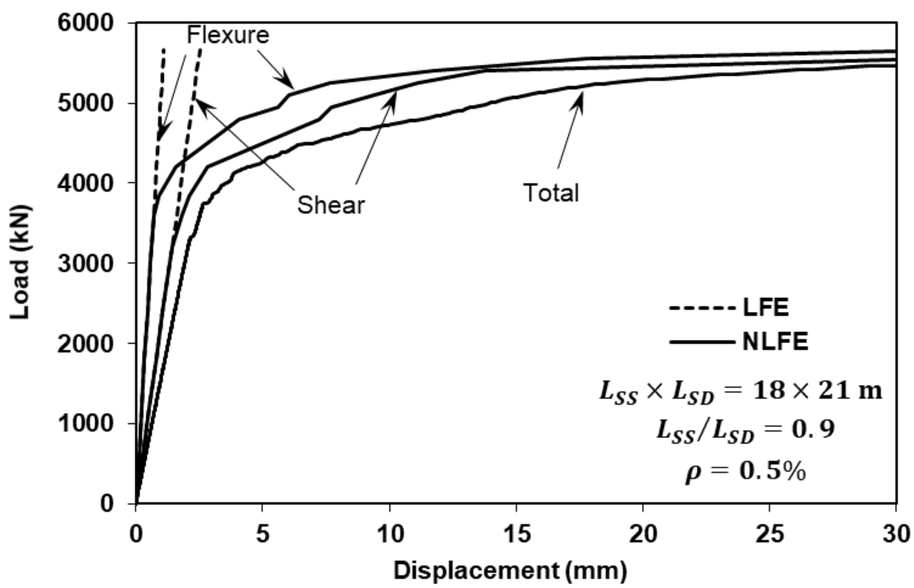

Figure C.8 – Force-deformation relationship showing portions due to shear and flexure for diaphragm with $L_{SS} \times L_{SD} = 18 \times 21$ m (Case 1) and $\rho = 0.5\%$

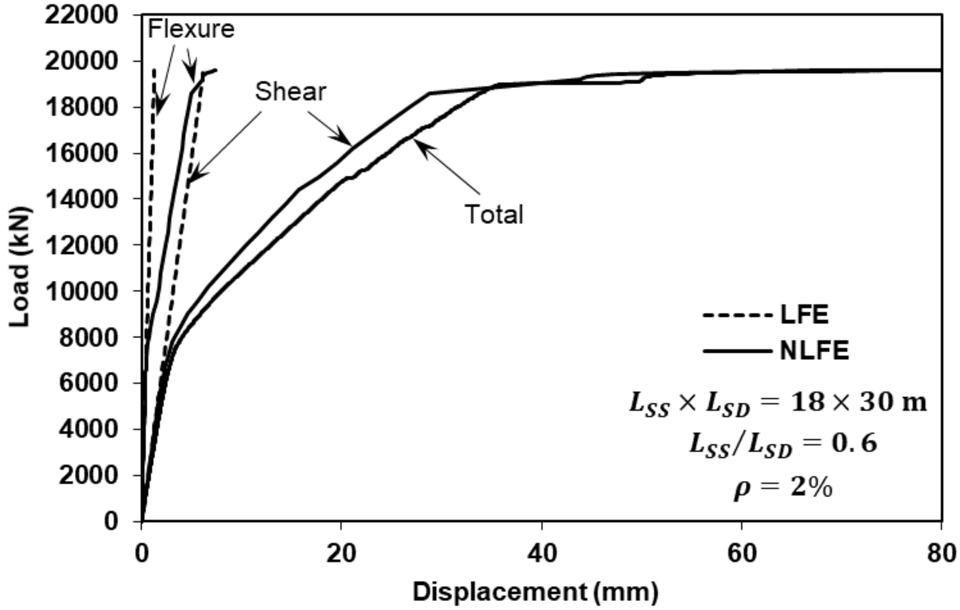

Figure C.9 – Force-deformation relationship showing portions due to shear and flexure for diaphragm with $L_{SS} \times L_{SD} = 18 \times 30$ m (Case 2) and $\rho = 2\%$

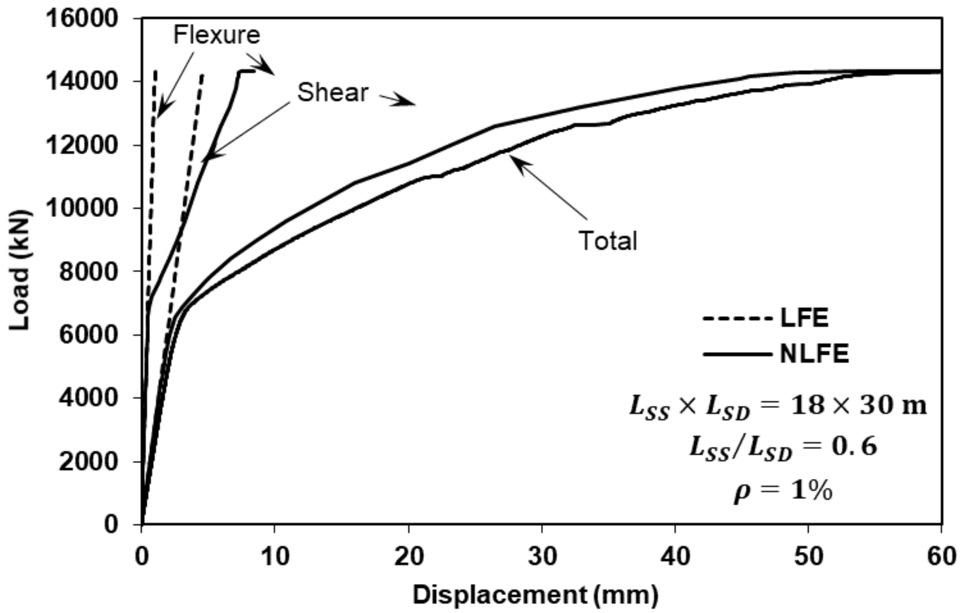

Figure C.10 – Force-deformation relationship showing portions due to shear and flexure for diaphragm with $L_{SS} \times L_{SD} = 18 \times 30$ m (Case 2) and $\rho = 1\%$

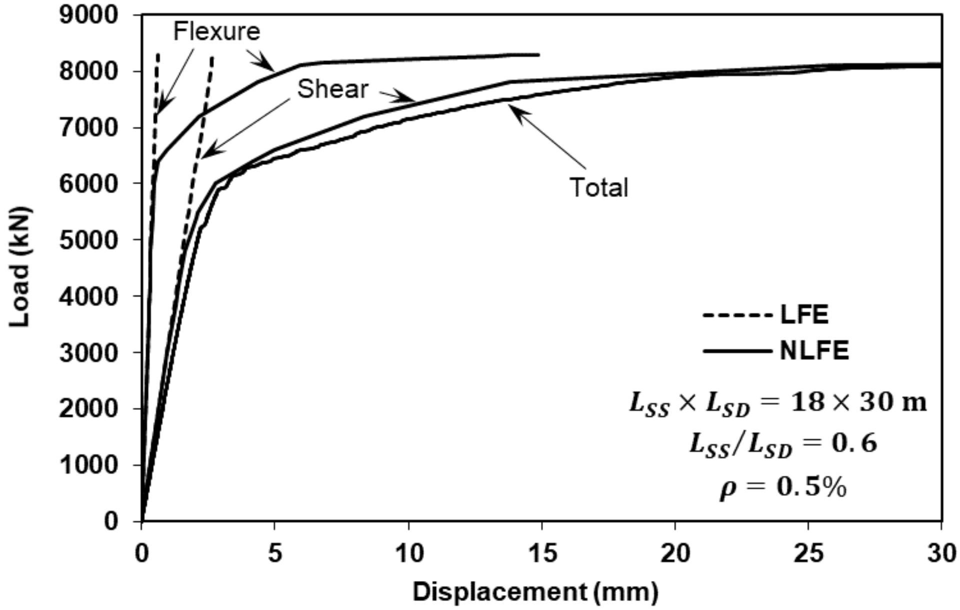

Figure C.11 – Force-deformation relationship showing portions due to shear and flexure for diaphragm with $L_{SS} \times L_{SD} = 18 \times 30$ m (Case 2) and $\rho = 0.5\%$

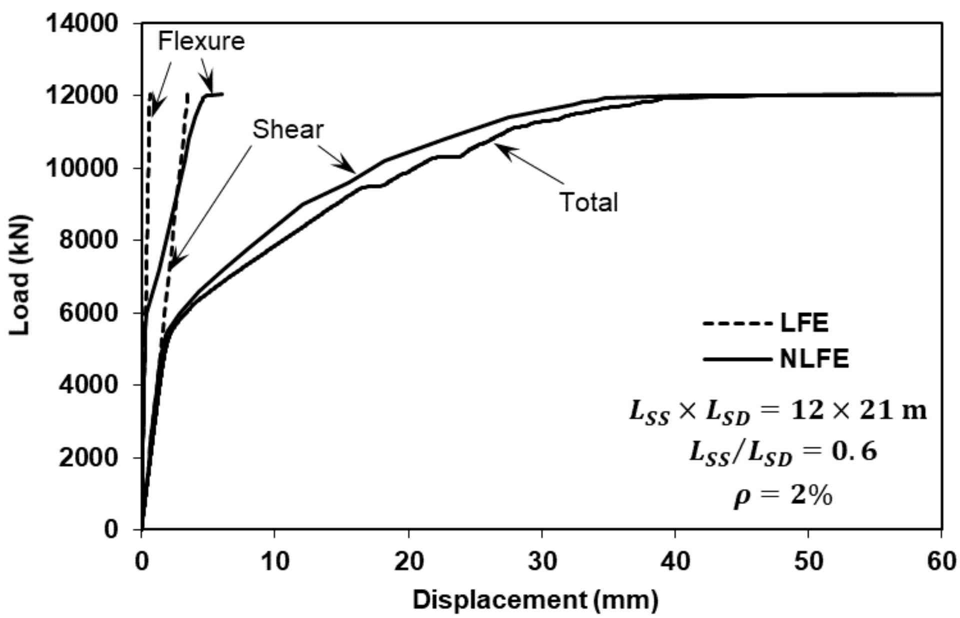

Figure C.1216 – Force-deformation relationship showing portions due to shear and flexure for diaphragm with $L_{SS} \times L_{SD} = 12 \times 21$ m (Case 3) and $\rho = 2\%$

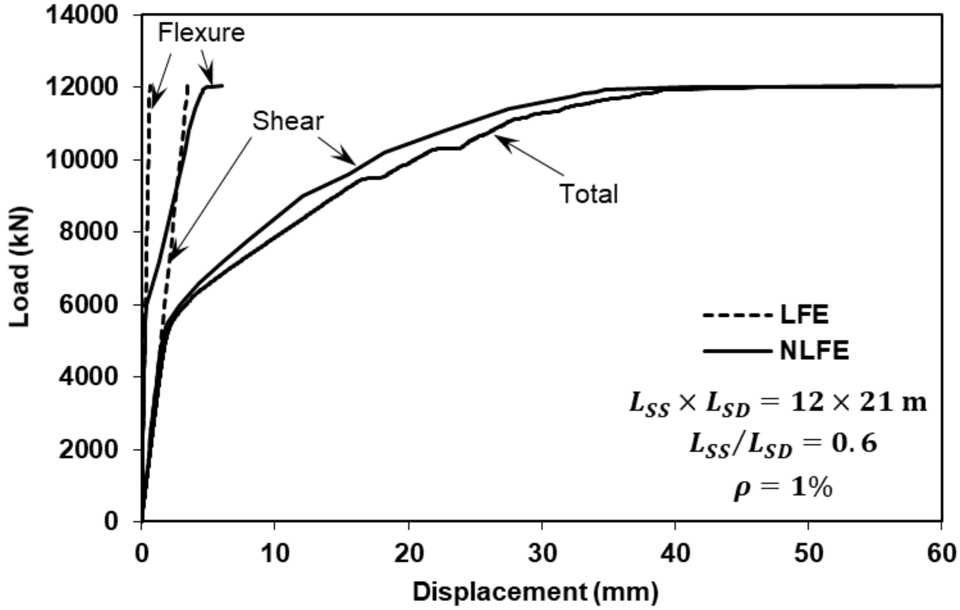

Figure C.13 – Force-deformation relationship showing portions due to shear and flexure for diaphragm with $L_{SS} \times L_{SD} = 12 \times 21$ m (Case 3) and $\rho = 1\%$

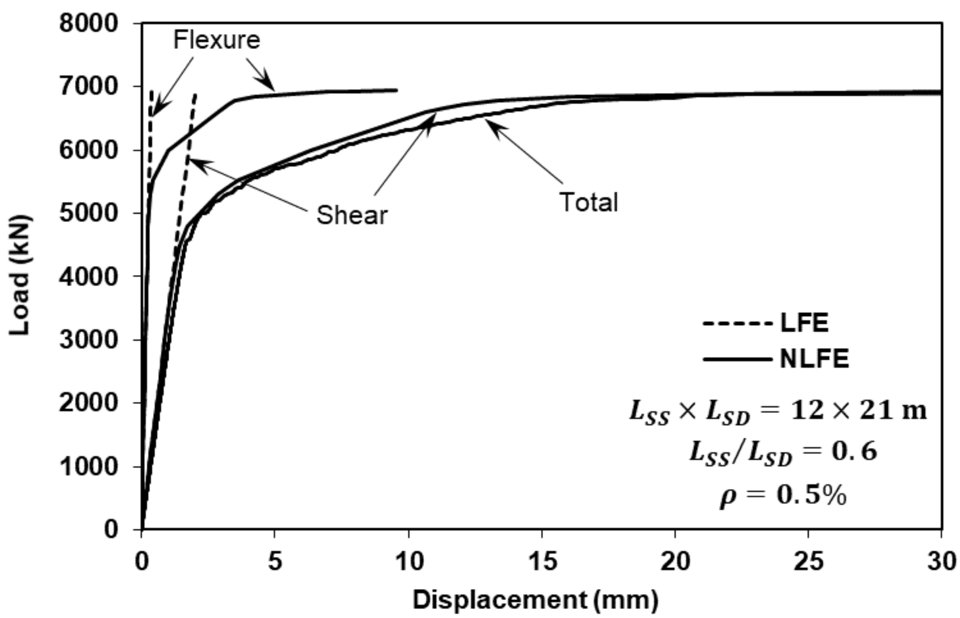

Figure C.14 – Force-deformation relationship showing portions due to shear and flexure for diaphragm with $L_{SS} \times L_{SD} = 12 \times 21$ m (Case 3) and $\rho = 0.5\%$

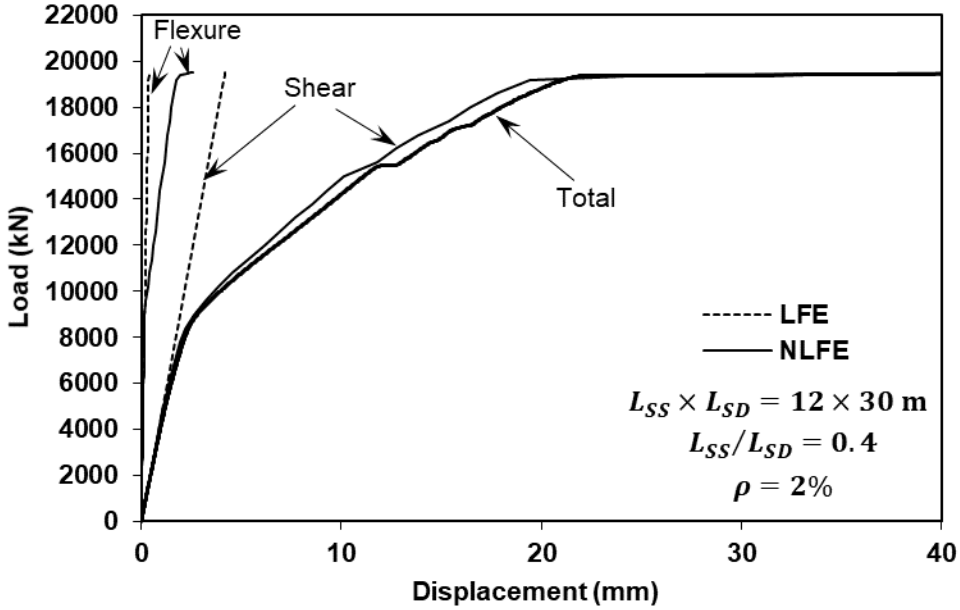

Figure C.15 – Force-deformation relationship showing portions due to shear and flexure for diaphragm with $L_{SS} \times L_{SD} = 12 \times 30$ m (Case 4) and $\rho = 2\%$

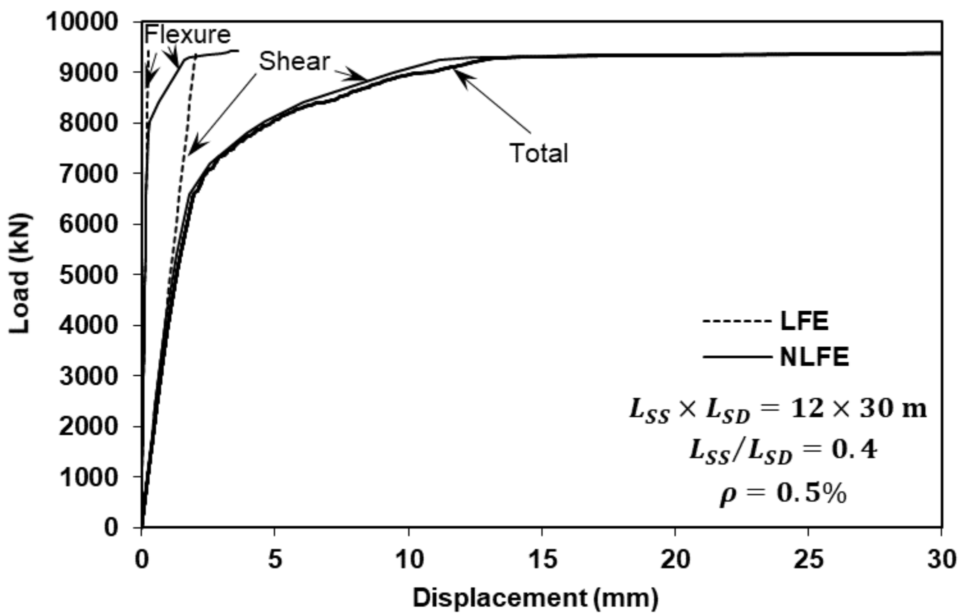

Figure C.16 – Force-deformation relationship showing portions due to shear and flexure for diaphragm with $L_{SS} \times L_{SD} = 12 \times 30$ m (Case 4) and $\rho = 0.5\%$

Shear and Flexural Stiffness Reduction Factors

Figures C.17 to C.26 present the shear, flexural and overall stiffness reduction factors versus load for diaphragms Cases 1, 2, 3 and with different reinforcement amount, respectively. As aforementioned, one of the important conclusions obtained from these figures is that the shear and flexural stiffness of diaphragm degrade simultaneously as the backstay force increases.

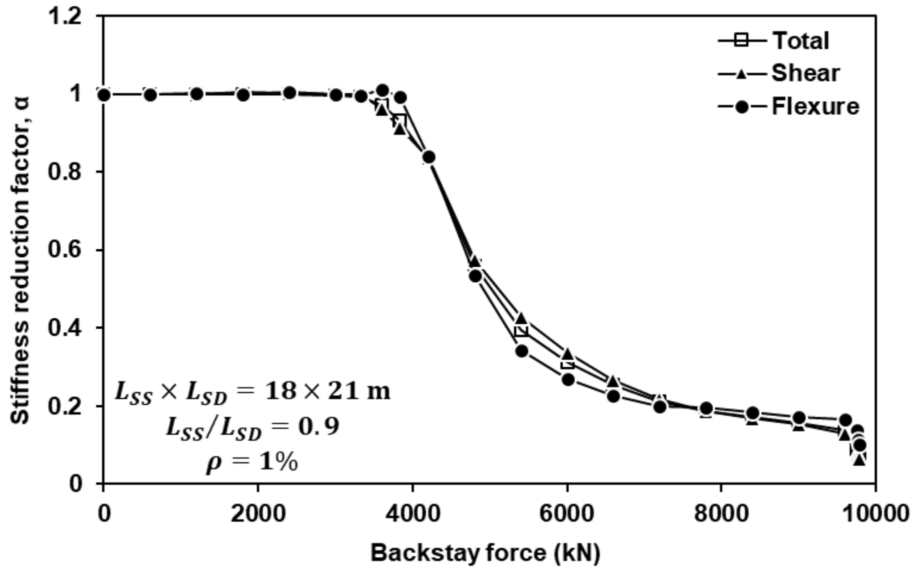

Figure C.17 – Shear and flexural stiffness reduction factors for diaphragm with $L_{SS} \times L_{SD} = 18 \times 21$ m (Case 1) and $\rho = 1\%$

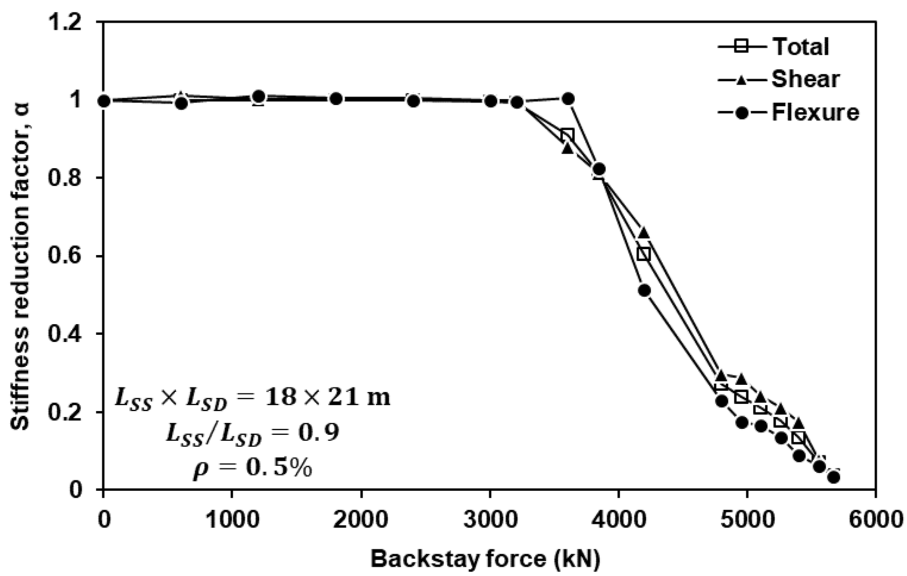

Figure C.18 – Shear and flexural stiffness reduction factors for diaphragm with $L_{SS} \times L_{SD} = 18 \times 21$ m (Case 1) and $\rho = 0.5\%$

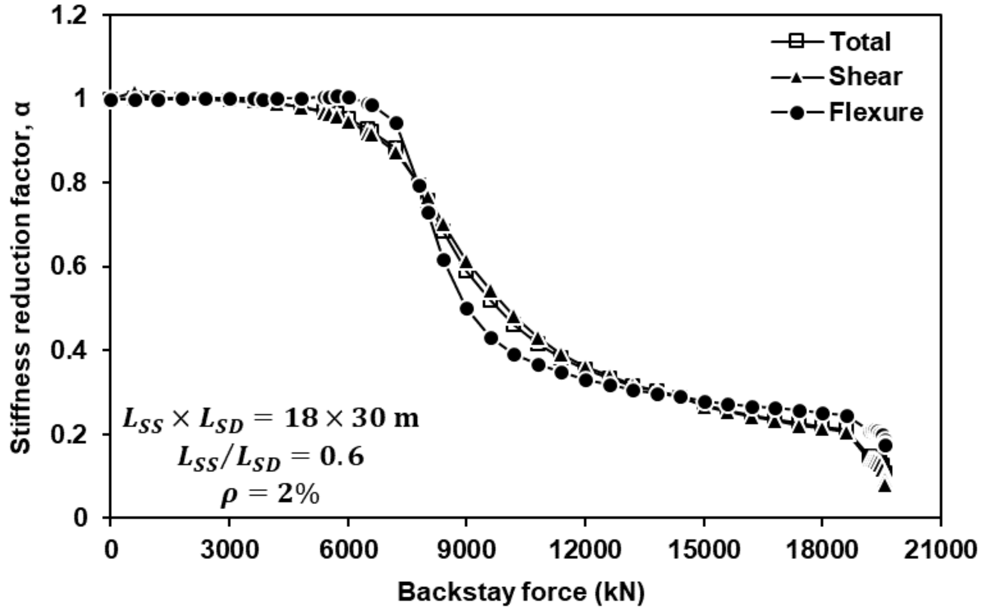

Figure C.19 – Shear and flexural stiffness reduction factors for diaphragm with $L_{SS} \times L_{SD} = 18 \times 30$ m (Case 2) and $\rho = 2\%$

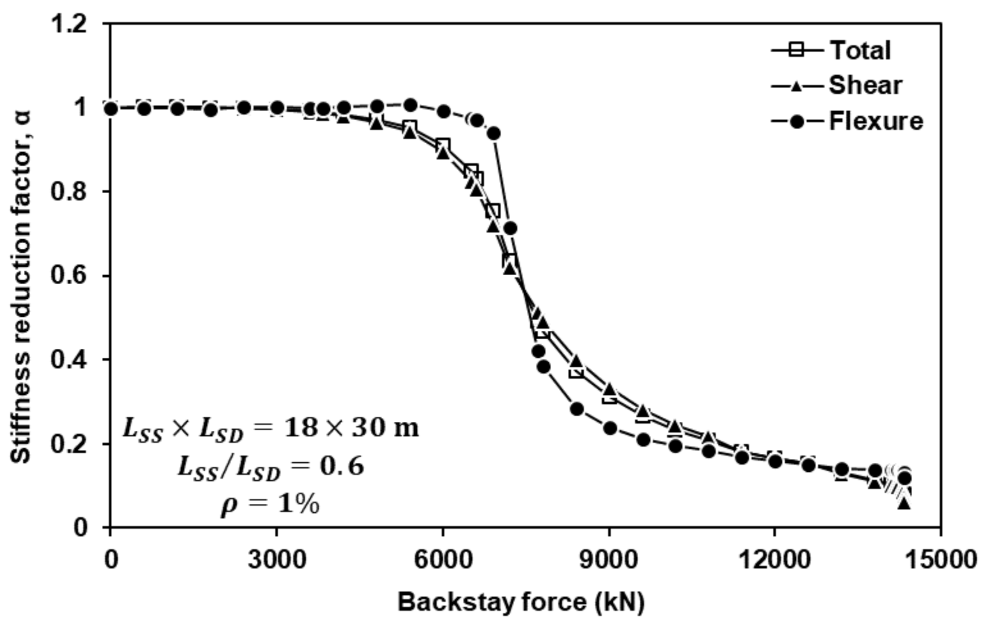

Figure C.20 – Shear and flexural stiffness reduction factors for diaphragm with $L_{SS} \times L_{SD} = 18 \times 30$ m (Case 2) and $\rho = 1\%$

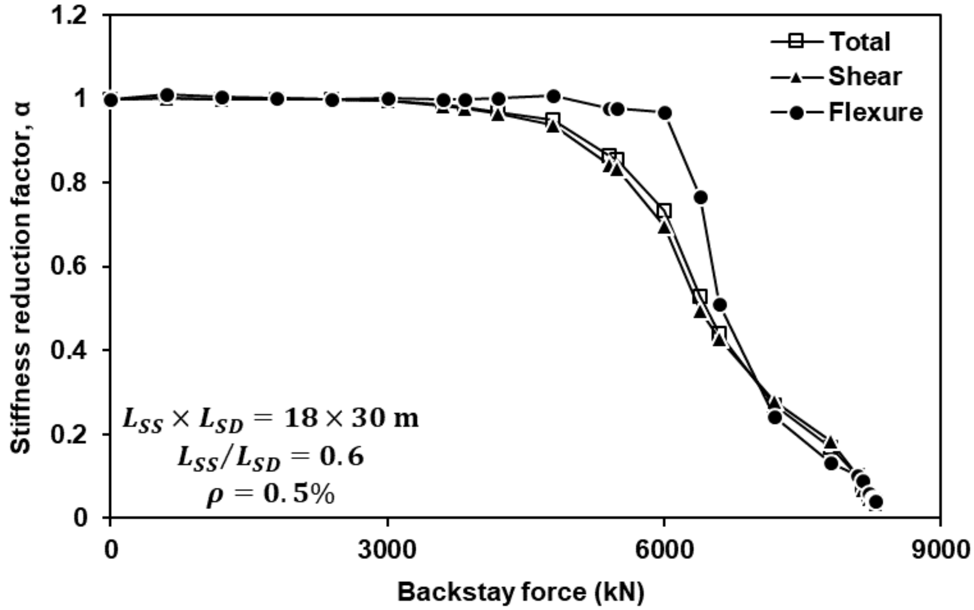

Figure C.21 – Shear and flexural stiffness reduction factors for diaphragm with $L_{SS} \times L_{SD} = 18 \times 30$ m (Case 2) and $\rho = 0.5\%$

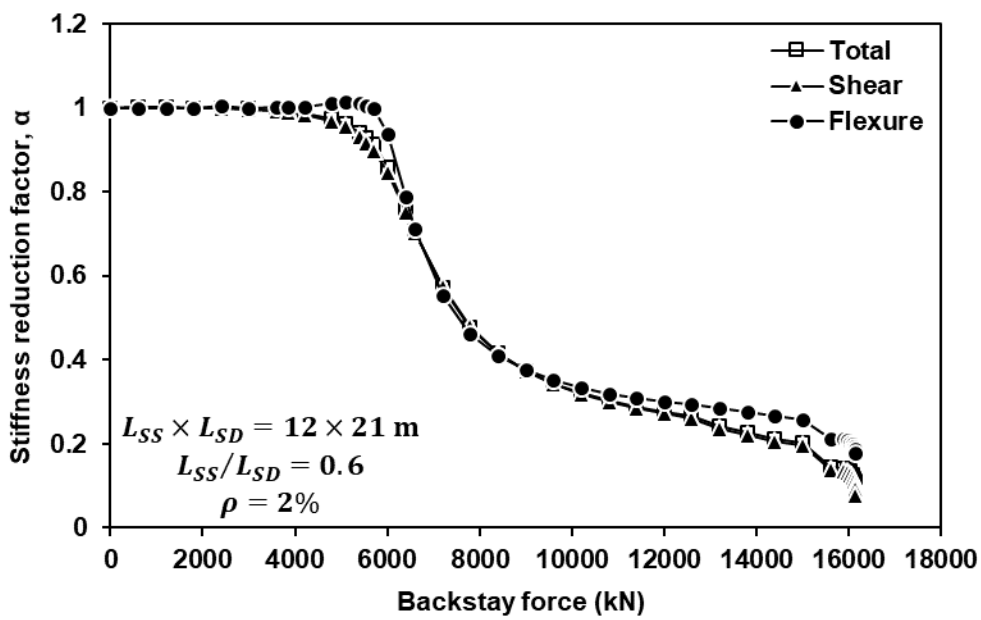

Figure C.22 – Shear and flexural stiffness reduction factors for diaphragm with $L_{SS} \times L_{SD} = 12 \times 21$ m (Case 3) and $\rho = 2\%$

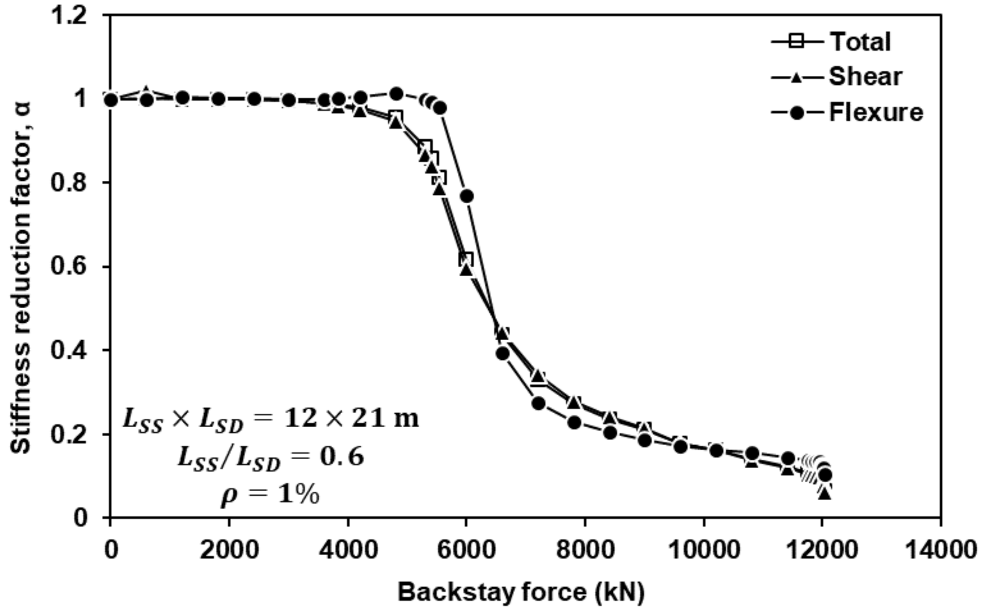

Figure C.23 – Shear and flexural stiffness reduction factors for diaphragm with $L_{SS} \times L_{SD} = 12 \times 21$ m (Case 3) and $\rho = 1\%$

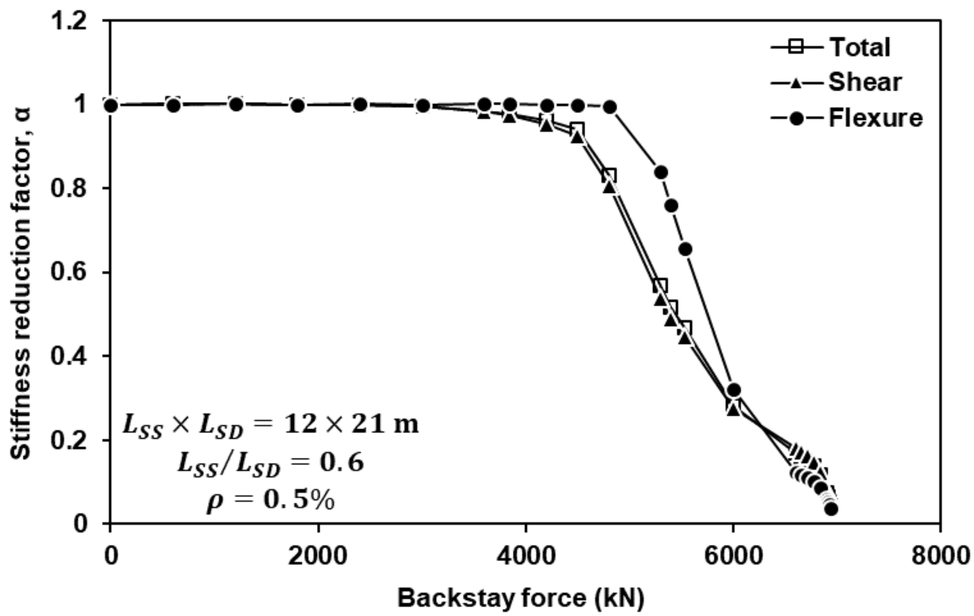

Figure C.24 – Shear and flexural stiffness reduction factors for diaphragm with $L_{SS} \times L_{SD} = 12 \times 21$ m (Case 3) and $\rho = 0.5\%$

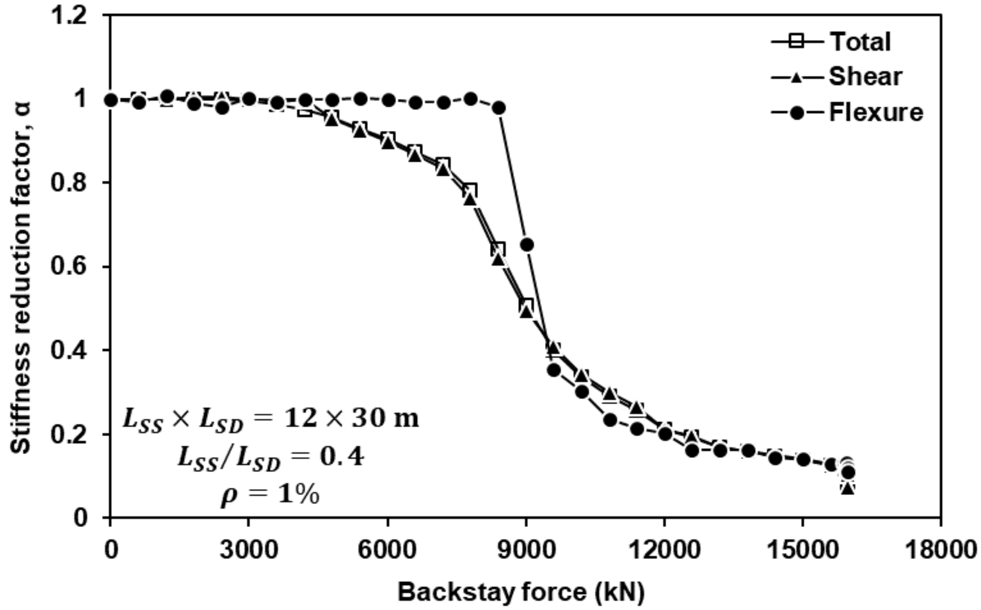

Figure C.25 – Shear and flexural stiffness reduction factors for diaphragm with $L_{SS} \times L_{SD} = 12 \times 30$ m (Case 4) and $\rho = 1\%$

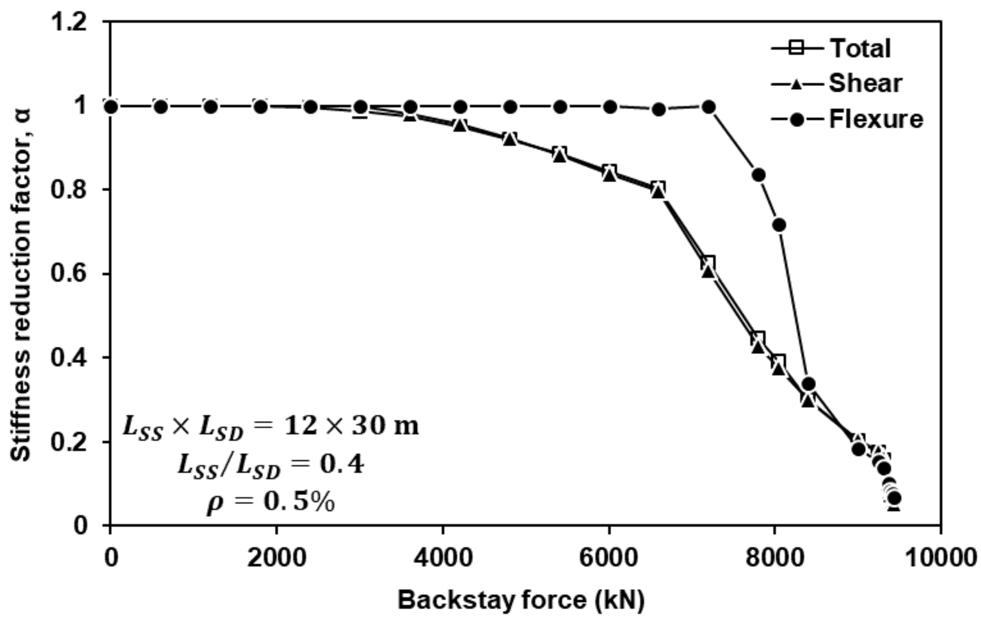

Figure C.26 – Shear and flexural stiffness reduction factors for diaphragm with $L_{SS} \times L_{SD} = 12 \times 30$ m (Case 4) and $\rho = 0.5\%$

Figures C.27, C.28 and C.29 compare the shear and flexural stiffness reductions for diaphragms with the aspect ratio of 0.9, 0.6 and 0.4 (Cases 1, 3 and 4) and different reinforcement amounts, respectively. The results reveal the influence of diaphragm reinforcement amount on shear and flexural stiffness reductions of diaphragms.

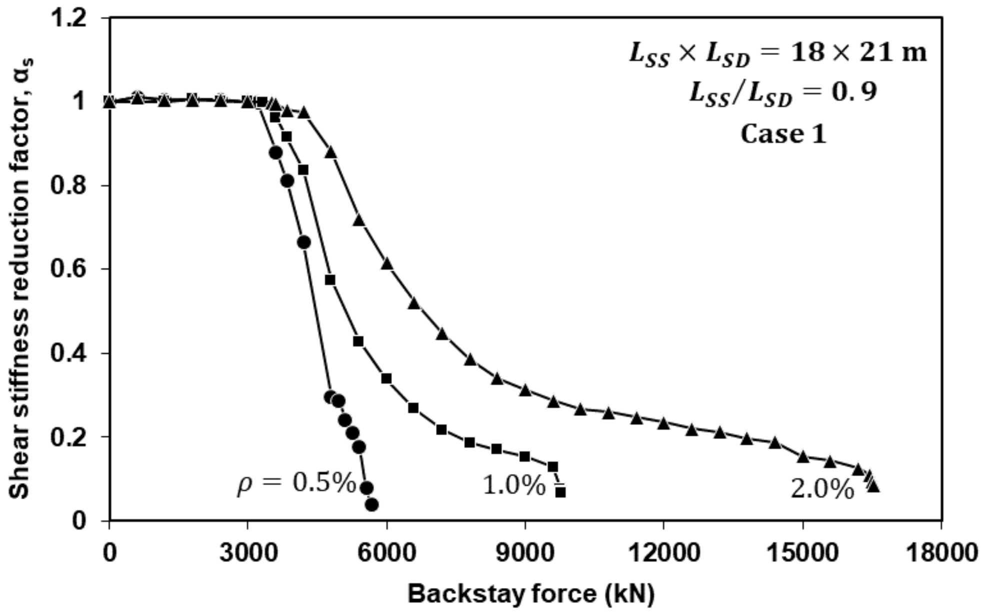

a)

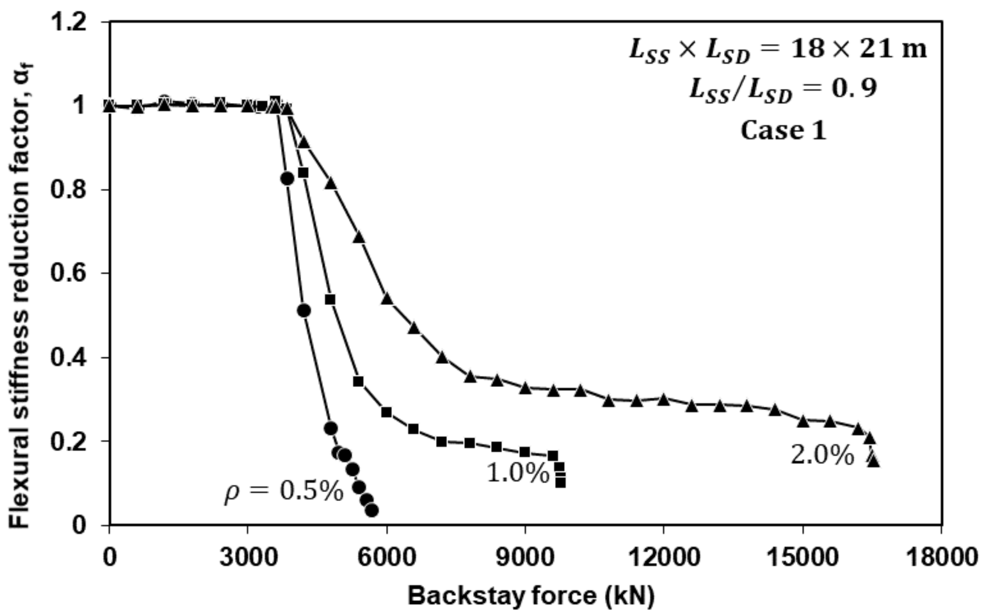

b)

Figure C.27 – Shear and flexural stiffness reduction factors for diaphragms with $L_{SS} \times L_{SD} = 18 \times 21$ m (Case 1) and different reinforcement amount: (a) shear; and (b) flexure

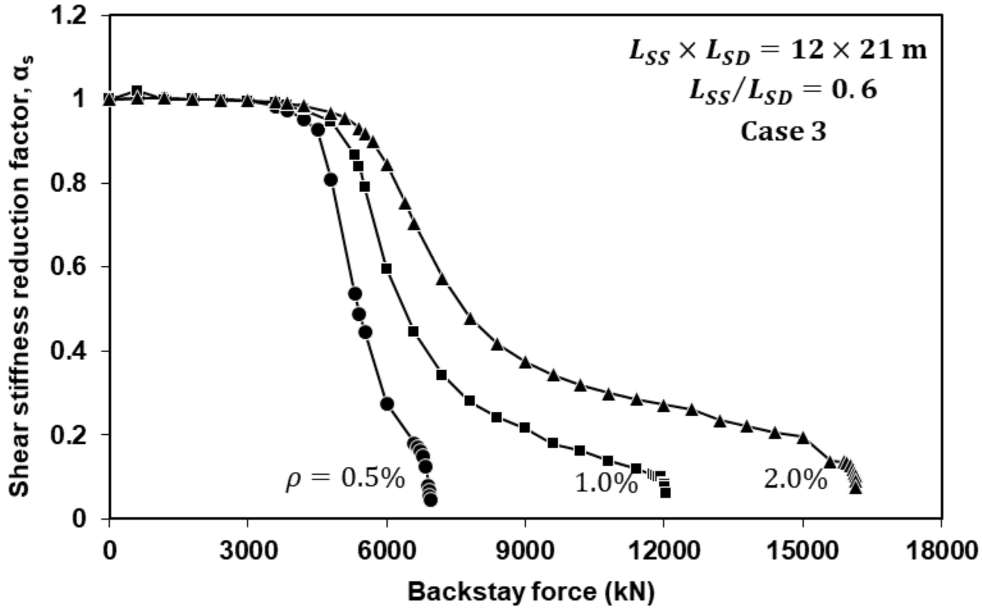

a)

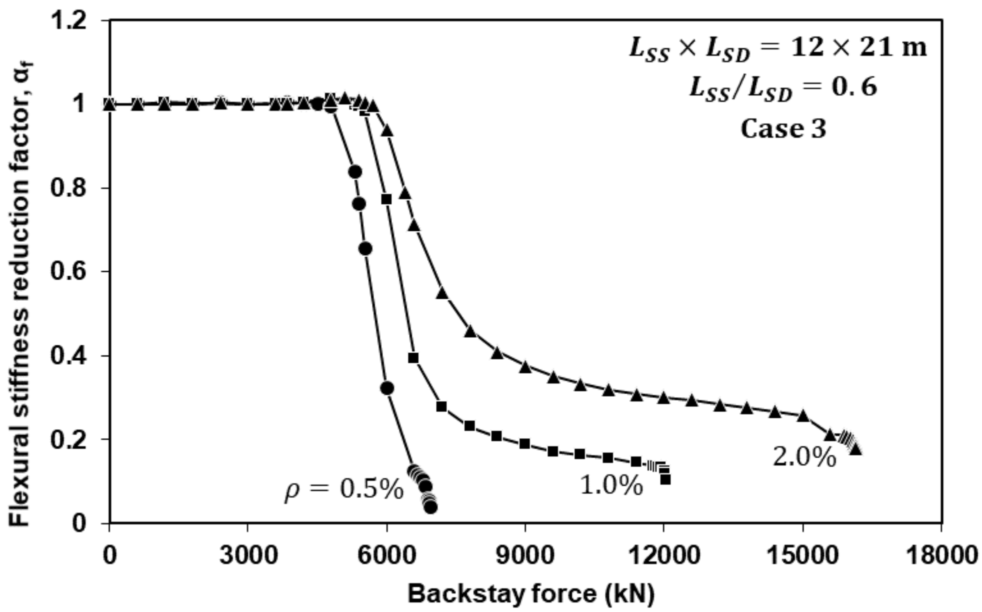

b)

Figure C.28 – Shear and flexural stiffness reduction factors for diaphragms with $L_{SS} \times L_{SD} = 12 \times 21$ m (Case 3) and different reinforcement amount: (a) shear; and (b) flexure

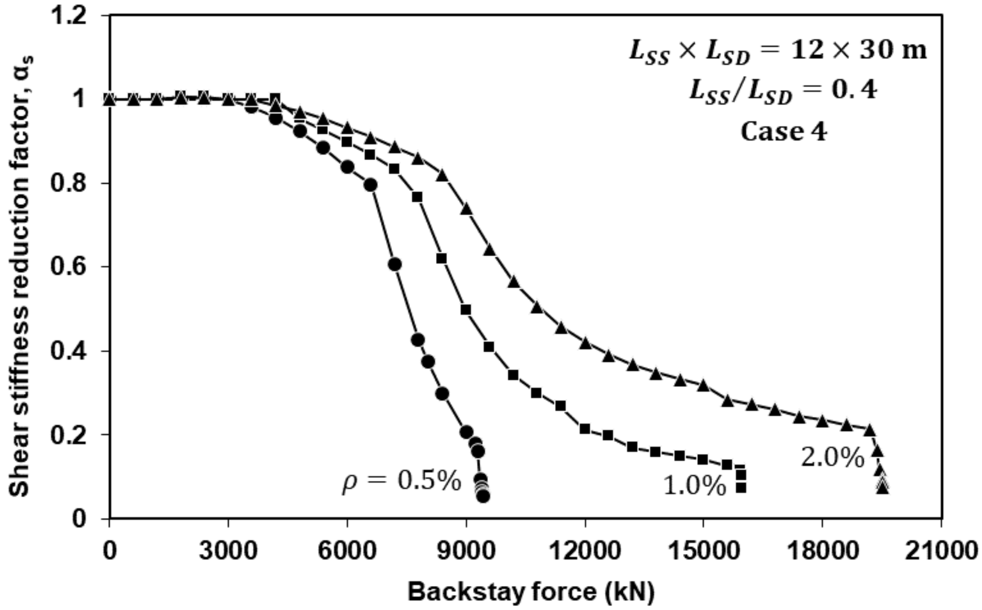

a)

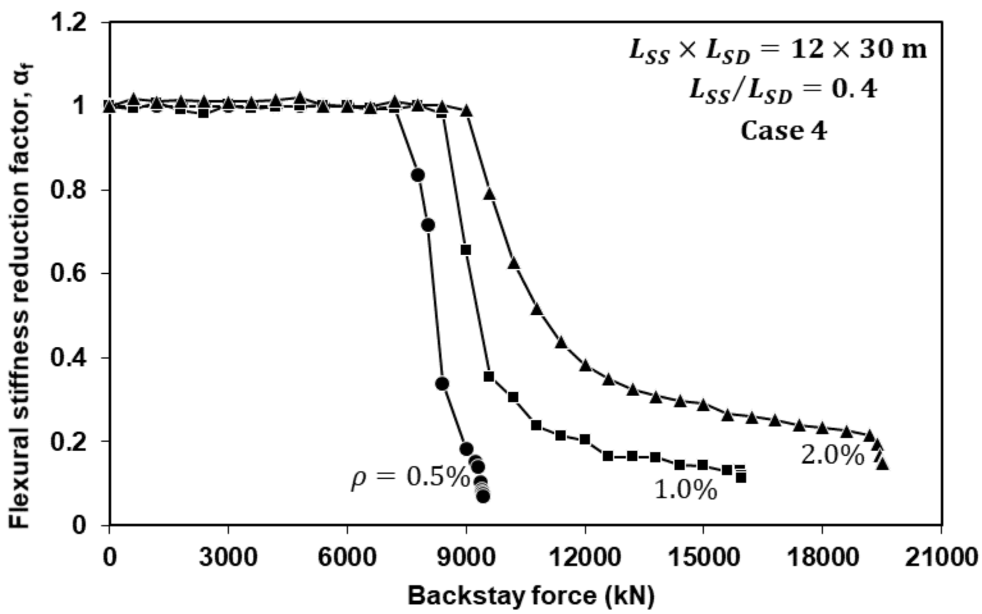

b)

Figure C.29 – Shear and flexural stiffness reduction factors for diaphragms with $L_{SS} \times L_{SD} = 12 \times 30$ m (Case 4) and different reinforcement amount: (a) shear; and (b) flexure

Comparison of Simplified Procedure with Analysis Results

Figures C.30 to C.40 compare the simplified procedure with analysis results for diaphragms Cases 1, 2, 3 and 4 with different reinforcement amount, respectively.

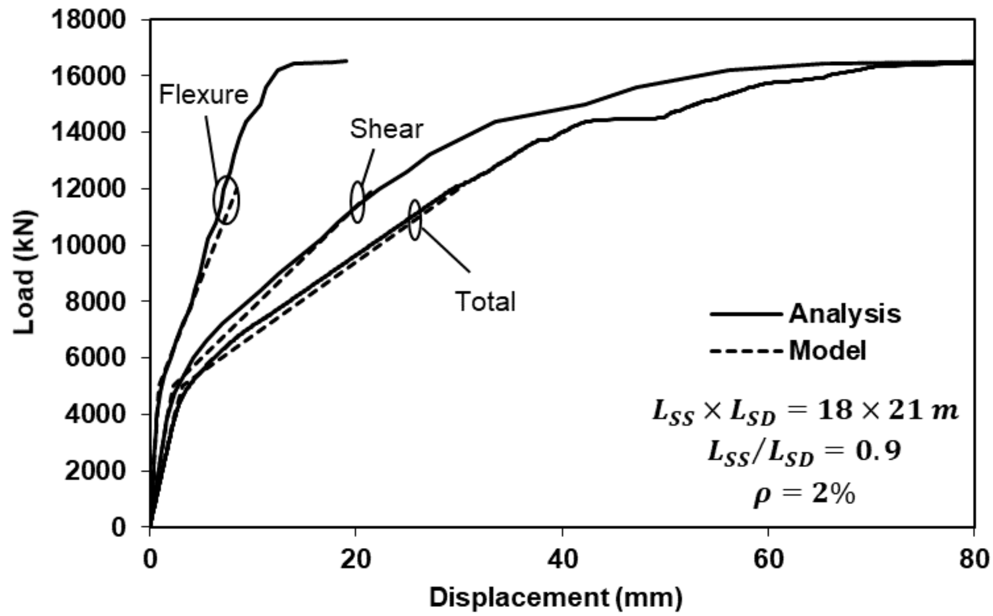

a)

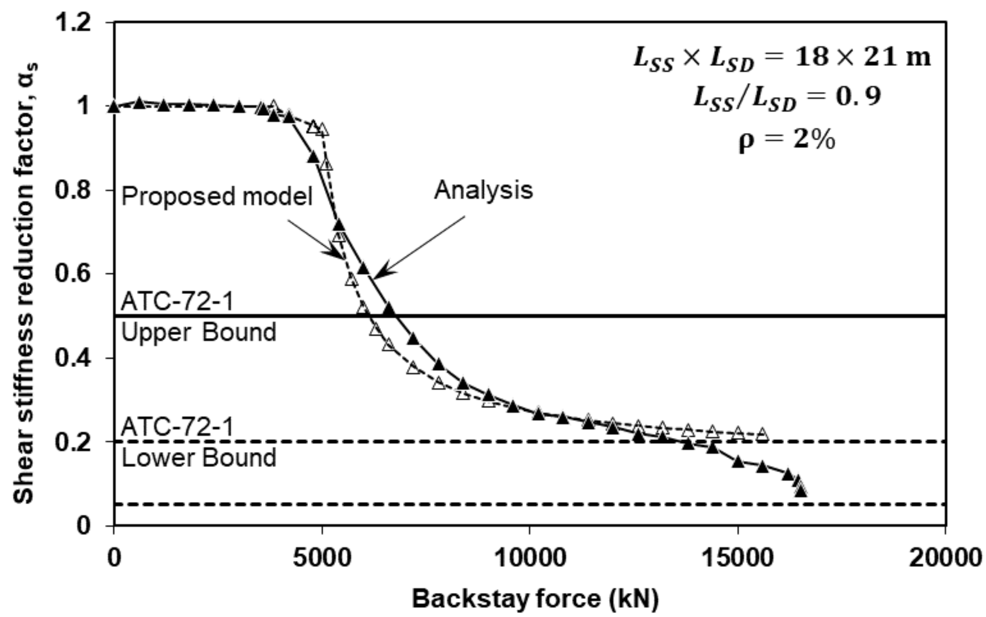

b)

Figure C.30 – Continued

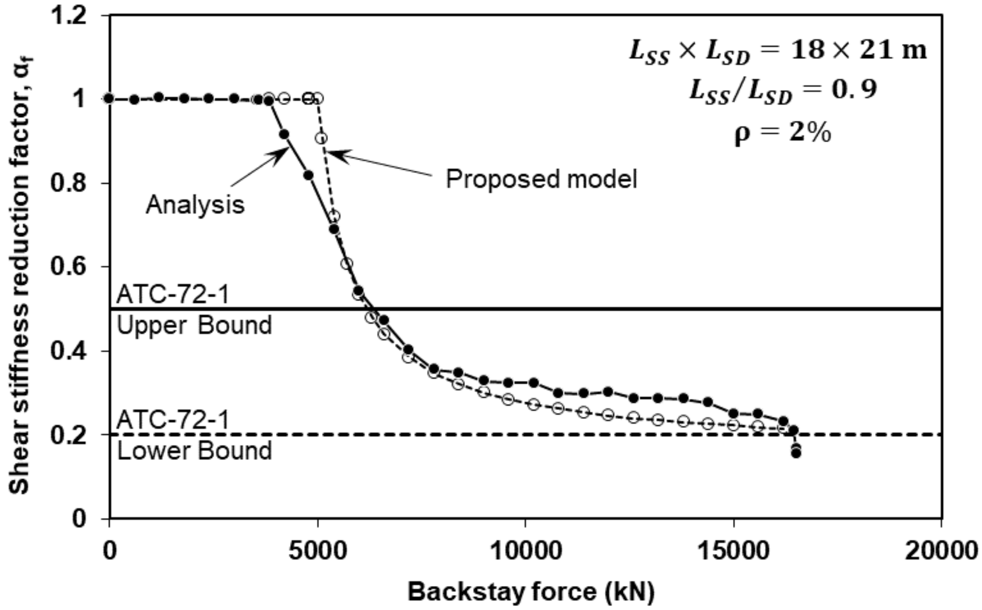

c)

Figure C.30 – Comparison of predicted and analytical results for diaphragm with $L_{SS} \times L_{SD} = 18 \times 21$ m (Case 1) and $\rho = 2\%$: (a) force-deformation relationship, (b) shear stiffness reduction factor, and (c) flexural stiffness reduction factor

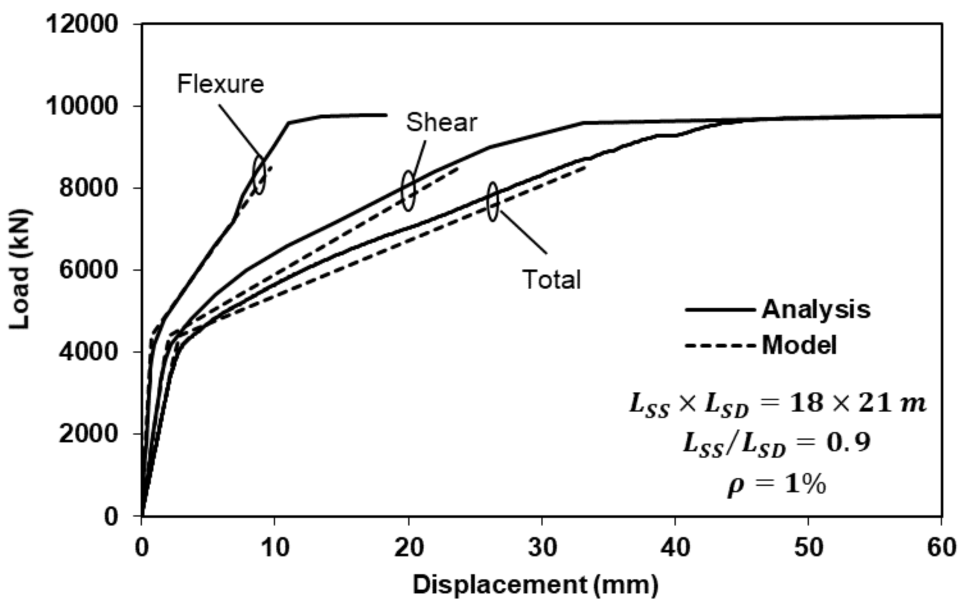

a)

Figure C.31 – Continued

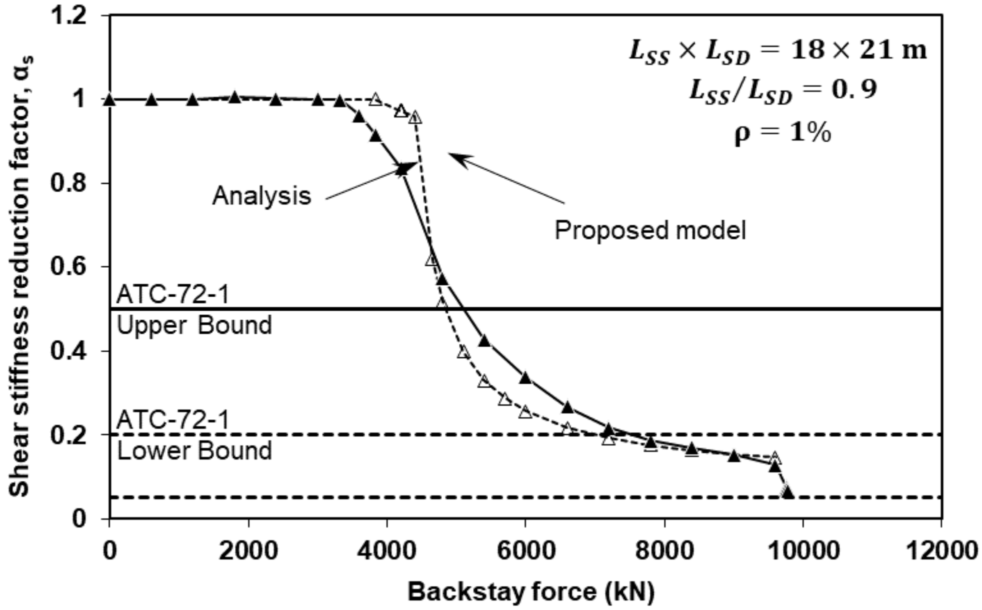

b)

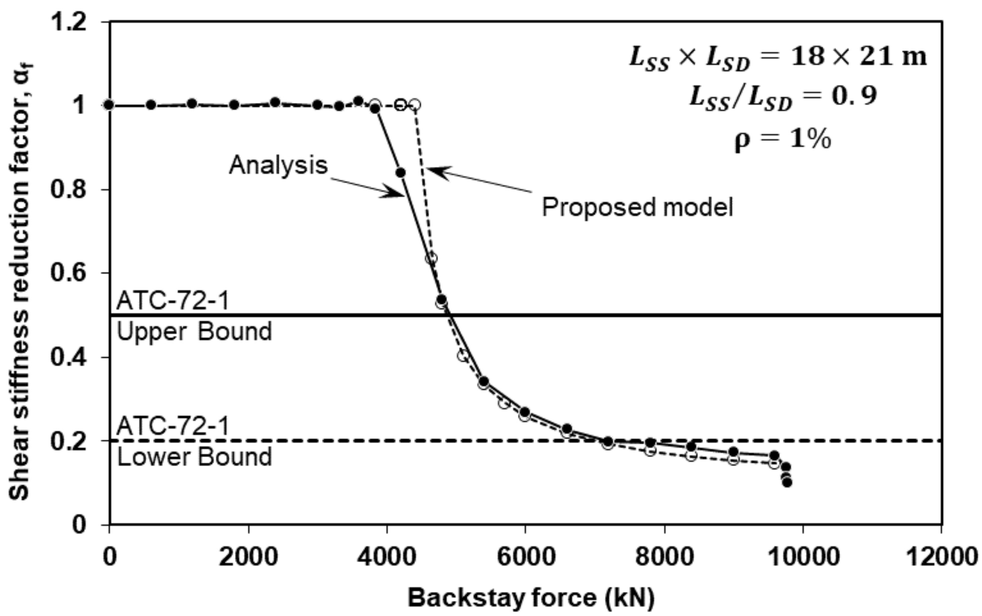

c)

Figure C.31 – Comparison of predicted and analytical results for diaphragm with $L_{SS} \times L_{SD} = 18 \times 21$ m (Case 1) and $\rho = 1\%$: (a) force-deformation relationship, (b) shear stiffness reduction factor, and (c) flexural stiffness reduction factor

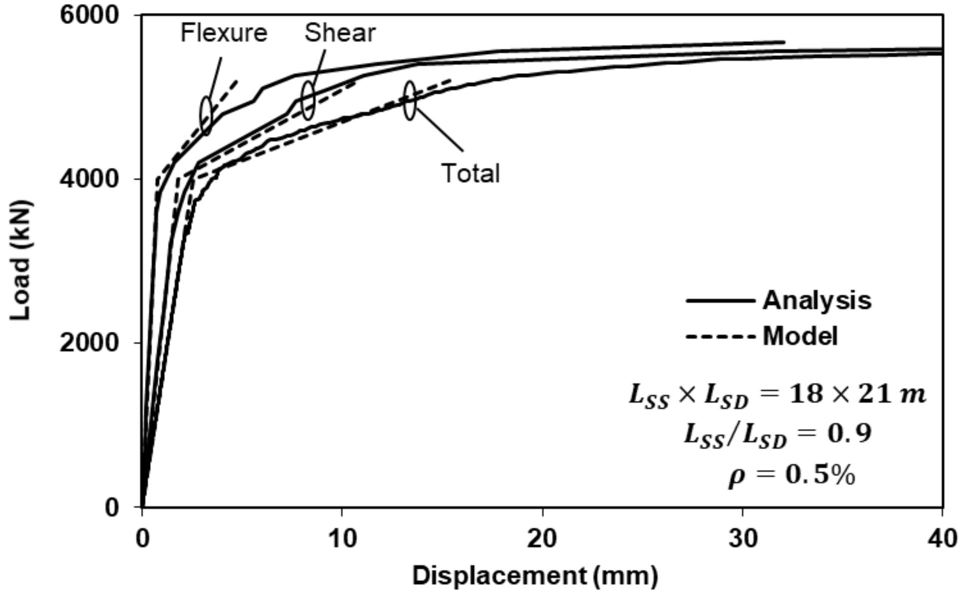

a)

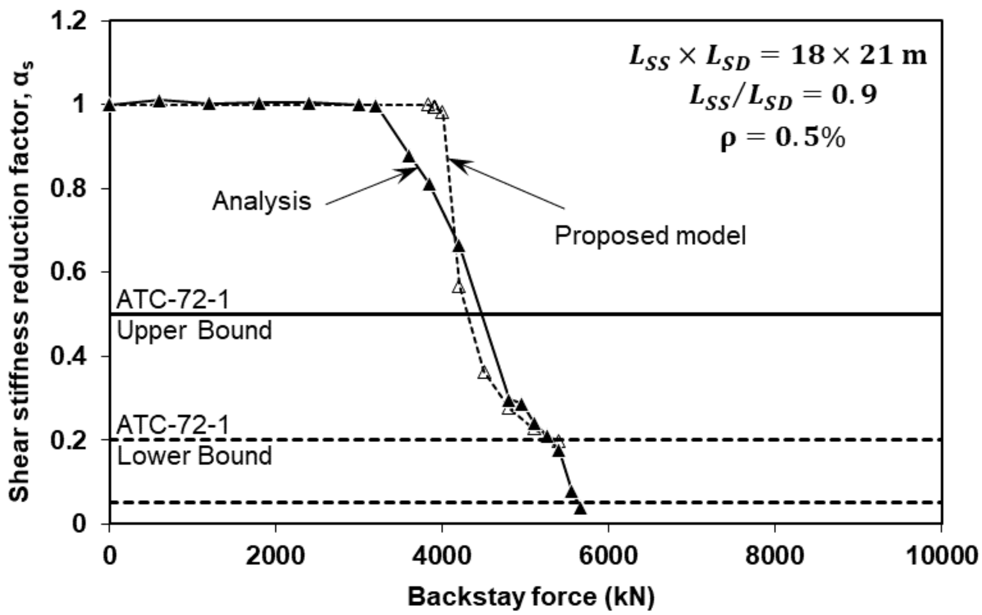

b)

Figure C.32 – Continued

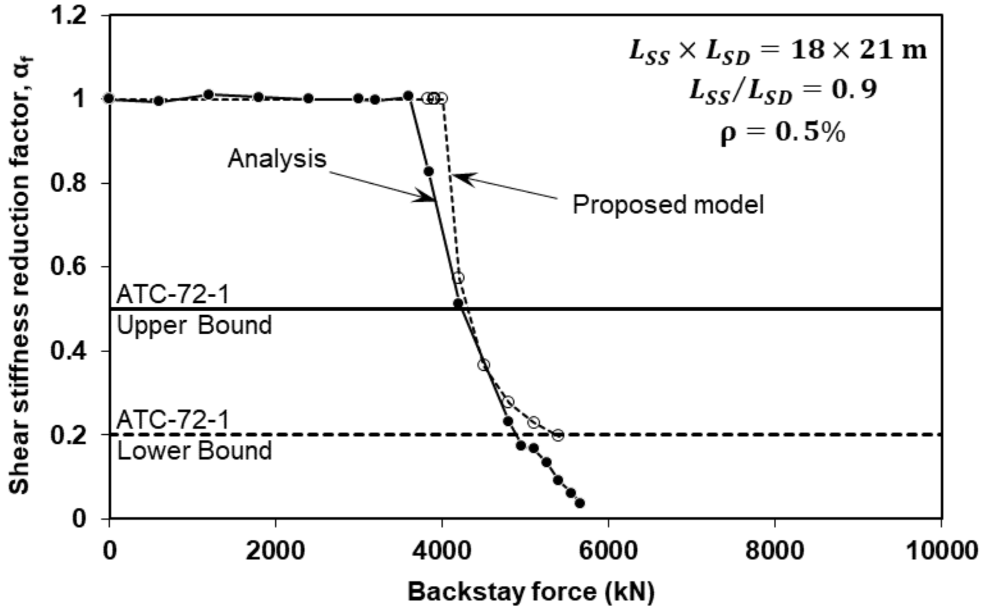

c)

Figure C.32 – Comparison of predicted and analytical results for diaphragm with $L_{SS} \times L_{SD} = 18 \times 21$ m (Case 1) and $\rho = 0.5\%$: (a) force-deformation relationship, (b) shear stiffness reduction factor, and (c) flexural stiffness reduction factor

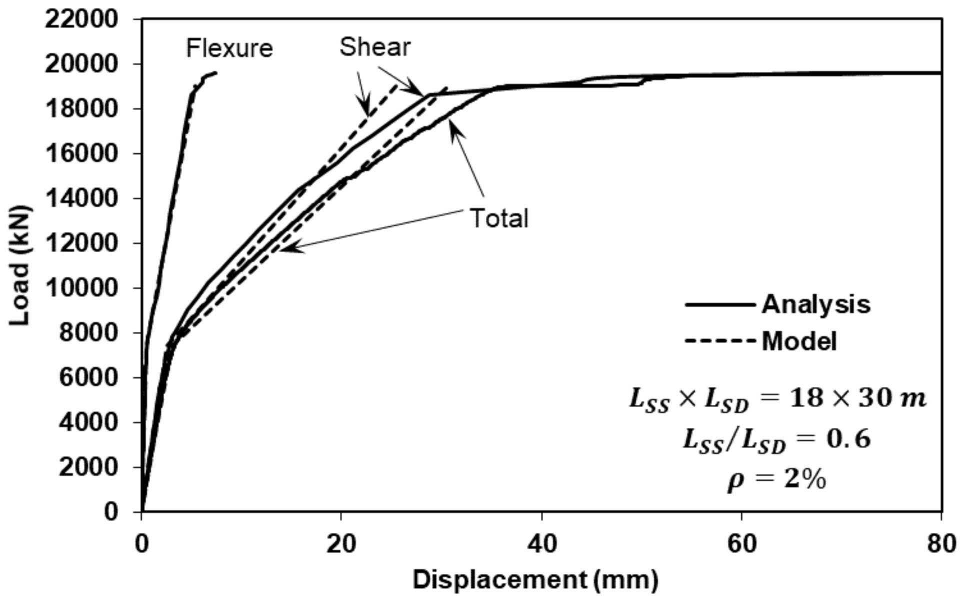

a)

Figure C.33 – Continued

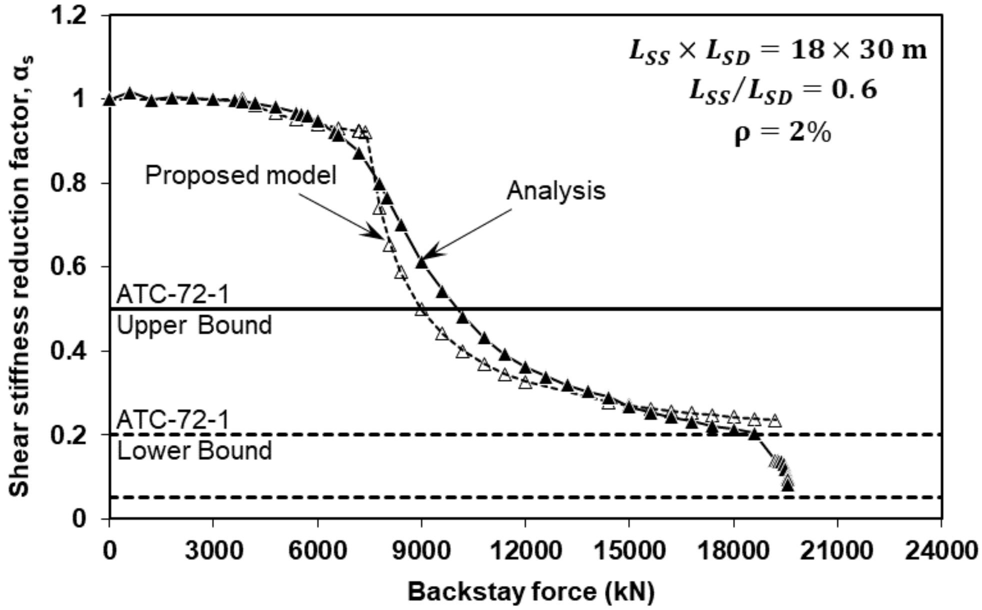

b)

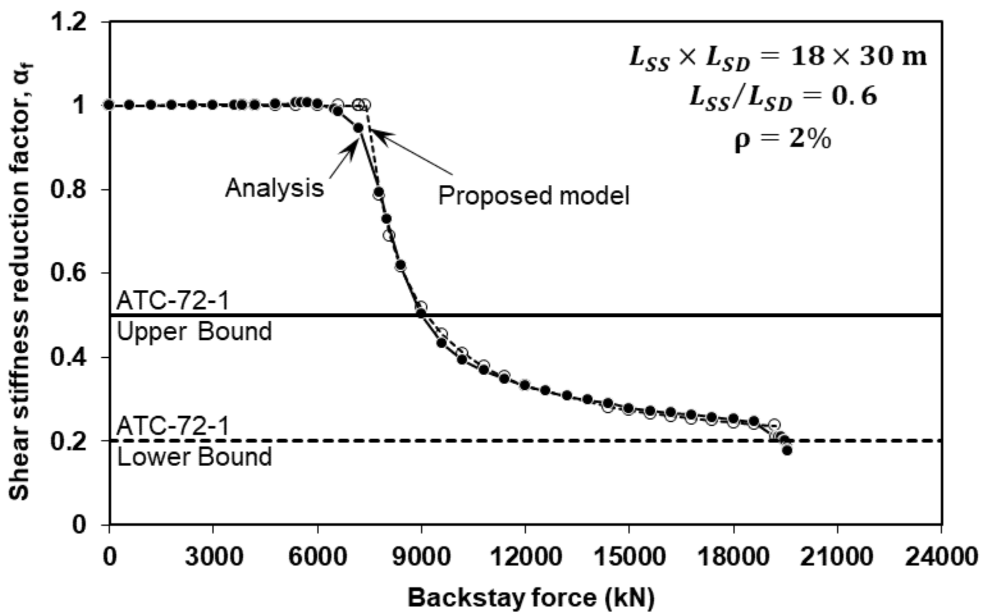

c)

Figure C.33 – Comparison of predicted and analytical results for diaphragm with $L_{SS} \times L_{SD} = 18 \times 30$ m (Case 2) and $\rho = 2\%$: (a) force-deformation relationship, (b) shear stiffness reduction factor, and (c) flexural stiffness reduction factor

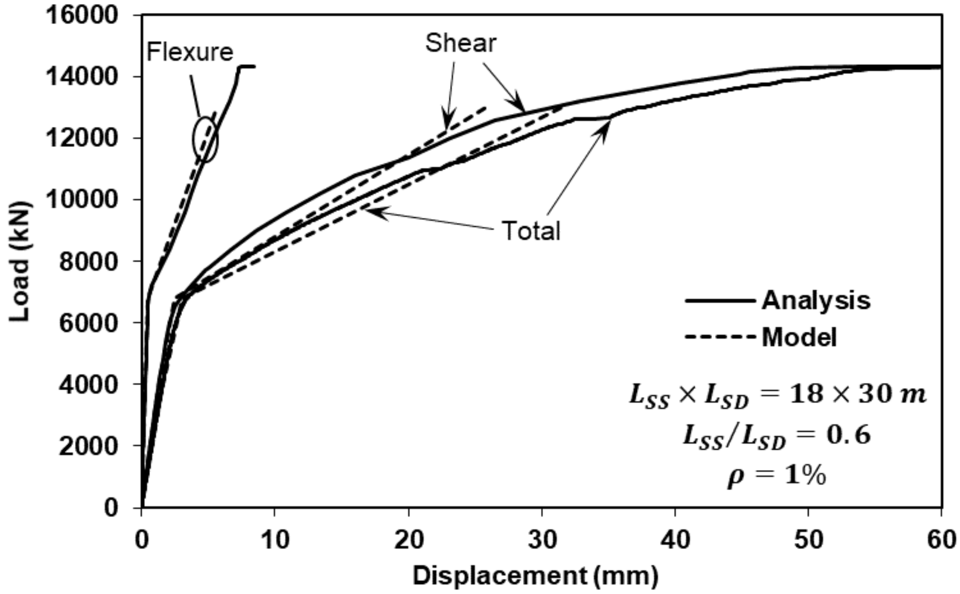

a)

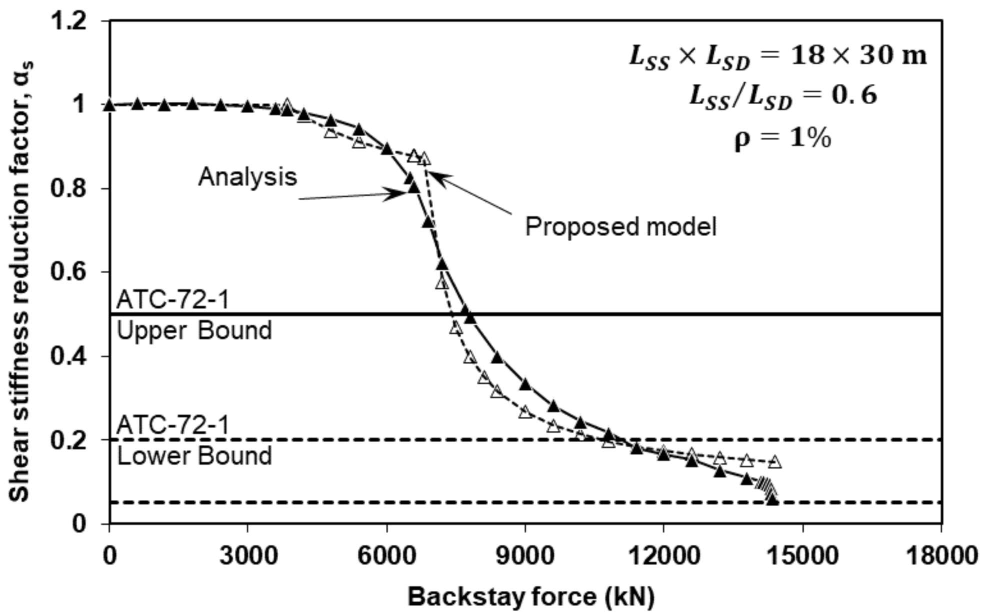

b)

Figure C.34 – Continued

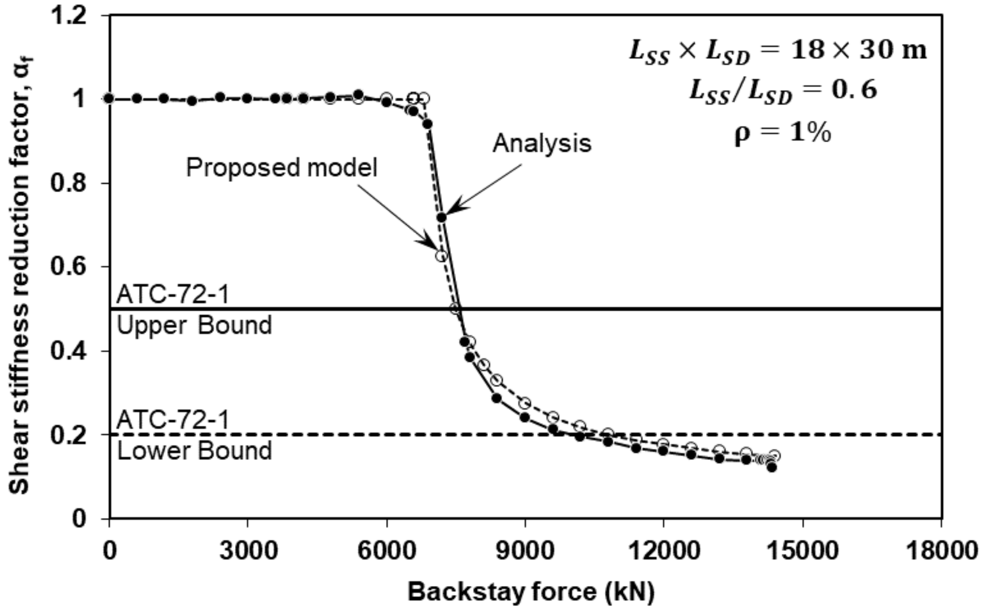

c)

Figure C.34 – Comparison of predicted and analytical results for diaphragm with $L_{SS} \times L_{SD} = 18 \times 30$ m (Case 2) and $\rho = 1\%$: (a) force-deformation relationship, (b) shear stiffness reduction factor, and (c) flexural stiffness reduction factor

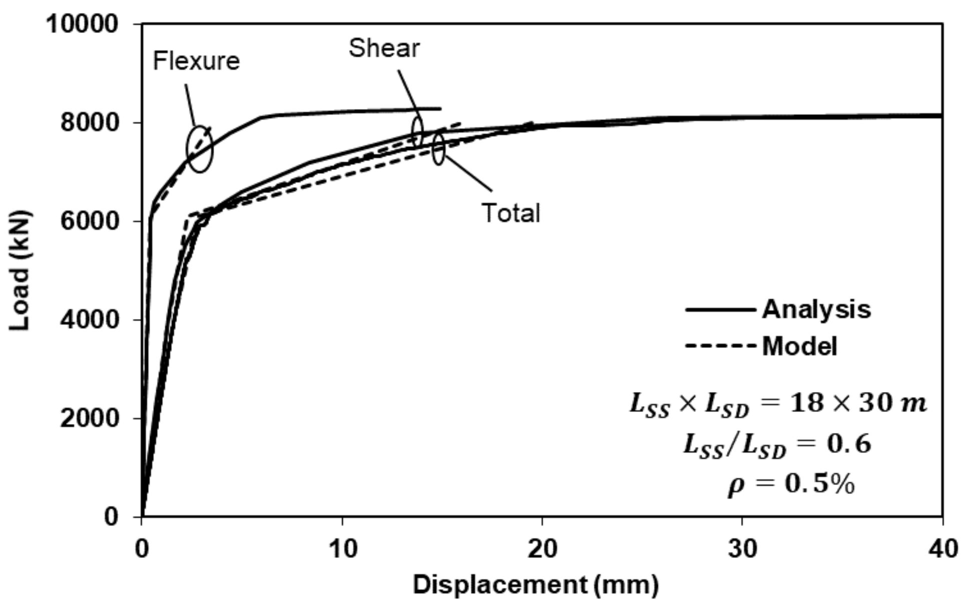

a)

Figure C.35 – Continued

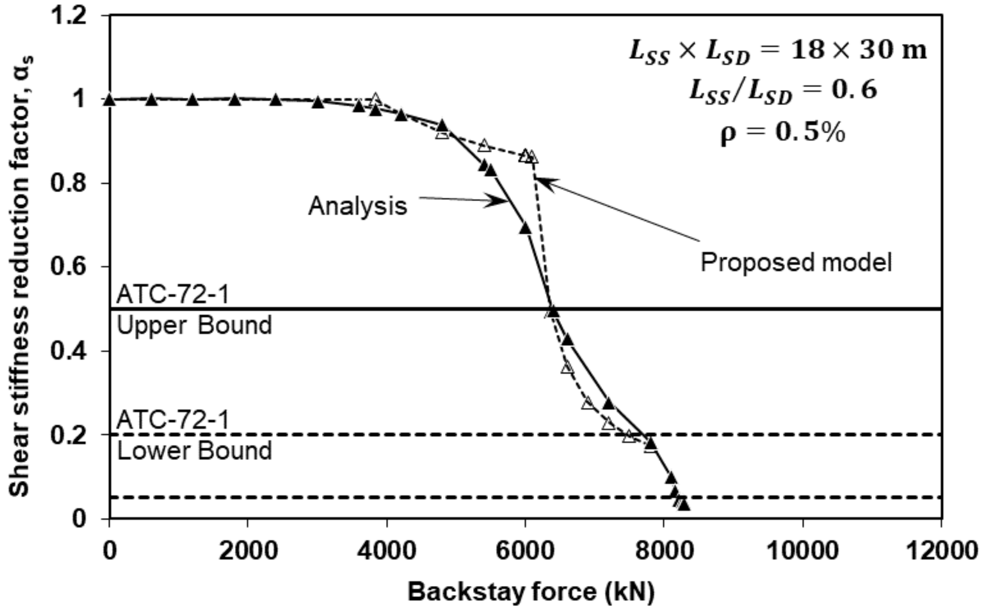

b)

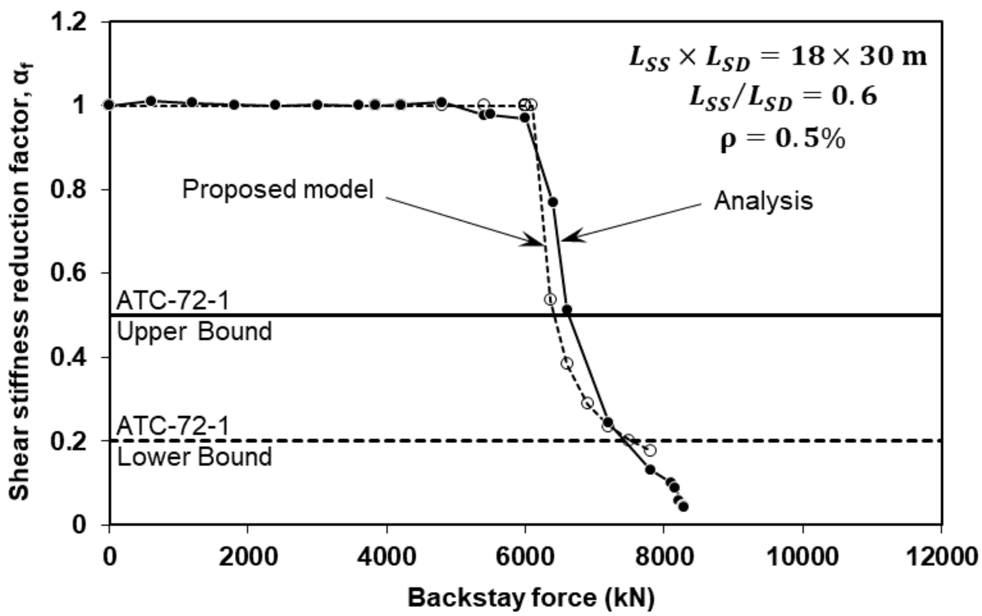

c)

Figure C.35 – Comparison of predicted and analytical results for diaphragm with $L_{SS} \times L_{SD} = 18 \times 30$ m (Case 2) and $\rho = 0.5\%$: (a) force-deformation relationship, (b) shear stiffness reduction factor, and (c) flexural stiffness reduction factor

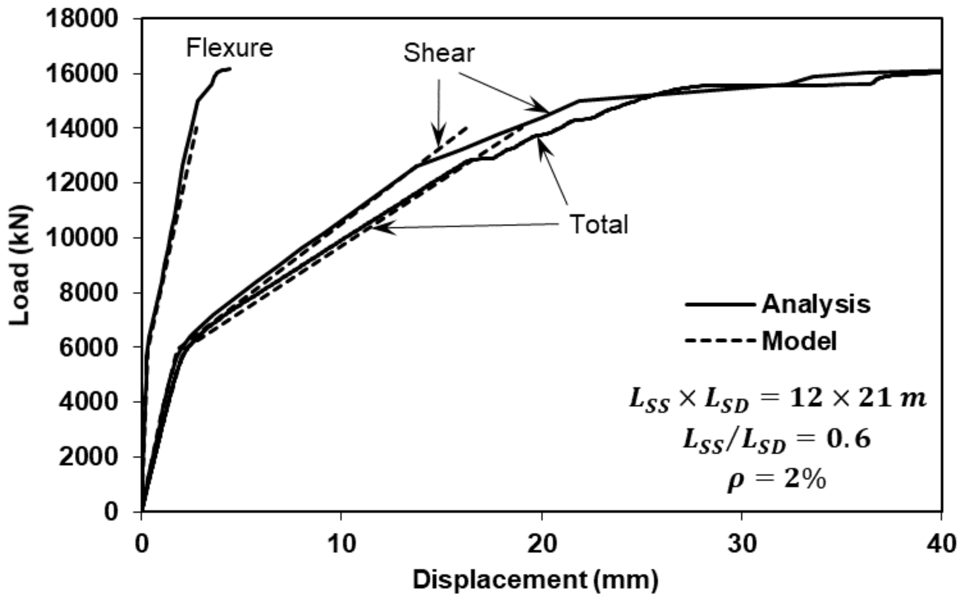

a)

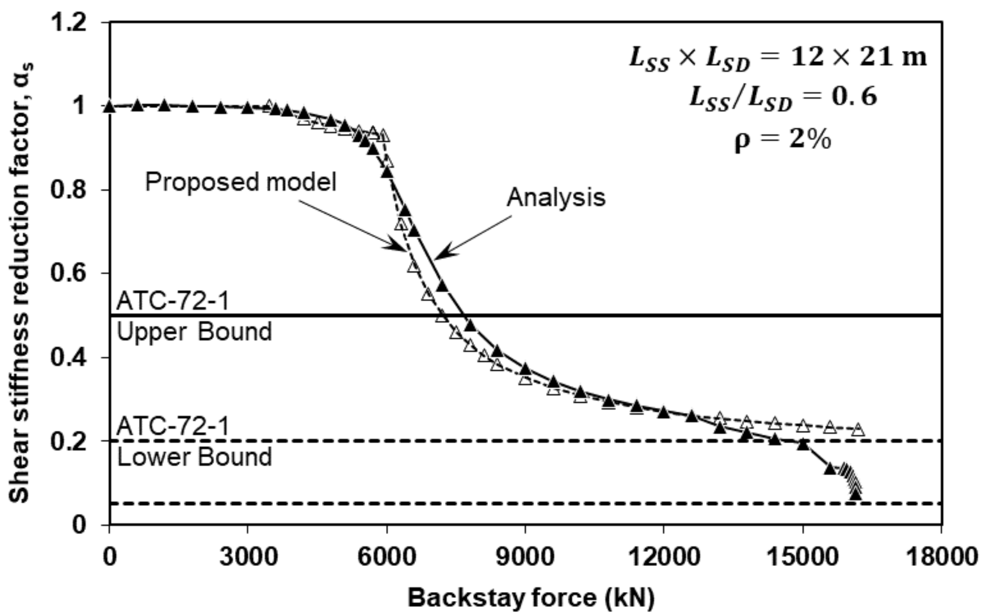

b)

Figure C.36 – Continued

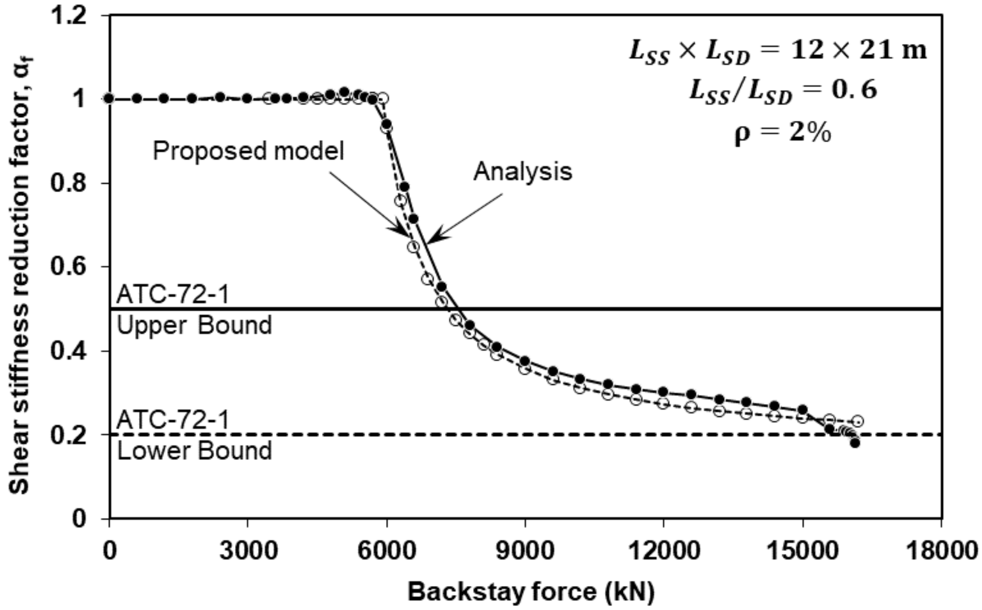

c)

Figure C.36 – Comparison of predicted and analytical results for diaphragm with $L_{SS} \times L_{SD} = 12 \times 21$ m (Case 3) and $\rho = 2\%$: (a) force-deformation relationship, (b) shear stiffness reduction factor, and (c) flexural stiffness reduction factor

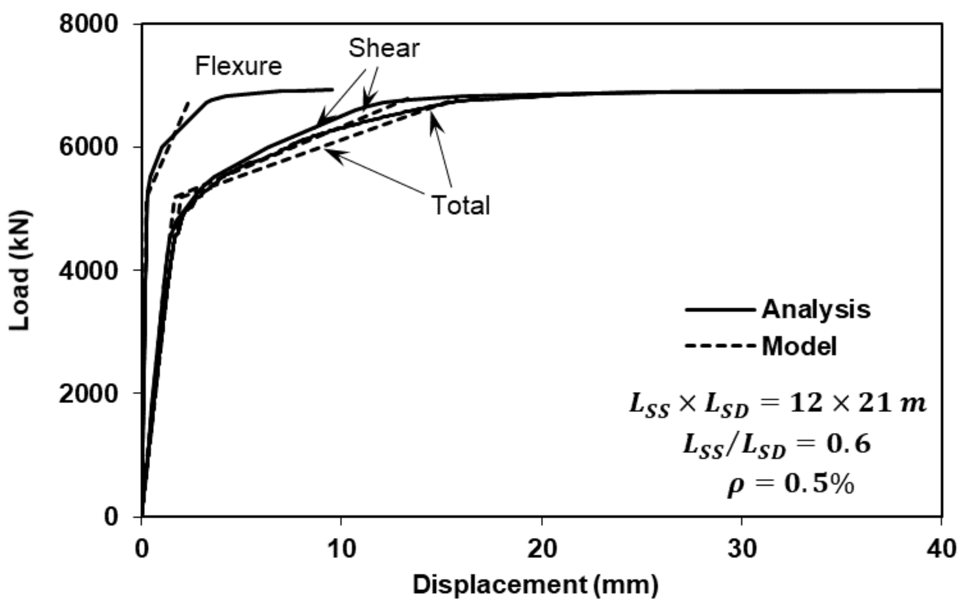

a)

Figure C.37 – Continued

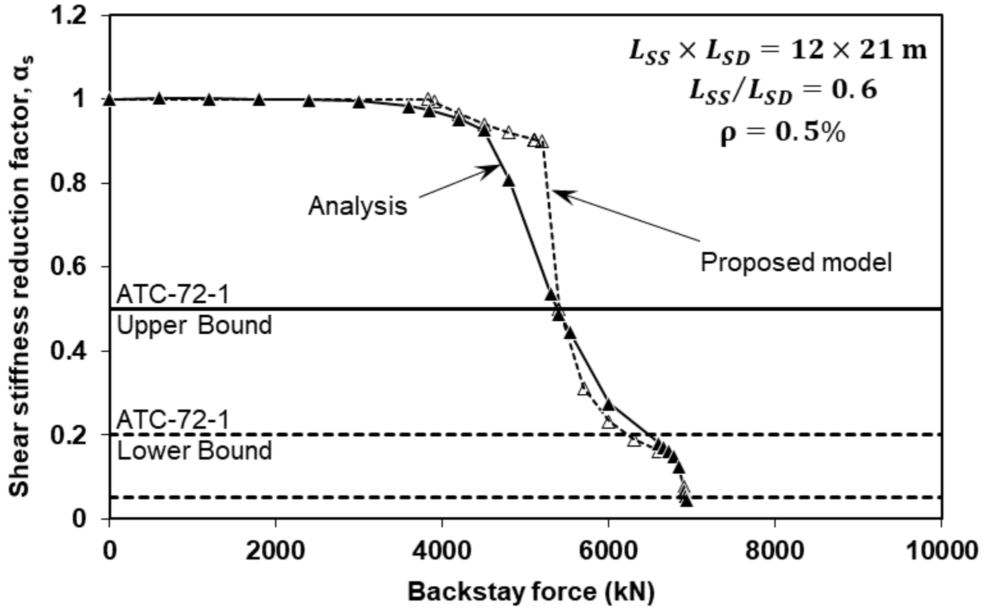

b)

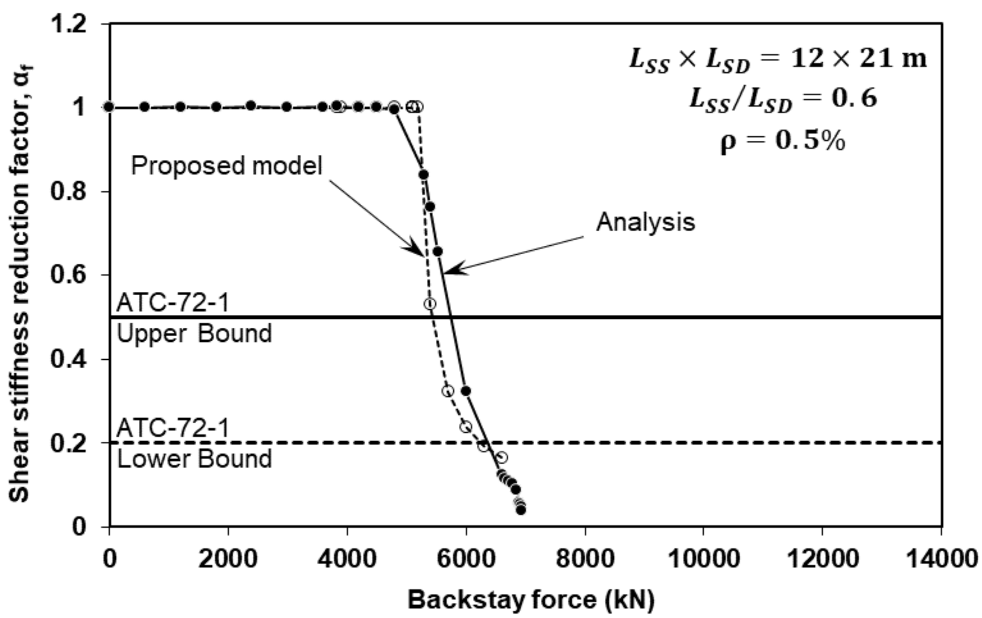

c)

Figure C.37 – Comparison of predicted and analytical results for diaphragm with $L_{SS} \times L_{SD} = 12 \times 21$ m (Case 3) and $\rho = 0.5\%$: (a) force-deformation relationship, (b) shear stiffness reduction factor, and (c) flexural stiffness reduction factor

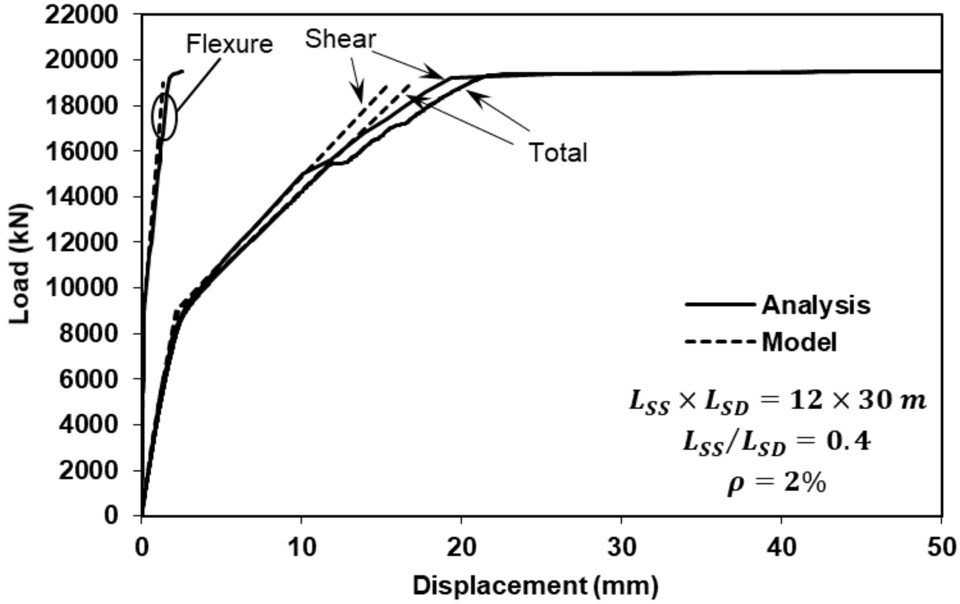

a)

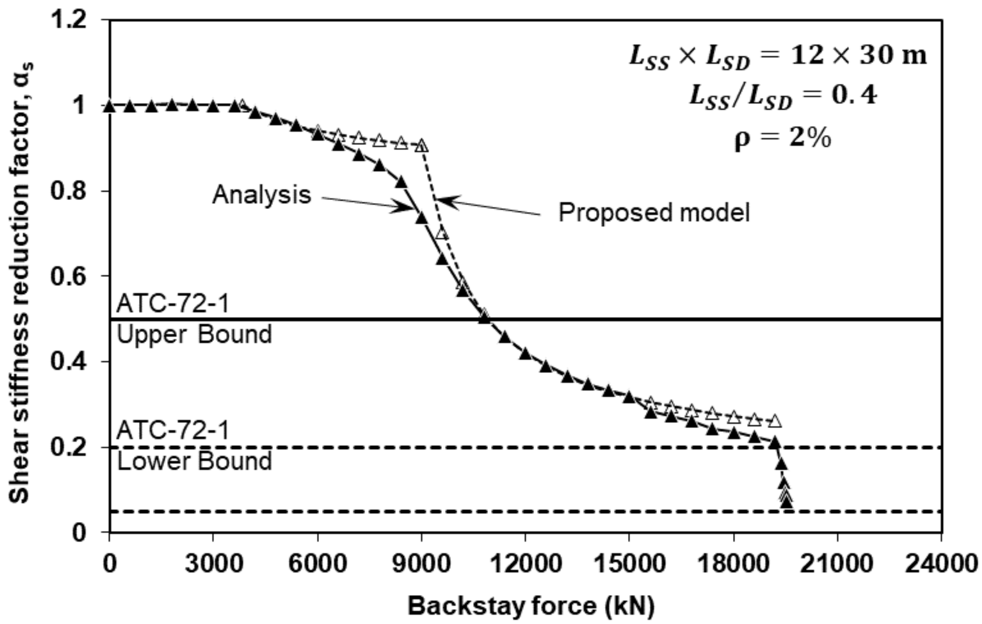

b)

Figure C.38 – Continued

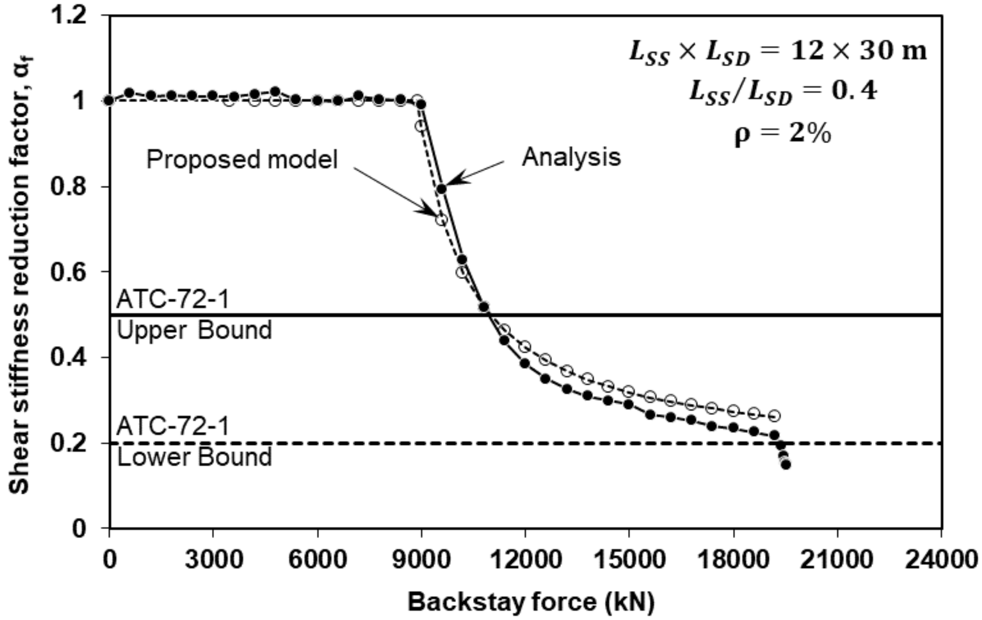

c)

Figure C.38 – Comparison of predicted and analytical results for diaphragm with $L_{SS} \times L_{SD} = 12 \times 30$ m (Case 4) and $\rho = 2\%$: (a) force-deformation relationship, (b) shear stiffness reduction factor, and (c) flexural stiffness reduction factor

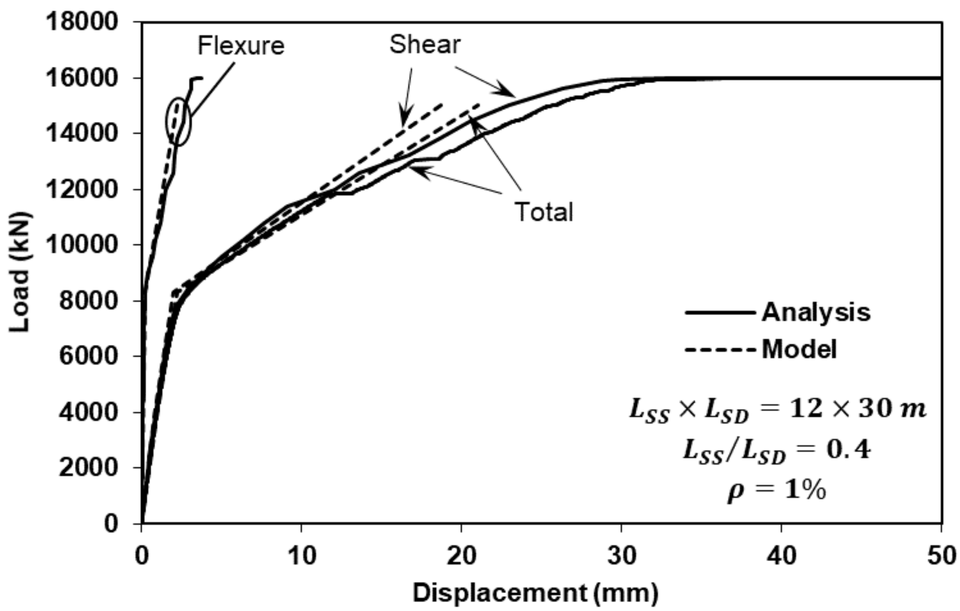

a)

Figure C.39 – Continued

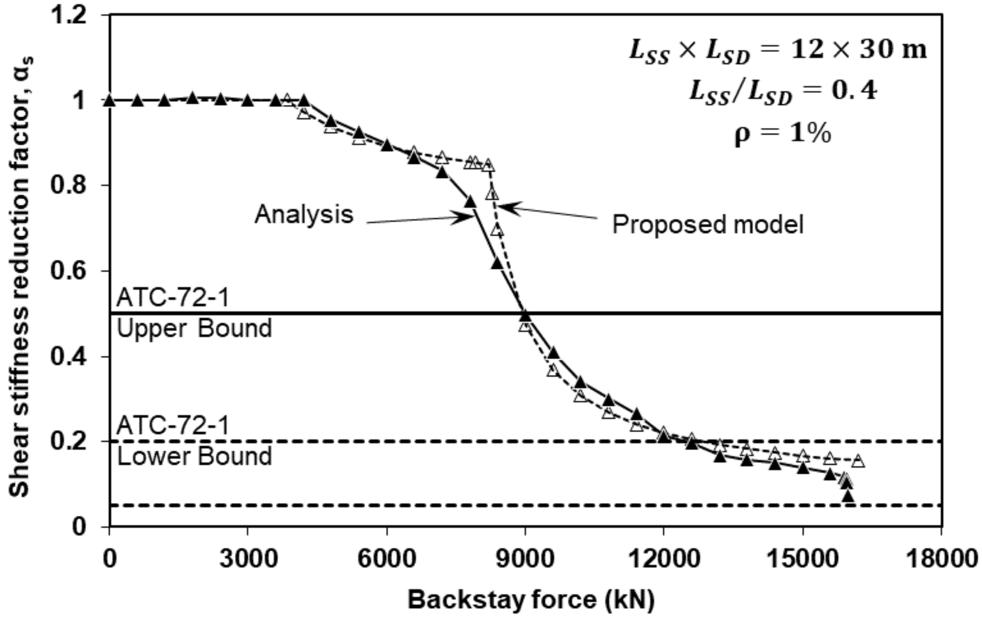

b)

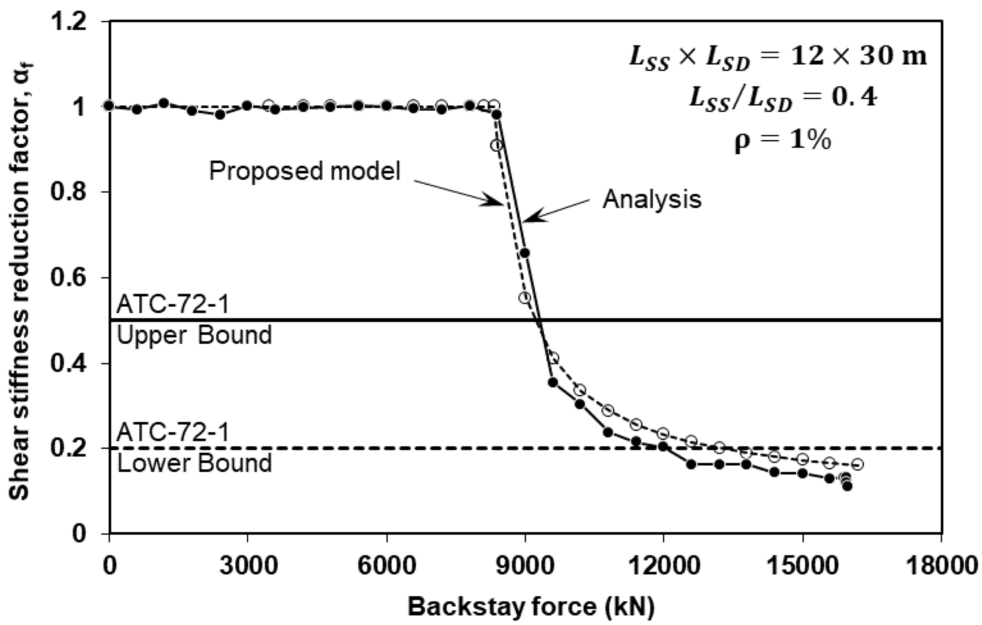

c)

Figure C.39 – Comparison of predicted and analytical results for diaphragm with $L_{SS} \times L_{SD} = 12 \times 30$ m (Case 4) and $\rho = 1\%$: (a) force-deformation relationship, (b) shear stiffness reduction factor, and (c) flexural stiffness reduction factor

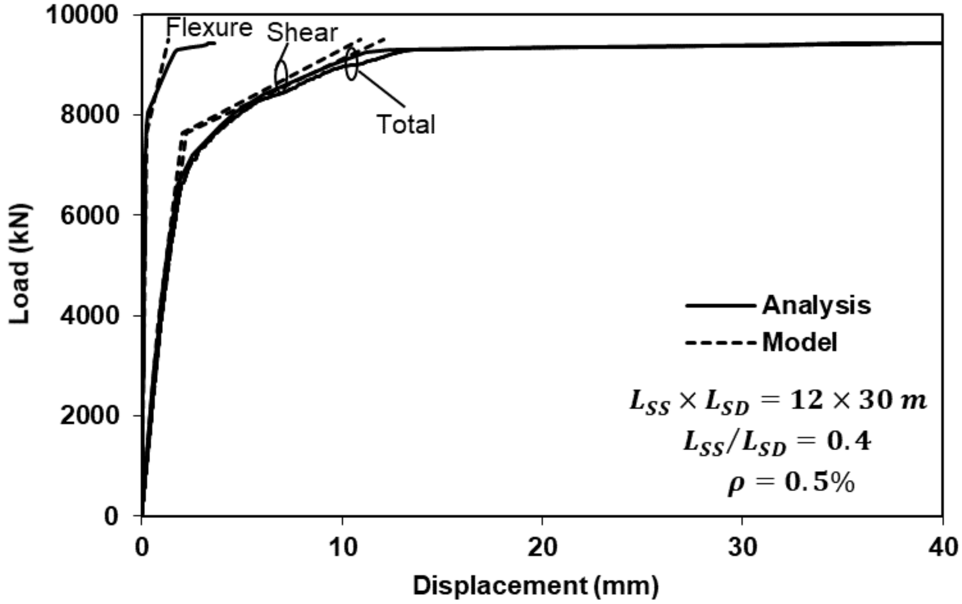

a)

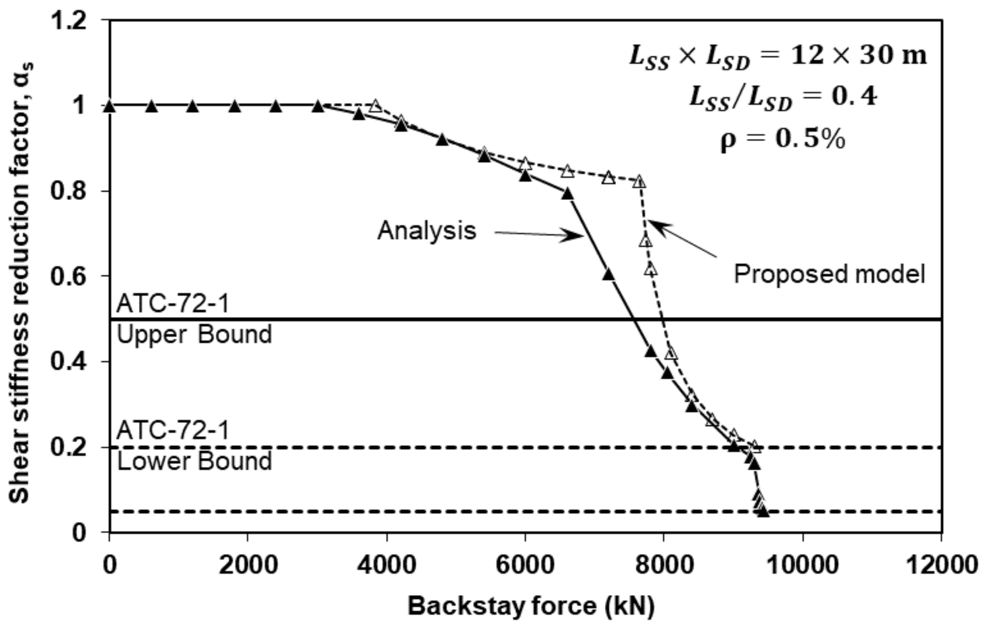

b)

Figure C.40 – Continued

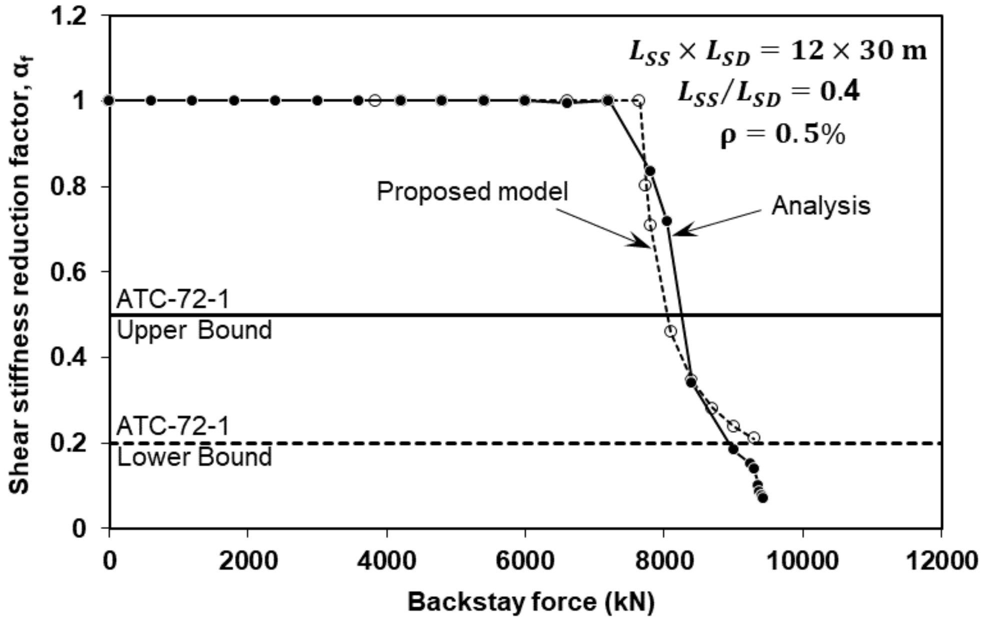

c)

Figure C.40 – Comparison of predicted and analytical results for diaphragm with $L_{SS} \times L_{SD} = 12 \times 30$ m (Case 4) and $\rho = 0.5\%$: (a) force-deformation relationship, (b) shear stiffness reduction factor, and (c) flexural stiffness reduction factor

Appendix D Deriving Expressions for Coefficients α_1 and α_2

Coefficients α_1 and α_1 are determined as a ratio of the cracked length to the diaphragm length at supports and mid-span, respectively, for a slab with fixed end supports subjected to a distributed load.

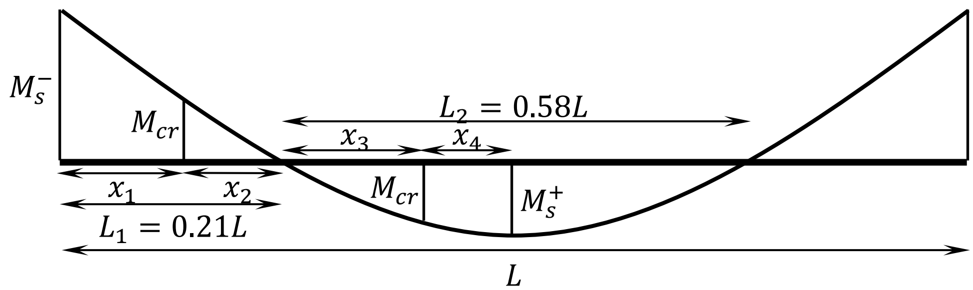

Figure D.1 – Bending moment diagram for a slab with fixed end supports subjected to a distributed load

The cracking moment and the maximum negative moment are defined as:

$$M_{cr} = \frac{f_r I_g}{y_t} \quad (D.1)$$

$$M_s^- = \frac{wL^2}{12} \quad (D.2)$$

For simplicity, the negative part of the bending moment diagram is considered as a rectangle, thus:

$$x_2 = L_1 \frac{M_{cr}}{M_s^-} \quad (D.3)$$

$$x_1 = L_1 - x_2 = L_1\left(1 - \frac{M_{cr}}{M_s^-}\right) = 0.21L\left(1 - \frac{M_{cr}}{M_s^-}\right) \quad (D.4)$$

$$\alpha_1 = \frac{x_1}{L/2} = 0.42\left(1 - \frac{M_{cr}}{M_s^-}\right) \quad (D.5)$$

$$M_s^+ = \frac{wL^2}{24} = \frac{wL_2^2}{8} \qquad (D.6)$$

$$x_3^2 - L_2 x_3 + \frac{M_{cr}}{w/2} = 0 \qquad (D.7)$$

$$x_3 = \frac{L_2 \pm \sqrt{L_2^2 - 4\,(\frac{M_{cr}}{w/2})}}{2} = \frac{L_2 \pm \sqrt{L_2^2\,(1 - \frac{M_{cr}}{wL_2^2/8})}}{2} = \frac{L_2}{2}\left(1 \pm \sqrt{1 - \frac{M_{cr}}{M_s^+}}\right) \qquad (D.8)$$

$$x_4 = \frac{L_2}{2} - x_3 = \frac{L_2}{2}\sqrt{1 - \frac{M_{cr}}{M_s^+}} \qquad (D.9)$$

$$\alpha_2 = \frac{x_4}{L/2} = \frac{L_2}{L}\sqrt{1 - \frac{M_{cr}}{M_s^+}} = 0.58\sqrt{1 - \frac{M_{cr}}{M_s^+}} \qquad (D.10)$$

Appendix E Reinforcement Details of Core Walls

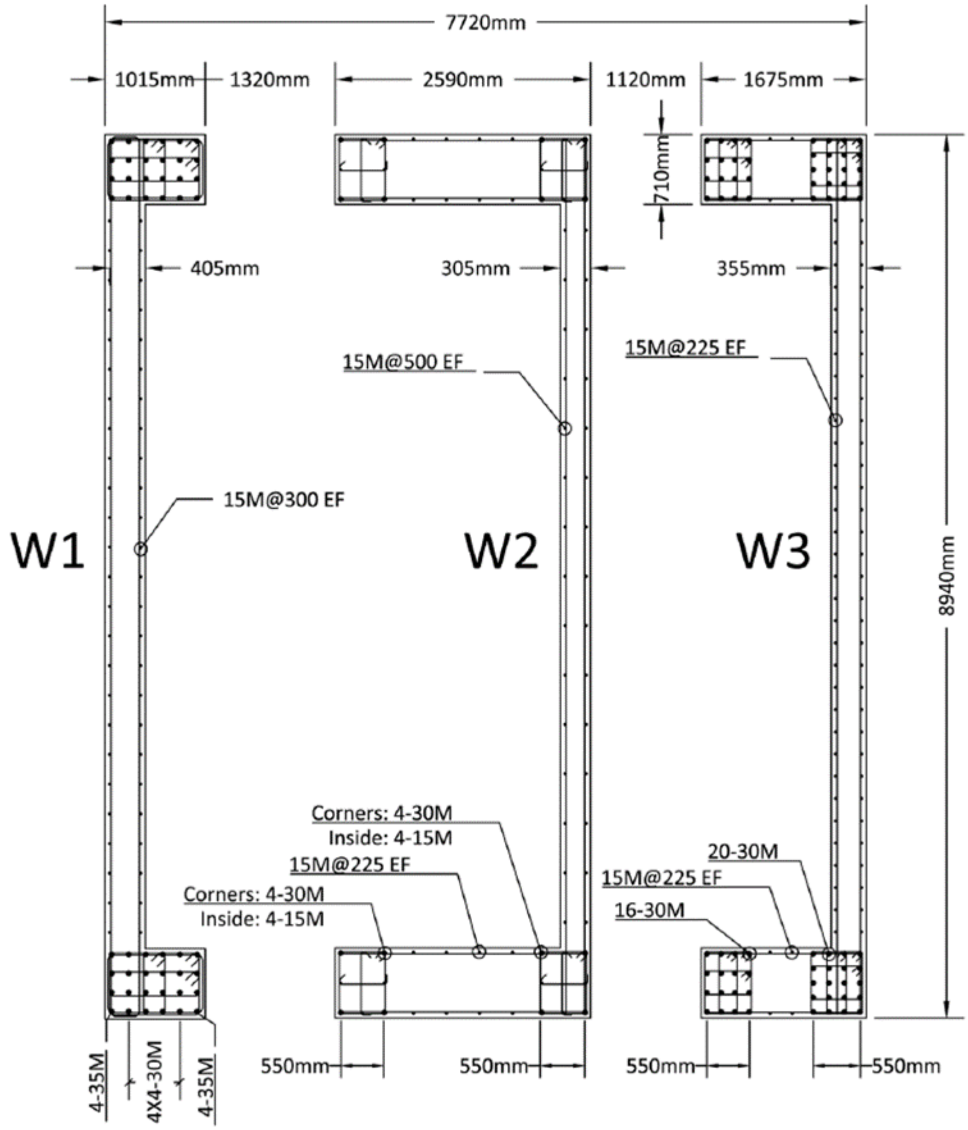

Figure E.1 – Plan view of core wall with details of vertical reinforcement at grade level (Mitchell, Paultre and Adebar, 2015)

Appendix F Analyzed Cases of High-Rise Core Wall Buildings with Sloped Columns

Definition of parameters used in the following tables:

SW: Shear wall
CW: Coupled wall
S: Symmetric
A: Asymmetric
RSA: Response spectrum analysis
LTHA: Linear time history analysis
NLTHA: Nonlinear time history analysis
GM: Ground motion
H: Horizontal
H+V: Horizontal and vertical

Table F.1 – Analyzed cases for understanding the physics of problem

Case	Column Slope (deg.)	Column Height (stories)	Column Base Story	Vert. Mass per Story in Weight Units (kN)	Wall Stiffness Modifier	Analysis Type	Excitation
1	3	16	0	1000	0.5	RSA	H
2	3	16	0	1000	0.85	RSA	H
2	3	16	0	1000	0.85	RSA	H
3	3	16	0	1000	0.85	RSA	H+V
1	3	16	0	1000	0.5	RSA	H
4	3	16	0	1000	0.5	LTHA (1 GM)	H
5	17	16	8	1000	0.85	RSA	H & H+V
6	17	16	8	1000	0.85	LTHA (1 GM)	H & H+V

- SAP 2D model, SW direction, Asymmetric sloped column
- Column stiffness modifier varies from 0.1 to 10

Table F.2 – Analyzed cases for comparing SRSS and CQC rules

Case	Column Slope (deg.)	Column Height (stories)	Column Base Story	Vert. Mass per Story in Weight Units (kN)	Wall Stiffness Modifier	Analysis Type	Excitation
1	3	16	0	1000	0.5	RSA (SRSS)	H
1	3	16	0	1000	0.5	RSA (CQC)	H

- SAP 2D model, SW direction, Asymmetric sloped column
- Column stiffness modifier varies from 0.1 to 10

Table F.3 – Analyzed cases for investigating influence of different characteristics of sloped columns

Case	Column Slope (deg.)	Column Height (stories)	Column Base Story	Vert. Mass per Story in Weight Units (kN)	Wall Stiffness Modifier
7	0	16	0	1000	0.5
8	3	16	0	1000	0.5
9	6	16	0	1000	0.5
10	9	16	0	1000	0.5
11	3	16	0	1000	0.5
12	3	8	0	1000	0.5
13	3	4	0	1000	0.5
14	6	16	0	1000	0.5
15	6	16	4	1000	0.5
16	6	16	8	1000	0.5
17	9	8	0	100	0.5
18	9	8	0	1000	0.5
19	9	8	0	3000	0.5
20	9	8	0	1000	0.5
21	9	8	0	1000	0.85
22	9	8	0	1000	1.0

- ETABS 3D model, SW & CW directions, S & A sloped columns, RSA, H & H+V excitations
- Column stiffness modifier varies from 0.1 to 10

Table F.4 – Analyzed cases for comparing SAP and ETABS models

Case	Column Slope (deg.)	Column Height (stories)	Column Base Story	Vert. Mass per Story in Weight Units (kN)	Wall Stiffness Modifier	Model
1	3	16	0	1000	0.5	SAP 2D
1	3	16	0	1000	0.5	ETABS 3D

- SW direction, Asymmetric sloped column, RSA, H excitation
- Column stiffness modifier varies from 0.1 to 10

Table F.5 – Analyzed cases for comparing RSA and LTHA

Case	Column Slope (deg.)	Column Height (stories)	Column Base Story	Vert. Mass per Story in Weight Units (kN)	Analysis Type	Excitation
23	0	16	0	1000	RSA	H & H+V
24	0	16	0	1000	LTHA (11 GMs)	H & H+V
2	3	16	0	1000	RSA	H & H+V
26	3	16	0	1000	LTHA (11 GMs)	H & H+V
26	6	16	0	1000	RSA	H & H+V
27	6	16	0	1000	LTHA (11 GMs)	H & H+V
28	9	16	0	1000	RSA	H & H+V
29	9	16	0	1000	LTHA (11 GMs)	H & H+V
30	12	16	0	1000	RSA	H & H+V
31	12	16	0	1000	LTHA (11 GMs)	H & H+V
32	15	16	0	1000	RSA	H & H+V
33	15	16	0	1000	LTHA (11 GMs)	H & H+V
5	17	16	0	1000	RSA	H & H+V
34	17	16	0	1000	LTHA (11 GMs)	H & H+V
35	20	16	0	1000	RSA	H & H+V
36	20	16	0	1000	LTHA (11 GMs)	H & H+V

- SAP 2D model, SW direction, Asymmetric sloped column
- Column stiffness modifier is 1, wall stiffness modifier is 0.85

Table F.6 – Analyzed cases for comparing RSA and LTHA analyses

Case	No. of Story	Column Slope (degree)	Column Height (story)	Column Base Location (story)	Vert. Mass per Story in Weight Units (kN)	Analysis Type	Excitation
37	30	3	4	0 - 26 (every 2 stories)	1000	LTHA (1 GM)	H
38	30	3	16	0 - 14 (every 2 stories)	1000	LTHA (1 GM)	H
39	50	17	30	0 - 15 (every 5 stories)	1000	LTHA (1 GM)	H & H+V
40	50	17	30	0 - 15 (every 5 stories)	1000	RSA	H & H+V

- SAP 2D model, SW direction, Asymmetric sloped column
- Column stiffness modifier is 1, wall stiffness modifier is 0.85

Table F.7 – Analyzed cases for developing simplified procedure

Case	Column Slope (deg.)	Column Height (stories)	Column Base Story	Vert. Mass per Story in Weight Units (kN)	Wall Stiffness Modifier	Analysis Type	Excitation
1	3	16	0	1000	0.5	RSA	H
41	6	16	0	1000	0.5	RSA	H
42	9	16	0	1000	0.5	RSA	H
43	12	16	0	1000	0.5	RSA	H
44	15	16	0	1000	0.5	RSA	H
45	17	16	0	1000	0.5	RSA	H
46	20	16	0	1000	0.5	RSA	H
47	3	16	0	1000	1	RSA	H
48	6	16	0	1000	1	RSA	H
49	9	16	0	1000	1	RSA	H
50	12	16	0	1000	1	RSA	H
51	15	16	0	1000	1	RSA	H
52	17	16	0	1000	1	RSA	H
53	20	16	0	1000	1	RSA	H
54	3	16	8	1000	0.5	RSA	H
55	12	16	8	1000	0.5	RSA	H
56	17	16	8	1000	0.5	RSA	H
57	20	16	8	1000	0.5	RSA	H
58	3	4	0	1000	1	RSA	H
59	12	4	0	1000	1	RSA	H
60	20	4	0	1000	1	RSA	H
61	3	4	8	1000	1	RSA	H
62	12	4	8	1000	1	RSA	H
63	20	4	8	1000	1	RSA	H

- SAP 2D model, SW direction, Asymmetric sloped column
- Column stiffness modifier varies from 0.1 to 10

Table F.8 – Analyzed cases for investigating the influence of effective stiffness of shear walls

Case	Column Slope (deg.)	Column Height (stories)	Column Base Story	Vert./Horz. Mass per Story in Weight Units (kN)	Wall Stiffness Modifier	Analysis Type	Excitation
64	17	16	8	1000/5000	1	LTHA (11 GMs)	H & H+V
65	17	16	8	1000/5000	-	NLTHA (11 GMs)	H & H+V
66	17	16	8	2000/5000	1	LTHA (11 GMs)	H & H+V
67	17	16	8	2000/5000	-	NLTHA (11 GMs)	H & H+V
68	17	16	8	1000/10000	1	LTHA (11 GMs)	H & H+V
69	17	16	8	1000/10000	-	NLTHA (11 GMs)	H & H+V
70	17	16	8	500/5000	1	LTHA (3 GMs)	H & H+V
71	17	16	8	500/5000	-	NLTHA (3 GMs)	H & H+V
64	17	16	8	1000/5000	1	LTHA (3 GMs)	H & H+V
65	17	16	8	1000/5000	-	NLTHA (3 GMs)	H & H+V
72	17	16	8	1500/5000	1	LTHA (3 GMs)	H & H+V
73	17	16	8	1500/5000	-	NLTHA (3 GMs)	H & H+V
66	17	16	8	2000/5000	1	LTHA (3 GMs)	H & H+V
67	17	16	8	2000/5000	-	NLTHA (3 GMs)	H & H+V
74	17	16	8	2500/5000	1	LTHA (3 GMs)	H & H+V
75	17	16	8	2500/5000	-	NLTHA (3 GMs)	H & H+V
76	17	16	8	3000/5000	1	LTHA (3 GMs)	H & H+V
77	17	16	8	3000/5000	-	NLTHA (3 GMs)	H & H+V

- PERFORM model, SW direction, Asymmetric sloped column
- Column stiffness modifier is 1

Table F.9 – Analyzed cases for comparing simplified procedure with NLTHA results

Case	Column Slope (deg.)	Column Height (stories)	Column Base Story	Vert./Horz. Mass per Story in Weight Units (kN)	Wall Direction	GMs	Column Stiffness Modifier
78	17	16	8	1000/10000	SW	22 Crustal	0.5
79	17	16	8	1000/10000	SW	22 Subcrustal	0.5
80	17	16	8	1000/10000	SW	22 Subduction	0.5
81	45	3	3	1000/5000	SW	22 Crustal	0.5
82	45	3	3	1000/5000	SW	22 Subcrustal	0.5
83	45	3	3	1000/5000	SW	22 Subduction	0.5
84	17	16	8	1000/10000	SW	22 Crustal 22 Subcrustal	0.1
85	17	16	8	1000/10000	SW	22 Crustal 22 Subcrustal	0.2
86	17	16	8	1000/10000	SW	22 Crustal 22 Subcrustal	0.3
87	17	16	8	1000/10000	SW	22 Crustal 22 Subcrustal	0.4
78 **79**	17	16	8	1000/10000	SW	22 Crustal 22 Subcrustal	0.5
88	17	16	8	1000/10000	SW	22 Crustal 22 Subcrustal	0.6
89	17	16	8	1000/10000	SW	22 Crustal 22 Subcrustal	0.7
90	17	16	8	1000/10000	SW	22 Crustal 22 Subcrustal	0.8
91	17	16	8	1000/10000	SW	22 Crustal 22 Subcrustal	0.9
92	17	16	8	1000/10000	SW	22 Crustal 22 Subcrustal	1.0
93	17	16	8	1000/10000	CW	22 Crustal 22 Subcrustal	0.5
94	17	16	8	1000/10000	CW	22 Crustal 22 Subcrustal	1.0

- PERFORM model, NLTHA, Asymmetric sloped column, H+V Excitation

Table F.10 – Analyzed cases for comparing simplified procedure with NLTHA results

Case	Column Slope (deg.)	Column Height (stories)	Column Base Story	Vert./Horz. Mass per Story in Weight Units (kN)	Wall Direction	GMs	Column Stiffness Modifier
95	45	3	3	1000/5000	SW	22 Crustal 22 Subcrustal	0.1
96	45	3	3	1000/5000	SW	22 Crustal 22 Subcrustal	0.2
97	45	3	3	1000/5000	SW	22 Crustal 22 Subcrustal	0.3
98	45	3	3	1000/5000	SW	22 Crustal 22 Subcrustal	0.4
81 **82**	45	3	3	1000/5000	SW	22 Crustal 22 Subcrustal	0.5
99	45	3	3	1000/5000	SW	22 Crustal 22 Subcrustal	0.6
100	45	3	3	1000/5000	SW	22 Crustal 22 Subcrustal	0.7
101	45	3	3	1000/5000	SW	22 Crustal 22 Subcrustal	0.8
102	45	3	3	1000/5000	SW	22 Crustal 22 Subcrustal	0.9
103	45	3	3	1000/5000	SW	22 Crustal 22 Subcrustal	1.0
104	45	3	3	1000/5000	CW	22 Crustal 22 Subcrustal	0.5
105	45	3	3	1000/5000	CW	22 Crustal 22 Subcrustal	1.0

- PERFORM model, NLTHA, Asymmetric sloped column, H+V Excitation

Appendix G Nonlinear Analysis Results for High-Rise Buildings with Sloped-Column Irregularity

Figures G.1 and G.2 compare the increase in column axial force obtained from simplified procedure and NLTHA for the case of sloped column with the slope of 17 deg. starting at 8th floor and going up for 16 floors (17D-16S-8) with different column stiffnesses for crustal and subcrustal ground motions, respectively.

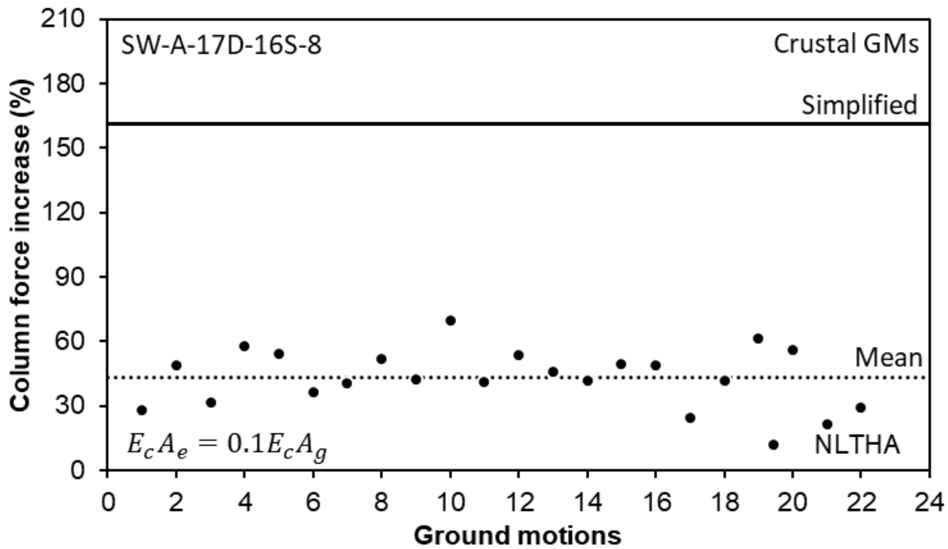

a)

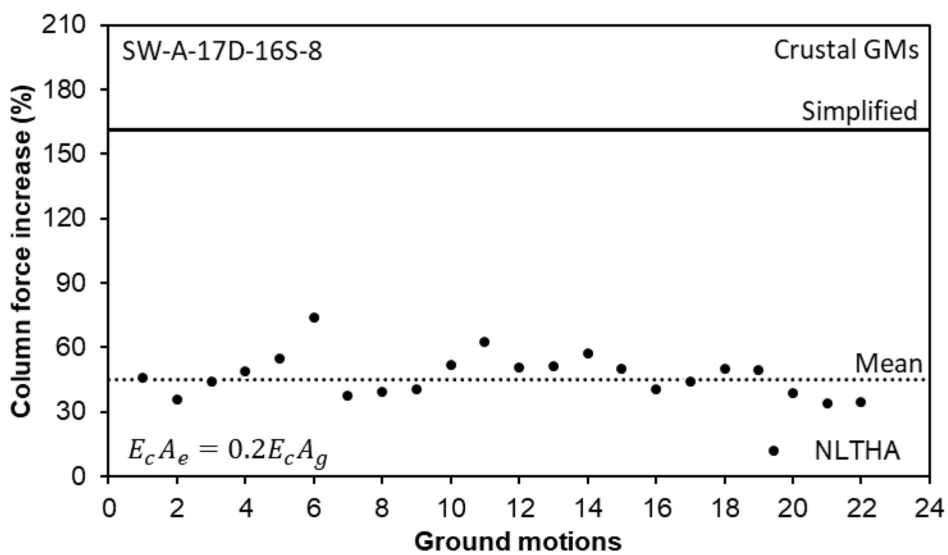

b)

Figure – Continued

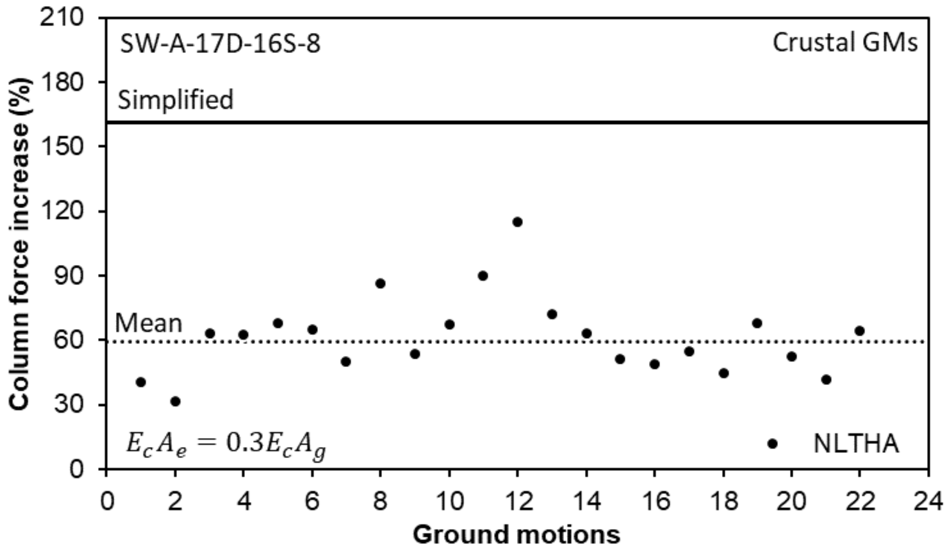

c)

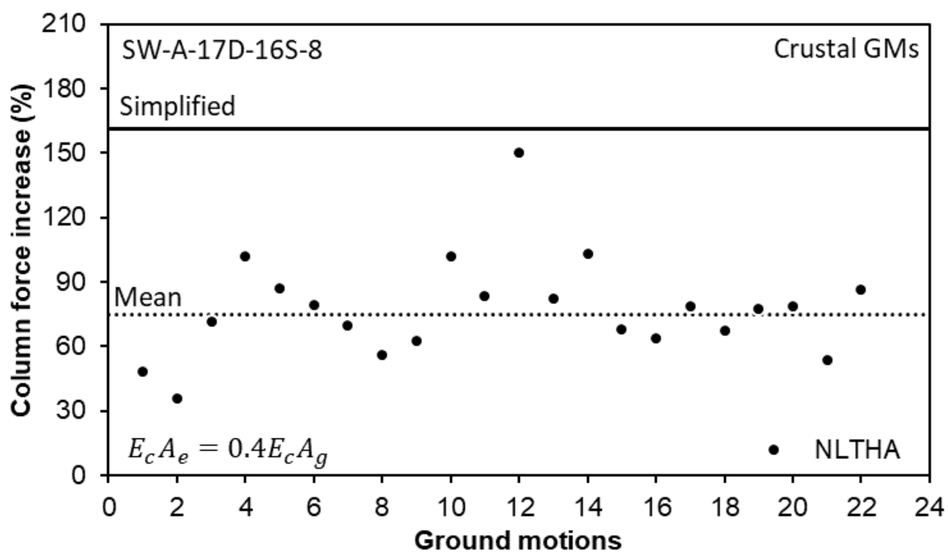

d)

Figure – Continued

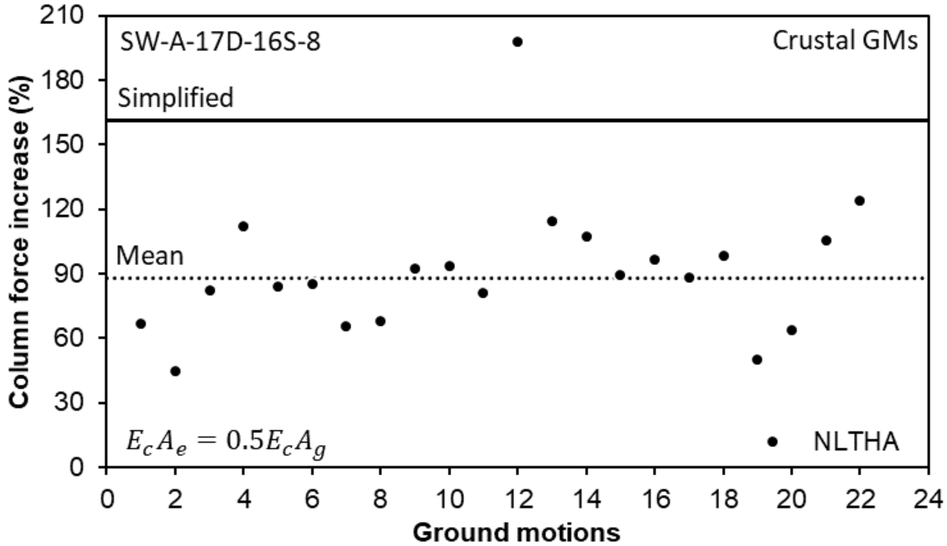

e)

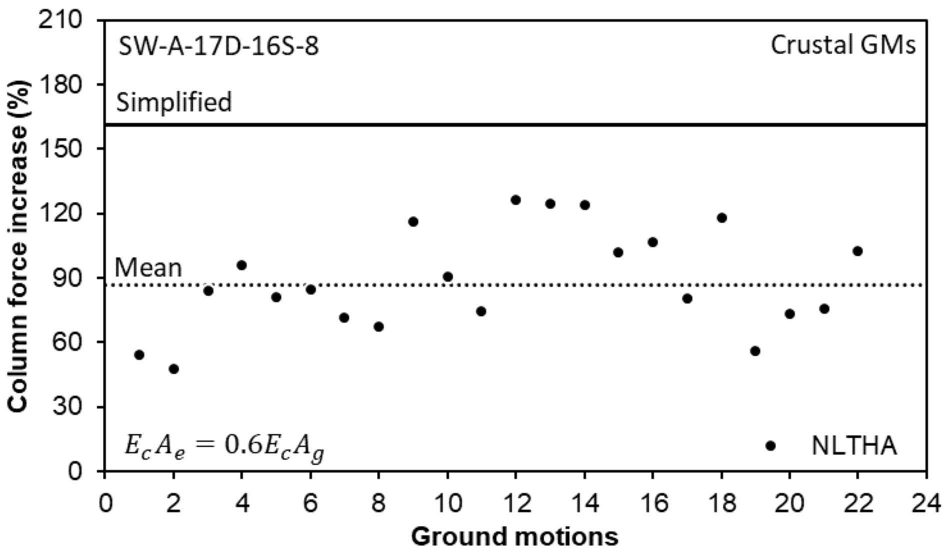

f)

**Figure – **Continued

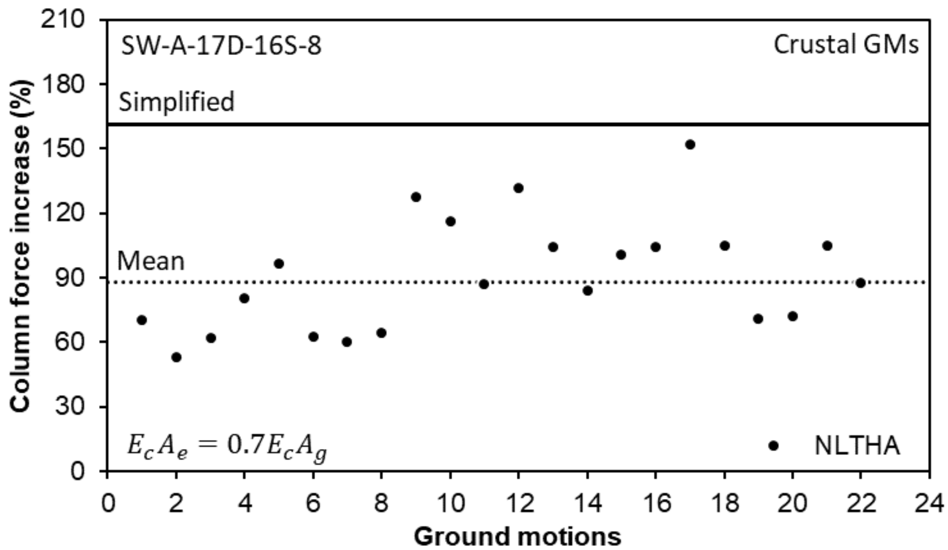

g)

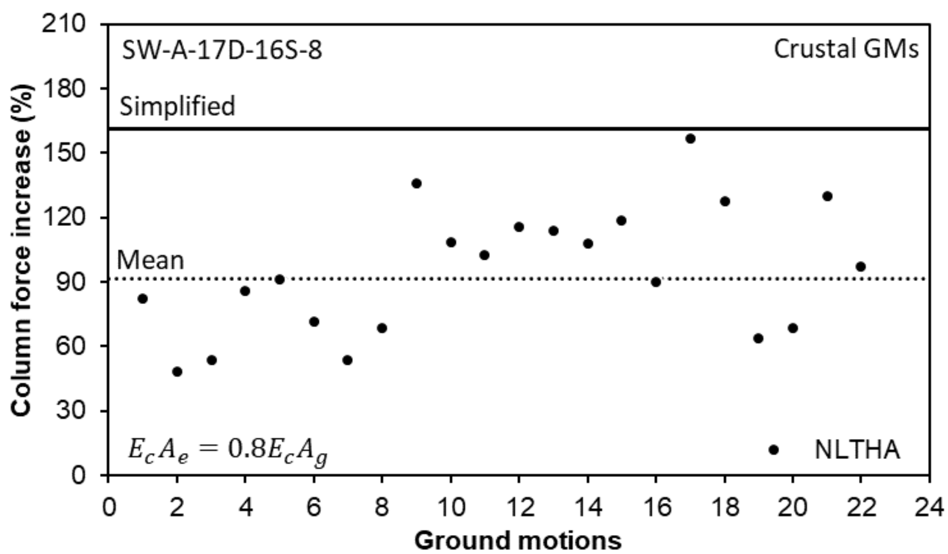

h)

Figure – Continued

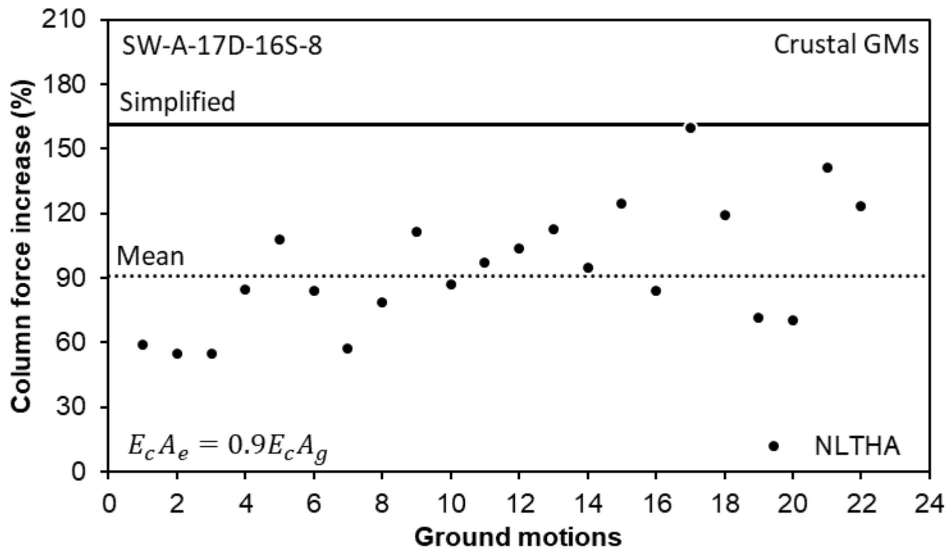

i)

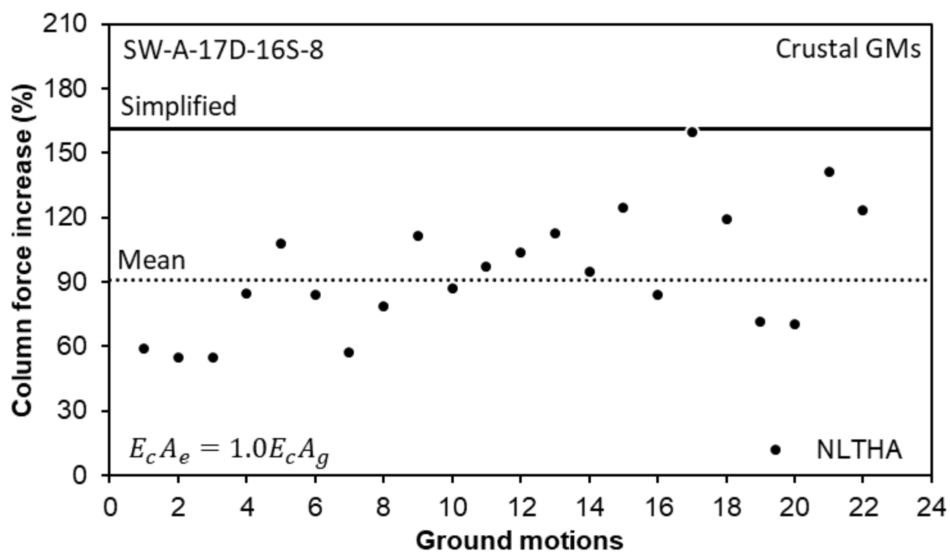

j)

Figure G.1 – Comparison of increase in column axial force obtained from simplified procedure and NLTHA with crustal ground motions for the case of sloped column with the slope of 17 deg. starting at 8th floor and going up for 16 floors (17D-16S-8) with different column stiffnesses of $E_cA_e =$: (a) $0.1E_cA_g$; (b) $0.2E_cA_g$; (c) $0.3E_cA_g$; (d) $0.4E_cA_g$; (e) $0.5E_cA_g$; (f) $0.6E_cA_g$; (g) $0.7E_cA_g$; (h) $0.8E_cA_g$; (i) $0.9E_cA_g$; (j) $1.0E_cA_g$

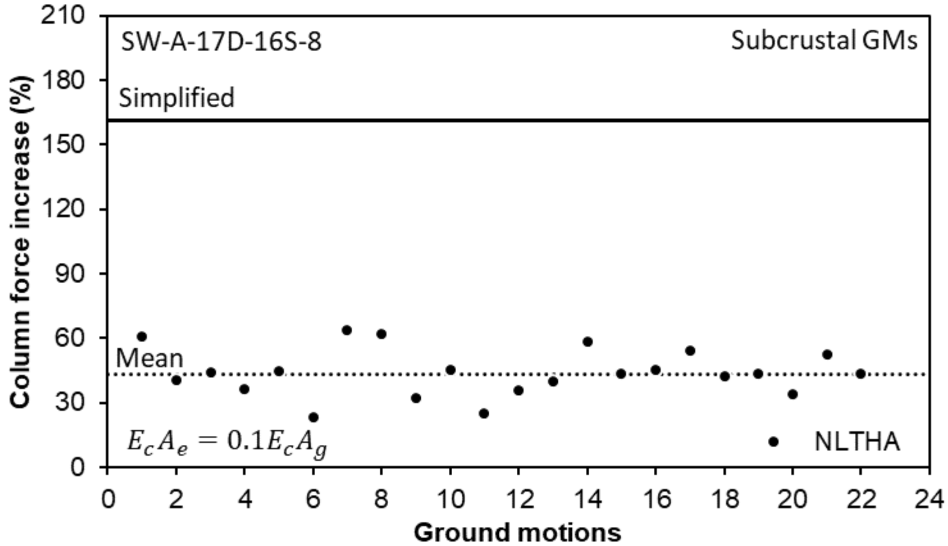

a)

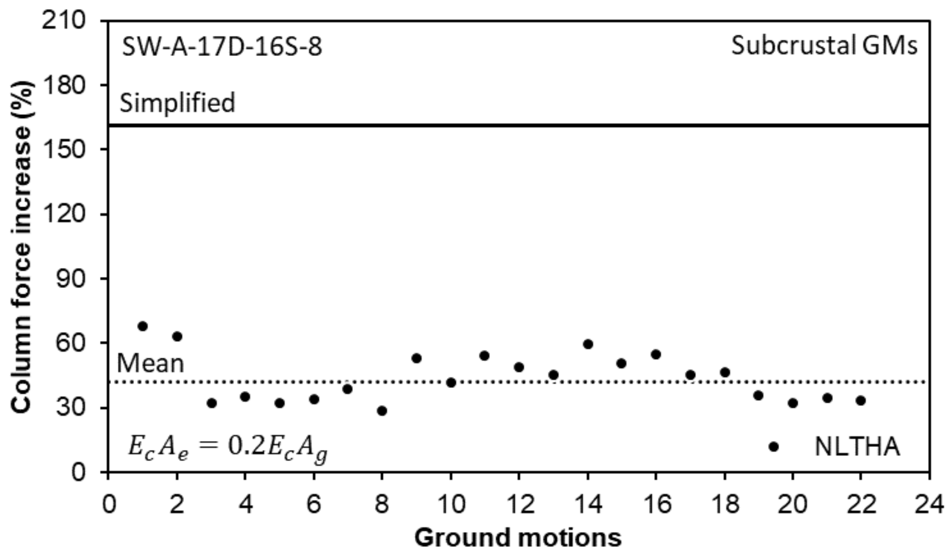

b)

Figure – Continued

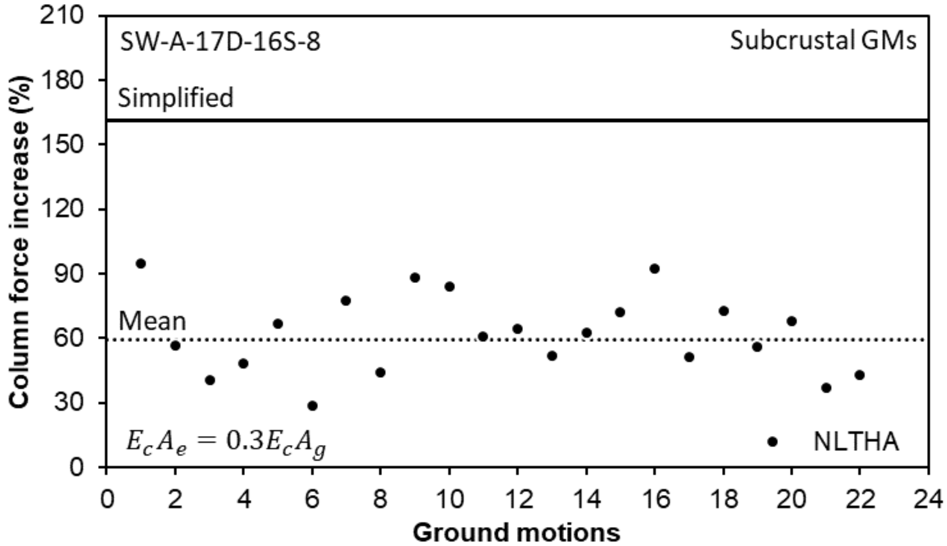

c)

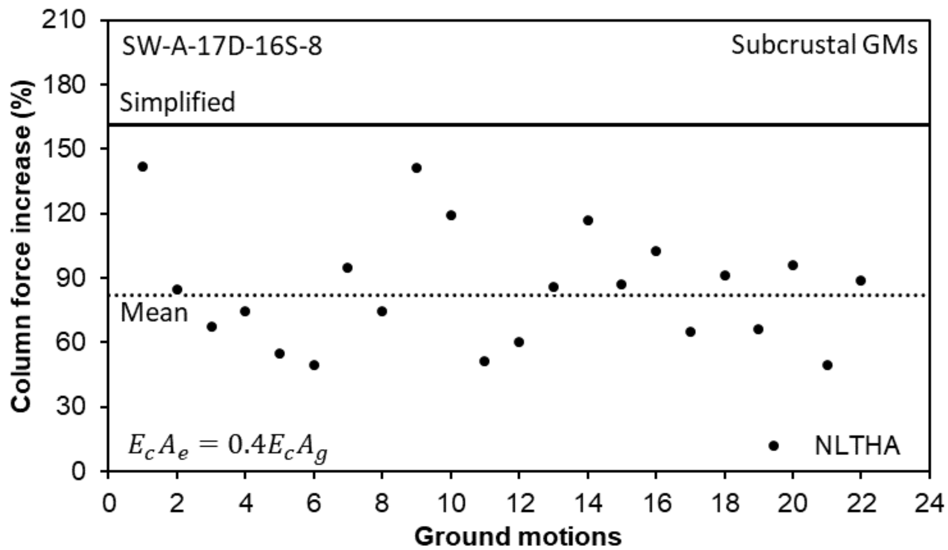

d)

Figure – Continued

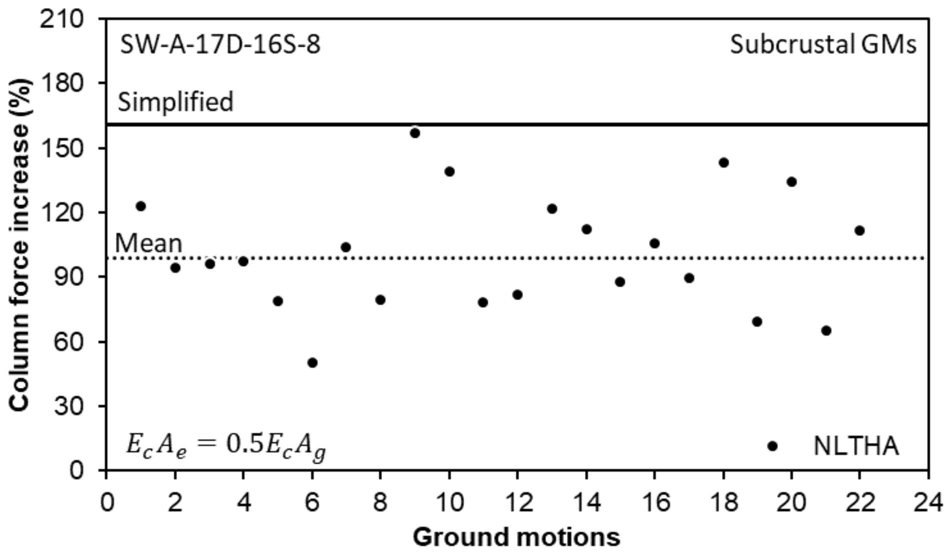

e)

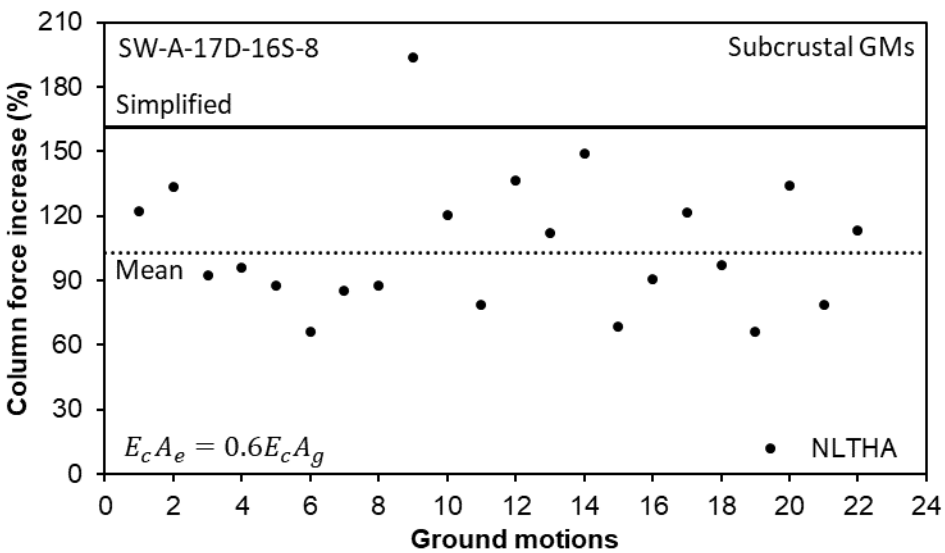

f)

Figure – Continued

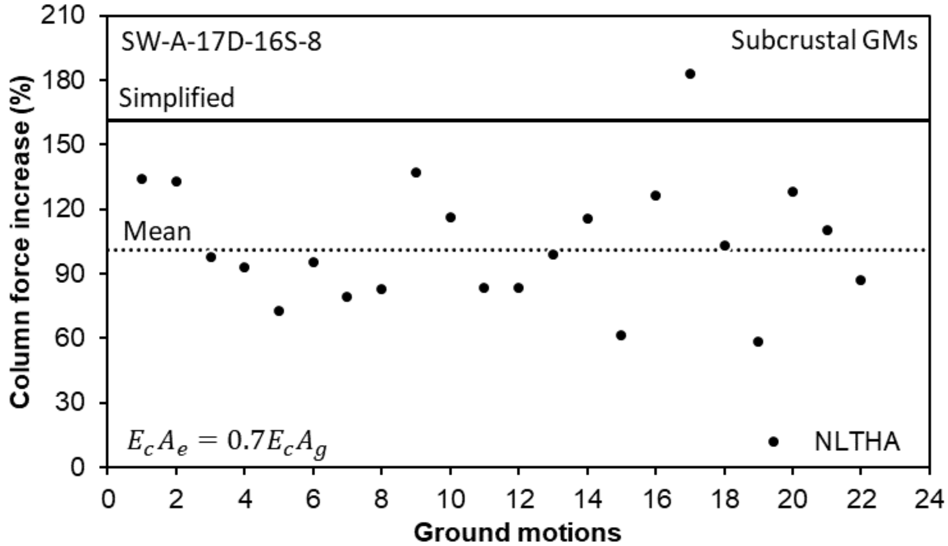

g)

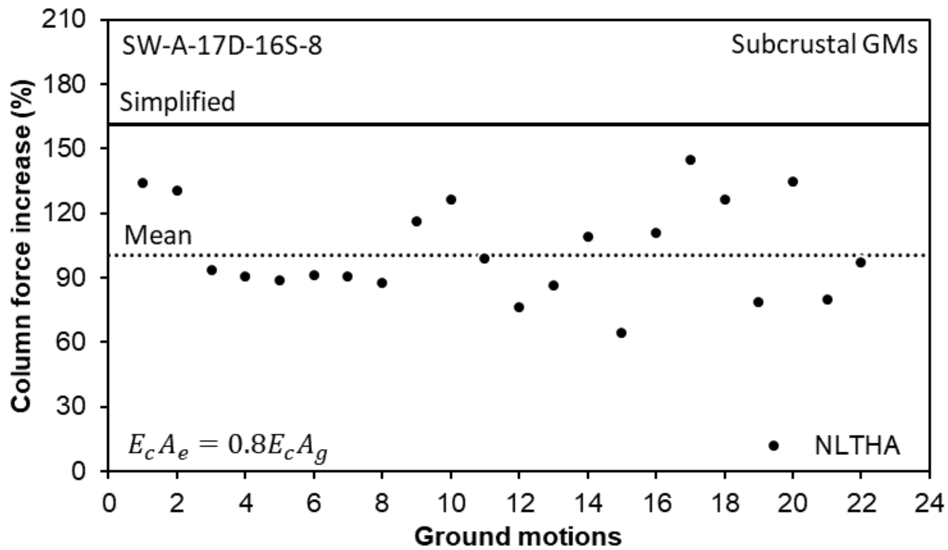

h)

Figure – Continued

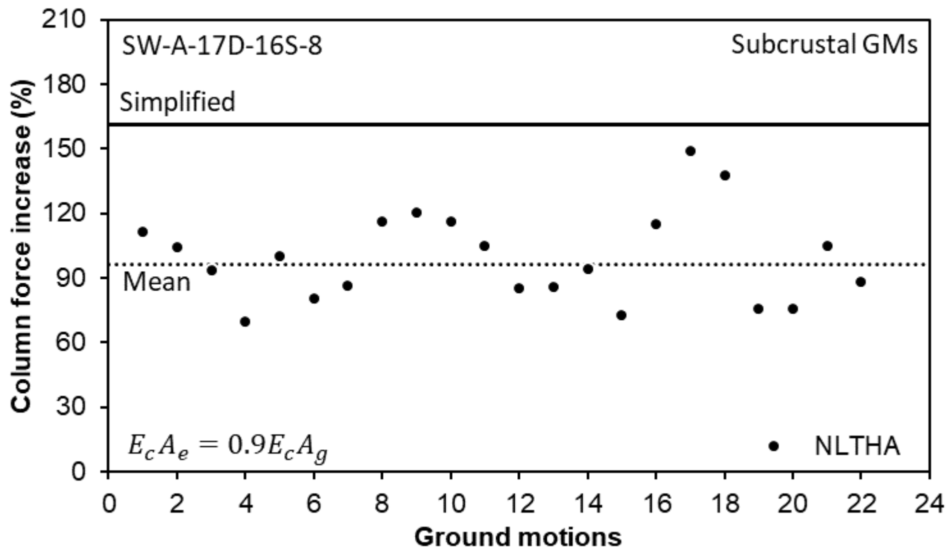

i)

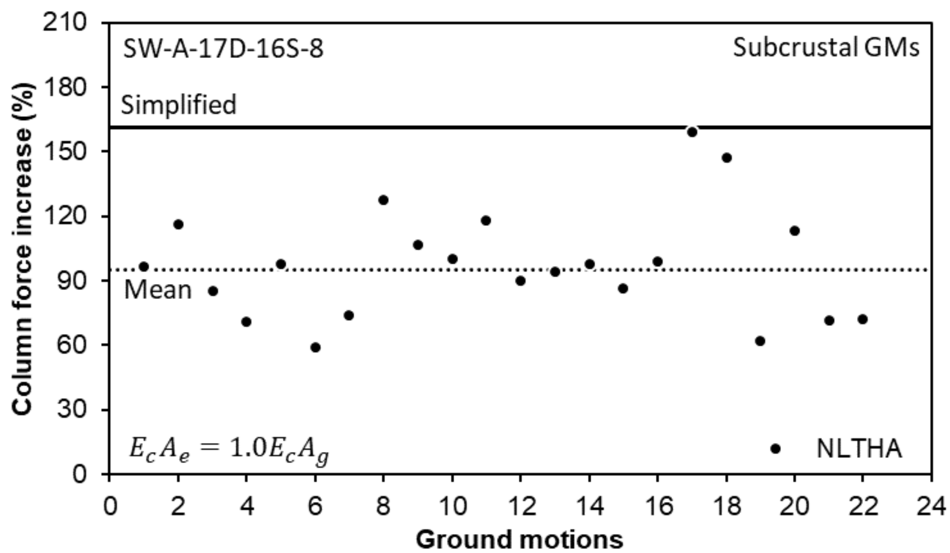

j)

Figure G.2 – Comparison of increase in column axial force obtained from simplified procedure and NLTHA with subcrustal ground motions for the case of sloped column with the slope of 17 deg. starting at 8th floor and going up for 16 floors (17D-16S-8) with different column stiffnesses of $E_cA_e =$: (a) $0.1E_cA_g$; (b) $0.2E_cA_g$; (c) $0.3E_cA_g$; (d) $0.4E_cA_g$; (e) $0.5E_cA_g$; (f) $0.6E_cA_g$; (g) $0.7E_cA_g$; (h) $0.8E_cA_g$; (i) $0.9E_cA_g$; (j) $1.0E_cA_g$

Figures G.3 and G.4 compare the increase in column axial force obtained from simplified procedure and NLTHA for the case of sloped column with the slope of 45 deg. starting at 3rd floor and going up for 3 floors (45D-3S-3) with different column stiffnesses for crustal and subcrustal ground motions, respectively.

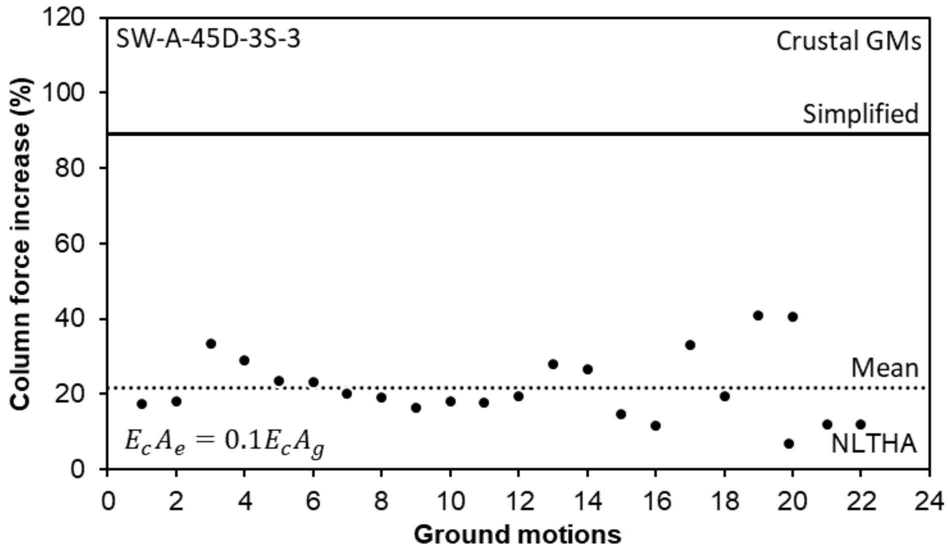

a)

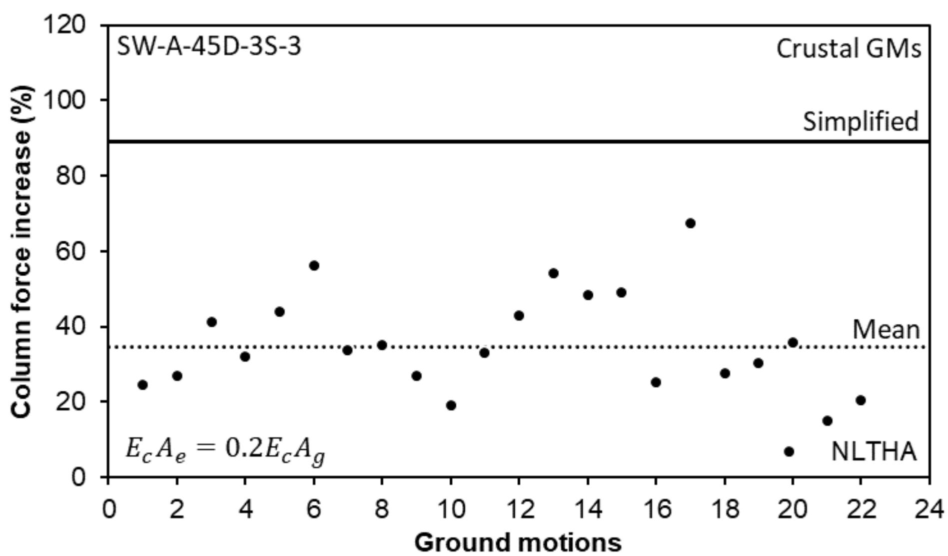

b)

Figure – Continued

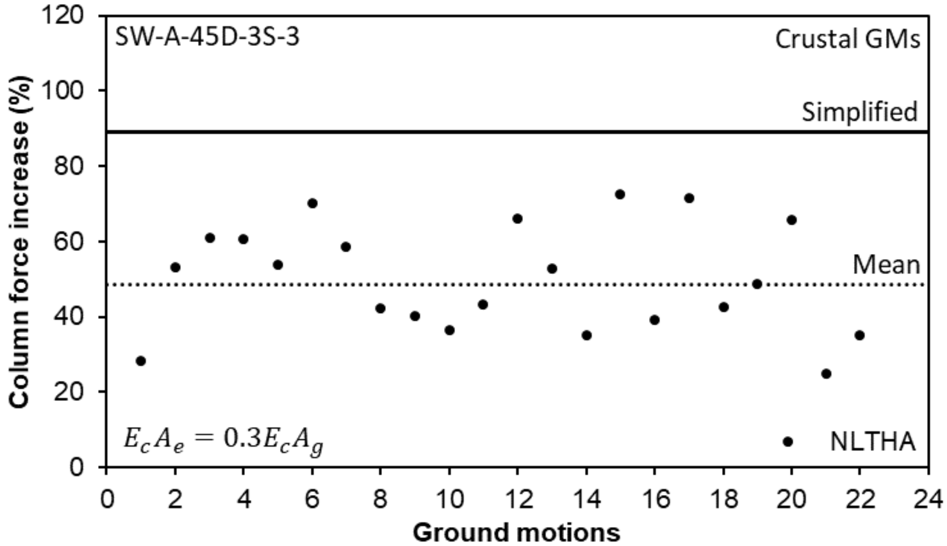

c)

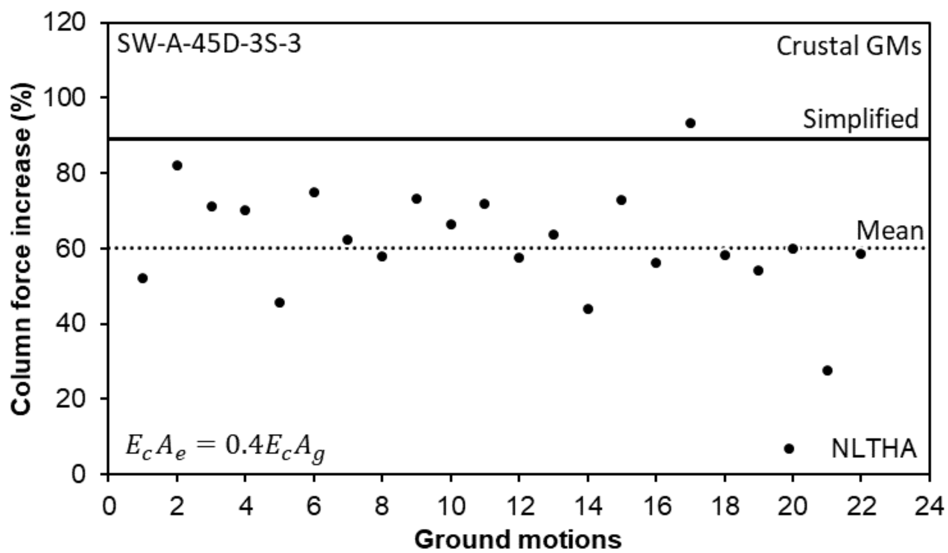

d)

Figure – Continued

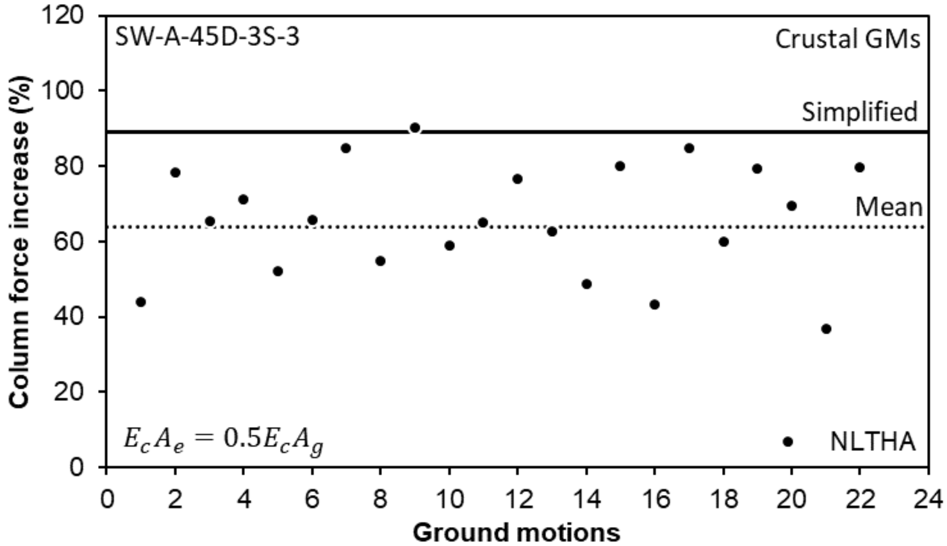

e)

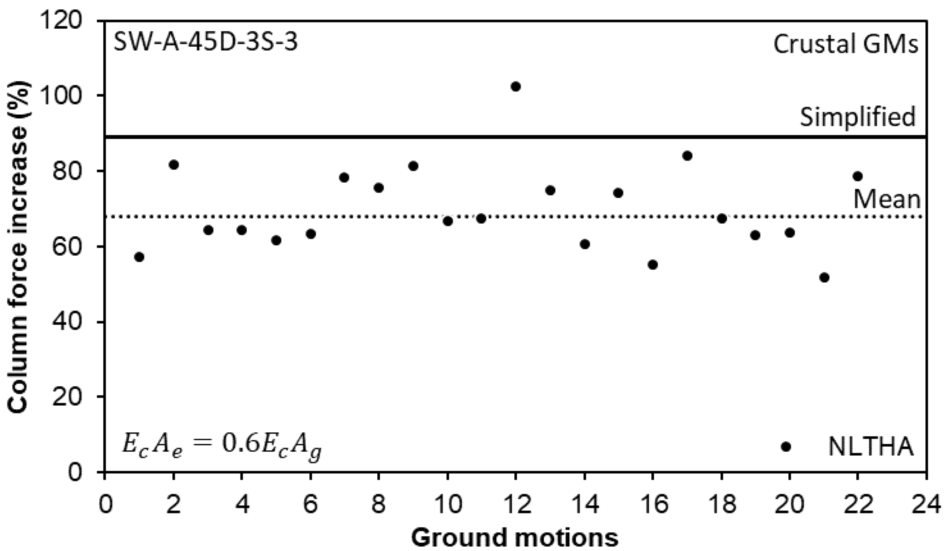

f)

Figure – Continued

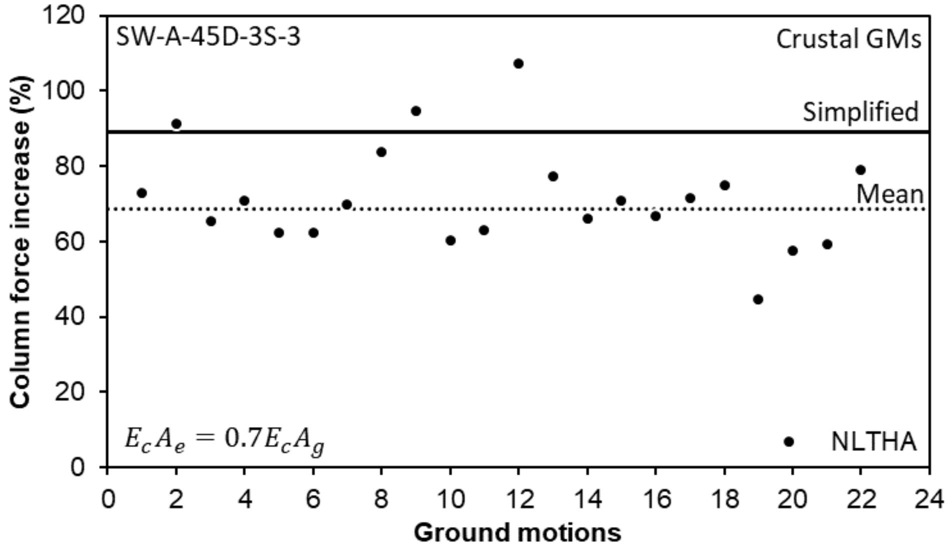

g)

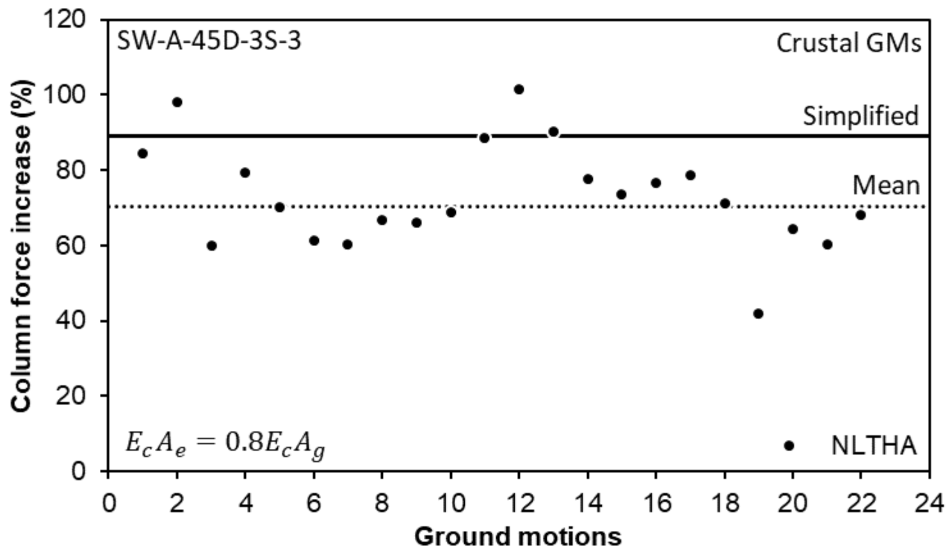

h)

Figure – Continued

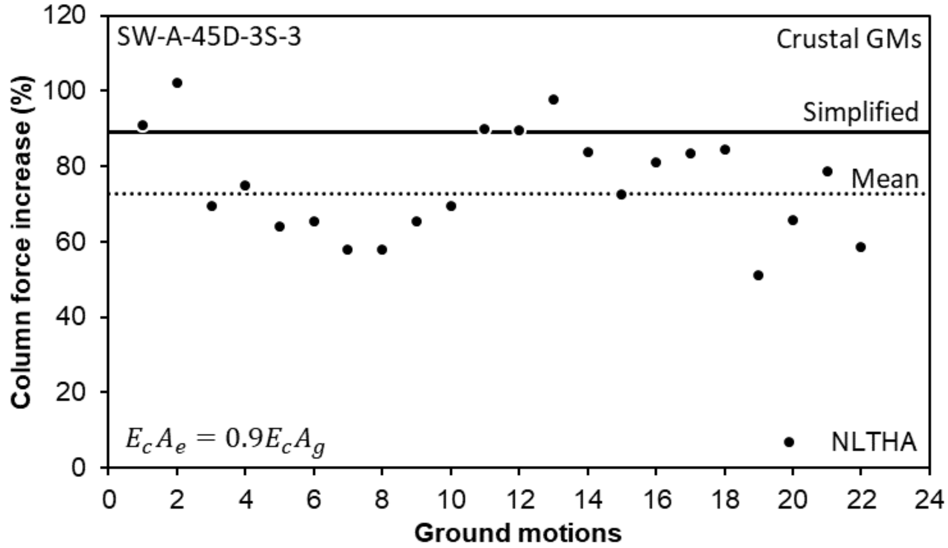

i)

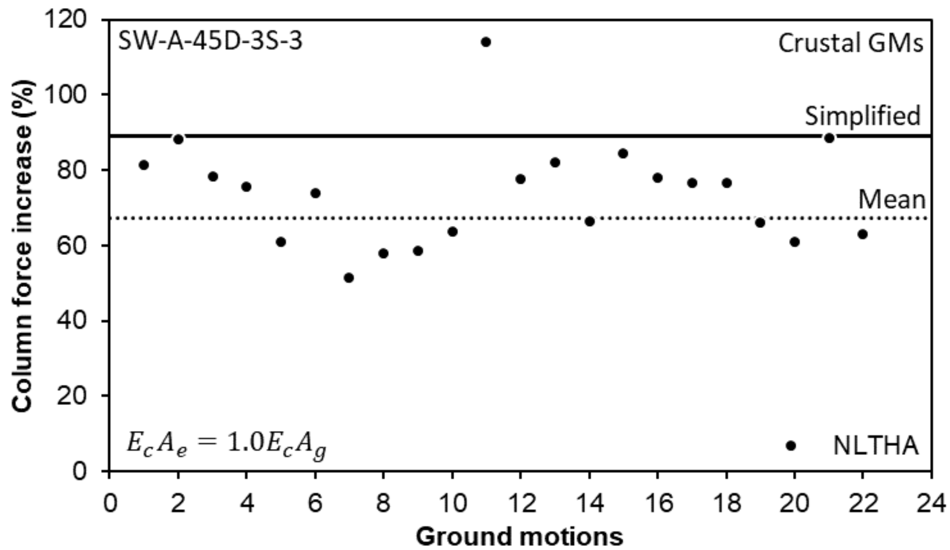

j)

Figure G.3 – Comparison of increase in column axial force obtained from simplified procedure and NLTHA with crustal ground motions for the case of sloped column with the slope of 45 deg. starting at 3rd floor and going up for 3 floors (45D-3S-3) with different column stiffnesses of $E_cA_e =$: (a) $0.1E_cA_g$; (b) $0.2E_cA_g$; (c) $0.3E_cA_g$; (d) $0.4E_cA_g$; (e) $0.5E_cA_g$; (f) $0.6E_cA_g$; (g) $0.7E_cA_g$; (h) $0.8E_cA_g$; (i) $0.9E_cA_g$; (j) $1.0E_cA_g$

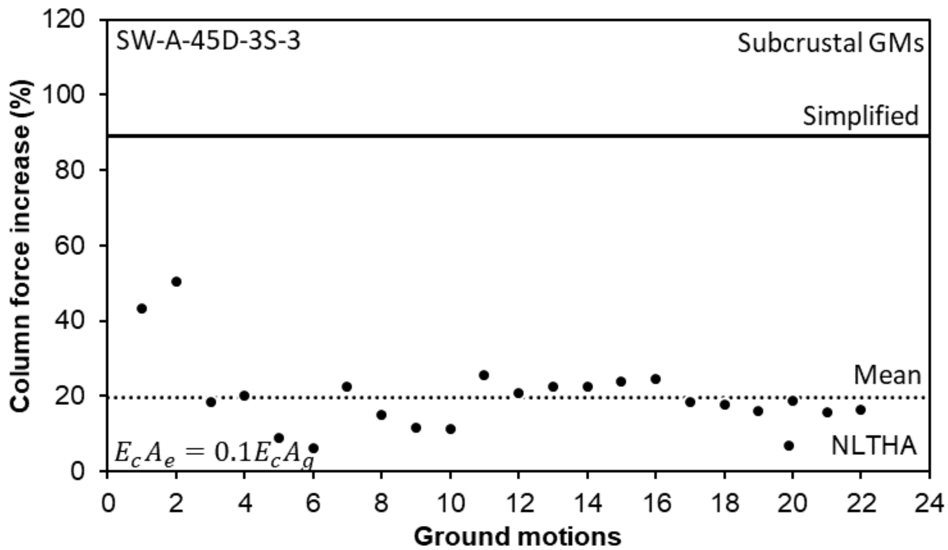

a)

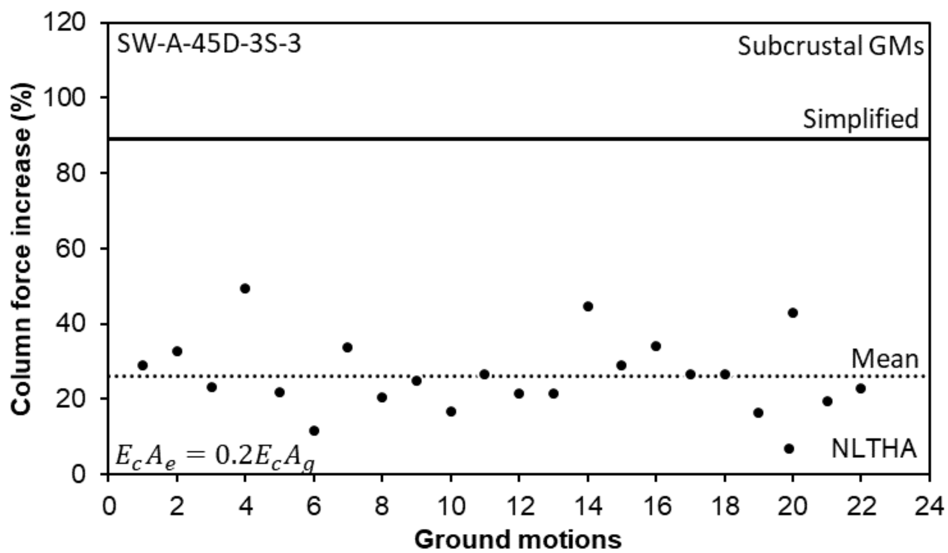

b)

Figure – Continued

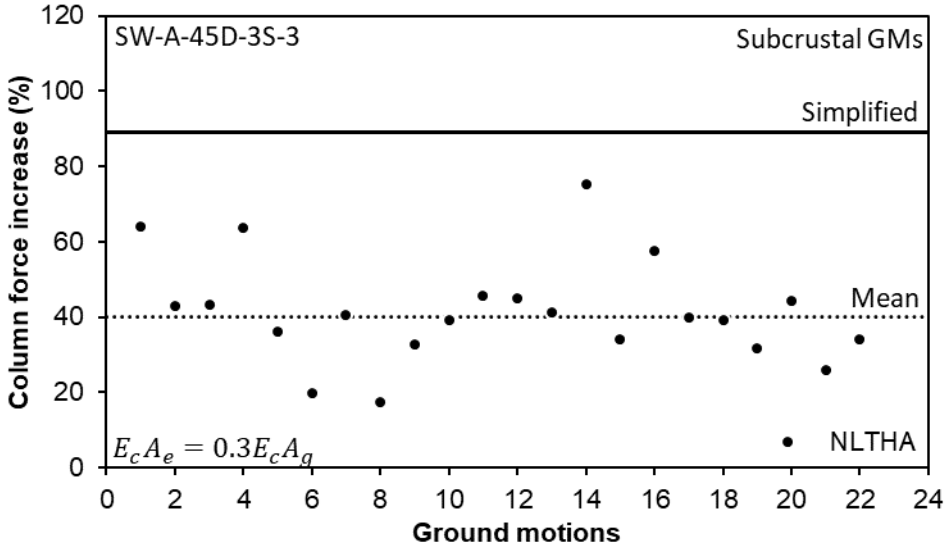

c)

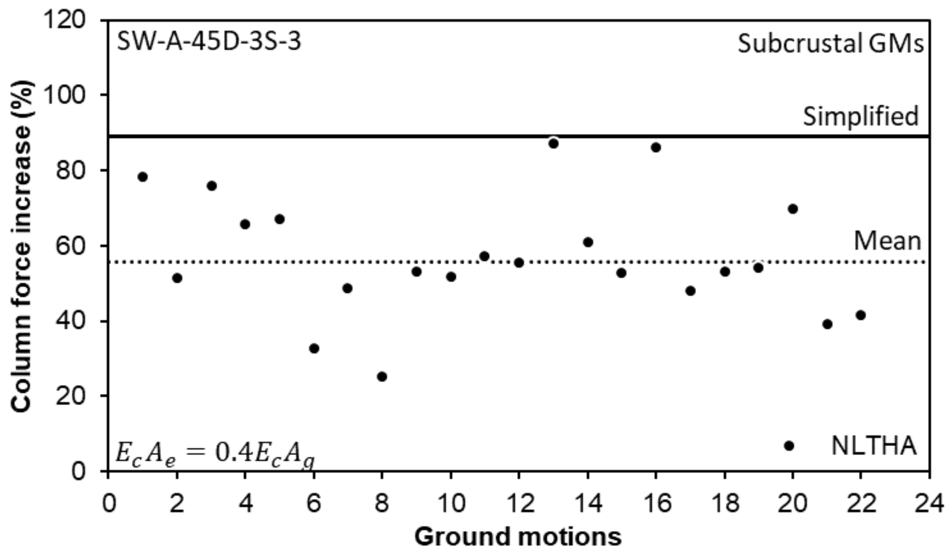

d)

Figure – Continued

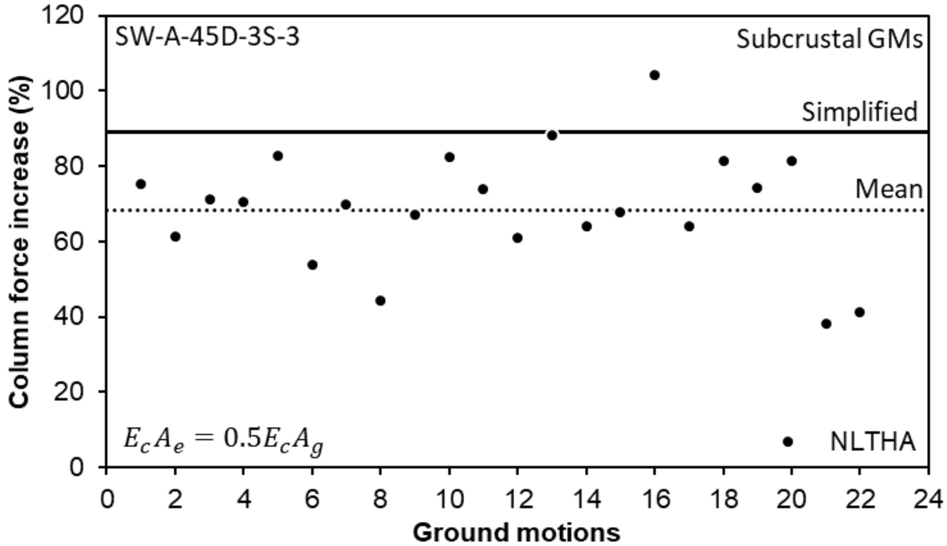

e)

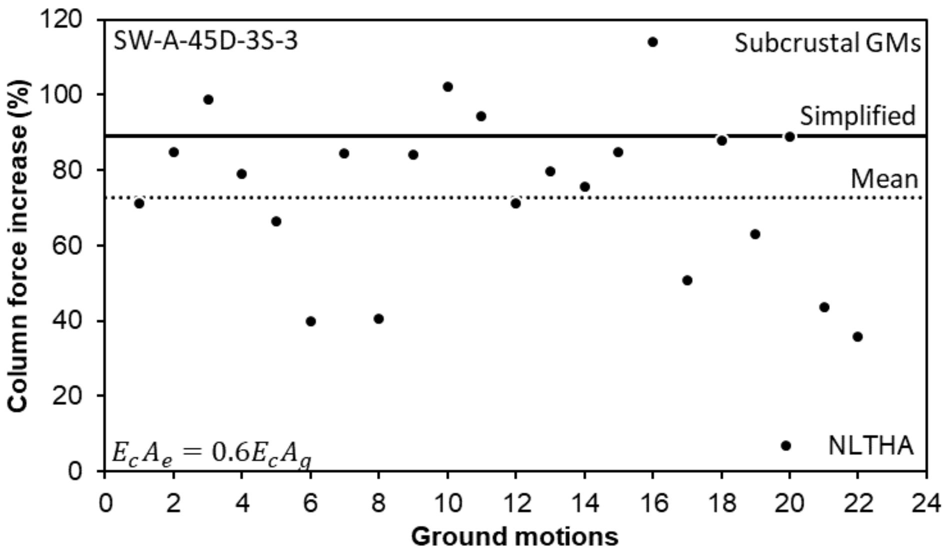

f)

Figure – Continued

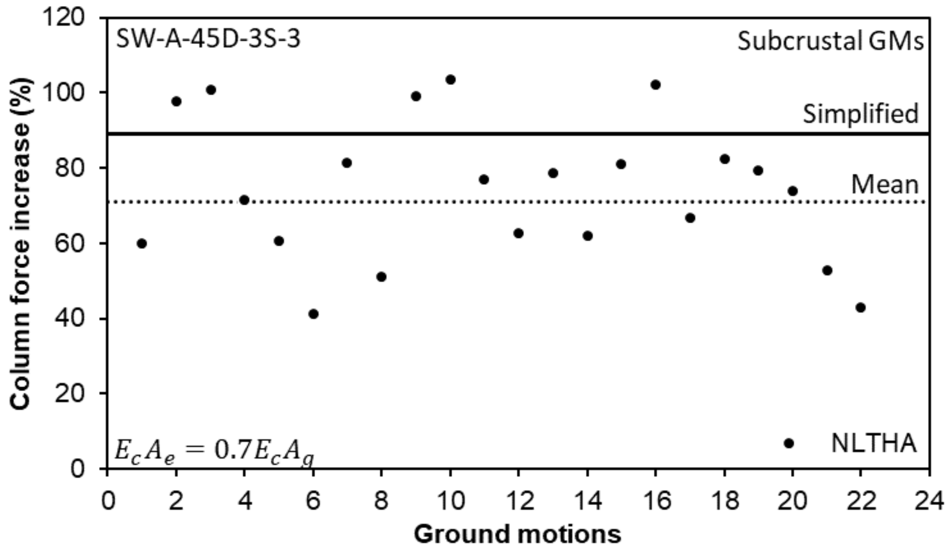

g)

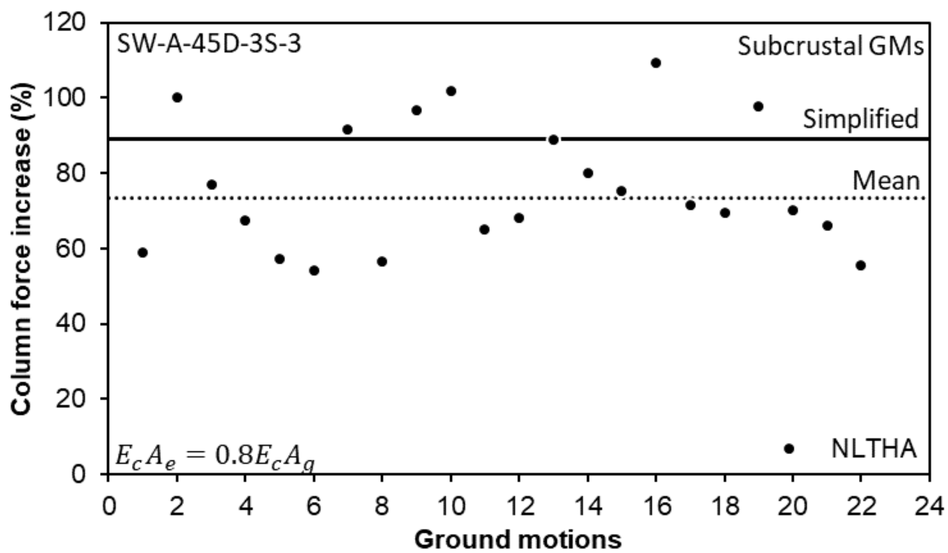

h)

Figure – Continued

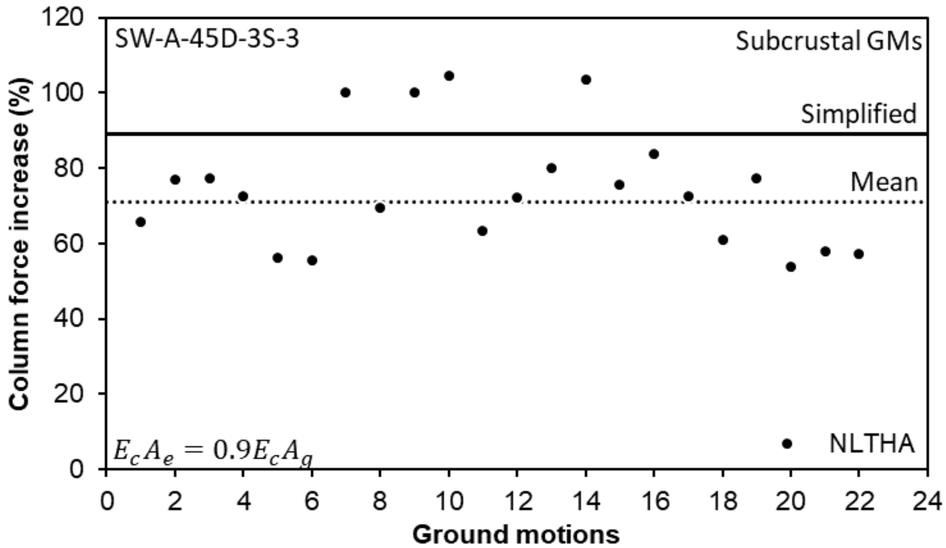

i)

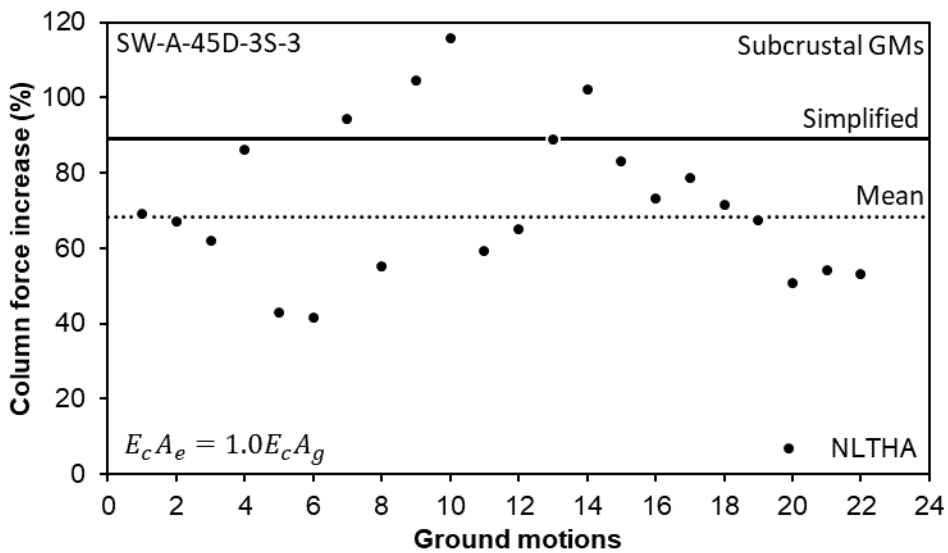

j)

Figure G.4 – Comparison of increase in column axial force obtained from simplified procedure and NLTHA with subcrustal ground motions for the case of sloped column with the slope of 45 deg. starting at 3rd floor and going up for 3 floors (45D-3S-3) with different column stiffnesses of $E_cA_e =$: (a) $0.1E_cA_g$; (b) $0.2E_cA_g$; (c) $0.3E_cA_g$; (d) $0.4E_cA_g$; (e) $0.5E_cA_g$; (f) $0.6E_cA_g$; (g) $0.7E_cA_g$; (h) $0.8E_cA_g$; (i) $0.9E_cA_g$; (j) $1.0E_cA_g$

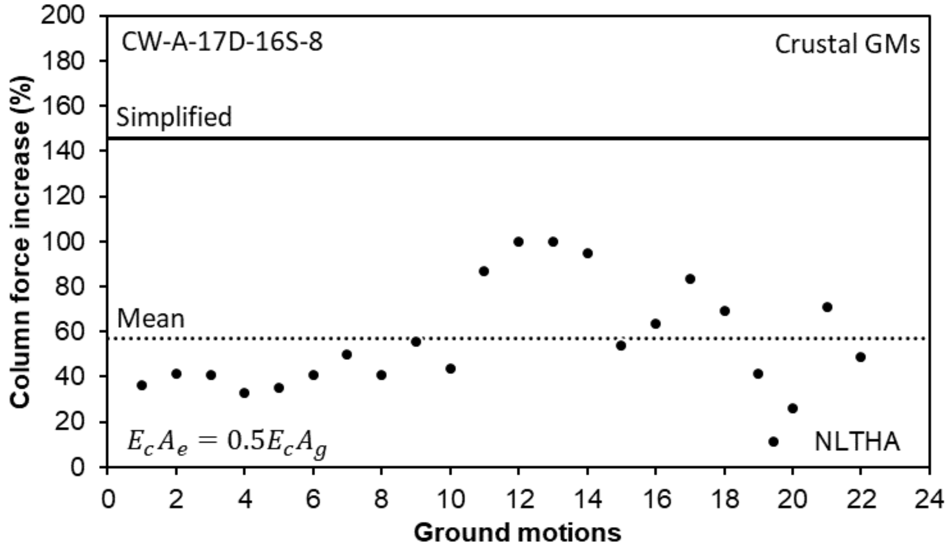

a)

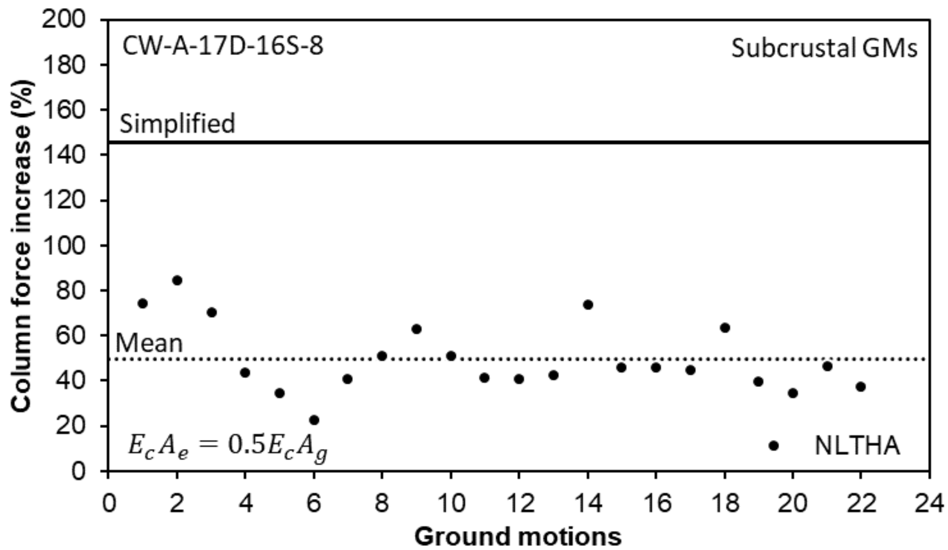

b)

Figure G.5 – Comparison of increase in column axial force of sloped column with the angle of 17 deg. starting at 8^{th} floor and going up for 16 floors in coupled wall direction obtained from simplified procedure and NLTHA with: (a) crustal ground motions; (b) subcrustal ground motions

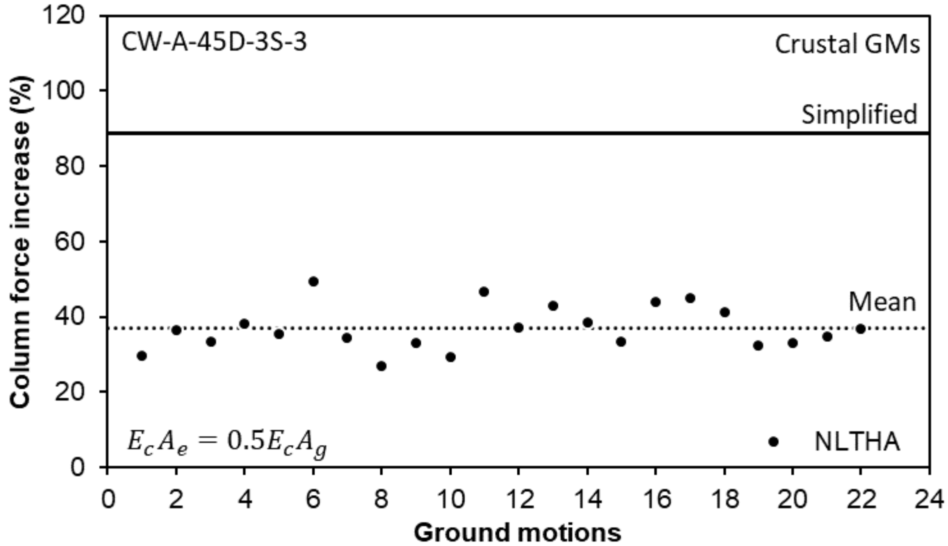

a)

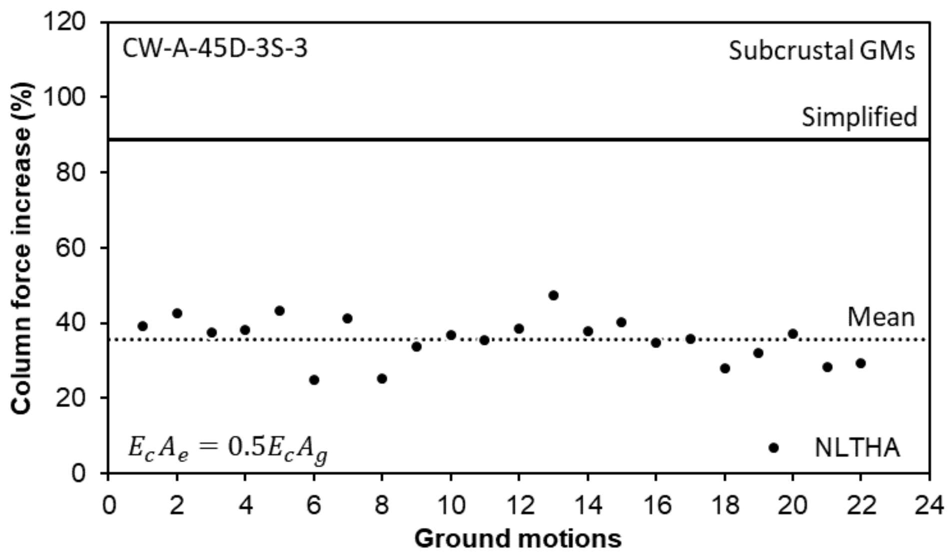

b)

Figure G.6 – Comparison of increase in column axial force of sloped column with the angle of 45 deg. starting at 3rd floor and going up for 3 floors in coupled wall direction obtained from simplified procedure and NLTHA with: (a) crustal ground motions; (b) subcrustal ground motions